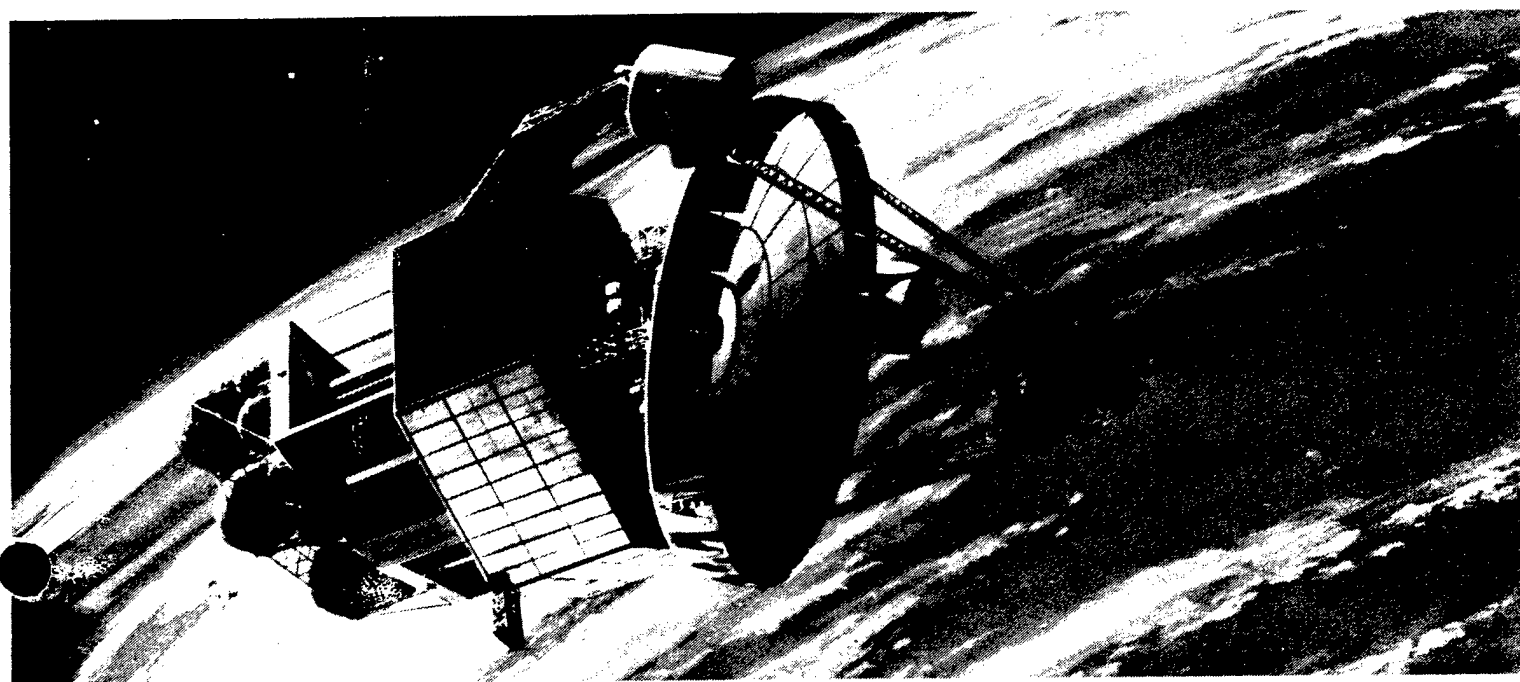


# Advanced Phased Array Chemical High Energy (APACHE) Laser Program



## Final Report – Volume I

19 January 1990

PLEASE RETURN TO:

BMD TECHNICAL INFORMATION CENTER  
BALLISTIC MISSILE DEFENSE ORGANIZATION  
7100 DEFENSE PENTAGON  
WASHINGTON D.C. 20301-7100

G. Koop  
J. Betts  
K. Bowler  
C. Clendening  
P. Schatzle  
S. Taylor  
M. Valley

Space & Technology Group  
TRW Inc.  
One Space Park  
Redondo Beach, CA 90278

19980819 155

Prepared for  
**Strategic Defense Initiative Organization**  
Directed Energy Office  
Pentagon  
Washington, DC 20301-7100

u 3245

**Naval Research Laboratory**  
4555 Overlook Avenue  
Washington, DC 20375

Unclassified

SECURITY CLASSIFICATION OF THIS PAGE

Volume I

## REPORT DOCUMENTATION PAGE

1a. REPORT SECURITY CLASSIFICATION Unclassified			1b. RESTRICTIVE MARKINGS		
2a. SECURITY CLASSIFICATION AUTHORITY OPNAVINST 5513.817			3. DISTRIBUTION/AVAILABILITY OF REPORT Unlimited		
2b. DECLASSIFICATION/DOWNGRADING SCHEDULE OADR					
4. PERFORMING ORGANIZATION REPORT NUMBER(S) AP-1984			5. MONITORING ORGANIZATION REPORT NUMBER(S)		
6a. NAME OF PERFORMING ORGANIZATION Applied Technology Division Space & Technology Group, TRW		6b. OFFICE SYMBOL (If applicable)	7a. NAME OF MONITORING ORGANIZATION Naval Research Laboratory		
6c. ADDRESS (City, State and ZIP Code) One Space Park Redondo Beach, California 90278			7b. ADDRESS (City, State and ZIP Code) Washington, D. C. 20375-5000		
8a. NAME OF FUNDING/SPONSORING ORGANIZATION Strategic Defense Initiative Organization		8b. OFFICE SYMBOL (If applicable) DEO	9. PROCUREMENT INSTRUMENT IDENTIFICATION NUMBER N00014-86-C-2345		
8c. ADDRESS (City, State and ZIP Code) Washington, D. C. 20301-7100			10. SOURCE OF FUNDING NOS.		
			PROGRAM ELEMENT NO.	PROJECT NO.	TASK NO.
			WORK UNIT NO.		
11. TITLE (Include Security Classification) Advanced Phased Array Chemical High Energy Laser System (APACHE)(U)					
12. PERSONAL AUTHOR(S) C. G. Koop, J. A. Betts, K. A. Bowler, C. Clendening, P. Schatzle, S. Taylor, and M. Valley					
13a. TYPE OF REPORT Final		13b. TIME COVERED FROM 03/09/86 TO 11/20/89		14. DATE OF REPORT (Yr., Mo., Day) 1990 January 19	
				15. PAGE COUNT 424	
16. SUPPLEMENTARY NOTATION					
17. COSATI CODES			18. SUBJECT TERMS (Continue on reverse if necessary and identify by block number)		
FIELD	GROUP	SUB. GR.	Stimulated Brillouin Scattering, phase conjugation, high power laser, flowing SBS cell, oscillator isolation, non- linear optics, segmented mirror		
19. ABSTRACT (Continue on reverse if necessary and identify by block number) Volume I of the final report for the Advanced Phased Array Chemical High Energy (APACHE) laser program presents phase conjugate laser technology which verifies and demonstrates the key technologies associated with phase conjugation of high power continuous wave chemical lasers using stimulated Brillouin scattering (SBS). These demonstrations include: SBS under long pulse conditions simulating CW operation that demonstrates the feasibility of using SBS for a high power, CW laser; near diffraction limited performance for beam combination at the HF wavelength using SBS in high pressure xenon; flowing-gas SBS cell experiments demonstrating fluid mechanics capability for using a flowing SBS medium for CW SBS applications; SBS conjugation experiments using a 19-element segmented mirror showing the ability of SBS to correct piston and tilt misalignment errors in a multielement segmented optic; and experiments to determine how feedback to the master oscillator from the SBS cell affects system performance.					
20. DISTRIBUTION/AVAILABILITY OF ABSTRACT CLASSIFIED/UNLIMITED <input checked="" type="checkbox"/> SAME AS RPT. <input type="checkbox"/> DTIC USERS <input type="checkbox"/>					
21. ABSTRACT SECURITY CLASSIFICATION Unclassified			22a. NAME OF RESPONSIBLE INDIVIDUAL C. G. Koop		
22b. TELEPHONE NUMBER (Include Area Code) (213) 813.9527			22c. OFFICE SYMBOL		

PLEASE RETURN TO:

BMD TECHNICAL INFORMATION CENTER  
BALLISTIC MISSILE DEFENSE ORGANIZATION  
7100 DEFENSE PENTAGON  
WASHINGTON D.C. 20301-7100

## CONTENTS

	Page
1. INTRODUCTION	1-1
1.1 APACHE SBL Concept Overview	1-2
1.2 Technical Issues	1-7
1.3 Summary	1-21
1.4 Final Report Organization	1-22
2. CW CONJUGATION EXPERIMENT	2-1
2.1 Introduction	2-1
2.2 Experiment Description	2-4
2.2.1 KMS Laser Facility and Operation	2-4
2.2.2 Layout of Optical Train and Diagnostics	2-4
2.2.3 Rotating Mirror Description and Operation	2-12
2.3 Experimental Results	2-17
2.3.1 SBS Reflectivity and Threshold Determination	2-17
2.3.2 Conjugation Fidelity for No Aberrator, Static, and Scanning Test Conditions	2-21
2.3.3 Wedge Aberrator Data, Static, and Scanning Test Conditions	2-33
2.3.4 Piston Aberrator Data, Static, and Scanning Test Conditions	2-40
2.3.5 Thermal Blooming Experiment	2-47
2.4 CWCS Experiment Analyses Dimensionless Scaling	2-55
2.4.1 Forward Scattering	2-55
2.4.2 Grating Convection	2-59
2.4.3 Thermal Blooming	2-60
2.5 Summary of Significant Results	2-66
2.6 References	2-67
3. HF SBS PHASE CONJUGATION STUDIES	3-1
3.1 Introduction	3-1
3.2 APACHE Experiment Description	3-3

## CONTENTS (Continued)

	Page
3.2.1 Laser Subsystem	3-3
3.2.2 Optical Train	3-7
3.2.3 Diagnostics	3-7
3.2.4 Phase Conjugation Subsystem	3-15
3.3 HFC Results	3-15
3.4 Conjugation Subsystem (COS) Experiment	3-21
3.5 Beam Combining (BC) Experiment	3-31
3.6 Threshold Reduction Experiments	3-38
3.7 SBS CW and Transient Threshold Behavior	3-46
3.7.1 CW Threshold Estimation	3-46
3.7.2 Pump Depletion Effects	3-52
3.7.3 Transient Threshold Behavior	3-54
3.7.4 Dimensionless Threshold Scaling	3-60
3.8 References	3-64
4. FLOWING-GAS SBS EXPERIMENTS	4-1
4.1 Overview	4-1
4.1.1 SBS Cell Concepts	4-1
4.1.2 Aerowindow Issues, Scaling Parameters	4-4
4.2 Subscale Experiments	4-10
4.2.1 Objectives	4-10
4.2.2 Facility Description	4-10
4.2.2.1 SBS Cell	4-12
4.2.2.2 Flow Control System	4-12
4.2.2.3 SBS Optical Train	4-16
4.2.2.4 Diagnostics	4-16
4.2.3 Fluid Mechanics Experiments	4-19
4.2.3.1 Experiment Description	4-19
4.2.3.2 Scaling Issues	4-21
4.2.3.3 Fundamental Wake Flow	4-22
4.2.3.4 Pressure Gradient Effects	4-26
4.2.3.5 Splitter Tip Suction	4-29
4.2.3.6 Splitter Tip Blowing	4-32
4.2.3.7 Discussion	4-32



## CONTENTS (Continued)

	Page
4.2.4 Flowing-Gas SBS Experiments	4-33
4.2.4.1 Experiment Description	4-33
4.2.4.2 Static-Cell SBS Results	4-35
4.2.4.3 Flowing-Gas SBS Results	4-35
4.2.4.4 Discussion	4-38
4.2.5 Summary	4-40
4.3 Full-Scale Experiments (CTS)	4-41
4.3.1 Objectives, Scaling Parameters	4-41
4.3.2 Facility Description	4-43
4.3.2.1 PAR Laser Upgrade	4-44
4.3.2.2 Flow Control System Design	4-44
4.3.2.3 SBS Cell	4-50
4.3.2.4 Multiple-Foci Optics	4-53
4.3.3 System Performance Tests	4-56
4.3.3.1 Upgraded PAR Laser	4-56
4.3.3.2 Flow Control System	4-58
4.3.3.3 SBS Cell	4-60
4.3.4 Preliminary SBS Experiments	4-62
4.3.4.1 Static-Xenon Results	4-64
4.3.4.2 Flowing-Gas SBS Results	4-64
4.3.5 Summary	4-66
4.4 Theoretical Support	4-69
4.4.1 Turbulence Model for BRIWON SBS Code	4-69
4.4.2 Computational Results and Discussion	4-71
4.5 References	4-82
5. ARRAY ALIGNMENT EXPERIMENT	5-1
5.1 Background	5-1
5.2 Array Alignment Experiment Description	5-3
5.3 Array Alignment Results	5-7

## CONTENTS (Continued)

	Page
5.3.1 Correction of Large Segment Piston	5-7
5.3.2 Threshold as Function of Segment Piston and Tilt	5-7
5.3.3 Threshold as Function of Number of Segments	5-11
5.3.4 Conjugation Fidelity as Function of Segment Tilt	5-16
5.4 Discussion of Results and Suggestions for Further Experiments	5-19
5.5 References	5-23
6. OSCILLATOR ISOLATION EXPERIMENT	6-1
6.1 Introduction	6-1
6.2 Theoretical Description	6-4
6.3 Experimental Description	6-9
6.3.1 CO <sub>2</sub> Laser Device and Operation	6-9
6.3.2 Resonator Description	6-10
6.3.2.1 Negative Branch Unstable Standing-Wave Resonator	6-10
6.3.2.2 Negative Branch Unstable Ring Resonator	6-14
6.3.3 Optical Layout and Diagnostics	6-18
6.4 Experimental Results	6-26
6.4.1 Negative Branch Unstable SW Resonator (CZAR)	6-26
6.4.1.1 Negative Branch Standing Wave Resonator Results for M = 1.5	6-26
6.4.1.2 NBSW Results for M = 2.0	6-34
6.4.2 Negative Branch Unstable Ring Resonator Experimental Results	6-34
6.4.2.1 Ring Resonator Results for M = 1.5	6-34
6.4.2.2 Ring Resonator Experimental Results for M = 1.77	6-43
6.4.3 Summary Comparison of Experimental Results for Standing-Wave and Ring Resonators	6-51

## CONTENTS (Continued)

	Page
6.5 Comparison Between Analysis and Experiment	6-54
6.5.1 Standing-Wave Resonators	6-54
6.5.2 Ring Resonators	6-60
6.5.3 Implications	6-64
7. OSCILLATOR ISOLATION VM EXPERIMENTS	7-1
7.1 Introduction and Motivation	7-1
7.2 Experiment Description	7-2
7.2.1 Resonator and High-Power Optical Train	7-2
7.2.2 External Optical Train	7-5
7.2.3 Diagnostics	7-5
7.3 Experimental Results	7-8
7.4 Recommendations for Future Work	7-14
8. PULSE STRETCHING EXPERIMENTS IN HF LASER	8-1
8.1 Introduction	8-1
8.2 Experimental Description	8-2
8.3 Experimental Results	8-4
8.4 Discussion	8-10
9. BIDIRECTIONAL AMPLIFIER CONCEPTUAL DESIGN STUDY	9-1
9.1 Background/Introduction	9-1
9.2 Amplifier Modeling and SBL Performance Predictions	9-6
9.2.1 CLAM Code	9-6
9.2.2 LFCM/HF Kinetics Code	9-10
9.3 Experiment Requirements	9-11
9.3.1 Gain Saturation as a Function of Frequency	9-11
9.3.2 Gain Saturation in the Amplifier	9-11
9.3.3 Amplifier Gain Length Product	9-14
9.3.4 Alignment of the Frequency Shifted Beam	9-14

## CONTENTS (Continued)

	Page
9.4 Experiment Design Approach	9-18
9.4.1 Optical Design	9-18
9.4.2 Mechanical Frequency Shifter Design	9-25
9.5 Small-Signal-Gain Measurements	9-33
9.5.1 Experiment Description	9-33
9.5.2 Experimental Results	9-36
9.6 References	9-47
10. ABSORPTION EXPERIMENT	10-1
10.1 Motivation and Requirements	10-1
10.2 Experiment Approach	10-1
10.2.1 Optical Attenuation Measurement	10-1
10.2.2 Photo-Acoustic Measurement	10-2
10.2.3 Gas Handling	10-4
10.3 Experimental Results	10-4

## ILLUSTRATIONS

	Page
1-1 Technology Issues Addressed by APACHE Program	1-3
1-2 APACHE SBL Design Concept	1-4
1-3 HF Phase Conjugation Issues Addressed Using New State-of-the-Art Test Facility	1-8
1-4 CW Phase Conjugation Issues Addressed	1-10
1-5 Flowing SBS Cell Technology Demonstrated	1-12
1-6 CTS Flowing Cell	1-13
1-7 Oscillator Isolation Issues Addressed	1-15
1-8 Conjugation Reduces Segment Piston Errors by Factor of 400	1-16
1-9 Conjugation Reduces Segment Misfigure Errors by Factor of 35 Over Range of Spatial Scales	1-17
1-10 Multielement Segmented Mirror Cophased Using SBS	1-19
1-11 Thousands of Waves Segment Piston Corrected to Greater Than $\lambda/20$ Using SBS Phase Conjugation	1-20
2.2-1 KMS Chroma Laser Facility	2-5
2.2-2 Pulse Shapes From Chroma Laser Used in CWCS Experiment	2-6
2.2-3 Far-Field Intensity Distributions for KMS Laser Beam	2-7
2.2-4 Incident Laser Beam Wavefront	2-8
2.2-5 Lateral Shearing Interferograms of Incident KMS Laser Beam Recorded by Fast-Framing Camera	2-9
2.2-6 CW Conjugation Scaling Experiment Optical Train and Diagnostics	2-10
2.2-7 CW Conjugation Scaling Experiment High-Pressure Xe SBS Cell	2-13
2.2-8 CWCS Experiment SBS Cell Fill/Drain System Schematic	2-14
2.2-9 CWCS Experiment Rotating Mirror Schematic	2-15
2.2-10 Oscilloscope Method of Rotating Mirror Position Control	2-16

## ILLUSTRATIONS (Continued)

	Page
2.3-17      Correction of Tilt Aberrated Wavefront by SBS Phase Conjugation, Static Focal Spot	2-37
2.3-18      Correction of Tilt Aberrated Wavefront by SBS Phase Conjugation, Scanning Focal Spot	2-38
2.3-19      BRIWON Code Calculations of Near-Field Phase for Wedge Aberrator, Static and Scanning Focal Spot	2-39
2.3-20      BRIWON Code Calculations of Far-Field Intensity for Wedge Aberrator, Static and Scanning Focal Spot	2-41
2.3-21      Grooved/Piston Aberrator Profilometer Traces	2-42
2.3-22      SBS Reflectivity Versus Time for Piston Aberrator, Static Focal Spot	2-43
2.3-23      Far-Field Intensity Distributions for Piston Aberrated Incident Beam and SBS Corrected Return Beam	2-44
2.3-24      Near-Field Phase of Incident Piston Aberrated Beam and SBS Corrected Beam	2-45
2.3-25      SBS Reflected Power Versus Pump Power (Threshold) for Piston Aberrator	2-46
2.3-26      Reflectivity Versus Focal Spot Velocity for Piston Aberrated Beam	2-48
2.3-27      Time-Integrated Incident and SBS Return Beam Far Fields for Piston Aberrator, Static and Scanning Focal Spot	2-49
2.3-28      Far-Field Intensity Distribution of Piston Aberrated Incident Beam and SBS Return Beam Before Second Pass Through Aberrator	2-50
2.3-29      Incident and SBS Return Beam Power Versus Time Traces for Absorber Added To Induce Thermal Blooming, Static Focal Spot	2-51
2.3-30      Suppression of Thermal Blooming by Scanning Focal Spot	2-53
2.3-31      Far-Field Conjugation Fidelity for Thermal Blooming Suppressed by Focal Spot Scanning	2-54
2.4-1        SBS Frequency Shift and Linewidth Angular Dependence	2-58

# ILLUSTRATIONS (Continued)

		Page
2.3-1	Reflectivity Versus Time Unaberrated Beam	2-18
2.3-2	Long Pulse Reflectivity Versus Time	2-19
2.3-3	Near-Field Intensity of Transmitted Beam Under Long Pulse Conditions	2-20
2.3-4	Reflected Versus Incident Power (Threshold) for No Aberrator, Static Focal Spot	2-22
2.3-5	Reflectivity Versus Incident Power for No Aberrator, Static Focal Spot	2-23
2.3-6	Experimental Results and BRIWON Theoretical Calculations of Reflectivity Versus Scan Speed for No Aberrator, 0 to 155 m/s Scan Speed	2-24
2.3-7	Conjugation Fidelity as Measured by Far-Field Beam-Quality Diagnostic for No Aberrator, Static Focal Spot	2-25
2.3-8	Time-Integrated Near-Field Phase of Incident and SBS Return Beams for No Aberrator, Static Focal Spot	2-27
2.3-9	Time-Resolved Near-Field Phase of SBS Return Beam for No Aberrator, Static Focal Spot	2-28
2.3-10	Time-Integrated Far-Field Intensity Distribution of Incident and SBS Return Beams for no Aberrator, 155 m/s Focal Spot Velocity	2-29
2.3-11	Experimental and BRIWON Theoretical Far-Field Beam Tilt Versus Focal Spot Scan Speed	2-30
2.3-12	BRIWON Code Calculations of Far-Field Intensity for No Aberrator, Static and Scanning Focal Spot Conditions	2-31
2.3-13	BRIWON Code Calculations of Near-Field Phase for No Aberrator, Static and Scanning Focal Spot	2-32
2.3-14	Wedge Aberrator and Corresponding Aberrated Wavefront (Double Pass)	2-34
2.3-15	Far-Field Intensity Distributions of Incident, Aberrated and SBS Return Beams for Wedge Aberrator, Static Focal Spot	2-35
2.3-16	SBS Power Versus Pump Power (Threshold) for Wedge Aberrator	2-36

## ILLUSTRATIONS (Continued)

		Page
2.4-2	Gaussian-Beam Thermal Blooming Strehl Ratio Correlation	2-62
2.4-3	Comparison Between Test Data and BRIWON Predictions	2-65
3.2-1	Apache Phase Conjugation Facility at CTS	3-4
3.2-2	Near-Field Intensity Film Burns	3-6
3.2-3	Pulse Temporal Profile from PAR Lasers	3-8
3.2-4	Optical Train for COS Experiment	3-9
3.2-5	Far-Field Beam at Spatial Filter	3-10
3.2-6	Diagnostics Layout	3-11
3.2-7	Near-Field Intensity Distribution of Incident Beam	3-13
3.2-8	Time-Integrated Beam Quality Diagnostic	3-14
3.2-9	Incident Beam Far-field Characteristics	3-16
3.3-1	Plot of Reflected Energy Versus Incident Energy, With No Aberrator	3-17
3.3-2	Plot of Transmitted Energy Versus Incident Energy	3-18
3.3-3	Far-Field Intensity Plots for Conjugated Beam With No Aberrator	3-19
3.3-4	Near-Field Intensity Plots of Incident and Conjugated Beam With No Aberrator	3-20
3.3-5	BRIWON Predictions of Far-Field Intensity of Conjugated Beam for Gaussian Input Beam	3-22
3.3-6	Plots of Reflected Energy Versus Incident Energy Showing Effect of SBS Telescope Alignment of Threshold	3-23
3.4-1	Far-Field Intensity Distributions of Incident Beam for Two-Dimensional Aberrator	3-24
3.4-2	Far-Field Intensity Distributions and Beam Quality Plots of Conjugated Beam for Two-Dimensional Aberrator	3-25
3.4-3	Temporal Plots of Incident and Transmitted Beams for Conditions Near Breakdown	3-26



# ILLUSTRATIONS (Continued)

		Page
3.4-6	Gas Breakdown Summary. (a) Peak Intensity Versus Threshold. (b) Relative Breakdown Intensity Versus Pulse Duration	3-30
3.5-1	Schematic of Wedge Separating Far-Field into Two Spots	3-32
3.5-2	Layout Showing Additional Diagnostics for Beam-Combining Aberrators	3-33
3.5-3	Transmitted Energy Versus Aberrator Alignment	3-34
3.5-4	Plots of Reflected Energy Versus Incident Energy for Wedge Aberrators	3-35
3.5-5	Plots of Far Fields of Incident, Aberrated and Conjugated Beams for Wedge Aberrator	3-36
3.5-6	Far-Field Intensity Plots From BRIWON Code for Beams Separated by 2.5 Spot Diameters	3-37
3.6-1	Optical Layout for Threshold Reduction Using Single Cell and Four Foci	3-39
3.6-2	Plot of Reflected Energy Versus Incident Energy for One, Two, and Four Foci	3-40
3.6-3	Reduction in Threshold Dependent on Focus-to-Focus Loss	3-41
3.6-4	Excellent Conjugation Fidelity Observed With Four-Foci Threshold Reduction	3-42
3.6-5	Beam Combination Demonstrated With Threshold Reduction	3-43
3.6-6	Four-Beam Phase-Conjugation Demonstration	3-45
3.7-1	Dependence of Threshold on Pump Beam Quality	3-51
3.7-2	BRIWON Steady-State Pump Depletion	3-55
3.7-3	BRIWON CW Reflectivity Predictions	3-56
3.7-4	Transient SBS Threshold Behavior	3-57
3.7-5	Predicted Transient SBS Response to Long Square Pulse	3-59
3.7-6	Subscale 1.06- $\mu$ m Reflectivity Data	3-61

## ILLUSTRATIONS (Continued)

	Page
3.7-7      Transient SBS Modeling	3-62
4.1-1      Axial Aerowindow Concept for SBS Cell (F/10 Configuration)	4-3
4.2-1      Subscale Flowing-Gas Facility	4-11
4.2-2      Schematic of Interior of Flowing-Gas Cell	4-13
4.2-3      Subscale Gas Handling Flow Control System	4-14
4.2-4      Optical Layout of Subscale SBS Experiments	4-17
4.2-5      Block Diagram of Subscale Optical Layout	4-18
4.2-6      Diagnostics Used in Subscale Fluid Mechanics Tests	4-20
4.2-7      Subscale Results for "Fundamental Wake Flow"	4-23
4.2-8      Variation of OPD With Interface Thickness; BRIWON Code With Turbulence Model	4-25
4.2-9      Flow Acceleration Ramps	4-27
4.2-10     Experimental Results for Flow Acceleration Ramps; Shadowgraphs and Interferograms	4-28
4.2-11     Results for Flow Acceleration Ramps; OPD, Comparison With Baseline Data	4-30
4.2-12     Splitter-Plate Tip Modified for Suction/Blowing Experiments	4-31
4.2-13     Placement of Pump Beam Focus Relative to Xe-He Interface	4-34
4.2-14     SBS Reflectivity for Static-Xe and Flowing-Gas Cases	4-36
4.2-15     Far-Field Intensity Pattern of Return Beam; Static Case and Flowing Case (pump energy = 60 mJ)	4-37
4.2-16     SBS Reflectivity as Function of Pump Focus Location; Model and Experimental Results (pump energy = 60 mJ)	4-39
4.3-1      Layout of Upgraded PAR Laser	4-45
4.3-2      Modified Segment of APACHE Facility Optical Train	4-46

# ILLUSTRATIONS (Continued)

		Page
4.3-3	Flow-Control System Schematic	4-47
4.3-4	Flowing-Gas SBS Cell Design (plan view)	4-51
4.3-5	Flowing-Gas SBS Cell Design (view along optical axis)	4-52
4.3-6	Flowing-Gas SBS Cell Integrated in Zone 3 of APACHE HF Facility	4-54
4.3-7	Multiple-Foci Optics Layout For SBS Cell	4-55
4.3-8	Temporal Behavior of PAR Multiline Pulse	4-57
4.3-9	Typical Pressure Histories for Key Flow Control Components	4-59
4.3-10	EHA Calibration for SBS Cell Pressure Control	4-61
4.3-11	SBS Cell Flow Behavior (shadowgraphs)	4-63
4.3-12	Temporal Behavior of Pump and Stokes Pulses	4-65
4.3-13	SBS Reflectivity Behavior for Static and Flowing Xe	4-67
5-1	Nineteen-Element Segmented Array	5-4
5-2	Experimental Layout	5-5
5-3	Thousands of Waves Segment Piston Corrected to Better Than $\lambda/20$ Using SBS Phase Conjugation	5-8
5-4	SBS Reflectivity Data Used To Establish Threshold Scaling With Array Parameters	5-10
5-5	Slope Efficiency of SBS Reflectivity	5-12
5-6	SBS Threshold as a Function of Segment Tilt (with random piston)	5-13
5-7	Segment Apertures Used To Correlate Threshold With Number of Segments	5-14
5-8	Technique Used for Threshold Scaling With Number of Segments Biases Measurement to Lower Values for Small N	5-15
5-9	SBS Threshold Scaling With Number of Segments	5-17

## ILLUSTRATIONS (Continued)

	Page
5-10 Representative Examples of Data Show High Degree of Piston and Tilt Conjugation	5-18
5-11 Interferograms Showing All Elements Cophased and One Segment Dropped Out	5-20
5-12 Piston Conjugation Scaling With RMS Segment Tilt	5-21
6-1(a) Pulsed CO <sub>2</sub> Laser Power Versus Time, No Return	6-11
6-1(b) Small Signal Gain Versus Run Current and Pressure	6-11
6-2 Negative Branch Unstable Standing Wave (CZAR) Resonator Layout	6-12
6-3 Negative Branch Standing-Wave Resonator (CZAR) Optical Schematic	6-13
6-4 Theoretical Near-Field Image of Negative Branch Standing-Wave Resonator	6-15
6-5 Negative Branch Unstable Ring Resonator Layouts	6-16
6-6 Near-field Intensity Profiles of Outcoupled Beam From OI Negative-Branch Unstable Ring Resonator	6-19
6-7 OI CO <sub>2</sub> Experiment Diagnostics	6-20
6-8 Detailed NBSW Optical Train and Diagnostics Layout	6-21
6-9 Acousto-optic Modulators Used to Frequency Shift Return Beam	6-23
6-10 CO <sub>2</sub> Oscillator Isolation Experiment Diagnostic Control Structure	6-25
6-11 Power Versus Time for NBSW Resonator, $M = 1.5$ , $\Delta\nu = 6.4$ MHz	6-27
6-12 Beam-Quality Degradation Versus Return for NBSW Resonator, $M = 1.5$	6-28
6-13 Frequency Content of Output Beam, NBSW Resonator, $M = 1.5$	6-30
6-14 Experimental and Theoretical Return Beam Amplification for the NBSW Resonator, $M = 1.5$ and $2.0$ for a Frequency Shift of $6.4$ MHz	6-32

# ILLUSTRATIONS (Continued)

	Page
6-15 Beam Quality Degradation Versus Return Beam Alignment for NBSW Resonator, $M = 1.5$	6-33
6-16 Beam-Quality Degradation Versus Return Fraction for NBSW CZAR, $M = 2$ (5% beam quality degradation for returns of $1.5 \times 10^{-4}$ )	6-35
6-17 Beam Quality Degradation Versus Return for NBSW Resonator, $\nu V = 6.4$ MHz, $M = 1.5$ and $2.0$ ( $M = 2$ is 5 x more sensitive to return)	6-36
6-18 Power Versus Time for NBSW Resonators for 6.4-MHz Shift and Comparable Return (Amplification greater for $M = 2$ resonator)	6-37
6-19 Power Versus Time for Ring Resonator and NBSW Resonator, $M = 1.5$ , $\Delta V = 6.4$ MHz	6-39
6-20 Intensity Drop Versus Return Fraction for Ring Resonator, $M = 1.5$	6-40
6-21 Ring Resonator, $M = 1.5$ , Gain of Return Beam	6-41
6-22 Beam-Quality Degradation Versus Return Fraction for Ring Resonator, $M = 1.5$	6-42
6-23 Intensity Drop Versus Frequency for Ring Resonator, $M = 1.5$	6-44
6-24 Gain Behavior Near Zero Frequency Shift	6-45
6-25 Ring Resonator, Effect of Frequency Shift Near Zero, $M = 1.5$	6-46
6-26 Intensity Drop for Ring Resonator, $M = 1.77$ , as Function of Return Fraction (Nonmode frequency shifts plotted)	6-47
6-27 Ring Resonator, $M = 1.77$ , Gain of Return Beam	6-48
6-28 Effect of Partially Blocking RWS Mirror, $M = -1.77$	6-50
6-29(a) Experimental and Theoretical Relative Brightness Versus Return for NBSW Resonators, $M = 1.5$ and $2.0$ , for a Frequency Shift of 6.4 MHz	6-53
6-29(b) Experimental and Theoretical Relative Brightness Versus Return for the Ring Resonators, $M = 1.5$ and $1.77$ , for a Frequency Shift of 6.4 MHz	6-53

# ILLUSTRATIONS (Continued)

	Page
6-30 Return Beam Outcoupling Fraction Dependence on Pass Number	6-55
6-31 Eigenvalues Used to Assess NBSW G(W) Values	6-56
6-32 Ring Resonator Outcoupling Ratio Pass Dependence, M = 1.5	6-62
6-33 HEXDARR Regenerative Mode Gain Versus Eigenmode Magnitude	6-65
7-1 Resonator Used for OIVM Experiment	7-3
7-2 OIVM Resonator Beam Footprint Before Clipper	7-4
7-3 Block Diagram of External Optical Train for OIVM Experiment	7-6
7-4 Detailed Layout of External Optical Train for OIVM Experiment	7-7
7-5 Near-Field Intensity of Propagated Beam	7-9
7-6 Spectrum of Laser Output	7-10
7-7 Horizontal Slice Plots of Intensity From Far Field Diagnostic at Two Times During Testing	7-11
7-8 Overlapping Slice Plots From Far Field Diagnostic, With and Without Return	7-13
8-1 Experimental Layout for Pulse Stretching Experiments	8-3
8-2 Power as Function of Time for Nominal Gas Mixture, F2/H2/He/O2 = 110/27.5/401.5/11, P = 550 torr Top traces are multiline power (a) Bottom Trace, P2(8) (b) Bottom Trace P2(7).	8-6
8-3 Power as Function of Time for Mixture With F2/H2/He/O2 = 45/15/701.5/3.5, P = 760 torr. Top traces are multiline pulses Bottom traces are P2(8) pulse (a) 50 kV, (b) 40 kV, (c) 35 kV.	8-7
8-4 Power as Function of Time for Mixture With F2/H2/He/O2 = 33/11/510/3, P = 560 torr Top traces are multiline pulse Bottom traces are P2(8) (a) 50kV, (b) 40 kV, (c) 35 kV	8-8

# ILLUSTRATIONS (Continued)

		Page
8-5	Power as Function of Time for Mixture With F <sub>2</sub> /H <sub>2</sub> /He/O <sub>2</sub> = 30/10/717/3, P = 760 torr	8-9
9.1-1	Aerospace Bidirectional Amplifier Experimental Setup	9-4
9.1-2	Predicted Extraction Efficiency Versus Input Intensity for Aerospace Experiment	9-5
9.2-1	CLAM Code Prediction of Bidirectional Amplifier Performance for SBL	9-8
9.2-2	CLAM Code Predictions of Bidirectional Amplifier Performance for High-Power Demonstration Experiment	9-9
9.3-1	CLAM Code Predictions for SBL and Three-Pass VM	9-13
9.3-2	CLAM Code Predictions of Extraction Efficiency as Function of Input Intensity	9-15
9.3-3	CLAM Code Predictions of Forward and Backward Amplifications Versus Number of Passes Through ALPHA-VM Gain Medium	9-16
9.3-4	Geometry Used to Determine Misalignment Tolerance	9-17
9.4-1	Sketch of Bidirectional Amplifier Concept for Oscillator and Four-Pass Amplifier	9-21
9.4-2	Bidirectional Amplifier Configuration for Oscillator and Four-Pass Amplifier	9-22
9.4-3	Sketch of Bidirectional Amplifier Experiment To Give Flexibility on Intensities of Counterpropagating Beams	9-23
9.4-4	Bidirectional Amplifier Configuration for Greatest Intensity Range of Counterpropagating Beams	9-24
9.4-5	Rotating Grating Shifter Concept	9-27
9.4-6	Translating Mirror Concept	9-29
9.4-7	Translating Coner Cube Concept	9-30
9.4-8	Velocity Required Versus Track Length for Different Numbers of Bounces	9-31
9.4-9	Internal and External Involute Wheels Compensate Astigmatic Focusing and Time-Varying Radial Velocity Dihedral Compensates Further	9-32

## ILLUSTRATIONS (Continued)

		Page
9.5-1	ALPHA VM Device	9-35
9.5-2	Schematic Experiment Showing Detector Scan From Shroud to Street	9-37
9.5-3	CLASP Small-Signal-Gain Schematic	9-38
9.5-4	Small-Signal-Gain Layout	9-40
9.5.3	Discussion of Data	9-41
9.5-5	Gain Uniformity From Strut to Shroud, P1(7) Line	9-42
9.5-6	Gain Uniformity From Strut to Shroud, P1(6) Line	9-43
9.5-7	Averaged Small-Signal-Gain Data on P1 Lines	9-44
9.5-8	Averaged Small-Signal-Gain Data on P2 Lines	9-45
10-1	Optical Attenuation Measurement Layout	10-3
10-2	PAS Experiment Optical Layout	10-5
10-3	Gas-Handling System for PAS Experiment	10-6



# TABLES

		Page
3.2-1	Summary of Diagnostics	3-12
4.1-1	Scaling Parameters for Flowing-Gas SBS Cell	4-5
4.2-1	Scaling Parameters in Fluid Mechanics Experiments	4-21
4.3-1	Important Scaling Parameters for Flowing-Gas SBS Cell DVT	4-42
4.4-1	SBS Reflectivity and BQ Dependence on Random Phase Aberration Realizations, Cell Length, and Interface Thickness	4-72
4.4-2	SBS Reflectivity and BQ Behavior for Random Phase-Aberration Realizations, $\Delta z = 0.05$ cm, Cell Length, = 3 RR (interface to focus)	4-73
4.4-3	SBS Reflectivity and BQ Behavior for Random Phase-Aberration Realizations, $\Delta z = 0.40$ cm, Cell Length = 3 RR	4-75
4.4-4	Phase Aberration Magnitudes at Interface for Random Realizations, $\Delta z = 0.05$ and 0. cm, Cell Length = 3 RR	4-76
4.4-5	Two-Foci Threshold Reduction, $\Delta z = 0.05$ cm, Cell Length = 3 RR	4-78
4.4-6	Three-Foci Threshold Reduction, $\Delta z = 0, 0.01$ , and 0.05 cm; 3 RR	4-79
4.4-7	Two-Foci Threshold Reduction With Turbulence and Grating Correction	4-81
5-1	Accuracy of Piston Conjugation	5-22
6-1	Traceability of Significant Nondimensional Parameters	6-3
6-2	Summary of Standing-Wave and Ring Resonator Results	6-52
6-3	Theoretical Eigenmodes for Standing-Wave Resonator, $M = 1.5$	6-57
6-4	Theoretical Eigenmodes for Standing-Wave Resonator, $M = 2.0$ , $L = 15.834$ m	6-59
7-1	Spectral Output of ALPHA-VM Device	7-12
8-1	Test Matrix for Pulse Stretching Experiments	8-4

## TABLES (Continued)

		Page
9.1-1	Bidirectional Amplifier Technical Issues	9-2
9.2-1	CLAM Code Results for SBL Bidirectional Amplifier Performance, With and Without Frequency Shift	9-7
9.2-2	CLAM Code Predictions of Intensities for ALPHA Run as Amplifier, With and Without Frequency Shift	9-10
9.3-1	Oscillator/Resonator Requirements	9-12
9.3-2	Amplifier Requirements	9-12
9.4-1	Options for Bidirectional Amplifier Experiment	9-19
9.4-2	Mechanical Frequency Shifter Design Requirements	9-26
9.4-3	Frequency Shifter Concept Evaluation	9-34
9.5-1	Nominal ALPHA-VM Run Conditions and Operating Time Line	9-39
10-1	Requirements for Xe HF Absorption Experiment	10-2
10-2	Xe HF Absorption Coefficients at 40 atm, Differential Optical Method	10-7

## 1. INTRODUCTION

The Advanced Phased Array Chemical High Energy (APACHE) laser program has developed an innovative approach to meeting strategic defense weapon system objectives for a high-power space-based laser (SBL) system. The cost and complexity of high-energy laser (HEL) weapon systems for strategic defense applications are typically dominated by the large-aperture beam projecting telescope and the laser subsystem. The APACHE approach uses nonlinear phase conjugation to reduce system size and complexity by providing a high-power beam of excellent beam quality while relaxing difficult optical design and fabrication tolerances in many cases by one to two orders of magnitude. In pursuit of this design, substantial technology development in the area of nonlinear optics with applications to high-energy laser systems has been developed. The maturity of this technology is such that nonlinear optics now represents a low technical risk approach for beam control in a strategic defense directed energy system. The groundwork has now been laid to support the next logical step which is an integrated demonstration of all of the key elements of the APACHE SBL concept at the highest laser powers available.

The APACHE space-based laser design approach integrates the hydrogen fluoride (HF) laser technology developed under the ALPHA program with nonlinear optical phase conjugation using stimulated Brillouin scattering (SBS). It has been demonstrated over a wide range of test conditions that stimulated Brillouin scattering provides an extremely effective means of passively correcting severe optical aberrations to levels commensurate with the diffraction limit. Additional experiments have demonstrated the utility of SBS to provide a means of coherently combining beams from multiple laser sources. The APACHE approach utilizes the aberration correction feature of SBS to produce a high-quality low-jitter laser beam while providing a growth path to extremely high powers using SBS to coherently couple the output of multiple laser sources. The result is a concept for a weapon class laser system which uses laser power efficiently, has low jitter for rapid and accurate line of sight retargeting, operates over a wide field of view to minimize constellation size, has applicability

over a broad range of system powers, and can be effectively scaled to very high levels of brightness for multiple strategic defense applications.

The overall goals of the APACHE program are identified as follows:

1. Develop a concept for a space-based laser system which fully exploits the inherent advantages of nonlinear optical phase conjugation for aberration and jitter correction and power scaling through coherent beam combination.
2. Identify critical technology issues associated with this SBL design concept, and address these issues through direct experimental studies. A parallel analytical modeling effort, with anchoring and validation provided through direct comparisons with the experimental results, provide the tools necessary to support the SBL design.
3. Update the SBL design concept, using the experimentally validated models, as the nonlinear optics technology matures.

The technical starting point for this effort began with the work completed under the Phased Array Laser System (PALS) and the Chemical Laser Phase Conjugation Technology (CLPCT) programs. The PALS program developed a preliminary SBL design concept implementing the use of SBS phase conjugation. This concept was further developed under the APACHE program to its present state. The CLPCT began the design of an SBS technology demonstration experiment to be conducted at HF wavelengths. The completion of this experiment design, followed by hardware integration and testing, was performed under APACHE. With the completion of APACHE, a follow-on program called APEX has been definitized which will extend the SBL conceptual design and provide an integrated technology demonstration of all of the subsystem concepts developed under APACHE.

### 1.1 APACHE SBL CONCEPT OVERVIEW

A schematic representation of the APACHE SBL design concept is shown in Figure 1-1. A detailed layout is presented in Figure 1-2. The system consists of essentially four major subsystems:

- Master oscillator subsystem
- Beam director subsystem
- Amplifier subsystem
- SBS subsystem.

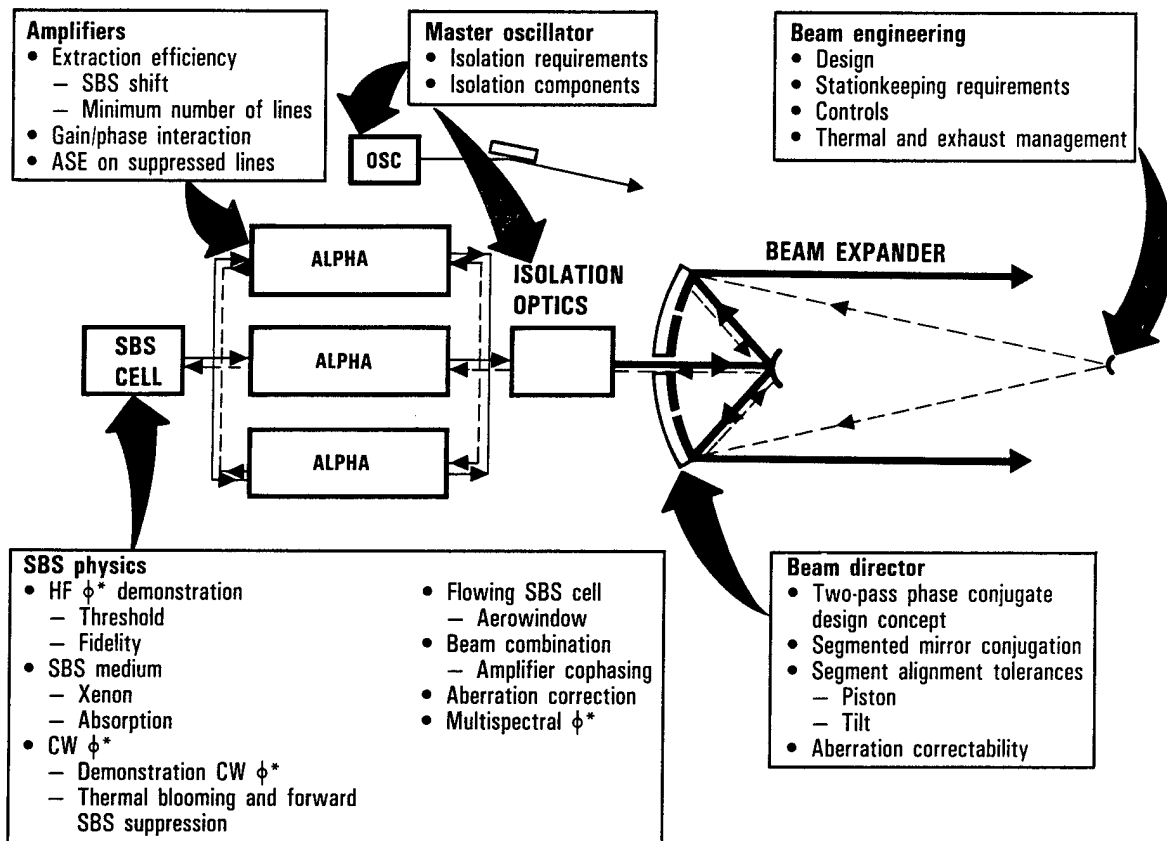


Figure 1-1. Technology Issues Addressed by APACHE Program

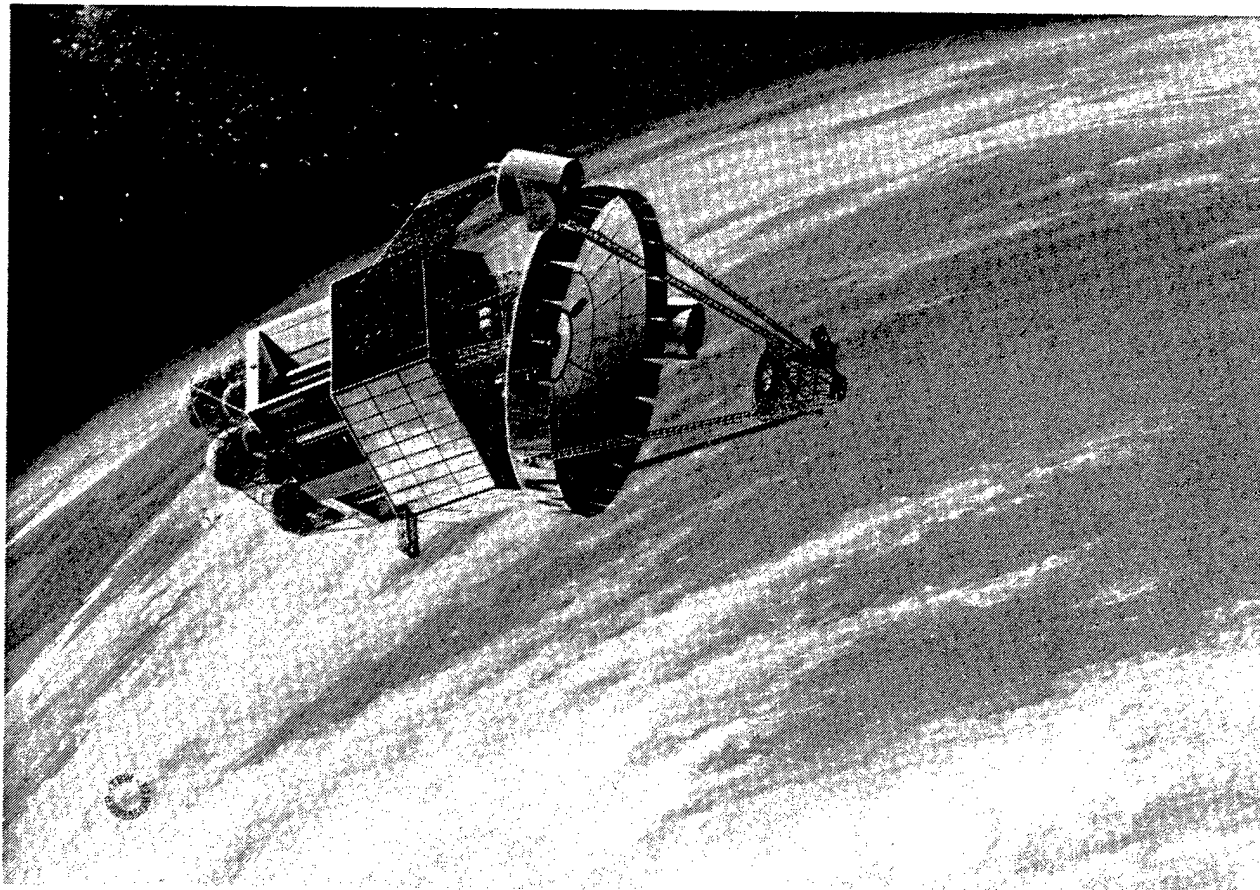
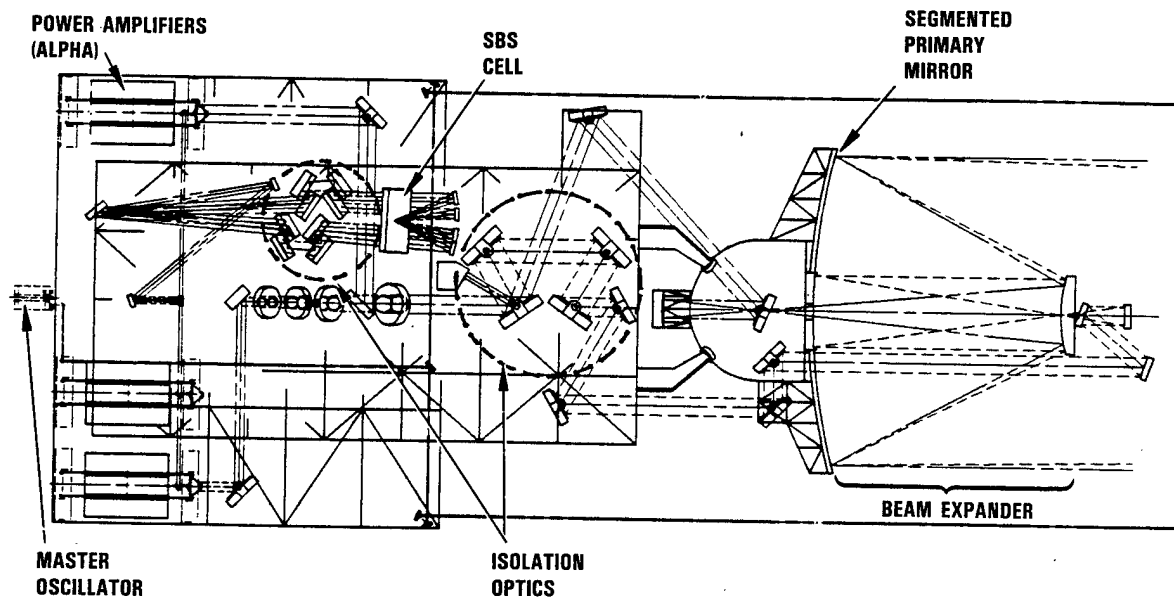


Figure 1-2. APACHE SBL Design Concept

The functional operation of this system is best understood by following the photons through the system, beginning with the master oscillator which is the source of the radiation. The master oscillator subsystem establishes the jitter and beam quality reference for the rest of the system. This subsystem consists of an ALPHA class cylindrical HF laser source and a quarter-wave retardation optic external to the HEXDARR resonator which produces a linearly polarized beam of relatively low power. The output of the laser propagates to a convex mirror located on a beacon separated from the host spacecraft by a distance corresponding to 25 primary mirror diameters. Here, the beam is diverged and reflects back toward the main part of the system. The location of this mirror is in the far field of the master oscillator beam, and serves the additional purpose of spatially filtering the master oscillator output to provide an nearly aberration free reference beam.

The high-quality low-power reference beam propagates to the beam director telescope. Impressed upon its phase distribution are the phase aberrations from the large aperture segmented primary mirror arising due to segment piston and tilt misalignment and misfigure. This aberrated low-power beam then propagates to the amplifier subsystem. The amplifier subsystem consists of multiple scaled-up ALPHA cylindrical gain generators configured to function as amplifiers rather than resonators. The beam next passes through quarter-wave retardation optics which converts the linearly polarized beam to circular polarization. It is then focused into the SBS cell. Within the SBS cell, the phase distribution arising from aberrations within the beam director and amplifier subsystems is conjugated or phase reversed.

When the beam reflects from the SBS cell and propagates back through the quarter-wave retardation optics, its linear polarization is restored but with an orientation orthogonal to that of the incident beam. This polarization rotation is used to discriminate between the low-power incident and high-power return beams, preventing the conjugated beam from returning to the master oscillator. Upon propagation back through the amplifiers the beam is further amplified. Aberrations generated in the amplifiers are corrected as a result of the conjugation process. Any

pathlength mismatch between the multiple amplifiers (which is simply treated like as other aberration by the SBS cell) is removed on this return pass. This passive means of pathlength control, which works for multiple line operation, eliminates the need for complex active control systems and phase detectors which must correct pathlength errors of tens to hundreds of centimeters with submicron accuracy.

After leaving the amplifier subsystem on the return pass, the high-power return beam is separated from the low-power incident beam using polarization sensitive grating rhombs. These gratings discriminate between the two beams on the basis of the orthogonal orientations of the polarization vectors. This high-power conjugated beam propagates back to the primary mirror where aberrations due to segment misalignment and misfigure are almost totally removed. A high-quality high-power beam is then directed toward the target.

The essential feature of the APACHE design calls for high-power beam control by passive means through the use of nonlinear optics. This beam control corrects primary mirror segment piston and tilt alignment. It also corrects for higher order aberration in mirror segments which result from fabrication errors, mechanical distortion, and thermo-optical processes. It also provides amplifier cophasing through coherent beam combination. Unnecessary in this design is the need for complex adaptive optics controls including deformable mirrors, wide field of view outgoing wave front sensors (WFOV OWS), active primaries with holographic optical elements (HOEs) for optical sampling, pathlength control optics ("optical trombone"), and hierarchical control systems (HACS) to provide closed-loop high-bandwidth active control over thousands of wavelength of light. In the APACHE concept, these rather complex systems are replaced by three new design elements, viz., a very simple passive control system (SBS cell), isolation optics, and a beacon satellite. As will be shown, these new subsystems have fairly benign design tolerances. Given the extensive amount of technology development which has occurred as part of the APACHE program, they represent a relatively low technical risk approach to the design of an effective SBL weapon system.

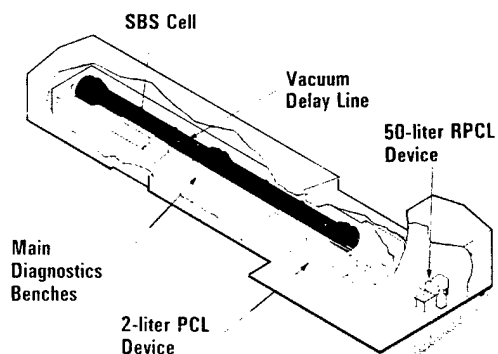


## 1.2 TECHNICAL ISSUES

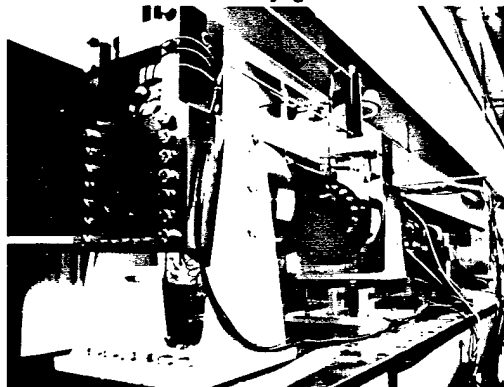
A major portion of the APACHE program involved identification of key technical issues associated with the SBL design concept employing SBS phase conjugation. Once identified, these technical issues were addressed experimentally. Models, validated by the results of the experiments, were used to further update the design. The primary focus of the APACHE technology development effort was to emphasize those issues specifically related to the implementation of SBS phase conjugation into an HF multiline continuous wave (CW) laser system. The key elements here are CW and HF. The implementation of SBS under CW conditions had received little attention prior to the start of APACHE, primarily due to the difficulty in exceeding the SBS threshold with a CW laser. Similarly, with the exception of the pioneering work performed by the Naval Research Laboratory (Whitney, Duignan, and Feldman), very little work in the area of HF conjugation had been done at the outset of APACHE.

Figure 1-1 shows a top-level summary, categorized by major subsystem, of the important technical issues addressed as part of the APACHE program.

Because of the unique nature of SBS phase conjugation, most of the technology issues identified at the start of the program were associated with this subsystem. One of the first technical issues needing resolution related to the demonstration of efficient SBS conjugation at HF wavelengths. With the exception of the NRL work, no other data on SBS at  $2.8 \mu\text{m}$  existed. Questions existed with regard to the optimum conjugating medium, the amount of power required to exceed the SBS threshold, the SBS reflectivity, the fidelity of the SBS process, the type of aberrations correctable by SBS, and the degree to which multiple beams can be cophased by SBS. To address HF conjugation questions, a new state-of-the-art test facility shown in Figure 1-3 was constructed at TRW's Capistrano Test Site (CTS). Using two pulsed HF chemical lasers produced by Pacific Applied Research (referred to hereafter as the PAR lasers), SBS experiments were conducted using a high-pressure Xe cell to produce a phase conjugate beam. Aberrations were intentionally introduced into the beam to quantify the fidelity of the SBS process to correct for optical distortions. Extensive diagnostics were used to monitor the fidelity and reflectivity of the SBS



APACHE HF Phase Conjugation Test Site



### HP Phase Conjugation Test Facility

- HF  $\phi^*$  demonstration
- SBS medium verification
- SBS threshold and fidelity
- Aberration correction
- Beam combination
- Threshold reduction

Experiment used to validate SBS physics model

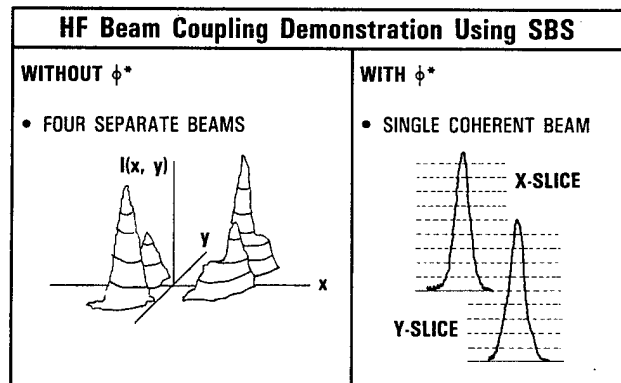
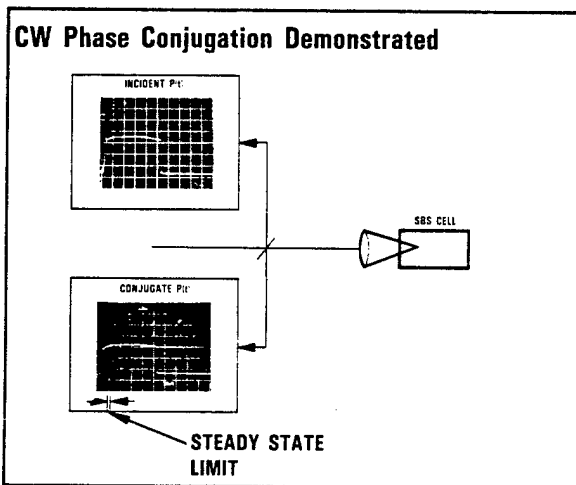


Figure 1-3. HF Phase Conjugation Issues Addressed Using New State-of-the-Art Test Facility

process over a wide range of test conditions. Shown in Figure 1-3 is a representative example of data from a beam combining experiment where coherent coupling of four separate beams using SBS was demonstrated. These experiments specified that Xe pressurized to 40 atm was the optimum choice for the conjugating medium. Xenon was chosen because of its high SBS gain (implying low threshold power), its relatively low absorption within the HF spectrum, and its small frequency shift. An important modeling activity conducted in parallel with the HF conjugation experiments was the development of an SBS physics model named BRIWON. The BRIWON model extended some of the previous SBS modeling work conducted at NRL to incorporate additional physical processes important for the APACHE SBL design. These included pump depletion, flow convection, turbulence, aberrations, thermal blooming, and self-focusing. The results of the HF conjugation experiments provided necessary information on threshold, reflectivity, fidelity, aberration correction, and beam combination for validation of the BRIWON SBS physics model used to support the SBL design effort. Additional data relating to methods for reducing the SBS threshold power using novel concepts demonstrated the applicability of the APACHE phase conjugate SBL design over a wide range of system brightness levels.

A second major issue associated with the application of phase conjugation for an ALPHA class laser is that the SBS process must work under CW conditions. Prior to the APACHE program, almost all of the SBS work had been performed in a pulsed regime. Questions relating to competition with other processes such as thermal blooming and forward SBS scatter required experimental verification. The primary issue was whether or not the SBS return would track the power and phase aberrations of the incoming beam over long periods of time. The approach taken was to use the KMS Fusion, Inc. CHROMAS Nd:YLF laser operated in a mode which simulated CW conditions. The CHROMA laser generated pulses which were substantially longer (of order 1000 to 2000 times) than the SBS phonon lifetime; the characteristic time scale of the SBS process. Representative examples of results of these experiments are shown in Figure 1-4. These data demonstrate nearly constant reflectivity for time scales well into the CW operating regime, thus confirming the applicability of SBS to perform in an SBL based on ALPHA HF laser technology operating under CW conditions. The



$\phi^*$  demonstrated for 200 times steady state limit

- Time invariant reflectivity

CW issues resolved

- Thermal blooming control using flow convection
- Forward SBS suppressed

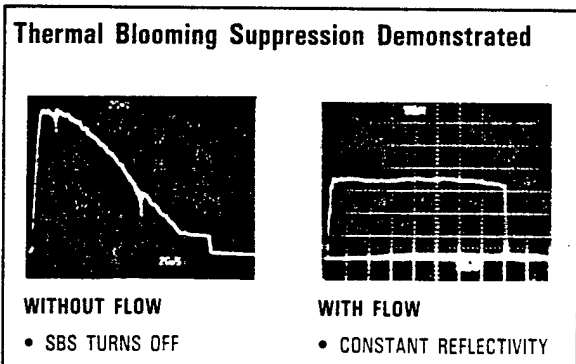
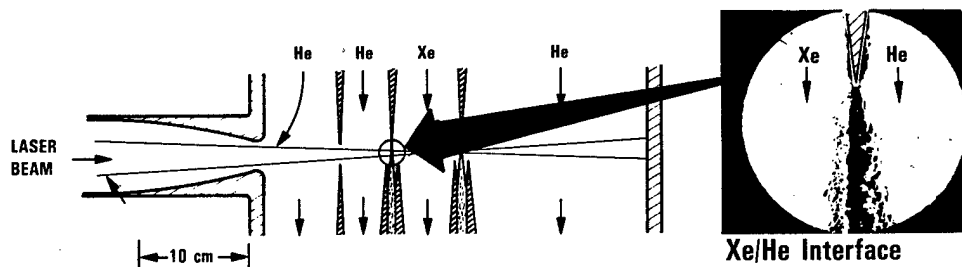


Figure 1-4. CW Phase Conjugation Issues Addressed

results of experiments to simulate the effects of thermal blooming in the SBS cell are also shown in this figure. These demonstrated that thermal blooming due to absorption in the Xe conjugation medium could be easily suppressed through the flow of the SBS medium at the moderate velocities of approximately 5 m/s. This constraint places unique requirements on the SBS cell design, and necessitated flowing SBS cell technology development.

A flowing cell design was defined on APACHE. A schematic of the concept is shown in Figure 1-5. The concept employs an aerodynamic window which allows the input and output of the high-power beam without the use of a material window which could not withstand the power fluxes (although consideration was also given to use of a material window as well). This aerowindow is coupled with a flow channel providing transverse flow of the conjugating Xe medium. To demonstrate this design concept, two approaches were taken. First, a series of subscale experiments were conducted at reduced pressure and  $1.06\text{ }\mu\text{m}$  to examine the interaction of fluid mechanics and SBS physics. Figure 1-5 shows a representative example of data generated on this subscale device. The critical area of the design is the interface between the aerowindow and flowing Xe where turbulent mixing between the gases of different refractive index produce optical aberrations in the beam to be conjugated. The results of these tests demonstrated that the effects of fluid mechanic aberrations could be controlled well enough to allow excellent fidelity in the conjugation of the beam. This is evidenced by the far-field intensity distributions shown in Figure 1-5. They show that the effect of the flow has virtually no effect on the fidelity of the conjugation process. Furthermore, the data show that the presence of the interface had minimal effect on the reflectivity or threshold power. Following these subscale experiments, a new cell designed to operate at the full 40 atm pressure was fabricated and integrated into the CTS phase conjugation test facility (depicted in Figure 1-3) for testing at HF wavelengths. A photograph of this full-scale device is shown in Figure 1-6. Under APACHE, the primary scope of this activity was to design, fabricate, and integrate the hardware into the CTS test facility. Preliminary checkout tests were also conducted to verify that the facility was operational. Further testing and detailed parameterization is scheduled as part of the APEX program.

Flowing cell concept uses unique aerowindow design



Flow convection

- Thermal control

Aerowindow

- High power CW operation

Flowing cell experiments demonstrate excellent  $\phi^*$  fidelity

$\phi^*$  Unaffected by Flowing Gas

Experimental Facility

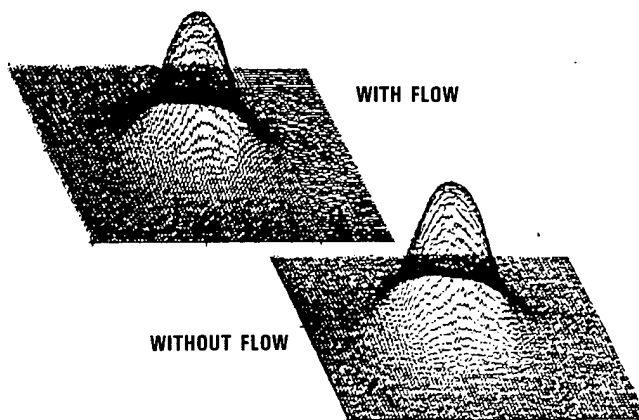
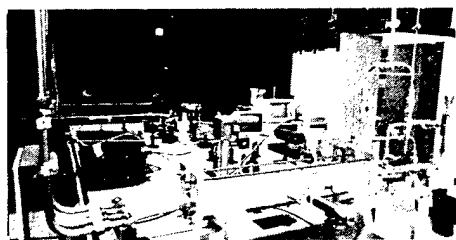


Figure 1-5. Flowing SBS Cell Technology Demonstrated

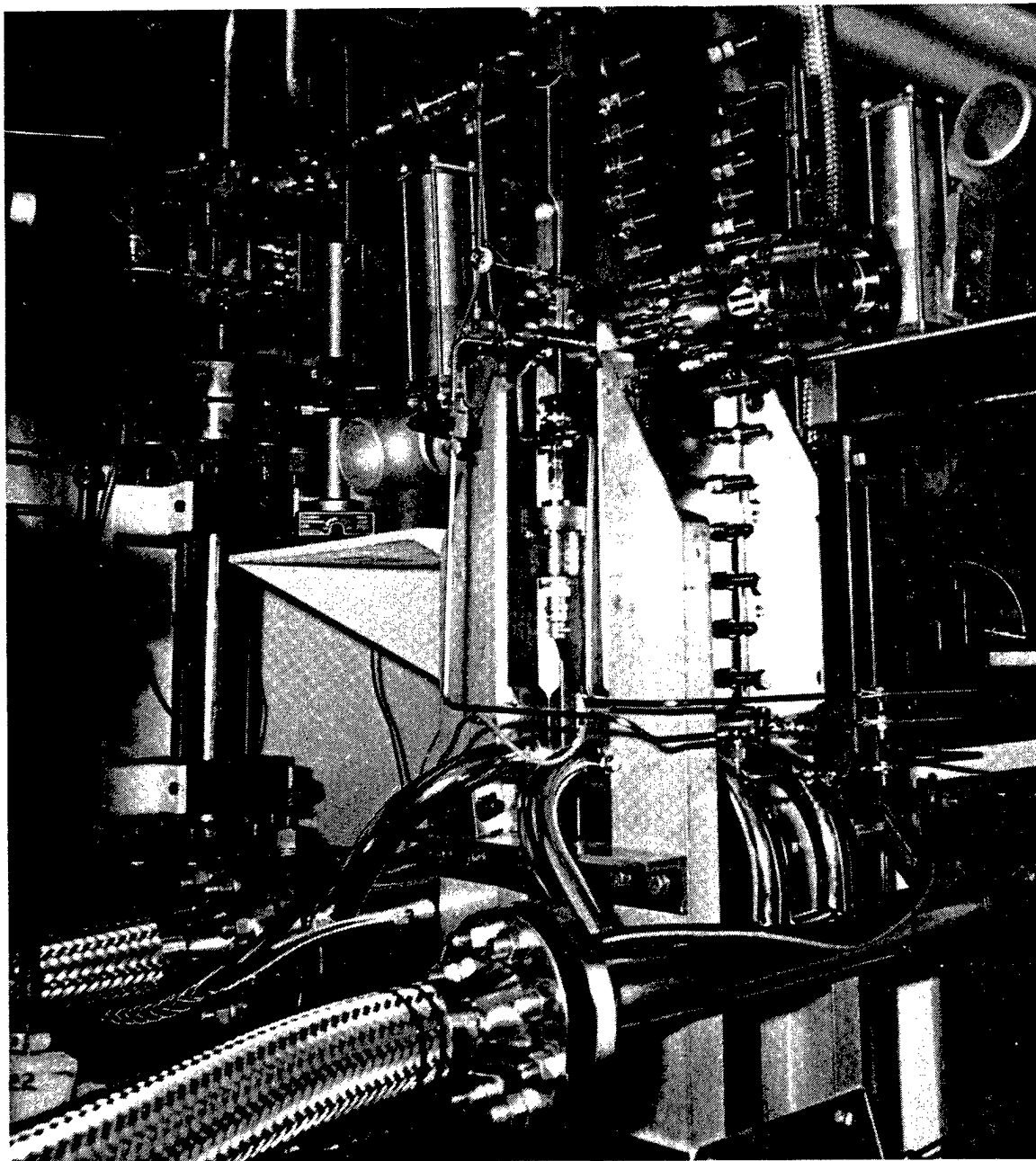


Figure 1-6. CTS Flowing Cell

Oscillator isolation was also a major technology issue for the SBL at the outset of the APACHE program. Here, the concern related to how feedback to the master oscillator from the SBS cell affects the SBL system performance. Feedback comes from imperfect isolation components and birefringence in the system. To examine isolation issues, experiments and analyses were performed to measure the impact of power leakage back into the master oscillator for several different resonator designs and test conditions. An representative example of results from this experiment is shown in Figure 1-7. Here oscillator brightness degradation, resulting from either a power decrease or a beam quality increase, is shown as a function of the normalized feedback power. These results were used to validate an isolation analysis. This analysis was subsequently used to model the performance of the ALPHA HEXDARR resonator operating with feedback to establish requirements for the various isolation components required in the SBL optical train.

The correction of large segment piston and tilt misalignment in the primary mirror is one of the driving motivations for pursuing the APACHE SBL concept. Consequently, this topic received a great deal of attention on the program, both analytically and experimentally. Using an optical design code, the beam-director subsystem, shown in detail in Figure 1-2, was analyzed in terms of its performance sensitivity to misalignment and misfigure of the optical segments which comprise the primary mirror. Typical results are shown in Figures 1-8 and 1-9. Performance sensitivity results to segment piston errors are presented in Figure 1-8. Here, it is seen that the beam director concept developed for the APACHE SBL design concept has the ability to reduce piston errors by 400-fold. For the example shown, nearly 15 waves (HF) RMS of segment piston errors produce  $<0.04$  waves residual OPD in the output beam directed toward the target. Similar calculations for segment misfigure, presented in Figure 1-9, show equally dramatic reductions in the effects of aberrations. Here, a spectrum of disturbance over a range of spatial scales between 0.5 to 10 cycles/m with an RMS OPD of about one wave was impressed on the segment surface contour. The net effect in the outcoupled beam to the target is smaller than  $1/35$  wave RMS OPD. Both of these calculations demonstrate the

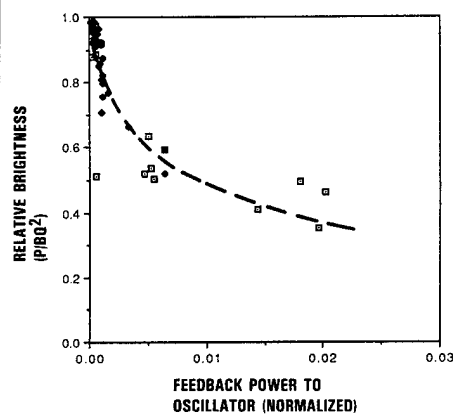


Experimentally validated analysis sets SBL system requirements

Test Facility



Brightness Sensitivity to Isolation  
Measured Experimentally



Experiments validate  
model

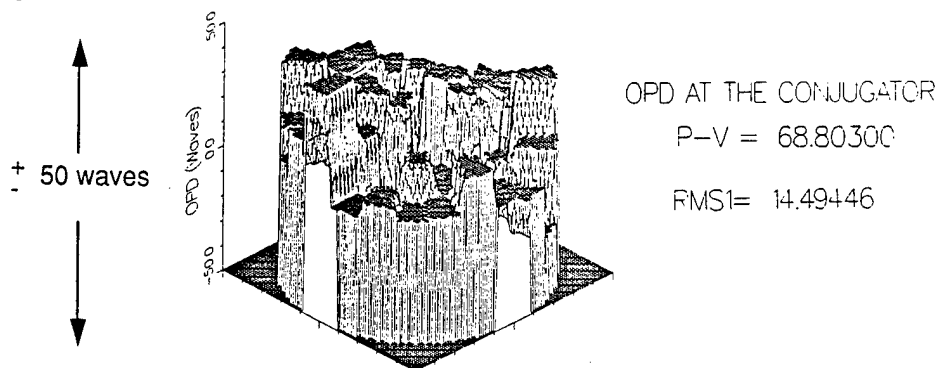
Model used to set  
SBL requirements

Components designed to meet isolation requirements

- Quarter wave retardation coatings
  - Low birefringence HR coatings
- } OCLI multiplayer dielectric design

Figure 1-7. Oscillator Isolation Issues Addressed

OPD due to segment piston corresponds to almost 15 waves RMS prior to phase conjugation



Residual OPD after phase conjugation reduced to less than 1/25 wave RMS

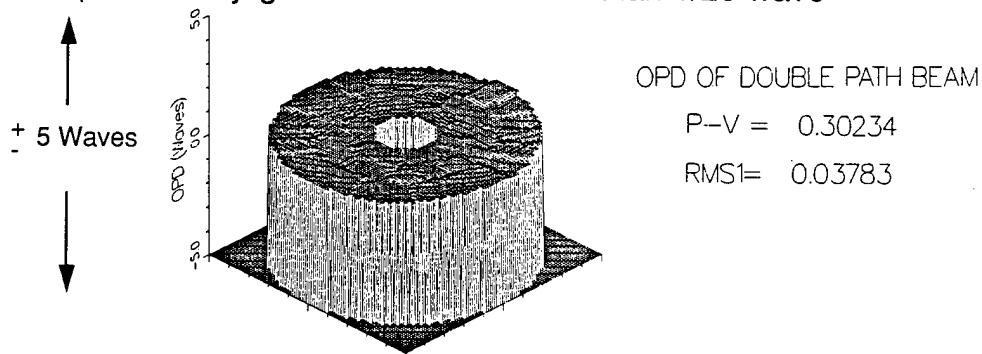
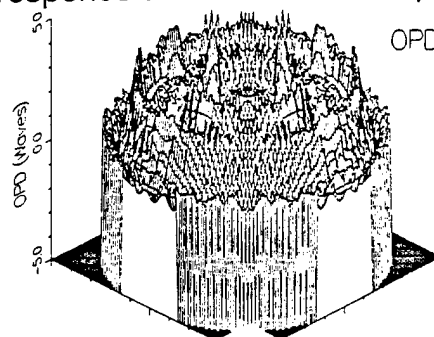


Figure 1-8. Conjugation Reduces Segment Piston Errors by Factor of 400

OPD due to segment misfigure corresponds to one wave RMS prior to phase conjugation

- Spectrum of disturbances extends over range .5 to 10 cycles per meter



OPD AT THE CONJUGATOR

P-V = 4.68691

RMS1= 0.97484

Residual OPD after phase conjugation reduced to approximately 1/35 wave RMS

OPD OF DOUBLE PATH BEAM

P-V = 0.13236

RMS1= 0.02858

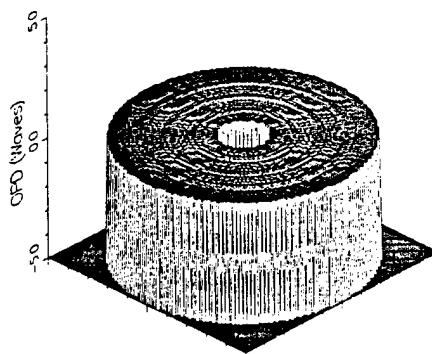


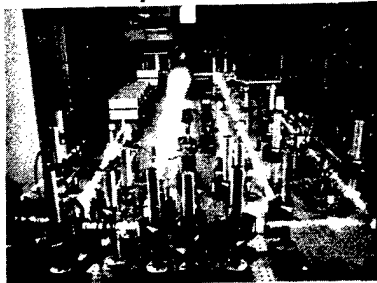
Figure 1-9. Conjugation Reduces Segment Misfigure Errors by Factor of 35 Over Range of Spatial Scales

potential for significant reduction in design, manufacturing, and control system tolerances afforded by the incorporation of nonlinear optics into the SBL design.

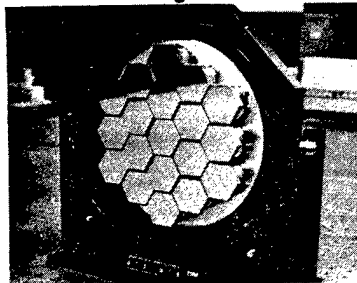
Experimental verification of the ability of SBS to correct piston and tilt misalignment errors in a multielement segmented optic was also provided. During this phase of the program, SBS conjugation experiments were conducted using a 19-element segmented mirror. Photographs of the hardware used and representative examples of results are shown in Figures 1-10 and 1-11. The segmented optic shown in Figure 1-10 consisted of 19 individual mirrors having exceptionally large (1000s of waves) random segment-to-segment piston misalignment, and segment tilts as large as three waves (RMS). Interferometry and far-field-intensity results shown in this figure demonstrate the dramatic effect phase conjugation has upon the optical performance of the mirror. Without phase conjugation, the near-field interferograms show the 19 segments acting independently of each other, with virtually no coherence between segments. The corresponding far-field-intensity distribution exhibits a very diffuse spot indicative of a highly aberrated beam. The effect that phase conjugation has on this picture is remarkable. Using SBS, the near-field phase distribution shows continuous fringes across the entire optic, indicating that all of the segments have been successfully cophased. Detailed measurements showed that this segment cophasing is accurate to better than  $1/25$  of a wave, even in the presence of large piston and tilt misalignment. The corresponding far-field-intensity map shows a tightly focused beam, with a peak intensity nearly 20 times that of the unconjugated case. Further verification of the ability of SBS to correct large piston displacements is shown in Figure 1-11. Here, the center segment of the array has been given a piston displacement so large (4500 waves) that it is visually observable. From the interferometric results one sees that without phase conjugation, the phase distributions of all of the segments (including the center segment) are randomly distributed. With SBS, however, phase continuity is observed across all of the segments, including the center segment which was grossly misaligned intentionally. These results demonstrate the versatility and wide dynamic range of the SBS process to correct exceptionally large

Test apparatus used 19-element segmented mirror

Test Facility



19-Element Segmented Mirror



- 1000's waves piston
- 3 waves tilt

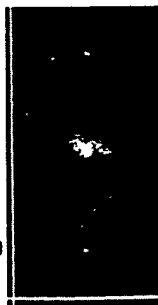
Cophasing to near diffraction limit demonstrated

Far Field Intensity

INCIDENT  
LASER  
BEAM

ABERRATED  
BEAM INTO  
SBS CELL

CONJUGATED  
BEAM



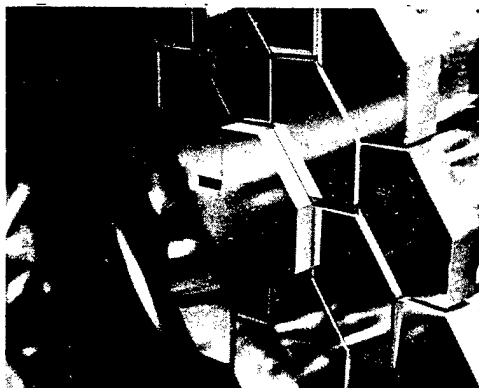
WITHOUT SBS



WITH SBS



Figure 1-10. Multielement Segmented Mirror Cophased Using SBS

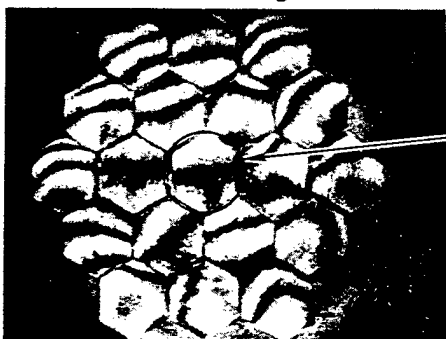


Segment intentionally misaligned by 4500 waves

- Large enough to be visually observable

Orders of magnitude relaxation in SBL alignment tolerances

**Gross Piston Misalignment Corrected to Near Diffraction Limit**



Intentionally  
Misaligned  
Segment

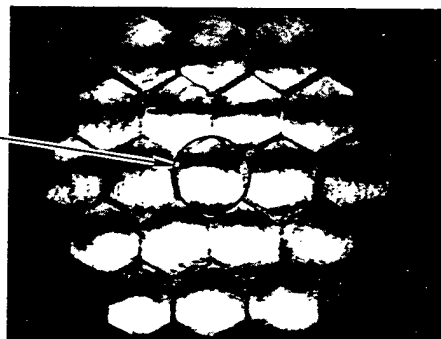


Figure 1-11. Thousands of Waves Segment Piston Corrected to Greater Than  $\lambda/20$  Using SBS Phase Conjugation

aberrations of the type to be encountered in a space based laser system using large segmented optics to levels near the diffraction limit.

### 1.3 SUMMARY

The APACHE program has made substantial progress in the development of both a design concept for a phase-conjugate space-based laser system, as well as providing technology support for the design. The design concept for the SBL employing SBS phase conjugation for aberration correction and beam combining has been developed to a mature state. A rigorous system engineering approach has been followed where system level requirements are tiered down to the major subsystems and assemblies, and detailed designs for all of these subsystems have been developed. As part of this design, technology issues for each of the subsystems were identified, and substantial experimental and theoretical effort was expended in addressing and resolving these issues. As result of this development effort, the SBS technology and its application to SBLs at this point can be considered to be in an advanced state and should no longer be considered a high-risk approach. All technology areas associated with the SBL design have been addressed, and significantly, no "show-stoppers" have been identified. In fact, for most cases, the implementation of phase conjugation not only improved performance but made design tasks easier. In the few areas where new subsystems or components are required, the design effort shows these new subsystems to be well within present day state of the art. Furthermore, the potential advantages of SBS envisioned at the start of the APACHE program to significantly relax optical tolerances and reduce overall cost, complexity, and technical risk have been born out under detailed scrutiny and quantitatively verified as part of an SBL system effectiveness studies conducted as part of the program.

At the present time, the basis for a phase conjugate SBL is well developed. Nearly all of the individual technology building blocks necessary to support the design of a phase conjugate SBL are reasonably complete. What is needed next is an integrated demonstration of all of the major components of the SBL concept at the highest power levels possible. This is the focus of the APEX program. Under APEX, a high-power CW phase-conjugation demonstration is being planned which will demonstrate in an

integrated fashion the coupling of a master oscillator with an amplifier, isolation optics, and a flowing SBS cell to demonstrate high aberration correctability using SBS with an HF chemical laser. Although still in the planning stages, subscale experiments are being planned which will support a high-power phase-conjugation experiment using either the ALPHA or MIRACL facilities as the laser source. This integrated experiment will provide the technical basis to support decisions regarding the future applications of this technology for strategic defense.

#### 1.4 FINAL REPORT ORGANIZATION

The presentation of the APACHE final report is divided into two separate volumes. In Volume I, the technology basis for the SBL design concept is presented. This is organized as follows:

<u>Section</u>	<u>Subject</u>
1	Introduction
2	CW SBS Conjugation Experiments and Analysis
3	HF Phase Conjugation Experiments and Analysis
4	Flowing SBS Cell Experiments and Analysis
5	Segmented Array Conjugation Experiments
6	Oscillator Isolation Experiments and Analysis
7	ALPHA-VM Isolation Experiments
8	PAR Pulse Stretching Experiments
9	Bidirectional Amplifier Experiment Design
10	Xenon Absorption Experiments

Volume II is devoted to a description of the SBL design concept and a discussion of the models developed to support the design. Also presented in Volume II is a discussion of the cost, weight, and resiliency analysis performed to quantitatively assess the system effectiveness of the APACHE SBL design concept, relative to that of an approach employing adaptive optics. Volume II is organized as follows:



<u>Section</u>	<u>Subject</u>
1	Introduction
2	APACHE SBL Requirements and Conceptual Design
3	Optical Modeling and Analysis
4	System Engineering Model Description
5	System Effectiveness Study

In the interest of keeping this document unclassified, all classified information has been deleted from Volumes I and II. In most cases, these data are simply specified as "XXX." A classified addendum to this final report contains all of the classified information deleted from the present document.

## 2. CW CONJUGATION EXPERIMENT

### 2.1 INTRODUCTION

The CW conjugation scaling (CWCS) experiments were designed to address several critical SBL issues. The SBL must operate for times long compared to the phonon rise time where competing processes may degrade the conjugation fidelity and reflectivity. For pulse lengths that are many hundreds of phonon lifetimes, the competing nonlinear processes include near-forward SBS, thermal blooming, and self-focusing. Since the SBL design approach includes flowing the SBS medium to eliminate these competing processes, one major objective of the CWCS experiment was to assess the effects of the CW SBS process on conjugation reflectivity and fidelity under conditions simulating the SBL flow. The CW technical concerns include definition of minimum SBS medium flow velocity that will eliminate competing processes and the maximum permitted before phonon grating convection degrades conjugation fidelity.

The technical issues addressed by this experiment can be divided into four main categories; SBS threshold, reflectivity and fidelity, near-forward SBS, SBS grating convection, and thermal blooming. Heating effects such as thermal blooming associated with absorption in the SBS medium can lead to transient SBS degradation. This sets SBL system requirements for minimum flow velocity of the SBS medium and the SBS medium (Xe) purity. The experimental approach to examine thermal blooming included introduction of a known absorber to simulate contamination in the SBL Xe cell and suppression of thermal blooming by scanning the focal spot across the medium to simulate flowing cell conditions. Also, a subscale experiment was performed as described in Section 10 to measure the Xe absorption at  $2.9 \mu\text{m}$ .

Although near-forward SBS develops on a slower time scale than backscattered SBS, it can compete for gain with backscattered SBS for sufficiently long pulse lengths. In the SBL this causes a loss in conjugated power and transient power fluctuations. To our knowledge, the longest previously reported pulse lengths for SBS scattering in the focused configuration are in the 1 to 5  $\mu\text{s}$  regime with  $\tau/\tau_{\text{PH}} = 50$  (References 2-1

through 2-5). We performed experiments at  $1.053 \mu\text{m}$  in high-pressure Xe with very long pulse lengths (typically,  $250 \mu\text{s}$  or  $\tau/\tau_{\text{PH}} = 6757$  and up to  $350 \mu\text{s}$  or  $\tau/\tau_{\text{PH}} = 9460$ ) and high pulse energy (typically  $50 \text{ J}$  or  $P/P_{\text{TH}} = 5$ , and up to  $80 \text{ J}$ ). Diagnostics were included to look for forward SBS under these long pulse conditions. Also, a transient SBS model was developed and is described in Section 2.4.

The SBL design includes a segmented primary mirror and several amplifiers to be combined to deliver a single beam on target. System brightness is a function of SBS fidelity and reflectivity which may depend on the type of aberration. Also, SBL system size and component fluences depend on SBS threshold. Thus, SBS threshold, fidelity, and reflectivity for typical SBL aberrations and the SBS capability to coherently couple multiple beams are issues addressed by the CWCS experiment. A random piston aberrator simulates the segmented beam director and beam combination is simulated with a wedge (tilt) aberrator. Power scaling is used to measure threshold. BRIWON model validation is presented in Section 2.4.

SBS grating convection is an issue that results from the requirement to flow the SBS medium to suppress thermal blooming and near-forward SBS. While relative motion should be able to suppress all competing effects with lifetime sufficiently larger than that for backward SBS, the relative motion may itself distort the conjugation fidelity. If the relative motion between the beam and the medium is fast compared to the phonon lifetime, the convection of the phonon grating past the beam produces reduced SBS reflectivity and a tilt in the Stokes beam relative to the pump. Specifically, grating convection may produce tilt in the return beam which can affect target pointing in the SBL. In the CWCS experiment a rotating mirror simulates the flowing SBS medium by scanning the beam across the focal region. Conjugation fidelity, reflectivity and tilt are measured as a function of scan speed. The experiment data is used to validate the BRIWON code as described in Section 2.4.

A description of the experiment is given in Section 2.2 and includes the laser facility and operation, optical layout and diagnostics, and rotating mirror configuration. The experimental results are presented in Section 2.3 for threshold measurement, conjugation fidelity, and

reflectivity under unaberrated and aberrated beam conditions, with and without beam scanning. Thermal blooming experiment results are presented in Section 2.3.5. Detailed discussions of the analyses including comparisons with BRIWON are given in Section 2.4. A brief summary of the most significant results is given in Section 2.5.

## 2.2 EXPERIMENT DESCRIPTION

Until the CWCS experiment, most SBS research had been performed in the short pulse regime. We have extended this research into the long pulse regime. This required sufficiently high power to reach SBS threshold and elimination of competing long pulse processes.

### 2.2.1 KMS Laser Facility and Operation

The Chroma laser fusion device at KMS Fusion, Ann Arbor, Michigan, is a Nd:YLF laser,  $1.053 \mu\text{m}$ . It supplied high power and long pulses typically  $250 \mu\text{s}$ . Pulse lengths of  $420 \mu\text{s}$ , i.e.,  $10^4$  times the phonon lifetime in Xe at 40 atm, are possible. Figure 2.2-1 shows the laser device. It consists of five rod amplifiers and eight disk amplifiers of which a maximum of five was used to supply 300 J to the TRW experiment. Typically, 50 J (200 kW or five times threshold) and up to 80 J were actually delivered to the SBS cell. Total gain for the laser system was  $10^9$ . The output polarization was linear at  $45^\circ$ . Permanent magnet and pulsed Faraday rotators were used to provide sufficient oscillator isolation. An acousto-optic modulator with a feedback diode adjusted the Q of the oscillator to generate different pulse shapes as shown in Figure 2.2-2. Square pulse shapes with less than 1% pulse ripple were most commonly used and triangular pulses were used for energy scaling studies. Threshold was obtained from a single shot with a triangular pulse or from the transmitted beam power. Mode structure was single axial mode and the beam size delivered to the TRW/KMS interface was 12.8 cm.

The beam quality of the laser was good and varied from 1.1 to 1.5 times diffraction limit. Figure 2.2-3 illustrates typical far field spots. There is little high-frequency structure in the far field. Also, the incident beam rms OPD is less than 0.09 waves, Figure 2.2-4, and the laser wavefront exhibits very little temporal variation, Figure 2.2-5, as measured by a lateral shearing interferometer and fast framing camera.

### 2.2.2 Layout of Optical Train and Diagnostics

The optical train and diagnostics are shown in Figure 2.2-6. A 4:1 reducing telescope gave a 3.2 cm beam at the beginning of the optical train. The beam was reduced further to 1.92 cm by a limiting iris placed

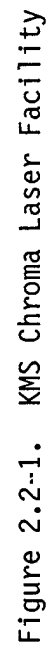


Figure 2.2-1. KMS Chroma Laser Facility

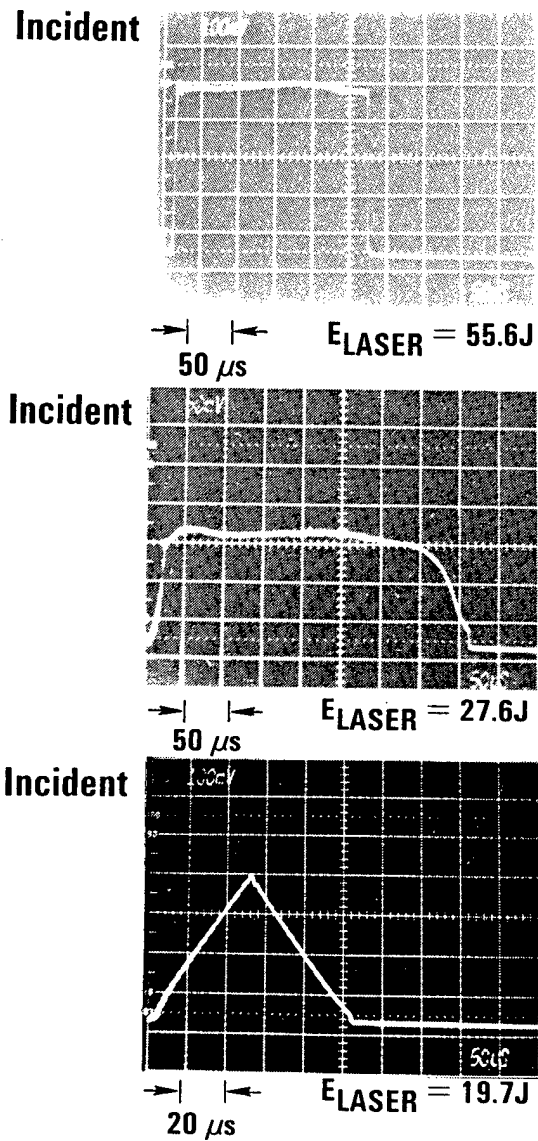


Figure 2.2-2. Pulse Shapes From Chroma Laser Used in CWCS Experiment

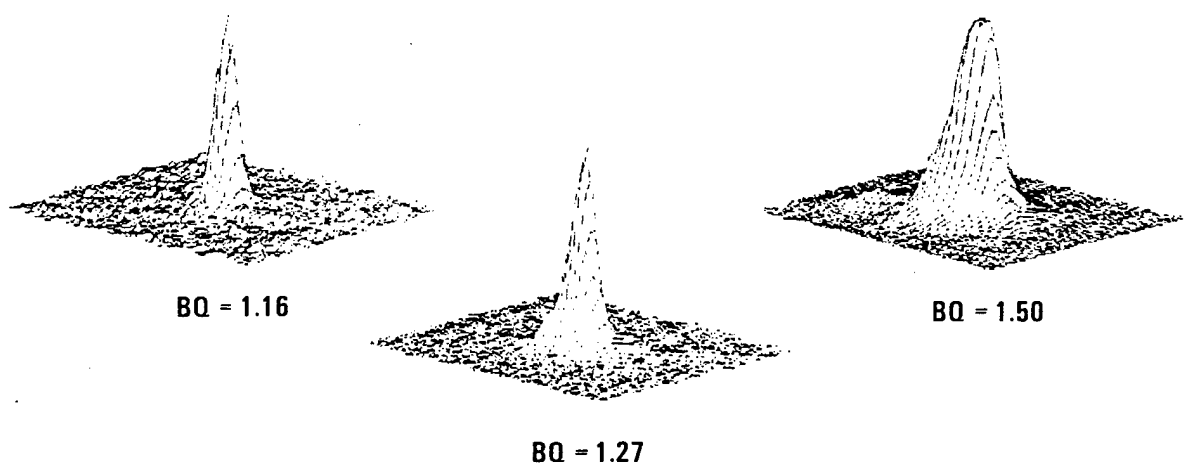


Figure 2.2-3. Far-Field Intensity Distributions for KMS Laser Beam



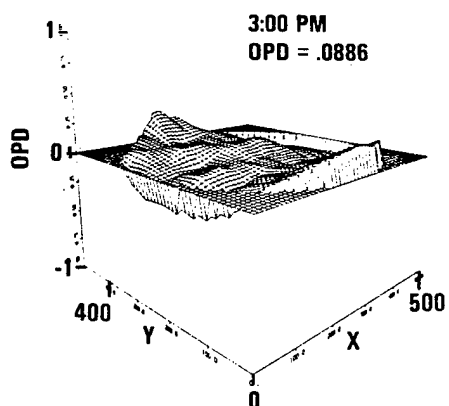
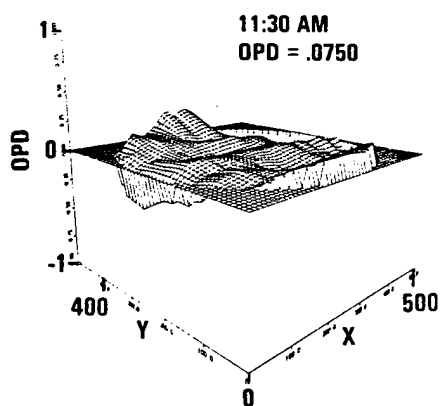
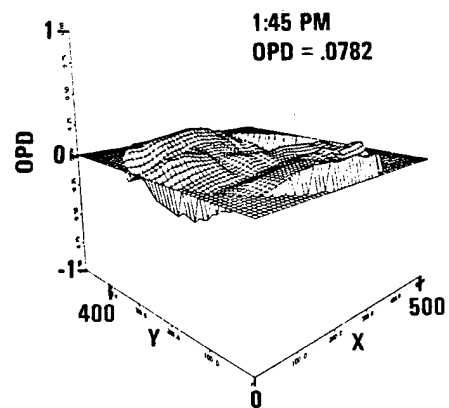
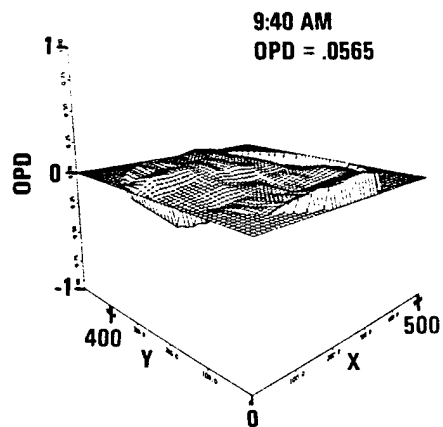


Figure 2.2-4. Incident Laser Beam Wavefront

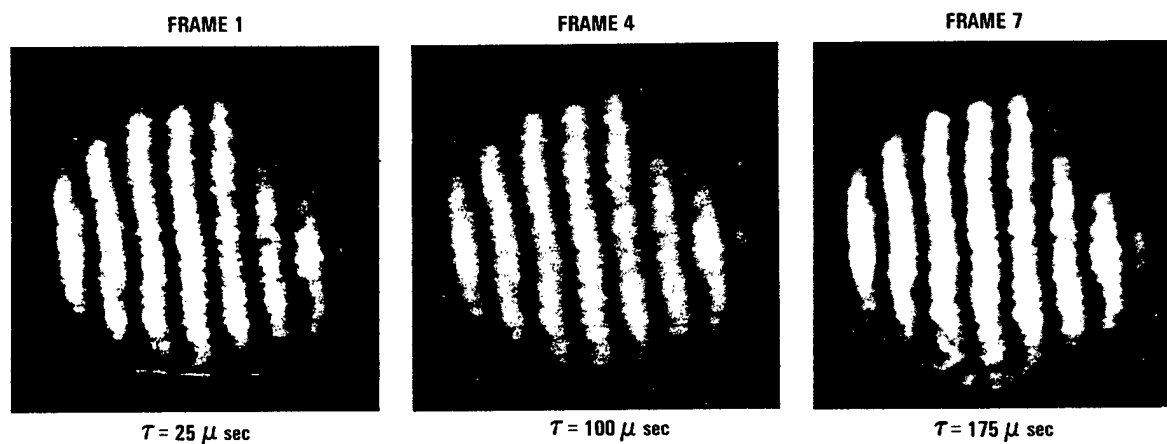


Figure 2.2-5. Lateral Shearing Interferograms of Incident KMS Laser Beam Recorded by Fast-Framing Camera

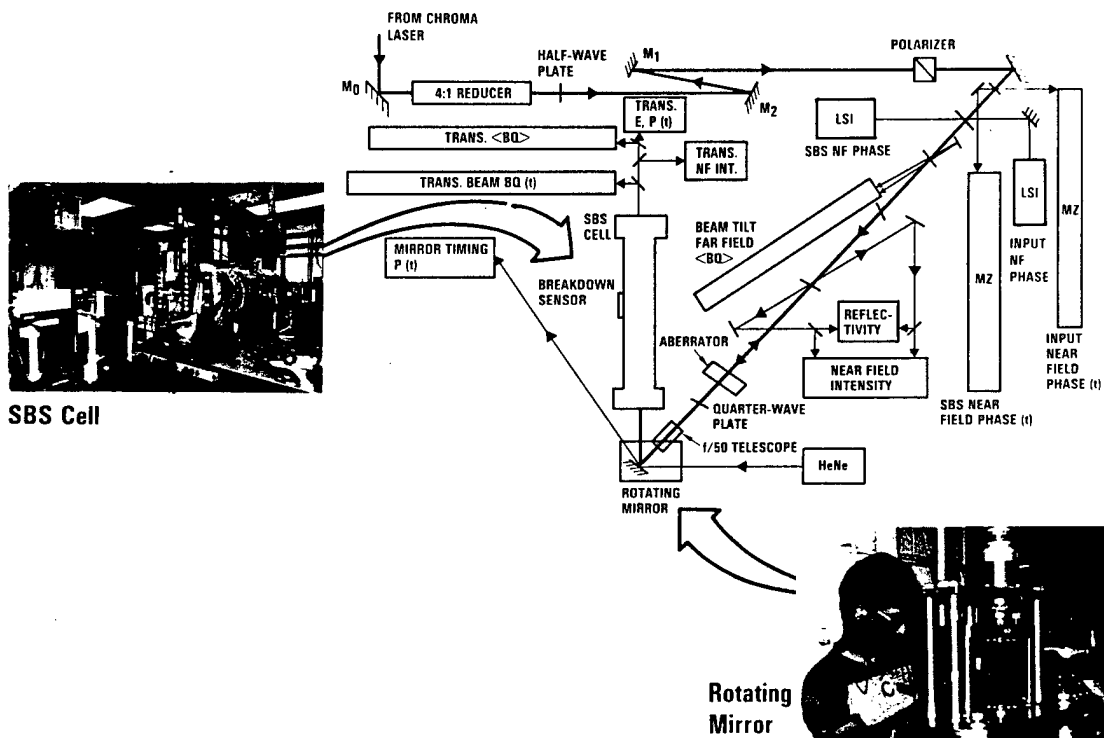


Figure 2.2-6. CW Conjugation Scaling Experiment Optical Train and Diagnostics

before the linear polarizer. The power from the laser was kept constant and the power into the SBS cell was controlled using a half-wave plate and polarizer in the main optical train. Angles of incidence for all beamsplitters were less than  $20^\circ$  to preserve both s and p polarization reflectivities. The figure of most of the optics was approximately 0.1 waves peak to valley at HeNe wavelength. The linear polarizer and quarter wave plate supplied circular polarization to the SBS cell and provided additional isolation of the laser from the SBS return beam. An F/50 focusing telescope gave a  $128\text{-}\mu\text{m}$  diffraction limited spot diameter at the center of the SBS cell, which is approximately 6 ft long. Plexiglass shields over the optical benches provided some thermal isolation.

We characterized the incident, return, and transmitted beams to obtain data on near field intensity and phase, beam quality, pulse shape, and energy. Two self-referencing Mach Zehnder interferometers with either CCD cameras or the fast framing camera, as well as a lateral shearing interferometer with a fast framing camera for time resolution within a pulse were used to measure near field phase of the incident and return beams. The fast framing camera can record an image every  $25\text{ }\mu\text{s}$  for an exposure time of approximately  $3\text{ }\mu\text{s}$ . Each CCD camera has a  $6 \times 8\text{ mm}$  array with  $23\text{-}\mu\text{m}$  horizontal and  $13.4\text{-}\mu\text{m}$  vertical center to center pixel separation, and pixel size of  $12 \times 13.4\text{ }\mu\text{m}$ . The data collected on the array was captured by a framegrabber and transferred to an IBM AT computer where it was processed. Time integrated beam quality was measured for incident and SBS return beams simultaneously on the same CCD camera. This diagnostic was also used to measure far-field displacement introduced by grating convection.

Incident, return and transmitted energies and power as a function of time were monitored for every shot with fast photodiodes. To provide fast time response, small area silicon photodiodes were used with a +45 V bias,  $50\text{ }\Omega$  scope termination and Tektronics 7104 oscilloscope. With this configuration the rise time was approximately 1 ns. An additional photodiode was placed exterior to a viewing window in the center of the SBS cell to monitor potential breakdown problems.

The SBS cell is a long, cylindrical pressure vessel capable of containing Xe up to 40 atm pressure. A sketch of the cell is shown in Figure 2.2-7. The cell has fused silica windows at both ends. Pneumatically actuated safety windows cover the quartz windows between shots. The windows are designed with a fluence safety factor of 7.5. The cell has a recirculation loop to suppress free convection OPD and to speed thermal equilibration after cryopumping.

A schematic of the SBS cell fill/drain system is shown in Figure 2.2-8. This system enables leak testing, cell evacuation and cryopumping of Xe for transfer to the cell or back into the bottles. An absorber may also be added to the cell through this system before it is pressurized with Xe.

### 2.2.3 Rotating Mirror Description and Operation

A key feature of the experiment was the rotating mirror which scanned the beam through the SBS medium to simulate a flowing cell. A schematic of the rotating mirror is shown in Figure 2.2-9. The mirror was configured for minimum surface distortion caused by assembly and rotation. It was enclosed in a vacuum chamber to eliminate OPD effects from air turbulence. The mirror could scan from focal velocities of 2 m/s up to 670 m/s. The typical focal speed ranged from 2.4 to 155 m/s.

Timing of the mirror was critical to keep the scanned beam within the SBS cell and was monitored continuously with a helium neon beam, photodiode and remote oscilloscope trace. Encoders on the motor provide redundant mirror position information to backup HeNe beam/photodiode signals. A sketch of the oscilloscope method of mirror position control is shown in Figure 2.2-10. The motor speed was controlled manually. The operator displayed the master clock and photodiode pulses on the oscilloscope and adjusted the time delay between pulses using the indexer. A counter was added in the clock pulse line to permit low speed operation.

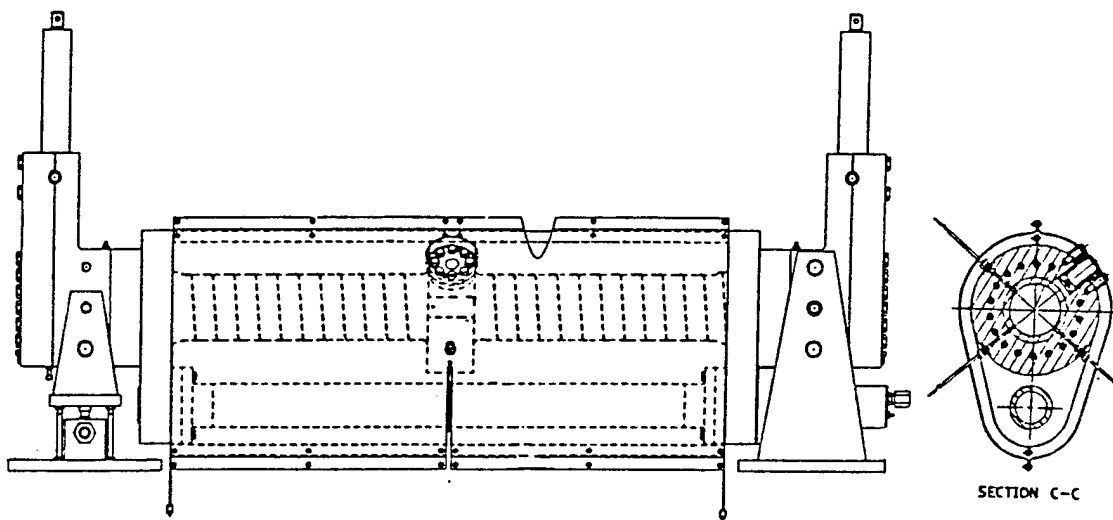


Figure 2.2-7. CW Conjugation Scaling Experiment  
High-Pressure Xe SBS Cell

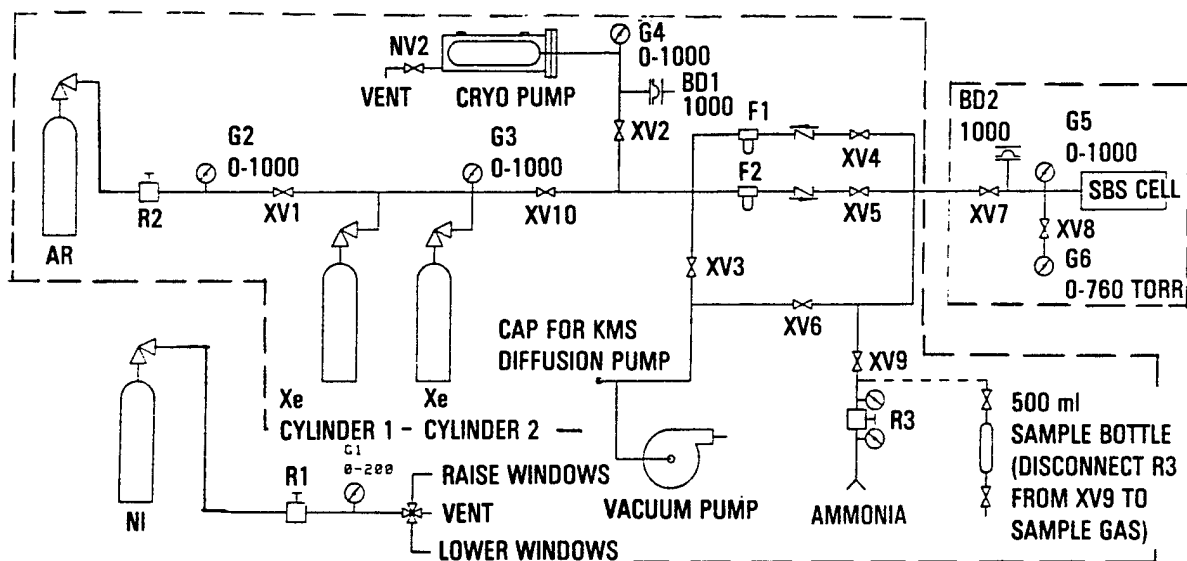


Figure 2.2-8. CWCS Experiment SBS Cell Fill/Drain System Schematic

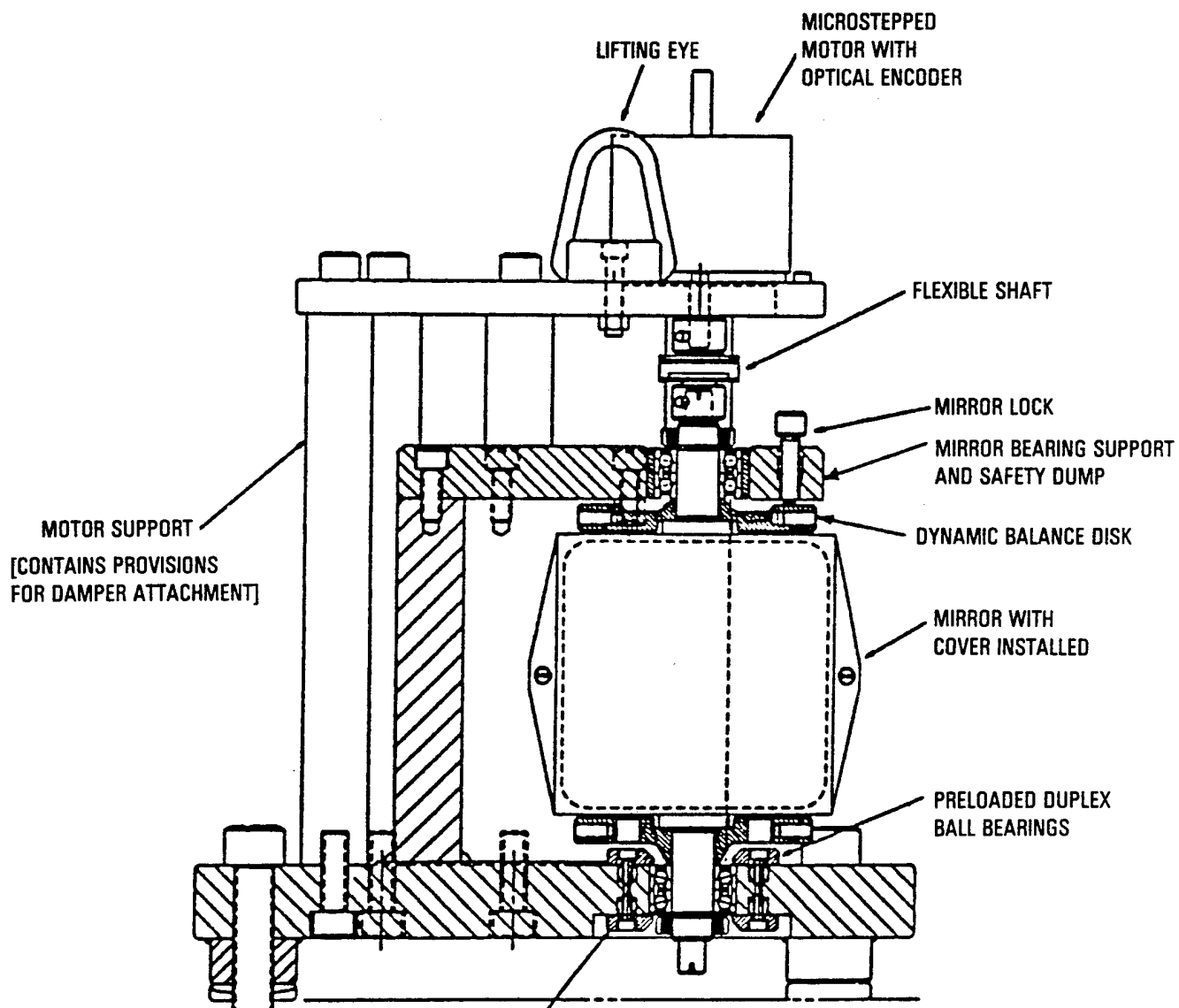


Figure 2.2-9. CWCS Experiment Rotating Mirror Schematic



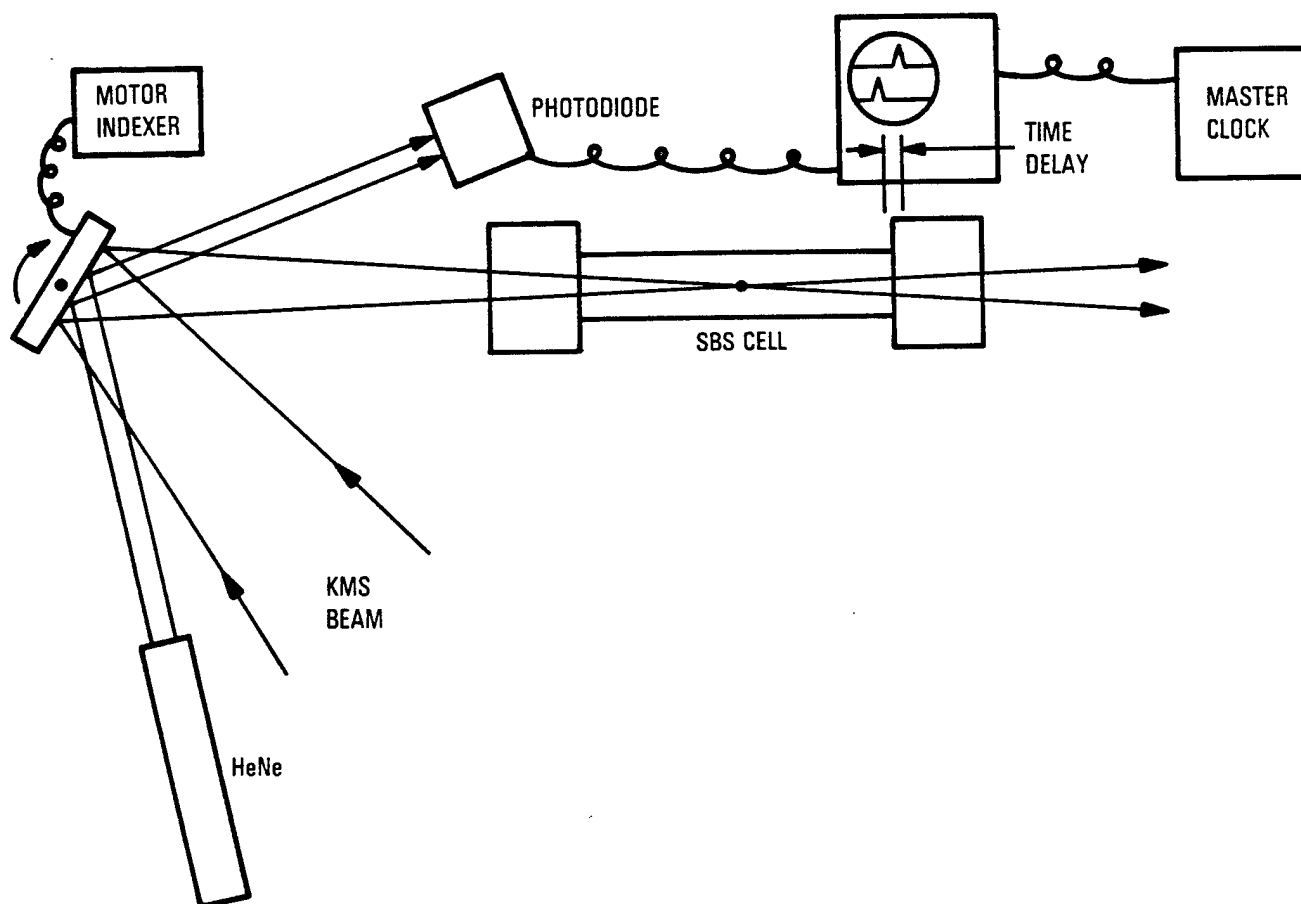


Figure 2.2-10. Oscilloscope Method of Rotating Mirror Position Control

## 2.3 EXPERIMENTAL RESULTS

The initial test series, presented in Section 2.3.1, characterized the SBS reflectivity under long pulse conditions, measured threshold, and looked for competing effects. Conjugation fidelity data without an aberrator with and without beam scanning are discussed in Section 2.3.2. Sections 2.3.3 and 2.3.4 present data for aberrated beams with and without scanning, and thermal blooming data are presented in Section 2.3.5.

### 2.3.1 SBS Reflectivity and Threshold Determination

Because the SBL must operate for times long compared to the phonon rise time, these experiments addressed the effects of long pulse operation on reflectivity, conjugation fidelity and competing effects. Most experiments were conducted with a pulse length of 250  $\mu$ s (7000 phonon lifetimes). For no aberrator and static test conditions SBS stayed on for 250  $\mu$ s as shown in Figure 2.3-1. The transmitted beam was clamped at threshold and the phase conjugate beam tracked the incident beam profile. No power fluctuations were seen in the SBS return beam, even with detectors capable of resolving 1 ns fluctuations. Reflectivity was approximately 50% for the pulse duration. For a few tests, the incident laser pulse was extended to approximately 420  $\mu$ s. As shown in Figure 2.3-2, it conjugated for 350  $\mu$ s or 104 phonon lifetimes with constant reflectivity of 250%.

No near-forward SBS, NFSBS, was present for these long pulse experiments in Xe. The near field intensity of the transmitted beam was monitored and is shown in Figure 2.3-3. The angle at which near-forward scatter first appears is predicted to be approximately  $0.5$  to  $1.0 \times 1/F\#$ , where  $F\#$  is the f-number for focusing the pump into the SBS cell. The camera field of view was twice that necessary to see the ring structure associated with NFSBS. Based on simple theory as described in Section 2.4 the expected turn on time is 60 to 100  $\mu$ s for  $F/50$  at 1.05  $\mu$ m in 40 atm Xe (Reference 2-6). However, NFSBS was not observed for pulses as long as 350  $\mu$ s. A more complex theory suggests that small changes in temperature and pressure cause speed of sound variations and lower the total integrated gain for NFSBS. Thus, NFSBS is difficult to observe and easily suppressed in Xe in contrast to liquid SBS media which are more favorable for forward scattering experiments. Detailed analysis of forward scattering is presented in Section 2.4.

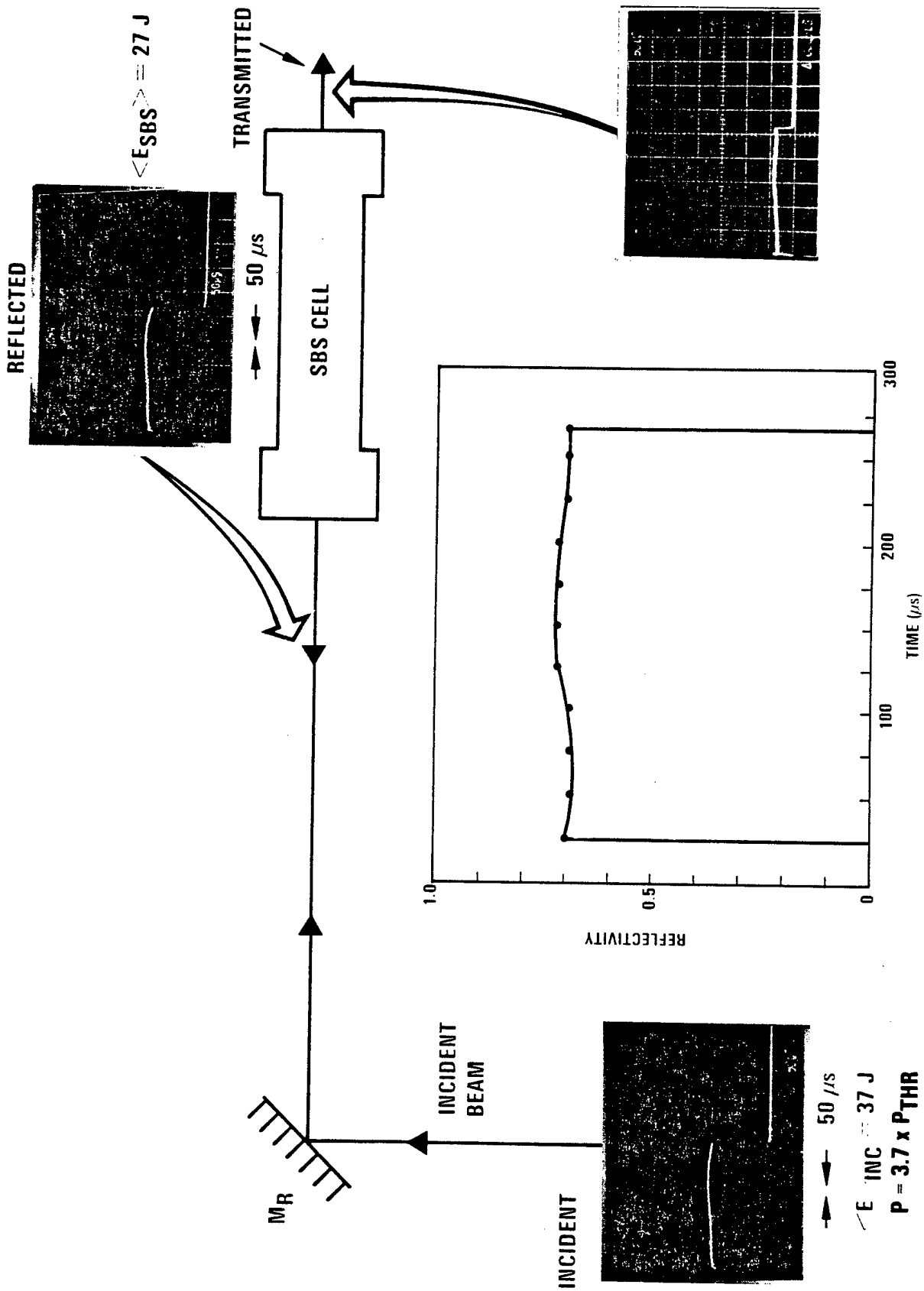


Figure 2.3-1. Reflectivity Versus Time Unaberrated Beam

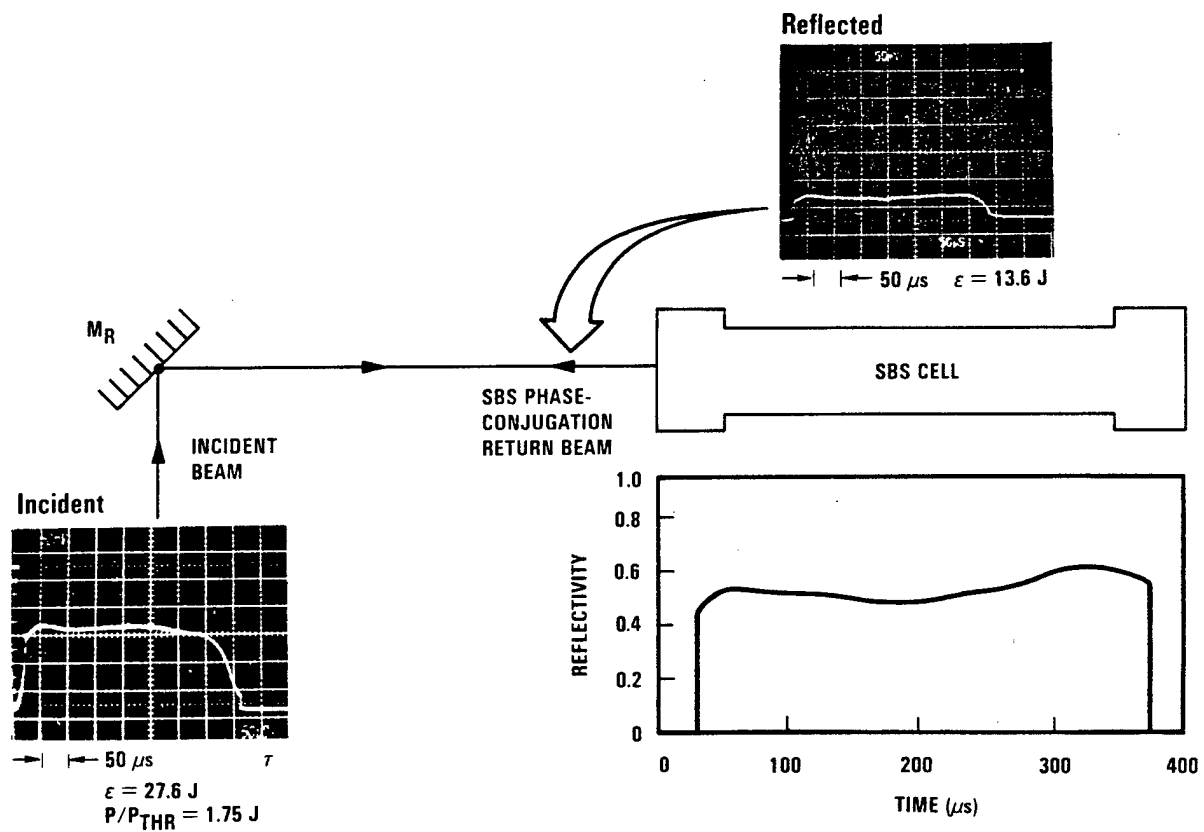


Figure 2.3-2. Long Pulse Reflectivity Versus Time

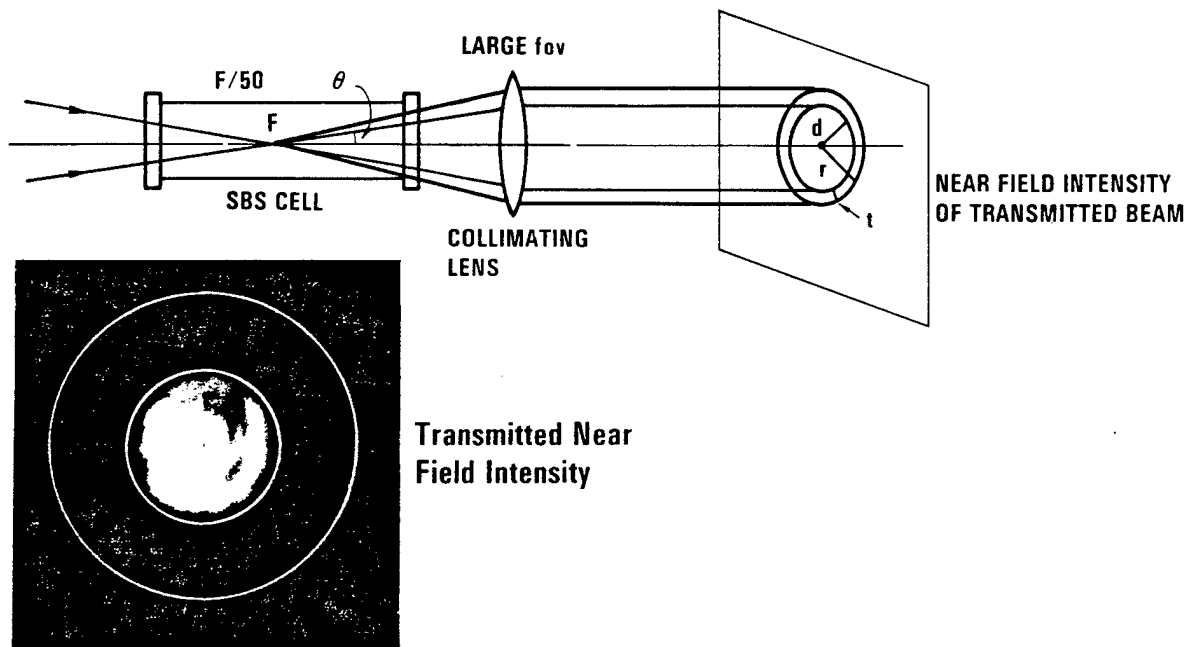


Figure 2.3-3. Near-Field Intensity of Transmitted Beam Under Long Pulse Conditions

Threshold was determined for no aberrator and static focal spot conditions. A triangular pulse shape was used to determine threshold with a single shot. Figure 2.3-4 illustrates the incident, reflected and transmitted pulses used to determine threshold. The SBS threshold is approximately 40 kW and the slope efficiency is 0.87. The transmitted beam is clamped at threshold.

Reflectivity is plotted as a function of incident power in Figure 2.3-5. Theoretical BRIWON code calculations predicted a threshold of approximately 29 kW for a diffraction limited beam at  $1.053 \mu\text{m}$ . Beam quality for the experimental threshold value of 40 kW was  $1.4 \pm 0.1$ . The measured threshold is consistent with the prediction if it is assumed that threshold scales approximately as beam quality to the first power for the low spatial frequency aberrations present in the input beam. If we scale threshold with wavelength, this implies an SBS threshold at  $2.8 \mu\text{m}$  of 77 kW for a diffraction-limited beam.

The SBS reflectivity was also studied while scanning the focal spot across the SBS medium for speeds of 0 to 155 m/s. High scan speeds were achieved with no significant degradation of SBS reflectivity. There was only a slight drop in SBS reflectivity apparent at the highest scan speed of 155 m/s as illustrated in Figure 2.3-6. As discussed in Section 2.3.5, this scan speed is at least 65 times that needed to suppress thermal blooming. Code calculations agree well with experimental data. A high-frequency "hash" on the SBS return was always present when scanning and may be the result of the same medium inhomogeneities that inhibited near forward SBS.

#### 2.3.2 Conjugation Fidelity for No Aberrator, Static, and Scanning Test Conditions

Conjugation fidelity was measured for a typical long pulse of  $250 \mu\text{s}$  with no aberrator under static and scanning test conditions. Time integrated beam quality, and time integrated and time resolved interferometric measurements of the incident and SBS return beams were made.

Excellent conjugation fidelity was observed for the unaberrated beam as shown in Figure 2.3-7. The time-integrated beam quality of the incident

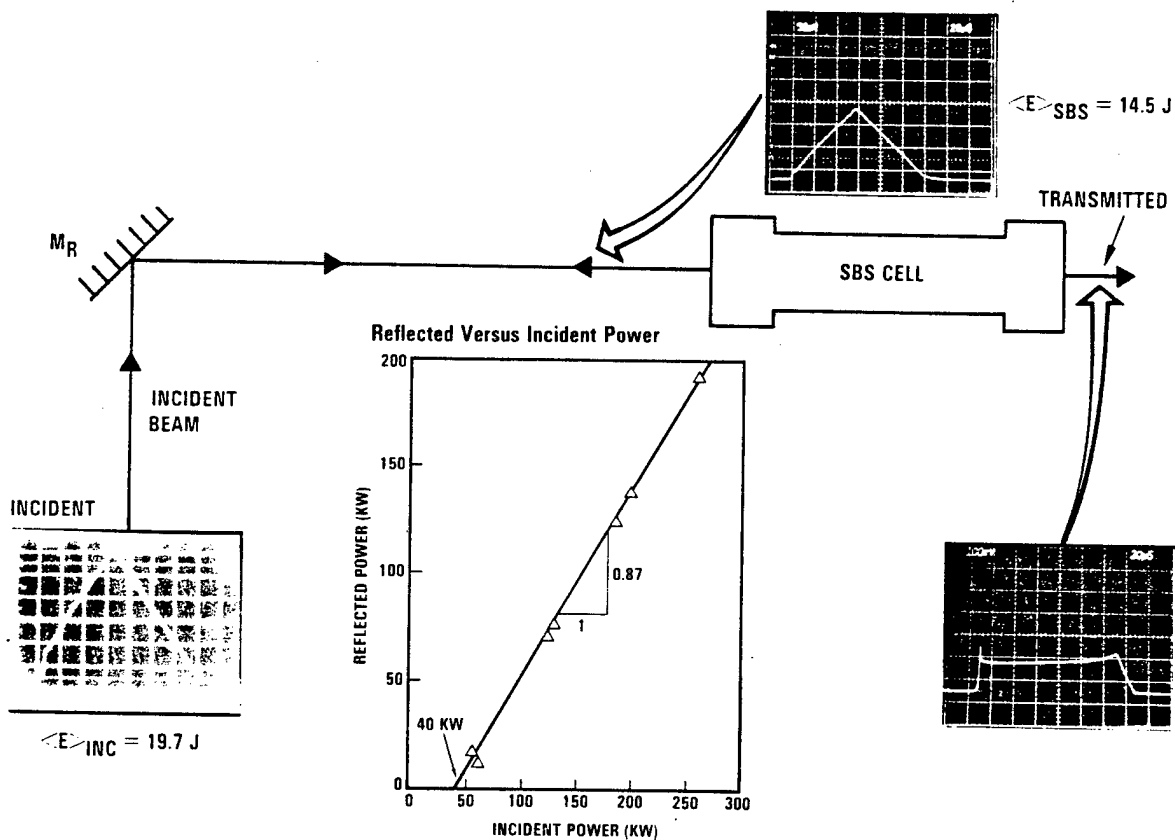


Figure 2.3-4. Reflected Versus Incident Power (Threshold) for No Aberrator, Static Focal Spot

$E_{\text{LASER}} = 19.7 \text{ J}$

$E_{\text{SBS}} = 14.5 \text{ J}$

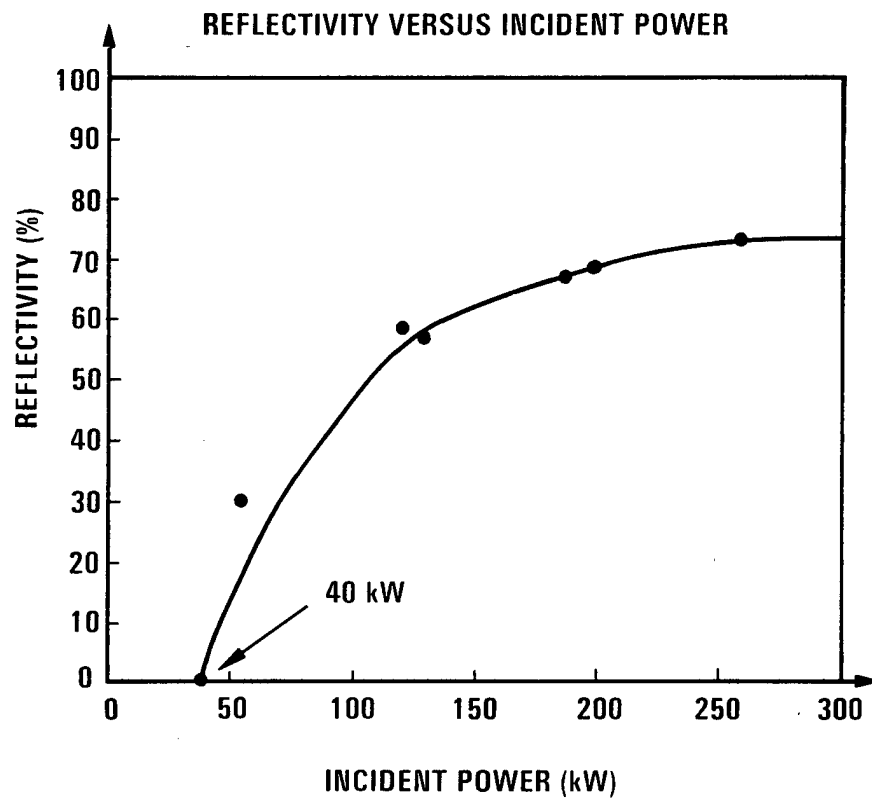
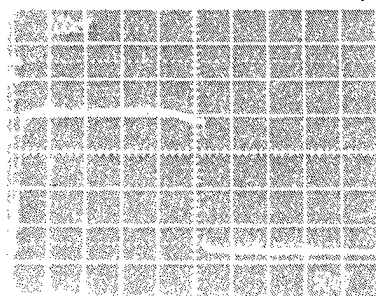
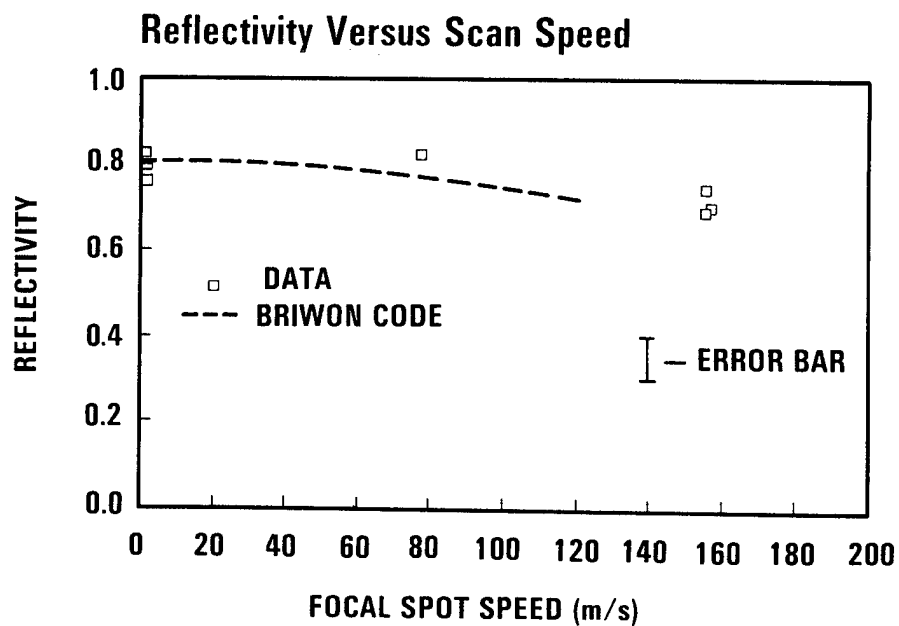
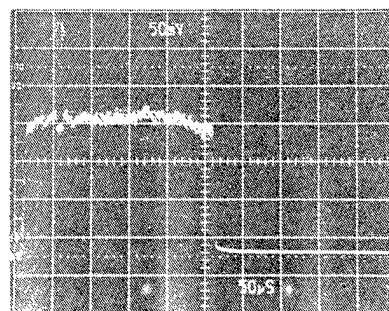


Figure 2.3-5. Reflectivity Versus Incident Power for No Aberrator, Static Focal Spot





**Incident 155 m/s**



**Reflected 155 m/s**

Figure 2.3-6. Experimental Results and BRIWON Theoretical Calculations of Reflectivity Versus Scan Speed for No Aberrator, 0 to 155 m/s Scan Speed

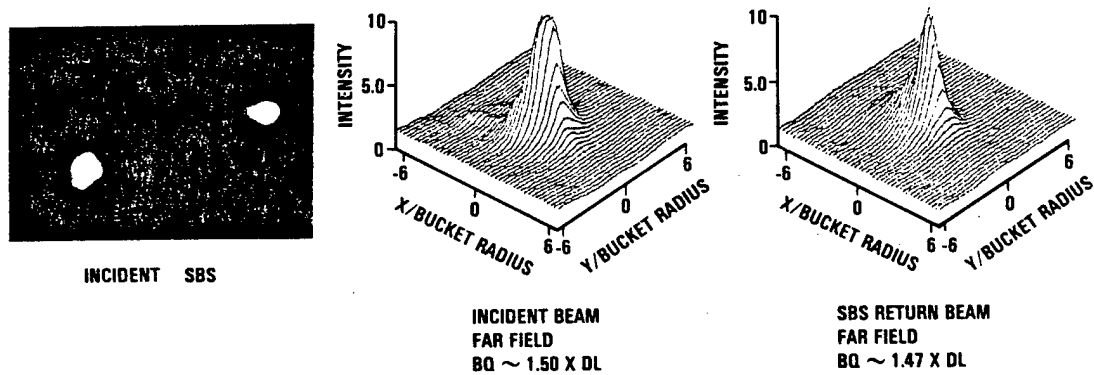


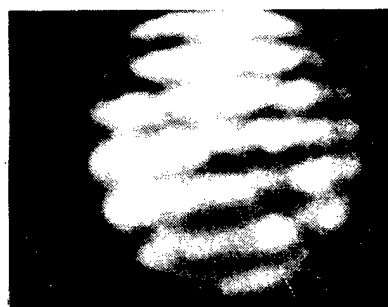
Figure 2.3-7. Conjugation Fidelity as Measured by Far-Field Beam-Quality Diagnostic for No Aberrator, Static Focal Spot

and return beams is the same within experimental measurement capability. Figure 2.3-8 shows the time-integrated near-field phase of the incident and return beam and indicates good conjugation fidelity. The incident beam and SBS return beam rms OPDs are  $0.1083 \pm 0.02$  and  $0.1176 \pm 0.02$  waves, respectively, and are the same within measurement capability. Fringe analysis of the interferograms was performed using TRW software FGRID. The software can measure fringes to within 0.0218 rms waves (1.01 BQ) as determined by digitizing an ideal plane wave pattern, i.e., straight fringes. Also, the incident and SBS Mach Zehnders were designed with identical optics specified at 0.10 waves peak to valley at HeNe to limit the residual beam-quality error between the two interferometers. Time resolved near-field phase of the SBS return beam was recorded by a lateral shearing interferometer and fast framing camera; three time slices are shown in Figure 2.3-9. The SBS reflected wavefront exhibits very little temporal variation over the typical 250- $\mu$ s pulse duration.

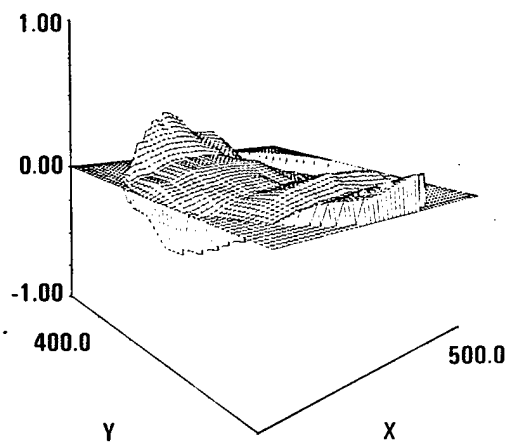
As described previously in Section 2.3.1, good reflectivity was observed for the maximum focal spot scan speed of 155 m/s. Good conjugation fidelity was also observed for an unaberrated beam at the 155 m/s scan rate. Figure 2.3-10 shows the time integrated far-field beam quality of the incident and SBS return beams. The beam quality is the same within experimental error. No deleterious effects from beam scanning were observed. However, one result of scanning the across the medium was to induce a slight tilt in the far field. Thus, while scanning fast enough to eliminate the effects of competing processes, one must scan slow enough to avoid the effects of grating convection, i.e., tilt in the far field. Far-field beam tilt versus focal spot scan speed is plotted in Figure 2.3-11 as well as BRIWON code predictions. For the fastest speed, 155 m/s, the far-field tilt was typically on the order of one diffraction limited spot size and would be an order of magnitude less for the slowest scan speed, 2.4 m/s. BRIWON code calculations predicted the tilt in the far field with a negligible change in the far-field beam quality with scanning. Code results in Figure 2.3-12 show the far-field intensity of the pump input and SBS return, no aberrator, for no scanning versus scanning at 100 m/s. Figure 2.3-13 a near-field phase shift predicted by BRIWON which is exhibited as displacement in the far-field. Detailed analysis of the effects of grating convection are presented in Section 2.4.



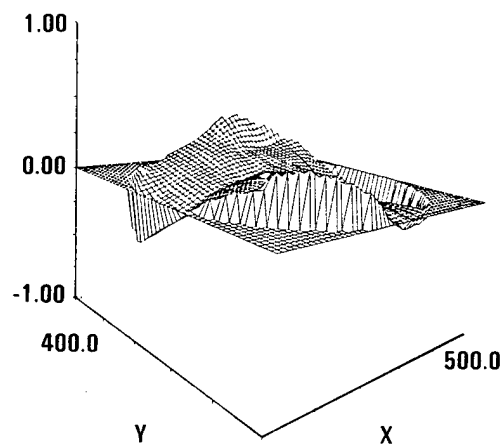
**Incident Interferogram**



**SBS Interferogram**



**(OPD) rms 0.1083 waves**



**(OPD) rms - 0.1176 waves**

**Figure 2.3-8. Time-Integrated Near-Field Phase of Incident and SBS Return Beams for No Aberrator, Static Focal Spot**

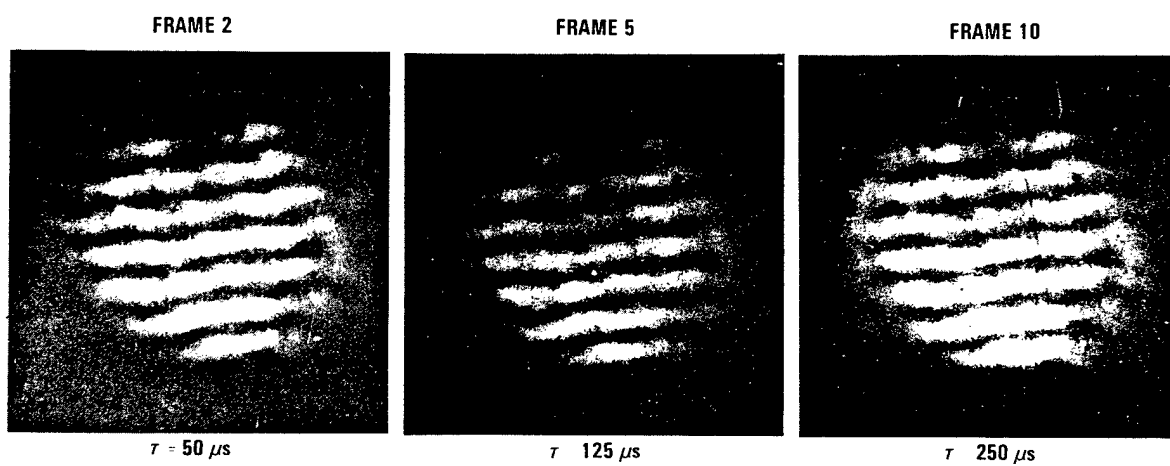
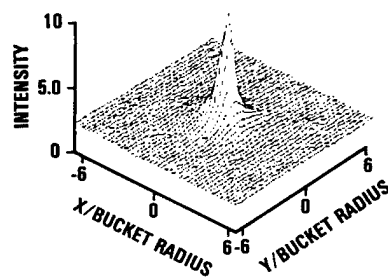


Figure 2.3-9. Time-Resolved Near-Field Phase of SBS Return Beam  
for No Aberrator, Static Focal Spot

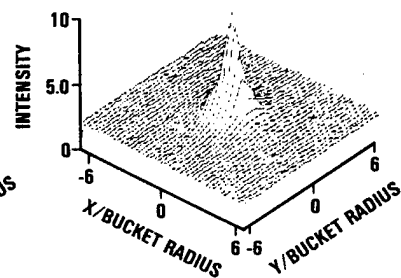


INCIDENT

SBS



INCIDENT BEAM  
FAR FIELD  
BQ ~ 1.4



SBS RETURN BEAM  
FAR FIELD  
DQ ~ 1.37

Figure 2.3-10. Time-Integrated Far-Field Intensity Distribution of Incident and SBS Return Beams for no Aberrator, 155 m/s Focal Spot Velocity

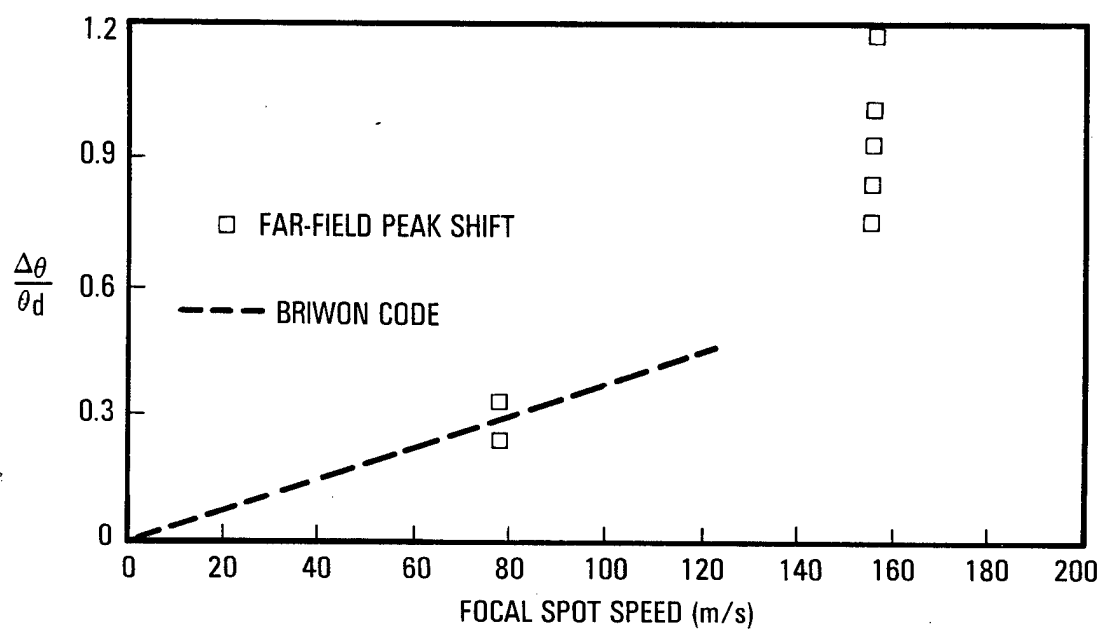


Figure 2.3-11. Experimental and BRIWON Theoretical Far-Field Beam Tilt Versus Focal Spot Scan Speed

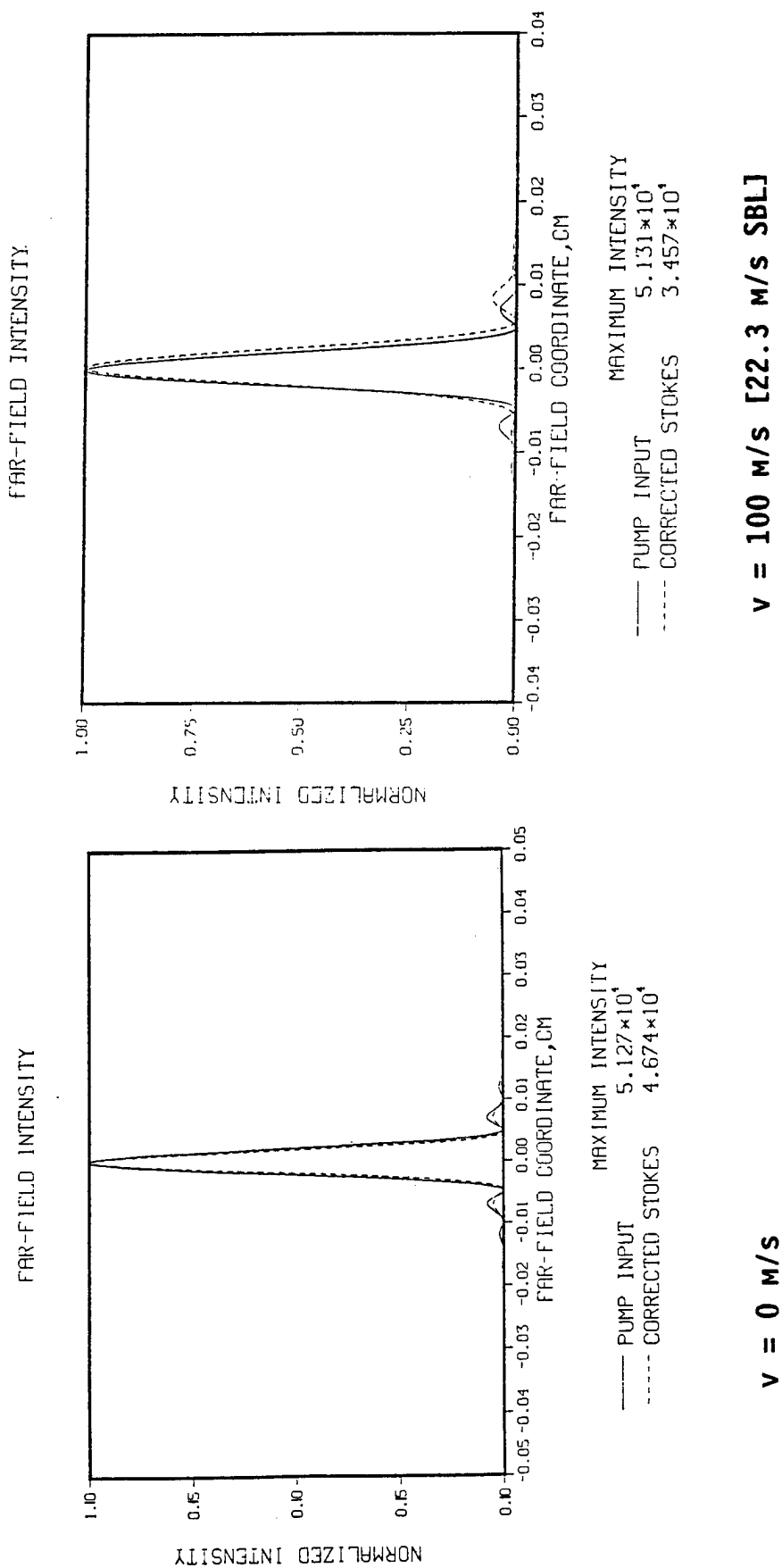


Figure 2.3-12. BRIWON Code Calculations of Far-Field Intensity for No Aberrator, Static and Scanning Focal Spot Conditions



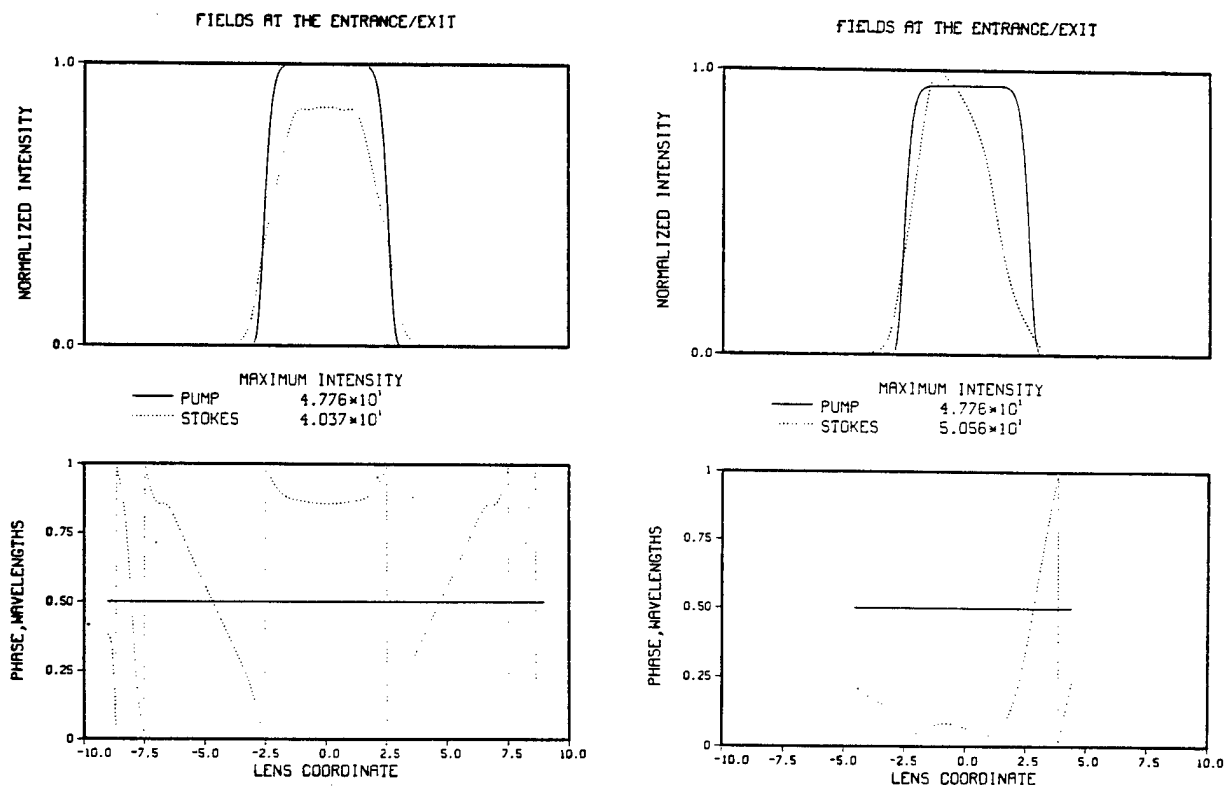


Figure 2.3-13. BRIWON Code Calculations of Near-Field Phase for No Aberrator, Static and Scanning Focal Spot

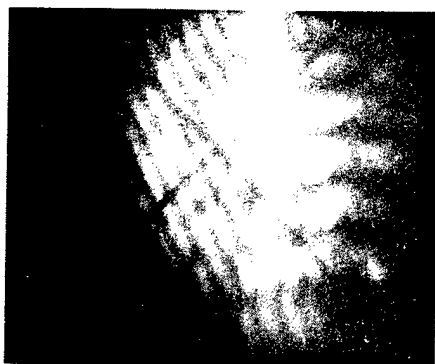
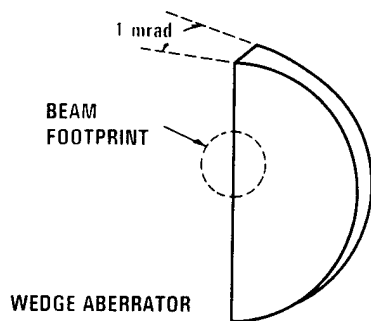
### 2.3.3 Wedge Aberrator Data, Static, and Scanning Test Conditions

The effects of typical aberrations such as segment tilt which may be present in the SBL design were studied for long pulses under static and scanning conditions. A 1 mrad wedge aberrator was used to generate two distinct far-field spots from the original good quality beam. This aberrator was placed just before the F/50 SBS telescope and each interferometer image relayed that position to the CCD cameras. Figure 2.3-14 shows an interferogram of the aberrated beam (double pass) without phase conjugation illustrating the large tilt in the wavefront with an rms OPD of 0.8351 waves. Figure 2.3-15 shows the time integrated far fields for the original incident beam, aberrated input beam, and SBS return beam. After conjugation of the two beams and a second pass through the aberrator, one spot was obtained with beam quality comparable to that of the incident beam. The beam quality of the SBS return is the same as the incident, unaberrated beam within experimental error.

Threshold for the beam with wedge aberrator was measured for long pulse, static focal spot test conditions. The SBS power is plotted versus pump power in Figure 2.3-16. The threshold power for the wedge aberrated beam was approximately 65 kW. This threshold is 60% higher than the unaberrated beam threshold. The slope efficiency was 0.62 for the aberrated beam compared to 0.87 for the unaberrated beam. Figure 2.3-17 shows that the tilt aberrated wavefront is well corrected with SBS phase conjugation. There is an order of magnitude improvement in the rms OPD from 0.84 rms waves aberrated to 0.09 rms waves SBS return.

Experiments with the wedge aberrated beam were performed under scanning conditions as well. For a maximum focal spot velocity of 155 m/s which corresponds to 35 m/s flow velocity in the SBL, good conjugation fidelity was obtained. The time integrated interferograms in Figure 2.3-18 show an order of magnitude improvement in the wavefront quality from 0.8351 rms waves aberrated to 0.0783 rms waves SBS return. The SBS beam far-field was comparable to the original incident beam quality.

BRIWON code calculations agree well with experimental data. As shown in Figure 2.3-19, they predicted shift in the near field phase caused by beam scanning, for wedge aberrator conditions. They also predicted



INTERFEROGRAM OF ABERRATED BEAM  
(DOUBLE PASS) WITHOUT PHASE CONJUGATION

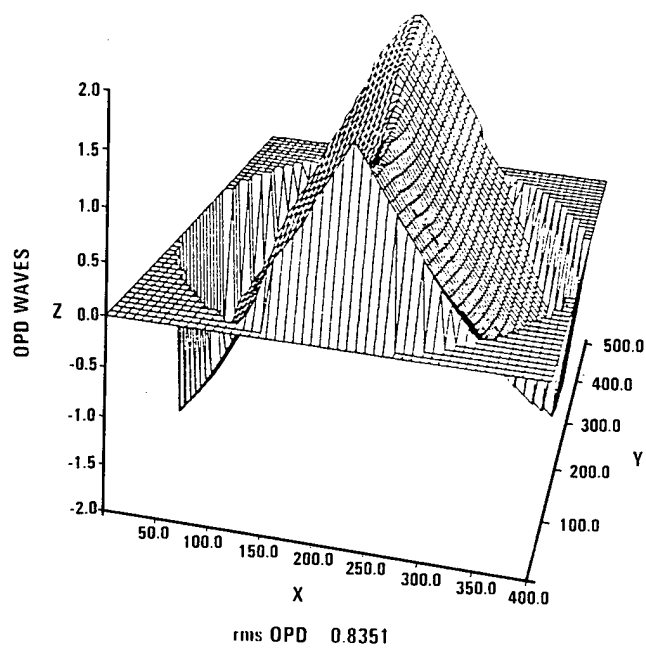


Figure 2.3-14. Wedge Aberrator and Corresponding Aberrated Wavefront  
(Double Pass)

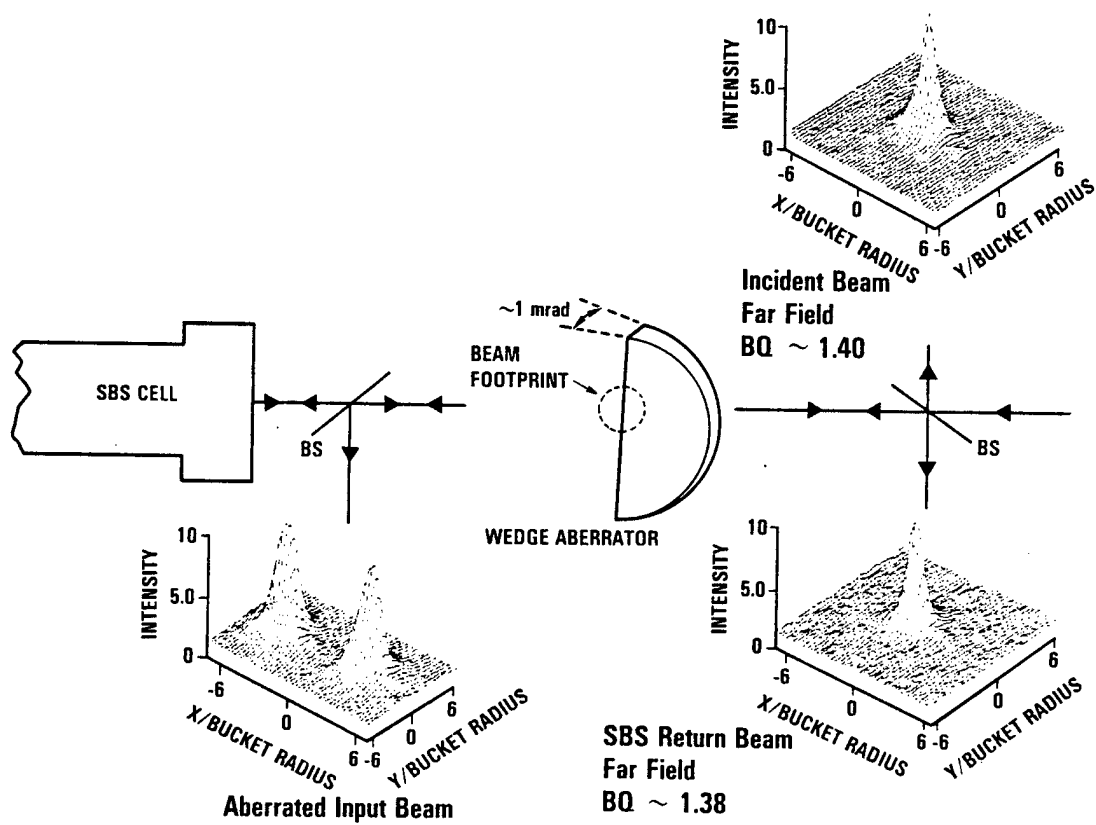
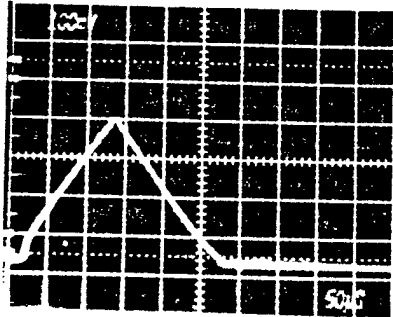
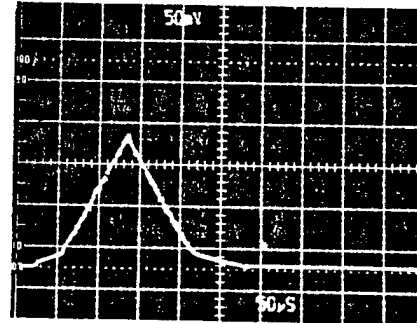


Figure 2.3-15. Far-Field Intensity Distributions of Incident, Aberrated and SBS Return Beams for Wedge Aberrator, Static Focal Spot



Incident



Reflected

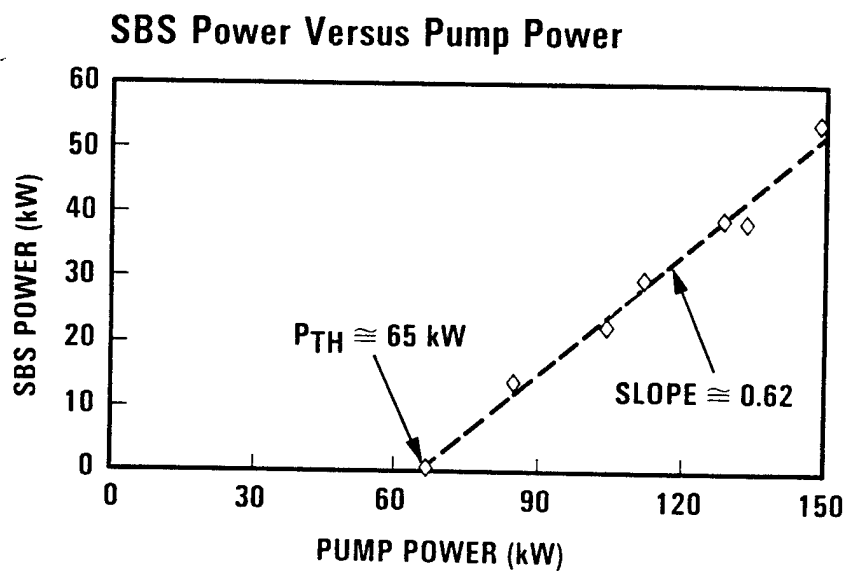


Figure 2.3-16. SBS Power Versus Pump Power (Threshold) for Wedge Aberrator

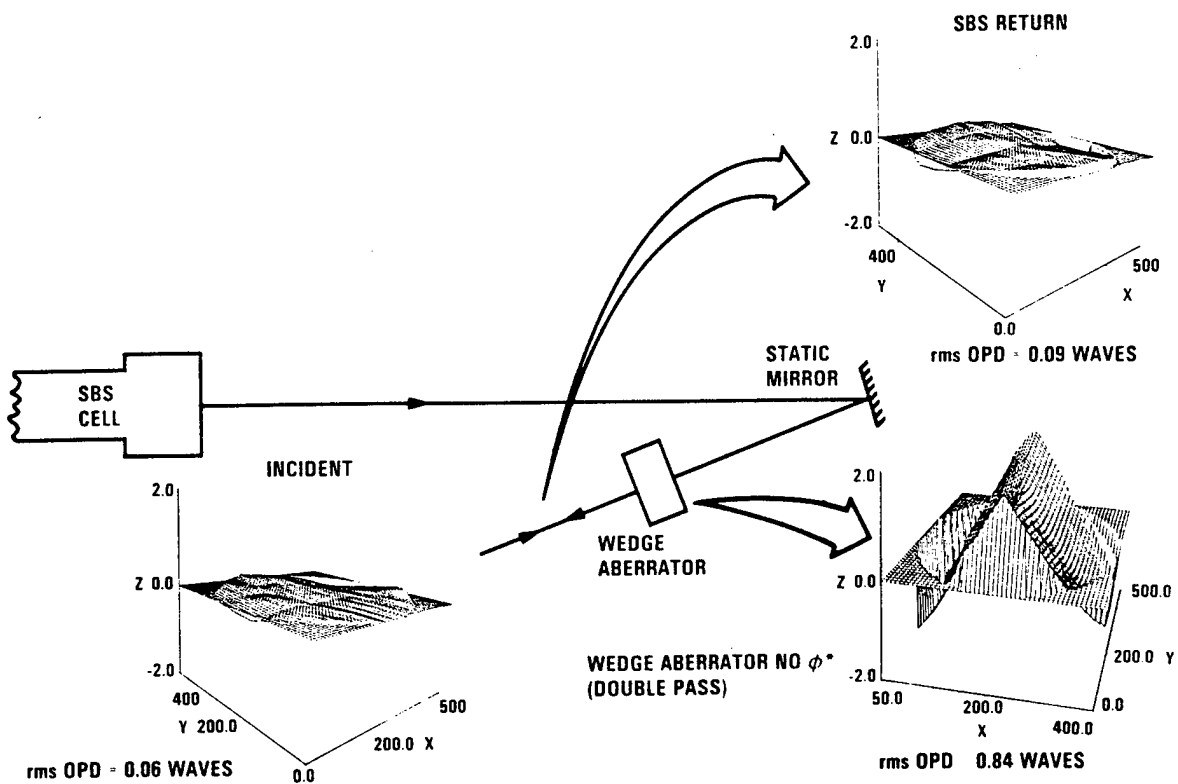


Figure 2.3-17. Correction of Tilt Aberrated Wavefront by SBS Phase Conjugation, Static Focal Spot

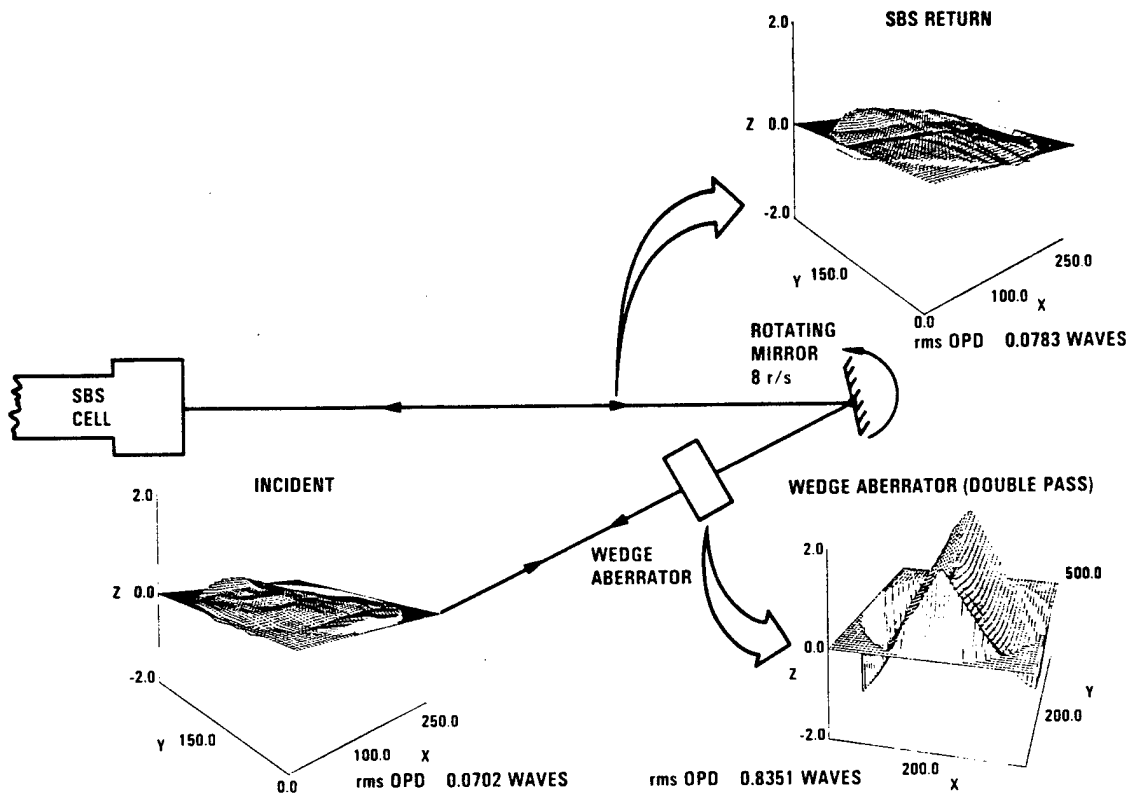
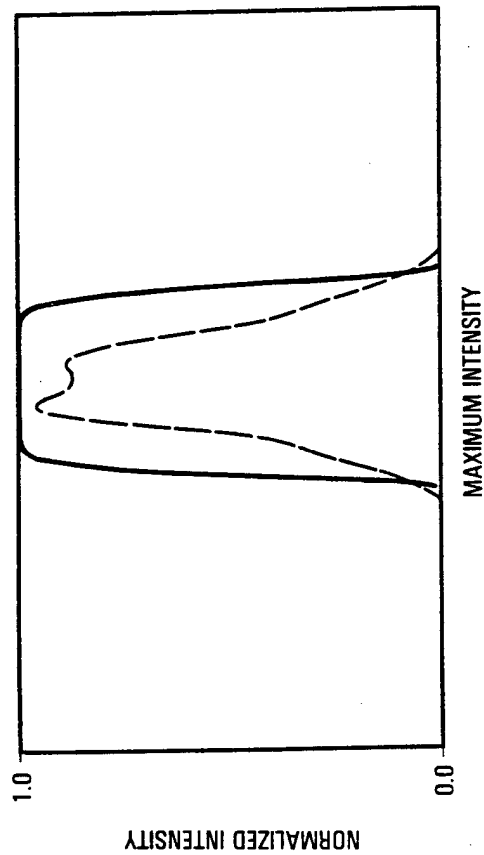
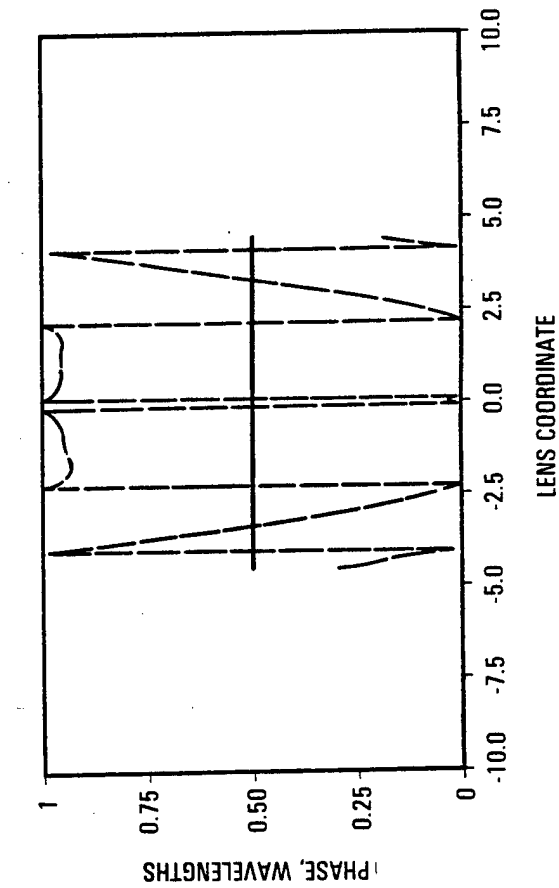
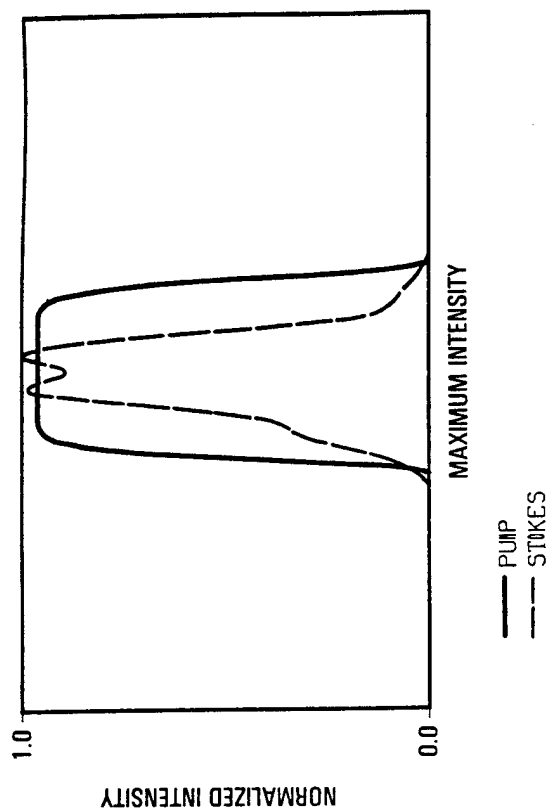


Figure 2.3-18. Correction of Tilt Aberrated Wavefront by SBS Phase Conjugation, Scanning Focal Spot

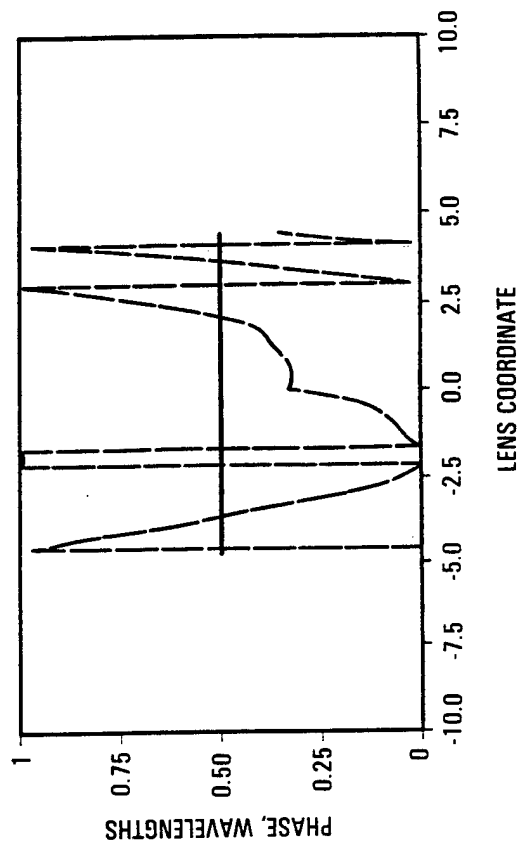
FIELDS AT THE ENTRANCE/EXIT



FIELDS AT THE ENTRANCE/EXIT



$v = 0 \text{ m/s}$



$v = 100 \text{ m/s [22.3 m/s SBL]}$

Figure 2.3-19. BRIVON Code Calculations of Near-Field Phase for Wedge Aberrator, Static and Scanning Focal Spot



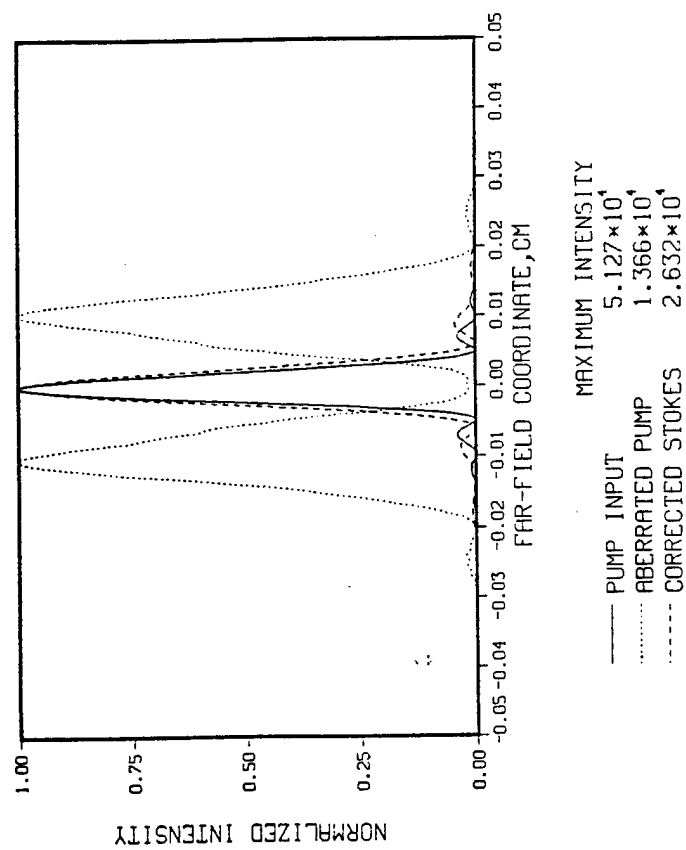
negligible degradation in beam quality with scan, Figure 2.3-20, for the beam combining (wedge) aberrator. The beam qualities for static versus scanning (100 m/s) conditions were  $1.006 \pm 0.1$  and  $1.032 \pm 0.1$ , respectively.

#### 2.3.4 Piston Aberrator Data, Static, and Scanning Test Conditions

A second aberration in the SBL design is piston caused by the multisegmented primary mirror. In these experiments a grooved aberrator was used to generate piston error in the incident beam. This aberrator is depicted in Figure 2.3-21. The grooves generated between 0.4 and 1.6 waves of piston. Profilometry indicates high spatial frequencies within the main groove structure.

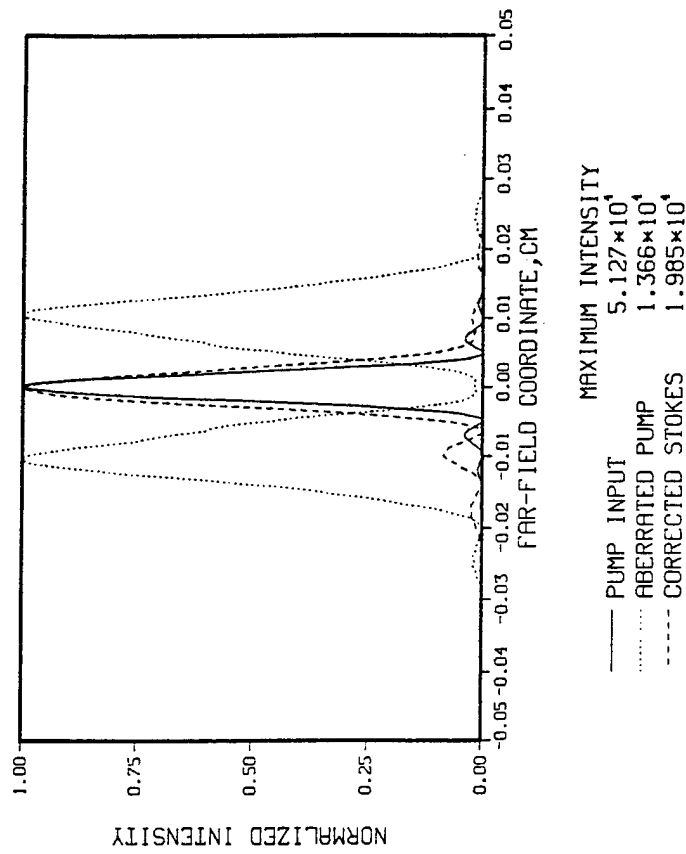
Good conjugation fidelity was obtained for static conditions. High SBS reflectivity, Figure 2.3-22, was maintained for thousands of phonon lifetimes. Figure 2.3-23 illustrates the far-field spot structure of the original unaberrated beam, the aberrated incident beam and the conjugated return beam. The aberrator tends to spread the beam in one dimension and generates an aberrated beam quality of 1.84. The beam quality of the SBS return through the aberrator was the same, 1.3, as the original unaberrated beam within experimental error. The interferograms in Figure 2.3-24 show correction of piston error for the static mirror case. A lateral shearing interferogram illustrates the piston error in the incident beam. Correction of the piston is evident in the SBS return beam interferogram in which the fringe offsets indicative of piston error are no longer present and fringe continuity is restored. This aberrator was more difficult to characterize given the variations in contrast across the interferogram caused by high-frequency scatter. Some residual error caused in part by digitization limitations and the quality of the interferograms was present even for the static mirror case.

Threshold was measured for the grooved aberrator using the triangular pulse. The reflected power versus incident power is plotted and power versus time traces for the incident, return and transmitted beams are shown in Figure 2.3-25. The transmitted energy is clamped at threshold, i.e., 78 kW. This is almost a factor of 2 higher than the unaberrated beam



**$v = 0 \text{ m/s}$**

**$BQ = 1.006$**



**$v = 100 \text{ m/s [22.3 m/s SBL]}$**

**$BQ = 1.032$**

Figure 2.3-20. BRIWON Code Calculations of Far-Field Intensity for Wedge Aberrator, Static and Scanning Focal Spot

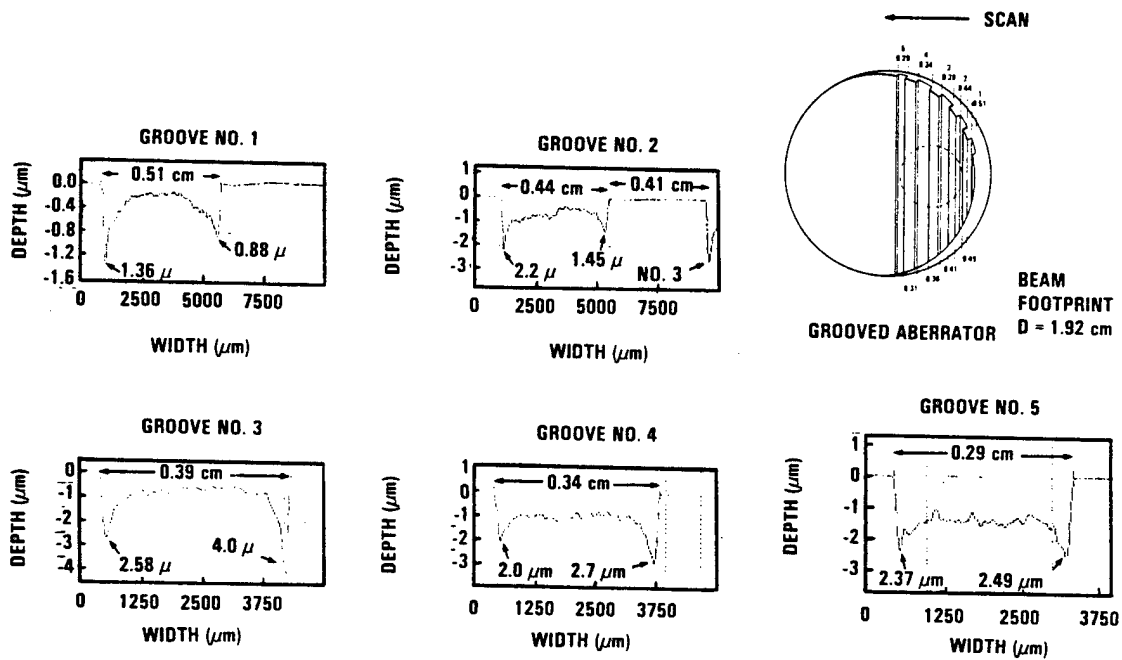


Figure 2.3-21. Grooved/Piston Aberrator Profilometer Traces

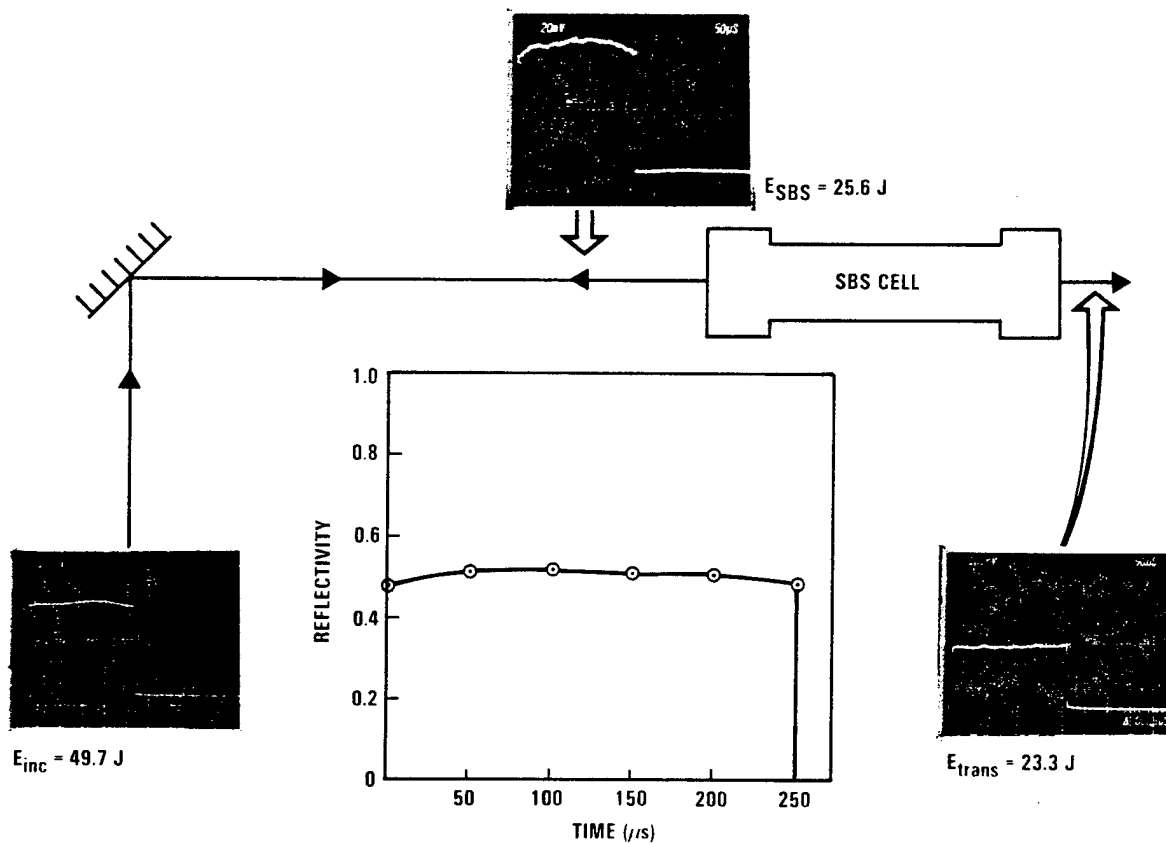


Figure 2.3-22. SBS Reflectivity Versus Time for Piston Aberrator, Static Focal Spot

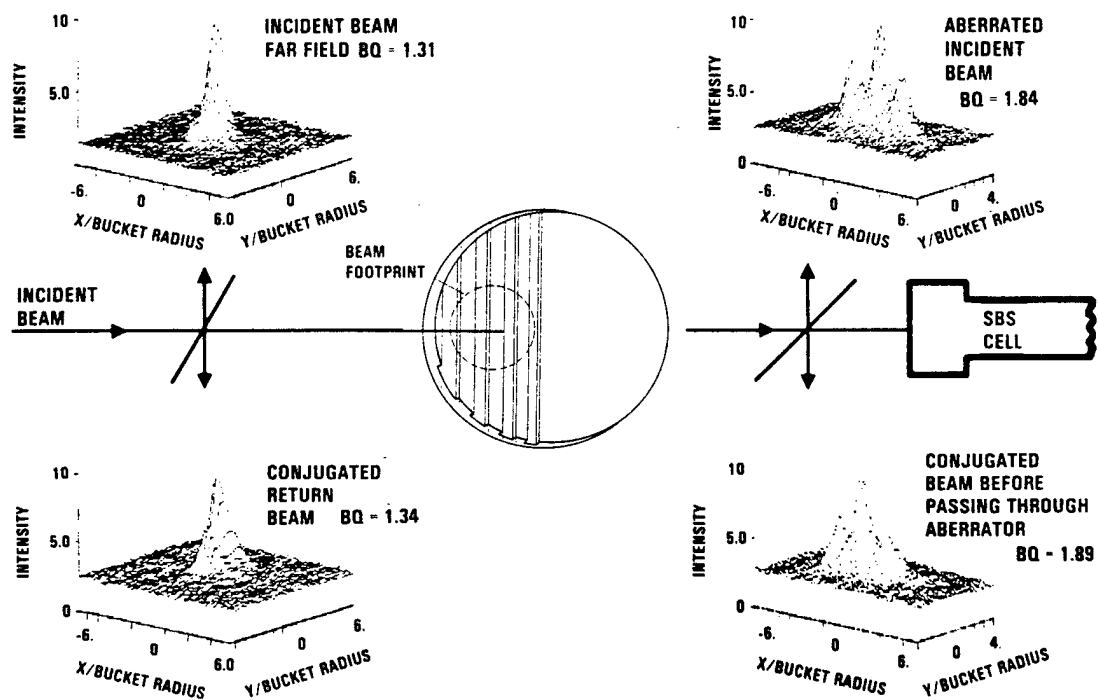
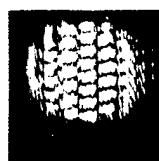


Figure 2.3-23. Far-Field Intensity Distributions for Piston Aberrated Incident Beam and SBS Corrected Return Beam



PISTON ABERRATOR  
INTERFEROGRAM —  
SINGLE PASS

LSI

INCIDENT BEAM



SBS RETURN DOUBLE PASS  
THROUGH GROOVE ABERRATOR

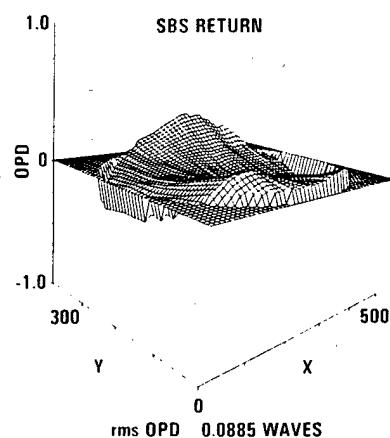
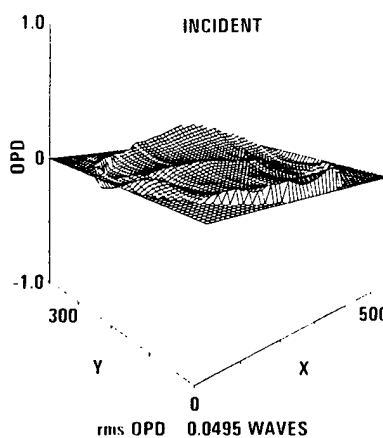


Figure 2.3-24. Near-Field Phase of Incident Piston Aberrated Beam and SBS Corrected Beam

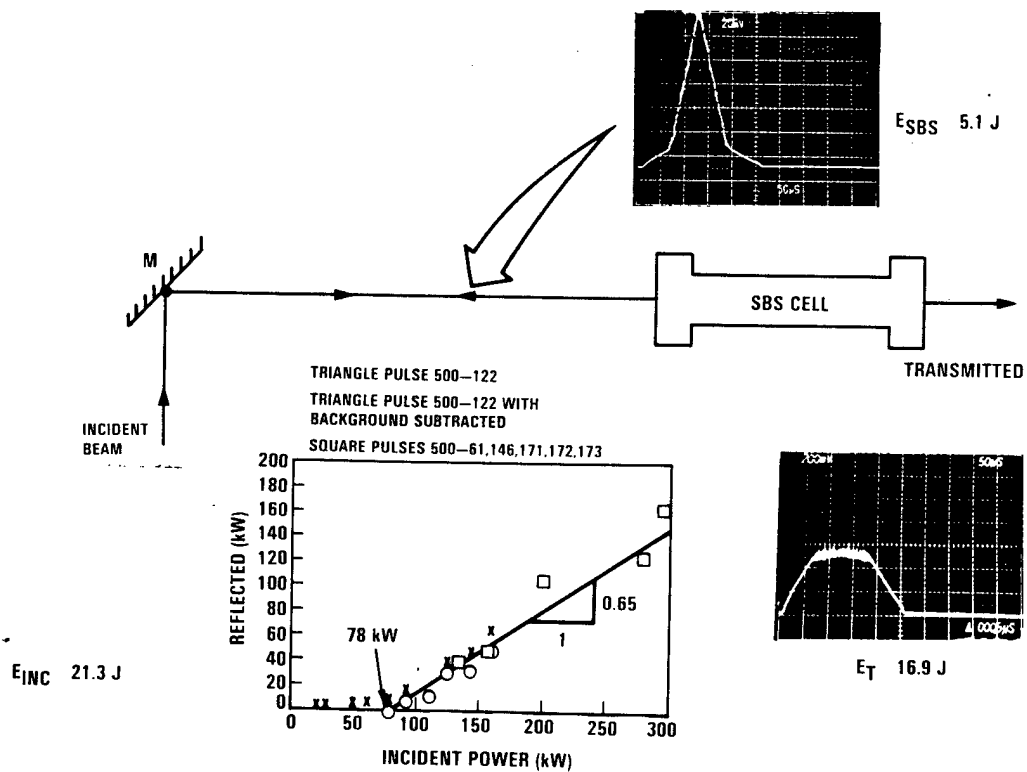


Figure 2.3-25. SBS Reflected Power Versus Pump Power (Threshold) for Piston Aberrator

threshold of 40 kW. The piston aberrator slope efficiency of 0.65 is comparable to the tilt aberrator case and lower than the unaberrated threshold slope efficiency of 0.87.

The grooved aberrator experiments were also performed under scanning mirror conditions. SBS maintained high reflectivity, 50%, with the grooved aberrator for scan speeds as high as 155 m/s. Reflectivity versus focal spot velocity is plotted in Figure 2.3-26. Although good reflectivity was maintained for this aberrator under scanning conditions, the grooved aberrator fidelity degraded at higher scan speeds. The time integrated far-field intensity distributions of the incident and SBS return beams, Figure 2.3-27, show a decrease in beam quality as scan speed was increased to 77 m/s. Data taken at 155 m/s, Figure 2.3-28, show that the far-field intensity distribution of the beam returning from the SBS cell is significantly different from the beam entering the cell. The large amplitude high spatial frequencies in this aberrator may have contributed to this difference. Also, the incident power was only approximately two times threshold for this test series.

#### 2.3.5 Thermal Blooming Experiment

Another competing process in the long pulse regime of particular interest is thermal blooming. Absorption induced heating effects degrade the beam quality which then raises SBS threshold power and lowers SBS reflectivities.

To induce thermal blooming, ammonia was added to the SBS cell to give an absorption coefficient of  $5 \times 10^{-6} \text{ cm}^{-1}$ . Three separate shots with successively greater input energies are shown in Figure 2.3-29. All shots were taken on the same day with no aberrator and with the wedge aberrator for 150- $\mu\text{s}$  square pulses. Heating effects quickly degraded the SBS return. Under static conditions, only 20  $\mu\text{s}$  was required to see degradation in reflectivity. The turn-off time was inversely related to the amount of input energy. However, the rate of degradation for all three input energies was the same even though turn-off times differed. The transmitted beam exhibited behavior complementary to that of the SBS return beam as expected.



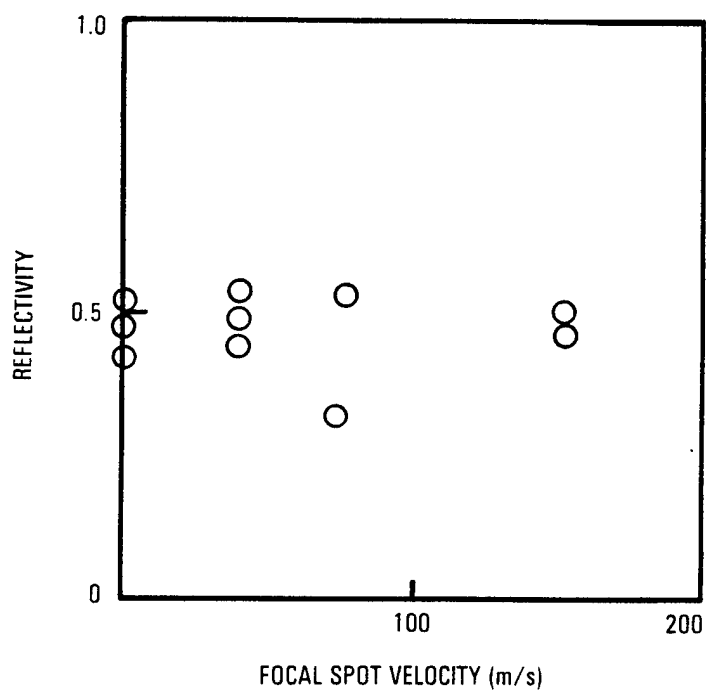


Figure 2.3-26. Reflectivity Versus Focal Spot Velocity for Piston Aberrated Beam

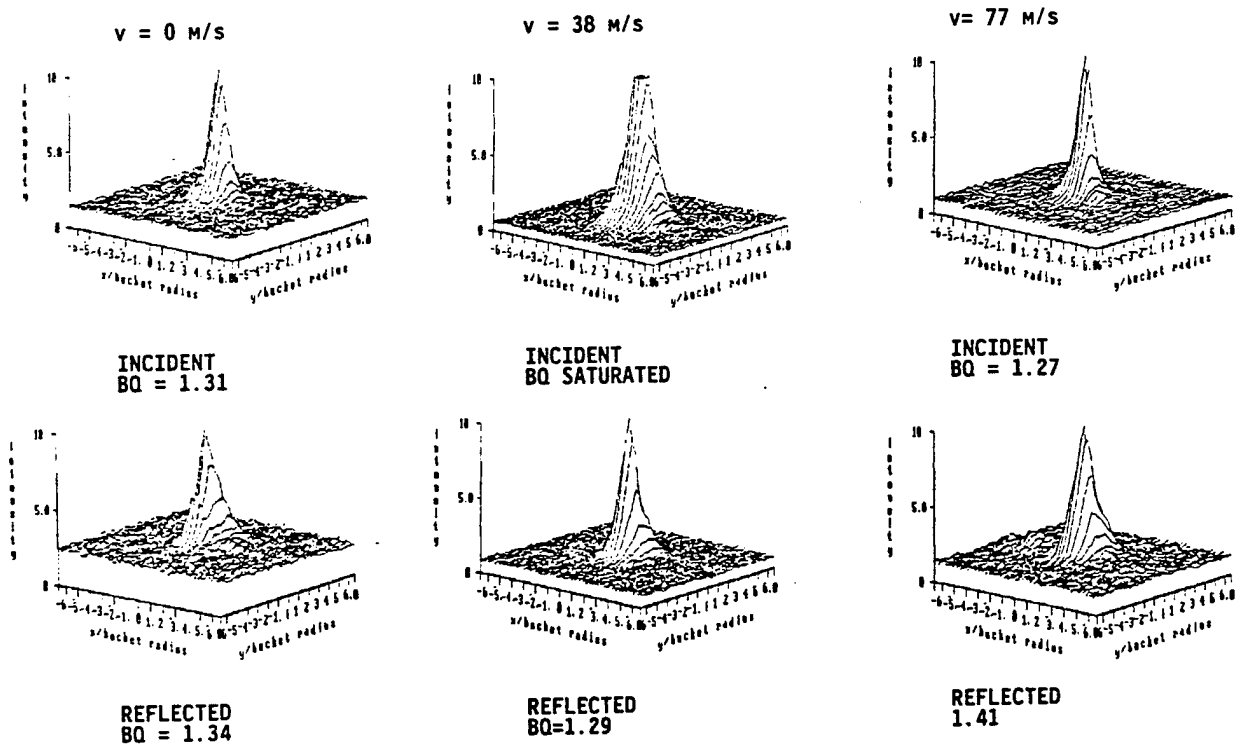


Figure 2.3-27. Time-Integrated Incident and SBS Return Beam Far Fields for Piston Aberrator, Static and Scanning Focal Spot

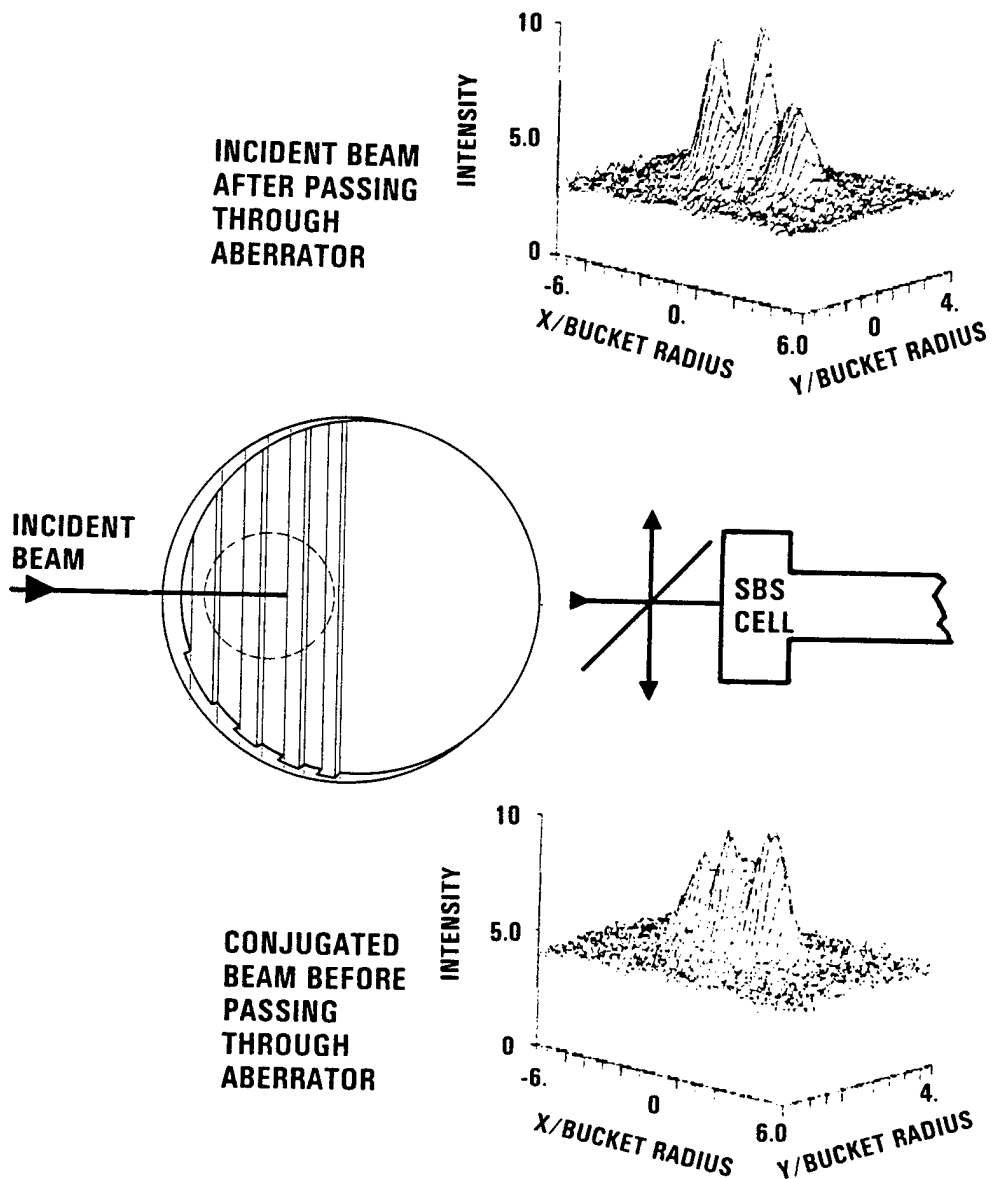
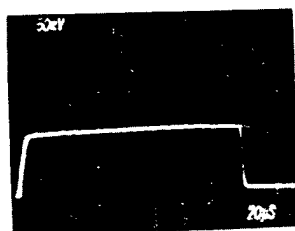
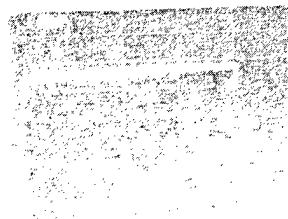


Figure 2.3-28. Far-Field Intensity Distribution of Piston Aberrated Incident Beam and SBS Return Beam Before Second Pass Through Aberrator



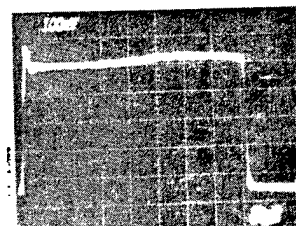
$E_{INC} = 12.25 \text{ J}$   
— NO ABERRATOR

(a)



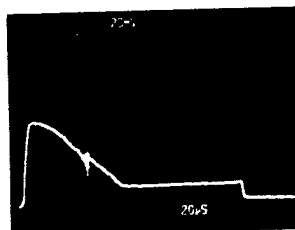
$E_{INC} = 22.7 \text{ J}$   
— NO ABERRATOR

(b)

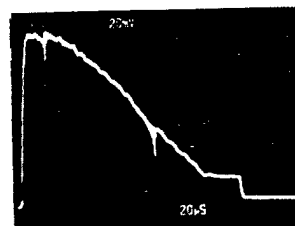


$E_{INC} = 49.9 \text{ J}$  — BEAM  
COMBINING ABERRATOR

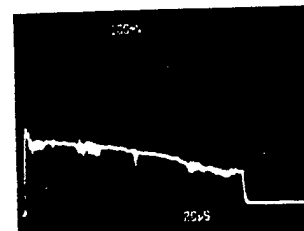
(c)



$E_{SBS} = 1.93 \text{ J}$



$E_{SBS} = 8.4 \text{ J}$



$E_{SBS} = 20.5 \text{ J}$

Figure 2.3-29. Incident and SBS Return Beam Power Versus Time Traces for Absorber Added To Induce Thermal Blooming, Static Focal Spot

To suppress the deleterious effects of thermal blooming, the beam was scanned across the SBS medium. Scans began at the highest focal speed of 155 m/s and the speed was successively decreased to find the slowest speed that would suppress thermal blooming. Even for the slowest speed of 2.4 m/s, thermal blooming was easily suppressed. As shown in Figure 2.3-30, the square pulse shape and thus, reflectivity was maintained. Because of the limitations of the rotating mirror velocity, the lower limit was never determined. The scan speed of 2.4 m/s corresponds to a movement of 50  $\mu\text{m}$  through the medium which is comparable to a focal point halfwidth.

Figure 2.3-31 shows good conjugation fidelity was also achieved with suppression of thermal blooming as measured in the far-field. The SBS return beam quality is comparable to the incident beam quality.

Detailed analysis of thermal blooming is presented in Section 2.4.

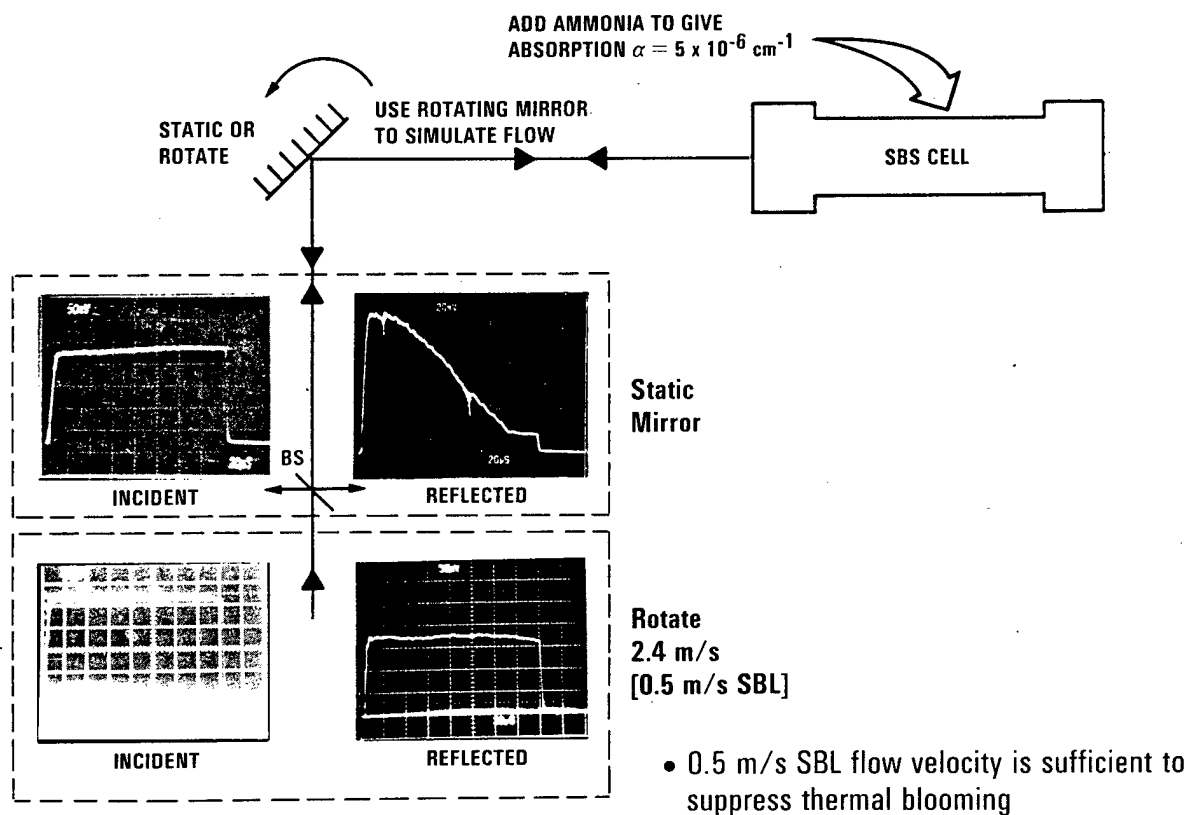


Figure 2.3-30. Suppression of Thermal Blooming by Scanning Focal Spot

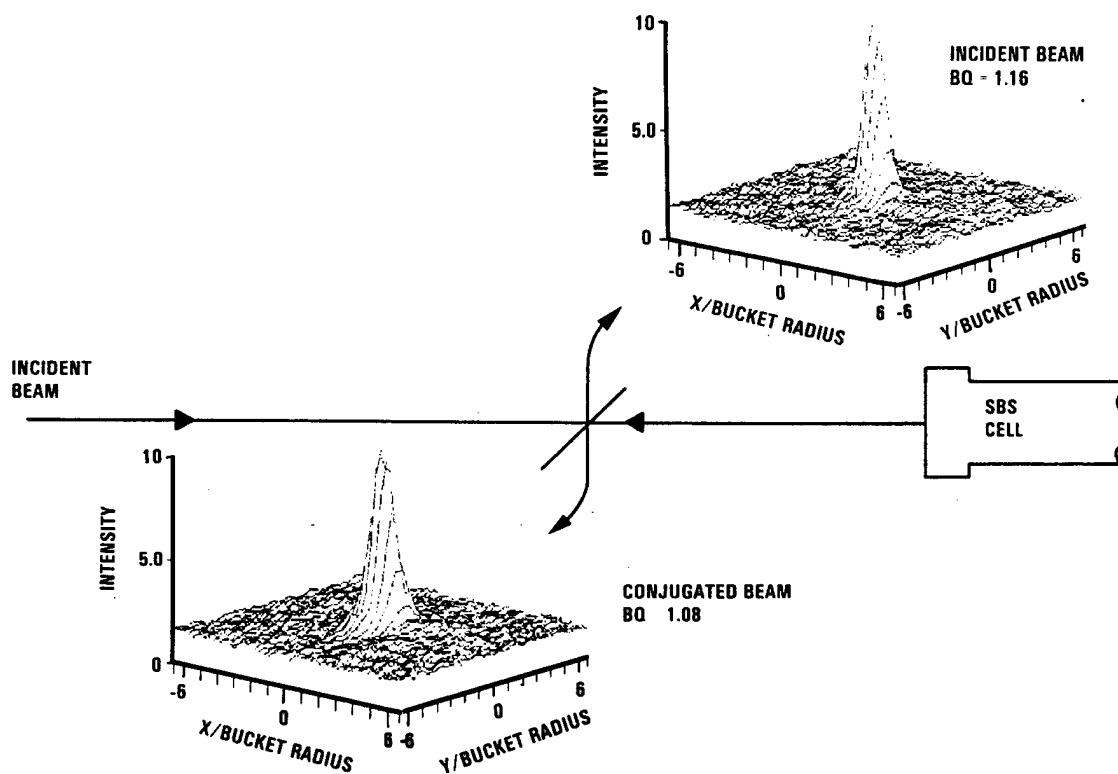


Figure 2.3-31. Far-Field Conjugation Fidelity for Thermal Blooming Suppressed by Focal Spot Scanning

## 2.4 CWCS EXPERIMENT ANALYSES DIMENSIONLESS SCALING

In analogy to the approach presented in detail in Section 3.7 scaling arguments can be applied to a variety of effects pertinent to the CWCS experiments. Further information on the basis of many of the equations used can be found in the discussion of the BRIWON computer code in Volume II, Section 3.5.

### 2.4.1 Forward Scattering

Originally, there was concern that in long pulse experiments forward scattering would eventually overpower backward SBS. Very conservative analyses suggested that moderate flow velocities could suppress the effect. More detailed assessments indicated that in the special case of Xe it was more difficult than anticipated to induce forward scattering. Indeed, forward scattering was not observed even in the case of no scanning and a 350- $\mu$ s pulse.

The reason that forward scattering was thought to be a potential problem is that under idealized conditions for scattering at an angle  $\theta$  the phonon lifetime and SBS gain scale as

$$t_{\text{phonon}}(\theta) = \frac{t_{\text{phonon}}(180)}{\sin^2(\theta/2)}$$

$$g_B(\theta) = \frac{g_B(180)}{\sin(\theta/2)}$$

The focal geometry strongly favors forward and backward scattering. These expressions suggest that eventually near forward scattering will dominate. However, transient analyses imply that backscattering turns on first. Simple scaling arguments were used to estimate the time required for forward scattering. Analogously to the backscattering gain quantity  $s$  ( $e^s = e^{25}$  as shown in Section 3.7), a scattering angle dependent  $S(\theta)$  can be defined base in the simple intensity model described in Section 3.7. The model includes a term for the gain over an appropriate length of the central Rayleigh range region and, where appropriate, an additional term



for gain outside the Rayleigh range but within the  $1/F\#$  geometrical cone. Specifically, the model assumed:

$$S(\theta) = \frac{2Pg_B(\theta)}{\pi\lambda(F\#)\sin(\theta)} \quad \frac{\pi}{2} > \theta > 1/F\#$$

$$\frac{2Pg_B(\theta)}{\pi\lambda(F\#)\sin(\theta)} + \frac{4Pg_B(\theta)(1 - \theta F\#)}{\pi\lambda} \quad 1/(2F\#) < \theta < 1/F\#$$

$$\frac{4Pg_B(\theta)(2 - \theta F\#)}{\pi\lambda} \quad 0 < \theta < 1/(2F\#)$$

Since pump depletion is quickly established,  $P$  is the conventional backward SBS threshold power. Using the same notation used in the Section 3.7 transient analyses, the ratio of transient to steady state threshold power is

$$C = \frac{S(\theta)}{\left[ \frac{8Pg_B(180)}{\pi\lambda} \right]}$$

and the predicted build up time (1.05  $\mu\text{m}$  laser) is

$$t = \frac{22 t_{\text{phonon}}(180^\circ)}{4 \sin^2(\theta/2) (C)}$$

Substitution shows that the minimum buildup time occurs for  $\theta = 1/(2F\#)$  and that

$$\begin{aligned} t_{\min} &= 29.3 t_{\text{phonon}}(180)(F\#) \\ &= (1.1 \mu\text{s})F\# \\ &\text{for HF } (9 \mu\text{s})F\# \end{aligned}$$

These time scales are long enough that it is relatively easy to eliminate forward scattering by flowing the gas at low velocities. However, even these estimated are too pessimistic. The model suffers from

several simplifying assumptions. The angular model is relatively uncertain, phonon propagation and diffraction are ignored, and most importantly the assumption that gain grows arbitrarily with decreasing angle is too pessimistic. Threshold calculations are based on line center gain and implicitly assume the same gain frequency dependence throughout the SBS cell. However, for gases near the critical point the speed of sound and thus the frequency shift is sensitive to local variations in temperature and pressure. The situation is summarized in Figure 2.4-1. The relative sensitivity increases inversely with the frequency shift. For 40 atm Xe,

$$\frac{\partial \nu}{\partial T} \sim 1 \text{ m/(sK)} \quad \frac{\partial \nu}{\partial P} \sim 1 \text{ m/(s atm)}$$

Even back scattering thresholds can be influenced by moderate temperature gradients. At 1.05  $\mu\text{m}$  temperature gradients of order  $\pm 1^\circ\text{K}$  induce a range of shifts in the peak SBS gain frequency comparable to the gain linewidth. The net gain is reduced just as it is in an inhomogeneously broadened laser. HF experiments are even more sensitive; near ideal performance requires that maximum gradients be of order a few tenths of a degree. Near forward scattering is much more sensitive to these variations. At 1.05  $\mu\text{m}$ , gradients of the order of a few millidegrees are sufficient to invalidate the simple near forward scattering analysis. It is very unlikely that the cell is that uniform. All these effects together could easily make the initial buildup estimate more than an order of magnitude too low. These arguments are equally applicable to HF and therefore the failure to observe forward scattering in the CWCS experiment indicates that very low flow velocities (less than 1 m/s) are sufficient to prevent forward scattering at HF wavelengths. Note that these arguments are not universally applicable. In particular, some liquids which are known as Kneser liquids have phonon lifetimes which do not scale inversely as frequency squared. The archetype example of such a liquid is carbon disulfide, and rough analyses suggest that it may be relatively easy to observe forward scattering in times scales of order tens of microseconds.

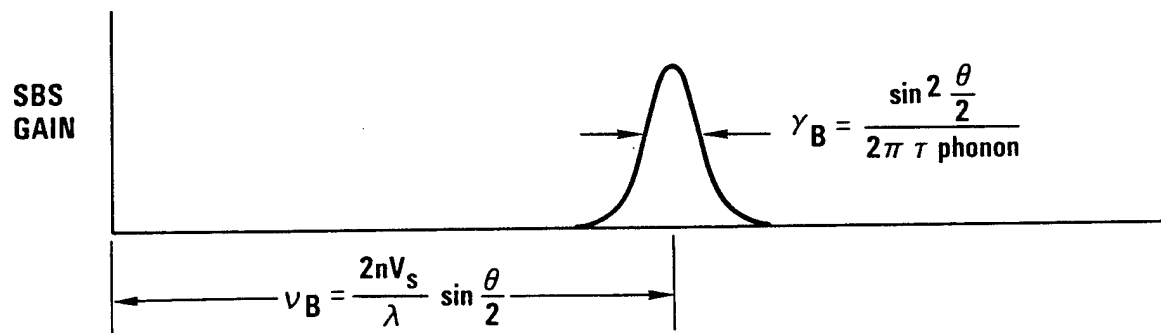


Figure 2.4-1. SBS Frequency Shift and Linewidth Angular Dependence

### 2.4.2 Grating Convection

The problem of grating convection in a flowing gas cell is treated in steady state (i.e.,  $\partial Q/\partial t = 0$ ) in BRIWON by adding a source term:

$$\frac{\partial E_S}{\partial z} \text{ source} = \frac{G_B}{2} |E_1|^2 E_B F(x, z, V)$$

where

$$F(x, z, v) = \frac{\Gamma}{2v} (1 + i \frac{2\Delta\omega}{\Gamma}) \frac{\int_{-\infty}^x E_L^* E_S \exp \left\{ -\frac{\Gamma}{2v} (1 + i \frac{2\Delta\omega}{\Gamma}) (x - x') \right\} dx'}{E_L^*(x) E_S(x)} \\ F \rightarrow 1, \text{ if } v \rightarrow 0$$

Here  $V$  is the convection velocity, and  $\Delta\omega/\Gamma$  is a small term which causes minimal wavelength dependence.

By converting to transverse coordinates measured in  $(\lambda F\#)$  units and making transformations analogous to those applied in Section 3.7.4 it can be shown that  $V$  can be adjusted to maintain  $F(x_1, z_1, V)$  invariant yielding a set of identical solutions provided the following translations are made simultaneously ( $K_1, K_2$  arbitrary):

$$\begin{aligned} k_1 \lambda & \rightarrow \lambda \\ k_2 (F\#) & \rightarrow F\# \\ E_1 / (k_2 * \text{SQR}(k_1)) & \rightarrow E_1 \\ v(k_2) / (k_1) & \rightarrow v \end{aligned}$$

Detailed BRIWON calculations show that at relatively low velocities the first effect of grating flow is to cause a small tilt in the reflected far-field signal (i.e., the grating is systematically shifted slightly downstream). Scaling arguments indicate that the angular shift measured as a fraction of the diffraction limit of the beam is the appropriate variable. Figures 2.3-6 and 2.3-11 show the agreement between CWCS data and BRIWON predictions. The illustrated behavior places limits on the maximum useful flow velocity. Scaling of the CWCS data to the HF wavelength and other  $F\#$ s can be done with the above transformations. From

a physical standpoint, the criteria is that translation of the gas near focus should occur slowly compared to the phonon lifetime:

$$\frac{2\lambda F\#}{V} \gg t_{\text{phonon}}$$

For example for the CWCS experiments this expression corresponds to approximately 35 phonon lifetimes for  $v = 80$  m/s, and at this velocity only moderate changes are apparent.

#### 2.4.3 Thermal Blooming

Control of heating effects due to absorption is the dominant factor in determining minimum flow velocity requirements. There are two basic effects which influence SBS behavior. First, absorption-induced Xe temperature spatial inhomogeneities can reduce total gain in the manner described in the forward scattering discussions. Second, as in conventional thermal blooming, the temperature gradients induce refractive index gradients which cause beam defocussing and consequently an increase in SBS threshold. Fortunately, in steady state the density gradients are phase conjugated so some degree of thermal blooming is tolerable. The effect has been modeled in the BRIWON computer code and verified experimentally at modest scan rates.

Simple scaling arguments can be used to estimate tolerances and scan speed requirements to reduce temperature spatial inhomogeneities. The approximate temperature rise near the focal region can be estimated with the expression:

$$\Delta T \sim \left[ \frac{a P_{\text{thres}}}{\pi (\lambda F\#)^2 C} \right] \left( \frac{2\lambda F\#}{V} \right) = \frac{2a P_{\text{thres}}}{V (\lambda F\#) C}$$

where

$a$  = absorption coefficient

$P_{\text{thres}}$  = SBS threshold power

$V$  = flow velocity

$C$  = heat capacity  $0.1 \text{ J}/(\text{K cm}^3)$

The use of  $P_{thres}$  in this expression implicitly assumes ideal pump depletion. Imperfect beam quality effects are not included but are anticipated to reduce sensitivity. For transient experiments which are performed without flow or scanning, the pulse duration is analogous to the flow transit time term,

$$\frac{2(\lambda F\#)}{V}$$

The earlier discussions indicate that substantial degradation should occur at temperature gradient levels of order  $1^\circ\text{K}$  for  $1.05 \mu\text{m}$  and  $0.3^\circ\text{K}$  for HF.

For typical flowing cell geometries conventional thermal blooming also begins to become important for transverse temperature gradients of a few tenths of a degree. Conventional thermal blooming (long cell limit) can be assessed in terms of the Gaussian beam distortion parameter,  $N_C$  where

$$N_C = \frac{-4 \text{ SQRT}(2) \alpha P_{thres}}{nVC} \left( \frac{\partial n}{\partial T} \right) F\#$$

Figure 2.4-2 shows the estimated scaling of Strehl ratio with  $N_C$ . Assuming threshold scales roughly linearly with beam quality (i.e., as the square root of Strehl ratio) modest degradations would be anticipated at  $N_C$  values of order 2 or less. Note that the CWCS experimental beam is not Gaussian and has imperfect beam quality. Thus, the use of Figure 2.4-2 as an estimator of velocity requirements is overly conservative.

For the CWCS experiments typical experimental parameters were

$$\lambda = 1.05 \mu\text{m}$$

$$P_{thres} = 22 \text{ kW}$$

$$\alpha = 5 \times 10^{-6} \text{ cm}^{-1}$$

$$F\# = 50$$

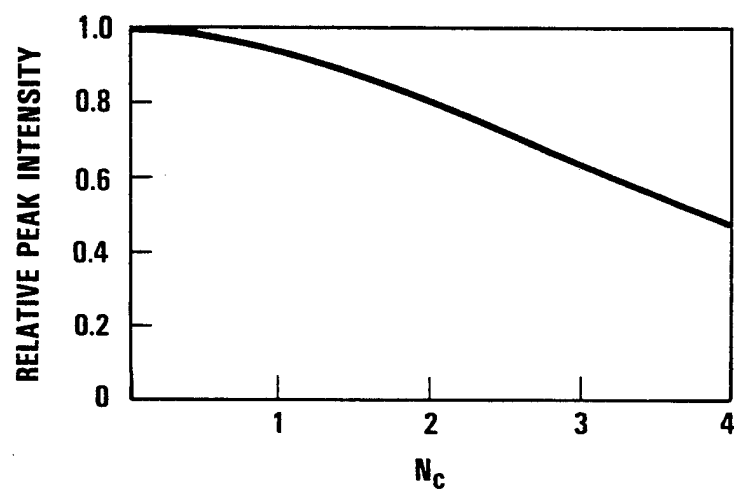


Figure 2.4-2. Gaussian-Beam Thermal Blooming Strehl Ratio Correlation

Figure 2.3-29 shows static cell test data all taken on the same day with a fixed amount of added absorber. Square input pulses of 150  $\mu\text{m}$  duration were used in all cases. Figure 2.3-30 shows the effect of scanning on temporal behavior. Back of the envelope calculations show these data are consistent with the earlier assessments.

1. A total temperature rise of order a few tenths of a degree should begin to impact SBS threshold and a  $1^\circ$  rise should substantially increase it. Substitution into the above expressions implies that for a diffraction limited beam the estimated time for a temperature rise of  $1^\circ$  is approximately 80  $\mu\text{m}$  (four divisions on the data traces). The reflectivity data evidently show declines on time scales of this order.
2. Since power at focus is independent of incident power, the time dependence of threshold should be the same for different incident powers. Moreover since transmitted power (i.e., threshold) and reflected power sum to incident power the time dependent decline in reflected power should also be independent of incident power until the incident power is below threshold. Comparison of the data in Figures 2.3-29(a) and (b) indicates that the observed shapes are virtually identical even for almost a factor of two difference in incident power. Note that the regions of constant reflectivity are background reflected signals and mark the regime where threshold exceeds the incident power.
3. Figure 2.3-29(c) shows that the sensitivity of a severely aberrated beam to thermal blooming is comparable to or less than that of better beam quality one.
4. The above arguments would suggest that very modest scan rates would eliminate thermal blooming effects. Specifically for the 2.4 m/s scan speed case the total focal volume transmit time is

$$\frac{2\lambda F\#}{V} = 44 \mu\text{s}$$

and the average temperature increase corresponds to half this value or only 22  $\mu\text{s}$ . Figure 2.3-29(b) shows that there is minimal reflectivity degradation on this time scale so one would expect this scan speed was sufficient to virtually eliminate thermal blooming effects. Indeed the observed reflectivity is comparable to the no absorber case and was not significantly changed by increasing the scanning speed. These results imply that for the SBL flow velocities or order a few meters per second are sufficient to accommodate anticipated impurity absorption levels of order  $1 \times 10^{-5} \text{ cm}^{-1}$ .



5. For the 2.4 m/s scan case the inferred Gaussian beam distortion parameter value is approximately 2.5. Figure 2.4-2 suggests that for an ideal beam this  $N_c$  value is marginal and that a modest increase in threshold due to absorption would be anticipated. However, the real beam has imperfect beam quality and is not Gaussian. Therefore, the estimate should be conservative. Within experimental uncertainties the data indicate that 2.4 m/s is sufficient to achieve near ideal performance.

For the steady state scanning cases the BRIWON code was used to more accurately assess behavior. Figure 2.4-3 compares observed and predicted reflectivity and beam quality behavior for the 2.4 m/s (the points near  $2 \times 10^{-8}$  s/cm<sup>2</sup> and higher scan speed cases. BRIWON does predict that 2.4 m/s is sufficient to control thermal blooming effects. Figure 2.3-31 shows the excellent conjugation behavior actually measured for the 2.4 m/s case.

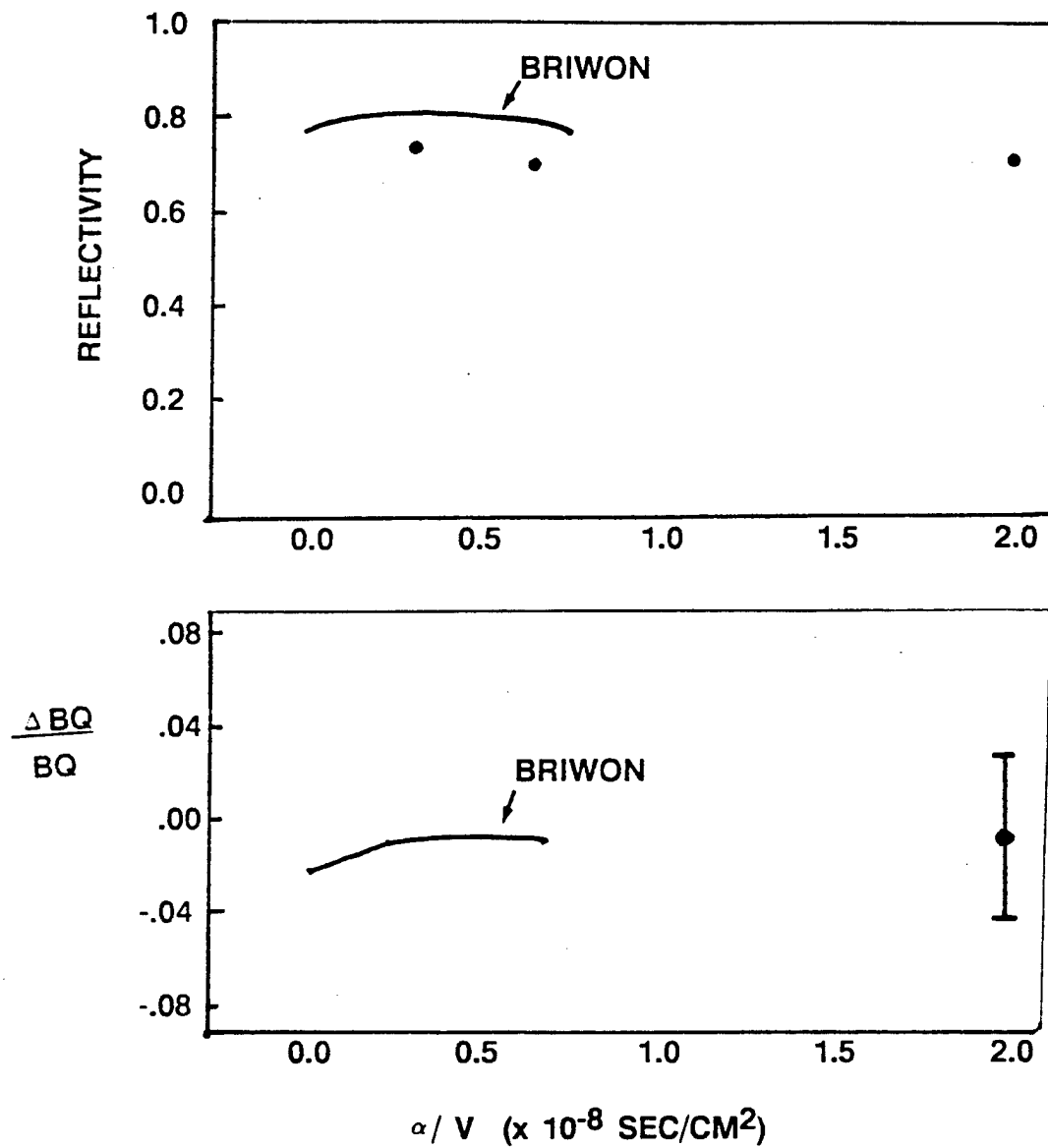


Figure 2.4-3. Comparison Between Test Data and BRIWON Predictions

## 2.5 SUMMARY OF SIGNIFICANT RESULTS

SBS has been successfully demonstrated in the long pulse regime for pulse lengths  $10^4$  times the phonon lifetime in 40 atm of Xe. Good reflectivity and conjugation fidelity are possible even for severely aberrated beams with and without beam scanning across the Brillouin medium. Good conjugation fidelity and reflectivity for the wedge aberrator show the feasibility of SBS phase conjugation for multiple beams under CW operation. Successful suppression of competing effects such as thermal blooming by beam scanning and the absence of near-forward SBS demonstrates the feasibility of long pulse SBS. For an SBL system, a flowing SBS medium would be used to suppress the competing effects. The slight tilt that is introduced in the far field as a result of the flowing medium (at low velocities) in the SBL would change the pointing angle much less than a diffraction limited spot.

## 2.6 REFERENCES

- 2-1. V. I. Bespalov, E. L. Bubis, O. V. Kulagin, G. A. Pasmanik, and A. A. Shilov, "Stimulated Brillouin Scattering and Stimulated Thermal Scattering of Microsecond Pulses," *Kvant. Elektron.* 13, 2044, 1986; *Sov. J. Quant. Electron.* 16, 1348, 1986.
- 2-2. Yu. V. Dolgoplov, V. A. Komarevskii, S. B. Kormer, G. G. Kochemasov, S. M. Kulikov, V. M. Murugov, V. D. Nikolaev, and S. A. Sukharev, "Experimental Investigation of the Feasibility of Application of the Wavefront Reversal Phenomenon in Stimulated Mandel'shtam-Brillouin Scattering," *Zh. Eksp. Teor. Fiz.* 76, 908, 1979; *Sov. Phys. JETP* 49, 458, 1979.
- 2-3. V. M. Volynkin, O. D. Gavrilov, and A. A. Chertkov, "Phase Conjugation of Microsecond-Range Pulses in Stimulated Brillouin Scattering of Light Beams Focused in a Liquid," *Sov. Tech. Phys. Lett.* 12, 167, 1986.
- 2-4. M. T. Duignan, B. J. Feldman, and W. T. Whitney, "Stimulated Brillouin Scattering and Phase Conjugation of Hydrogen Fluoride Laser Radiation," *Optics Lett.* 12, 111, 1987.
- 2-5. E. L. Bubis, V. V. Dobrotenko, O. V. Kulagin, G. A. Pasmanik, N. I. Stasyuk, and A. A. Shilov, "Influence of Thermal Self-Interaction on the Excitation of Stimulated Brillouin Scattering in Absorbing Media," *Kvant. Elektron.* 15, 147, 1988; *Sov. J. Quant. Electron.* 18, 94, 1988.
- 2-6. D. Bullock and C. Clendening, TRW Inc., private communication.

### 3. HF SBS PHASE CONJUGATION STUDIES

#### 3.1 INTRODUCTION

At the beginning of the APACHE program, most SBS phase conjugation demonstrations had been performed at wavelengths shorter than  $1.3 \mu\text{m}$ . The single exception was the preliminary work getting under way at the Naval Research Laboratory (NRL), where a pulsed HF laser device was being used. (Reference 2-1). Because the APACHE concept is based on SBS, our highest priority was to demonstrate SBS phase conjugation at HF wavelengths of  $\sim 2.8 \mu\text{m}$ .

The HF SBS phase conjugation studies conducted for the APACHE program were divided into four major test series:

- HF conjugation (HFC) experiments
- Conjugation subsystem (COS) experiments
- Beam combination (BC) experiments
- Threshold reduction (TR) experiments.

The primary focus of the HFC tests was the development of a state-of-the-art test facility to study SBS phase conjugation at HF wavelengths, and to obtain a preliminary set of data verifying that the facility was operational.

In the COS experiments, SBS parameterization as a function of aberrator characteristics and f-number and piston aberrations simulating those expected from a segmented-beam director in an SBL were studied. The motivation for the f-number tests was the establishment of a breakdown threshold for 40 atm of Xe.

The BC experiments demonstrated the ability of SBS phase conjugation to coherently combine two or more beams without actively controlling the propagation path of the individual beams. This was motivated by the SBL concept, which relies on SBS phase conjugation to combine beams from two or more amplifiers.

The TR experiments demonstrated a novel approach to reducing the SBS threshold in a manner that is scalable to a high-power continuous-wave (CW) device.

A design approach to provide high-quality data at this wavelength was chosen. Some of the major design trades considered were laser source, conjugating medium, oscillator isolation, and beam propagation in air.

The first consideration was the laser source for the conjugation experiments. To achieve the power estimated to exceed threshold for SBS, a pulsed HF chemical laser was chosen. This device is capable of high peak power and is relatively compact, in contrast to a CW HF chemical laser, which requires a relatively large device to provide the high power needed for SBS. Preliminary power budgets indicated that a device the size of the RPCL pulsed laser might be needed. Therefore, the experiment was performed at CTS, and a dedicated facility was built adjacent to the RPCL building to allow the option to use this device.

High absorption in the HF wavelength band eliminated many common SBS media. High-pressure Xe was chosen as the conjugating medium because of its low absorption at the desired wavelengths, large electrostrictive coefficient necessary for high SBS gain, and relatively small frequency shift (107 MHz). This shift falls well within the gain bandwidth of the HF medium, which is necessary for efficient extraction in an SBL utilizing a phase-conjugated bidirectional amplifier.

Isolation of the master oscillator from the returning SBS pulse was also an early design issue. An optical delay was used for isolation, i.e., propagating the beam a long distance so that the SBS return did not enter the oscillator until after lasing had terminated. This prevented confusing side issues concerning changes in oscillator output caused by SBS return and its effect on SBS conjugation. Use of the delay line also allowed the incident beam to be spatially filtered, providing an almost perfect reference beam for high-precision measurement of SBS conjugation fidelity.

Another design issue was propagation of the beam down the long distance needed for the optical delay line. The delay line was placed in a vacuum, and the rest of beam train, with the exception of the laser subsystem, was enclosed in an environmentally conditioned room with temperature and humidity accurately controlled. This permitted lines strongly absorbed by the atmosphere to be studied and also ensured that thermal effects would not alter shot-to-shot alignment.

The experiments conducted at NRL (Reference 3-1) provided preliminary SBS data at HF wavelengths useful during the integration phase of the HF phase-conjugation facility at CTS. These experiments provided the first experimental data at HF wavelengths and demonstrated that high-pressure Xe is a suitable SBS medium. Also provided were the first measurements of conjugation fidelity under these conditions, although the measurements were limited by the imperfect beam quality of the launched beam, resolution accuracy of the far-field diagnostic, and imperfect oscillator isolation. With the TRW facility (with its nearly diffraction-limited reference beam quality and perfect oscillator isolation eliminating ambiguous results), improved data were obtained.

### 3.2 APACHE EXPERIMENT DESCRIPTION

A diagram of the dedicated facility built to study SBS phase conjugation at HF wavelengths is shown in Figure 3.2-1. The facility consists of several subsystems: the oscillator/amplifier, main optical train, diagnostics, and phase-conjugation cell.

#### 3.2.1 Laser Subsystem

The experiment was designed to use either the 50-liter RPCL device or two 2-liter pulsed HF lasers obtained from Pacific Applied Research (PAR) as the laser source. Experiments indicate that the PAR lasers have sufficient energy to exceed the SBS threshold with wide margin, and consequently the option to use RPCL was never exercised. Furthermore, as a recent upgrade to conjugate a larger range of aberrations, two new PAR lasers with a total capacity of 10 liters recently were purchased with TRW funds and integrated into the system.

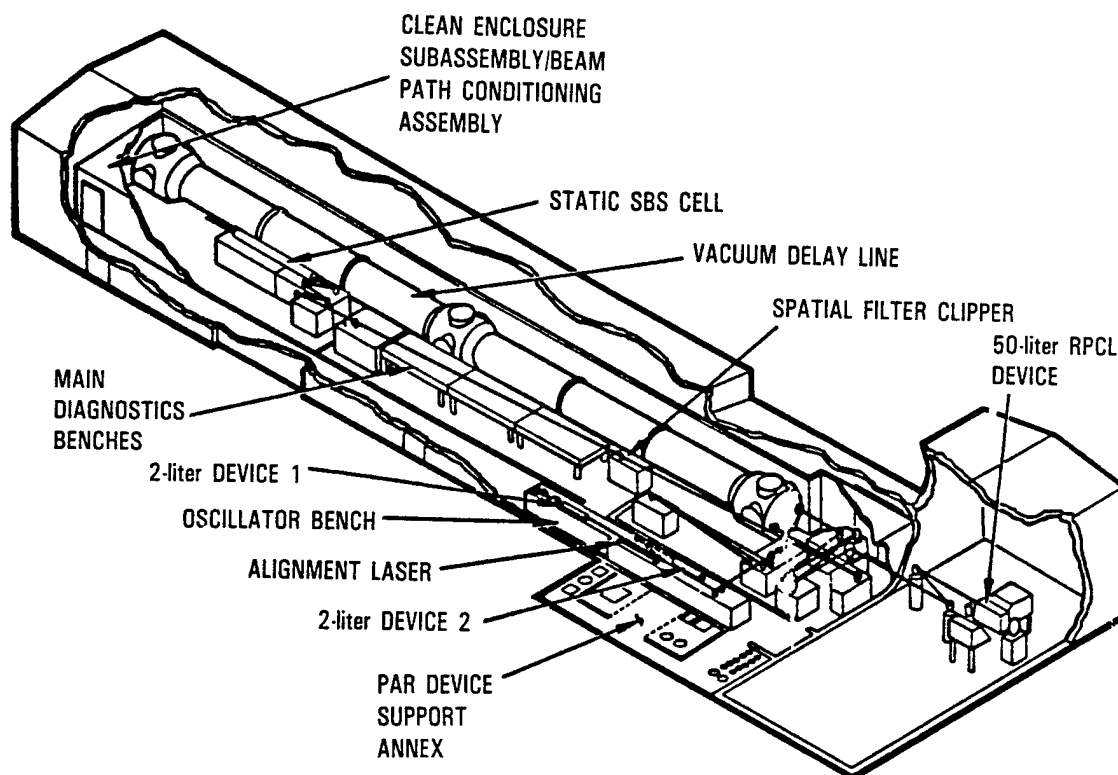


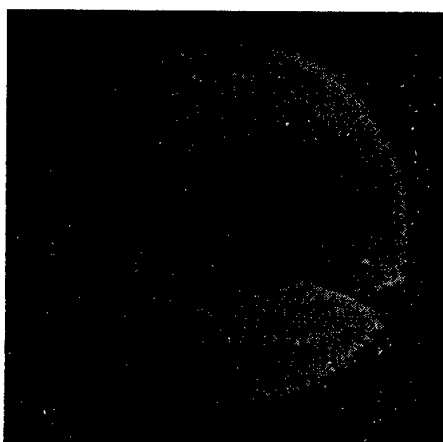
Figure 3.2-1. Apache Phase Conjugation Facility at CTS



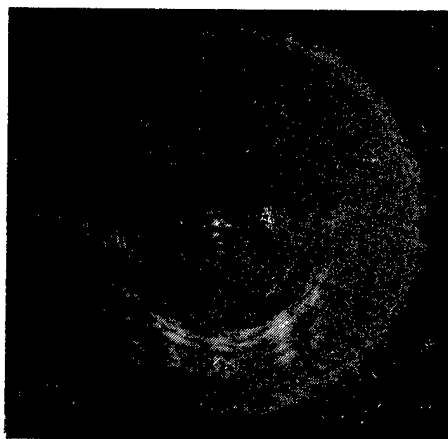
The PAR laser heads are flashlamp initiated and contain a 2-liter active gain volume. The gain volume is 1 m long and 2.5 cm in diameter. The gain medium is contained by a Suprasil quartz tube. The ends are sealed with  $\text{CaF}_2$  windows canted at an angle of  $5^\circ$  to normal to prevent parasitic oscillations. The two laser heads are operated in a master oscillator/power amplifier (MOPA) configuration. The oscillator has an on-axis annular unstable resonator with a magnification of 2.5. The cavity was long enough so that the PAR head fit completely on one-half of the length, ensuring that no closed-path existed between the end mirrors as a result of a grazing reflection off an inside wall of the laser. The cavity length was set at a half-integer Fresnel number for maximum transverse mode separation. The final design has a mirror separation of 304 cm and an equivalent Fresnel number of 8.5.  $\text{CaF}_2$  windows at Brewster's angle are included intracavity to linearly polarize the output in the horizontal direction. The outcoupled beam has a hole in the middle and radial lines caused by the struts holding the convex mirror as shown in Figure 3.2-2(a). To ensure a relatively uniform beam at the entrance to the amplifier, there is a propagation distance of 15 m between the oscillator and amplifier to diffractively fill in the hole in the mode caused by the feedback mirror. The beam shape after exiting the amplifier is shown in Figure 3.2-2(b). The entire oscillator/amplifier system is positioned on an optical bench external to the environmental conditioning system. A turning flat is used to direct the beam through a  $\text{CaF}_2$  window into the environmentally conditioned enclosure.

PAR laser operation was characterized and about 10% of the power was found to be from the  $\text{P}_2(8)$  line. Different gas mixtures were studied. The gas mixture recommended by the manufacturer contained 25%  $\text{SF}_6$  in addition to  $\text{F}_2$ ,  $\text{H}_2$ , and He. Because of its large index, the  $\text{SF}_6$  caused the beam to spread as the beam propagated to the far field. Consequently,  $\text{SF}_6$  was eliminated, and the nominal gas mixture used consisted of 20%  $\text{F}_2$ , 5%  $\text{H}_2$ , 73% He, and 2%  $\text{O}_2$ . This mixture was typically used at a pressure of 550 torr to prevent over pressure in the laser cavity which could cause damage. The maximum laser energy obtained from the PAR lasers was approximately 100 J. This degraded with time as the flashlamps and laser tube became dirty. The lasers have to be refurbished after about 300

### **DP-4 Film Burns**



**OSCILLATOR ONLY**



**OSCILLATOR PLUS  
AMPLIFIER**

Figure 3.2-2. Near-Field Intensity Film Burns

shots. A typical pulse shape is shown in Figure 3.2-3. Almost the same amount of energy was obtained from the amplifier as from the oscillator. The laser medium was homogeneously broadened, indicating that the laser operated in single mode. No evidence of mode beating was observed on the power versus time diagnostic.

### 3.2.2 Optical Train

A diagram of the high-power optical train is shown in Figure 3.2-4. The section from the turning flat behind the amplifier up to but not including the spatial filter is contained in zone 1 of the environmental conditioning system. The beam passes through beam shaping and steering optics and is directed through a 2.2- $\mu$ s (two-pass) optical delay line. This delays the SBS return such that there is no gain in the PAR laser by the time any SBS return enters the cavity. The long path produced a very low Fresnel number ( $\sim 0.25$ ). Spatial filtering downstream produces a beam of excellent quality ( $\sim 1.01$ ). The delay line mirrors are coated for high reflectivity, and the CaF<sub>2</sub> delay line windows are antireflection coated. The delay line can be run in vacuum. In early tests, the grating was placed upstream of the delay line to spectrally disperse the HF lines so only the P<sub>2</sub>(8) line reached the spatial filter. However, the high fluxes caused grating damage. Since the P<sub>2</sub>(8) line has very good air propagation compared to the other HF lines produced by the PAR laser, air attenuation can be used to reduce the flux in unwanted lines. Consequently, the delay line was left at atmospheric pressure, and the system was reconfigured with the grating downstream of the delay line. The spatial filter is downstream of the grating, far enough away that the P<sub>2</sub>(8) line is the only line passing through the spatial filter. A sketch of the beam at the upstream side of the spatial filter is shown as Figure 3.2-5.

### 3.2.3 Diagnostics

The diagnostics subsystem provides the instrumentation to monitor the performance of the launched and SBS return beams and is contained in zone 2 of the environmental conditioning system. A summary of diagnostic measurements is shown in Table 3.2-1 and the diagnostics layout is shown in Figure 3.2-6. The major diagnostics include the temporal power, energy, integrated beam quality, and near-field intensity for the launched and SBS return beams.

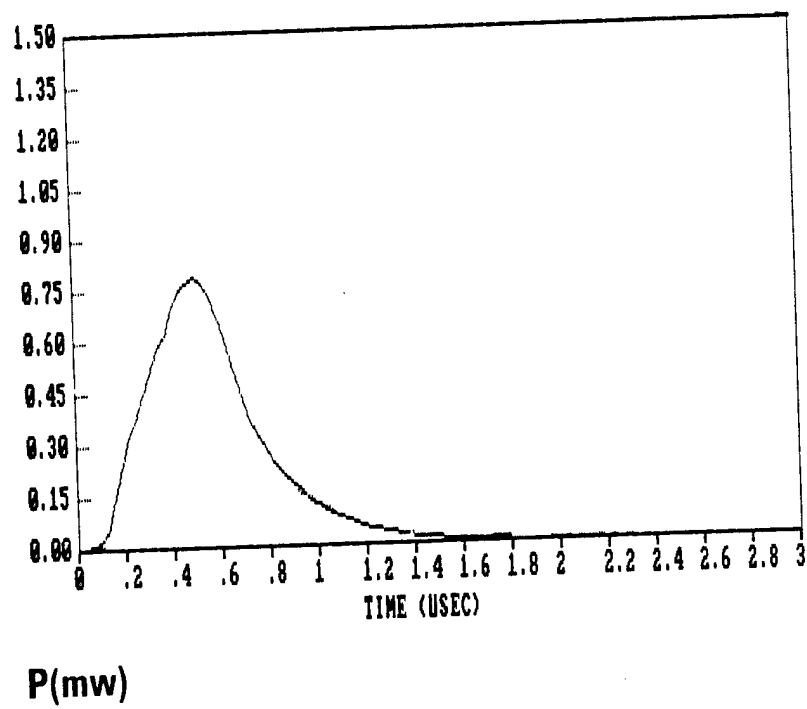


Figure 3.2-3. Pulse Temporal Profile from PAR Lasers

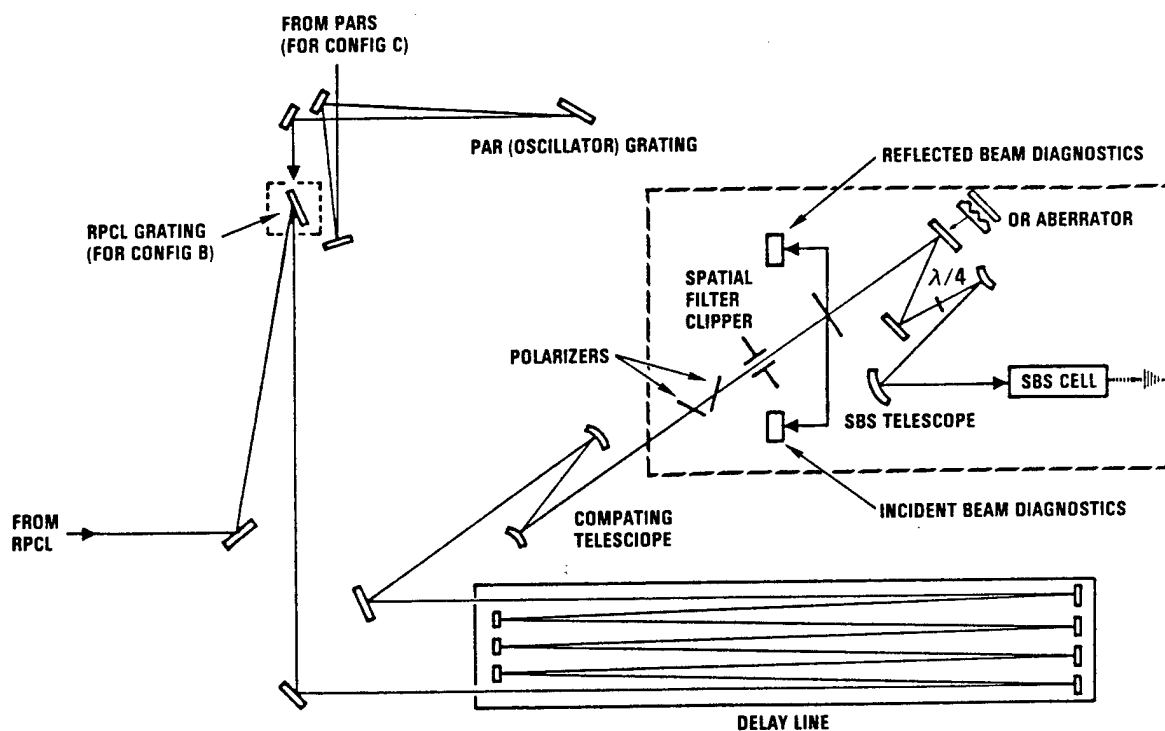


Figure 3.2-4. Optical Train for COS Experiment

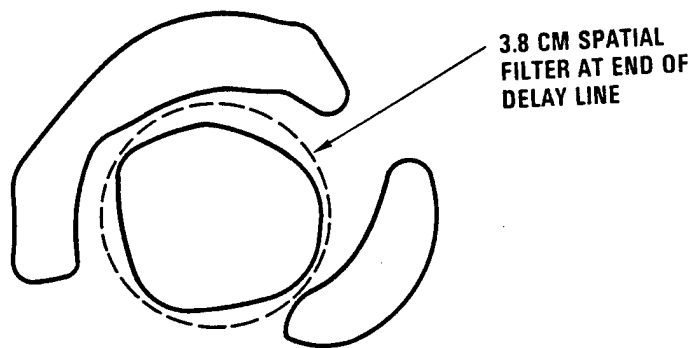


Figure 3.2-5. Far-Field Beam at Spatial Filter

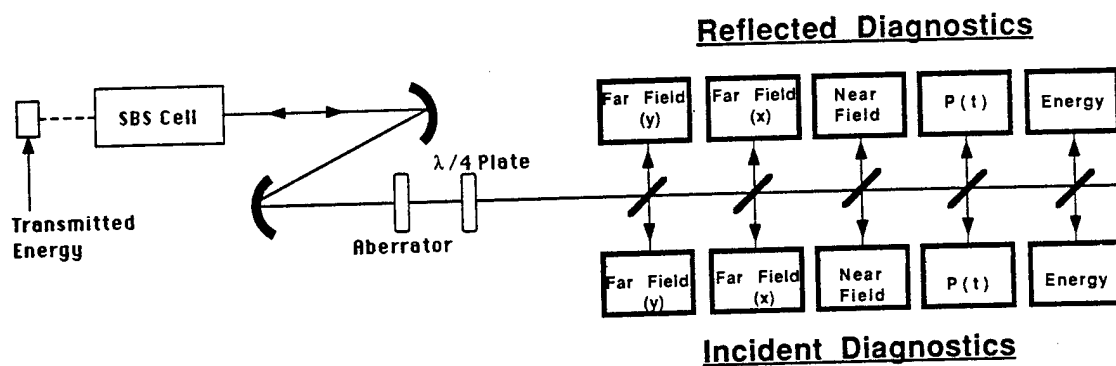


Figure 3.2-6. Diagnostics Layout

Table 3.2-1. Summary of Diagnostics

Measurement	Launched	Return	Method
Temporal power [P(t)]	x	x	InAs detectors
Energy (E)	x	x	Calorimeters
Near-field intensity	x	x	16 x 16 pyroelectric arrays
Beam quality (BQ)	x	x	Crossed linear 256 element arrays

Energy measurements are made with 1-in. Judson calorimeters which give  $\pm 5\%$  accuracy. Beamsplitters leading to the calorimeters are calibrated to ratio the amount of power entering and leaving the SBS cell over the power sent to the calorimeter. Temporal power measurements are made with a pair of Judson InAs detectors with integrating spheres. The responsivity of the power measurement is calibrated against the energy measured by the calorimeter. Power measurements are recorded by LeCroy transient digitizers and plotted by the control computer.

Near-field intensity is measured with a Spiricon 16 by 16 element pyroelectric detector array. The beam diameter measured with this diagnostic is used to compute the theoretical beam shape in the far field. The near-field intensity distribution closely approximates that of a Gaussian (Figure 3.2-7).

Spiricon linear arrays are used to measure time-integrated beam quality. This diagnostic consists of high-resolution pyroelectric detector arrays made up of 256 elements,  $85 \times 1000 \mu\text{m}$  in size, and spaced  $100 \mu\text{m}$  center to center, with a  $3 \times 10^5 \text{ V/J}$  (per element) responsivity and a dynamic range of  $10^4$ . Calibrations were performed by illumination with a spatially filtered chopped HeNe laser beam, with a beam quality of  $1 \times \text{DL}$ . For each measurement, the arrays are orthogonally oriented with cylindrical lenses condensing the beam to one dimension as shown in Figure 3.2-8. Beam quality is calculated using the measured near-field intensity distribution approximated as a Gaussian. The measured far-field pattern is then



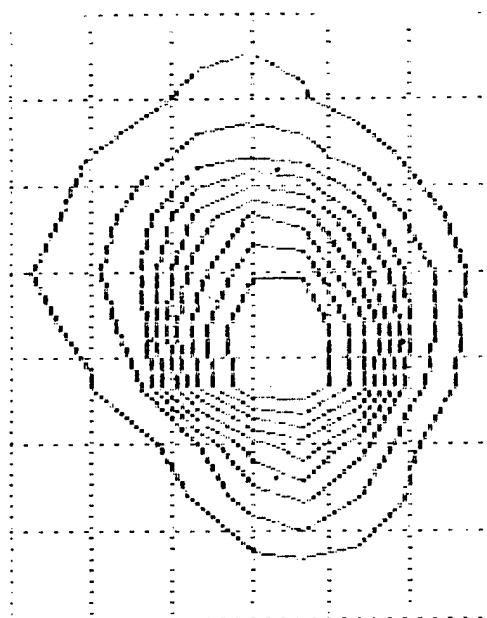


Figure 3.2-7. Near-Field Intensity Distribution of Incident Beam

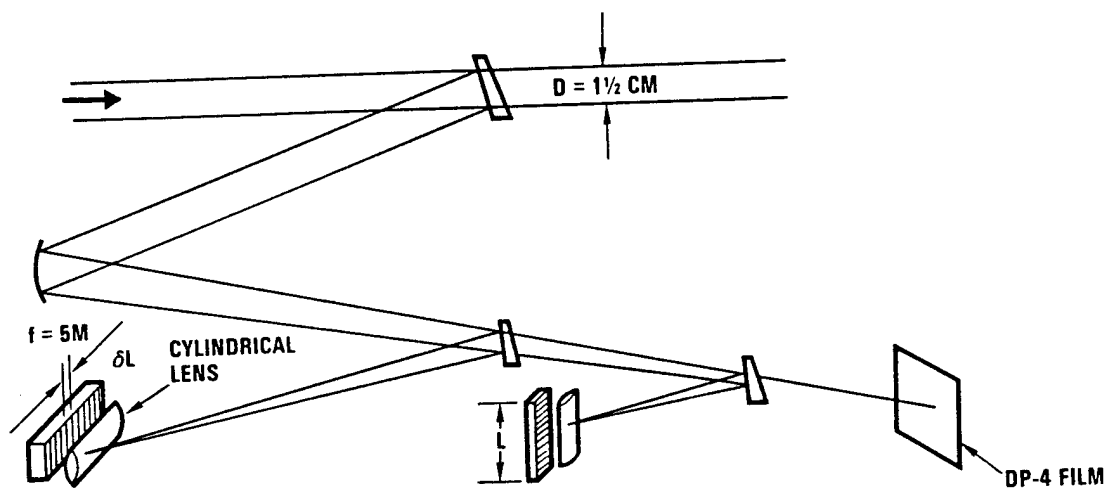


Figure 3.2-8. Time-Integrated Beam Quality Diagnostic

compared to the theoretical pattern for a Gaussian. Beam-quality plots are shown in Figure 3.2-9.

#### 3.2.4 Phase Conjugation Subsystem

Downstream of the diagnostic beamsplitter, the beam propagates to the SBS telescope. This telescope consists of a changeable convex mirror to adjust the telescope f-number, followed by a large concave mirror which focuses the beam into the SBS cell with the desired f-number.

The SBS medium is Xe gas at 40 atm. The SBS cell has Lucite safety windows which are lowered when personnel are in the area and lifted during an experiment. Xe is purified before it enters the cell by passing it through a hydrox purifier and a line filter to remove particulates. The SBS cell was carefully cleaned and assembled in a cleanroom environment before initial filling with Xe gas.

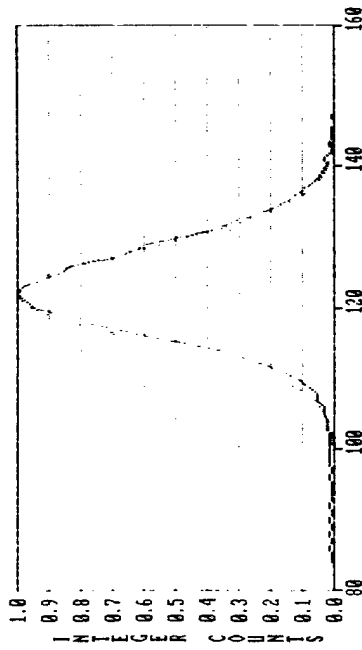
### 3.3 HFC RESULTS

Experiments were performed to establish the SBS threshold and conjugation fidelity in 40 atm of Xe at HF wavelengths for an f-number of 30. Measurements were made of beam quality in the far field and reflected energy versus incident energy. Plots of reflected energy versus incident energy are shown in Figure 3.3-1. The plot closely approximates a straight line with a slope of  $\sim 1$  and an intercept of 0.3 J. A second plot of the transmitted energy through the SBS cell, shown in Figure 3.3-2, exhibits a relatively constant transmitted energy once threshold is reached. Sometimes the threshold appeared to be substantially lower (typically  $\sim 0.2$  J), as evidenced by both the intercept of the plot and by the transmitted energy. This appeared to be correlated with the pulse length and shape of the laser output. This behavior is not well understood.

Plots of the far-field intensity distributions in the vertical and horizontal directions for the conjugated beam are shown in Figure 3.3-3. These can be compared with incident beam plots in Figure 3.2-9. Similar plots of the near-field intensity distribution for the incident and conjugated beams are shown in Figure 3.3-4. Note that the beam quality of

# Horizontally Aligned Array

BO = 1.00 ± 0.03

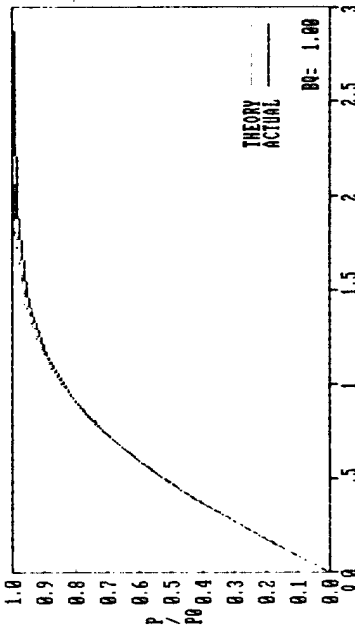
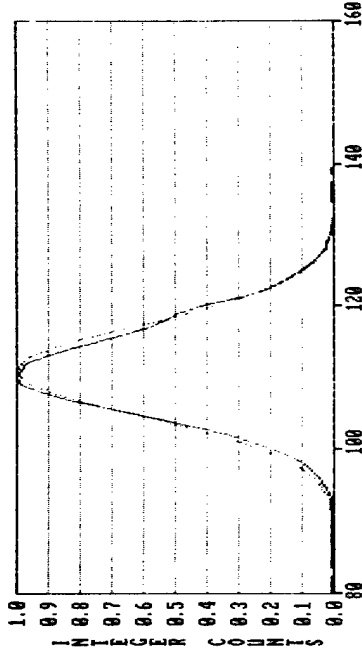


## (a) Far-Field Intensity Distribution

— MEASURED  
--- DIFFRACTION LIMITED

# Vertically Aligned Array

BO = 0.99 ± 0.03



## (b) P/P<sub>0</sub> Distribution

— MEASURED  
--- DIFFRACTION LIMITED

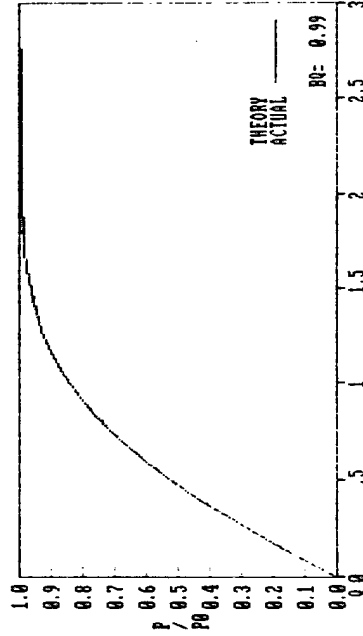


Figure 3.2-9. Incident Beam Far-field Characteristics

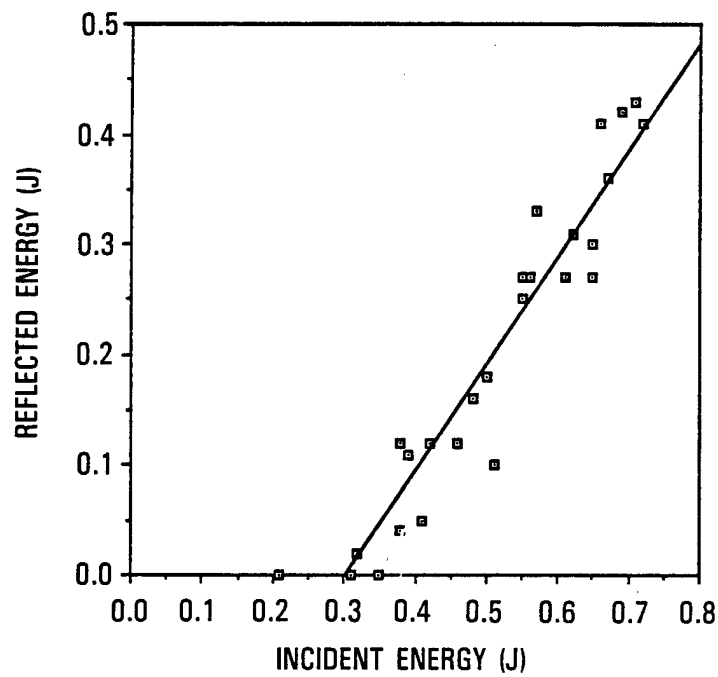


Figure 3.3-1. Plot of Reflected Energy Versus Incident Energy, With No Aberrator

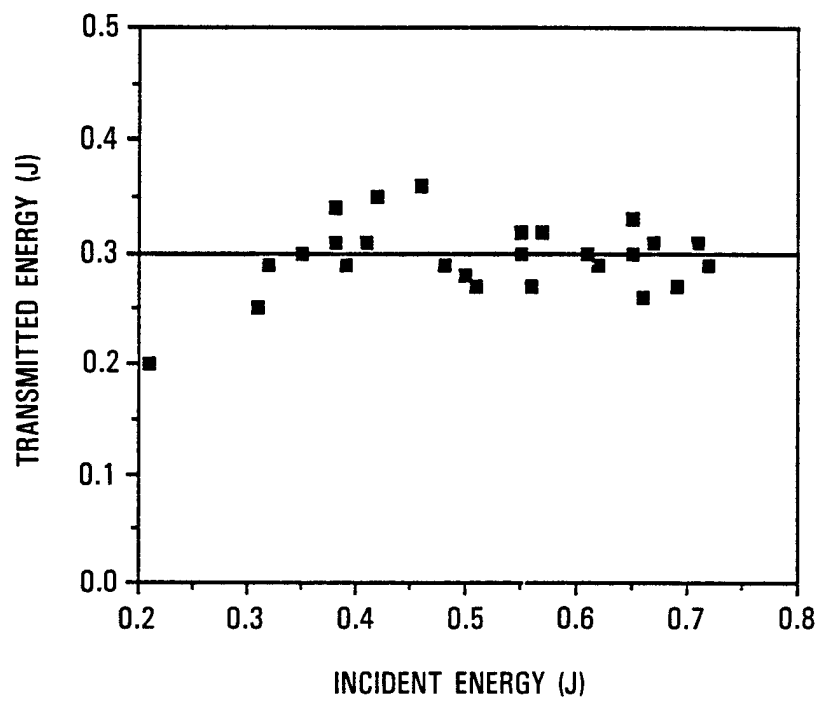
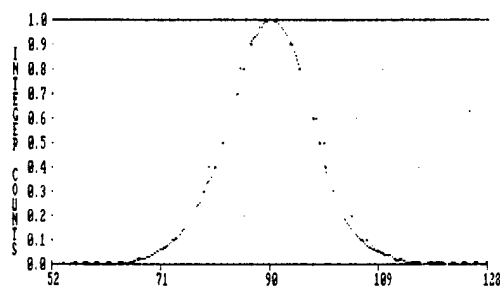


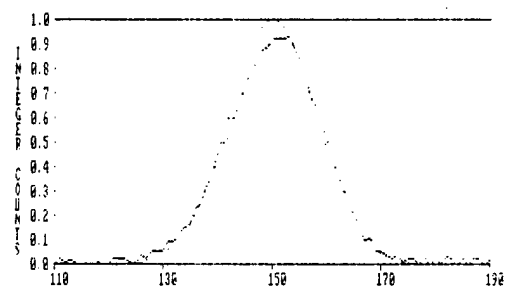
Figure 3.3-2. Plot of Transmitted Energy Versus Incident Energy

## Far field intensity distribution

### Horizontal Array

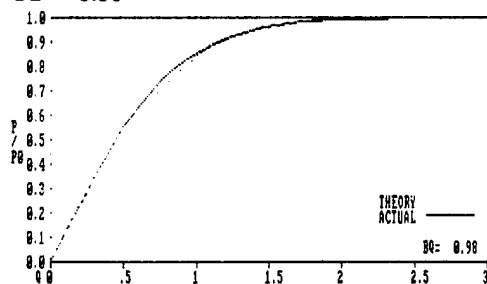


### Vertical Array



— DATA  
 ---- DIFFRACTION  
 LIMIT

### P/P<sub>0</sub> distribution and beam quality BQ = 0.98



### BQ = 1.04

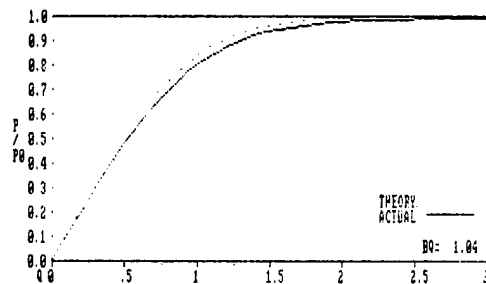


Figure 3.3-3. Far-Field Intensity Plots for Conjugated Beam With No Aberrator

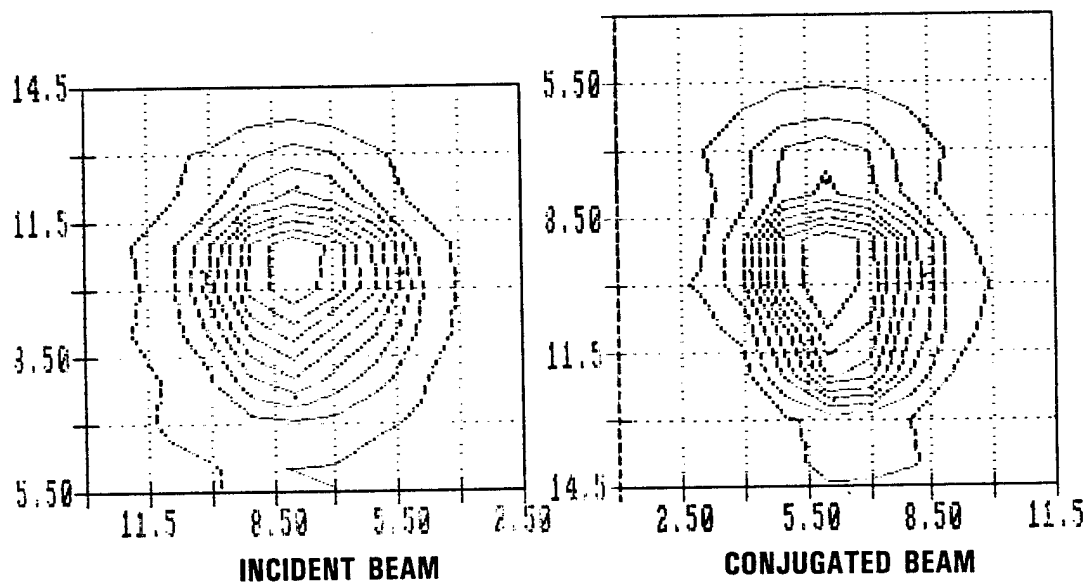


Figure 3.3-4. Near-Field Intensity Plots of Incident and Conjugated Beam, With No Aberrator



both incident and conjugated beams in both directions is 1.00 within experimental error of  $\pm 0.05$ . BRIWON code calculations were performed for a Gaussian beam at  $2.9 \mu\text{m}$ . Far-field plot of the intensity of the input pump and corrected stokes is shown in Figure 3.3-5. The predicted beam quality is 1.00, in good agreement with the experiment.

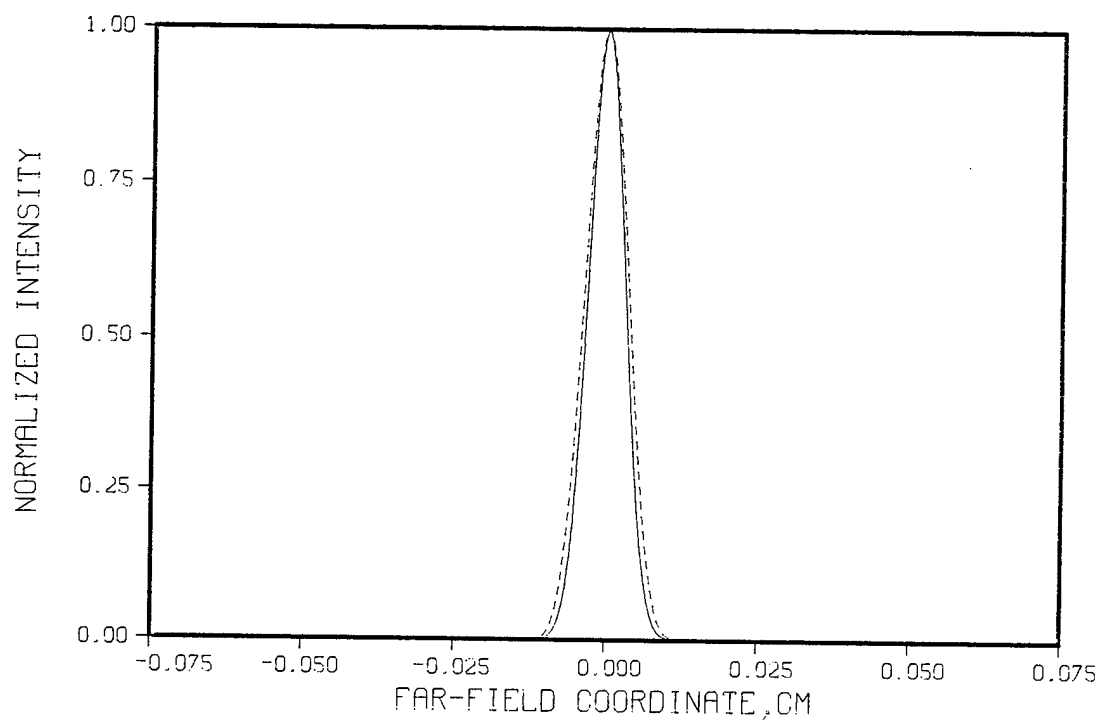
Seidel aberrations introduced by misalignment of the SBS telescope had a measureable effect on SBS threshold. This is shown in Figure 3.3-6 for both aligned and misaligned telescope configurations. Interferometry showed substantial astigmatism (vertical and horizontal foci separated by almost 6 in.) for the misaligned telescope, which resulted in a higher threshold, 0.45 J. When the telescope was aligned interferometrically, the threshold was reduced to 0.3 J.

### 3.4 CONJUGATION SUBSYSTEM (COS) EXPERIMENT

The purpose of the conjugation subsystem (COS) experiments was to establish an HF data base scalable to an SBL. Variables included aberrations and f-number into the SBS cell.

Aberration experiments were conducted with aberrators consisting of one-dimensional irregularly spaced piston stops. Conjugation of two one-dimensional aberrators oriented orthogonally to each other was studied. The wavefront error was 0.4 waves peak to peak in the vertically oriented aberrator and 0.8 waves peak to peak in the horizontally oriented aberrator. Far-field intensity distributions are shown in Figure 3.4-1. Conjugation fidelity is shown in Figure 3.4-2. The beam quality in both directions was close to unity, indicating excellent conjugation fidelity.

A second part of the COS experiment was to vary the f-number. The major objective of this exercise was to establish the "clean Xe" breakdown threshold. The onset of breakdown was established by observing the incident and transmitted  $P(t)$ s. Breakdown resulted in plasma formation, which absorbed the incident radiation. Consequently, the pulse shape of the transmitted beam with breakdown changes from that of the transmitted beam without breakdown. Pulse shapes with no breakdown, incipient breakdown, and full breakdown are shown in Figure 3.4-3. An f-number of



	MAXIMUM INTENSITY
—— PUMP INPUT	$2.828 \times 10^5$
----- CORRECTED STOKES	$1.947 \times 10^5$

Figure 3.3-5. BRIWON Predictions of Far-Field Intensity of Conjugated Beam for Gaussian Input Beam

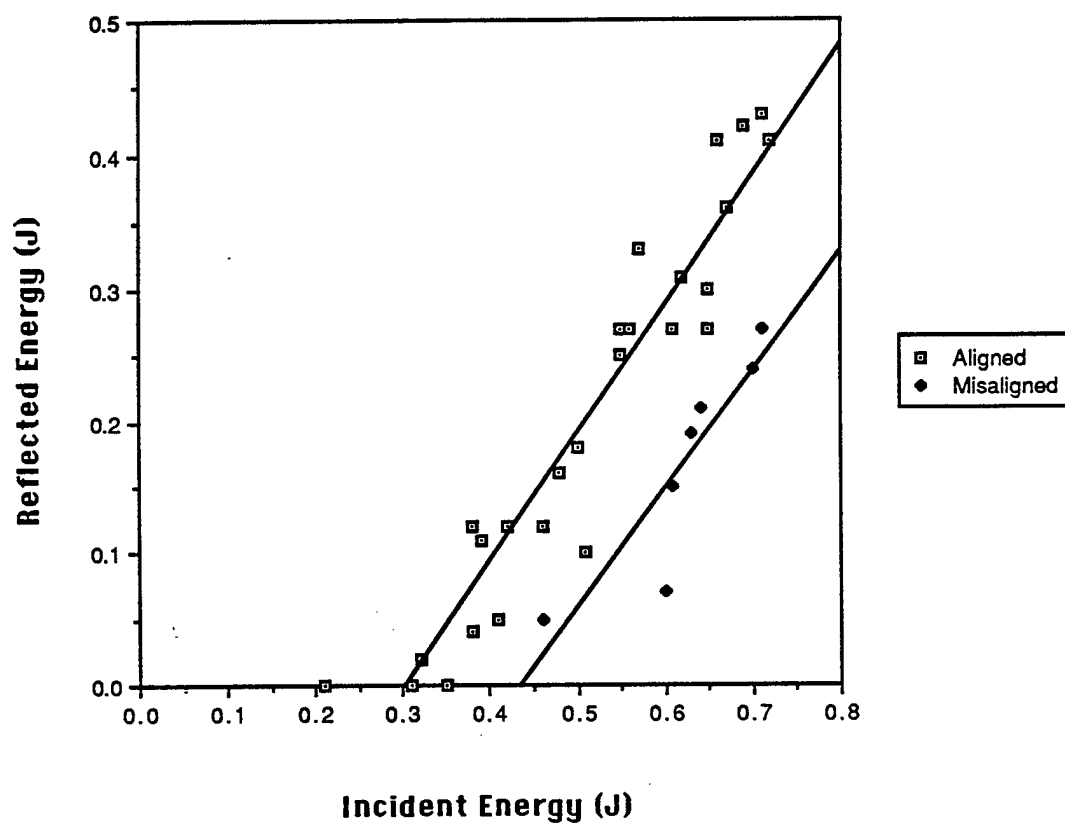
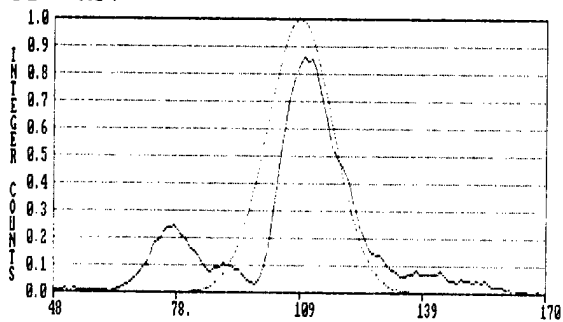


Figure 3.3-6. Plots of Reflected Energy Versus Incident Energy Showing Effect of SBS Telescope Alignment of Threshold

### Horizontal Array

BQ = 1.34



### Vertical Array

BQ = 1.43

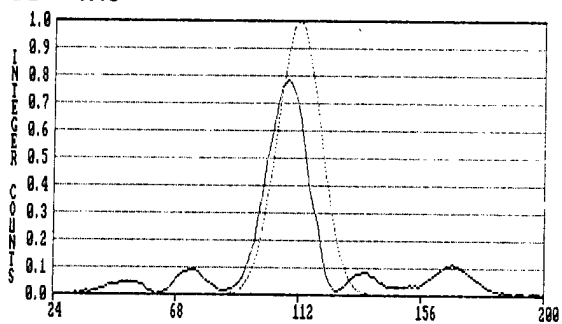
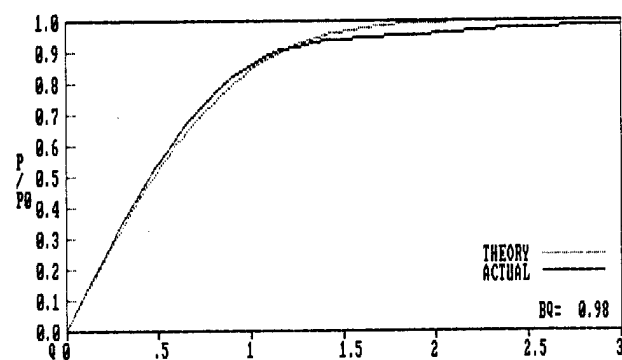
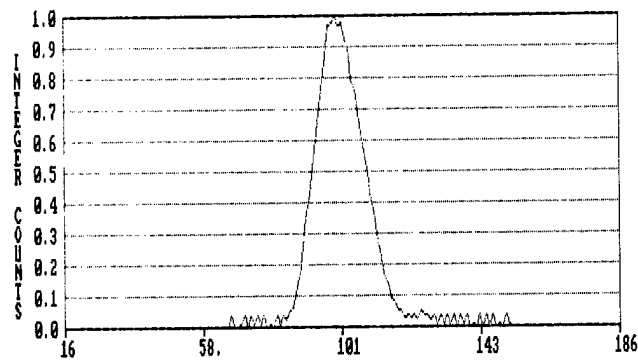


Figure 3.4-1. Far-Field Intensity Distributions of Incident Beam for Two-Dimensional Aberrator

## Far field beam quality

### Horizontal Array

BQ = 0.98



### Vertical Array

BQ = 1.04

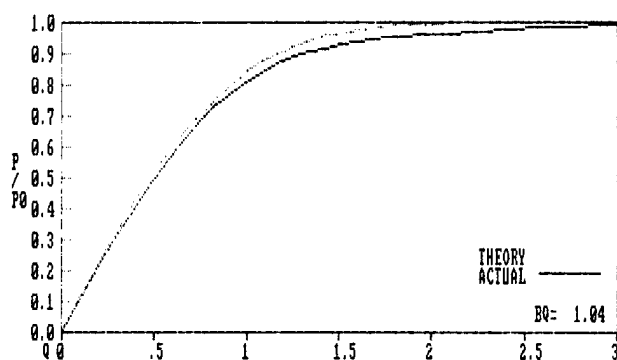
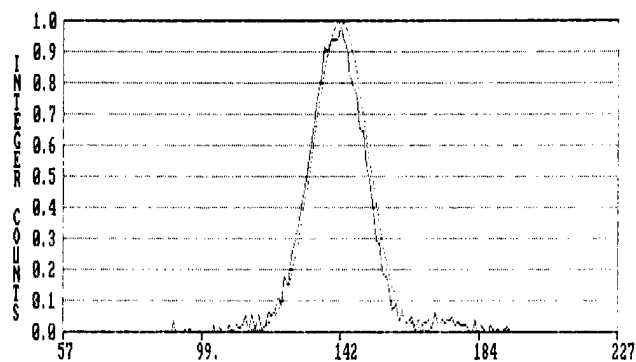


Figure 3.4-2. Far-Field Intensity Distributions and Beam Quality Plots of Conjugated Beam for Two-Dimensional Aberrator

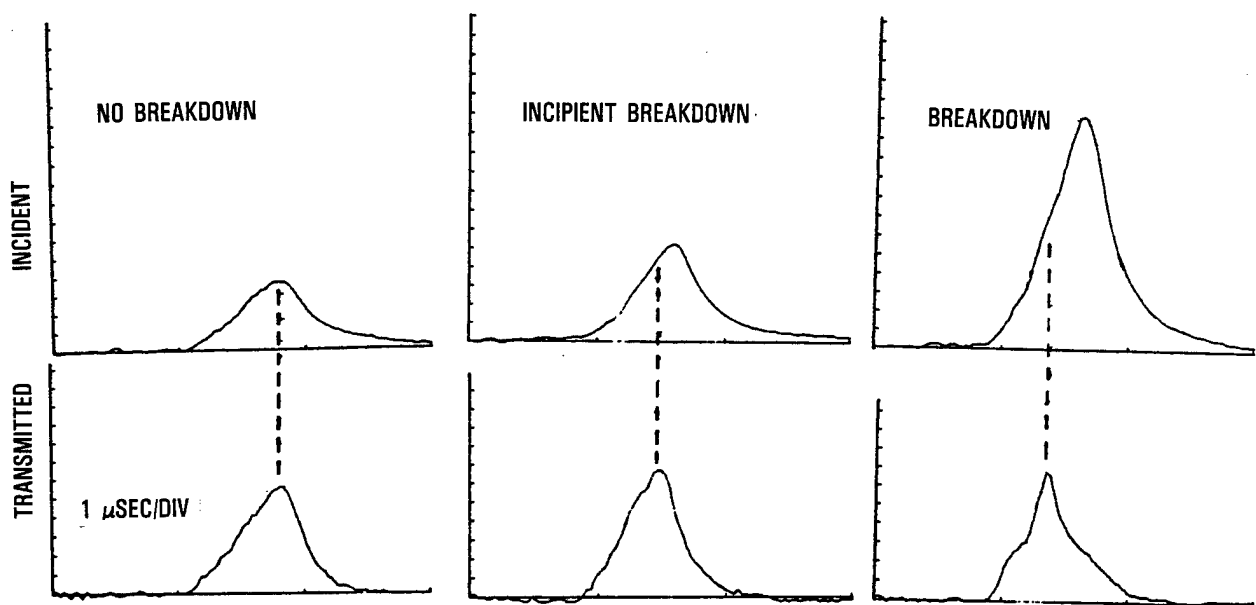


Figure 3.4-3. Temporal Plots of Incident and Transmitted Beams for Conditions Near Breakdown

~13 was required to obtain a high enough intensity to achieve breakdown. The breakdown threshold established from this experiment was approximately  $4.5 \times 10^{10} \text{ W/cm}^2$ .

To scale the this result to CW HF, it is important to understand the mechanisms for breakdown. The two basic processes which can lead to optically induced breakdown in pure Xe are direct multiphoton ionization and cascade or collision-induced absorption. The multiphoton ionization directly ionizes Xe atoms and is unimportant at the wavelengths and power levels of interest for the APACHE program. In the cascade process, free electrons absorb energy from the laser radiation during collisions with Xe atoms and exponentially multiply in number due to a series of ionizing collisions. Breakdown occurs when the intensity is sufficiently high that energy gained by induced absorption exceeds all losses. The number of cascades required for breakdown is reasonably small, typically of the order of 40 to 60. For long pulses or CW operation, the breakdown limit is determined by intensity.

The primary electron energy loss mechanisms which determine the breakdown threshold are (1) electron diffusion out of the laser beam, (2) elastic Xe collision losses, and (3) inelastic Xe collisional losses. Analysis (References 3-2 and 3-3) indicates that inelastic collision losses strongly dominate at the high pressures of interest. Rough calculations were performed using the numerical values in Reference 2. The predicted optical breakdown intensities for 40 atm Xe were  $4 \times 10^9 \text{ W/cm}^2$  at  $2.9 \mu\text{m}$  and were weakly dependent on pressure over the range of interest. This model is very simplistic; thus, the experiments described above.

Breakdown is commonly observed at intensities well below the intrinsic limit due to aerosols. A typical symptom of aerosol-induced breakdown is a f-number-dependent breakdown intensity. There are several theoretical treatments to assess scaling with particle size and pressure, but their accuracy is limited. Even if an accurate model were available, it would depend on such intangibles as the composition of the aerosols. The approach outlined by Smith (Reference 3-4) will be used to estimate the consequences of different particle sizes. Smith's results imply that there

is a radius-dependent particulate breakdown threshold for the vaporized particle material and that the intrinsic gas breakdown limit is reached when all particles are sufficiently small that their breakdown limit is larger than the clean gas value. Substitution into his expressions and comparisons between them and the earlier theoretical clean gas values imply that the intrinsic limit is approached for maximum particle diameters of order 0.1 to 0.3  $\mu\text{m}$ . It appears likely that the presence of larger particulates will decrease the breakdown threshold somewhere between inversely and inversely as the square of their ratio to this size.

Experimentally apparently higher breakdown intensities can also be observed. At long wavelengths there may not always be an initiating electron (or very small aerosol) at the intensity peak in the focal region and therefore, there is variation in the observed value. The SBS process itself can also substantially influence breakdown. If the rise time of the laser pulse is sufficiently long that the phonon grating is established before breakdown occurs, the transmitted power and inferred focal point power flux is reduced by the transmission factor of the phonon grating.

Data interpretation is also complicated by the difficulty in estimating the peak intensity and deciding whether the need for an initiating electron source implies that the average focal volume value is more appropriate. Typical intensity estimates include:

Focal volume	$P/[\pi(\lambda F/\#)^2]$
Circular focus (peak)	$P\pi/[4(\lambda F/\#)^2]$
Gaussian beam (peak)	$P\pi/[2(\lambda F/\#)^2]$

Using an analytical breakdown intensity estimate for a wavelength of 1.06  $\mu\text{m}$ , these correspond to peak incident powers of 590, 240, and 120 kW, respectively.

Subscale breakdown measurements were performed early in the APACHE program using a 1.06- $\mu\text{m}$  laser. Breakdown was observed to occasionally occur at levels commensurate with the highest power condition. After correcting for the reflected beam, the experimental transmitted power was



approximately 700 kW. The estimated beam quality of the laser is 1.2. Assuming breakdown scales as beam quality squared, breakdown could be approximated as

$$I_{\text{break}} = 500 \text{ kW } (BQ)^2 (F\#/30)^2$$

This value is higher than the analytical estimates except for the average focal volume assumption. Extrapolation to HF wavelengths implies a correlation

$$I_{\text{break}} = 700 \text{ kW } (BQ)^2 (F\#/30)^2$$

The HF data for F/13, assuming an intensity calculated for a Gaussian beam, gives an inferred breakdown intensity at 2.9  $\mu\text{m}$  of

$$I_{\text{break}} = 1800 \text{ kW } (BQ)^2 (F\#/30)^2$$

with a range of uncertainty of 0.9 to 3.4 MW for the 1.8 MW value. This value and the earlier value inferred from the 1.06- $\mu\text{m}$  data are large compared to the 2.9- $\mu\text{m}$  SBS threshold (75 kW) and indicate that for pure Xe breakdown is not a significant problem over the range of f-numbers considered in the SBL design ( $>20$ ). Figure 3.4-6(a) summarizes the the SBS threshold in relation to the breakdown threshold as a function of f-number. Figure 3.4-6(b) shows that the pulse duration of the PAR lasers was sufficiently long to simulate CW breakdown.

In extrapolating results to CW conditions, the main consideration is the much larger volume sampled due to the gas flow which makes stringent particle control essential. On very rare occasions one might be unlucky and a large particle might induce breakdown. After a few tens of microseconds the particle would be removed from the beam by the flow and the question naturally arises as to whether the plasma would then extinguish. Under some conditions maintenance of a stable plasma is possible (References 3-5 and 3-6). However, the arguments in Reference 3-7

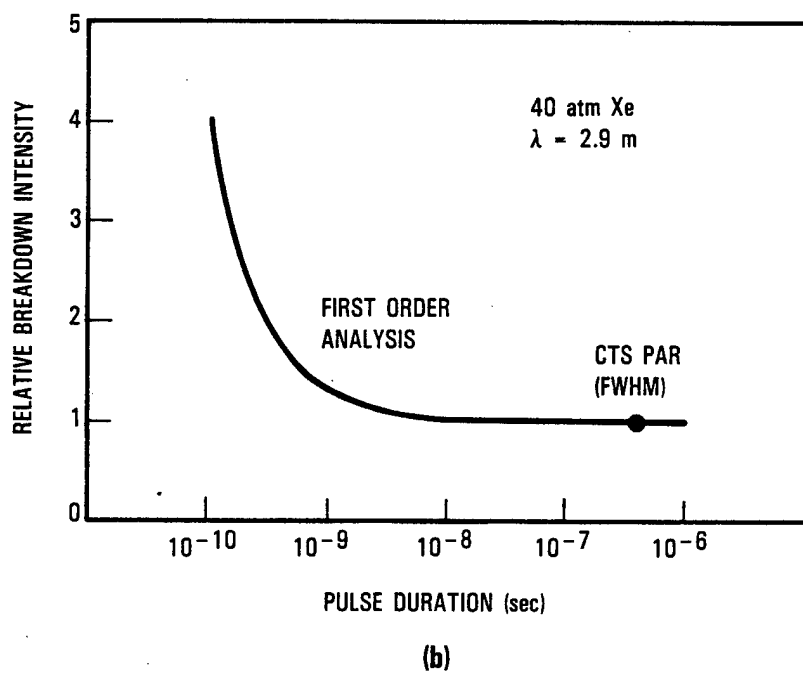
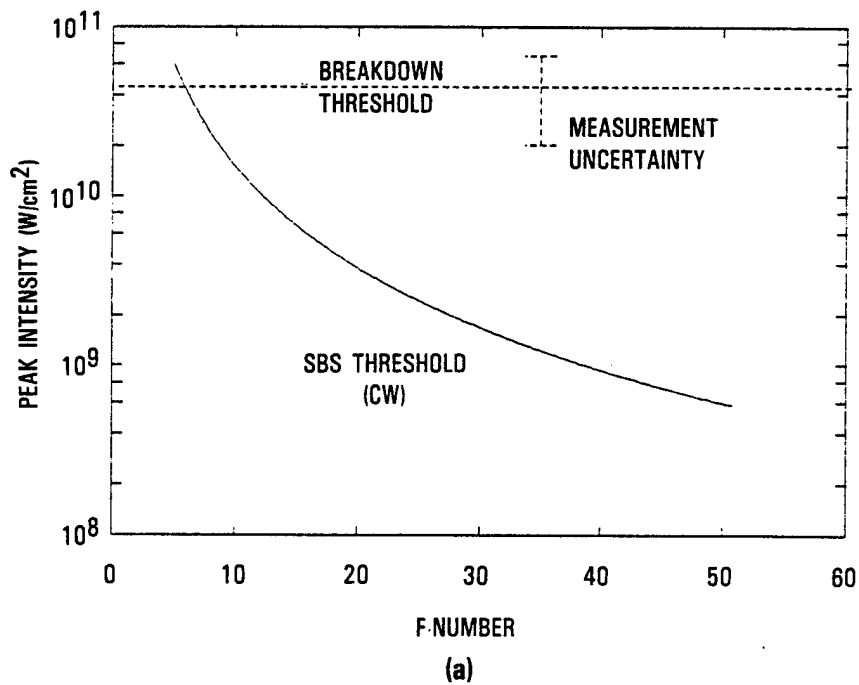


Figure 3.4-6. Gas Breakdown Summary. (a) Peak Intensity Versus Threshold  
(b) Relative Breakdown Intensity Versus Pulse Duration

indicate that often the plasma is unstable. Further effort is required to assess this possibility.

### 3.5 BEAM COMBINING (BC) EXPERIMENT

For the beam combining experiments, a  $\text{CaF}_2$  wedge was inserted into half the beam as shown in Figure 3.5-1. The wedge separates the far field into two spots. In this configuration, the beams overlapped before focus. Four wedges were studied which provided beam separations of 1.25, 2.5, 5, and 10 spot diameters. Alignment of the beam on the wedge was found to be critical to obtain a reproducible experiment. To aid in measurement of alignment and to discriminate between "good" and "bad" shots, a new diagnostic was added to the train, as shown in Figure 3.5-2. A calorimeter was used to look at the reflection off the wedge and was used to quantify the percentage of the beam hitting the wedge. In addition, a piece of carbon paper (which "burns" to show the beam footprint) was placed in the transmitted beam to show the relative energy of the two beams at the SBS cell. Sensitivity to wedge alignment is shown in Figure 3.5-3, where transmitted energy ( $\approx$  threshold) is plotted versus the percentage of the beam on the aberrator. There is a local maximum in the threshold as a function of aberrator alignment, and threshold is highest when the beam is split into two equal halves. This diagnostic was used to reject misaligned shots. The energy in the PAR lasers without threshold reduction was sufficient to study only the beams separated by 1.25 and 2.5 spot diameters. A plot of threshold energy with these beam combining aberrators versus unaberrated threshold energy is shown in Figure 3.5-4. Further beam combination experiments were performed using threshold reduction which allowed study of wider spot separations in the far field. These results are provided in Section 2.6. Conjugation fidelity was measured for the beam combining aberrator. An example of this is shown in Figure 3.5-5 where the input beam with a beam quality (BQ) of 1.10 is split into two spots separated by 2.5 spot diameters and conjugated into a single spot with a BQ of 1.07. A BRIWON code calculation for spots separated by 2.5 spot diameters is shown in Figure 3.5-6. The code prediction for conjugated beam quality is 1.014.

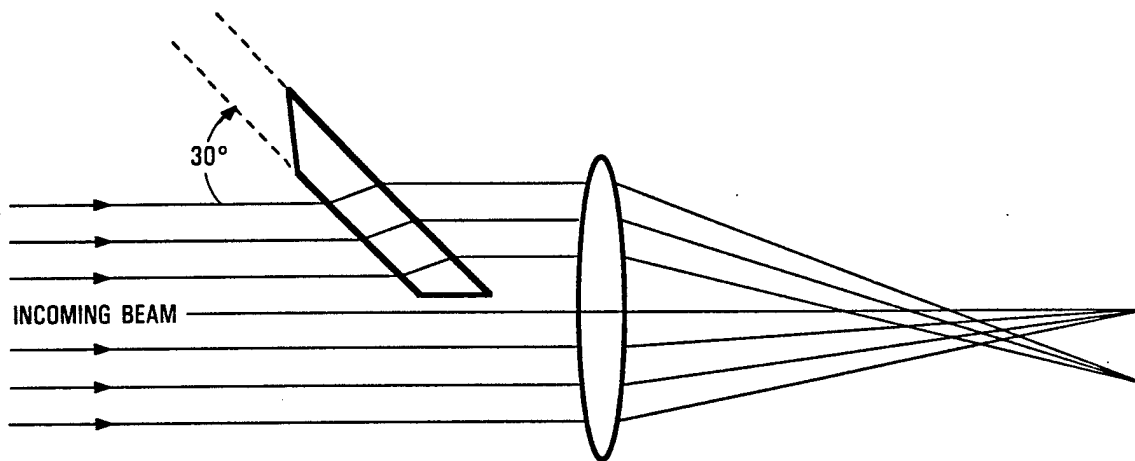


Figure 3.5-1. Schematic of Wedge Separating Far-Field into Two Spots

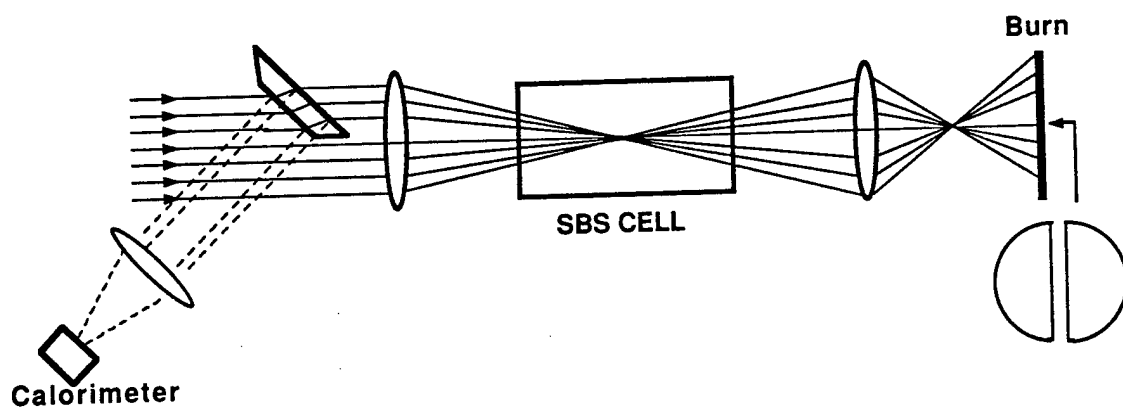


Figure 3.5-2. Layout Showing Additional Diagnostics for Beam-Combining Aberrators

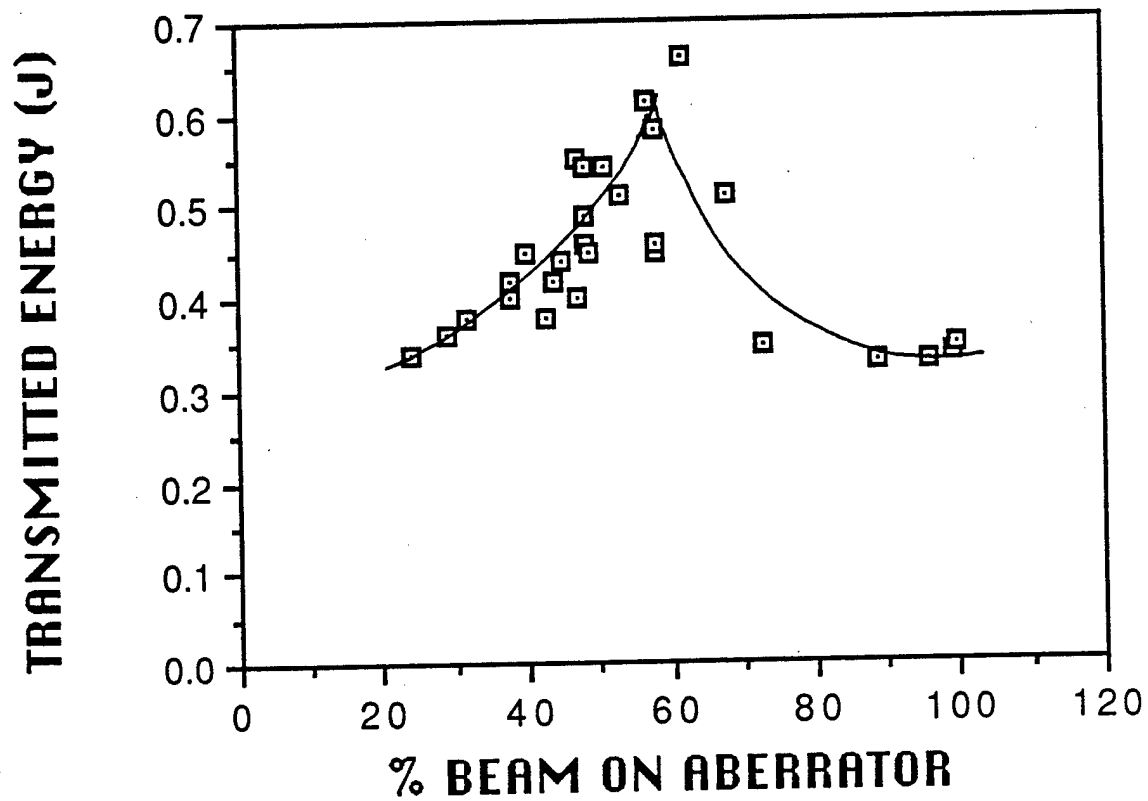


Figure 3.5-3. Transmitted Energy Versus Aberrator Alignment

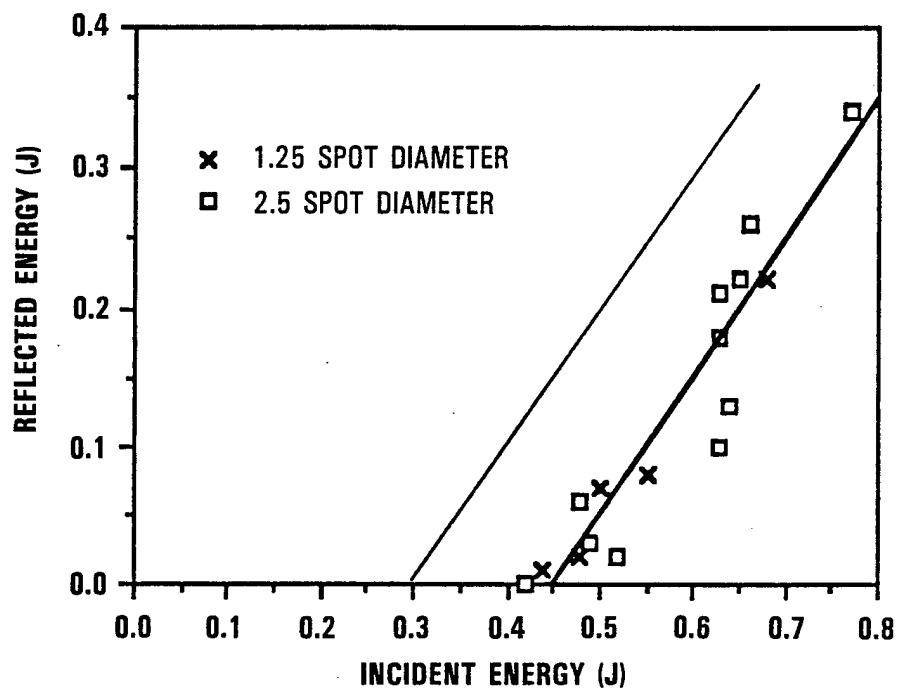


Figure 3.5-4. Plots of Reflected Energy Versus Incident Energy for Wedge Aberrators

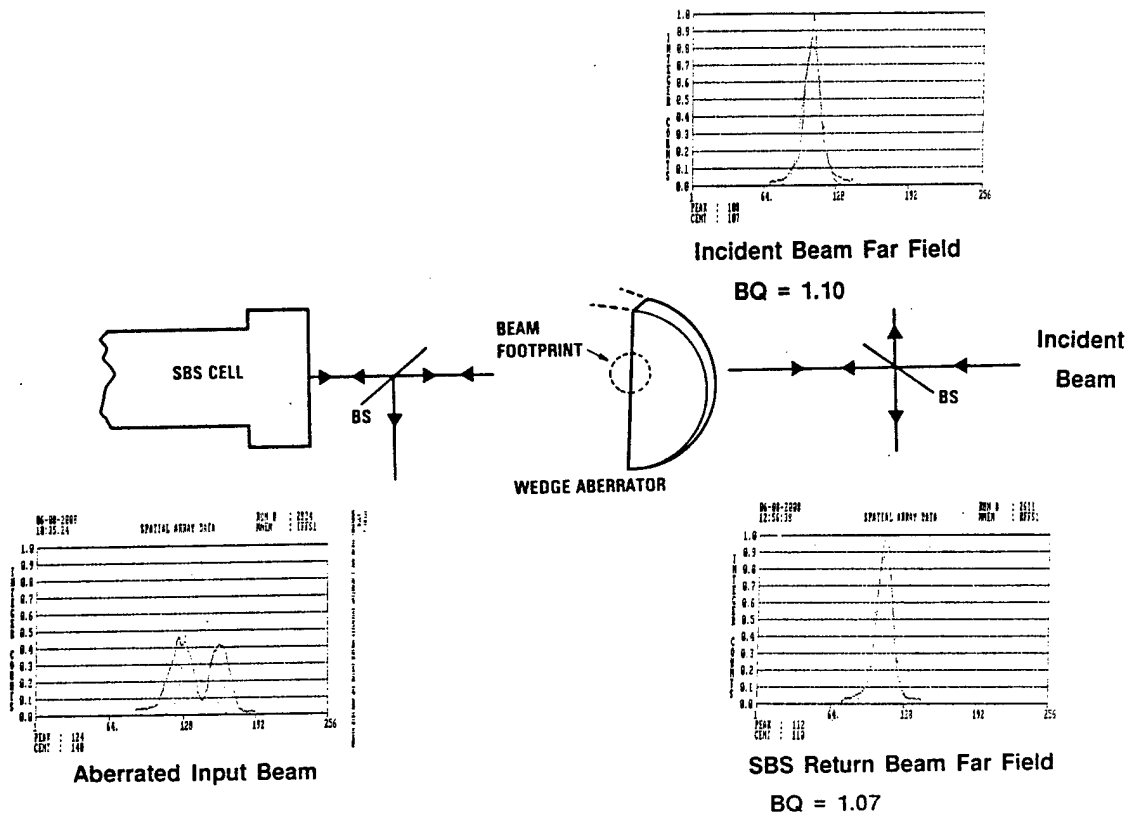
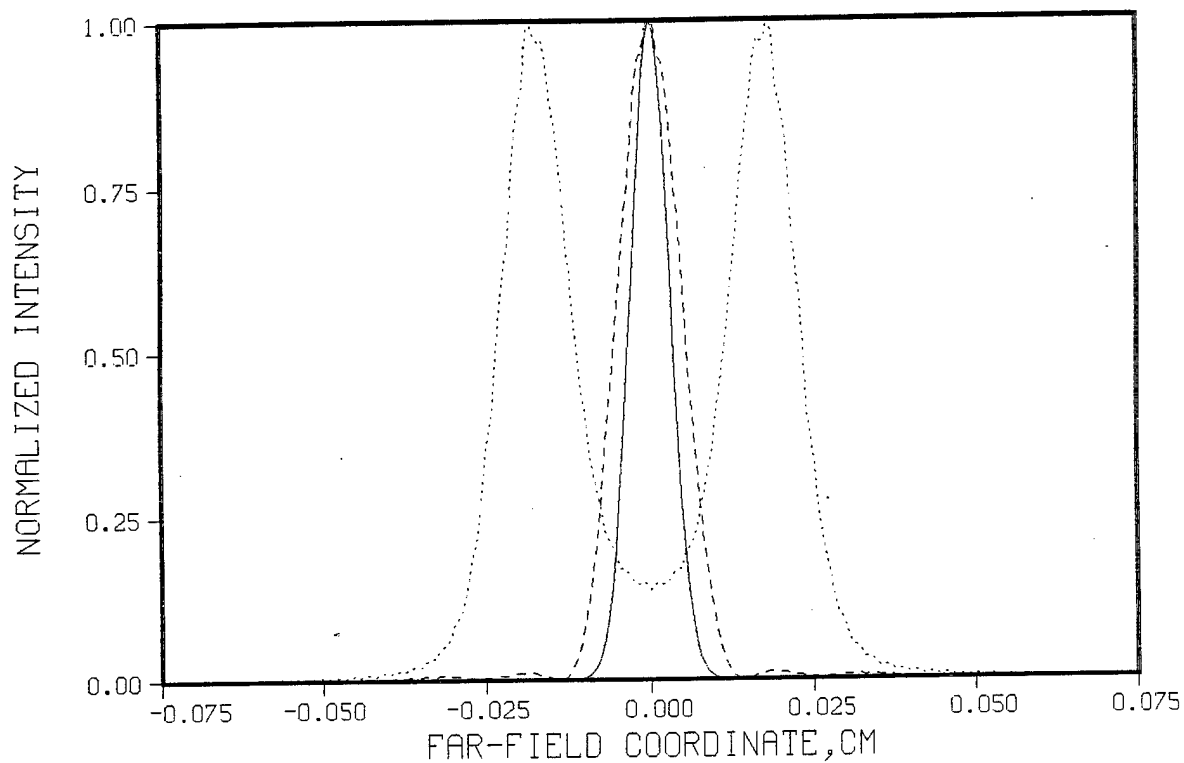


Figure 3.5-5. Plots of Far Fields of Incident, Aberrated and Conjugated Beams for Wedge Aberrator





	MAXIMUM INTENSITY
— PUMP INPUT	$2.828 \times 10^5$
..... ABERRATED PUMP	$7.320 \times 10^4$
---- CORRECTED STOKES	$1.230 \times 10^5$

Figure 3.5-6. Far-Field Intensity Plots From BRIWON Code for Beams Separated by 2.5 Spot Diameters

### 3.6 THRESHOLD REDUCTION EXPERIMENTS

The threshold reduction concept studied in these experiments was to use successive foci in the SBS medium, each providing a backseed for the one in front. Initial experiments were conducted using two separate SBS cells with a focussing lens between cells. The first experiment was performed with a doubled YAG laser with hexane used as the SBS medium by R. Aprahamian and C. Clendening on TRW IR&D funds. In the first HF experiments two cells were also used, but high-pressure Xe was used as the SBS medium. Subsequent experiments were conducted with a single cell using curved mirrors to allow two or four nonoverlapping foci in the cell. A schematic of this setup is shown in Figure 3.6-1. Plots of reflected energy versus incident energy are shown in Figure 3.6-2 for two and four foci. The slope efficiency stays near 1 for all configurations, but the intercept (threshold) decreases with increasing number of foci. A threshold reduction of almost 2.6 was demonstrated with four foci.

One of the limitations of this experiment was the uncoated  $\text{CaF}_2$  windows on the SBS cell. Reflection off the window surfaces resulted in a transmission loss focus to focus. A study of focus-to-focus loss was made both experimentally and with the BRIWON code. The minimum loss caused by reflection off the SBS cell windows and the retro mirror equals 0.78. To verify the dependence of threshold on focus-to-focus loss, flats were inserted between the retro mirror and the SBS cell. Results are plotted in Figure 3.6-3. BRIWON code results for two and four foci were also plotted. Both the code and experiment indicate a larger threshold reduction enhancement factor for increasing round-trip transmission. This illustrates the need to minimize the losses between foci when using this technique. Conjugation fidelity measured with threshold reduction remained good as shown in Figure 3.6-4. Both incident and reflected beam qualities were  $1.00 \pm 0.05$ .

Threshold reduction with four foci was also used to study conjugation fidelity. In particular, the beam-combining aberrators were chosen for this study. Far-field spot separations of 1.25, 2.5, 5, and 10 spot diameters were studied. Figure 3.6-5 shows a plot of threshold (ratioed to

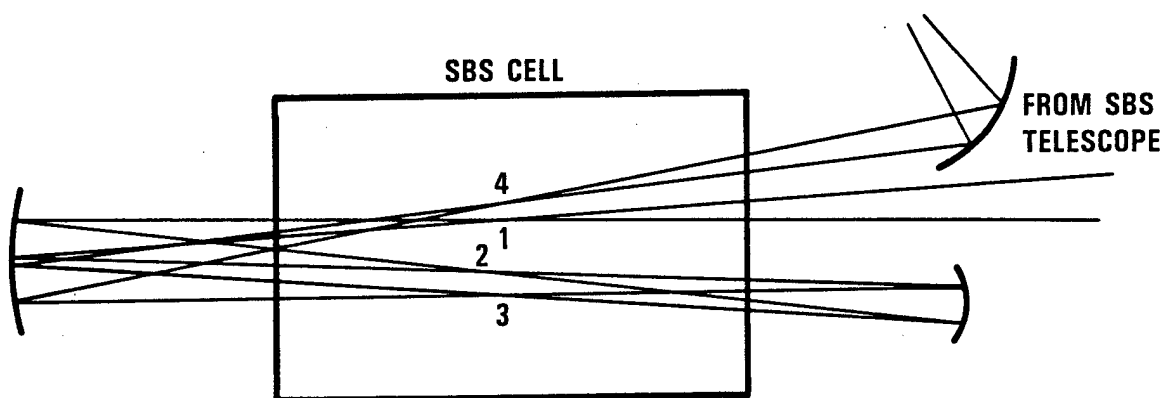


Figure 3.6-1. Optical Layout for Threshold Reduction Using Single Cell and Four Foci

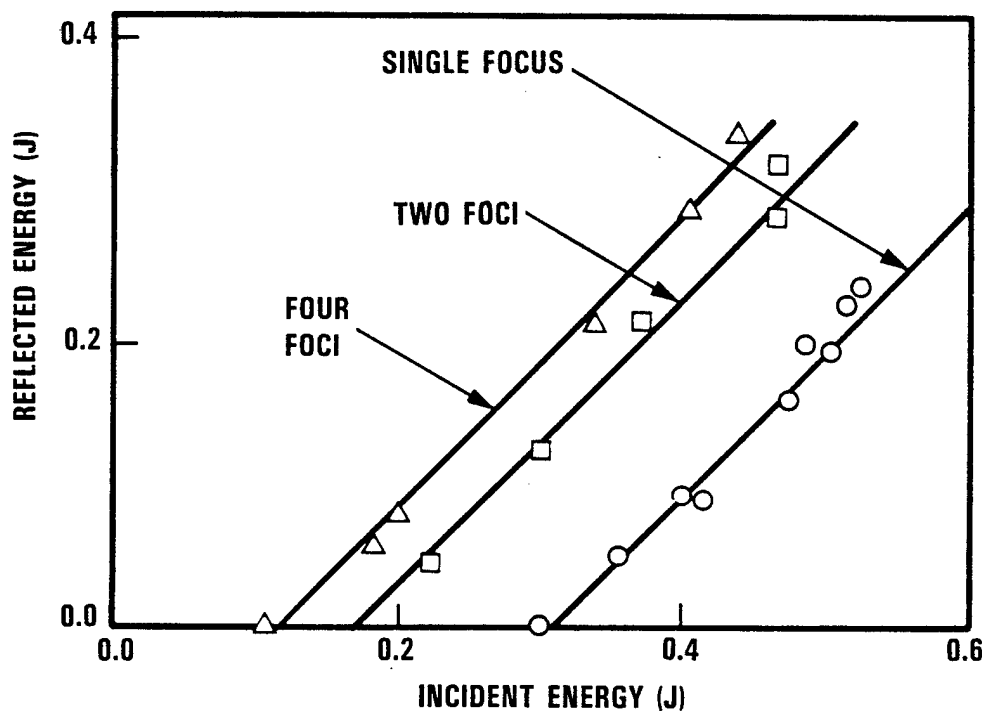


Figure 3.6-2. Plot of Reflected Energy Versus Incident Energy for One, Two, and Four Foci

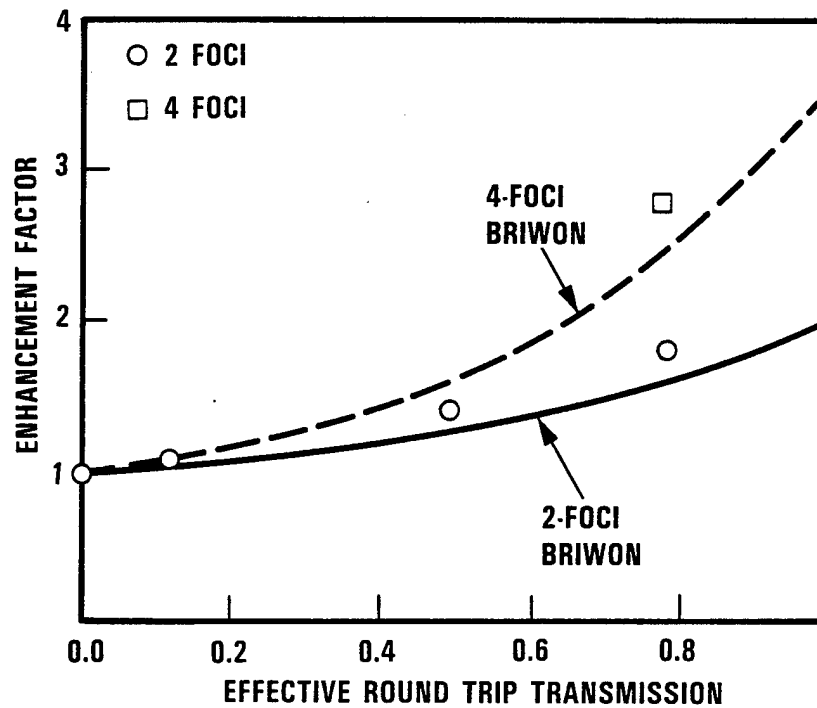


Figure 3.6-3. Reduction in Threshold Dependent on Focus-to-Focus Loss

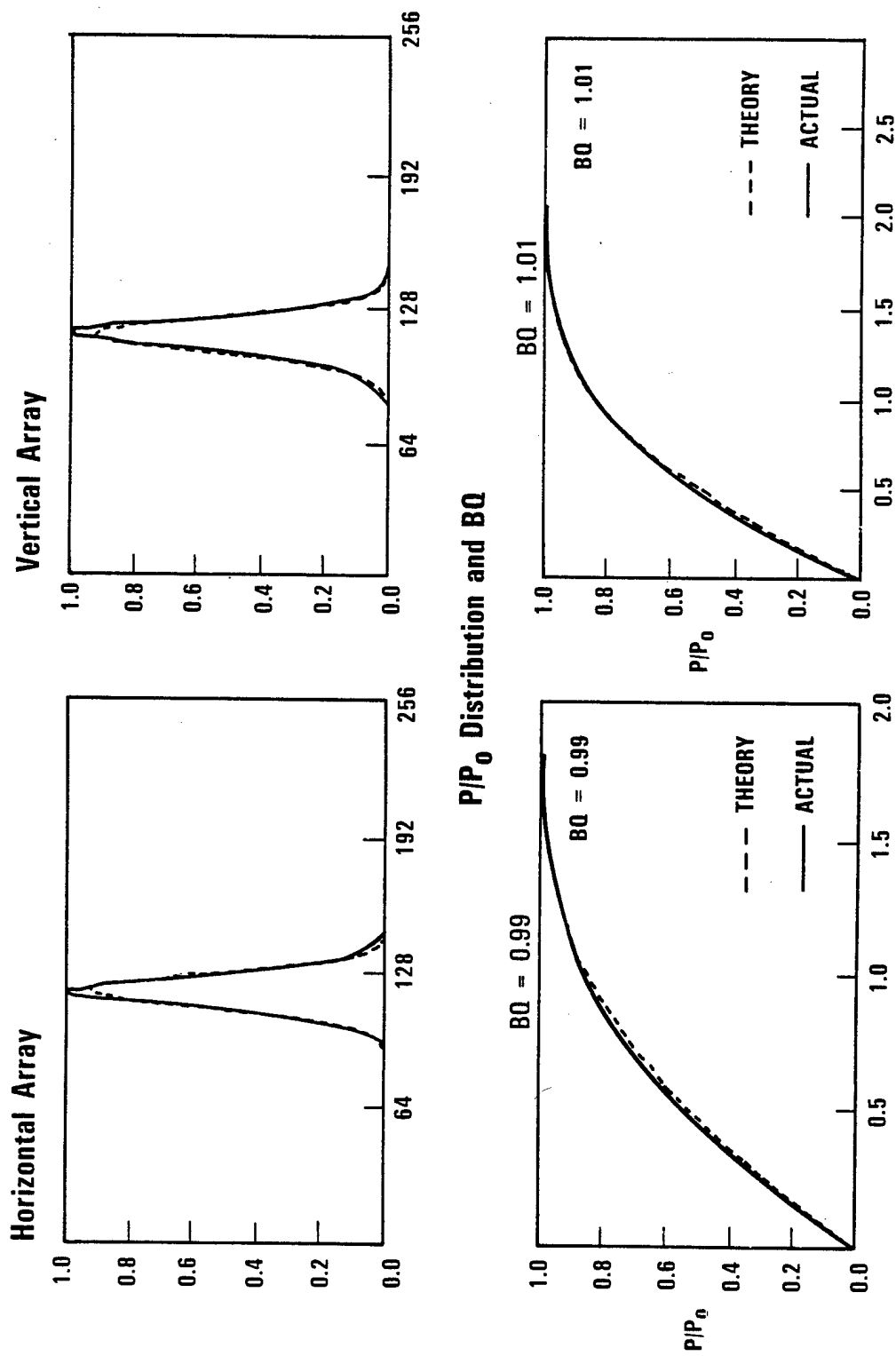


Figure 3.6-4. Excellent Conjugation Fidelity Observed With Four-Foci Threshold Reduction

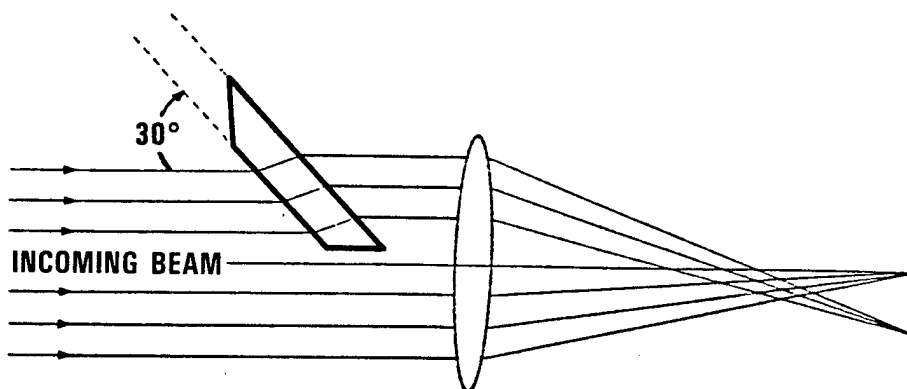
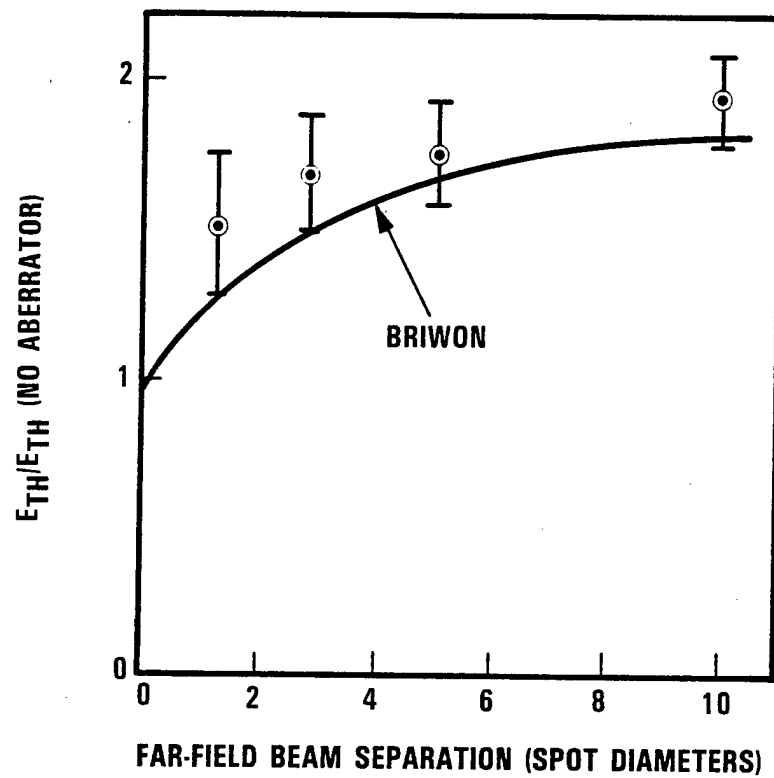


Figure 3.6-5. Beam Combination Demonstrated With Threshold Reduction

the unaberrated threshold) versus far-field beam separation in spot diameters. Also shown in this figure are BRIWON calculations for the same condition. Both the experiment and code predicted an increased threshold with increased spot separation in the far field. Conjugation fidelity remained good with incident and reflected beam qualities of  $1.00 \pm 0.05$ .

Another experiment was conducted in which two wedge aberrators were crossed at right angles to produce four separate beams in the SBS cell. A two-foci threshold reduction was used to keep the incident power above threshold. The phase-conjugated return showed excellent beam quality as illustrated in Figure 3.6-6. This was the first successful demonstration of four-beam combination at HF wavelengths by SBS and is important for scaling to the SBL as it simulates combination of beams from four amplifiers.

In summary, successive foci in an SBS cell was found to be effective in reducing threshold while maintaining good conjugation fidelity. Minimization of focus-to-focus loss is important in fully utilizing this technique.

The reduction of threshold by focusing the pump and Stokes fields several times within the cell, with the focal points suitably separated, was modeled by assuming a tandem arrangement of SBS cells. The pump field leaving the back of one cell is propagated to the near field and re-focused into the next cell. Similarly, the Stokes field leaving the front of one cell is propagated to a near-field lens and is refocused into the preceding cell. The boundary conditions for the fields are now specified for the pump at the front of the first cell and for the Stokes, as noise, at the rear of the last cell. The iteration procedure in BRIWON for solving the coupled field equations then requires the propagation of the pump and Stokes through all cells on each iteration. The velocity-dependent aberrations (thermal blooming and grating convection) are the same for each cell since only one physical cell is present and the flow velocity is assumed to be uniform throughout the interior of the cell. On the other hand, the turbulence characteristics of the flowing layer forming an aerowindow may vary with distance downstream from the nozzle so that, in



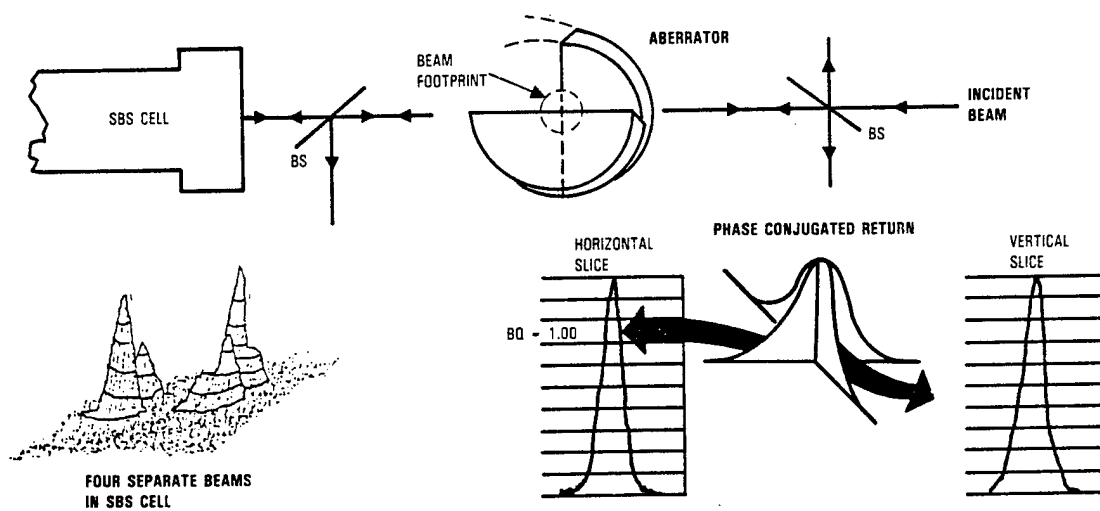


Figure 3.6-6. Four-Beam Phase-Conjugation Demonstration

the multicell model, the turbulence parameters are allowed to vary from cell to cell.

For a particular case of an F/30 system, a Gaussian pump beam of 500 kW, and a total cell length of  $6\lambda(F/\#)^2$ , the threshold values were calculated with BRIWON to be 86-, 51-, and 40-kW for 1, 2, and 3 cells, respectively. Another case of a wedge aberrator applied at the focusing lens which produced a focal-plane spot separation of 2.5 beam diameters gave a single-cell threshold of 157 kW, which, when 2 cells were used, was reduced to 86 kW. Grating convection aberrations were also examined for a two-cell case at  $\lambda = 2.8 \mu\text{m}$ , and it was found that over a range of flow velocities of 0 to 10 m/s threshold increased by about 10%, or approximately half the increase for a single cell.

### 3.7 SBS CW AND TRANSIENT THRESHOLD BEHAVIOR

Both analytical and computer calculations were performed to assess the threshold and reflectivity dependence of the SBS process at conditions of interest. In this section the assumptions and results are summarized and compared with experimental measurements at both 1.06- and 2.9- $\mu\text{m}$  laser wavelengths.

#### 3.7.1 CW Threshold Estimation

The SBS gain coefficient  $g_B$  can be obtained from the expression

$$g_B = \frac{w_s^2 (\gamma_e)^2 t_{\text{phonon}}}{c^3 n v \rho}$$

where

- $w_s$  = scattered light angular frequency
- $\gamma_e$  = electrostriction coupling constant
- $c$  = speed of light
- $n$  = refractive index
- $v$  = sound speed
- $\rho$  = gas density
- $t_{\text{phonon}}$  = phonon lifetime.

For high-pressure Xe  $t_{\text{phonon}}$  is inversely proportional to the scattered-light frequency squared, so  $g_B$  is frequency independent. The gain-gas-density dependence is approximately quadratic. This results from the explicit inverse dependence on density, the implicit dependencies of electrostriction and phonon lifetime (both approximately proportional to density), and the relatively weak density dependence of  $n$  and  $v$ . For 40 atm Xe, the inferred  $g_B$  value is 46 cm/GW. The phonon lifetime for 2.91  $\mu\text{m}$  laser scattering is estimated to be 280 ns.

CW threshold can be estimated by determining the effective gain length product necessary to amplify spontaneous Brillouin Stokes backscattering to detectable levels. The dominant initial spontaneous scattering occurs at the back of the cell and the effective gain can be estimated by some simple integrals. The average gain (appropriately weighted by the photon distribution) at a given  $z$  location is

$$G(z) = \frac{g_B \int I^2 dA}{\int I dA} = \frac{g_B \int I^2 dA}{P}$$

where

$I$  = intensity

$dA$  =  $dx dy$

$P$  = incident power

$g_B$  = Brillouin gain coefficient,  $\text{cm}^{-1}/(\text{W}/\text{cm}^2)$ .

For purposes of threshold estimation, there is no pump depletion and as a first approximation for a focusing circular beam and a long SBS cell of length  $2L$  the following intensity profile was assumed:

$$I(z) = \frac{P}{\pi (\lambda F/\#)^2} \quad |z| < 2\lambda (F/\#)^2$$

$$\frac{4 P (F/\#)^2}{\pi z^2} \quad L > |z| > 2\lambda (F/\#)^2$$

The net gain between  $z = +2 \lambda (F/\#)^2$  and  $+L$  can be shown to equal

$$\exp \left[ \frac{s(1 - 1/L^*)}{4} \right]^*$$

where

$$S = \frac{8g_B P}{\pi \lambda}$$

and

$$L^* = \frac{L}{2 \lambda (F/\#)^2}$$

The gain in the focal region  $|z| < 2 \lambda (F/\#)^2$  is  $\exp(S/2)$ .

The net gain over the entire length is

$$\exp \left[ \frac{S}{2} + \frac{S}{2} \left( 1 - \frac{1}{L^*} \right) \right]^*$$

For large  $L^*$  values and a source at the cell back the total gain is

$$\exp(S)$$

By comparing the last two expressions, it is possible to estimate threshold scaling versus cell length. Note that for long cells, half the gain comes from regions more than one Rayleigh range from focus. This large contribution is the primary reason why threshold need not simply scale as beam quality squared for aberrated beams.

The spontaneous emission which is being amplified is actually distributed spatially and for a diffraction-limited beam was roughly approximated using the following formula:

$$\Delta\theta \sim \frac{1}{(2F/\#)} \quad |z| < 2\lambda (F/\#)^2$$

$$\Delta\theta \sim \lambda \frac{F\#}{z} \quad -L^* < z < -2\lambda (F/\#)^2$$

$$\Omega(z) = \frac{2\pi (\Delta\theta)^2}{2}$$

For a cell which is several Rayleigh ranges long the dominant contribution comes from well behind the focus. Assuming a spontaneous source term:

$$\frac{d\sigma}{d\Omega} P \Omega(z) dz \quad -L < z < -2\lambda (F/\#)^2$$

and integrating the gain, implies a net amplified signal

$$\frac{Pd\sigma}{d\Omega} \frac{2\pi\lambda}{S} \exp\left(\frac{S}{4}\right) * \left[ \exp\left(\frac{-S}{4L^*}\right) - \exp\left(\frac{-S}{4}\right) \right] * \exp\left(\frac{S}{2}\right) * \left\{ \exp\left[\left(\frac{S}{4}\right) * \left(1 - \frac{1}{L^*}\right)\right] \right\}$$

As shown below, S is of order 25, and thus for large L\* values this expression is almost exactly

$$\frac{Pd\sigma}{d\Omega} \frac{2\pi\lambda}{S} \exp(S)$$

and the predicted gain factor is dominated by the exp(S) factor.

The spontaneous cross section ( $d\sigma/d\Omega$ ) is proportional to the fourth power of laser frequency and varies approximately linearly with gas density. For typical HF laser frequencies and a 40-atm Xe cell, its value is approximately  $2 \times 10^{-9}/\text{cm.st}$ . If threshold is defined as a 1% reflectivity then, the threshold condition is that:

$$0.01 P = P \frac{d\sigma}{d\Omega} \frac{2\pi\lambda}{S} \exp(S)$$

A numerical solution yields an S value of 25. For a 1.06  $\mu\text{m}$  laser, this drops to  $S = 22$ . The associated HF threshold power is 62 kW and for YAG wavelengths is 20 kW. Moderately higher values (i.e., 68 kW and 22 kW) are predicted if a 10% definition of threshold is used.

Similar analyses can be applied to beams which are not uniform. The intensity weighted gains are then used. For example, a real flat-top circular beam has a more complex profile than the simple uniform profiles assumed above. For purposes of comparison, the actual intensities calculated based on appropriate Fourier Bessel integrals were used to calculate an intensity weighted net average gain. The result agreed within a few percent with the approximation. The intensity weighted gain was also calculated for a Gaussian beam and the inferred threshold was reduced by a factor of  $8/(\pi^2) = 0.81$  when compared to the uniform beam approximation. More detailed analyses with the more comprehensive BRIWON computer code agree well with the predicted thresholds and show comparable effects associated with effects of beam apodization. After BRIWON was modified to include a spontaneous scattering source term it predicted a long cell limit threshold power for HF of 72 kW, and when one focusing dimension was made Gaussian, it predicted a threshold reduction factor of 0.89.

As discussed in Section 2, the CW  $P_{\text{threshold}}$  at 1.05  $\mu\text{m}$  was measured to be 40 kW for a beam quality = 1.5. This compares quite well with diffraction-limited BRIWON analyses and the above analytical estimates which imply that the threshold for a diffraction limited beam is 22 to 29 kW. A threshold scaling of  $\sim BQ^1$  is sufficient to explain the data. BRIWON calculations shown in Figure 3.7-1 for a one-half cycle cosine astigmatic aberrator similar to the actual measured beam aberration agree with this scaling. Note that a simple beam quality scaling law is probably not in general appropriate. Clearly, threshold scaling depends on the nature of the aberration. Some preliminary numerical calculations which used methods analogous to those used to estimate threshold suggest that even for phase aberrations which are geometrically similar but have different amplitudes a simple power law is not always appropriate.

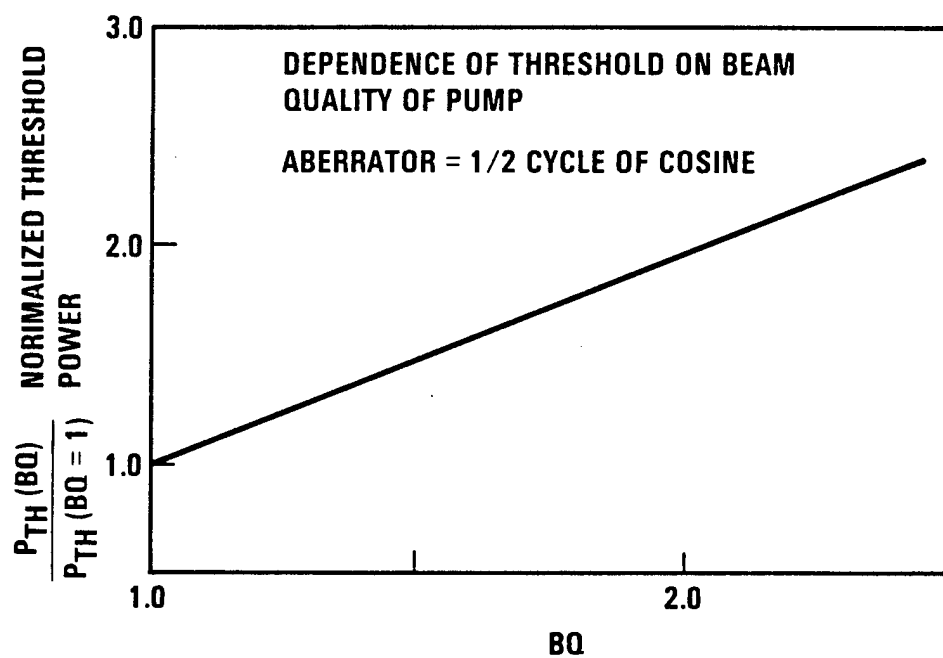


Figure 3.7-1. Dependence of Threshold on Pump Beam Quality

Similar arguments apply to the N multiple sequential foci case and imply that for perfect beams threshold falls nearly inversely with the number of foci. The analysis can easily be extended to include losses between foci. If the transmission factor loss at each cell interface is T, then to achieve a net gain factor of exp(25) the following approximate equation must be satisfied:

$$\exp(25) = \sum_{I=1}^N T^{(4I-2)} \exp \left[ \frac{TS_R (T^{2I} - 1)}{T^2 - 1} \right]$$

where  $25/S_R$  is the threshold reduction factor.

### 3.7.2 Pump Depletion Effects

The analysis was also used to assess the effects of pump depletion in the uniform beam approximation. For a moderately long cell, the argument is as follows for a cell of length 2L: Ignoring the trivial energy in the phonons, energy conservation requires that the laser and Stokes power spatial derivatives are equal.

$$\frac{dp_1(z)}{dz} = \frac{dp_s(z)}{dz}$$

Integrating yields

$$P_1(z) - P_s(z) = \text{constant} = P_{\text{threshold}}$$

The SBS gain equation implies the relationship

$$\frac{dP_s(z)}{dz} = \frac{P_s(z) P_1(z) g_B}{A(z)}$$

where  $A(z)$  = beam area.



Integrating backward from the front of the cell to a location  $z$  more than a Rayleigh range in front of focus yields

$$P_1(z) = \frac{P_1(L) P_{\text{threshold}}}{P_1(L) - (P_1(L) - P_{\text{threshold}}) \exp[s(z)]}$$

where

$$s(z) = 4P_{\text{threshold}} (F/\#)^2 g_B (1/L - 1/z) / \pi$$

Transforming to reduced coordinates and using the analytical threshold estimate for HF yields:

$$P_1(z^*) = \frac{K P_{\text{threshold}}}{K - (K-1) \exp[s(z^*)]}$$

$$s(z^*) = \frac{25(1/L^* - 1/z^*)}{4 - 2/L^*}$$

where

$$P_1(L) = K P_{\text{threshold}}$$

$$L^* = L / (2\lambda (F/\#)^2)$$

$$z^* = z / (2\lambda (F/\#)^2)$$

Substitution shows that for cells which are at least several Rayleigh ranges long pump depletion occurs predominantly in front of focus. In the limit of a long cell the transmitted pump power is

$$P_1(z^*) = \frac{K P_{\text{threshold}}}{K - (K-1) \exp(-6.25/z^*)}$$

Clearly, the incident beam is depleted well in front of focus. This is important when assessing competing processes such as optically induced breakdown because it means that in steady state the peak intensity is primarily determined by the threshold rather than by the incident power.

Figure 3.7-2 shows a typical BRIWON calculation substantiating this conclusion. Note that the calculation was performed with an early noise model which underestimated the spontaneous scattering. Figure 3.7-3 shows BRIWON predicted reflectivity and transmitted power dependence.

### 3.7.3 Transient Threshold Behavior

Transient SBS behavior can also be approximated analytically. Using the formulation in Reference 3-8 for a rectangular pulse, it can be shown that threshold is just reached when

$$-2\Gamma t_p + \sqrt{8(C)(S)(\Gamma t_p)} = S$$

where

- $\Gamma = 1/(2 t_{\text{phonon}})$
- $t_{\text{phonon}} =$  phonon lifetime
- $C =$  ratio of transient to steady-state threshold power
- $t_p =$  pulse duration
- $S =$  effective gain factor ( $\exp(S) =$  gain) required to reach threshold {e.g., 25 for 2.9  $\mu\text{m}$  (HF), 22 for 1.06  $\mu\text{m}$ }

The formula can easily be recast in terms of energy required to reach threshold. In the limit of short pulses threshold is just an energy requirement and the required pulse energy is

$$E_{\text{threshold}} = (S) \frac{(t_{\text{phonon}}) (P_{\text{threshold}})}{4}$$

Figure 3.7-4 shows results when the pulse is not short and also shows results for a linear ramp pulse shape. Evidently, until a pulse is several phonon lifetimes long the pulse shape is relatively unimportant. Also shown is the threshold energy requirement if transient effects could be ignored and the pulse power could simply be  $P_{\text{threshold}}$  ( $S = 24$  assumed). To evaluate transient behavior under conditions well above the energy threshold a transient computer model was constructed based on the simple

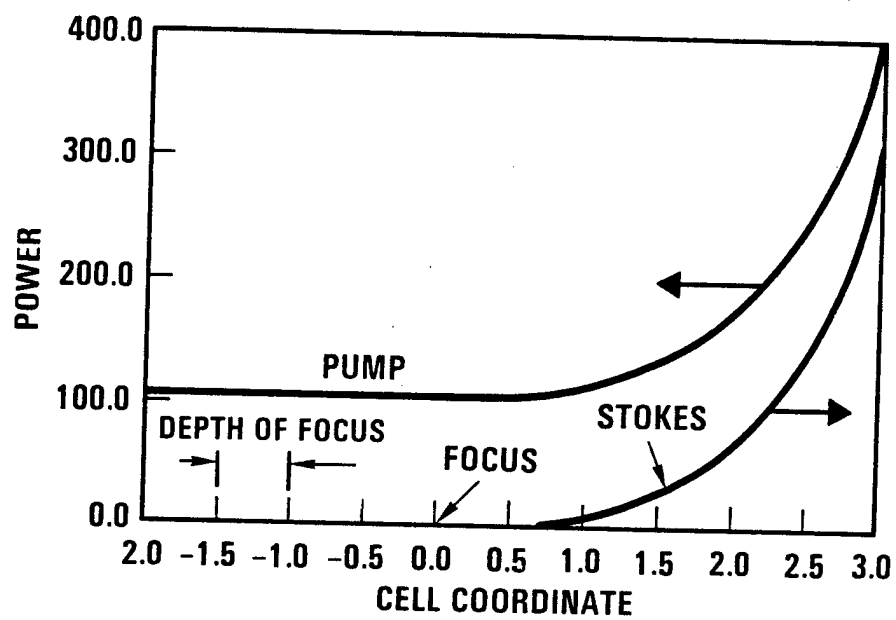
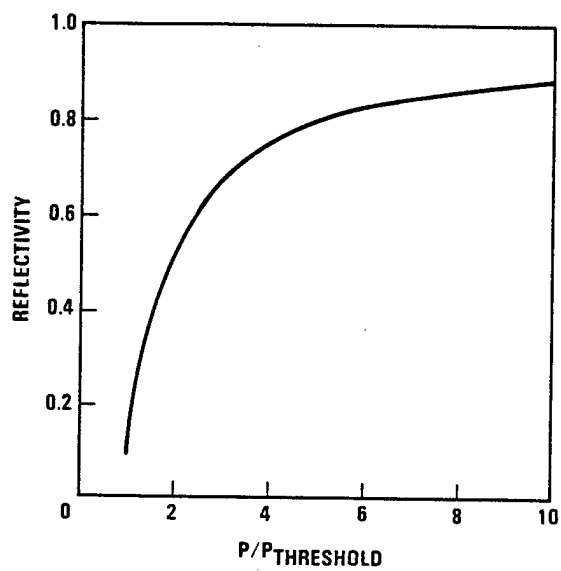
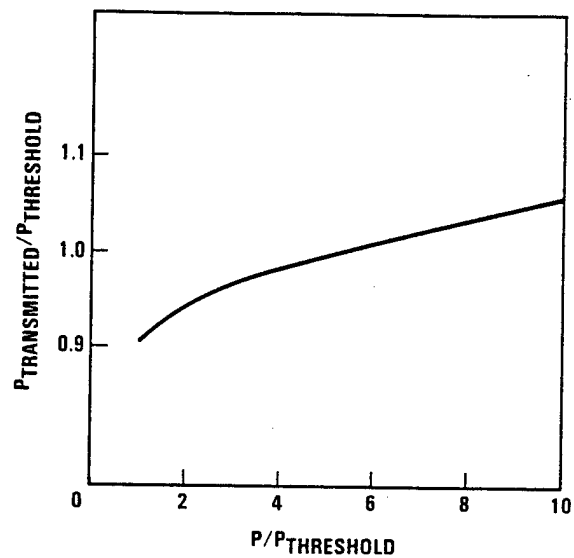


Figure 3.7-2. BRIWON Steady-State Pump Depletion



**Reflectivity Dependence  
on Incident Power**



**Transmitted Power Dependence  
on Incident Power**

Figure 3.7-3. BRIWON CW Reflectivity Predictions

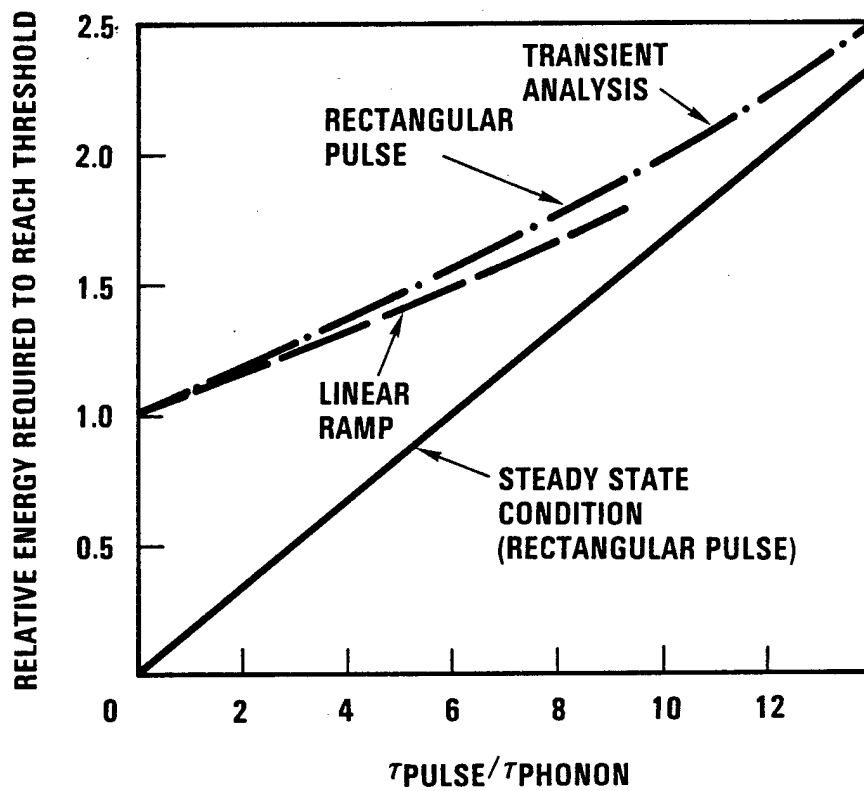


Figure 3.7-4. Transient SBS Threshold Behavior

uniform intensity focused beam approximation and spontaneous source model used to estimate CW thresholds. The basic amplification terms (Reference 3-8) used to estimate local buildup of the grating and pump depletion were:

$$\frac{\partial E_s}{\partial z} = iAE_1Q$$

and

$$\frac{\partial Q}{\partial t} + \Gamma Q = -iBE_1^*E_s$$

where

- Q = phonon amplitude
- E<sub>1</sub> = laser field amplitude, excluding traveling wave phase
- E<sub>s</sub> = Stokes field amplitude, excluding traveling wave phase
- g<sub>B</sub> = 2AB/Γ
- A/B = 2v<sub>n</sub>/c = 10<sup>-6</sup> for Xe
- v = sound speed
- n = refractive index
- c = speed of light

Focused-beam diffraction effects were implicitly included through additional spatial derivatives based on a scheduled beam area z dependence. A large number of z positions and small time steps were used and iterative adjustments made to achieve self consistent solutions for incident and reflected beams. Typical results for incident square pulses are shown in Figure 3.7-5. the overshoot is due to evolution of the spatial distribution of the grating. Calculations done with short high power pulses predicted that approximately the same amount of energy is required to achieve near unity reflectivity as is required to reach threshold. On a plot of reflected versus incident energy this implies a line with unity slope and a zero reflectivity intercept of approximately 1.5 E<sub>threshold</sub> rather than E<sub>threshold</sub>. Naturally for pulse energies only moderately larger than E<sub>threshold</sub>, the data do not fall on the line.

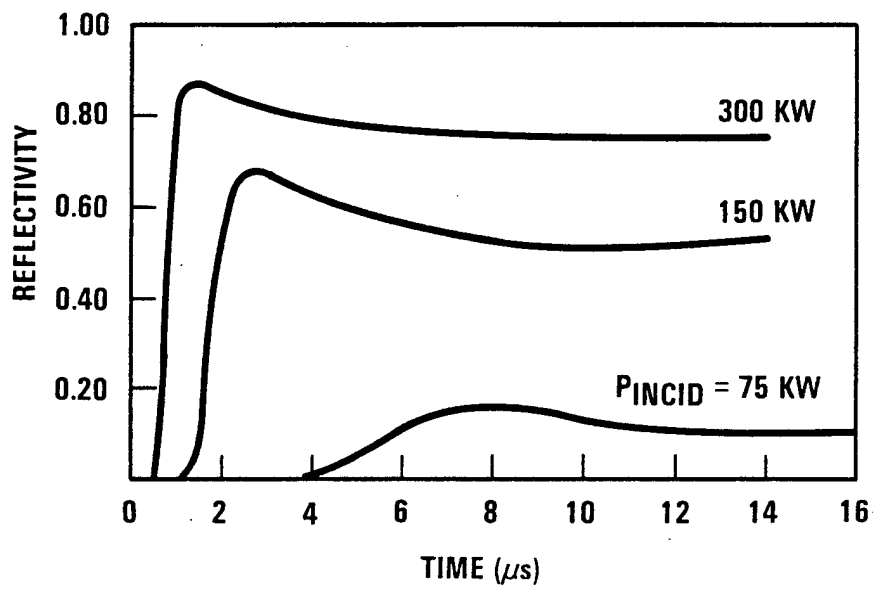


Figure 3.7-5. Predicted Transient SBS Response to Long Square Pulse

Model comparisons were made with both subscale 1.06- and 2.91- $\mu\text{m}$  transient data. Figure 3.7-6 summarizes typical subscale 1.06  $\mu\text{m}$  reflectivity data. Figure 3.7-7 indicates good agreement between predicted and measured dependence of the relative energy intercept on gas density. The calculations included corrections for pulse duration and density dependence for all pertinent gain parameters. The absolute intercept was also well predicted. For a diffraction-limited beam the inferred  $E_{\text{threshold}}$  value for 600 psi was 4.2 mJ for a predicted intercept of 6.3 mJ. This agrees well with the measured value of roughly 7 mJ, especially since the laser had an estimated beam quality of 1.1 to 1.2. Note that there is a disagreement in slope. The simple theory predicts a unity slope but the data slope is less. A similar experimental trend was observed in quasi-CW 1.054- $\mu\text{m}$  experiments where the reflectivity peaked at 87% regardless of input power.

In contrast to the 1.05- $\mu\text{m}$  experiments the HFC 2.91- $\mu\text{m}$  experiments demonstrated a unity slope. The zero reflectivity intercept was  $0.3 \pm 0.05$  J. This is somewhat larger than expected. For a diffraction-limited Gaussian beam with the measured temporal behavior, the predicted intercept is 0.2 J. Possible explanations for the discrepancy are (1) calibration errors, (2) unknown laser source temporal variations, and (3) additional competing processes which are not adequately modeled. Some variability in threshold was observed with a probable correlation between input pulse rise time and threshold. Faster rise times yielded lower thresholds. This could be symptomatic of an unknown laser temporal variation.

#### 3.7.4 Dimensionless Threshold Scaling

If the small effects associated with the frequency dependence of the spontaneous noise term are neglected (e.g., 22 versus 25 for 1.06 versus 2.9  $\mu\text{m}$  lasers), it is possible to use dimensional scaling arguments to show the similarity between transient focused beam experiments at different wavelengths and f-number values. These arguments are equally applicable to non uniform beams with transverse amplitude and phase variations. The basic transient equations including diffraction in the paraxial limit and the implicit wavelength dependencies of A and B (both inverse with wavelength) are



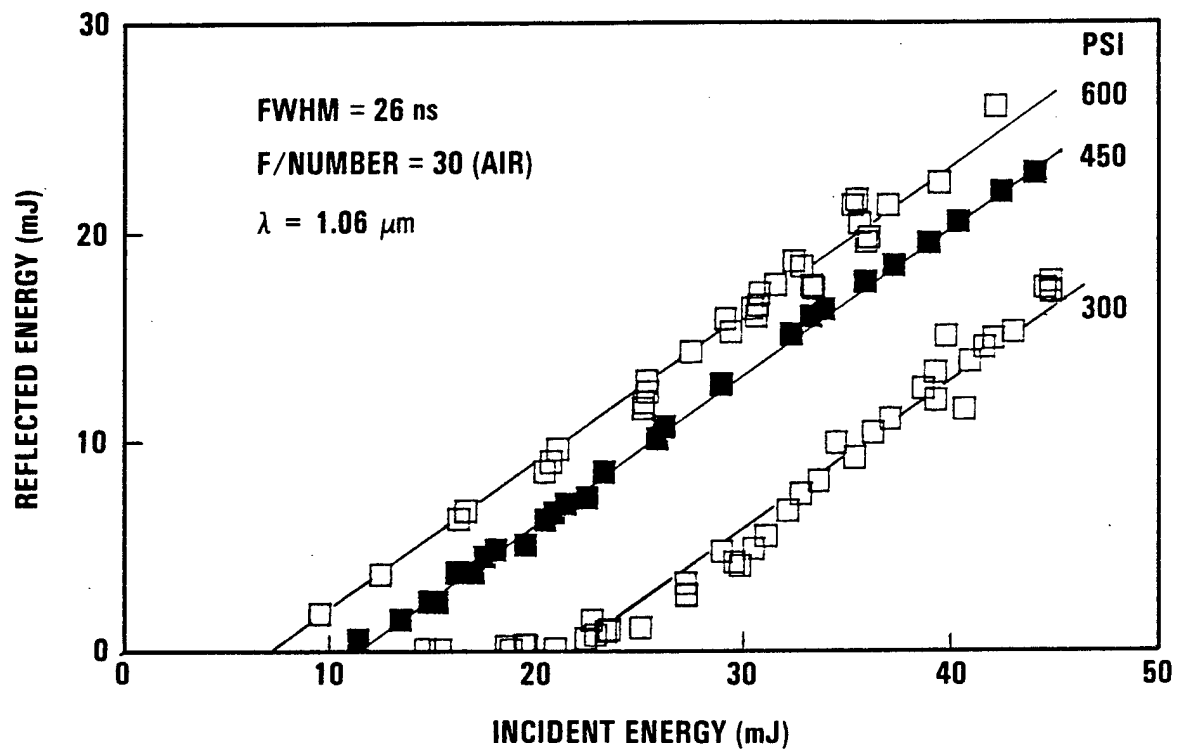


Figure 3.7-6. Subscale 1.06- $\mu\text{m}$  Reflectivity Data

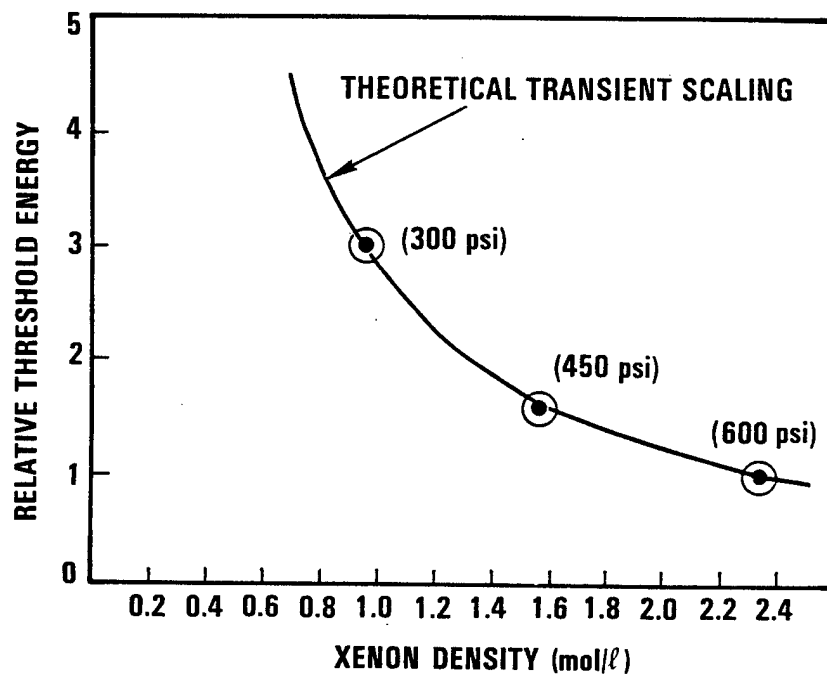


Figure 3.7-7. Transient SBS Modeling

$$\frac{\partial E_s}{\partial z} = \frac{iA_1 E_1 Q}{\lambda} - \frac{i\lambda}{4\pi} \left[ \frac{\partial^2 E_s}{\partial x^2} + \frac{\partial^2 E_s}{\partial y^2} \right]$$

$$\frac{\partial Q}{\partial t} + \frac{2Q}{t_{\text{phonon}}} = \frac{-iB_1 E_1^* E_s}{\lambda}$$

If we measure time in units of  $t_{\text{phonon}}$ ,  $x$  and  $y$  in units of  $\lambda F/\#$ , and  $z$  in units of  $\lambda (F/\#)^2$  then these equations become:

$$\frac{\partial E_s}{\partial z_1} = iA_1 E_1 Q (F/\#)^2 - \frac{i}{4\pi} \left[ \frac{\partial^2 E_s}{\partial x_1^2} + \frac{\partial^2 E_s}{\partial y_1^2} \right]$$

$$\frac{\partial Q}{\partial t_1} + 2Q = \frac{-iB_1 E_1^* E_s t_{\text{phonon}}}{\lambda}$$

If these equations are solved for a new f-number value of  $k(F/\#)$  and cell lengths are adjusted to maintain an equal number of Rayleigh ranges, then substitution shows that a new solution is

$$E_s \rightarrow \frac{E_s}{k}, \quad E_1 \rightarrow \frac{E_1}{k}, \quad Q \rightarrow \frac{Q}{k^2}$$

Since power is proportional to the transverse spatial integral of field squared (i.e.,  $dA = dx_1 dy_1 (\lambda F/\#)^2$ ) the new solution corresponds to the same laser and Stokes power, a result consistent with the expectation that threshold power behavior is f-number independent. Note that the acoustic energy density (proportional to  $Q^2$ ) scales differently than laser intensity and is a much stronger function of f-number.

Using the excellent approximation that  $t_{\text{phonon}}$  is proportional to wavelength squared, similar arguments indicate that the effect of multiplying the wavelength by a factor  $k$  is to result in new solutions:

$$E_s + \frac{E_s}{\sqrt{Q}(k)} \quad E_1 + \frac{E_1}{\sqrt{Q}(k)} \quad Q + Q$$

Squaring the field and doing the transverse spatial integral shows that powers scale linearly with wavelength. Thus, CW threshold power scales linearly with wavelength. On the other hand, energy thresholds also include a time integral and since time is measured in phonon lifetimes (proportional to  $k^2$ ) the energy threshold scales as wavelength cubed.

### 3.8 REFERENCES

- 3-1. M.T. Duignan, B.J. Feldman and W.T. Whitney, "Stimulated Brillouin Scattering and Phase Conjugation of Hydrogen Fluoride Laser Radiation," *Opt. Lett.* 12, 111-113, 1987.
- 3-2. D. Smith and R. Meyerand, "Laser Radiation Induced Gas Breakdown", Chapter 11, Principles of Laser Plasmas, Wiley-Interscience 1976.
- 3-3. N. Generalov et.al., "Gas Breakdown Under the Influence of Long-Wave Infrared Radiation of a CO<sub>2</sub> Laser, *ZhEtf Pis. Red.* 11, (7) 343, 5 April 1970.
- 3-4. D. Smith, "Gas Breakdown Initiated by Laser Radiation Interaction with Aerosols and Solid Surfaces," *J. Appl. Phys.* 48, (6) 2217, 1977.
- 3-5. N. Generalov et.al., "Experimental Investigation of a Continuous Optical Discharge, *Sov. Phys.-JETP* 34, (4), 763, 1972.
- 3-6. Y. Raizer, "Optical Discharges", *Sov. Phys. Usp.*, 23 (11), 789 1980.
- 3-7. G. Kozlof et.al., *Sov. Phys. JETP* 39, 463, 1974.
- 3-8. B. Ya. Zel'dovich, et.al., Principles of Phase Conjugation, Springer-Verlag, 1985.

## 4. FLOWING-GAS SBS EXPERIMENTS

The SBS cell is an important component of the APACHE conceptual design. The conjugating medium is Xe gas maintained at a nominal pressure of 40 atm and a nominal temperature of 300 K. Three key issues of the design are: (1) pressure isolation of the high-pressure Xe from the ambient vacuum, (2) thermal blooming of the gas due to the high intensity of the focused HF beam, and (3) SBS threshold reduction.

This section describes experiments and related analyses performed under the APACHE program to support the design of a high-pressure SBS cell. Concepts considered are briefly discussed in Section 4.1 with emphasis given to the issues and relevant scaling parameters of an axial aerowindow design. Fluid mechanics and SBS experiments performed using a subscale flowing-gas SBS cell are discussed in Section 4.2. A full-scale flowing cell was also integrated into the APACHE HF facility at CTS. The design, integration, and preliminary testing were performed under the APACHE program, as discussed in Section 4.3. The bulk of the testing, including multiple-foci threshold reduction, is to be performed under the APEX program. A turbulence model was also developed and incorporated into the BRIWON SBS code to serve not only as a design tool but to provide a better understanding of the coupling between flow-induced turbulent aberrations and SBS behavior.

### 4.1 OVERVIEW

This section first briefly describes concepts considered for an SBS cell that provides high-pressure isolation, prevents thermal blooming, and accommodates multiple foci. The conceptual design of a flowing-Xe SBS cell with a He axial aerowindow is identified as the focal point for SBS cell experiments performed under the APACHE program. Technical issues and the relevant scaling parameters for this concept are then discussed.

#### 4.1.1 SBS Cell Concepts

Two concepts are under consideration for isolating the high-pressure Xe gas from the ambient vacuum: an aerowindow, which provides a fluid mechanical pressure drop; and a material window, which physically isolates

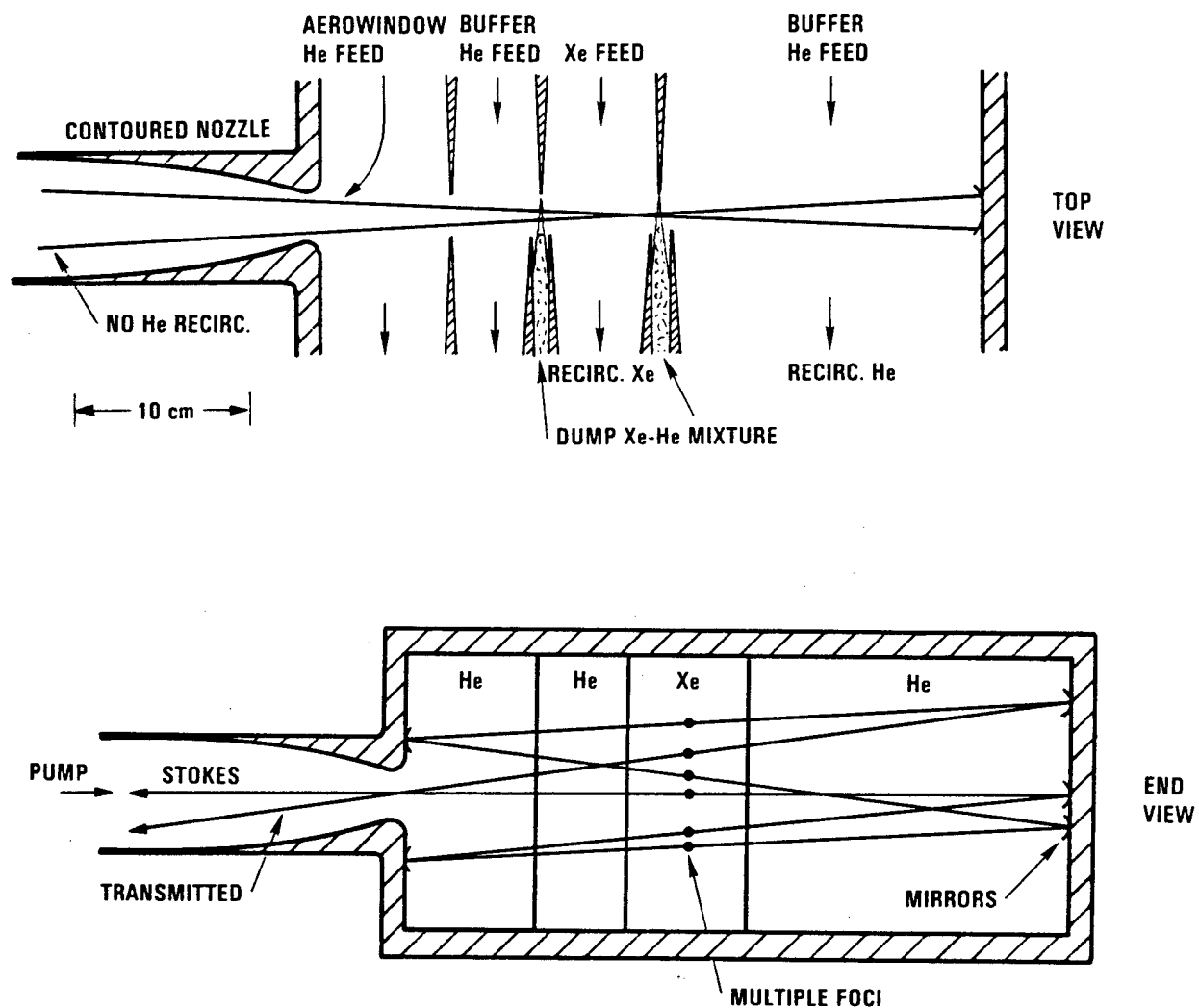
the high-pressure gas from the vacuum. Key issues associated with both concepts are the effects of aberrations introduced by the windows on SBS threshold and conjugation fidelity. In the case of the aerowindow, the aberrations are caused by flow-induced density variations of the gas(es). Aberrations introduced by the material window arise not only from the glass itself but from the thermal boundary layer along the convectively cooled surfaces.

Although parallel efforts are under way to investigate both concepts, as discussed in greater detail in APACHE Systems Engineering, Volume II, the experimental work under the program has concentrated on the axial aerowindow concept. A transverse aerowindow concept was also considered (Volume II) but was found to have larger dry weight, higher flow losses, larger flow-induced aberrations, and greater complexity than the axial aerowindow.

The second fundamental issue associated with the SBS cell is thermal blooming of the Xe. Two possible approaches to avoid thermal blooming include flowing the Xe gas and scanning the beam(s). Beam scanning was actually used in the APACHE CW conjugation experiment (Section 2). Although this approach was useful for defining the velocity of the beam relative to the Xe required to avoid thermal blooming, the application of the approach to a multiline, multibeam system is unduly complex. The approach taken presently is to maintain a fixed beam geometry and to flow the Xe.

The flowing-gas SBS cell, in its present state of development, accommodates multiple foci in an attempt to minimize SBS threshold. Although a single focus (per line) is suitable for the SBL baseline design, the multiple-foci threshold reduction concept may be required for ground-based demonstration experiments. The effect of multiple foci is to extend the characteristic SBS gain length. A detailed discussion of the multiple foci concept is given in Section 3.6, in which PAR laser HF pulses were multiply focused in a static-Xe SBS cell, and in Section 4.1.2 in which requirements are defined for the multiple-foci geometry.

A schematic of the conceptual design for the flowing-Xe, axial aerowindow SBS cell is shown in Figure 4.1-1 and forms the basis for



NOTE: DESIGN IS APPLICABLE TO HIGH- AND LOW-BRIGHTNESS SYSTEMS

Figure 4.1-1. Axial Aerowindow Concept for SBS Cell (F/10 Configuration)

experiments and analyses. The laser beam enters the cell from the left and focuses in the center of the Xe channel. Xenon gas flows transverse to the axis of the beam thus providing fresh, thermally uniform gas to the conjugating region. Analysis based on the results of the CWCS experiments (Section 2) suggests that the Xe velocity be high enough to avoid thermal blooming ( $\sim 5$  m/s for an absorption coefficient of  $1 \times 10^{-5} \text{ cm}^{-1}$ ), but not high enough to smear the phonon grating ( $\sim 20$  m/s).

Pressure isolation is provided by a supersonic nozzle whose axis is directed into the beam path. Xenon was discarded as a possible aerowindow gas because it tends to condense in the nozzle, it has a relatively large refractive index, and it imposes a large penalty in weight. By using He for the aerowindow gas, most of the flow-induced aberrations are restricted to a thin interface between the Xe and He flow channels. An intermediate He channel whose velocity is matched to that of the Xe channel is provided to buffer the He aerowindow flow from the Xe channel. A wider He channel whose velocity is also matched to the Xe velocity provides a low optical-index path for the multiple-focus geometry.

The SBS cell concept is applicable to a single-focus configuration as well as to a multiple-focus design employed to reduce the SBS threshold power. In the multiple-foci configuration, the beam is reimaged by cooled mirrors to produce six foci in the conjugating region. The requirements on the geometry of the multiple foci are discussed in the following section. After the last focus, the beam exits the SBS cell through the aerowindow at an angle relative to the pump beam.

A discussion of the concept at the systems level, including gas flow rates and dry weights of the cell, turbopumps, heat exchangers, and other hardware, is given in Volume II.

#### 4.1.2 Aerowindow Issues, Scaling Parameters

Issues and associated nondimensional scaling parameters for the axial aerowindow conceptual design are summarized in Table 4.1-1. Nominal values of the parameters are listed for both the baseline SBL design and a potential ground-based demonstration using the ALPHA laser, which is the main focus of the APEX program. The parameters are divided into four



Table 4.1-1. Scaling Parameters for Flowing-Gas SBS Cell

Issue	Parameter	SBL Baseline	ALPHA Demo
<b>General</b>			
Pump power	$P/P_{TH}$	3-5	3
Conjugating depth (half-width)	$L/(2\lambda f_{\#}^2)$	3.0	3.0
Optical thickness of conjugating region	$(n-1) L/\lambda$	500	500
Laser pulse width ( $\tau_{PL}$ = phonon lifetime)	$\tau_{laser}/\tau_{PL}$	$\gg 10$	$\gg 10$
Beamlet f-number	$f_{\#}$	30-50	30-50
Conglomerate f-number	$F_{\#}$	6-10	6-10
Laser coherence length (single focus)	$L_C/(4\lambda f_{\#}^2)$	$\gg 1$	$\gg 1$
Self-seeding of adjacent longitudinal modes (n an integer)	$\frac{ \Delta\nu_{shift} - n\Delta\nu_{model} }{\Delta\nu_{SBS BW}}$	$> 1$	$> 1$
<b>Xenon Convection</b>			
Thermal blooming	$\frac{4\sqrt{2} \alpha P_{TH} \partial n/\partial T f_{\#}}{\pi n \rho C_p u}$	0(1)	0(1)
Thermal blooming	$u_s \tau_{laser}/(2\lambda f_{\#})$	$\gg 10$	$\gg 10$
Thermal homogeneity of conjugating medium	$(\Delta T)_{rms}/T$	$< 5 \times 10^{-4}$	$< 5 \times 10^{-4}$
Grating convection	$u \tau_{PL}/(2\lambda f_{\#})$	0.01	0.01
<b>Turbulence</b>			
OPD (nom, rms)	$\Delta\lambda/\lambda$	0.1	0.1
Optical thickness	$\Delta n \delta/\lambda$	$< 10$	$< 10$

Table 4.1-1. Scaling Parameters for Flowing-Gas SBS Cell (Continued)

Issue	Parameter	SBL Baseline	ALPHA Demo
Beamlet diameter at wake	$L/(f_{\#}\delta)$	1	1
Conglomerate beam diameter at wake	$L/(F_{\#}\delta)$	5	5
Wake Reynolds number	$Re_{\delta}$	$5 \times 10^4$	$5 \times 10^4$
Characteristic turbulent time scale ( $\tau_{PR} \equiv$ phonon rise time)	$\tau_T/\tau_{PR}$	$\sim 25$	$\sim 25$
Turbulence correlation length	$1/\delta$	0.2	0.2
Threshold Reduction			
Number of foci (per line)	N	1	TBD
Foci lateral separation	$s/(2\lambda f_{\#})$	NA	$>20$
Beam overlap in conjugating region	-	NA	None
Laser coherence length ( $f_m =$ reimaging focal length)	$L_C/(N-1) f_m$	NA	$>1$

categories: (1) general SBS parameters that are relevant with or without flowing gases, (2) parameters introduced by flowing Xe, independent of the window used, (3) turbulence parameters of the Xe-He wake associated with the axial aerowindow, and (4) parameters related to the multiple-foci threshold reduction concept.

Note from Table 4.1-1 that the values of the SBS cell parameters for an ALPHA demonstration experiment are well matched to the values of the nominal SBL design. It is required that the pump power exceed SBS threshold by a factor of roughly three to achieve acceptable conjugation fidelity. The half-width of the conjugating region, three Rayleigh ranges, is driven by the segment tilt allowance on the segmented mirror. For a single beamlet the minimum required half-width would be reduced to approximately one Rayleigh range. Because the present concept for the segmented mirror utilizes two annular rows of mirror elements with a central obscuration, the conglomerate f-number is one-fifth of the beamlet f-number.

Both the SBL system and the ALPHA demonstration experiment utilize CW lasers in that the "pulse" duration is large compared to the phonon lifetime ( $\sim 250$  ns under the nominal conditions). The coherence length of the laser for a single focus must be greater than one depth of focus (two Rayleigh ranges), and is observed to be much greater than a depth-of-focus. To avoid self-seeding of adjacent longitudinal modes, it is necessary that the spectral content of one SBS-shifted mode not overlap neighboring longitudinal modes of the pump. This parameter is not directly related to the design of the SBS cell, but is included for completeness of the general SBS parameters.

Three issues are associated with flowing the Xe: thermal blooming, thermal homogeneity of the freestream gas, and grating convection. The first thermal blooming parameter in Table 4.1-1 is indicative of the temperature behavior in the focal region, and is derived from the balance between that fraction of the threshold power absorbed by Xe in the focal region and the convection of energy out of the region at the flow velocity,  $u$ . The CWCS experiment suggests that this parameter be of order 1 or less to avoid unacceptable thermal blooming effects.

For short enough laser pulses thermal blooming is not expected to play a role. The second parameter reflects the fact that the pulse length of both the SBL and the ALPHA demonstration are much longer than the time required for disturbances to propagate at the acoustic velocity,  $u_s$ , across the characteristic focal diameter.

Even in the absence thermal blooming effects, thermal homogeneity of the Xe must be maintained to avoid degradation in SBS performance due to variations in the phonon propagation velocity (i.e., sonic speed) within the conjugating region. A first-order analysis suggests that the rms temperature fluctuations not exceed approximately 0.1 to 0.2°C for Xe at room temperature. This value, reflected in Table 4.1-1, is only representative. The magnitude of the allowable rms level depends as well on the characteristic correlation length of the thermal variations. Although this parameter is also relevant to static SBS cells, it is particularly important to flowing gas designs.

Several nondimensional parameters can be formed that characterize the Xe-He wake and its influence on the incident beam. Given a nominal flow velocity of 10 m/s and the very low kinematic viscosity of high-pressure Xe, the boundary layer approaching the splitter tip is turbulent. Thus, the wake is also expected to be turbulent without the application of flow control techniques. A wake thickness of 0.5 mm is used in Table 4.1-1 as a representative, practically achievable value just downstream of the splitter plate. Based on experimental data (Section 4.2) and turbulence modeling (Section 4.4), the nominal rms OPD introduced by the wake under these conditions is approximately one-tenth of a wave. The effects of wake thickness on SBS threshold and conjugation fidelity are discussed in greater detail in Section 4.4.

As discussed in Sections 4.2 and 4.4, the diameter of the beam at the Xe-He interface relative to the turbulent integral scale is also a parameter of significance. Aberrations can be minimized if the beam diameter can be kept small compared to the integral scale, suggesting that focus be kept close to the wake. Requirements on conjugating depth and the desirability of very thin wakes (small integral scales), however, reduce this benefit.

To achieve good conjugation fidelity it is also necessary that turbulence induced aberrations, or any time-varying aberrations, occur on time scales that are large compared to the phonon rise time. At present this requirement is not well quantified. Note that in Table 4.1-1 the characteristic turbulence time scale of the nominal wake is approximately 25 times the phonon rise time.

The last parameter category listed in Table 4.1-1 relates to the multiple-foci threshold reduction concept. Although the conceptual design of the flowing-gas cell accommodates six foci, the requirement on number of foci is not precisely defined. Threshold reduction techniques are generally more important for low-power SBL concepts and laboratory scale experiments. Regardless of the number of foci, it is necessary that the foci be separated by a sufficient distance that possible crosstalk between counterpropagating beams be eliminated. It is presently assumed that ten aberrated spot diameters are sufficient. For similar reasons, it is required that the beams not cross within the conjugation region. Finally, it is required that the coherence length of the laser exceed the distance from the first focus to the last. In the event that this distance is greater than the coherence length, it is possible, in principle, to side step this requirement by including an additional path length equal to the cavity length of the laser resonator between appropriate foci.

## 4.2 SUBSCALE EXPERIMENTS

### 4.2.1 Objectives

The objectives of the subscale flowing-gas SBS experiments are as follows:

1. Provide a hardware simulation of the baseline design of the APACHE SBL flowing-gas SBS cell, including geometrical, optical, and fluid mechanical characteristics
2. Characterize the optical aberrations imposed on a laser beam that passes through the turbulent interface between coflowing Xe (conjugation) and He (aerowindow) gas streams
3. Evaluate the effects of these aberrations on the phase-conjugation process.

Two classes of experiments were undertaken in an effort to meet these objectives. The first class was intended to explore the fluid mechanical aspects of the turbulent interface between the gas streams, in particular, to study various ways of manipulating the interface to reduce the aberrations it imposes on the pump laser beam that traverses it. The second class of experiments was designed to study the SBS process within the flowing-gas cell, with special consideration given to determination of threshold energy and SBS reflectivity.

The next three sections of this report describe the facility used in the experiments, the fluid mechanics experiments, and finally, the flowing-gas SBS experiments.

### 4.2.2 Facility Description

The subscale flowing-gas experiments were conducted in the TRW Technology Test Center, Building 67, Space Park. The test facility, (Figure 4.2-1), consisted of a flowing-gas SBS cell, a gas handling/flow control system, an optical train to introduce laser pulses into the SBS cell, and an array of diagnostic instrumentation for fluid mechanical as well as phase conjugation studies. The various components of the facility are described in the following sections.

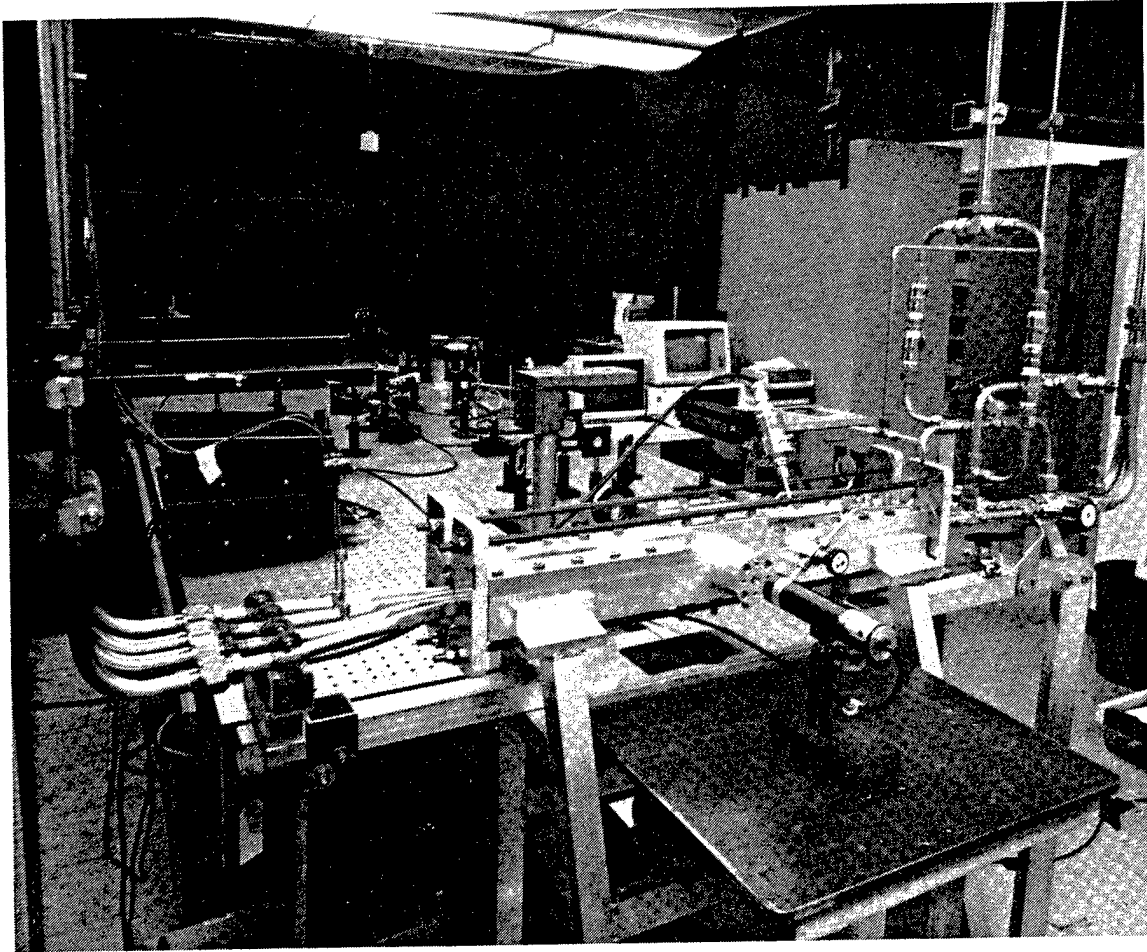


Figure 4.2-1. Subscale Flowing-Gas Facility

#### 4.2.2.1 SBS Cell

The flowing-gas SBS cell used in these experiments was constructed by milling a long, straight channel of rectangular cross section from a large Al block. A thick Al lid bolted on top of the block could be removed to allow access into the cell. The two test gases were admitted into one end of the cell, and were prevented from mixing by the presence of a partition down the middle of the cell. Approximately halfway along the cell this partition, also called a splitter plate, was terminated with a sharp tip. Downstream from this tip the two gas streams was allowed to come into contact; the gases subsequently mixed together and flow out the other end of the test cell.

Figure 4.2-2 is a schematic showing the interior of the cell in the region near the tip of the splitter plate. Also shown in the figure are two windows that provide for passage of the SBS pump/return beams through the cell walls; the windows are mounted on spacers extending out from the walls to keep the energy fluence below the damage threshold of the window material. Two larger windows are also included in this region to allow visual access to the interior of the cell and for shadowgraph photography. These windows are located on the upper and lower surfaces of the cell to provide a "cross-section" view of the mixing region. Also shown in the figure are the flow-conditioning screens located shortly upstream of the splitter-plate tip. Not shown in the figure, but present nevertheless, is a set of high-porosity nylon pads immediately downstream of the test section. These pads completely fill the cross section of the cell and are intended to mix the two gas streams thoroughly prior to their exiting the cell. This action was found to be necessary to stabilize the interface between the two gas streams.

#### 4.2.2.2 Flow Control System

Figure 4.2-3 is a schematic of the system used to control the flow of gases in this experiment. The gases are supplied to the SBS cell through two sets of lines (one set for the He side and one for the Xe side). Each line contains a regulated flow of gas from a pressurized reservoir; the flow rate is determined by a sonic orifice located between each regulator and the SBS cell. The reservoir on the He side is either the building's He



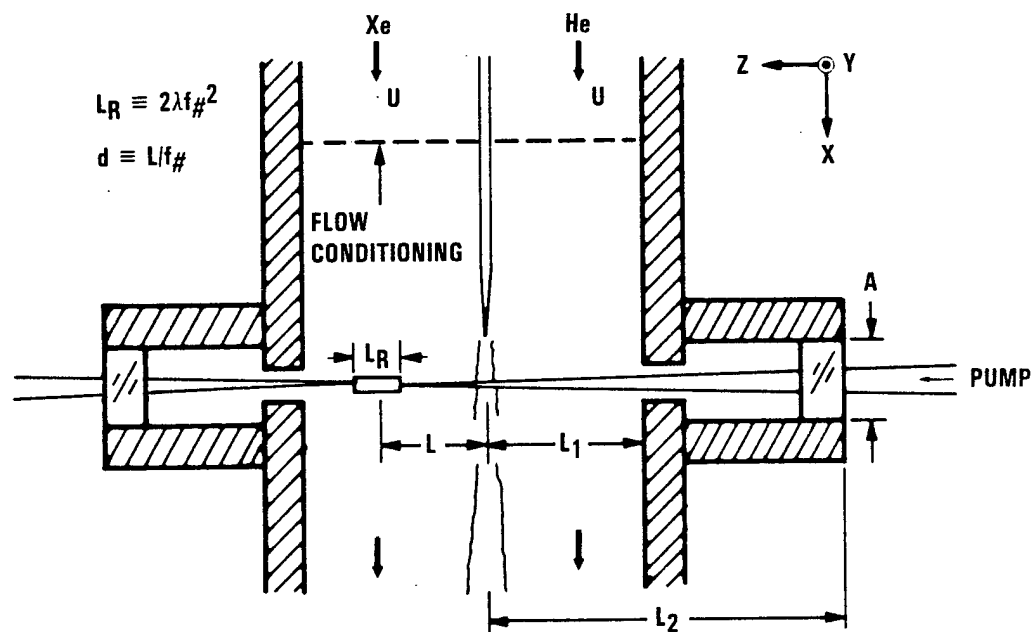


Figure 4.2-2. Schematic of Interior of Flowing-Gas Cell

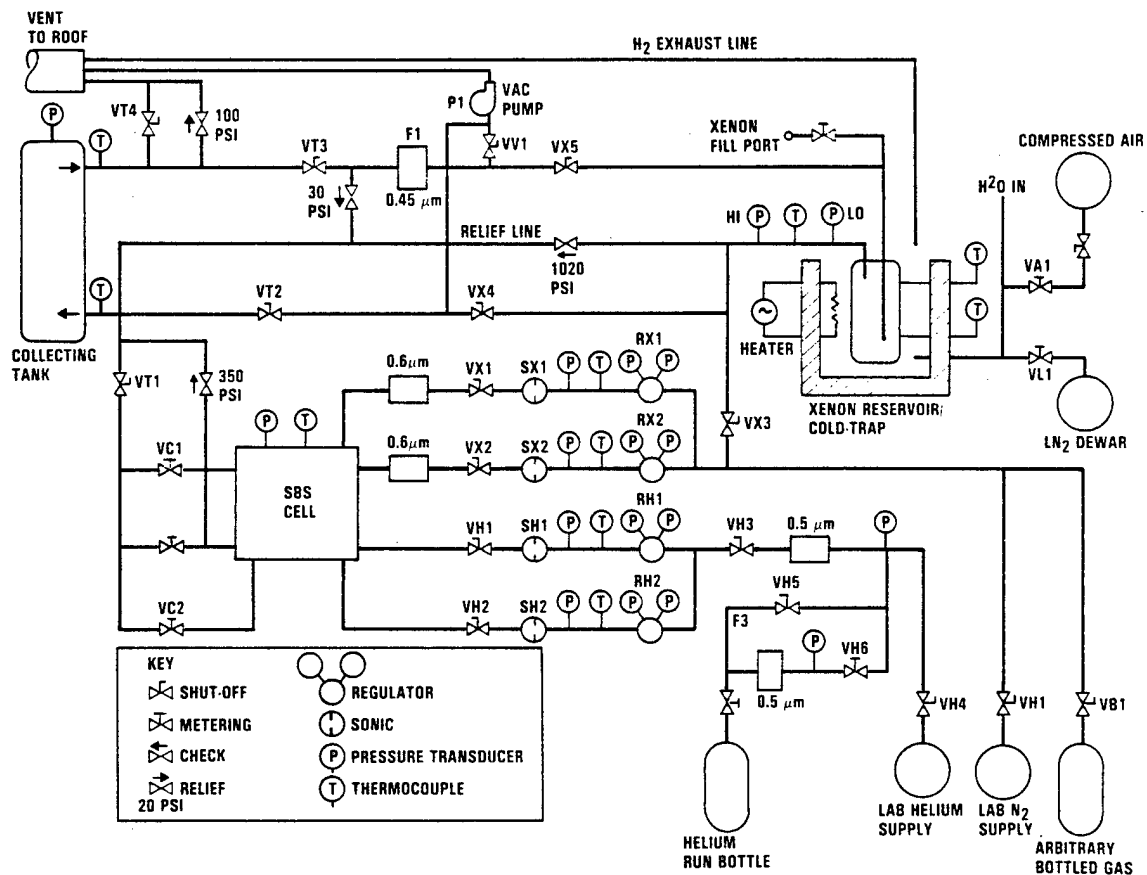


Figure 4.2-3. Subscale Gas Handling Flow Control System

supply or a separate gas bottle. In either case, the He flows through a 0.5- $\mu\text{m}$  particle filter prior to entering the cell. The primary reservoir on the Xe side also serves as a cryogenic separator, and will be explained in more detail shortly. Other gases are sometimes used in the "Xe" side of the system, and the reservoir in those cases is either the building's tank farm for the gas or a separate gas bottle. The gas in the Xe side flows through a 0.6- $\mu\text{m}$  filter before entering the SBS cell.

The pressure of the gases inside the SBS cell is controlled by diaphragm valves in the exit lines downstream of the cell. The gas mixture which leaves the cell flows through these valves and into a collecting tank during each run. For the tests involving phase conjugation, the gas in the Xe side of the system actually is Xe. Since Xe is relatively expensive, it is recovered from the mixture in the collection tank by a cryogenic separation process. The Xe-He mixture is slowly passed through a network of stainless-steel tubing immersed in a liquid  $\text{N}_2$  bath; the Xe freezes out onto the walls of the tubing, while the He remains in the vapor state. After all of the gas mixture has been processed in this manner, the He is pumped away and, the walls of the tubing are heated to thaw and vaporize the Xe. This tubing then serves as a supply reservoir for the next gas flow cycle.

One additional feature of the Xe reservoir that should be mentioned is the means for preheating the Xe prior to a test run. This heating is necessary to compensate for the Joule-Thompson temperature loss that occurs when the Xe flows from the higher reservoir pressure to the lower operating pressure inside the SBS cell. The space surrounding the tubing is filled with water and heated by the same resistance element used to vaporize the frozen Xe. In order to heat the gas inside the tubing uniformly, it is necessary to agitate the water inside the tank. This agitation is accomplished by bubbling air forcefully up from the bottom of the tank.

Finally, the flow of gases through the system during a run is initiated by simultaneous opening of ball valves located upstream and downstream of the SBS cell; this process is done manually.

#### 4.2.2.3 SBS Optical Train

The optical layout used in the phase conjugation experiments is shown in Figure 4.2-4, and a block diagram of the setup is given in Figure 4.2-5. Pulses from a Nd:YAG laser are first sent through a variable attenuator formed by a linear polarizer and half-wave plate. The attenuated pulses are then spatially filtered and admitted into the rest of the optical train by the action of a mechanical shutter under computer control. A pair of apertures down beam of the shutter are used to check alignment of the system. A wedged beamsplitter is used to pick off a portion of the incident beam for diagnostics (energy, power versus time, and far-field intensity). The remainder of the pump beam is focused into the flowing-gas cell by a lens mounted on a pair of linear traversing stages; in this way, it is possible to change the position of the focal point within the cell. The phase-conjugated return beam is optically isolated from the laser by the combination of a linear polarizer and quarter-wave plate down beam of the incident-beam diagnostics. This optical combination also serves to divert the return beam into a diagnostic setup similar to the one used for the incident beam.

#### 4.2.2.4 Diagnostics

Two sets of diagnostics were employed in this experiment (one set for the phase-conjugation study and one for the fluid mechanical investigation).

The phase-conjugation diagnostics have already been mentioned (pulse energy, power versus time, and far-field intensity for both the incident pump and phase conjugate return beams). The pulse energies are sensed by a pair of joulemeters and displayed on digital readouts. The temporal makeup of each of the pulses is revealed by a photodiode; the traces for both beams are displayed on an oscilloscope. The far-field intensities of the pulses are recorded simultaneously by focusing the beams down onto the array of a CCD video camera. The joulemeter displays and oscilloscope display are located close together on the laboratory table so that they may be videotaped simultaneously. In addition, a video monitor with a shadowgraph display of the flow in the SBS cell is located within the field of view of this video camera. The images on this video camera are

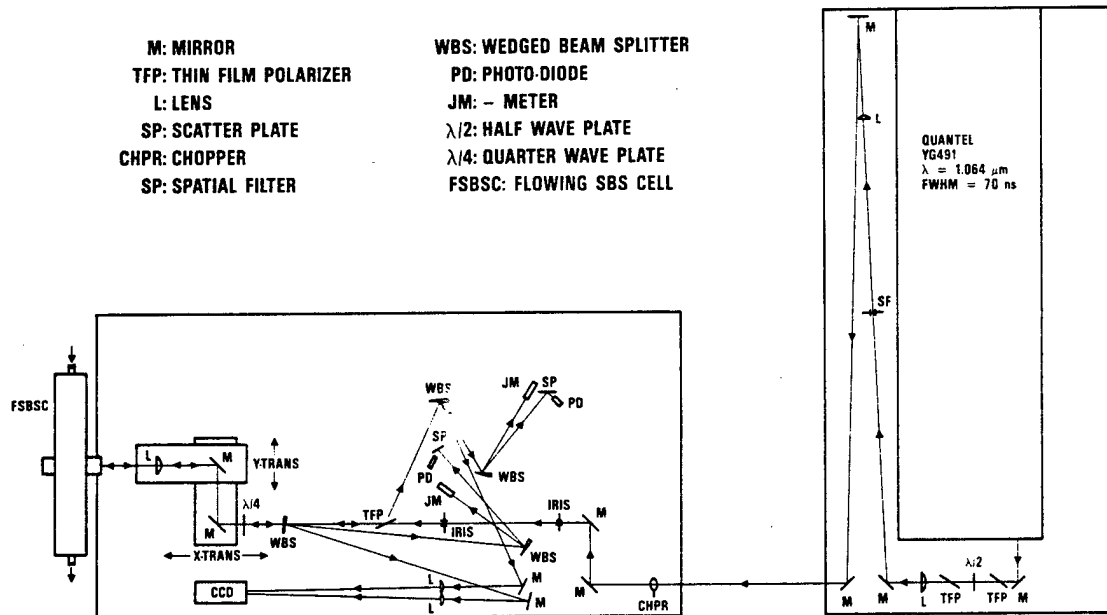


Figure 4.2-4. Optical Layout of Subscale SBS Experiments

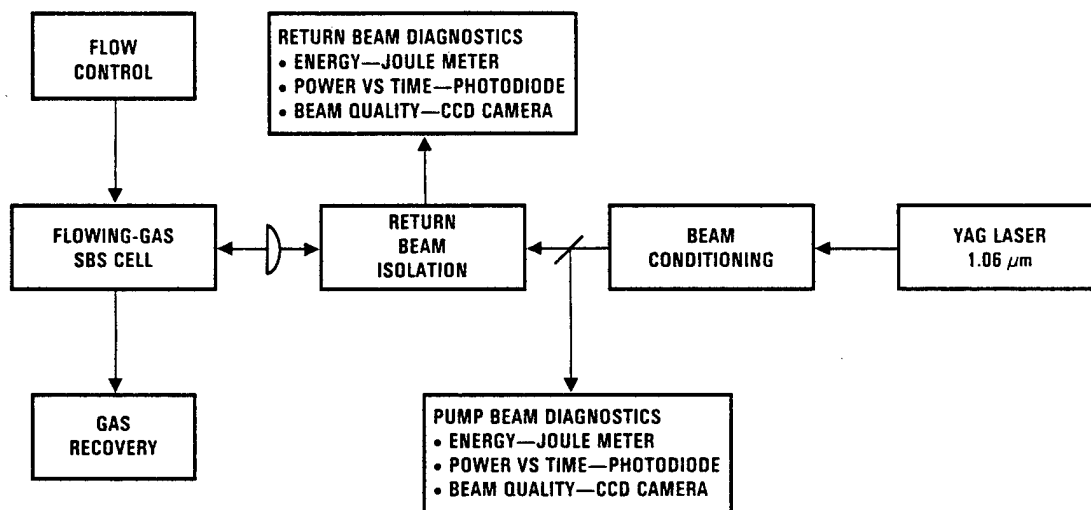


Figure 4.2-5. Block Diagram of Subscale Optical Layout

synchronized with those on the CCD camera recording the far-field spots by a momentary flash of light in the room.

Two types of diagnostics are used in the fluid mechanical investigation. A focused shadowgraph system is used to obtain visual information on the flow structure inside the SBS cell. Instantaneous pictures are obtained by using a sparkgap for the light source, while a tensor lamp provides illumination for real-time video display of the flow. The other diagnostic technique used in the fluid mechanical study is interferometry. The output beam from a Zygo interferometer is apertured and focused down into the flowing-gas cell to mimic the geometry of the pump beam used in the SBS studies. The reason for using a focusing geometry is ensure that the interferometer beam "sees" the same optical aberrations as the pump beam. The interferograms are short-duration exposures, and are recorded either by a Polaroid camera or a CCD video camera.

#### 4.2.3 Fluid Mechanics Experiments

##### 4.2.3.1 Experiment Description

The goals of the fluid mechanical investigation were to characterize the aberration imposed on a laser beam that propagates through the turbulent gas interface, and to seek ways to reduce that aberration. For these experiments,  $N_2$  was substituted for Xe in the flowing-gas cell, while He was still used as the aerowindow gas. This substitution was made to allow for longer test run times and to shorten the amount of down time between tests.

The arrangement used in most of the tests is illustrated in Figure 4.2-6. The speed of each gas stream was 2 m/s and the nominal operating pressure in the cell was 20 atm; a few tests were performed at a flow speed of 5 m/s. The shadowgraph beam was collimated through the test section, and the camera that collected the beam was focused on the edge of the gas interface nearest the camera. The location of the interferometer beam focus was varied both along the optical axis (normal to the gas interface) and in the streamwise direction. The interferometer was used in double-pass mode.

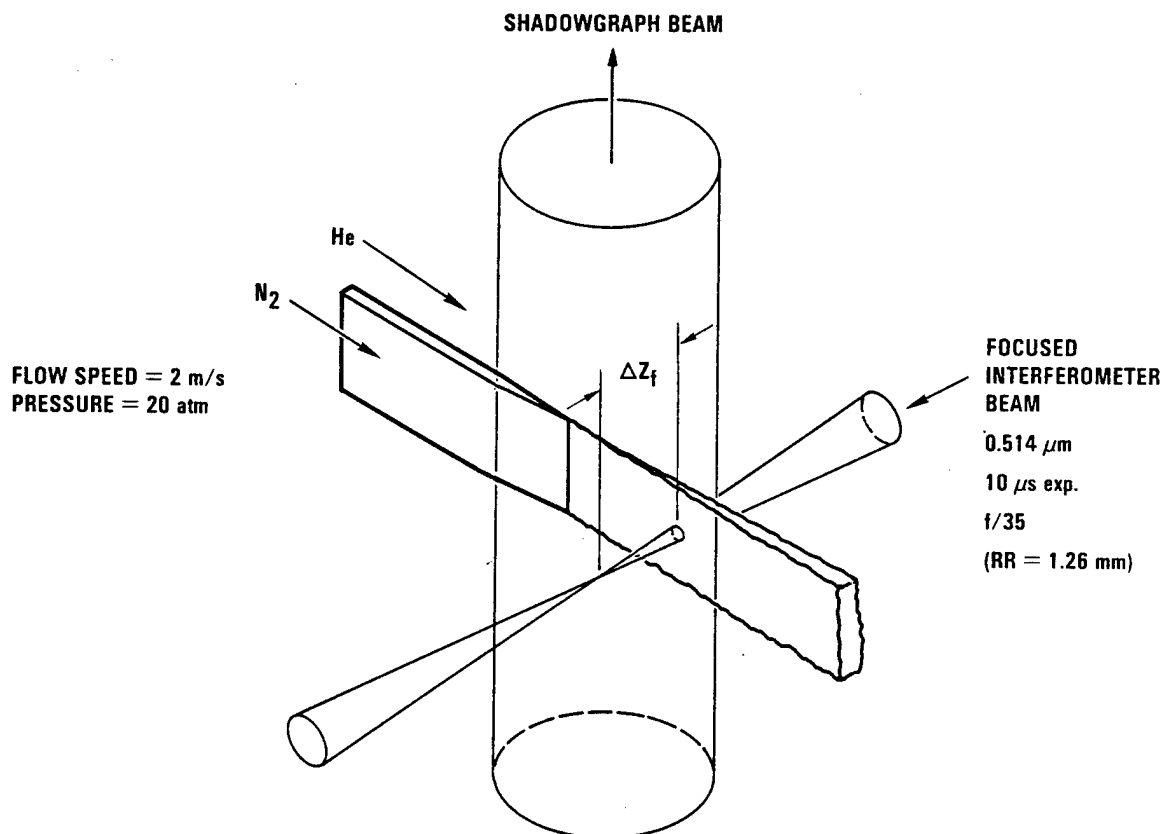


Figure 4.2-6. Diagnostics Used in Subscale Fluid Mechanics Tests



#### 4.2.3.2 Scaling Issues

The fluid mechanics experiments to be discussed involved testing conducted on a subscale experimental device with test conditions different from those of the full scale SBS cell that would be used in an SBL. It is necessary, therefore, to provide scaling relationships in order that the experimental results may be properly interpreted in terms of what would be observed under full scale conditions. The primary distinctions between the subscale and full scale test parameters are summarized in Table 4.2-1.

Table 4.2-1. Scaling Parameters in Fluid Mechanics Experiments

Parameter	Subscale Experiments	Full Scale (SBL)
"Conjugating" Medium		
Gas	N <sub>2</sub>	Xe
Pressure (atm)	20	40
Normalized Density, $\rho/\rho_{\text{ref}}$	20	55
Gladstone-Dale coefficient, $\beta \times 10^4$	2.96	6.46
Aerowindow Medium		
Gas	He	He
Pressure (atm)	20	40
Normalized Density, $\rho/\rho_{\text{ref}}$	20	40
Gladstone-Dale coefficient, $\beta \times 10^4$	0.32	0.32
Nominal Interface Thickness, L (cm)	0.3	0.3
Optical Wavelength, $\lambda$ ( $\mu\text{m}$ )	0.5145	2.8
OPD Factor: $\Delta(\beta\rho/\rho_{\text{ref}}) L/\lambda$	30.8	36.7

From an optical distortion standpoint, the most critical scaling relation between the two test conditions is the optical path difference going through the turbulent interface separating the aerowindow gas from the conjugating medium. The OPD is proportional to the "OPD Factor" listed in the table above. It can be seen that the OPD Factor for the subscale interface is about 85% of that which would exist within the full-scale SBS cell. Thus, the interferograms obtained in the subscale apparatus using

the 0.5145  $\mu\text{m}$  Zygo laser source will quite similar to what one would have obtained if the experiment had been conducted on the full-scale device using the HF wavelength of 2.8  $\mu\text{m}$ .

#### 4.2.3.3 Fundamental Wake Flow

Figure 4.2-7 presents the results of investigating the fundamental wake flow described in the previous section. In the shadowgraph, the flow direction is from top to bottom and the  $\text{N}_2$  stream is on the left side; in addition, the picture is approximately true size. Also indicated on the photograph is the width of the gas interface at the point where the interferometer beam penetrates the interface.

The two interferograms in the figure were taken at distances of 4 and 8 Rayleigh ranges (5 and 10 mm, respectively) from the gas interface into the  $\text{N}_2$  stream. The turbulent nature of the interface introduces shot-to-shot variation in the interferograms, so several interferograms were made at each location. During a typical test run, the position of the beam focus was fixed. The run would begin with a baseline "no-flow" interferogram having three or four waves of tilt, and was followed by the flow test during which seven or eight interferograms would be made. Note that the Zygo Fizeau interferometer used to generate these interferograms double passes the beam through the interface. Thus the OPD produced by a single pass through the interface (i.e., what would occur in a real system as the beam propagates into the Xe to be conjugated) would be reduced by a factor of two from what is depicted in the interferograms. However, this factor of two is taken into account in the presentation of the OPD data.

The interferograms obtained from these tests were processed using the VFAST! fringe analysis package developed by Phase Shift Technology. This package allows the user to input fringe data either manually (using a digitizing tablet) or automatically (using a video source). An interactive feature of the software also allows the user to "touch up" fringes to compensate for regions of poor contrast in the original interferogram. The procedure used to process the interferograms is as follows.

The baseline interferogram was digitized by one of the previously mentioned methods and stored in the computer. The flow interferogram was

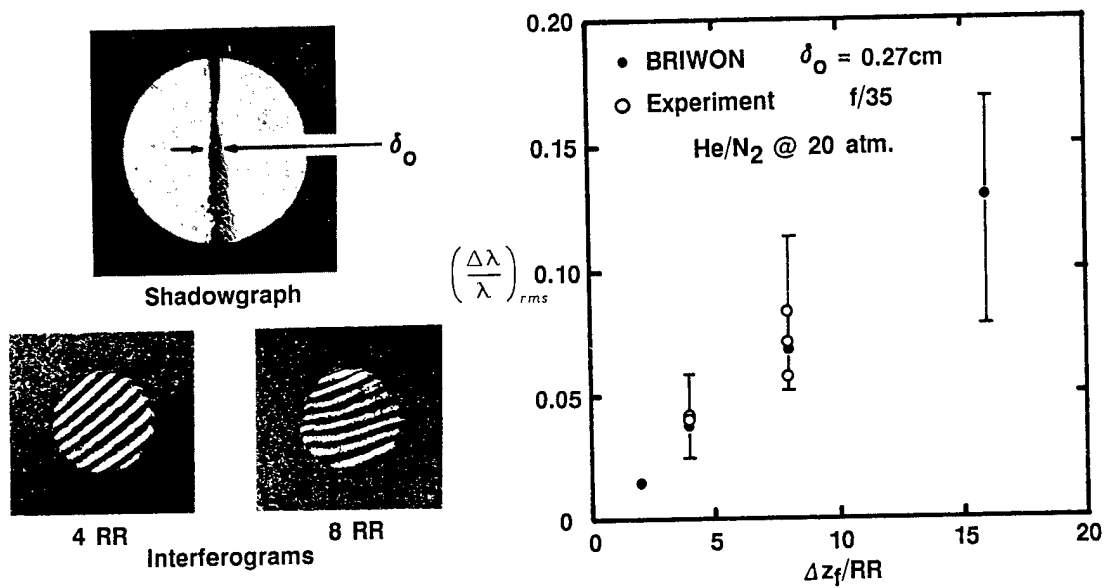


Figure 4.2-7. Subscale Results for "Fundamental Wake Flow"

then digitized and stored in the same way. A phase map was generated for each interferogram by interpolating the digitized fringe locations onto a uniform rectangular grid. These interpolated phase maps were then compared to the original interferograms to check the fidelity of the interpolation procedure; if the result was unacceptable, the interferogram was reprocessed. Once good phase maps existed for both the baseline and flow interferograms, the phase maps were subtracted point by point to produce a phase map corresponding to the flow aberration. Any residual tilt was then removed from this aberration phase map, and the rms was computed of the remaining phase difference. The rms optical path difference (OPD) was then calculated using this rms phase difference.

Figure 4.2-7 shows the OPD as a function of focal point location in the  $N_2$  stream. The open circles represent the experimental data, while the solid circles are results from the BRIWON code using the turbulence model described in Section 4.4. The bars on the BRIWON results indicate the range of values obtained for a number of statistical realizations of the flow. Two things are evident in this figure. First, the OPD is small near the gas interface and increases with increasing depth into the  $N_2$  side. Second, the amount of scatter in the results increases as the focal point is placed farther away from the interface. It is encouraging that such good agreement is obtained between the data and the model predictions for both of these observations.

As discussed in Section 4.2.3, one of the goals of the fluid mechanics experiments was to characterize the optical aberrations produced by the turbulent gas interface; the data in Figure 4.2-7 are the desired characterization. The other goal was to seek ways to reduce those aberrations. The turbulence model used in the BRIWON code suggests that the OPD across the gas interface can be reduced by decreasing the thickness of the interface. Figure 4.2-8 shows the model predictions for the case where the beam diameter at the interface is fixed and where the turbulence length scale is proportional to the interface thickness. The next three sections of this report describe three different schemes that were investigated in attempts to reduce the interface thickness.

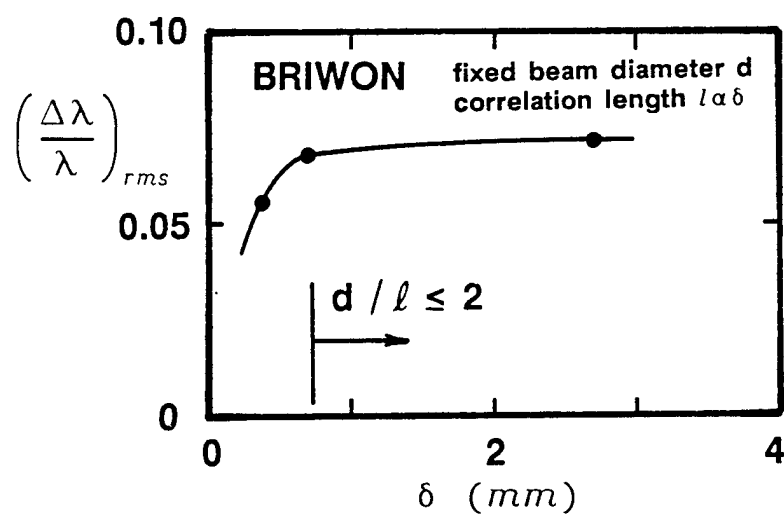


Figure 4.2-8. Variation of OPD With Interface Thickness; BRIWON Code With Turbulence Model

#### 4.2.3.4 Pressure Gradient Effects

In Reference 4-1, Prabhu and Narasima describe experiments in which plane, turbulent wakes were subjected to axial pressure gradients. The pressure gradients in their study were produced by reducing the cross-sectional area of the flow channel. They determined, among other things, that the thickness of the wake decreased as the flow accelerated through the reduced-area region of the channel. In view of this result, it was decided to subject the turbulent wake in the flowing-gas SBS cell to an axial pressure gradient. This pressure gradient was produced by placing inserts in the test section of the cell to reduce the cross-sectional area. Two sets of inserts were fabricated and are shown in Figure 4.2-9. The first insert, referred to as Mod 1, was simply a ramp made of plexiglas that was attached to the floor of the cell. The cell cross-sectional area was reduced only to 80% of its original value, and so the resulting pressure gradient was rather mild. The second insert, Mod 2, provided a dramatic reduction in cell area, down to about 22% of original value.

The shadowgraphs and interferograms of the flows produced by the two pressure gradient devices are shown in Figure 4.2-10. The first thing to note about the shadowgraphs is that the thickness of the interface produced by the Mod 1 device is about three-fourths of that corresponding to the unaccelerated flow, while the Mod 2 device gives an interface thickness of about one-half the original value. The second thing to note is that the interfaces are deflected towards the He side; this deflection is observed to be quite small for the Mod 1 device but appreciable for Mod 2. The fact that the interface deflects toward the He side is attributed to the higher flow speed produced in that side by the action of the pressure gradient. In effect, the lighter gas is accelerated more readily than is the heavier one. Corresponding to the increased flow speed is a reduction in the static pressure, and the reduced pressure deflects the flow to that side.

It can be seen from the figure that the interferograms recorded for these flows are not as well defined as those from the original flow. There are at least two reasons for this lack of definition. The first reason is simply that the accelerated flow speed smears the fringes during the exposure of the interferogram. The second reason is that the tilted

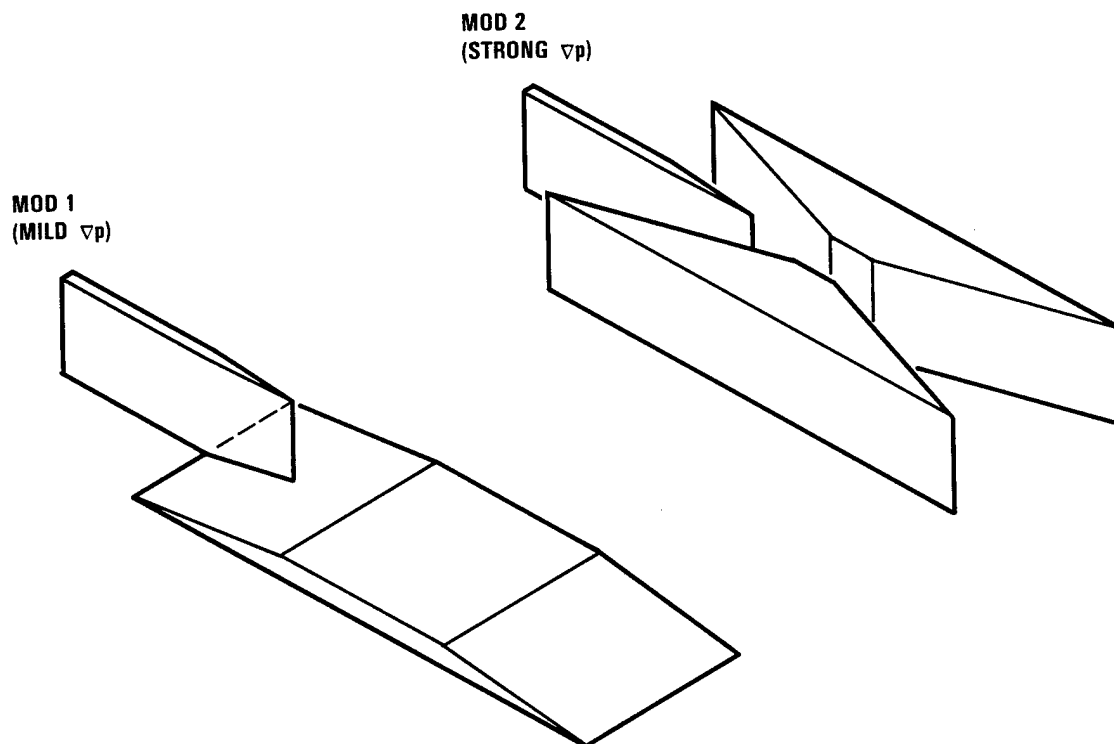
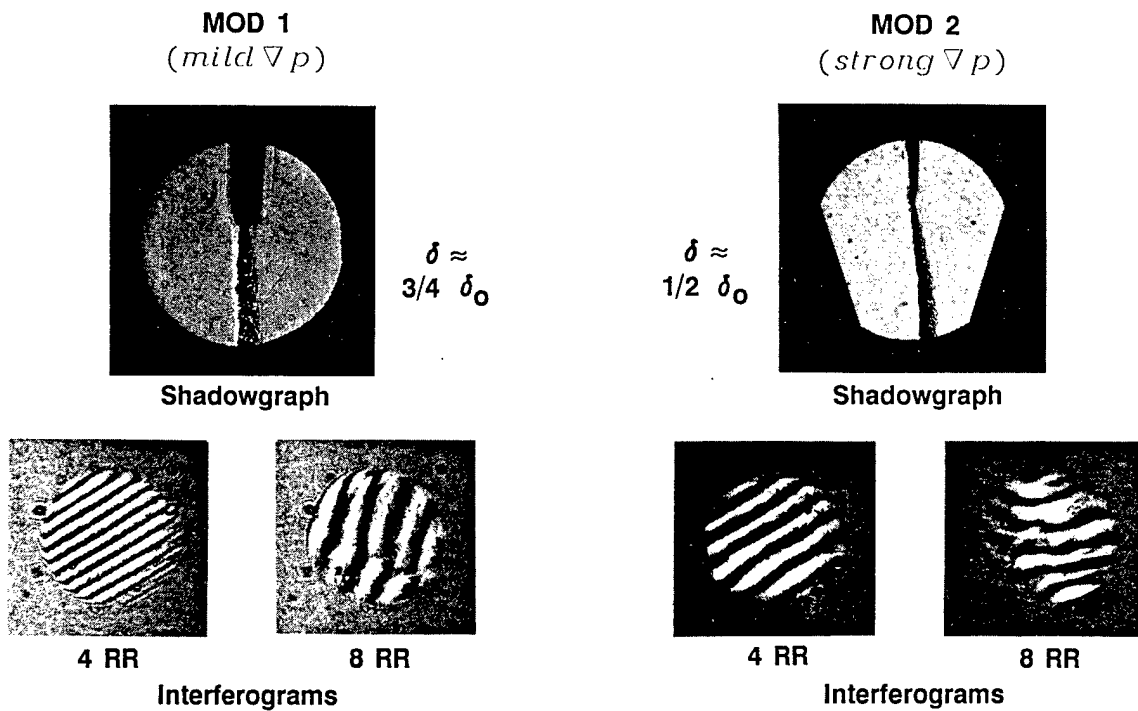


Figure 4.2-9. Flow Acceleration Ramps



NOTE: Fringe spacing for 40 atm Xe-He and  $2.8 \mu\text{m}$  is 20% larger

Figure 4.2-10. Experimental Results for Flow Acceleration Ramps; Shadowgraphs and Interferograms



interface deflects the interferometer beams and thus alters the optical alignment of the system. These facts complicate the data-reduction process and make it difficult to obtain a reliable value for the OPD across the accelerated interface.

A smaller data set thus exists for the flows with pressure gradient, and the results from this limited set are shown in Figure 4.2-11. This figure shows the variation of OPD with distance from the interface for the same conditions as in the "fundamental wake flow" (Figure 4.2-7). The BRIWON results and the results for the unaccelerated flow are simply carried over from that earlier figure. The results from the Mod 1 device (mild pressure gradient) show an apparent small reduction in the OPD, consistent with the observed slight thinning of the interface; however, the magnitude of the reduction is comparable to the measurement uncertainty. It was not possible to process the Mod 2 interferograms reliably, for the reasons mentioned earlier, so those results cannot be presented here.

The conclusion to be drawn from the pressure gradient study is that accelerating the flow in the wake region does, indeed, thin the wake; it also appears that this acceleration reduces the optical aberration by a small amount, but the actual reduction is difficult to quantify.

#### 4.2.3.5 Splitter Tip Suction

Another method for reducing the thickness of the turbulent gas interface is to suck away the boundary layers that flow along the splitter plate and eventually merge to form the near-wake region. In the present experiment, this suction was accomplished by cutting a very narrow slot (0.010-in. width) in the sharp trailing edge of the splitter plate, as indicated in Figure 4.2-12. This narrow slot was cut into a duplicate of the original splitter plate using a fine EDM wire. The suction is driven by the large pressure difference that exists between the test cell and the collector tank attached to the suction outlet. The flow rate of the gas sucked from the cell through this tip was controlled by a throttling valve and a sonic orifice that were installed in the line between the test cell and collector tank. The flow rate could therefore be adjusted, but the nominal value corresponded to the combined mass flow rate of the He and N<sub>2</sub> boundary layers.

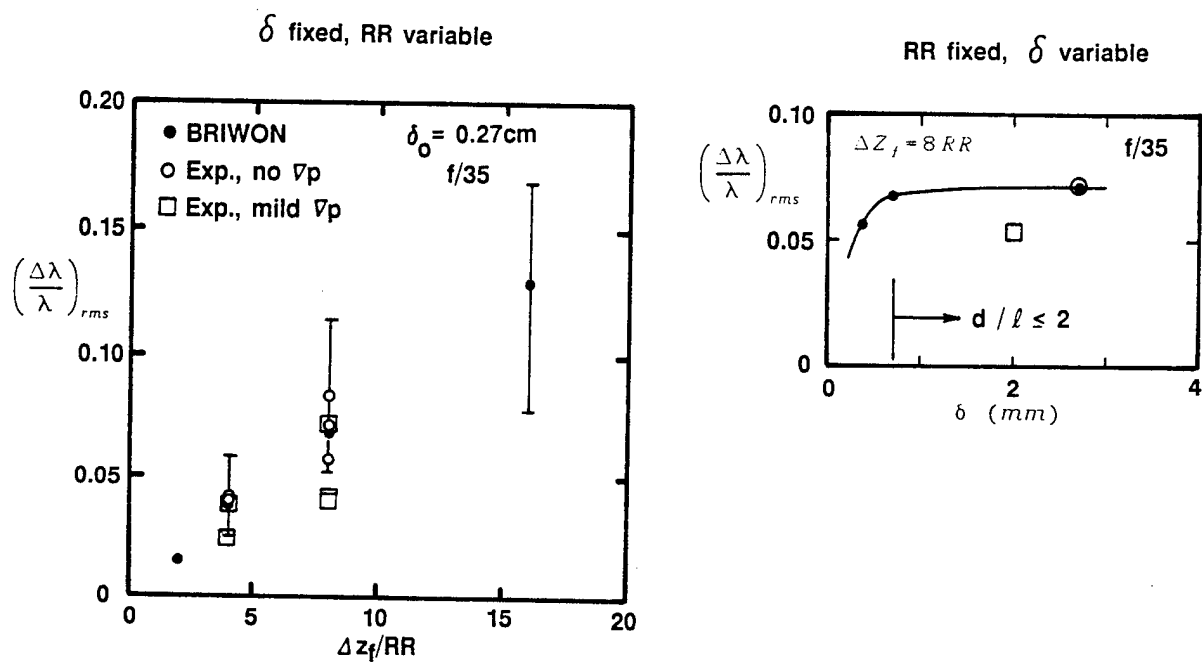


Figure 4.2-11. Results for Flow Acceleration Ramps; OPD, Comparison With Baseline Data

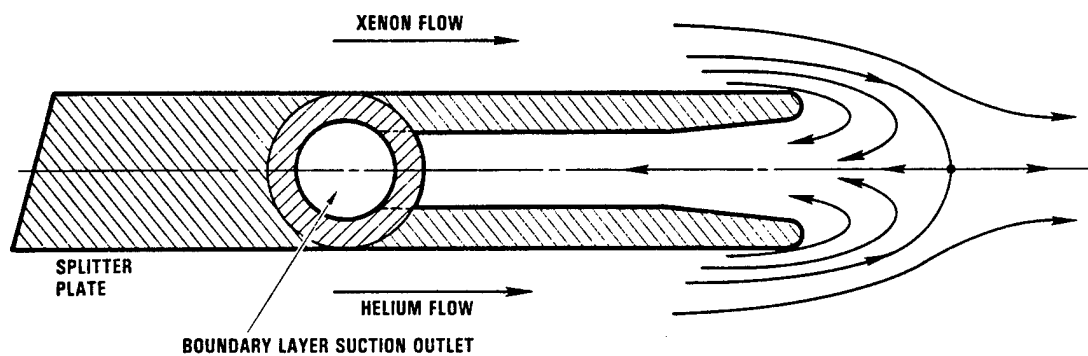


Figure 4.2-12. Splitter-Plate Tip Modified for Suction/Blowing Experiments

The results of these tests indicate that trailing-edge suction does not improve the quality of the baseline flow. In fact, any amount of suction causes the interface to thicken, suggesting that turbulent mixing between the two gas streams has somehow been enhanced. If the amount of suction increases beyond a certain range, the interface grows catastrophically and fills the He channel. Interferograms made through this interface are, for the most part, meaningless.

#### 4.2.3.6 Splitter Tip Blowing

The third method that was tried for reducing the thickness of the turbulent gas interface also employed the slotted splitter-plate tip developed for the suction experiments. In this case, however, a thin two-dimensional jet of fluid was introduced into the interface. The rationale behind the use of a jet was to inhibit the cross-stream mixing of the two gas streams and thereby make the interface thinner. The composition of the jet fluid varied from pure  $N_2$  to pure He. In addition, the jet velocity was varied over the range from one to four times the velocity of the He and  $N_2$  streams in the test cell.

Shadowgraphs suggest that, for a fixed composition of jet fluid, increasing the jet speed relative to the freestream speed causes a very slight thinning of the interface immediately downstream of the splitter tip, and a slight widening of the interface at greater downstream distances. These changes in the width of the interface are less pronounced for heavier (more  $N_2$ ) compositions of jet fluid.

A qualitative examination of the interferograms suggests that the jet reduces the magnitude of the optical aberrations compared to those of the original, sharp-edged splitter plate, but the reduction is quite small. Furthermore, this result appears to be relatively insensitive to the composition and speed of the gas jet. In view of the complexity of this type of flow device, it does not offer a clear advantage over the sharp-edged tip.

#### 4.2.3.7 Discussion

The results of the fluid mechanics experiments described above indicate that it has not yet been possible to improve the baseline flow

quality significantly. The most promising approach investigated thus far has been flow acceleration, and this method deserves further attention. It may also be worthwhile to investigate a different approach to boundary-layer suction, one that involves sucking the fluid away from the walls in a distributed fashion, rather than sucking only from the tip of the splitter plate. In either case, it will be necessary to improve the interferometric setup to allow for shorter exposure times (thereby reducing the amount of fringe smearing) and to overcome the "shadowgraph effect" present on many of the interferograms.

#### 4.2.4 Flowing-Gas SBS Experiments

##### 4.2.4.1 Experiment Description

The goal of the flowing-gas SBS experiments is to characterize the effect of the turbulent Xe-He interface on SBS reflectivity and conjugation fidelity. The experiments are conducted in the near-transient SBS regime, in which the pulse width is approximately five times the phonon lifetime; the characteristic fluid time scales, however, are large compared to the phonon lifetime. In all of these experiments, the nominal flow speed of each gas stream is 2 m/s, and the cell pressure is 20 atm.

The layout of the optical train and the diagnostics employed in this experiment have already been described in Section 4.2.2. Figure 4.2-13 illustrates the focusing pump beam geometry in relation to the turbulent Xe-He interface. Laser pulses at a wavelength of  $1.06\ \mu\text{m}$  (70 ns FWHM at 5-Hz repetition rate) are focused into the Xe gas stream. The position of the focal point relative to the interface is varied in both the streamwise direction and along the axis of the pump beam. The boundaries of focal point displacement are indicated in the figure; with the wavelength and focusing geometry employed here (F/35), the Rayleigh range is about 2.5 mm, and so the extent of focal point displacement is about 4 Rayleigh ranges in each direction. Referring to the previous discussion of Section 4.2.3.2 regarding scaling relations, the OPD through the interface for the subscale SBS experiments (20 atm Xe at  $1.06\ \mu\text{m}$ ) is approximately 8% greater than what would obtain under full scale conditions (40 atm Xe at  $2.8\ \mu\text{m}$ ). Thus, the results of these experiments yield a conservative estimate of what will occur in the SBL.

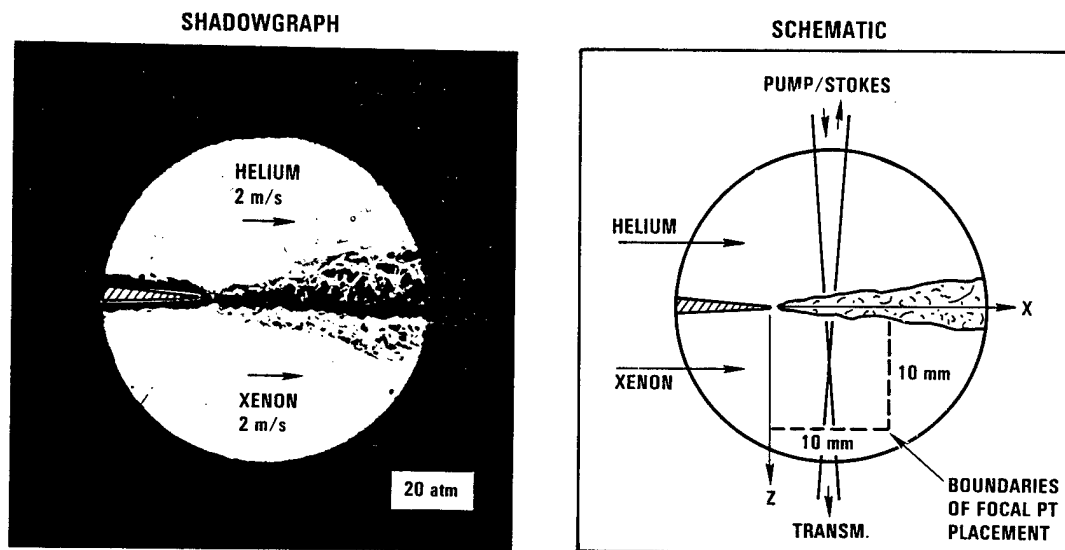


Figure 4.2-13. Placement of Pump Beam Focus Relative to Xe-He Interface

#### 4.2.4.2 Static-Cell SBS Results

Figure 4.2-14 shows the reflectivity of the SBS process when the test cell is pressurized to 20 atm with Xe only (the Xe is not flowing, and there is no He stream). This case, therefore, represents a baseline with which the flowing-cell data will be compared. These reference data are shown as open squares in the figure. Each point is the average value of ten consecutive shots into the cell, and the vertical bars on the datum at 60 mJ indicates the typical range of the individual data points composing the average. A least-squares straight-line fit to the data above 50 mJ pump energy yields an energy threshold of about 29 mJ and an SBS reflection efficiency of about 93%.

#### 4.2.4.3 Flowing-Gas SBS Results

Prior to conducting the flowing-gas SBS tests, our main concern was that the fidelity of the conjugation process could be seriously degraded by the presence of the turbulent gas interface. The test results, however, indicate that such concern was unwarranted. Figure 4.2-15 shows the far-field intensity patterns of the conjugated return beams for a static Xe test and for a test with a turbulent Xe-He interface. In each case, the nominal pump energy is 60 mJ. Very little difference is observed between the two far-field distributions, demonstrating that the gas interface has only a minimal effect on conjugation fidelity.

Included on the static reflectivity curve for pure Xe, (Figure 4.2-14) are the first reflectivity data generated in the flowing-gas SBS cell. The data were accumulated during a single test run. Throughout that run, the focal point was positioned about two Rayleigh ranges into the Xe stream (5 mm) and slightly more than half a Rayleigh range downstream from the tip of the splitter plate (1.5 mm).

The duration of the run was about 20s; during that time, the pulse energy incident on the cell was varied by manually adjusting the attenuator in the optical train. The filled-in squares in Figure 4.2-14 are actually averages of a half dozen or so pulses at each pump energy level. The vertical bars indicate the range of return energies recorded at each pump energy level. The first thing to note about the data is that the flowing-

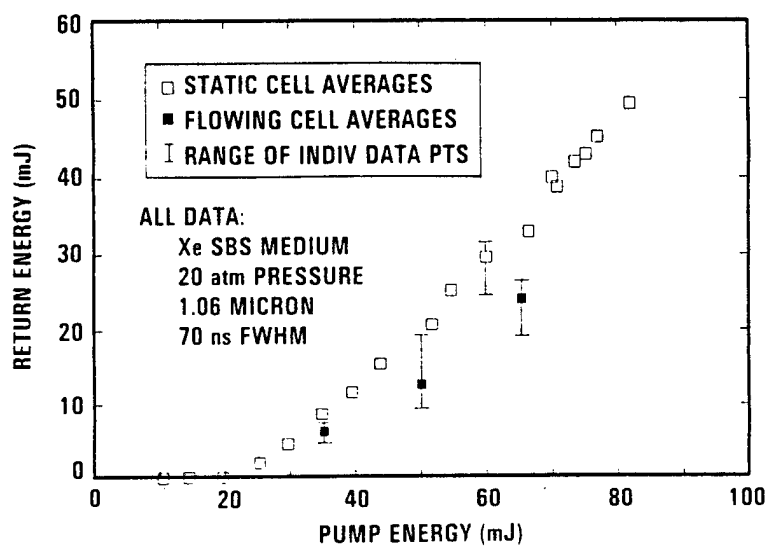
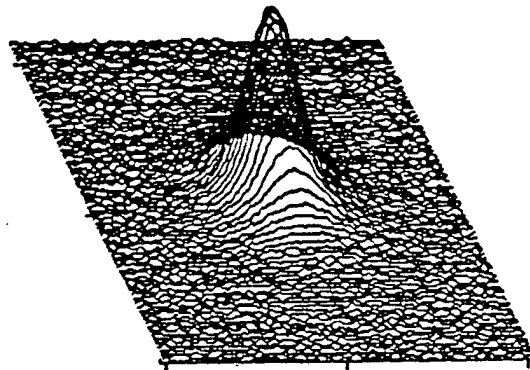
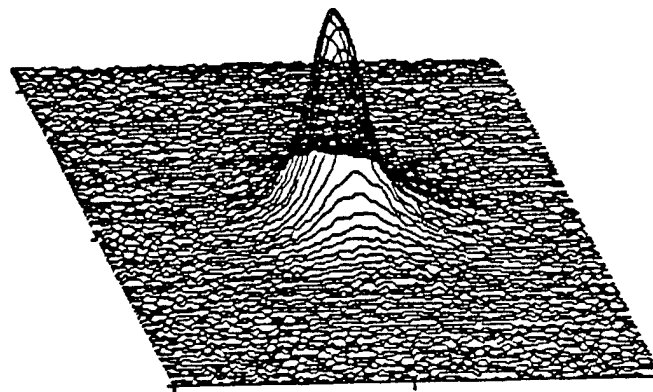


Figure 4.2-14. SBS Reflectivity for Static-Xe and Flowing-Gas Cases





**STATIC**



**FLOWING GAS**

Figure 4.2-15. Far-Field Intensity Pattern of Return Beam; Static Case and Flowing Case (pump energy = 60 mJ)

gas return energies are slightly lower than the static cell values. However, as the pump energy increases beyond about twice the unaberrated energy threshold, the slope of the flowing-gas curve approaches that of the static Xe curve. This observation suggests that, for high enough pump energy, the reflection efficiency of the SBS process is almost unaffected by turbulence-induced aberrations; of course, the penalty imposed by larger aberrations is an increased threshold energy.

In contrast to Figure 4.2-14, which shows reflectivity at a fixed location as a function of pump energy, is Figure 4.2-16, in which the reflectivity is presented as a function of focal point location for a fixed pump energy (60 mJ). All of the data in this case have been normalized by the unaberrated SBS return energy from the static-Xe case (about 30 mJ return for a 60-mJ pump). The figure shows data from tests in which the focusing lens was manually traversed along the pump-beam axis at three streamwise stations. These stations were located about 0.6, 2.1, and 3.6 Rayleigh ranges downstream from the tip of the splitter plate. Also shown in the figure are filled-in circles, which represent predictions from the BRIWON code with the turbulence model. The inset in the figure shows the approximate value of wake thickness at the three streamwise measurement stations.

#### 4.2.4.4 Discussion

In Figure 4.2-16, the reflectivity is observed to attain a maximum at each downstream position as the focal point is traversed along the beam axis. Furthermore, the magnitude of the maximum decreases and its transverse location extends deeper into the conjugating region as the focal point is moved downstream. The decrease in reflectivity as the focal point is moved close to the interface (less than about a Rayleigh range) is expected, because the extent of the high-gain SBS region is reduced by such movement. However, as the focal point is moved away from the interface, the benefit associated with the longer gain region is offset by an increase in the magnitude of turbulence-induced aberrations, which affects SBS threshold and, thus, reflectivity. It is proposed that the magnitude of the aberrations depends not only on the thickness of the turbulent layer, but also on the diameter of the beam at the interface relative to the

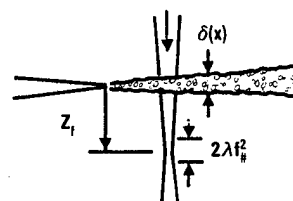
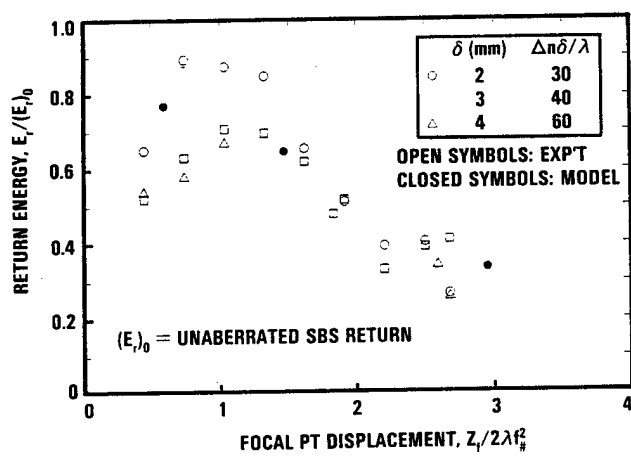


Figure 4.2-16. SBS Reflectivity as Function of Pump Focus Location; Model and Experimental Results (pump energy = 60 mJ)

integral scale of the turbulence. Although turbulent fluctuations in the optical path are introduced over a wide range of scales, the largest contributions are expected from a range of scales whose size is on the order of the integral scale. For a sufficiently small beam diameter, the larger turbulent scales introduce only tilt, which does not significantly affect SBS threshold. Therefore, for a fixed thickness of the turbulent layer, the maximum reflectivity occurs at a focal position far enough into the conjugating region to yield reasonable SBS gain, but close enough to the turbulent layer to keep the beam diameter at the interface small compared to the integral scale of the turbulence.

#### 4.2.5 Summary

The results of the subscale flowing-gas experiments may be summarized as follows:

1. The turbulent gas interface has very little effect on conjugation fidelity; the effect is expected to decrease as the ratio of pump energy to threshold energy increases.
2. The optical aberration imposed on the pump beam by the turbulent gas interface increases as the beam focus is moved farther from the interface. By itself, this increased aberration decreases the SBS reflectivity.
3. SBS reflectivity is also reduced if the focus is moved too close to the interface due to the reduced conjugating depth available in that area.
4. The maximum SBS reflectivity occurs when the pump beam is focused approximately one Rayleigh range away from the turbulent gas interface.
5. The effect of the aberrations on the SBS energy threshold is to increase the threshold.
6. Good agreement is obtained between the experimental results and the BRIWON turbulence model.
7. The most promising approach to improving the quality of the baseline flow is application of a favorable pressure gradient to thin the turbulent interface.

### 4.3 FULL-SCALE EXPERIMENTS (CTS)

The results of the subscale flowing-gas SBS experiments provided insight into the effects of the aerowindow turbulent interface on SBS physics, and provided design criteria for minimizing such effects. Results from the subscale experiments also guided the development of the BRIWON SBS-turbulence model described in Section 4.4.

Although the subscale facility is useful for proof-of-principle experiments, it is not amenable to experiments involving multiple foci, HF wavelengths, long pulses, or full-scale flow conditions. Described in this section are the designs and preliminary test results from a full-scale flowing gas system that was integrated into the existing APACHE HF facility at CTS. Objectives and relevant nondimensional parameters are discussed in Section 4.3.1. Description of the facility, including the flowing-gas SBS cell, are given in Section 4.3.2. The performance of the major components are discussed in Section 4.3.3, and results from preliminary phase conjugation experiments are presented and discussed in Section 4.3.4.

#### 4.3.1 Objectives, Scaling Parameters

The overall objectives of the CTS flowing-gas SBS experiments are two-fold: (1) to investigate the effects of the aerowindow Xe-He wake on SBS threshold and conjugation fidelity under full-scale flow conditions using an HF laser, and (2) to quantify the effect of the wakes on multiple-foci threshold reduction. The objective under the APACHE program was to design and integrate the flowing-gas hardware and to obtain preliminary flowing-gas data. The bulk of the testing is to be performed under the APEX program.

The SBS cell designed for the APACHE flowing-gas DVT is a full-scale simulation of the critical features of the SBL aerowindow concept. Of primary interest is the behavior of the Xe-He wake and its effects on the SBS conjugation process. Material windows are used in place of the aerowindow nozzle to simplify the experiment. Details of the SBS cell design are given in Section 4.3.2.3.

Nondimensional scaling parameters that are most relevant to the APACHE flowing-gas DVT are listed in Table 4.3-1, a condensed version of Table

Table 4.3-1. Important Scaling Parameters for Flowing-Gas SBS Cell DVT

Issue	Parameter	SBL Baseline	ALPHA Demo	APACHE SBS Cell DVT
Pump power	$P/P_{TH}$	3-5	3	1-7
Conjugating depth (half-width)	$L/(2\lambda f_{\#}^2)$	3.0	3.0	2.2-4.4
Laser pulse width ( $\tau_{PL}$ = phonon lifetime)	$\tau_{laser}/\tau_{PL}$	$\gg 10$	$\gg 10$	$> 4$
Beamlet f-number	$f_{\#}$	30-50	30-50	30
Thermal homogeneity of conjugating medium	$(\Delta T)_{rms}/T$	$< 5 \times 10^{-4}$	$< 5 \times 10^{-4}$	$< 5 \times 10^{-4}$
OPD (rms, nom.)	$\Delta\lambda/\lambda$	0.1	0.1	0.1
Optical thickness	$\Delta n \delta/\lambda$	$< 10$	$< 10$	$< 10$
Beamlet diameter at wake	$L/(f_{\#}\delta)$	1	1	1
Wake Reynolds number	$Re_{\delta}$	$5 \times 10^4$	$5 \times 10^4$	$5 \times 10^4$
Characteristic turbu- lent time scale ( $\tau_{PR}$ = phonon rise time)	$\tau_T/\tau_{PR}$	$\sim 25$	$\sim 25$	$\sim 25$
Turbulence correlation length	$1/\delta$	0.2	0.2	0.2
Threshold Reduction				
Number of foci (per line)	$N$	1	TBD	1-4
Foci lateral separation	$s/(2\lambda f_{\#})$	NA	$> 20$	30
Beam overlap in conjugating region		NA	None	None
Laser coherence length ( $f_m$ = reimaging focal length)	$L_C/(N-1) f_m$	NA	$> 1$	$> 1$

4.1-1. Values of the parameters are given for the present experiment and compared with nominal values for the SBL baseline design and the ALPHA demonstration nominal design. As these parameters were discussed in Section 4.1.2 for the SBL and ALPHA designs, only those parameter values of the APACHE DVT that differ from those of the SBL will be mentioned.

The most important difference between the present experiments and the SBL is the pulse width of the lasers. Although pulse stretching techniques are under consideration for future use, the pulse width of the upgraded PAR lasers on the  $P_2(8)$  line is three to four times the phonon lifetime. The two phenomena most affected by the shorter pulse width are thermal blooming and SBS behavior in the presence of time-varying aberrations (induced by the turbulent wake). Thermal blooming was adequately addressed in the CWCS experiments, but the latter phenomenon remains an issue. It is desirable to have a pulse width greater than several phonon response times (several microseconds), whereas the pulse width in the APACHE DVT is approximately  $1 \mu s$ .

Another issue not addressed in the present experiments is beam combination in a flowing cell, and is a potential subject for future investigation. Beam combination experiments conducted in a static cell are discussed in Section 3.5. Future experiments that include a turbulent interface have been proposed for the APEX program.

Thus, the APACHE flowing-gas SBS DVT is a full-scale, single-line simulation of the nominal SBL conceptual design in all respects except pulse and beam combination.

#### 4.3.2 Facility Description

Three components of the APACHE HF facility were modified to accommodate the flowing-gas SBS cell: (1) the PAR laser was upgraded from two 2-liter devices to two 5-liter devices, as described in Section 4.3.2.1, to provide a greater margin of pump energy over SBS threshold, (2) a Xe-He flow control system was added to the existing Xe gas-handling system, described in Section 4.3.2.2, and (3) a multiple-foci optical segment was integrated around the SBS cell, described in Section 4.3.2.4. The design and construction of the flowing SBS cell itself is discussed in Section 4.3.2.3.

#### 4.3.2.1 PAR Laser Upgrade

The PAR laser system was upgraded using TRW capital to support the flowing-gas SBS experiments. The  $P_2(8)$  output energy delivered to the SBS cell from the original PAR laser system was approximately three times the unaberrated threshold. To accommodate a possible factor of two increase in the SBS threshold introduced by the Xe-He wake, a larger laser system was needed.

The approach taken was to employ the basic design of the two original PAR heads, but to increase the diameter of the heads from 5 to 8 cm. The gain volume for each head increased from 2 to 5 liters. Because the length of the heads remained the same, the original flashlamps and high-voltage system were compatible with the new heads.

The laser configuration was also modified. In the original design, one head was employed in a positive-branch, unstable resonator and the other served as a single-pass amplifier. Both 5-liter heads are now used in one positive-branch, unstable resonator (Figure 4.3-1). The magnification of the upgraded laser is 2.77.

The larger beam diameter, however, required a compacting telescope located in zone 1 prior to the delay line (Figure 4.3-2) to ensure that the Fresnel number at the exit of the delay line met the original requirements of the APACHE optical system ( $\sim 1.6$ ). A second expanding telescope was required at the exit of the delay line to reduce the fluence on the grating. The compacting telescope originally located in zone 2 was modified to yield a beam diameter equal to that of the original design, thus avoiding any modifications of the diagnostic legs in zone 2.

The performance of the new PAR laser design is discussed in Section 4.3.3.1.

#### 4.3.2.2 Flow Control System Design

The purposes of the flow control system are: (1) deliver Xe and He gases to the SBS cell at specified flowrates, pressures, and mean temperatures, (2) purify and filter gases entering the SBS cell, and (3) provide the ability to recover Xe from the He-Xe mixture exhausted from the SBS cell. A schematic of the flow control system is shown in Figure 4.3-3.



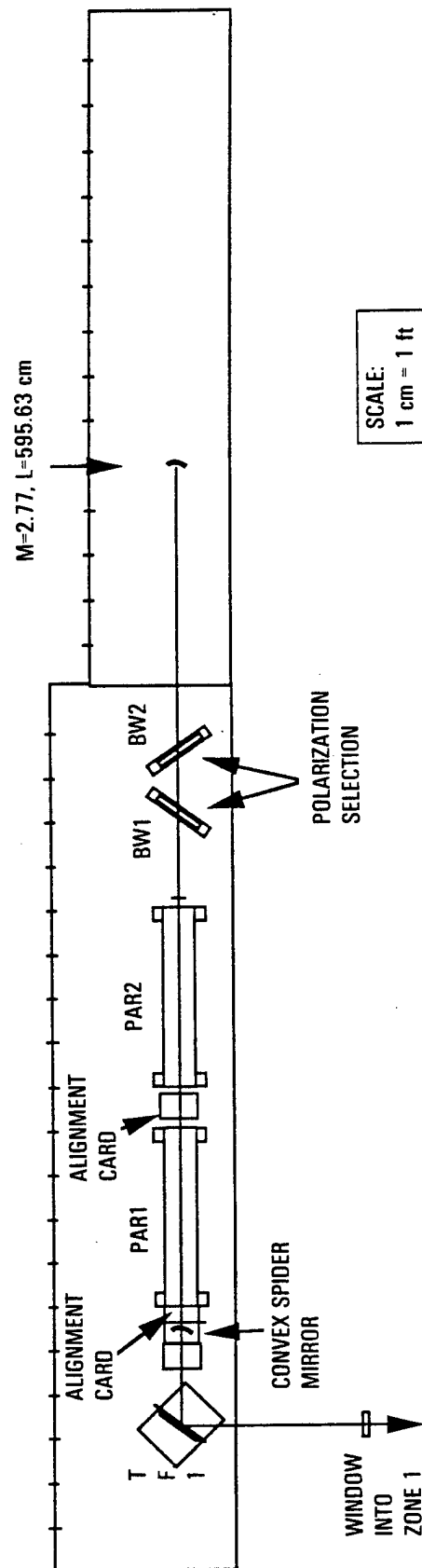


Figure 4.3-1. Layout of Upgraded PAR Laser

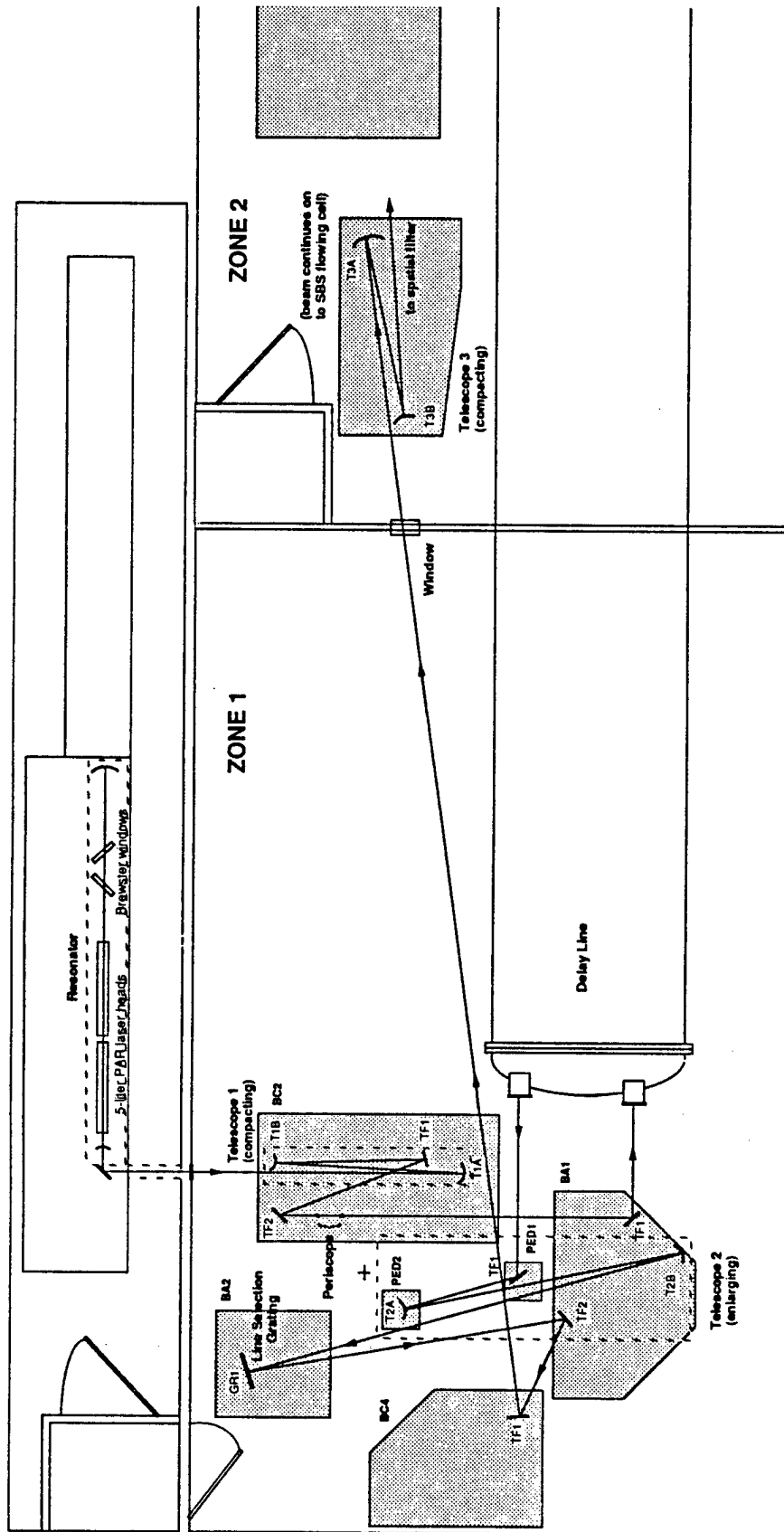


Figure 4.3-2. Modified Segment of APACHE Facility Optical Train

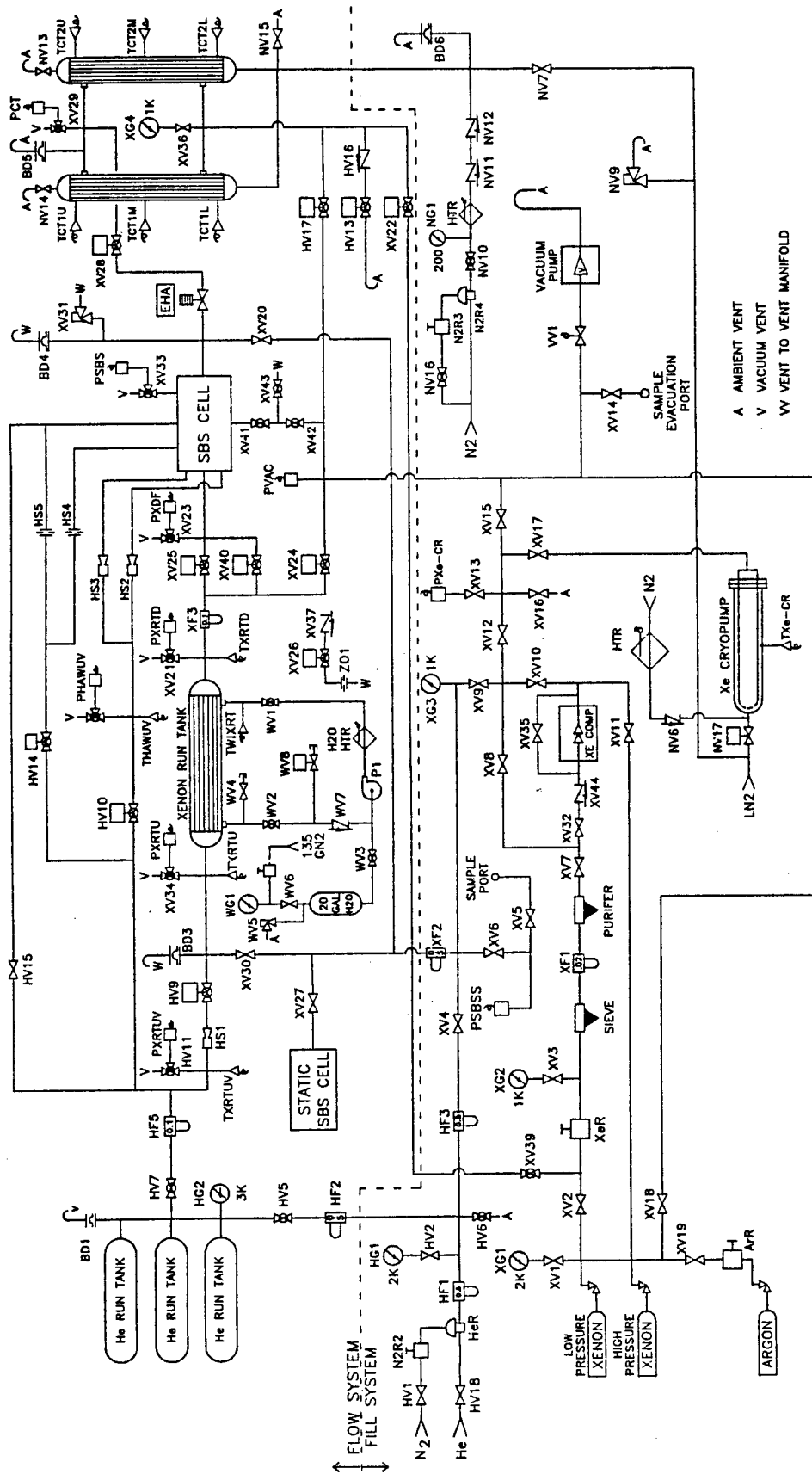


Figure 4.3-3. Flow-Control System Schematic

The dotted line across the middle of the figure is a convenient functional demarcation of the system. Components located in the upper half of the figure are generally related to the delivery of Xe and He gases to the cell during a flowing-gas test, and components in the lower half of the figure are related to posttest Xe recovery and purification.

Velocity and pressure in the SBS cell are controlled by the combination of upstream sonics and an electro-hydraulically actuated (EHA) control valve located downstream. The upstream sonics control the mass flowrate through each of the three channels, and the EHA controls the mean pressure level in the SBS cell, generally set to 40 atm.

The He run tanks are large (100 ft<sup>3</sup>) surplus storage vessels utilized to maintain approximately constant pressure for the sonics (80 atm) during the course of a flow test. He gas from sonics HS2 and HS3 (Figure 4.3-3) are fed directly to the aerowindow buffer channels at velocities matched to that of the Xe channel.

Helium from sonic HS1, however, is used as a piston for gas in the Xe run tank. The Xe run tank is comprised of a bundle of seventeen 3/4-in. diameter, 20-ft tubes encased in a 6-in. diameter shell. Xenon is pressurized in the tubes and temperature-controlled water is circulated in the region surrounding the tubes. The purpose of this design is twofold: (1) the long, slender tubes ensure that the mixing region between the He and Xe is relatively short, and (2) the temperature-controlled water flow ensures that the Xe is maintained at a prespecified, uniform temperature. The latter feature is particularly important for the delivery of thermally uniform Xe gas to the SBS cell at a temperature that is closely matched to the wall of the cell. Thermal analysis suggests that the Xe gas must be matched to within 1.5°C of the cell wall temperature to ensure that thermal fluctuations not exceed 0.2°C (rms) in the conjugating region. Thermal fluctuations larger than approximately 0.2°C are predicted to noticeably degrade conjugation fidelity and increase SBS threshold.

During flowing gas operation, the He driver gas forces the slug of Xe from the run tank, through filter XF3 and into the SBS cell. Xenon is kept separate from the two adjoining He channels until the gases reach the splitter plate tip in the SBS cell conjugating region.

An important feature of the flow system is the utilization of on-the-fly particulate filters. Such filters are necessary because it is not practically possible to maintain the required particulate level in either the He run tanks or the Xe run tank. It is required that particulates greater than approximately  $0.3\text{ }\mu\text{m}$  diameter be removed to achieve the "clean air" limit for Xe under the present nominal experimental conditions. Two high flowrate filters, HF5 and XF3 (Figure 4.3-3) are used to remove particulates from the He and Xe streams, respectively. These components are advertised by the Millipore Corporation as  $0.05\text{-}\mu\text{m}$  absolute filters with a retention efficiency of greater than 99.99999%

The Xe-He mixture exits the SBS cell and flows to the EHA valve. The EHA valve provides pressure control for the SBS cell throughout a flowing gas test. It operates in a sonic condition until the catch tank pressure rises to a pressure of roughly 25 atm, well after the Xe-He mixture exits the SBS cell. Although the EHA valve is capable of operating in a pressure feedback mode, it is simply commanded to one of two positions in the present operation. The first position corresponds to a pure He flow which occurs during the initial phase of a flow run when the Xe has not yet reached the EHA valve from the Xe run tank. The second valve position corresponds to the Xe-He flow. Each position is chosen to maintain the specified SBS cell pressure, generally 40 atm.

All gases exiting the SBS cell and EHA valve are dumped into catch tanks that also serve as cold traps. The two 20-ft-long catch tanks are of a shell and tube design in which the gases are collected in the volume located within the main outer shell but outside the inner tube bundle. Seven  $3/4$ -in. tubes run the length of the catch tanks and are filled with  $\text{LN}_2$  to freeze out the Xe.

The catch tanks have the capacity to hold six runs of Xe before a recovery operation is required. Xenon is recovered by first venting and vacuum pumping He gas from the catch tanks. The  $\text{LN}_2$  is then drained from the tubes which are subsequently heated to ambient temperature by hot, flowing  $\text{GN}_2$ . External band heaters are also required to heat the outer shell. Finally, the Xe gas is pumped back into high-pressure K-bottles for future use.

A description of the system operational procedure and performance is given in Section 4.3.3.2.

#### 4.3.2.3 SBS Cell

The CTS flowing-gas SBS cell is a 40-atm pressure vessel comprised of three separate flow channels (Figures 4.3-4, plan view, and 4.3-5, view along optical axis). Xenon gas flows in the center channel and He gas flows in the two outer channels at velocities typically matched to that of the Xe. Flow velocities are limited to 20 m/s by upstream filters and by the maximum  $C_dA$  of the downstream pressure-control valve (Section 4.3.2.2). The width of the Xe channel is 2.2 cm, which translates to 4.4 Rayleigh ranges for an f-number of 30 and a laser wavelength of 2.9  $\mu\text{m}$ . Both He channels are 2.5 cm wide.

One unique feature of the cell design is the sandwich construction which permits any of the three channels to be modified or replaced without affecting the remaining channels. Other features of the cell include a 3.3:1 contraction section, perforated plates and screens in the upstream plenum to control fluctuations of velocity and temperature, and a 4.75° half-angle diffusor section located downstream of the conjugating region.

The HF beam enters the cell through a 7.6-cm-diameter, 2.5-cm-thick  $\text{CaF}_2$  window (Figure 4.3-4) and is focused in the Xe channel. The transmitted beam exits the cell through an identical window mounted on the opposite side. Each window mount is canted at 3° about an axis parallel to the trailing edge of the splitter plates to direct reflections away not only from the main beam path but from the multiple-foci region as well (Section 4.3.2.4). The windows are also offset from the main body of the cell to keep the fluence below the damage level.

The body of the SBS cell was machined from 17-4PH stainless steel. The Xe channel, which contains both splitter plates, was machined from two individual plates that were subsequently brazed together. Preparation of the two halves for brazing included a machining operation to ensure flatness of the faces, Ni plating of the faces, and electropolishing. A thin Ni sheet was placed between the two halves and the entire assembly was heated to 1950°F. All machined parts of the SBS cell were then heat

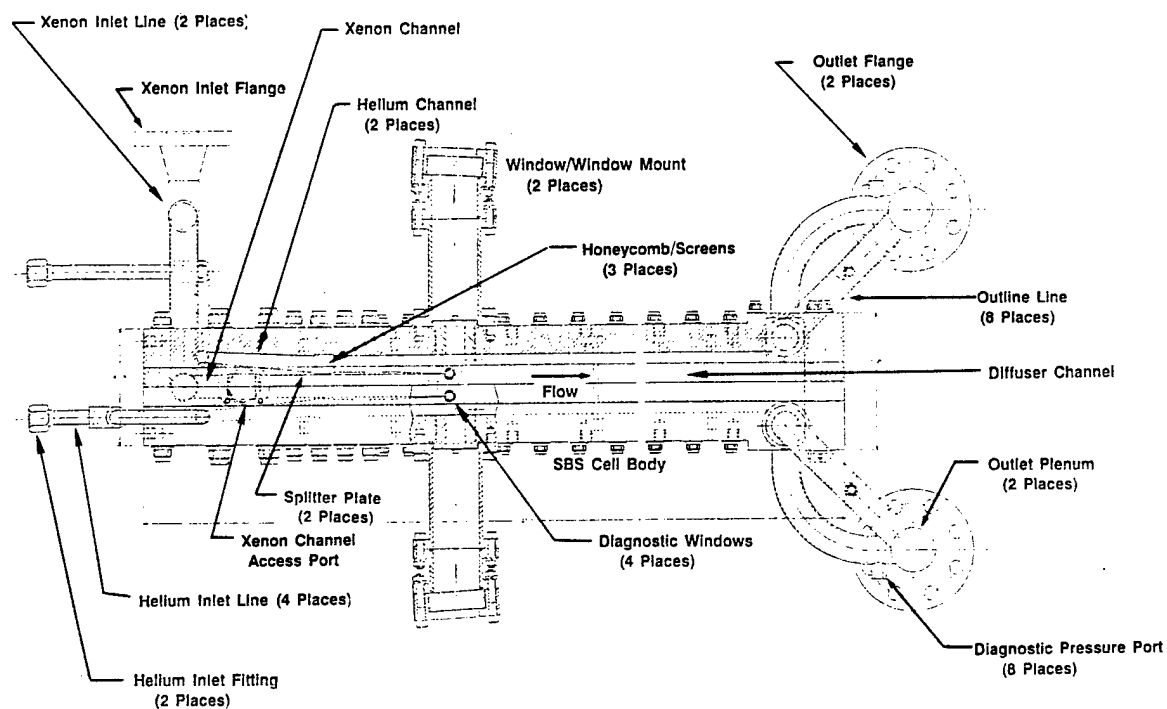


Figure 4.3-4. Flowing-Gas SBS Cell Design (plan view)

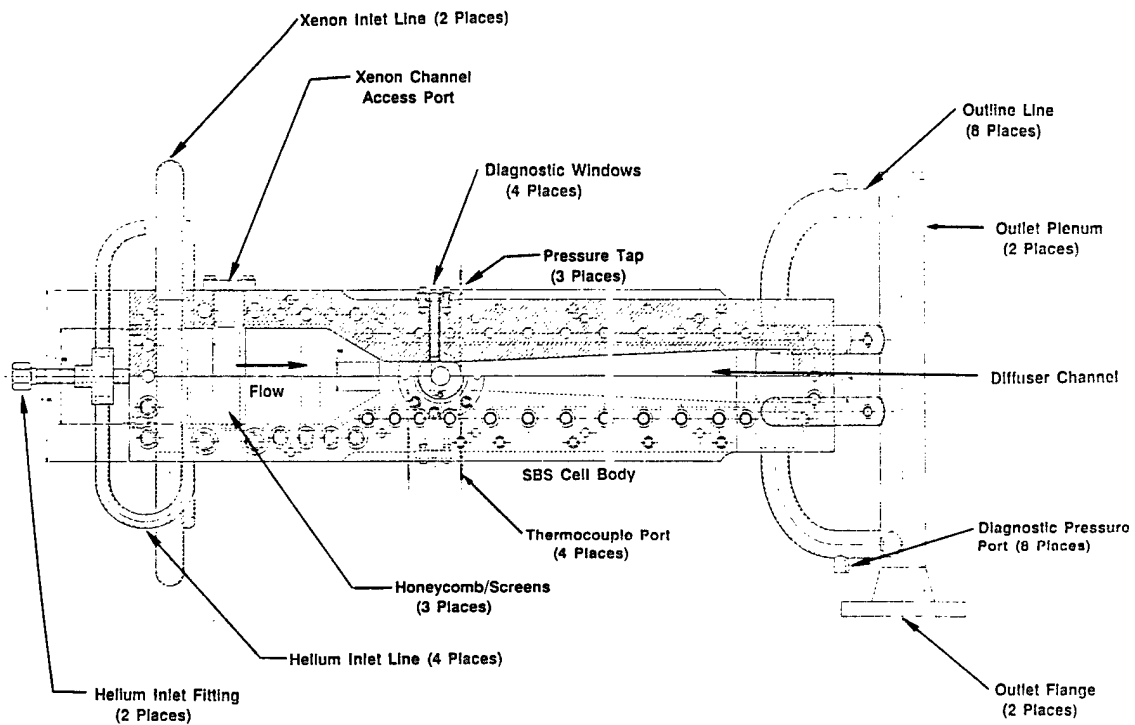


Figure 4.3-5. Flowing-Gas SBS Cell Design (view along optical axis)



treated to 1050°F. After final machining operations were completed, e.g., the cutting of O-ring grooves, all parts to be exposed to gas flow were electropolished, including inlet and exit tubing, manifolds, and screens.

Upon completion of the fabrication process, all components were inspected and assembled to ensure that the product met design specifications. The cell was then pressurized to 60 atm (50% above the working pressure) to ensure structural integrity. Pressure decay and He "sniffer" tests were performed with the cell pressurized to 40 atm. The cell was then disassembled and all parts were cleaned in the TRW Space Park cleanroom per PR 2-2-12 (level S). After cleaning, all components were shipped to the CTS cleanroom for final assembly and leak tests.

The SBS cell was mounted vertically in zone 3 of the APACHE HF facility (Figure 4.3-6) and plumbed to the flow control system. System flow tests were performed first, as described in Section 4.3.3.2, to ensure that Xe and He were delivered to the SBS cell at the proper pressures, temperatures, and flow rates, and that the Xe recovery system performed to design specifications. Fluid mechanics tests of the wakes in the SBS cell were then performed using the shadowgraph technique (Section 4.3.3.3).

#### 4.3.2.4 Multiple-Foci Optics

The multiple-foci optics were designed to place one, two, or four foci at precise locations within the SBS cell. The geometry of the design satisfies the SBL requirements on foci separation and beam overlap (Table 4.3-1).

A schematic of the layout is illustrated in Figure 4.3-7. As in the original APACHE optical train, a Schief-Spiegler telescope first brings the incident collimated beam to focus in the SBS cell. A reimaging mirror located on the transmitted side of the cell brings the beam to a second focus displaced from the first. A second reimaging mirror on the incident side of the cell brings the beam to a third focus, and the first reimaging mirror brings the beam to a fourth focus. The beam exits the optical train to a dump after the last focus.

Also shown in the figure is a mirror mounted on a translation stage designed to control the precise position of the first focal point, and a

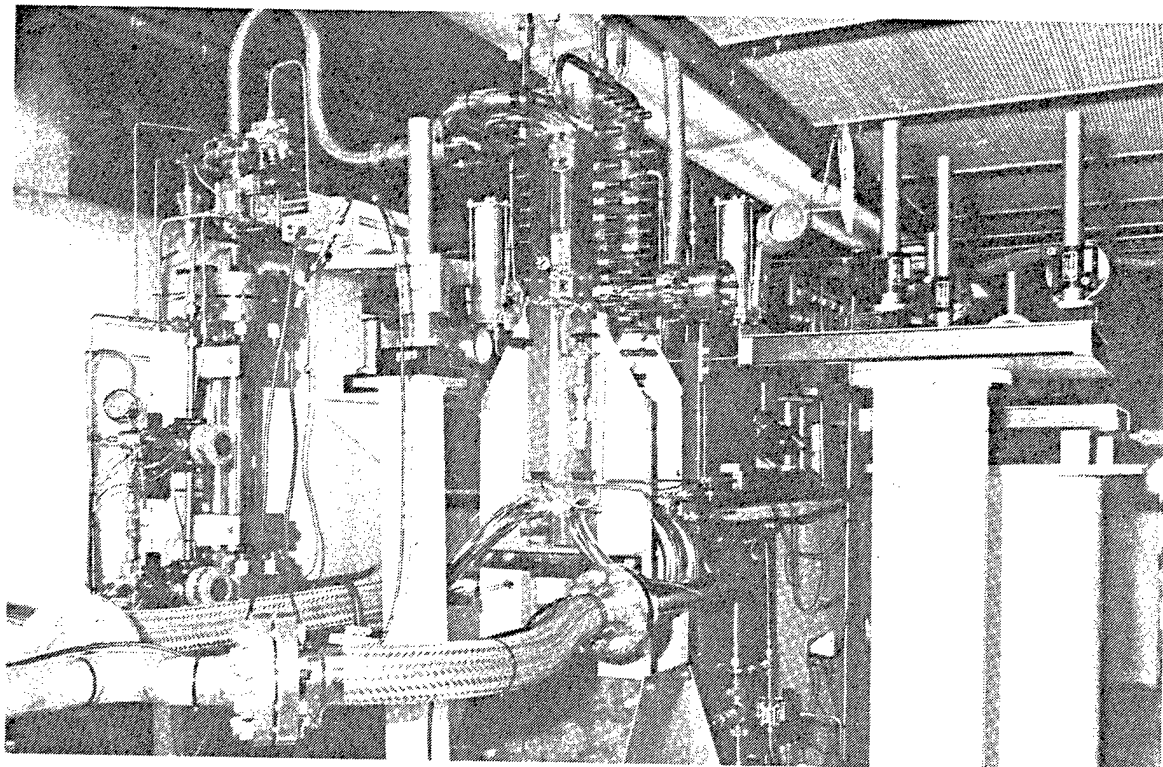


Figure 4.3-6. Flowing-Gas SBS Cell Integrated in Zone 3  
of APACHE HF Facility

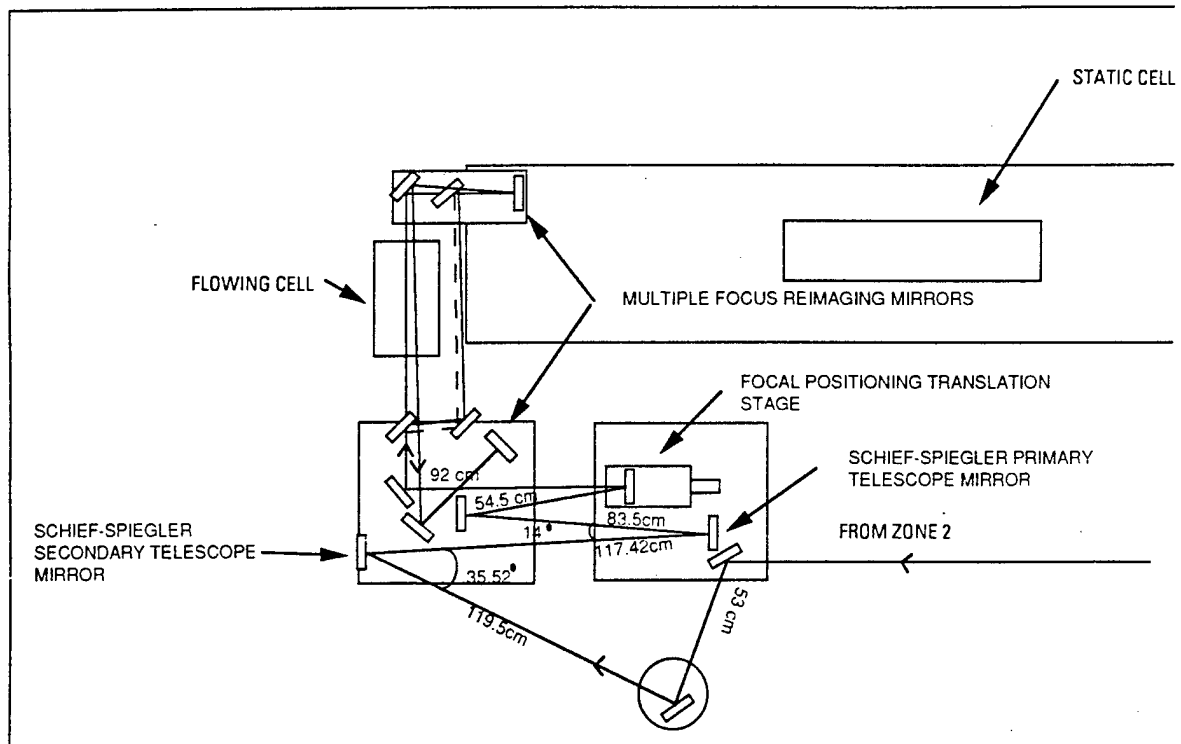


Figure 4.3-7. Multiple-Foci Optics Layout For SBS Cell

bypass leg to permit the observation of the relative positions of the foci at a reference location outside the SBS cell.

These optics were employed in single-focus experiments under the APACHE program. Multiple-foci experiments are to be performed under the APEX program.

#### 4.3.3 System Performance Tests

This section describes component checkout tests performed prior to the SBS phase conjugation experiments. The three major component included the upgraded PAR lasers, the flow control and gas recovery system, and the flowing-gas SBS cell.

##### 4.3.3.1 Upgraded PAR Laser

The upgraded PAR laser was found to exceed expectations for output energy. Using the same gas mixture employed in the original PAR heads, the new laser outputs more than twice as much energy at a lower flashlamp voltage and a lower laser gas pressure. The original PAR laser delivered roughly 60 J of multiline energy for a flashlamp voltage of 50 kV and a gas pressure of 580 torr. The upgraded laser delivers 150 J at 40 kV flashlamp voltage and 460 torr pressure.

In terms of energy delivered to the SBS cell the upgraded PAR laser provides over 2 J of spatially filtered  $P_2(8)$  energy, an order of magnitude above the unaberrated SBS threshold. The original PAR laser typically delivered 0.8 J.

A typical  $p(t)$  trace taken very near the PAR laser is shown in Figure 4.3-8. The FWHM of the multiline pulse is estimated to 1.3  $\mu s$ . The contribution of EMI to the transducer behavior is also illustrated in the lower trace of Figure 4.3-8. The trace was obtained by triggering the lamps with an empty cavity.

The alignment system was also modified to improve the pointing precision of the beam. A He-Ne coalignment laser is now injected into the laser cavity through one of the Brewster windows. This approach dramatically improves the ability to consistently "hit" the spatial filter. It is now possible to obtain 20 to 25 valid laser shots per day.

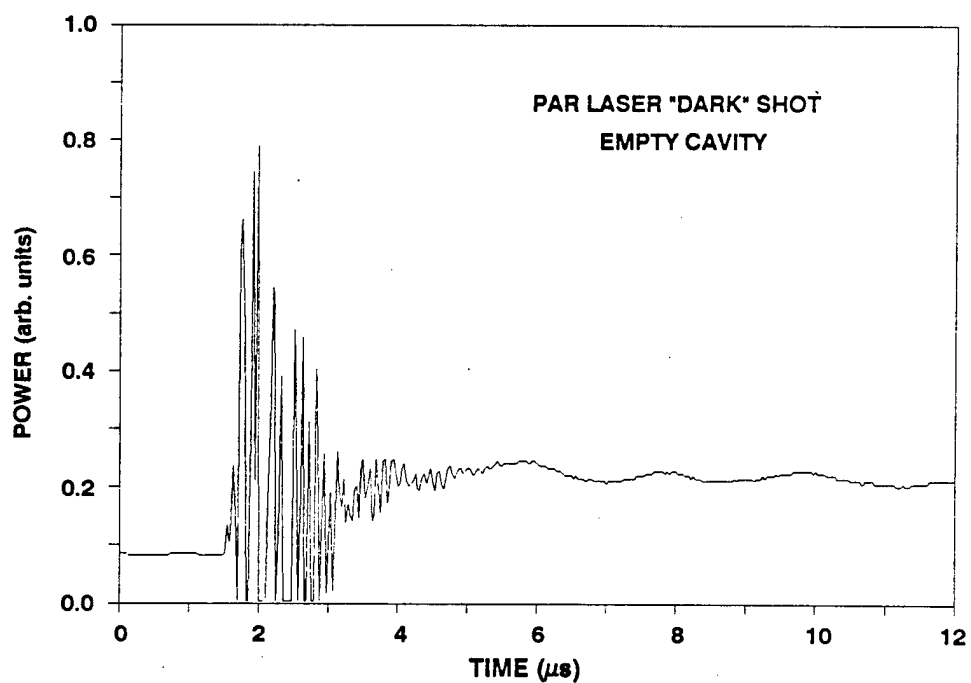
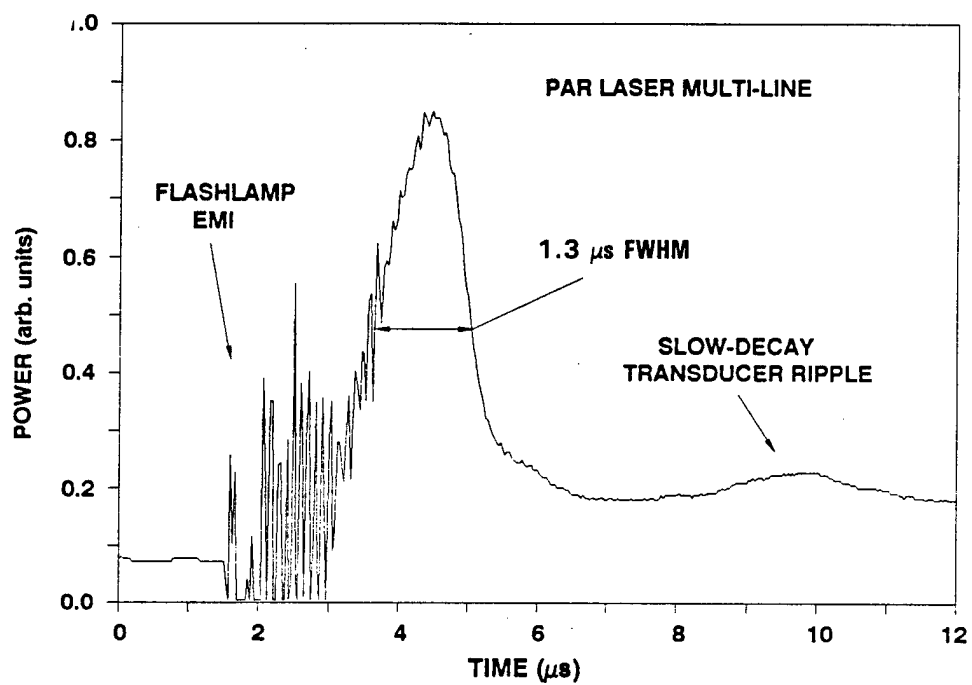


Figure 4.3-8. Temporal Behavior of PAR Multiline Pulse

#### 4.3.3.2 Flow Control System

The performance of the flow control system was evaluated at low and moderate flowrates and was found to meet design specifications. The system was designed to deliver both Xe and He gases filtered at  $0.05\ \mu\text{m}$  to the SBS cell at pressures of up to 40 atm and velocities of up to 17 m/s. General system tests were performed at pressures of 15 to 40 atm and velocities of 2 to 10 m/s using Ar-He in initial tests and Xe-He in final tests.

The operational procedure developed for the system is as follows (Figure 4.3-3). The SBS cell is filled with He to 40 atm and is initially isolated from the rest of the system by valves, HV10, HV14, XV25, and the EHA. The Xe run tank is filled to 40 atm and is initially isolated from other components by valves HV9 and XV25. The He run tanks, which supply gas to the aerowindow buffer channels and to the Xe run tank (acting as a gas piston), are filled to 82 atm to ensure sonic flow across all mass flow control venturies. The catch tanks are vented to roughly atmospheric pressure and are kept near  $\text{LN}_2$  temperature.

Just prior to a run all valves are in a closed position except HV7 and XV28. When the system is triggered, a timer-based control panel commands valves HV9, HV10, HV14, and XV25 to their open positions. The EHA is simultaneously commanded to the first of two positions. The first position corresponds to pure He flow prior to the arrival of Xe at the EHA. After a preset time delay, the EHA is commanded to its final "Xe-He" position. A second timer on the control panel triggers the PAR laser after the flow has attained a steady state. After the He gas from sonic HS1 has pushed all Xe into the catch tanks from the Xe run tank and the SBS cell, all remote valves are commanded closed and the run is complete.

Typical pressure histories for the Xe run tank, the SBS cell, and the catch tanks are shown in Figure 4.3-9. This particular run corresponds to a Xe-He flow at 7.3 m/s and 40 atm cell pressure. Transients are observed to occur at  $t = 0$  when the fire valves open and again at  $t = 1.4\ \text{s}$  when Xe arrives at the EHA cell pressure control valve. The sharp pressure drop starting at  $t = 5.8\ \text{s}$  corresponds to the arrival at the EHA of He gas used to push Xe from the run tank. Helium is flowed through the Xe run tank and SBS cell until shutdown at  $t = 9.3\ \text{s}$  to ensure that all Xe is flushed into the catch tanks.

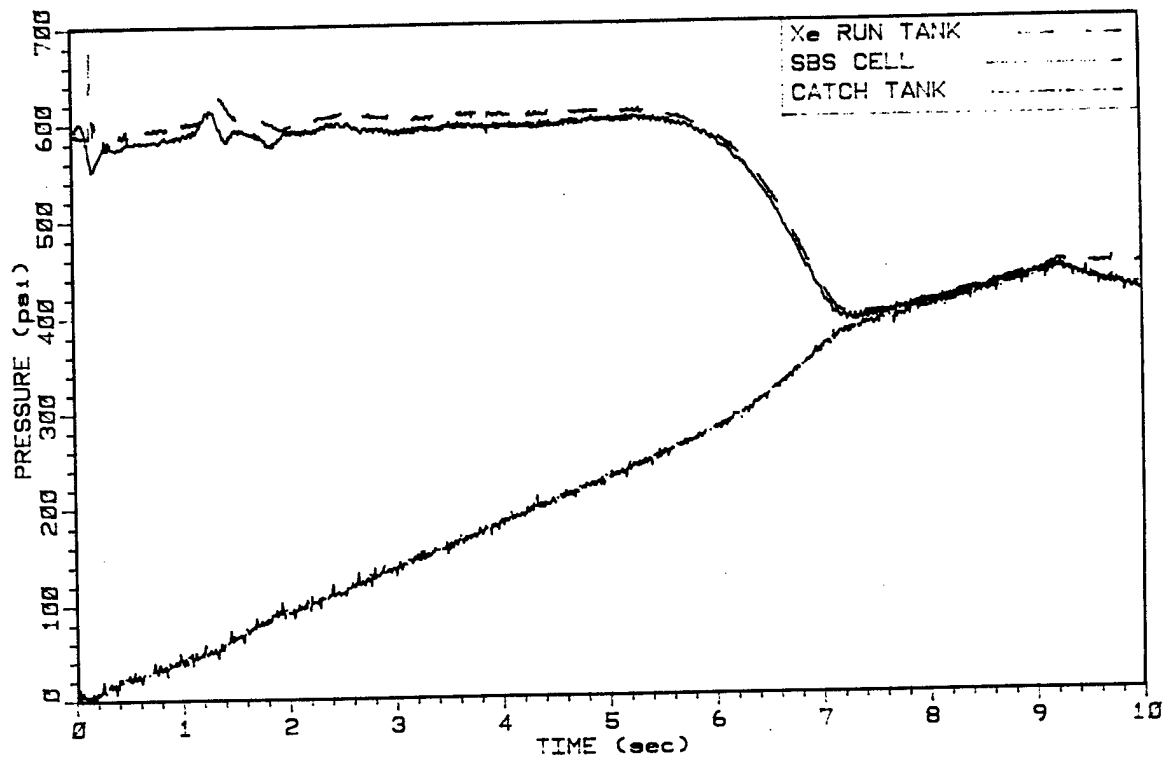


Figure 4.3-9. Typical Pressure Histories for Key Flow Control Components

The flow system has been calibrated to allow operation over the design range of SBS cell flow velocities and pressures. The calibration includes valve timings, mass flow controlling sonics, and EHA position. The most critical calibration is of the EHA valve, used for cell pressure control. Shown in Figure 4.3-10 is the flowrate calibration curve obtained for one of two available EHA valve pintles, and represents the key to controlling SBS cell pressure.

After all gas is collected at the conclusion of test, the Xe gas is allowed to freeze on the LN<sub>2</sub> tubes located within the catch tanks. The He gas is then vented to the atmosphere, and a vacuum is pulled on the catch tanks to remove all He. The catch tanks hold up to six runs of Xe. In preparation for the next test, all other tanks are filled to their appropriate pressures in parallel with the catch tank operation. The turnaround time from test to test is approximately 1 h, yielding a practical maximum of six runs per day. Xenon is recovered at the end of the day and pumped back into high-pressure K-bottles for future use.

#### 4.3.3.3 SBS Cell

Flowing-gas tests were performed on the SBS cell prior to the phase conjugation tests to check the behavior of the wake and to scrutinize the performance of the 0.05- $\mu$ m particulate filters. Early in the checkout phase the PAR laser was used to test for particulate breakdown by flowing pure He. No breakdown was observed in these tests for pulse energies as high as 2 J, a pulse width of 0.85  $\mu$ s (FWHM), and an f-number of 30.

Initial shadowgraph tests of the Xe-He wake indicated that unacceptably large index variations were present in the Xe freestream. The possibility of thermal variations was eliminated by flowing pure Xe and by varying the temperature of the gas relative to the SBS cell wall temperature, thus leaving He contamination as the source of the index variations.

One candidate considered as the source of the contamination was the inadequate flushing of He by the Xe in upstream sections of the SBS cell. However, tests performed with a Xe prefill of the SBS cell instead of the usual He prefill yielded the same behavior.



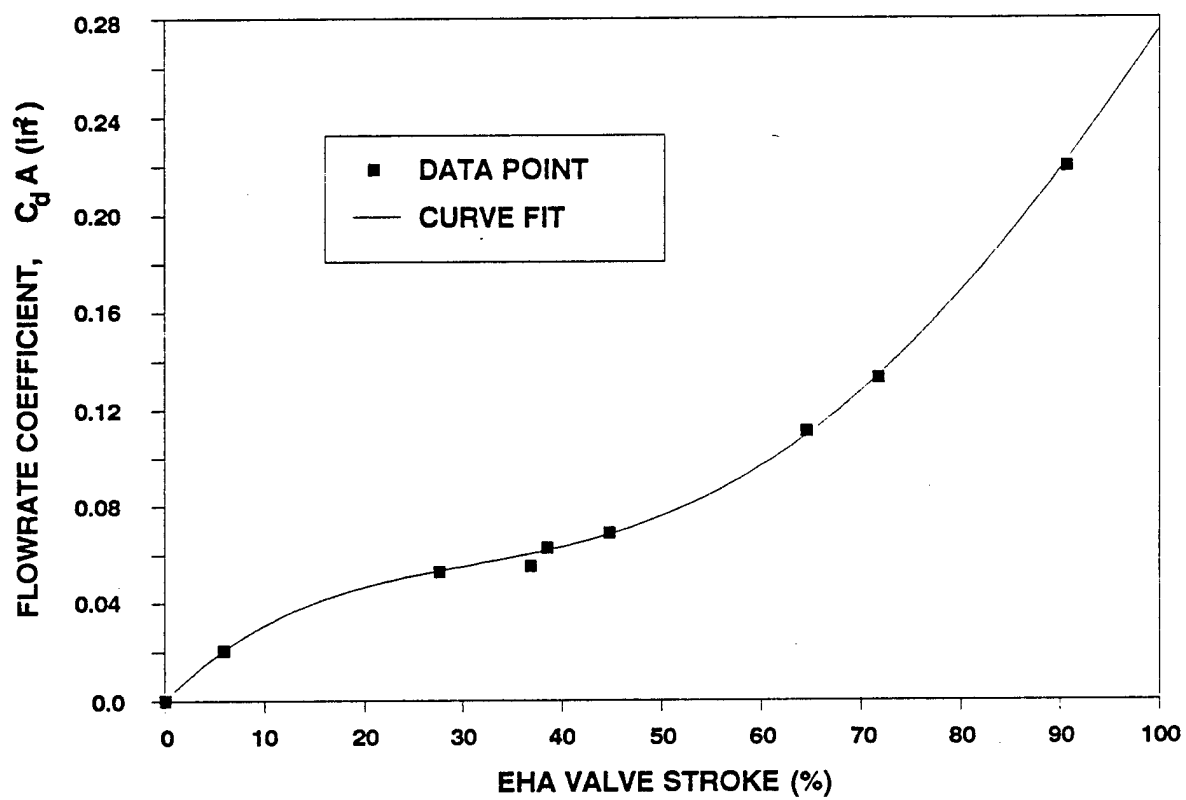


Figure 4.3-10. EHA Calibration for SBS Cell Pressure Control

Flow oscillations induced by unsteady behavior downstream of the conjugating region, a problem encountered in the subscale flowing-gas experiments but not expected in the present design, were considered next as a possible source. Small, stainless-steel springs were added to the lower section of the diffuser to ensure adequate mixing of the Xe and He and to attenuate oscillations that could possibly occur between the cell and the EHA valve. Although there seemed to be some improvement, the flow was not satisfactory.

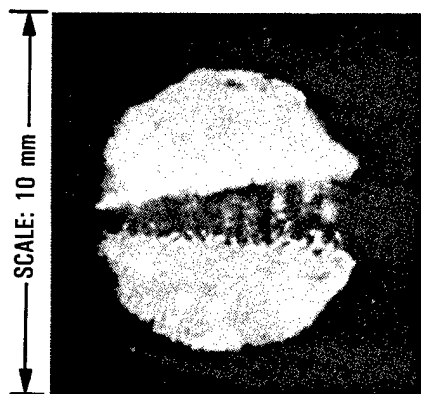
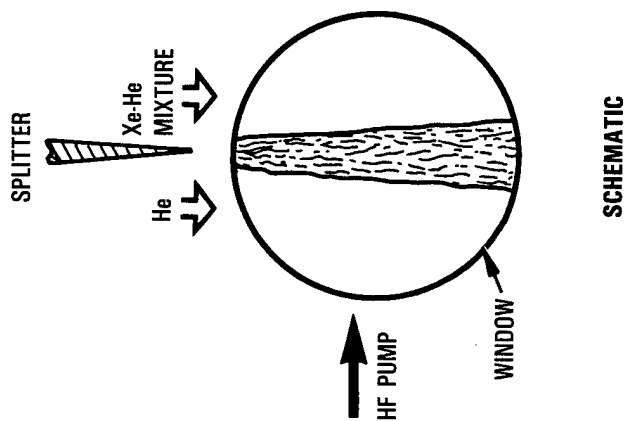
A major contributor to the adverse flow behavior was identified to be check valves in the He channel feed lines that chattered. The valves were removed, and the Xe freestream exhibited a significant improvement. However, index fluctuations were still evident in the freestream.

The character of the index variations is illustrated in the spark shadowgraphs in Figure 4.3-11. The shadowgraphs were taken while examining the effect of density ratio on the overall flow behavior. Shadowgraphs are presented for density ratios of 2.4 and 10 obtained by mixing He with Xe in the run tank. The index variations mentioned are evident in the flow corresponding to the higher density ratio, suggesting that buoyancy effects may be present. Note, however, that the sensitivity of the shadowgraph for the lower density ratio is correspondingly lower than for the higher density ratio flow.

Despite the index variations evident in the shadowgraphs, attempts were made to phase conjugate in the flowing-gas SBS cell. These experiments are described below in Section 4.3.4.

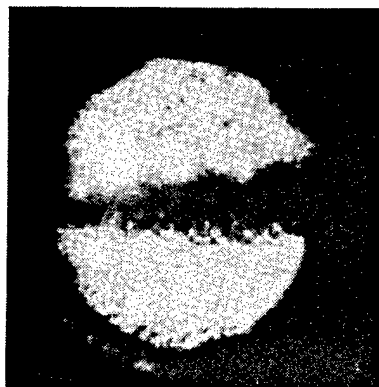
#### 4.3.4 Preliminary SBS Experiments

Preliminary phase conjugation experiments using the flowing-gas SBS cell were performed near the conclusion of the APACHE program. These experiments included static Xe SBS tests to provide baseline data, tests with flowing Xe only to validate the thermal homogeneity of the Xe, and flowing Xe-He tests.



DENSITY RATIO = 2.4

40 atm PRESSURE  
7.2 m/s VELOCITIES



DENSITY RATIO = 10.0

Figure 4.3-11. SBS Cell Flow Behavior (shadowgraphs)

#### 4.3.4.1 Static-Xenon Results

Static Xe tests were conducted using the flowing cell and the PAR laser to provide baseline data for subsequent flowing-gas SBS experiments. The flowing cell was simply filled with Xe to 40 atm pressure and allowed to thermally equilibrate for a minimum of 2 h. The depth of the conjugating region, from window to window, was tens of Rayleigh ranges.

Typical power-time histories for the pump and Stokes beams are shown in the upper and lower traces, respectively, in Figure 4.3-12. The pump energy measured for this particular test was 1.9 J, and the return energy was approximately 1.5 J. The FWHM of the incident pulse was measured to be 0.88  $\mu$ s for a flashlamp voltage of 40 kV and a laser gas pressure of 460 torr. This width is noticeably larger than the original PAR pulse width of 0.5  $\mu$ s obtained at 50 kV and 580 torr.

Preliminary reflectivity data were obtained for various pump energies up to a maximum of 2.1 J, roughly twice as high as that achieved in earlier tests using the original PAR laser. The minimal scatter observed in the data is attributed to better pointing precision at the spatial filter. More data are needed at the moderate and high energy levels to ascertain the asymptotic slope and intercept. Using data points for pump energies less than 1 J, as in previous APACHE SBS experiments, the intercept occurs at or slightly above 0.3 J. Although the SBS telescope alignment was found to introduce less than a tenth wave peak-to-valley aberration, the combined optical quality of the remaining optics and their possible effect on threshold were not characterized for this experiment. These data should be considered primarily as a reference for flowing-gas tests performed under the same conditions.

#### 4.3.4.2 Flowing-Gas SBS Results

Flowing-gas SBS tests were conducted first using Xe only to ensure that thermal control of the flowing Xe was satisfactory. This was accomplished by prefilling the SBS cell with pure Xe and disconnecting the control signals to the He channel feed valves. Therefore, a strong velocity shear layer existed between Xe in the center conjugating channel and stagnant Xe in the two He channels and window cavities.

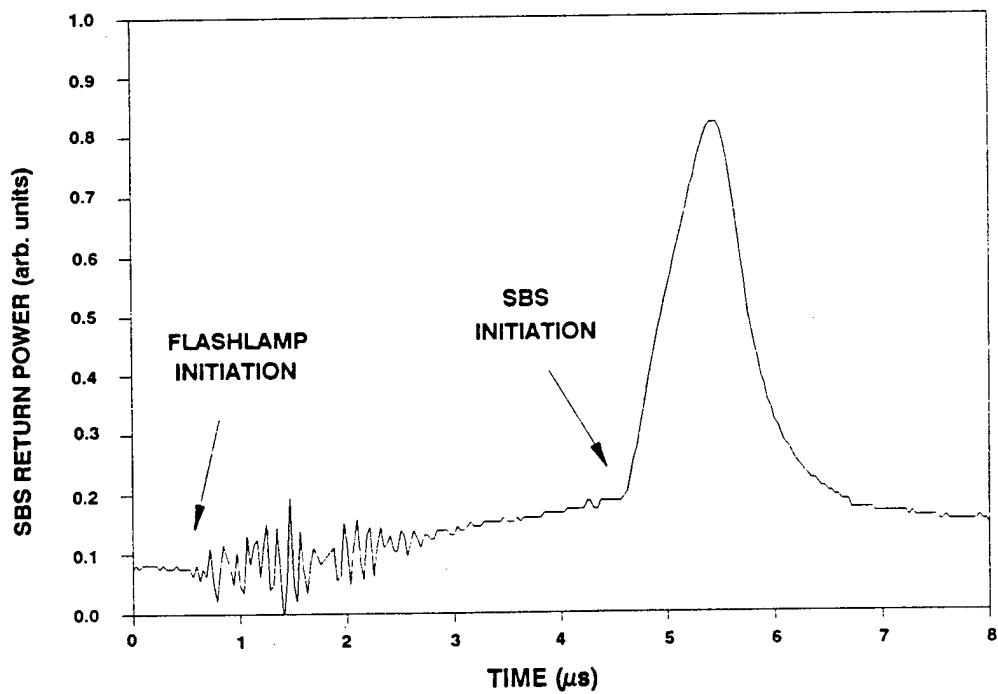
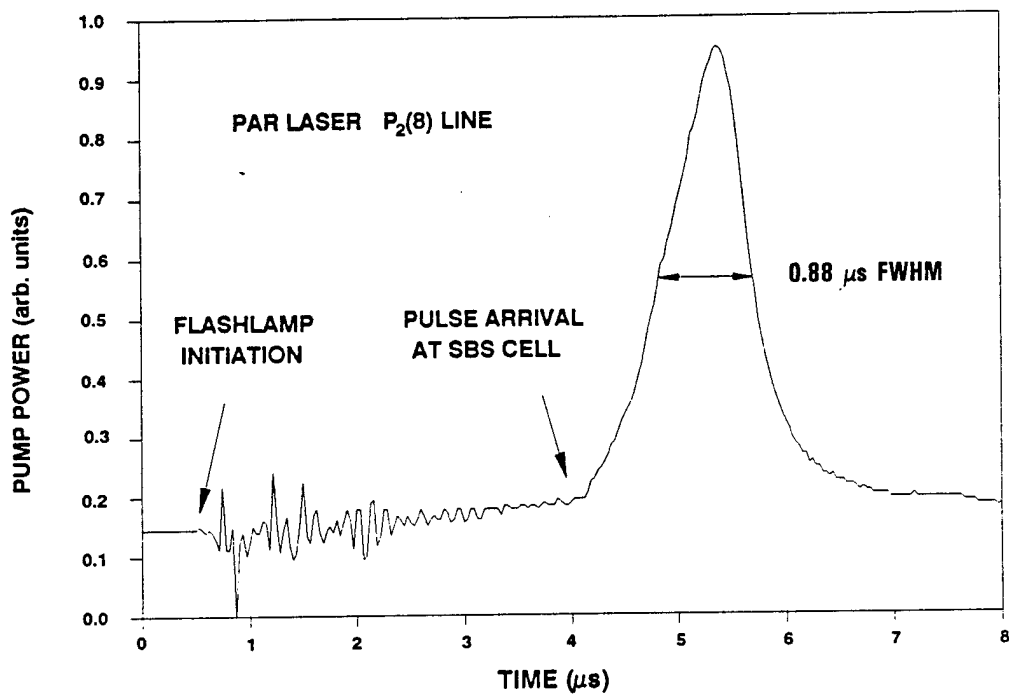


Figure 4.3-12. Temporal Behavior of Pump and Stokes Pulses

Despite a thin thermal shear layer evident on shadowgraphs, SBS reflectivity for the pure Xe flow was approximately equal to that obtained in the static SBS experiments, as shown in Figure 4.3-13. Note that breakdown was not observed in either the static or flowing Xe SBS tests.

Flowing-gas SBS tests conducted using Xe in the center channel and He in the two outer channels, however, yielded no calibrated returns. Although a weak return was observed on both a calorimeter and a  $p(t)$  transducer for one flow test, the signal-to-noise was too low to be considered a viable data point. Several other tests performed under the same conditions produced no return energy, suggesting that the freestream index variations discussed in Section 4.3.3.3 must be reduced further.

A high probability of breakdown was also observed during the flowing Xe-He experiments. Two possible sources of the breakdown include particulates in the He channels that are convected into Xe channel (this convection is also responsible for the observed index variations in the Xe channel), and local "hot spots" produced by flow-induced aberrations. In either case, it is recommended that efforts focus on eliminating the He contamination in the Xe channel.

It is further recommended that future flowing-gas SBS tests, conducted under the APEX program, be performed with the SBS cell oriented in a horizontal position rather than in its present vertical position to eliminate buoyancy effects as a possible source of the index variations.

#### 4.3.5 Summary

Status of the full-scale flowing SBS cell experiments conducted on the APACHE program is summarized below:

1. The full-scale flowing-cell hardware has been successfully integrated into the APACHE HF phase-conjugation test facility at the TRW Capistrano Test Site and is fully operational.
2. An upgrade to the original Pacific Applied Research (PAR) pulsed HF lasers has been completed under TRW capital funds. The primary motivation for this work was to provide additional margin in terms of the amount of energy supplied to the SBS cell relative to the SBS threshold. The system now delivers approximately ten times the energy required for a diffraction-limited beam to exceed the SBS threshold.

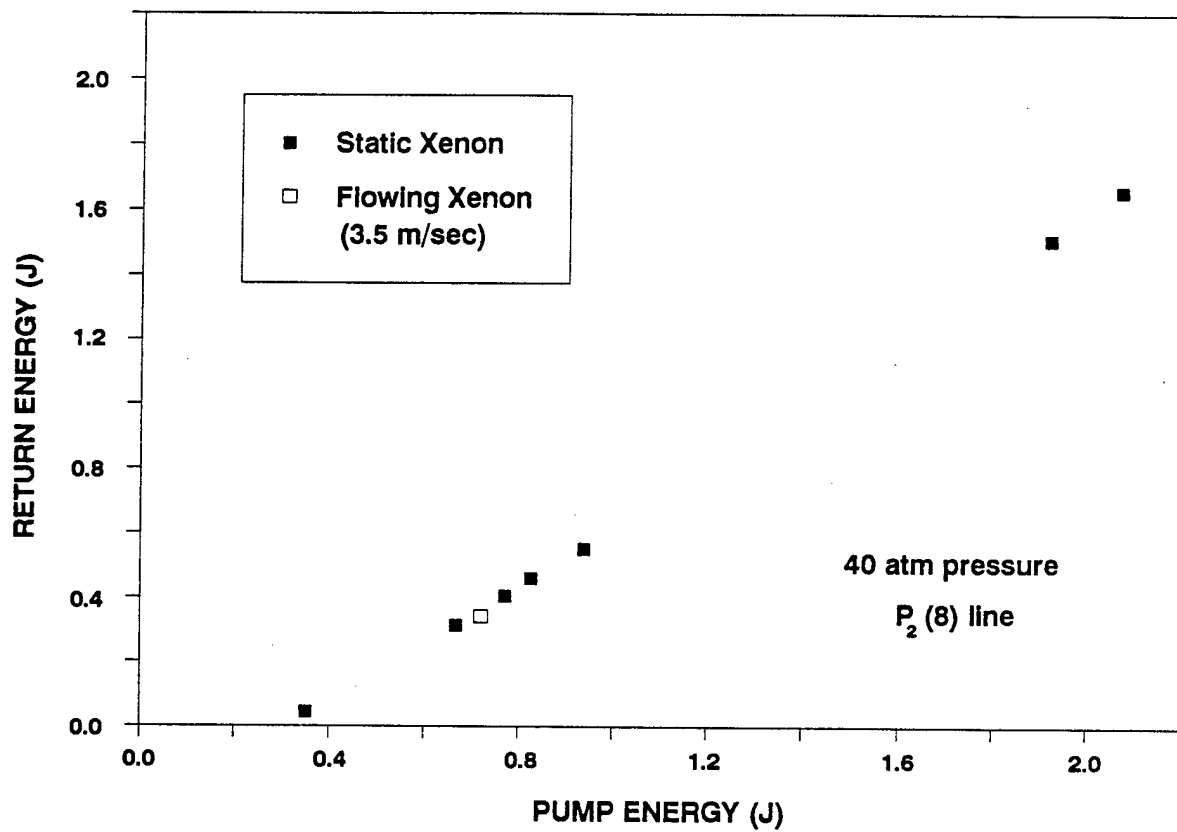


Figure 4.3-13. SBS Reflectivity Behavior for Static and Flowing Xe

3. Preliminary SBS data have been obtained in a flowing-gas medium. Data obtained with flowing Xe alone showed results nearly identical to that of static Xe, indicating that the fluid mechanical requirements for thermal uniformity in the Xe were achieved. A limited amount of data with both Xe and He flowing showed problems with He entrainment into the Xe, which suppressed the SBS process. This problem is presently being remedied as part of the APEX program, and additional testing is planned to be conducted under APEX.



#### 4.4 THEORETICAL SUPPORT

This section describes the derivation of the power spectral density of the phase, as used in the BRIWON code, from an empirical index-of-refraction spectrum describing turbulent refractive-index inhomogeneities in the Xe-He interface of an aerowindow in the SBS cell. The results of applying the code to the prediction of turbulence effects on the SBS process in both single-cell and multicell configurations are reported.

##### 4.4.1 Turbulence Model for BRIWON SBS Code

A two-dimensional geometry is assumed in which the  $z$  direction is the direction of propagation of a field incident on the turbulent layer, and the  $x$  direction is the flow direction of the gas stream. The change in phase on passing through the layer is

$$\phi(x) = k_0 \int_{-\Delta z/2}^{\Delta z/2} \Delta n(x, z') dz' \quad (4.4-1)$$

where  $\Delta z$  is the thickness of the turbulent layer and  $\Delta n$  is the deviation from the mean of the index of refraction;  $k_0$  is the free-space wave number,  $2\pi/\lambda$ . The autocovariance function of the phase is

$$\begin{aligned} B_\phi(\xi) &= \langle \phi(x) \phi(x+\xi) \rangle \\ &= k_0^2 \Delta z \int_{-\Delta z}^{\Delta z} (1 - |z'|/\Delta z) B_n(\xi, z') dz' \end{aligned} \quad (4.4-2)$$

where  $B_n(\xi, z)$  is the two-dimensional autocovariance function of the index of refraction; see Papoulis (Reference 4-2) for the transformation of the double integral.

The measured one-dimensional power spectral density of the index of refraction for shear flows is of the form (Batt, Reference 4-3; Taylor, Reference 4-4)

$$S_n(k) = \frac{C_0}{1 + L^2 k^2} \quad (4.4-3)$$

where  $C_0 = (\Delta n^2)L/\pi$ ,  $L$  = the correlation length, and  $(\Delta n^2)$  is the mean-square deviation from the mean of the index of refraction across the thickness of the layer. The corresponding one-dimensional autocovariance function is its Fourier Transform

$$B_n(\xi) = \int_{-\infty}^{\infty} e^{iK\xi} S_n(K) dK \quad (4.4-4)$$

$$(4.4-4)$$

$$= \frac{\pi C_0}{L} e^{-|\xi|L}$$

One choice for a two-dimensional autocovariance function  $B_n(\xi, \eta)$  which is symmetric in  $\xi$  and  $\eta$  and which has the above form for  $\eta = 0$  is

$$B_n(\xi, \eta) = \frac{\pi C_0}{L} \exp\{-(\xi^2 + \eta^2)^{1/2}/L\}. \quad (4.4-5)$$

(Alternative forms have been suggested by Litvak, Reference 4-5.)

Substituting this expression into the integral for the phase autocovariance function and taking its Fourier transform gives the phase PSD:

$$S_\phi(K) = 4k_0^2 C_0 \frac{L^2}{A^4} \left[ \beta K_1(\beta) - 1 + \frac{\beta}{2} \int_0^\beta K_0(u) du \right] \quad (4.4-6)$$

where

$$A = (1 + K^2 L^2)^{1/2} \quad (4.4-7)$$

and

$$\beta = A\Delta z/L \quad (4.4-8)$$

and  $K_0$  and  $K_1$  are modified Bessel functions of order 0 and 1. The limiting form for large  $\beta$  may be shown to be

$$S_{\phi}(K) = 4k_0^2 C_0 \frac{L^2}{A^4} \left( \frac{\pi}{4} \beta \right)$$

(4.4-9)

$$= \frac{k_0^2 \Delta z L^2 \Delta n'^2}{(1 + K^2 L^2)^{3/2}}$$

The general form of the phase PSD (Equation 4.4-6) is used in the BRIWON code to generate, by standard harmonic synthesis methods (Knepp, Reference 4-6), a realization of the normally distributed random phase across the SBS cell. The phase aberration is applied as a phase screen to the pump and Stokes fields at any location within the cell; up to two such screens may be used within the cell. In the case of turbulence due to flow in an aerowindow the screen locations are necessarily at the front and back boundaries of the SBS cell.

#### 4.4.2 Computational Results and Discussion

The turbulence model in the BRIWON code has been exercised to provide a limited parametric study of the effects on the SBS process of cell geometry and medium-flow characteristics. The results to date are reported in Tables 4.4-1 through 4.4-7. For all cases, the wavelength was 2.8  $\mu\text{m}$ , the f number was 30, the medium 40 atm Xe, and the pump power 500 kW (~6 times the unaberrated threshold power) except in Table 4.4-2 for which the pump power is 250 kW. The value of  $(\Delta n'^2)^{1/2}$  was set at 0.1  $\Delta n$ , where  $\Delta n$  is the mean index difference between Xe and He, and the ratio of autocorrelation length, L, to layer thickness,  $\Delta z$ , was fixed at 0.27 (Taylor, Reference 4-4). The "cell length" in the tables refers to the distance from the focal plane to the front of the cell, expressed in units of the Rayleigh Range,  $2\lambda f^2$  number. In all cases the back of the cell is an equal distance from the focal plane.

Table 4.4-1 shows the reflectivity, conjugation fidelity, threshold power, and the beam quality of both the Stokes return and the transmitted pump for either different cell lengths, turbulent layer thicknesses  $\Delta z$ , or realizations of the random phase (different realizations are identified by

Table 4.4-1. SBS Reflectivity and BQ Dependence on Random Phase Aberration Realizations, Cell Length, and Interface Thickness

Seed	Run #	dz (cm)	Cell Length ( X RR )	Reflectivity	CF	Threshold (KW)	BQ (Stokes)	BQ (Trans. Pump)
(a)	761	0.20	3	0.679	0.885	161	1.019 / 1.003	1.83 / 1.10
(b)	762	0.20	3	0.667	0.777	166	1.049 / 1.028	1.38 / 1.09
(c)	763	0.20	3	0.808	0.917	97	1.003 / 0.995	1.94 / 1.39
(d)	764	0.20	3	0.730	0.878	135	1.000 / 1.000	1.31 / 1.14
(e)	765	0.20	3	0.779	0.878	110	1.027 / 0.993	1.15 / 1.12
(f)	766	0.20	3	0.705	0.817	147	1.034 / 1.034	1.73 / 1.43
(g)	767	0.20	3	0.736	0.709	132	1.049 / 1.026	1.40 / 1.29
Mean:				0.729	0.837	135	1.026 / 1.011	1.53 / 1.22
Std. Dev.:				0.05	0.07	25	0.02 / 0.02	0.30 / 0.14
(f)	780	0.20	0.5	0.642	0.702	179	0.974 / 0.973	1.06 / 1.05
(f)	781	0.20	0.75	0.727	0.786	136	0.978 / 0.973	1.11 / 1.06
(f)	769	0.20	1	0.754	0.840	124	0.989 / 0.975	1.17 / 1.08
(f)	770	0.20	6	0.650	0.901	175	1.021 / 1.016	1.49 / 1.43
(f)	772	0.40	1	0.746	0.832	126	0.989 / 0.975	1.19 / 1.08
(f)	771	0.40	3	0.704	0.811	148	1.037 / 1.037	2.17 / 1.41
(f)	773	0.40	6	0.609	0.494	196	1.113 / 1.112	1.87 / 1.79
(f)	776	0.05	1	0.763	0.843	119	0.987 / 0.975	1.11 / 1.07
(f)	775	0.05	3	0.729	0.824	135	1.033 / 1.015	1.41 / 1.31
(f)	777	0.05	6	0.749	0.914	126	1.018 / 1.011	1.39 / 1.32
-	783	-	0.50	0.656	0.844	172	0.975 / 0.973	1.05 / 1.03
-	782	-	0.75	0.739	0.850	131	0.976 / 0.973	1.06 / 1.03
-	758	-	1	0.771	0.846	114	0.981 / 0.975	1.08 / 1.03
-	779	-	3	0.828	0.875	86	0.995 / 0.979	1.11 / 1.06
-	778	-	6	0.832	0.884	84	1.009 / 1.009	1.09 / 1.06

Table 4.4-2. SBS Reflectivity and BQ Behavior for Random Phase-Aberration Realizations,  $\Delta z = 0.05$  cm, Cell Length, = 3 RR (interface to focus)

Seed	Run #	dz (cm)	Cell Length ( X RR )	Reflectivity	CF	Threshold (KW)	BQ (Stokes)	BQ (Trans. Pump)
(a)	784	0.05	3	0.746	0.895	127	1.016 / 1.000	1.49 / 1.16
(b)	785	0.05	3	0.766	0.807	117	1.029 / 0.997	1.20 / 1.06
(c)	786	0.05	3	0.810	0.913	95	1.002 / 0.993	1.12 / 1.10
(d)	787	0.05	3	0.773	0.873	112	0.996 / 0.996	1.23 / 1.16
(e)	788	0.05	3	0.805	0.877	98	1.015 / 0.988	1.17 / 1.10
(f)	775	0.05	3	0.729	0.824	135	1.033 / 1.015	1.41 / 1.31
(g)	789	0.05	3	0.782	0.845	109	1.014 / 1.002	1.20 / 1.12
(h)	790	0.05	3	0.798	0.833	101	1.015 / 0.986	1.21 / 1.06
(i)	791	0.05	3	0.691	0.753	155	1.073 / 1.038	1.46 / 1.34
(j)	792	0.05	3	0.759	0.890	120	1.009 / 1.001	1.26 / 1.19
Mean:				0.766	0.851	117	1.020 / 1.002	1.28 / 1.16
Std. Dev.:				0.04	0.05	18	0.02 / 0.015	0.13 / 0.10

different letters in Column 1). The second of each pair of beam quality numbers is the value when corrected for tilt and focus. Threshold power is defined as the power of the pump beam transmitted through the back of the cell, so there will be a slight variation of these numbers with input power.

The first seven cases listed in Table 4.4-1 are identical except for the realization of the random phase. Following these are the mean and standard deviation of the computed values, averaged over the seven realizations. Next in the table is a set of 10 cases, all with the same phase realizations, but with varying cell lengths and layer thicknesses. The next group of five cases is included for comparison purposes and shows the dependence of the SBS results on cell length when there is no turbulence.

Tables 4.4-2 and 4.4-3 summarize the results for 10 different realizations of phase aberration. The cell length is fixed at 3 Rayleigh ranges and the layer thickness is fixed at 0.05 cm in Table 4.4-2 and at 0.40 cm in Table 4.4-3. The results in Tables 4.4-1 through 4.4-3 suggest a fairly weak dependence on the thickness of the turbulent layer (for thicknesses  $\geq 0.05$  cm) and that, if some turbulence exists, an optimum choice of cell length might be  $\geq 1$  Rayleigh range. A shorter cell length provides inadequate interaction length for the phase conjugate field to develop fully, while for longer cell lengths the beam diameter at the turbulent interface is of sufficient size to include many correlation lengths of the refractive index resulting in a poorly focused beam.

Threshold powers for the same ten realizations and two layer thicknesses are listed in Table 4.4-4 along with the values of the RMS phase over the beam, with the mean tilt removed, and with both mean tilt and focus removed (labeled Phase 1 and Phase 2, respectively). The correlation of threshold with RMS phase variation (of either type) is rather weak, with a considerable spread in threshold values sometimes occurring for nearly equal values of phase.

Table 4.4-3. SBS Reflectivity and BQ Behavior for Random Phase-Aberration Realizations,  $\Delta z = 0.40$  cm, Cell Length = 3 RR

Seed	Run #	dz (cm)	Cell Length ( X RR )	Reflectivity	CF	Threshold (KW)	BQ (Stokes)	BQ (Trans. Pump)
(a)	793	0.40	3	0.669	0.883	165	1.020 / 1.003	1.65 / 1.11
(b)	794	0.40	3	0.703	0.749	149	1.060 / 1.045	1.37 / 1.10
(c)	795	0.40	3	0.808	0.917	96	1.003 / 0.995	1.99 / 1.39
(d)	796	0.40	3	0.724	0.878	138	1.001 / 1.001	1.29 / 1.14
(e)	797	0.40	3	0.779	0.878	110	1.028 / 0.994	1.22 / 1.13
(f)	771	0.40	3	0.704	0.811	148	1.037 / 1.037	2.17 / 1.41
(g)	798	0.40	3	0.698	0.562	151	1.093 / 1.049	1.54 / 1.54
(h)	799	0.40	3	0.796	0.872	102	1.017 / 0.990	3.28 / 1.82
(i)	800	0.40	3	0.656	0.740	172	1.072 / 1.050	1.66 / 1.56
(j)	801	0.40	3	0.719	0.902	141	1.007 / 1.001	1.39 / 1.20
Mean:				0.726	0.819	137	1.034 / 1.017	1.76 / 1.34
Std. Dev.:				0.05	0.11	26	0.03 / 0.025	0.61 / 0.25

Table 4.4-4. Phase Aberration Magnitudes at Interface for  
Random Realizations,  $\Delta z = 0.05$  and  $0.40$  cm,  
Cell Length = 3 RR

Seed	..... $dz = 0.05$ .....			..... $dz = 0.40$ .....		
	Phase1 (waves)	Phase2 (waves)	Threshold (KW)	Phase1 (waves)	Phase2 (waves)	Threshold (KW)
(a)	0.173	0.076	127	0.298	0.082	165
(b)	0.104	0.071	117	0.153	0.083	149
(c)	0.086	0.084	95	0.098	0.092	96
(d)	0.111	0.071	112	0.170	0.082	138
(e)	0.061	0.049	98	0.087	0.050	110
(f)		0.096	135		0.113	148
(g)	0.096	0.095	109	0.120	0.114	151
(h)	0.068	0.059	101	0.064	0.062	102
(i)	0.128	0.121	155	0.170	0.146	172
(j)	0.114	0.098	120	0.166	0.109	141
Mean:	0.105	0.082	115	0.147	0.093	136
Std Dev:	0.03	.02	18	0.07	.03	27

Phase1 = rms phase over beam with tilt removed

Phase2 = rms phase over beam with tilt and focus removed



The results of initial modeling of the effects of turbulence on the multiple-foci method of threshold reduction are summarized in Table 4.4-5. Two cells were assumed, each of total length  $6(2\lambda f^2_{\#})$ , and with each turbulent interface having a thickness of 0.05 cm; the pump power for these cases was 500 kW. The first case in Table 4.4-5 is listed for reference and is the mean result for the single cell with turbulence. The remaining four cases have different combinations of realizations of the random phase at the three interfaces. The threshold power decreases by almost a factor of 2 in some cases, and the conjugation fidelity remains fairly high. Beam quality values for these cases are not available since the multicell version of BRIWON was not complete at the time of the computer runs.

The study was then extended to three cells and to thinner turbulent layer thicknesses, with results as shown in Table 4.4-6. For the thinnest layer considered,  $\Delta z = dz = 0.01$  cm, the threshold value for three cells drops to a value approximately one-half that of a single cell with no turbulence. As the layer thickness goes to zero the effects of turbulence diminish, of course, but not in a simple way. Since the correlation length of the index of refraction variations decreases in proportion to the layer thickness, the spectrum of the phase decreases as  $(dz)^3$  for low frequencies, but less rapidly at higher frequencies. Thus, the phase PSD will emphasize higher spatial frequencies as the layer gets thinner. The variance of the phase, given by the integral over all frequencies of the phase spectrum, or, equivalently, by the phase autocovariance function  $B_{\phi}(\xi)$  at  $\xi = 0$ , may be shown, using Equations 4.4-2 and 4.4-5, to be proportional to the square of the layer thickness. However, the RMS phase, proportional to  $\Delta z$ , is not by itself an adequate measure of the dependence on layer thickness of the SBS process since it cannot characterize the shift in the spectrum toward higher frequencies (with decreasing layer thickness) and the consequent tendency toward larger-angle, and less effectively conjugated, scattering in the cell.

Table 4.4-5. Two-Foci Threshold Reduction,  $\Delta z = 0.05$  cm, Cell Length = 3 RR

Run No.	dz	Seed at Interface			Ref1	CF	Threshold (kW)	BQ (Stokes)	
784-792	0.05	-	-	-	0.766	0.851	117	NA	One-cell mean results
806	0.05	(j)	(c)	(b)	0.838	0.930	81	NA	
807	0.05	(a)	(h)	(d)	0.803	0.916	98	NA	
808	0.05	(e)	(f)	(g)	0.864	0.914	68	NA	
809	0.05	(f)	(g)	(e)	0.815	0.926	92	NA	

Interface: (1) - At front of Cell 1  
 (2) - At back of Cell 1  
 (3) - At front to Cell 2

Table 4.4-6. Three-Foci Threshold Reduction,  
 $\Delta z = 0, 0.01, \text{ and } 0.05 \text{ cm}; 3 \text{ RR}$

# of Cells	Run #	dz	Seed At Interface					Refl	CF	Threshold (KW)	BQ (Stokes)
			(1)	(2)	(3)	(4)	(5)				
1	779	0	-	-	-	-	-	0.828	0.875	86	0.995/0.979
2	805	0	-	-	-	-	-	0.895	0.929	51	NA
3	882	0	-	-	-	-	-	0.920	0.957	40	0.982/0.980
1	784	0.05	(a)	-	-	-	-	0.746	0.895	127	1.016/1.000
2	807	0.05	(a)	(h)	(d)	-	-	0.803	0.916	98	NA
3	816	0.05	(a)	(h)	(d)	(f)	(g)	0.854	0.936	73	1.003/0.999
1	792	0.05	(j)	-	-	-	-	0.759	0.890	120	1.009/1.001
2	806	0.05	(j)	(c)	(b)	-	-	0.838	0.930	81	NA
3	815	0.05	(j)	(c)	(b)	(a)	(h)	0.876	0.937	62	0.998/0.998
1	818	0.01	(j)	-	-	-	-	0.813	0.871	93	1.002/0.988
2	819	0.01	(j)	(c)	(b)	-	-	0.884	0.924	58	0.991/0.991
3	820	0.01	(j)	(c)	(b)	(a)	(h)	0.908	0.944	46	0.988/0.986

Interface: (1) - At front of Cell 1  
 (2) - At back of cell 1  
 (3) - At front of Cell 2  
 (4) - At back of Cell 2  
 (5) - At front of Cell 3

The effect of grating convection on the SBS process in the two-cell configuration is suggested by the results shown in Table 4.4-7, in which flow velocities from 0 to 10 m/s and turbulent layer thicknesses of 0.0 and 0.01 cm were considered. For these runs, the input pump power was 250 kW, whereas the results in the preceding tables were for a power of 500 kW. Thus, the values of reflectivity and conjugation fidelity for the unaberrated case are somewhat lower than their values in Table 4.4-5; the threshold power is also lower because of its definition (in this report) as the power transmitted through the back of the cell. Two values of conjugation fidelity are shown; the first is for the Stokes field at the focusing lens; the second is calculated with the flow-induced tilt removed. The latter is reported in the second from last column and is in units of  $2\lambda/D$ . The effect of the turbulent interfaces on the flow-induced tilt is small, amounting to an approximately constant increase of 0.02 of the diffraction-limited spot angle (at least for the single combination of phase realizations considered). As in the other tables in this report, the second beam quality number is its value with both near-field tilt and focus removed.

Table 4.4-7. Two-Foci Threshold Reduction With Turbulence and Grating Correction

Run #	Flow Vel. (m/s)	dz	Seed At Interface			Refl	CF	Threshold (KW)	Stokes Tilt (X DL Spot Size)	BQ (Stokes)
(1)	(2)	(3)	(1)	(2)	(3)					
827	0	0	-	-	-	0.814	0.906	46	0	0.985/0.979
828	2	0	-	-	-	0.813	0.903/0.906	47	0.016	0.985/0.979
829	4	0	-	-	-	0.811	0.891/0.905	47	0.042	0.985/0.979
830	6	0	-	-	-	0.809	0.872/0.902	48	0.063	0.984/0.979
831	8	0	-	-	-	0.804	0.845/0.899	49	0.085	0.984/0.979
832	10	0	-	-	-	0.801	0.810/0.892	50	0.112	0.983/0.979
834	2	0.01	(j)	(c)	(b)	0.789	0.889/0.894	53	0.034	0.996/0.995
836	4	0.01	(j)	(c)	(b)	0.786	0.875/0.892	54	0.061	0.996/0.994
837	6	0.01	(j)	(c)	(b)	0.783	0.849/0.892	55	0.080	0.996/0.994
838	8	0.01	(j)	(c)	(b)	0.775	0.813/0.886	56	0.109	0.997/0.990
839	10	0.01	(j)	(c)	(b)	0.770	0.765/0.879	58	0.135	0.998/0.991

Interface: (1) - At front of Cell 1  
(2) - At back of cell 1  
(3) - At front of Cell 2

#### 4.5 REFERENCES

- 4-1. Prabhu, A, and Narasima, R. (1972). "Turbulent non-equilibrium wakes." J. Fluid Mech., Vol. 54, pp. 19-38.
- 4-2. Papoulis, A., Probability, Random Variables, and Stochastic Processes. McGraw-Hill, New York, 1965.
- 4-3. Batt, R.G., "Turbulent Mixing of Passive and Chemically Reacting Species in a Low-Speed Shear Layer," J. Fluid Mech., 82, Part 1, 53-95, 1977.
- 4-4. Taylor, S., "Relevance of PSD Used in BRIWON to Model Turbulent Index Variations," TRW IOC AP-1556, 31 May 1988.
- 4-5. Litvak, M., "Laser Scatter from Xe-He Interface," TRW IOC AP-1554, Rev. A, 28 June 1988.
- 4-6. Knepp, Dennis L., "Multiple Phase Screen Calculation of the Temporal Behavior of Stochastic Waves," Proc. IEEE, 71, (6), 722-737, 1983.

## 5. ARRAY ALIGNMENT EXPERIMENT

An important issue for the SBL is the beam-quality budget allocation for SBS conjugation of the multiple beams produced by the primary mirror segmentation and by partitioning into individual amplifiers. This beam quality budget must be consistent with requirements on the number of segments and on the piston and tilt between segments. In the APACHE concept, the piston and tilt between primary mirror segments, as well as the optical path differences through the multiple amplifiers, are corrected using SBS beam combination. SBS beam combination phase locks the beams to each other and conjugates their relative piston. In the APACHE concept, beam combination is produced by overlapping the beams in the SBS interaction region (approximately three times the depth of focus centered about the focal plane). In this case, the phonon grating that is created is common to all the beams so that the Stokes output beam is the ensemble conjugate of the input beams.

### 5.1 BACKGROUND

SBS beam combination in overlapping interaction regions was first used by Basov, et al. (Reference 5-1) to correct for birefringence. Subsequently, References 5-2 through 5-6 have discussed and demonstrated the use of SBS to combine the output from several laser amplifiers. However, these papers did not quantify the alignment parameters required to obtain good piston conjugation. Basov et al. (Reference 5-2) did demonstrate that the total path length difference between two beams (piston) was limited by the SBS frequency shift. The residual piston error after conjugation,  $\delta$  (in waves), is proportional to the SBS shift in wave numbers,  $\Delta_B$  the path difference between the beams,  $\Delta L$  (in cm):

$$\delta = \Delta_B \Delta L \quad 5-1$$

Proof-of-principle experiments and analyses were performed at TRW on IRAD (References 5-7, 5-8, and 5-9), and more detailed parameterization was performed on the NOMES program (References 5-10 and 5-11) and on the RSELE program (Reference 5-12 and 5-13). These references all considered the

case of two beams and demonstrated that good piston conjugation was obtained under the following conditions:

- Piston less than both the laser coherence length and the coherence length defined by the SBS shift (Equation 5-1)
- Far-field separation up to 2.5 spot diameters with near-field separation up to 10% of beam diameter
- Near-field separation up to 3.5 beam diameters for complete overlap in the focal plane
- Beam energy ratio up to 5:1
- Polarization mismatch up to 20°.

In addition, aberrations were shown to increase the angular range for good coupling. The RSELE program (References 5-12 and 5-13) also demonstrated that the angular alignment requirement was tighter for out-of-plane misalignment than for in-plane misalignment. (Here, the plane referred to is that defined by the centers of the two near-field spots and the focal point for perfectly aligned beams.) These results are all consistent with the hypothesis that good beam coupling occurs when the overlap between the two interaction volumes is maximized.

The objective of the APACHE array alignment experiments was to demonstrate beam combination (correction of piston and tilt errors) for a large number of segments, simulating the SBL primary mirror. Specific objectives were to parameterize SBS threshold and reflectivity as a function of segment piston and tilt and as a function of the number of segments, and to determine the requirements on segment tilt for good piston conjugation. A related objective was to determine if the geometric asymmetry in alignment requirements (i.e., in-plane versus out-of-plane) observed for two beams in the RSELE experiments would be mitigated by a two-dimensional distribution of array segments. The quantitative results from these experiments have been incorporated in the APACHE systems analysis model (Volume II, Section 4) and subsequently in analysis and design of the SBL.

The following sections describe the experimental setup (Section 5.2) and results (Section 5.3), and discuss the significance of the results and suggestions for further experiments (Section 5.4).



## 5.2 ARRAY ALIGNMENT EXPERIMENT DESCRIPTION

The array alignment experiment was designed to provide high-accuracy data on multisegment beam combination by SBS while minimizing experimental complexity. In line with this philosophy, a doubled Nd:YAG laser was chosen to provide a visible source for easy alignment, and n-hexane was chosen as the SBS medium since it had been found to provide a reasonably low threshold, high reflectivity, and good conjugation fidelity at this wavelength.

The array itself was designed to provide accurate control of segment tilt, while providing only rough control of segment piston. These requirements are consistent with previous results on SBS beam combination: tilt alignment to within a few waves is necessary, while the piston requirement is determined by the shorter of the laser coherence length ( $>1$  m for this experiment) and the maximum path length difference consistent with the SBS shift ( $\sim 2.5$  cm for an  $0.5 \lambda$  piston error). The array (Figure 5-1) consisted of 19 segments, each with an f-number of 34 and giving an array f-number of 7. Each segment was mounted on three supports, consisting of one micrometer and two piezo translators. The micrometer provided coarse piston control with  $\sim 5$  waves of resolution; however, the accuracy of piston control was determined by visual alignment, with an accuracy of a few tenths of a millimeter (several hundred waves). Such large piston errors are consistent with the requirements for good SBS beam combination, and no further attempt was made to control piston. The two piezo translators provided 0.04 wave accuracy for tilt control of the segments. Segment tilt was measured using a Mach-Zehnder interferometer (Figure 5-2). The piezo translators were controlled by function generators to produce "random" shot-to-shot variations in segment tilt. Thirteen function generators were connected in a pseudo-random pattern to the 38 piezo translators. As can be seen from the interferograms showing the array alignment in Section 5.3, the segments themselves were of poor optical quality, typically having 0.5 to 1.0 wave of error (PV).

A schematic of the experimental setup is shown in Figure 5-2. The laser source was a doubled, Q-switched Nd:YAG laser producing 10 ns,  $\sim 100$  mJ pulses with linear polarization. Because the array aberrations

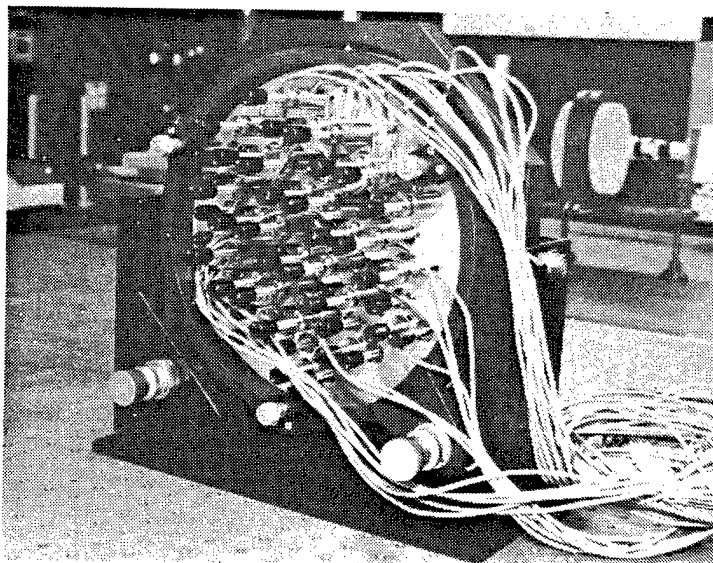
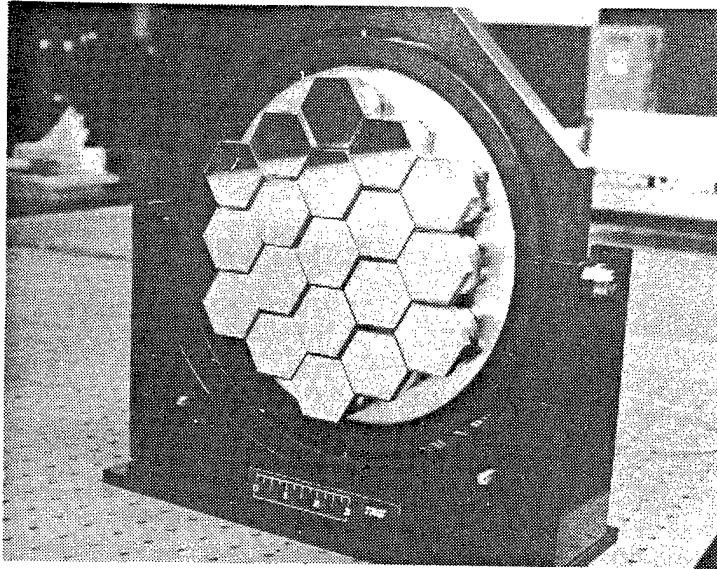


Figure 5-1. Nineteen-Element Segmented Array

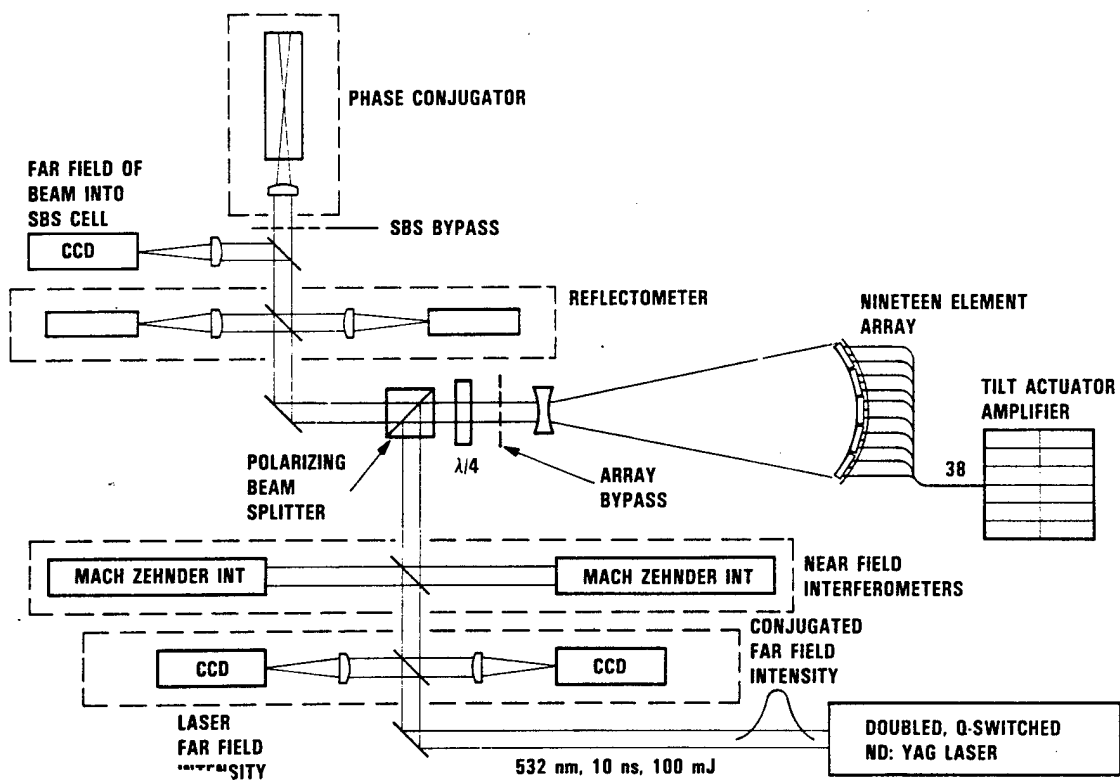


Figure 5-2. Experimental Layout

increased the SBS threshold substantially, it was decided to accept the less than ideal beam quality of the laser ( $\sim 1.3$ ) as a reference for conjugation fidelity measurements in exchange for higher power at the SBS cell, which would enable the study of more severely aberrated beams. Isolation from the return beam was provided by a Faraday rotator, frequency doubling, and time of flight. The input beam passes diagnostic beamsplitters before reflection from the polarizing beamsplitter, which sends it toward the array. A quarter-wave plate produces a circularly polarized beam that is then reflected from the array. After a second pass through the quarter-wave plate, the beam passes through the polarizing beam splitter to the SBS cell. After reflection from the SBS cell, the beam passes back through the polarizing beam splitter and the quarter-wave plate to reflect a second time from the array. If the SBS cell has produced accurate conjugation of the array piston and tilt errors, the beam reflected from the array will have the same beam quality as the incident beam. The outgoing beam is then reflected from the polarizing beam splitter in the direction of the laser.

The diagnostics between the laser and the array measure the input and output (conjugated) beam quality for assessment of conjugation fidelity. Both far-field and near-field data are collected. The near-field beam quality is measured interferometrically with a pair of Mach-Zehnder interferometers (one for input and one for output). The overall quality of the beam is measured by calculating the rms phase over the aperture, while piston conjugation is determined by measuring the fringe displacement across the segment boundaries. [Fringes that are continuous across a boundary indicate an absence of piston ( $\text{mod } 2\pi$ ).] The array alignment and beam quality produced by the array can also be measured using the "output" diagnostics by rotating the quarter-wave plate so that the beam reflected from the array is sent immediately to the output path rather than to the SBS cell. In addition, the "array bypass" mirror can be inserted in front of the array to provide a calibration beam for the Mach-Zehnders or to provide baseline data on whole (nonsegmented) beam conjugation.

The diagnostics between the array and the SBS cell measure incident and reflected energy and incident beam quality (in the far field). The

energy measurements are used to calculate SBS reflectivity and threshold. The far-field diagnostic at the SBS cell provides a measure of the array alignment for each shot when the array alignment is being varied in the rep. pulse mode. This diagnostic is also used to calibrate the array alignment and the piezo controllers.

This diagnostic setup provides interferometric data on the input laser and on the conjugated output on each shot for accurate conjugation fidelity measurements. The far-field beam quality of the beam incident on the SBS cell is also recorded on each shot. However, an interferometric record of the array alignment is only available when the beam is diverted from the SBS cell. Consequently, when the array segments were dithered using the function generators, the only instantaneous measurement of the array alignment on each shot was the far-field data at the SBS cell.

### 5.3 ARRAY ALIGNMENT RESULTS

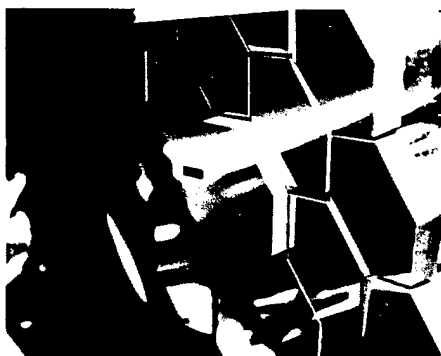
Data was collected on over 5000 shots, including ~100 shots for which interferometric data was collected. The resulting data reduction has been divided into four subject areas, which are discussed in Paragraphs 5.3-1 through 5.3-4.

#### 5.3.1 Correction of Large Segment Piston

As discussed in Section 5.1, the limit on conjugation of segment piston should be either the coherence length of the laser or the coherence length corresponding to the SBS shift. The magnitude of piston that can be corrected using SBS was illustrated dramatically by intentionally misaligning one segment by ~4500 waves (2.4 mm) as shown in Figure 5-3. There were large amounts of segment-to-segment tilt [see interferogram in Figure 5-3(b)] and piston [note visible piston in Figure 5-3(a)] in addition to the one grossly pistoned segment. The interferogram of the output, phase-conjugated beam [Figure 5-3(c)] demonstrates that the 4500 waves of piston have been corrected in addition to correction of the piston and tilt on the remaining segments.

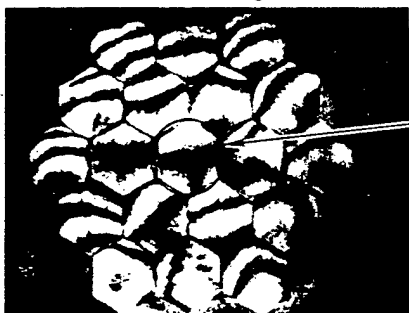
#### 5.3.2 Threshold as Function of Segment Piston and Tilt

These threshold measurements consisted of two test series: (1) threshold was measured with random piston alone (of undetermined absolute



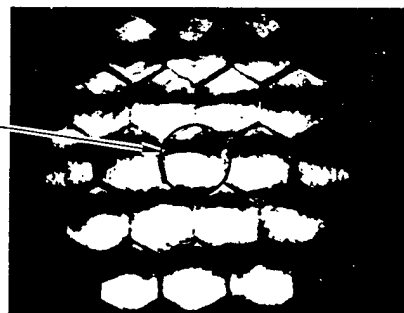
(a)

**Gross Piston Misalignment Corrected to Near Diffraction Limit**



(b)

**Intentionally  
Misaligned  
Segment**



(c)

Figure 5-3. Thousands of Waves Segment Piston Corrected to Better Than  $\lambda/20$  Using SBS Phase Conjugation

magnitude), using the "best aligned" configuration, and (2) threshold was measured with random piston of undetermined magnitude and random tilt controlled by the piezo translators. For all the array alignment experiments, threshold is defined as the x-intercept of the best-fit straight line through a plot of reflected energy versus incident energy (e.g., Figure 5-4(a)). The slope of this line is reported as the slope efficiency of the SBS process. Threshold measurements were compared to a baseline defined as the threshold for the laser beam without any aberrations produced by the array, i.e., the "array bypass" threshold. The beam quality of the "array bypass" beam was  $\sim 1.3$  and the threshold was 0.55 mJ.

Measurement of the threshold for piston aberration alone was accomplished using several "best aligned" array configurations. A "best aligned" configuration was obtained by adjusting the tilt controls on the segments to produce an interferogram of the array surface that had fringes that were as straight as possible in both the vertical and horizontal directions (Figure 5-4(b), an example). Deviations from straightness are unavoidable due to the poor quality of the individual segments. Since the absolute value of segment piston is not controlled, each "best aligned" configuration should be assumed to have a different distribution and rms piston. The random piston in the "best aligned" configuration increased the beam quality to  $\sim 5$  to 6 and the threshold to  $\sim 1.6$  mJ. Both the "array bypass" and the "best aligned" reflectivity curves had a slope efficiency of  $\sim 1.0$ .

Measurement of the threshold for random piston and tilt was performed using shot-to-shot dither of the tilts on all the segments. The voltages supplied to the function generators were calibrated in terms of segment focal-spot motion. The voltages were set to give a chosen rms tilt over the entire array, while random frequencies and phase offsets were supplied to produce a pseudo-random change in tilt distribution from shot to shot. An example of the resulting segment alignment is shown in Figure 5-4(c) for 4.3 waves rms tilt. The SBS reflectivity curve was generated by setting the input energy and averaging the SBS reflected energy over a large number of array settings ( $\sim 100$ ). An example of threshold determination for random

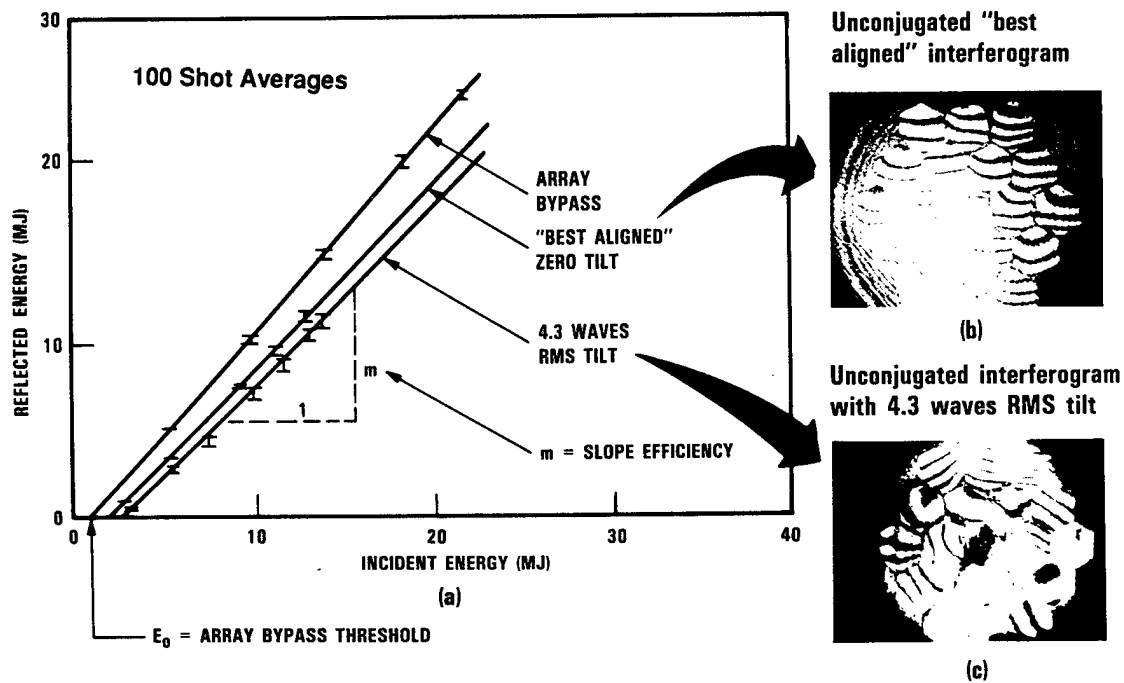


Figure 5-4. SBS Reflectivity Data Used To Establish Threshold Scaling With Array Parameters



piston and 4.3 waves rms tilt is shown in Figure 5-4. The slope efficiency for the tilt cases was found to be slightly less than 1.0. The decrease in slope efficiency with large amounts of tilt may be produced by individual segments that have a higher threshold due to reduced overlap with the rest of the beam. The dependence of slope efficiency on rms tilt is shown in Figure 5-5, and the dependence of threshold on rms tilt is shown in Figure 5-6. The major effect on threshold is produced by the segment piston, while the addition of tilt has a relatively small effect over the range studied.

### 5.3.3 Threshold as Function of Number of Segments

The SBS threshold was also measured for arrays consisting of 1 to 19 segments. These measurements were obtained by inserting apertures in the beam to choose the number of array segments illuminated (Figure 5-7). In all cases, a "best aligned" configuration was used so that only piston errors affected the threshold.

Although this procedure was simple to carry out, there are several considerations that complicate interpretation of the results. Since the beam quality of the incident laser beam was  $\sim 1.3$ , masks with a small aperture area (few segments) spatially filter the beam, producing an incident BQ that increases as the number of segments increases. Thus, the BQ at the SBS cell and, therefore, the SBS threshold also increase as the number of segments, even without any segment piston. For small N (number of segments), the mask blocks a large fraction of the aperture, so the total energy available is limited in these cases to a few times threshold. Because the threshold is defined by an asymptotic-slope intercept, this limitation biases the experimentally determined threshold toward smaller values for small N (Figure 5-8). Finally, since the absolute piston settings are random, the beam quality can vary greatly as the number of segments changes.

Given these considerations, it is apparent that the most consistent set of threshold data is obtained from the "array bypass" configuration (one segment) and the 19 segment "best aligned" configuration, both of which use the same beam aperture. As the number of segments is decreased using the mask, the threshold scaling becomes less consistent. This can be

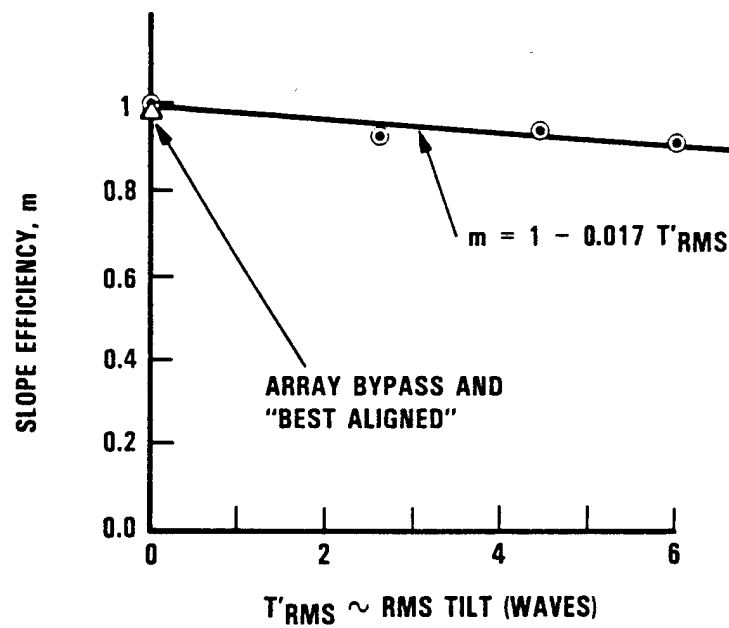


Figure 5-5. Slope Efficiency of SBS Reflectivity

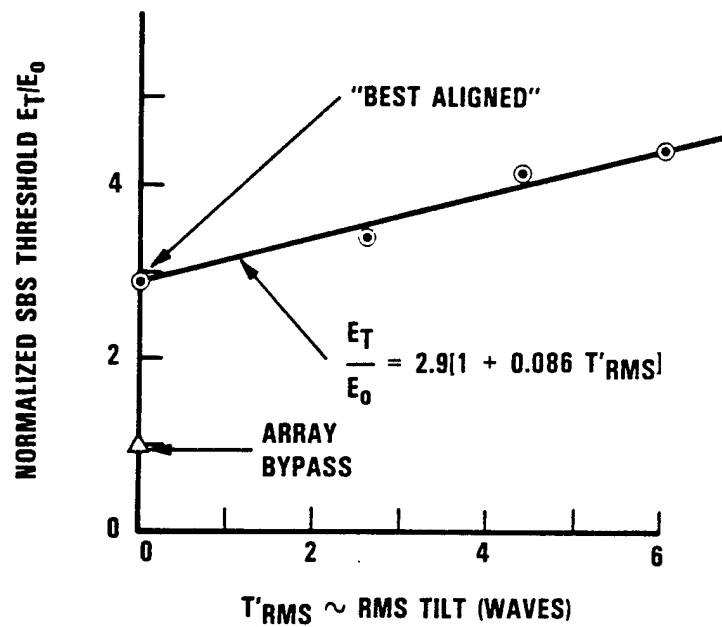


Figure 5-6. SBS Threshold as a Function of Segment Tilt (with random piston)

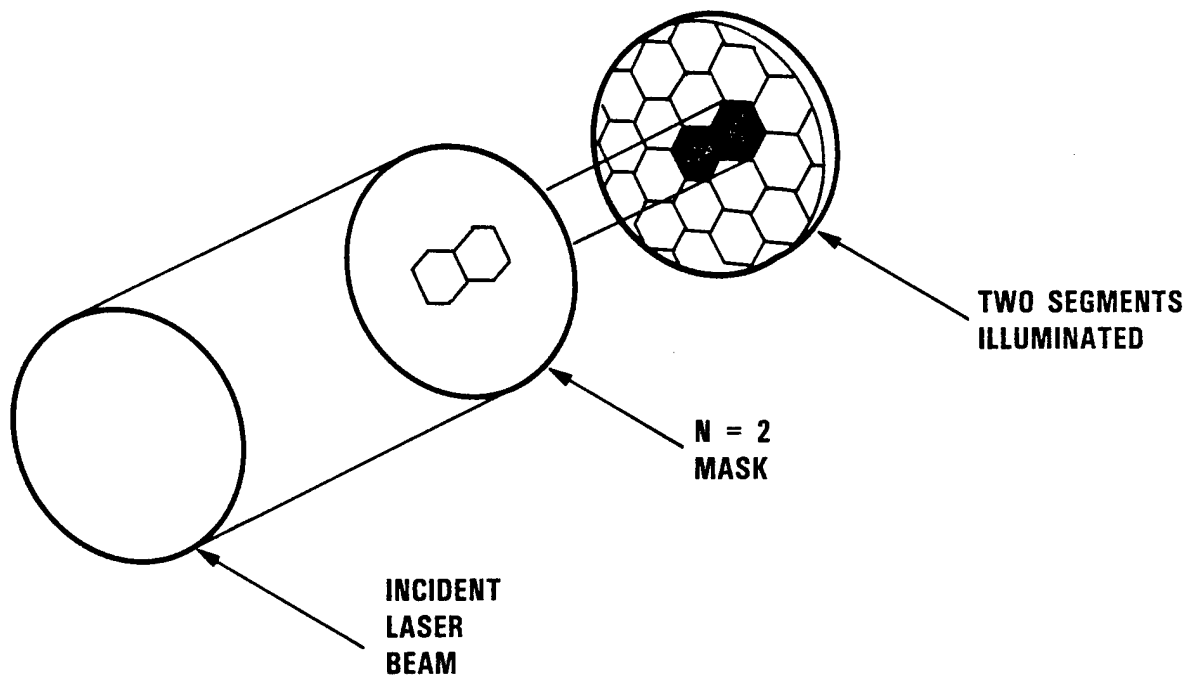


Figure 5-7. Segment Apertures Used To Correlate Threshold With Number of Segments

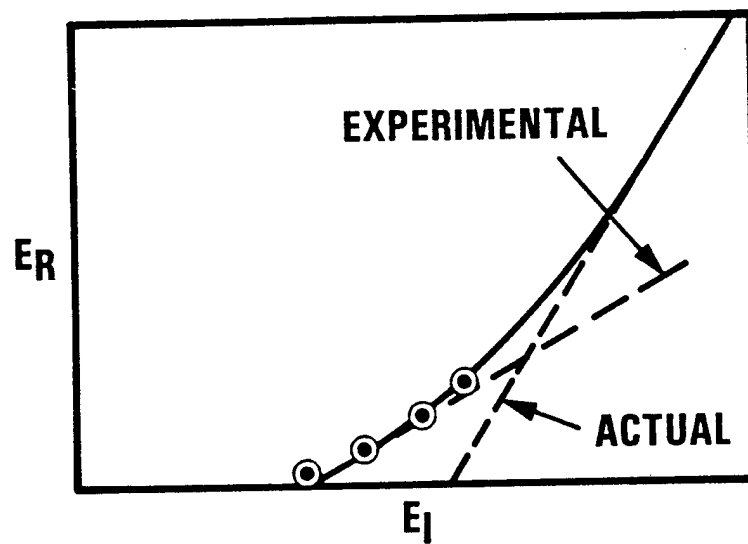


Figure 5-8. Technique Used for Threshold Scaling With Number of Segments Biases Measurement to Lower Values for Small N

seen in Figure 5-9, where the threshold data for 12 to 19 segments appears to lie on a straight line with the point defined by the "array bypass" threshold. This line gives an  $N^{1/3}$  dependence of threshold on the number of segments. A simplified analysis that assumes threshold scales as BQ predicts an  $N^{1/2}$  scaling with the number of segments (assuming random piston between segments). The slower increase seen in the experiment may not be significant for several reasons: First, the considerations discussed above also complicate the deduction of a scaling relation from this data, and second, the data were collected for a single piston setting of the array.

#### 5.3.4 Conjugation Fidelity as Function of Segment Tilt

Interferometric and far-field data was collected both as a function of segment tilt and as a function of power incident on the SBS cell. To quantify the limitations on beam combination produced by segment tilt, the following paragraphs consider only shots with energy  $>5$  times threshold. Data taken with lower incident energies indicate that the alignment tolerances decrease as threshold is approached from above.

A representative example of data showing a high degree of piston and tilt conjugation is shown in Figure 5-10 for a shot taken from the 2.6 wave rms tilt series. An interferogram representative of the array alignment during this series is shown in Figure 5-10(c). In addition to the tilt, which was controlled by the function generators, an unknown, large amount of segment piston, estimated to be on the order of  $10$  to  $10^3$  waves, was present. Figure 5-10(a) shows the far-field spots for the input laser beam, the aberrated beam incident on the SBS cell, and the conjugated output beam. Figure 5-10(b) shows three-dimensional plots illustrating the improvement in far-field brightness produced by conjugation. Finally, Figure 5-10(d) shows an interferogram of the conjugated output; the continuity of the fringes demonstrates accurate piston conjugation, and their straightness indicates high fidelity correction of the segment tilts and misfigures.

The limitation on segment tilt for good beam combination (conjugation of both piston and tilt) was determined by analyzing the fringe continuity across segment boundaries in the interferograms of the conjugated output

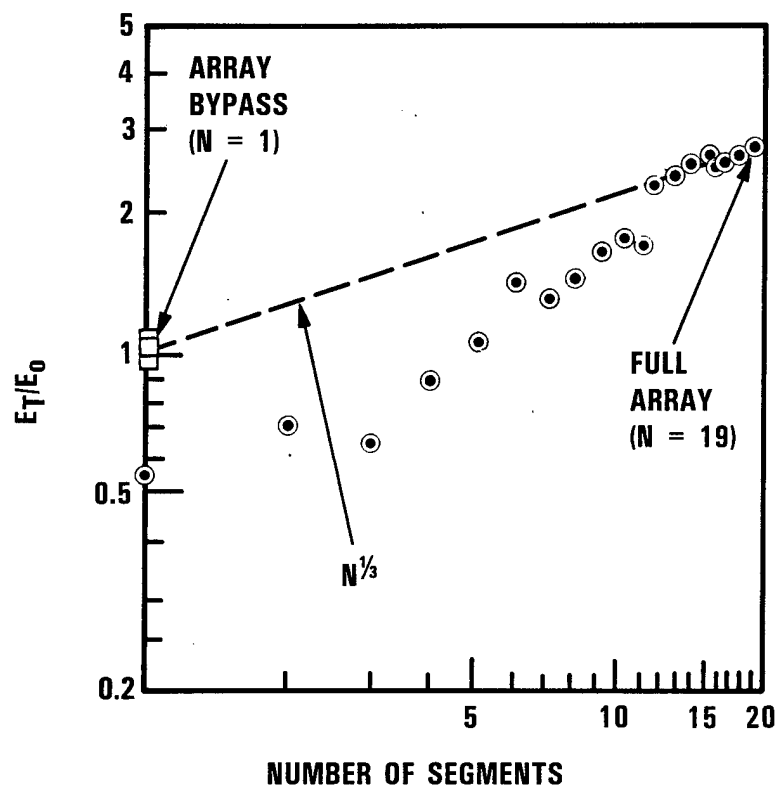


Figure 5-9. SBS Threshold Scaling With Number of Segments

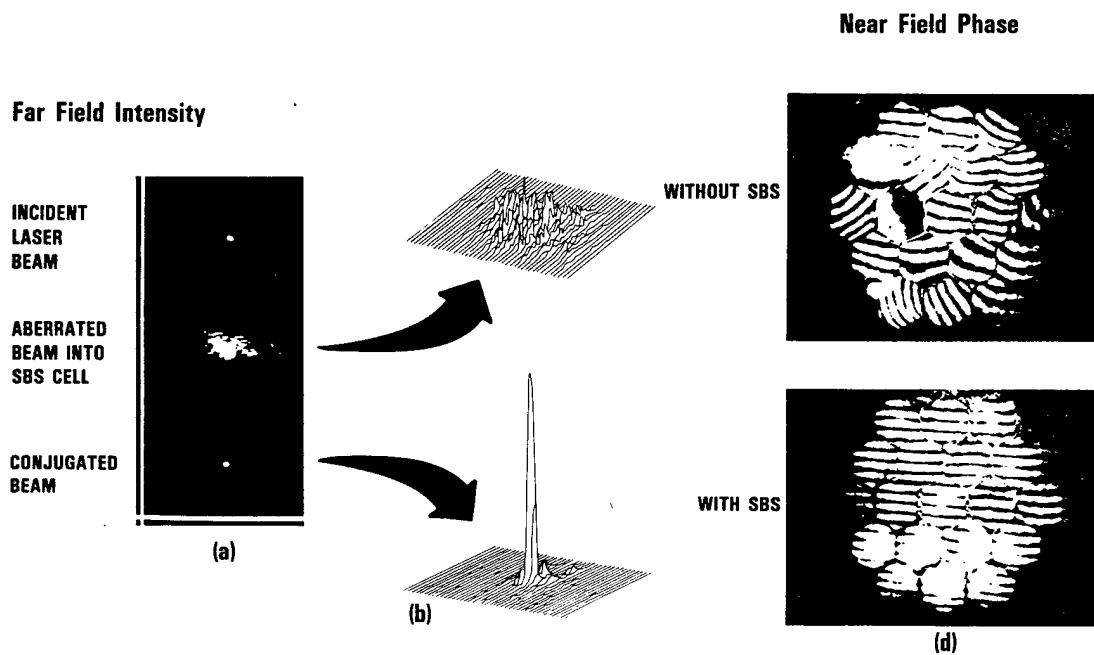


Figure 5-10. Representative Examples of Data Show High Degree of Piston and Tilt Conjugation

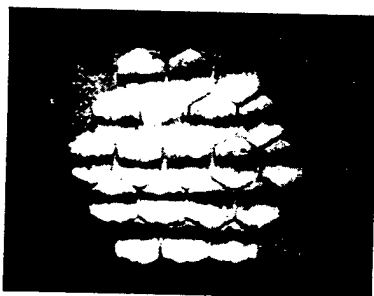


(after the second reflection from the array). These interferograms were obtained using the "random" dither technique described earlier. At least 20 interferograms were obtained for each value of rms segment tilt, with an exception in the case of "best aligned" where only six interferograms were analyzed. For each interferogram, the number of segments that had "dropped out" of phase was catalogued. Interferograms demonstrating all 19 segments cophased and one segment dropped out are shown in Figure 5-11. These data are presented as histograms in Figure 5-12. For the "best aligned" configuration (with 0 tilt), all the segments were cophased for all the shots. For 2.6 rms waves of tilt, 19 out of 20 shots had all 19 segments cophased, and only one segment was out of phase in the remaining shot [Figure 5-11(b)]. As the rms tilt increases to 4.3 and 6.0 waves, the number of shots with all segments cophased decreases, and the number of segments out of phase in a given shot increases. These results are in general agreement with the earlier NOMES and RSELE results for in-plane alignment of two segments. Thus, the 19 segment results indicate that a two-dimensional array of segments alleviates the tighter out-of-plane alignment requirements found for two segments.

The accuracy of piston conjugation was determined by reducing interferograms for the cases of 0 and 2.6 waves (rms) of tilt. The interferograms were digitized and the fringe intensity profiles across adjacent segments extracted and compared to deduce the relative phase shift across a segment boundary. These phase shifts were then rms'd over the entire array. The results are presented in Table 5-1. For both sets of data, piston was conjugated to within  $\lambda/20$ . The accuracy of this measurement procedure was assessed by analyzing fringes within a segment (as opposed to across a segment boundary), where the fringes should be continuous. The accuracy thus deduced was  $\lambda/45$ .

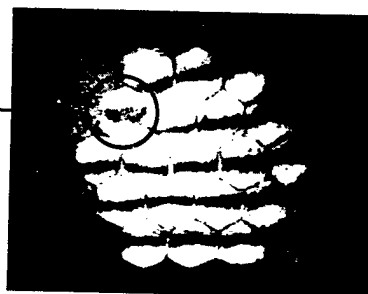
#### 5.4 DISCUSSION OF RESULTS AND SUGGESTIONS FOR FURTHER EXPERIMENTS

The array alignment results have successfully demonstrated scaling of the SBS beam combining technique to a 19-element array. A piston error of  $\sim 4500$  waves was corrected by SBS, vividly demonstrating the large dynamic range for piston conjugation. (Note that in the SBL, while this dynamic range can be applied to path length differences between the amplifiers, the



All 19 segments cophased  
(a)

SEGMENT  
"DROPPED  
OUT"



Example of segment dropout  
(b)

Figure 5-11. Interferograms Showing All Elements Cophased and One Segment Dropped Out

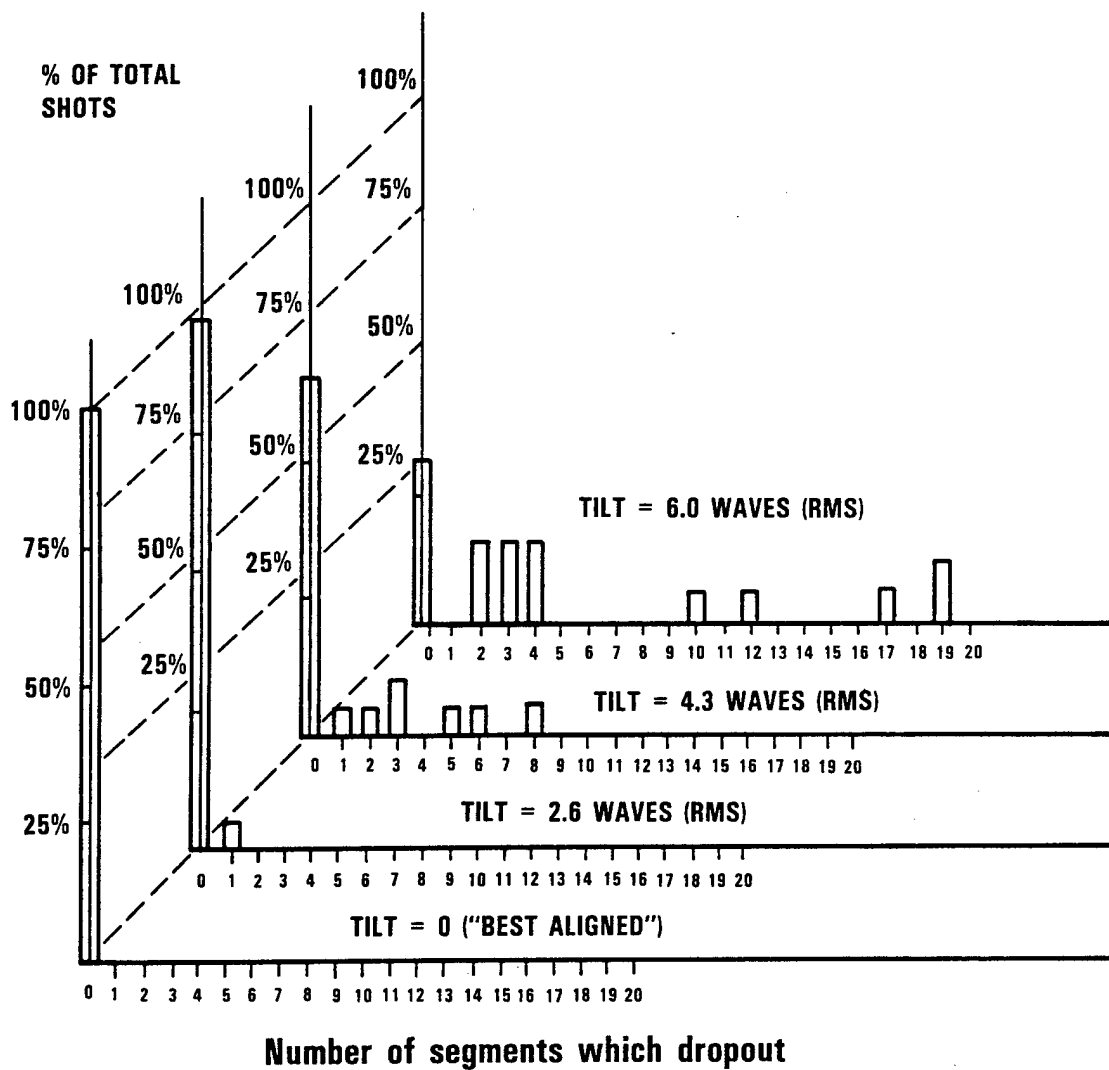


Figure 5-12. Piston Conjugation Scaling With RMS Segment Tilt

Table 5-1. Accuracy of Piston Conjugation

RMS Tilt (waves)	Conjugated RMS Piston (waves)	Number Shots Analyzed
0	0.036 $\pm$ 0.022	5
2.6	0.048 $\pm$ 0.022	7

piston correction on the primary is more severely limited by the optical design of the beam director, specifically the distance to the beacon.) The array alignment results also demonstrated excellent phase fidelity for configurations with random piston and up to  $\sim 2.5$  waves rms of tilt. Preliminary scaling relationships were deduced for threshold as a function of rms tilt, beam quality (produced by segment piston and tilt), and number of segments.

It is our intention in the APEX program to refine these preliminary results. Data sets collected with an array alignment interferogram for each shot will allow us to determine if segment dropout is correlated with specific alignment conditions, e.g., when the segment in question is tilted away from the rest of the beam. It would also be desirable to collect a data set for threshold as a function of number of segments that is free from the considerations complicating interpretation discussed in Section 5.3.

## 5.5 REFERENCES

- 5-1. N. G. Basov, V. F. Efimkov, I. G. Zubarev, A. V. Kotov, S. I. Mikhailov, and M. G. Smirnov, "Inversion of Wavefront in SMBS of a Depolarized Pump," *Pis'ma Zh. Eksp. Teor. Fiz.* 28, 215-219, 1978; [*JETP Lett.* 18, 197-201, 1978].
- 5-2. N. G. Basov, I. G. Zubarev, A. B. Mironov, S. I. Mikhailov, and A. Y. Okulov, "Laser Interferometer with Wavefront-Reversing Mirrors," *Zh. Eksp. Teor. Fiz.* 79, 1687-1686, 1980; [*Sov. Phys. JETP* 52, 847-851, 1980].
- 5-3. N. G. Basov, V. F. Efimkov, A. V. Kotov, A. B. Mironov, S. I. Mikhailov, and V. G. Smirnov, "Influence of Certain Radiation Parameters on Wavefront Reversal of a Pump Wave in a Brillouin Mirror," *Kvantovaya Elektron.* 6, 765-771, 1979; [*Sov. J. Quantum Electron.* 9, 455-458, 1979].
- 5-4. A. F. Vasil'ev, A. A. Mak, V. M. Mit'kin, V. A. Serebryakov, and V. E. Yashin, "Correction of Thermally Induced Optical Aberrations and Coherent Phasing of Beams During Stimulated Brillouin Scattering," *Zh. Tekh. Fiz.* 56, 312-316, 1986; [*Sov. Phys. Tech. Phys.* 31, 191-193, 1986].
- 5-5. D. A. Rockwell and C. R. Giuliano, "Coherent Coupling of Laser Gain Media Using Phase Conjugation," *Opt. Lett.* 11, 147-149, 1986.
- 5-6. K. V. Gratsianov, A. F. Kornev, V. V. Lyubimov, A. A. Mak, V. G. Pankov, and A. I. Stepanov, "Investigation of an Amplifier With a Composite Active Element and a Stimulated Brillouin Scattering Mirror," *Kvantovaya Elektron.* 13, 2337-2339, 1986; [*Sov. J. Quantum Electron.* 16, 1544-1546, 1986].
- 5-7. G. Linford, Phased Array Combination of Laser Beams, Experimental, IR&D Report 85324033, March 1985.
- 5-8. M. Valley, Phased Analysis Array Combination of Laser Beams, Analysis, IR&D Report 85324023, March 1985 (Confidential).
- 5-9. M. Valley, G. Lombardi, and R. Aprahamian, "Beam Combination by Stimulated Brillouin Scattering," *J. Opt. Soc. Am.* B3, 1492-1497, 1986.
- 5-10. NOMES Final Report, AFWL-TR-86-5, May 1986.
- 5-11. R. H. Moyer, M. Valley, and M. Cimolino, "Beam Combination Through Stimulated Brillouin Scattering," *J. Opt. Soc. Am.* B5, 2473, 1988.
- 5-12. RSELE Final Report.
- 5-13. D. Carroll, R. Johnson, S. Pfeifer, and R. Moyer, Experimental Study of SBS Beam Combination, to be submitted to JOSA B.

## 6. OSCILLATOR ISOLATION EXPERIMENT

The issue of oscillator isolation has been addressed in a series of experiments and analyses. Several technical approaches have been taken to establish isolation requirements and to optimize the oscillator design. The subscale CO<sub>2</sub> laser experiments described in this section provide data for model validation. The standing-wave resonator and a ring resonator similar to the ALPHA HEXDARR resonator provided a data base. Experiments on the ALPHA VM (Section 7) extend that data base to CW HF. In addition, a physics model applicable to laboratory experiments and APEX/SBL HEXDARR resonators was developed to scale the experimental results to APEX and the SBL and to optimize resonator design.

Isolation component development, as discussed in Volume II, Section 2-11, has been performed. This includes coating designs for quarter-wave retardation, low birefringence annular optics and turning flats, and a birefringent wedge required to fully utilize the capability of the coating designs.

The CO<sub>2</sub> oscillator isolation experiment design began in February 1988, and testing concluded with both standing-wave and ring resonator experiments in July 1989. The following sections describe the objectives, approach, experiment, and resonator design and present the results for a negative-branch standing-wave CO<sub>2</sub> resonator ( $M = 1.5$  and  $2.0$ ) and the negative branch CO<sub>2</sub> ring resonator ( $M = 1.5$  and  $1.77$ ). Section 6.1 is an introduction to the experiment and describes the main objectives. Theory and derivations are presented in Section 6.2. Descriptions of the CO<sub>2</sub> resonators, optical train design, and experiment are given in Section 6.3. Experimental results are presented in Section 6.4 for both resonators. In addition, discussions and comparisons of the results for different resonators and magnifications and theoretical results are given in Section 6.5.

### 6.1 INTRODUCTION

In a CW phase-conjugated system, power returning to the master oscillator may degrade its performance. Systems analysis for the SBL discussed in Volume II, Section 2-11 sets the requirement that the system

brightness (power/BQ<sup>2</sup>) must degrade by less than 1% as a result of feedback to the master oscillator. Performance modeling of the SBL presented in Volume II shows that the system brightness is very insensitive to oscillator power, provided the power at the SBS cell is well above threshold for the high brightness SBL. This 1% system degradation corresponds to approximately 50% decrease in master oscillator power. The oscillator isolation experiments were designed to help establish isolation requirements and optimize oscillator design with minimal risk. The goal of these experiments was to provide a data base upon which an isolation model could be validated. This validated model is then used to set requirements for both the SBL and the high-power CW phase-conjugation demonstration to be performed on the APEX program. These isolation requirements set design requirements for both the master oscillator and the isolation component hardware.

The oscillator isolation experiment on the CO<sub>2</sub> device was selected as an initial approach to characterizing behavior of an oscillator in the presence of feedback because CO<sub>2</sub> allows an easier understanding of the basic physics issues. For example, the CO<sub>2</sub> gain is significantly less complex than HF as we can ignore coupled transitions with single spectral line operation. The mode spectrum is less complex and therefore it is easier to understand what happens to the dominant mode at different return beam frequencies. This basic understanding is then used to perform analyses and create a validated isolation model which can be scaled to the more complex case of HF. Table 6-1 shows the traceability of significant nondimensional parameters for the CO<sub>2</sub> experiments, an APEX demonstration and the SBL device.

The CO<sub>2</sub> laser device had several practical advantages. The device provides a high data acquisition rate with real-time, nonremote adjustments possible. The resonator parameters are easily varied to understand the leverage to be obtained in isolation by resonator design. Feedback power is also easily varied. Single spectral line operation is possible, and gas pressure can be varied to change the homogeneous width/mode spacing ratio. Also, an acousto-optic modulator can be used to vary return beam frequency as opposed to a complex mechanical frequency shifter which would be required on a larger scale device.

Table 6-1. Traceability of Significant Nondimensional Parameters

Parameter	SBL	APEX	CO <sub>2</sub>
Resonator Type	Ring	Ring or SW	SW and Ring
G <sub>0</sub> L	4	4	1 to 2
Magnification	3	~3	1.2, 1.5, 2
Number Passes to Fresnel Core	1-2	1-2	2
Lorentz Width/Mode Spacing	1.25	0.6 to 1	0.54 to 3.2
Doppler Width/Mode Spacing	34	16 to 34	6
Doppler Width/Lorentz Width	27	27	2
Location of Frequency Shift/ Mode Spacing	0-1	0-1	0-1

The experimental technical approach includes subscale CO<sub>2</sub> laser experiments to provide data for model validation. A standing-wave resonator provides the initial validation data, and a ring resonator traceable to the ALPHA HEXDARR resonator is studied for further model validation. Specifically, the performance degradation of each of these two resonators is studied as a function of returned power and resonator parameters. The parameters of interest include the fraction of return power, resonator magnification and  $G_{sat}L$ , return beam frequency, i.e., SBS shift relative to gain bandwidth, longitudinal, mode spacing, and position of higher order transverse modes, as well as return beam alignment.

When the fed-back beam returns at a frequency that is different from any of the lowest loss transverse modes, as in the case of an SBS phase conjugator, it is likely to excite a higher order mode with poor beam quality. If the feedback is large enough, significant power may be transferred from the lowest loss mode to a mode with poor beam quality. For a ring resonator, this results in a power loss in the forward wave, while for a standing-wave resonator, the primary effect may be a degradation in beam quality. For small amount of feedback, the saturated gain in the resonator can be assumed to be unperturbed by the feedback.



## 6.2 THEORETICAL DESCRIPTION

It is feasible to make approximate estimates of oscillator sensitivity to frequency-shifted feedback based on a simple model which treats feedback as a two-step process: (1) the reinjected beam is amplified at the resonator threshold gain while it walks into and out of the resonator Fresnel core; and (2) the amplified signal then serves as an input to a regenerative amplifier. In a standing-wave resonator when the injected frequency differs substantially from the resonator lowest loss eigenfrequencies, the amplified beam is eventually outcoupled at the outcoupling scraper but typically has such bad beam quality compared to the fundamental mode that it contributes negligibly to the far field central spot. Thus, the primary effect of frequency shifted feedback on a standing-wave resonator is to degrade beam quality. For feedback near resonance with fundamental mode frequencies the amplification factor is higher but the amplified signal itself also is expected to have good beam quality so there is not a substantial resonance in beam quality degradation. In a ring resonator, the injected signal produces a reverse wave which is "outcoupled" internally. In this case the amplified signal reduces the outcoupled power but does not degrade its beam quality. For feedback near resonance with resonator eigenfrequencies the power reduction is expected to exhibit a resonance.

There are several levels of sophistication at which this analysis can be pursued. Ideally, one would construct a model that included (1) two dimensional physical optics, (2) high-resolution multiple-saturable gain sheets, (3) adjustable self-consistent feedback, and (4) an iterative transient algorithm which converged to a near steady-state result. Such a model should implicitly predict characteristics similar to those summarized earlier. Some progress was made in constructing a simple one-dimensional version of such a model (the MOI code) but it was not completed. The model did manifest many of the sensitivities discussed earlier and served as a primary motivating factor for formulating the simpler models which were used.

At the next level of complexity, one can use one series of physical optics calculations to assess the relative outcoupling as the beam walks into and out of the Fresnel core and another set of calculations to assess resonator eigenvalues. The first series of calculations is used to estimate the effective number of gain passes to walk into and out of the Fresnel core and also provides an estimate of the correction required to account for the outcoupling which occurs before the last pass. The lowest loss eigenvalue is used to estimate the saturated gain per pass during the amplification passes. The higher loss eigenvalues are used as inputs to regenerative amplification analyses. Analyses of this type were performed for the test resonators and are presented in Section 6.5.

Finally, it is possible to use simple resonator ABCD matrices to estimate the number of passes to walk into and out of the resonator, to assume that in the geometrical limit the saturated power gain per round trip is simply magnification squared, and to use simple injection locking expressions to estimate the magnitude of the regenerative amplification term. The net amplification expression for a standing-wave resonator is

$$I_{out} = I_{in} G_A G_L G(W) = I_{in} G_{Total}$$

where

$I_{out}$  = amplified output

$I_{in}$  = input

$G_A$  = net gain during walk into and out of the Fresnel core  
 =  $(M^2)^n$  in geometric limit, where  $n$  = effective number of passes

$G_L$  = fractional loss during amplification (1 in geometric limit)

$G(W)$  = contribution due to regenerative amplification

$G_{Total}$  = total gain.

As an example, consider a confocal telescopic resonator with diameter  $D$ , mirror separation length  $L$ , magnification  $M$  and laser wavelength  $\lambda$ . Assuming an approximate reversal criteria that for a mode annulus width  $W_m$  on the  $m$ th pass reversal occurs when rotation through the

diffractive half angle  $\lambda/2W$  transforms a forward into a reverse ray, then based on a series of ABCD matrix calculations the net inferred  $G_A$  value is

$$\frac{D^4 (M+1)^2 (M-1)^4}{16L^2 M^4 \lambda^2}$$

This expression can be quite large. For example for  $D = 3\text{cm}$ ,  $L = 800\text{ cm}$ ,  $M = 3$ , and  $\lambda = 2.8 \times 10^{-4}\text{ cm}$ , it equals 300.

It should not be supposed that this is a general result applicable to other types of resonator but it does provide some insight into the general scaling. The result implies a strong sensitivity dependence on resonator parameters. For example, holding other parameters constant and varying magnification from 1.5 to 2 increases  $G_A$  by a factor of 7. Although they were a different type of resonator, the two standing-wave CZAR resonators experimentally exhibited a comparable increase (actually approximately a factor of 5) in  $G_{\text{Total}}$  over this range of magnifications.

Regenerative amplification can be assessed using the conventional one dimensional analysis approach used to assess injection locking. Suppose an input signal  $E_x$  (amplitude) is injected at the scraper hole and just fills it. During a round trip it experiences a net amplitude gain  $G_R$  ( $M$  in the geometric limit) which is determined by the resonator threshold condition for the fundamental lasing mode. Suppose the round trip amplitude outcoupling fraction for the fundamental is  $T_F$  and the retained fraction is  $R_F$  (the notation is borrowed from transmissive optics). The following relations hold:

$$T_F^2 + R_F^2 = 1$$

and

$$G_R R_F = 1$$

If the mode matched the profile of some transverse mode and approximated its frequency, then the amplitude loss fraction per round trip should approximately equal the outcoupling fraction associated with the mode  $T_M$ . Assuming that there is a frequency mismatch  $\Delta\gamma$  between the injected signal and this mode and that the resonator round trip length is  $2L$ , the accumulated phase shift associated with a round trip is given by the expression:

$$\phi = \frac{4\pi\Delta\gamma L}{c}$$

Based on these assumptions and summing the appropriate geometrical progression, the net outcoupling after converting to intensity is

$$\frac{(E_I)^2 (G_R^2 T_M^2)}{(1 - R_M G_R \cos(\phi))^2 + (R_M G_R \sin(\phi))^2}$$

Because of the way  $E_I$  is defined the last pass in  $G_A$  has been double counted in this expression and the appropriate expression for  $G(W)$  is

$$G(W) = G(\phi) = \frac{(T_M^2)}{(1 - R_M G_R \cos(\phi))^2 + (R_M G_R \sin(\phi))^2}$$

$R_M$  can be related to the mode eigenvalue,  $E_M$  by the equations

$$T_M^2 = 1 - E_M^4$$

and

$$T_M^2 + R_M^2 = 1$$

The  $G(W)$  expression diverges inversely as the square of  $\Delta\gamma$  for a fundamental mode as  $\Delta\gamma$  tends to zero. For higher loss modes  $R_M G_R < 1$  and

although there is a local maximum at  $\Delta\gamma = 0$  the width of the resonance is large and its amplitude weak. Indeed as discussed in Section 6.5 for resonators with good mode discrimination, this factor is almost frequency independent and of order unity except very near the fundamental modes.

Experimental observables can be easily related to  $G_{Total}$ . In the limit where the feedback perturbations are small enough that substantial fractions of the unperturbed output remain, the observed net beam quality can be related to  $G_{Total}$  based on the assumption that the amplified signal contributes nothing to the far field central spot. Since the experimentally observed unperturbed beam qualities were all excellent and physical optics calculations suggest amplified beam qualities in excess of 3, typically 5 or more, this assumption is probably reasonable even when half the output power is frequency shifted due to feedback. The equations are as follows:

$S$  = return fraction

$F = S \times G_{Total}$

$\Delta BQ$  = observed change in beam quality ( $BQ = 1$  before perturbation)

$Q$  = beam quality of frequency shifted output

$P$  = power through far field pinhole without feedback

The power through the far field pinhole with feedback drops to

$$P(1 - F + F/Q^2) \quad \text{and by definition}$$

$$(1 + \Delta BQ)^2 = 1/(1 - F + F/Q^2)$$

and

$$\frac{(1 + \Delta BQ)^2 - 1}{(1 + \Delta BQ)^2} = (1 - 1/Q^2)SG_{Total} \approx SG_{Total}$$

Thus, if the left-hand  $\Delta BQ$  expression is plotted versus  $S$  the inferred slope can be used to estimate  $G_{Total}$ .

In the case of a ring resonator similar arguments can be applied to infer  $G_{Total}$  in terms of the fractional intensity decline. Based on the approximation that the total power produced is constant:

$$P_{init} = P_{out} + FP_{out}$$

$$\Delta I = \frac{P_{init} - P_{out}}{P_{init}}$$

where

$P_{init}$  = initial power output

$P_{out}$  = feedback perturbed power output

Substitution shows that

$$\Delta I / (1 - \Delta I) = SG_{Total}$$

and, therefore, plotting this expression versus  $S$  yields  $G_{Total}$  as a slope.

## 6.3 EXPERIMENTAL DESCRIPTION

### 6.3.1 CO<sub>2</sub> Laser Device and Operation

The CO<sub>2</sub> laser testbed was established in TRW's Technology Test Center, located in Building 67 on site at Space Park, and serves as a subscale testbed for future oscillator isolation (OI) experiments. The CO<sub>2</sub> device is pulsed with pulse length controlled by a square-wave current pulse. A small sustainer discharge current of 50 mA continuously passes through the device to maintain ionization of the laser medium. Typical pulse lengths are between 1 and 2 ms in duration. The gain medium is 1.5 m long with a circular cross section approximately 20 cm in diameter. The gas flow is longitudinal, along the optical axis, and the medium is transversely excited. The gasses used in the laser are CO<sub>2</sub>, He, and N<sub>2</sub>. For operation at 6 torr the gauge pressures for He/N<sub>2</sub>/CO<sub>2</sub> are 115/85/20 psig, and, thus, the pumping requirement to maintain this flow rate is about 750 cfm. The theoretical Doppler width is approximately 60 MHz with typically one longitudinal mode lasing as measured in the experiments.

The typical pulse rate and pulse length for these experiments are approximately 1 Hz and 2 ms, respectively. The operating current is 2.5 amp, with an operating voltage of 16 kV. This supplies sufficient energy and relatively square and repeatable pulse shapes. Gauge pressures for 6 torr operation of He/N<sub>2</sub>/CO<sub>2</sub> = 115/85/20 psig correspond to 0.035/0.015/0.062 moles/s. The maximum energy output for these experiments has been approximately 800 mJ for a 2 ms pulse.

The small signal gain was measured in the initial risk reduction experiments with a California probe laser for line P(20). It was found to be 0.85% cm<sup>-1</sup> on axis at 6 torr cavity pressure. Figure 6-1(a) illustrates the 2 ms pulse shape, and Figure 6-1(b) is a graph of the small signal gain versus horizontal scan position across (perpendicular to the optical axis) the gain medium. Curves are shown for different operating currents at 6 torr and 10 kV operating voltage. For lower pressure operation at 1.8 torr, the small signal gain decreases noticeably on axis. There is also an asymmetry across the cavity even at the higher pressure. A run current of 2 amp has the highest overall small signal gain.

### 6.3.2 Resonator Description

Two different resonator types were studied in the CO<sub>2</sub> oscillator isolation experiments. A negative branch unstable standing-wave resonator at M = 1.5 and M = 2.0, and a negative branch ring resonator at M = 1.5 and M = 1.77 are discussed.

#### 6.3.2.1 Negative Branch Unstable Standing-Wave Resonator

Figure 6-2 is a layout of the negative branch unstable standing-wave resonator, CZAR (conjugate zoom resonator), for three magnifications, 1.2, 1.5, and 2.0. Magnifications 1.5 and 2.0 were studied. The gain medium is double passed and the beam is folded in the x dimension, i.e., parallel to the optical bench. Folding about the x-axis homogenizes the asymmetric gain profile by mapping the inner diameter into the outer diameter.

A schematic of the negative branch resonator design is shown in Figure 6-3. Since the scraper is at focus, the Fresnel number is infinite and the intensity fluctuations are minimized in the outcoupled beam. An example of the theoretical near-field intensity profile is shown in

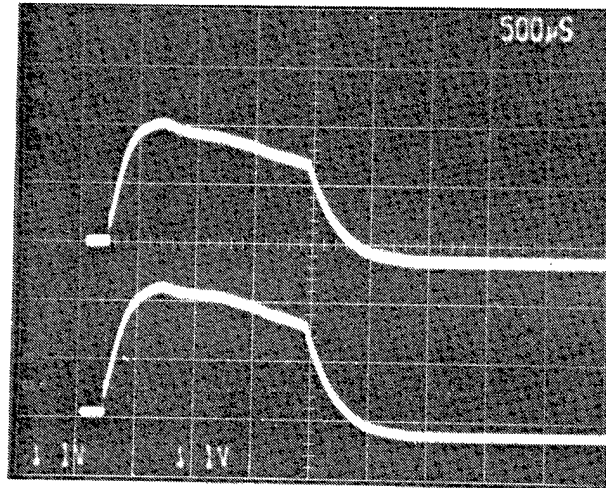


Figure 6-1(a). Pulsed CO<sub>2</sub> Laser Power Versus Time, No Return

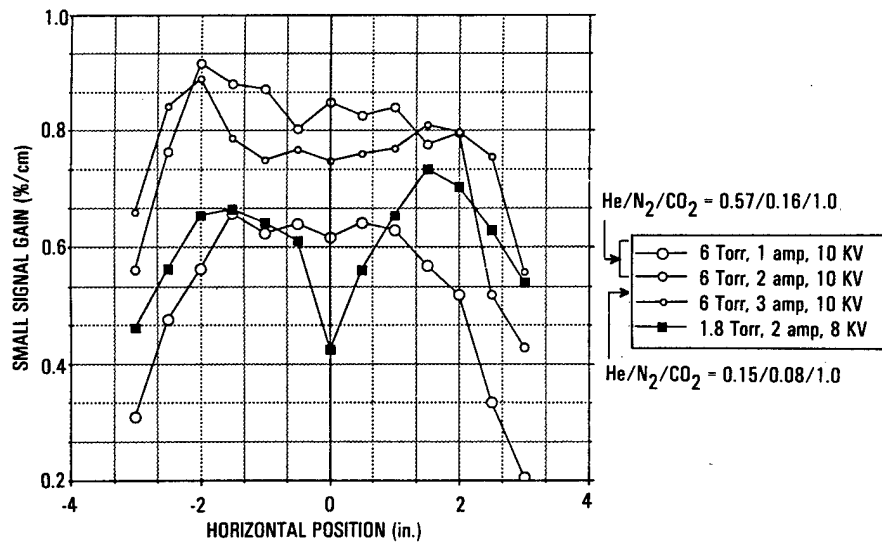


Figure 6-1(b). Small Signal Gain Versus Run Current and Pressure



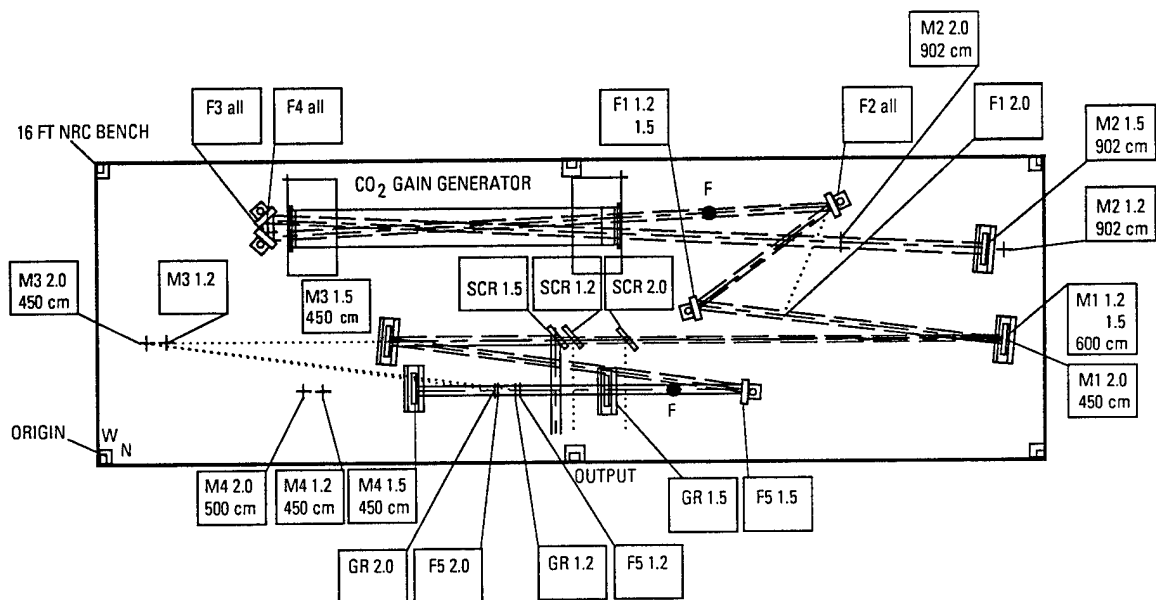


Figure 6-2. Negative Branch Unstable Standing Wave (CZAR) Resonator Layout

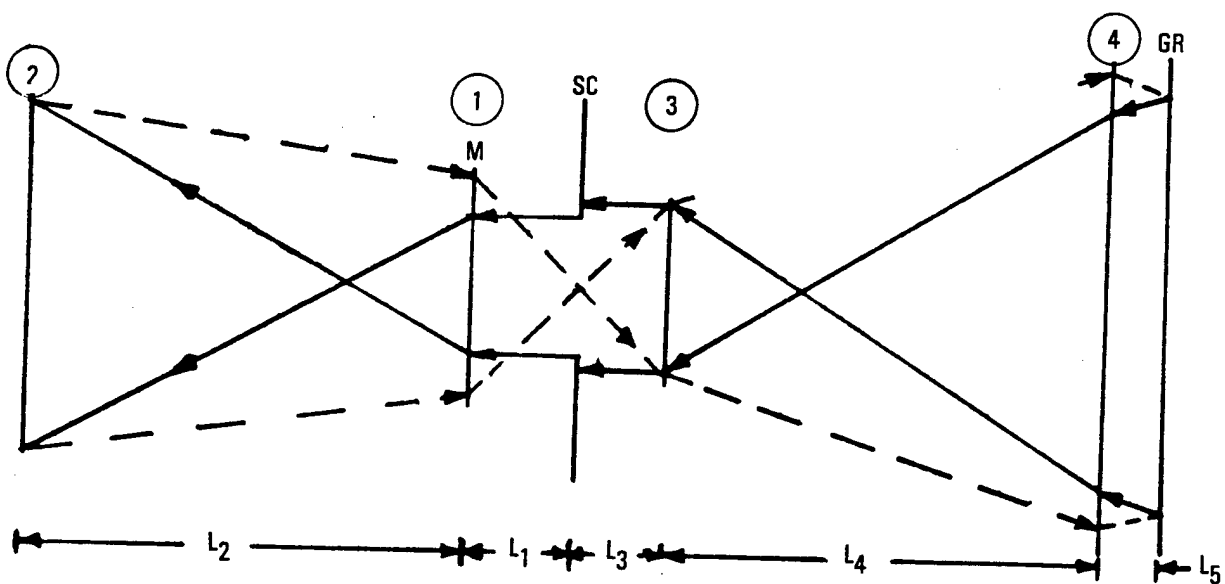


Figure 6-3. Negative Branch Standing-Wave Resonator (CZAR)  
Optical Schematic

Figure 6-4. The inner beam size, 2.54 cm square, is the same for  $M = 1.5$  and  $M = 2$ , while the outer dimensions are 3.81 and 5.08 cm, respectively.

Line selection was initially attempted with a grating (150 1/mm) in the Littrow configuration to suppress all lines but P20. However, the dispersion was not sufficient since five spectral lines lased equally well. The grating was replaced with a dielectric flat at normal incidence. Optimum alignment of this turning flat gives two spectral lines: the 10.58  $\mu\text{m}$ , P(18), line is present about 99% of the time, and 10.56  $\mu\text{m}$ , P16, is present concurrently approximately 30% of the time. The wavelength was also observed to shift suddenly from one line to another. However, when the cavity is slightly misaligned, the 10.58  $\mu\text{m}$  line is always present and the second spectral line is seen infrequently ( $<2\%$ ). Small changes in cavity length can cause the spectral output to change. Data are typically taken under single-line, single-mode operation because multimoding is not repeatable and rarely seen for the duration of the pulse.

The length of the resonator for  $M = 1.5$  is 16.31 m, and thus, the longitudinal mode spacing is 9.196 MHz. The resonator for  $M = 2.0$  is slightly shorter, 15.76 m, and has a longitudinal mode spacing of 9.519 MHz. Most of the components in the resonator are coated for vertical, s, polarization. The output is 95% vertically polarized which is the orientation required by optics and acousto-optic modulators in the external optical train. The far-field beam quality is 1.09 for both  $M = 1.5$  and  $M = 2.0$ .

The output energies for a 2 ms pulse at  $M = 1.5$  and  $M = 2$  are approximately 600 and 800 mJ, respectively.

#### 6.3.2.2 Negative Branch Unstable Ring Resonator

Figure 6-5 illustrates the negative branch unstable ring resonator. The magnification is set by the two powered mirrors and in these experiments  $M = -1.5$  and  $M = -1.77$  are studied. There are 11 elements including the output scraper mirror and a periscope which rotates the intracavity beam by  $90^\circ$  around the optical axis each round trip.

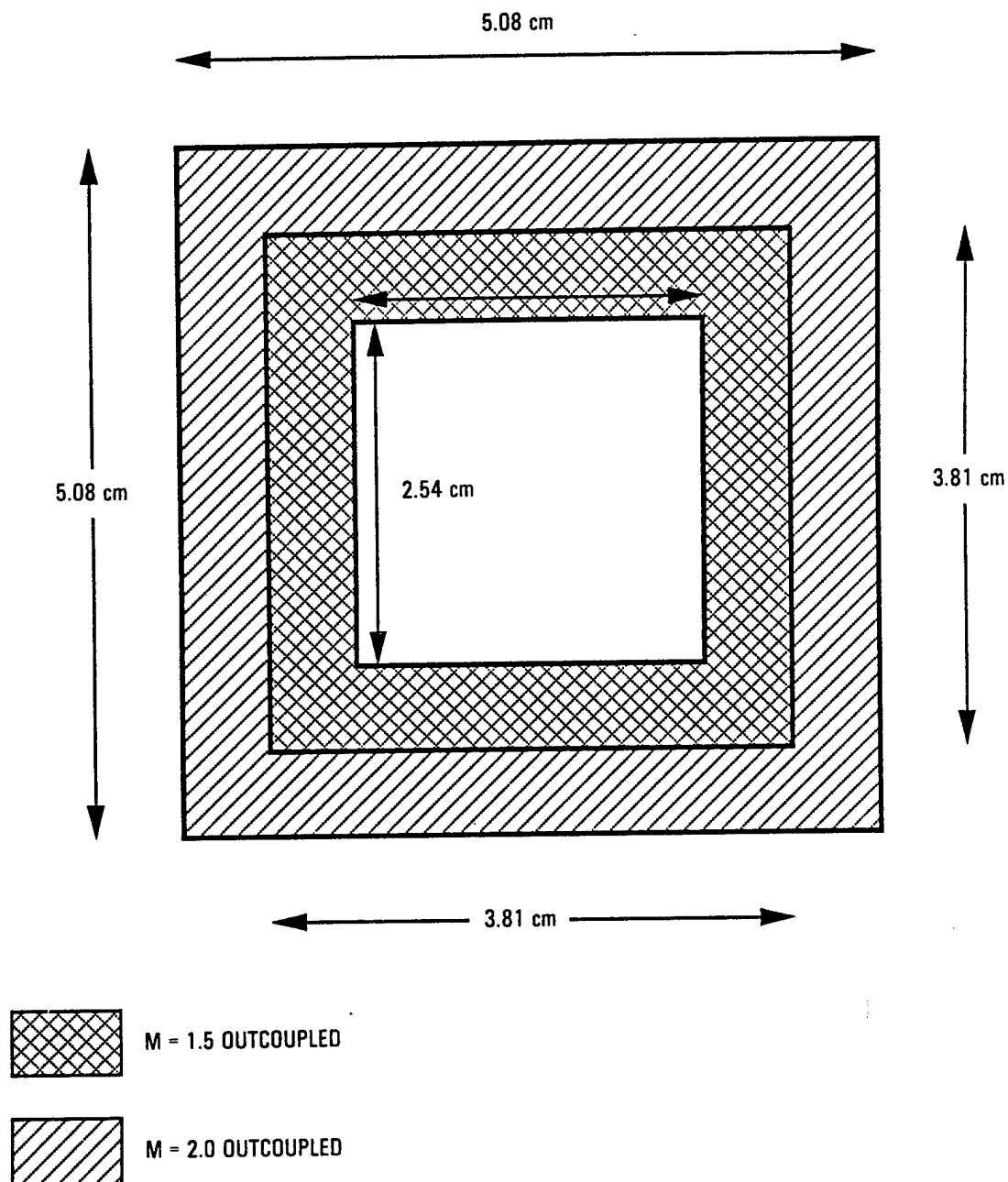
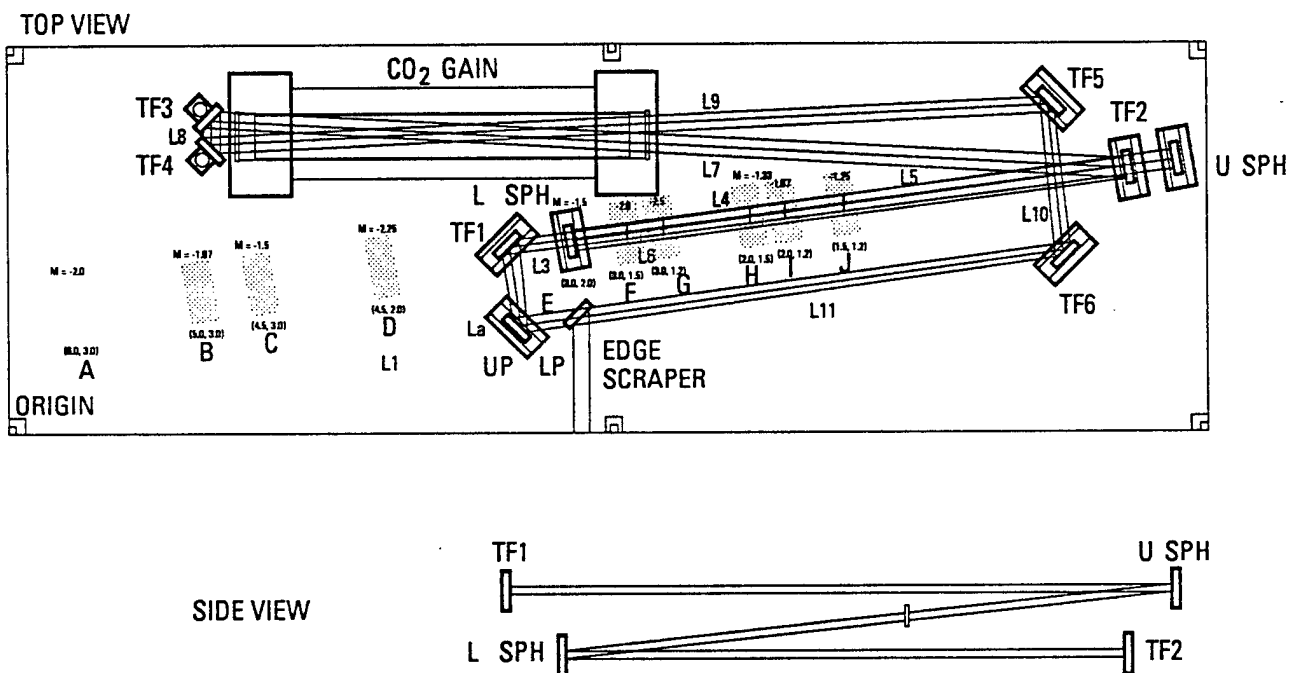


Figure 6-4. Theoretical Near-Field Image of Negative Branch Standing-Wave Resonator



01M.160.90.08-5005

Figure 6-5. Negative Branch Unstable Ring Resonator Layouts

The design includes an internal focus to study reimaging and potential reverse wave suppression techniques, although an additional reverse wave suppressor mirror is included behind the scraper. For  $M = 1.5$ , the reverse wave suppressor (RWS) mirror, is located between the periscope lower mirror and the scraper, 53 cm behind the scraper.

Ring resonators are attractive for high-power chemical lasers. However, these resonators can support waves that propagate in either the forward or reverse directions. Efficient extraction requires either suppression or utilization of the reverse wave. In resonators such as the one used on ALPHA, there is an automatic suppression associated with the fact that the forward-wave mode envelope is well matched to the gain region, and the reverse-wave envelope is not. Sometimes further suppression is achieved by means of a RWS mirror. The RWS mirror reinjects the reverse wave output into the resonator forward direction and is adjusted to reinforce the forward wave while suppressing the reverse wave. Only a small fractional return is necessary to achieve excellent rejection. Experimentally, for the selected OI resonators it was found that a flat located behind the outcoupling scraper was sufficient. At that location the reverse wave has a substantial radius of curvature and thus is not mode matched to the RWS mirror. The RWS mirror is approximately aligned normal to the optical axis. In the geometrical optics limit when a portion of the reverse wave is reflected by the RWS mirror, it makes one pass through the gain medium and then is absorbed by the beam-clipping aperture located near the scraper. Some further leakage into the forward wave occurs as a result of diffraction. In addition, the alignment process may lead to minor deviations from the nominal position.

The beam double passes the gain medium and crosses in the middle of the gain generator similar to the previously described negative branch unstable standing wave resonators. The round-trip path length for  $M = 1.5$  is 18.87 m, and thus,  $c/2L$  and  $c/L$  are 7.95 and 15.9 MHz, respectively. For  $M = 1.77$ , the round-trip path length is 16.59 m, and  $c/2L$  and  $c/L$  are 9.04 and 18.08 MHz, respectively.

The output polarization is circular and exhibits a temporal periodicity in handedness, i.e., left-handed circular versus right-handed circular as measured by a quarter waveplate (300 order) and linear polarizer. Typically, data are collected for the vertical, s, polarization because this is the polarization least attenuated by the optical train and acousto-optic modulators.

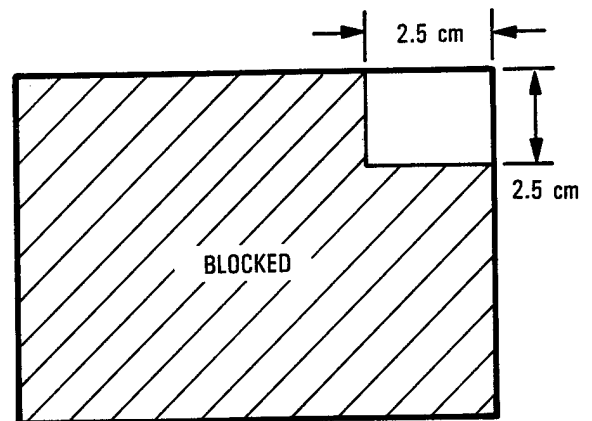
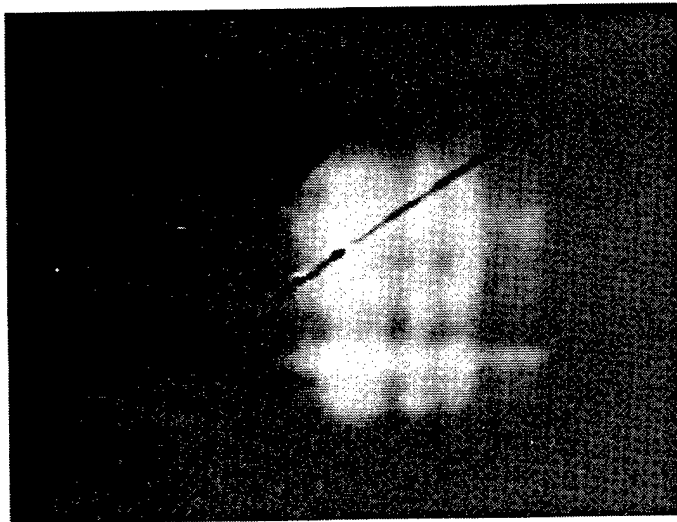
The outcoupled forward-wave energy of the ring resonator for  $M = 1.5$  is approximately 400 mJ without the reverse-wave suppressor. However, with the reverse wave suppressor, the energies increased to  $\geq 600$  mJ ( $M = 1.5$ ) and 1.0 J ( $M = 1.77$ ).

The near-field profile of the intracavity beam is rectangular and exhibits slight Fresnel ringing as does the outcoupled beam. Figure 6-6 illustrates the near-field intensity pattern for  $M = 1.5$ . The theoretical outcoupled beam height and width are approximately  $4.85 \times 5.71$  cm ( $M = 1.5$ ), and  $7.56 \times 6.27$  cm ( $M = 1.77$ ). Measured values are  $4.1 \times 4.95$  cm ( $M = 1.5$ ), and  $7.2 \times 6.5$  cm ( $M = 1.77$ ). The beam quality for both magnifications is approximately  $1.07 \pm 0.02$  for the unperturbed ring resonator, and was found to be independent of the reverse wave suppressor mirror.

### 6.3.3 Optical Layout and Diagnostics

The optical system layout for the oscillator isolation experiments is shown as a block diagram in Figure 6-7, and in detail in Figure 6-8. The optical system is designed to accommodate variable resonators, scraper positions, and resonator magnifications with minimal change. One optical bench is dedicated to the resonator, and three additional benches house the external optical train and diagnostics. The benches are enclosed in plexiglass to reduce atmospheric turbulence and for operational safety.

Significant design characteristics of the optical train are as follows. The scraper is image relayed through the acousto-optic modulators (AOMs) and onto the return flat mirror to maintain integrity of the near-field intensity distribution fed-back to the resonator. Two telescopes provide the image relaying and also reduce the beam size to fit through the small AOM apertures. The optical train favors vertical polarization, and



**REVERSE WAVE SUPPRESSOR  
MIRROR PARTIALLY BLOCKED**

Figure 6-6. Near-field Intensity Profiles of Outcoupled Beam From  
OI Negative-Branch Unstable Ring Resonator



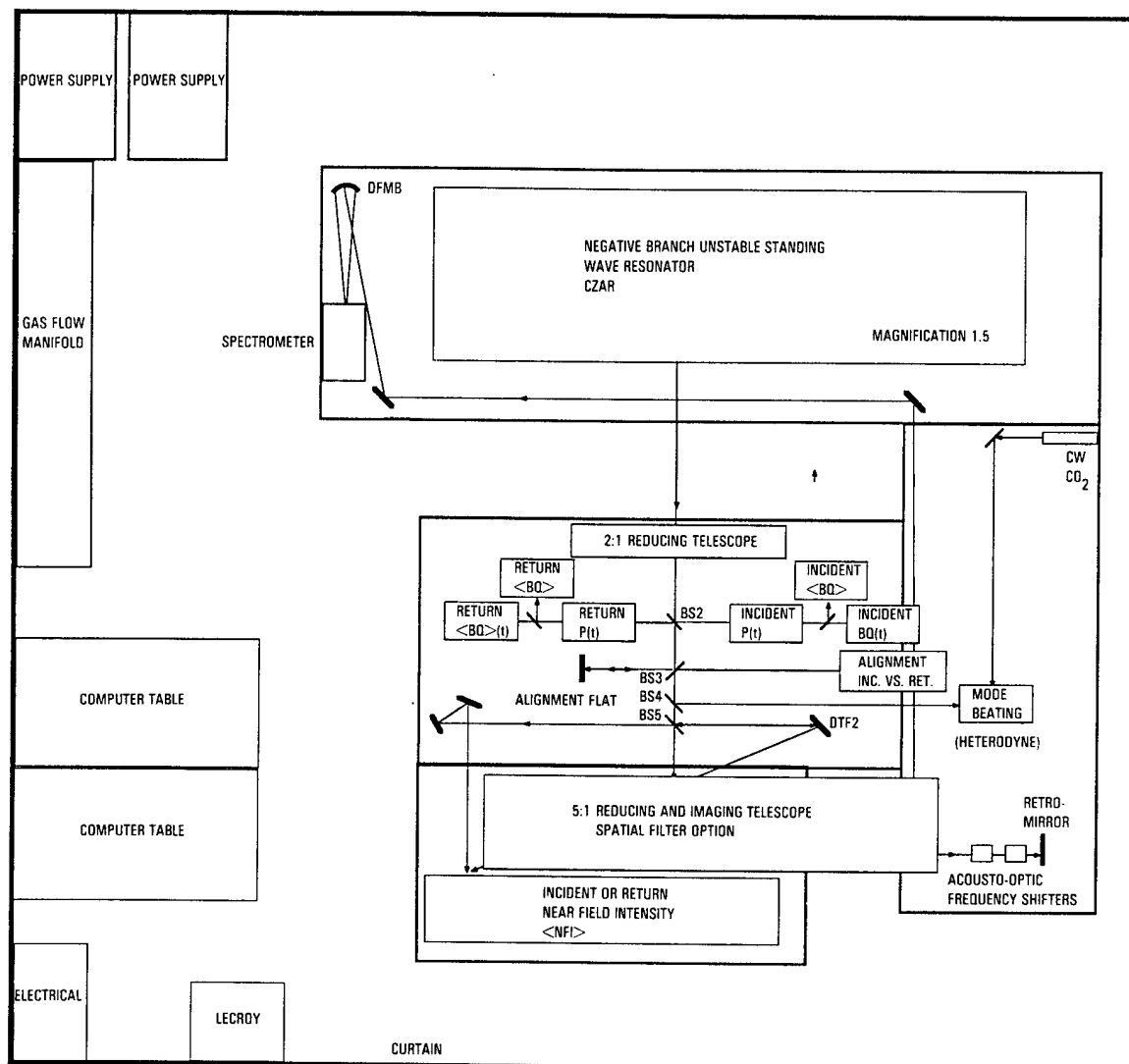


Figure 6-7. OI CO<sub>2</sub> Experiment Diagnostics

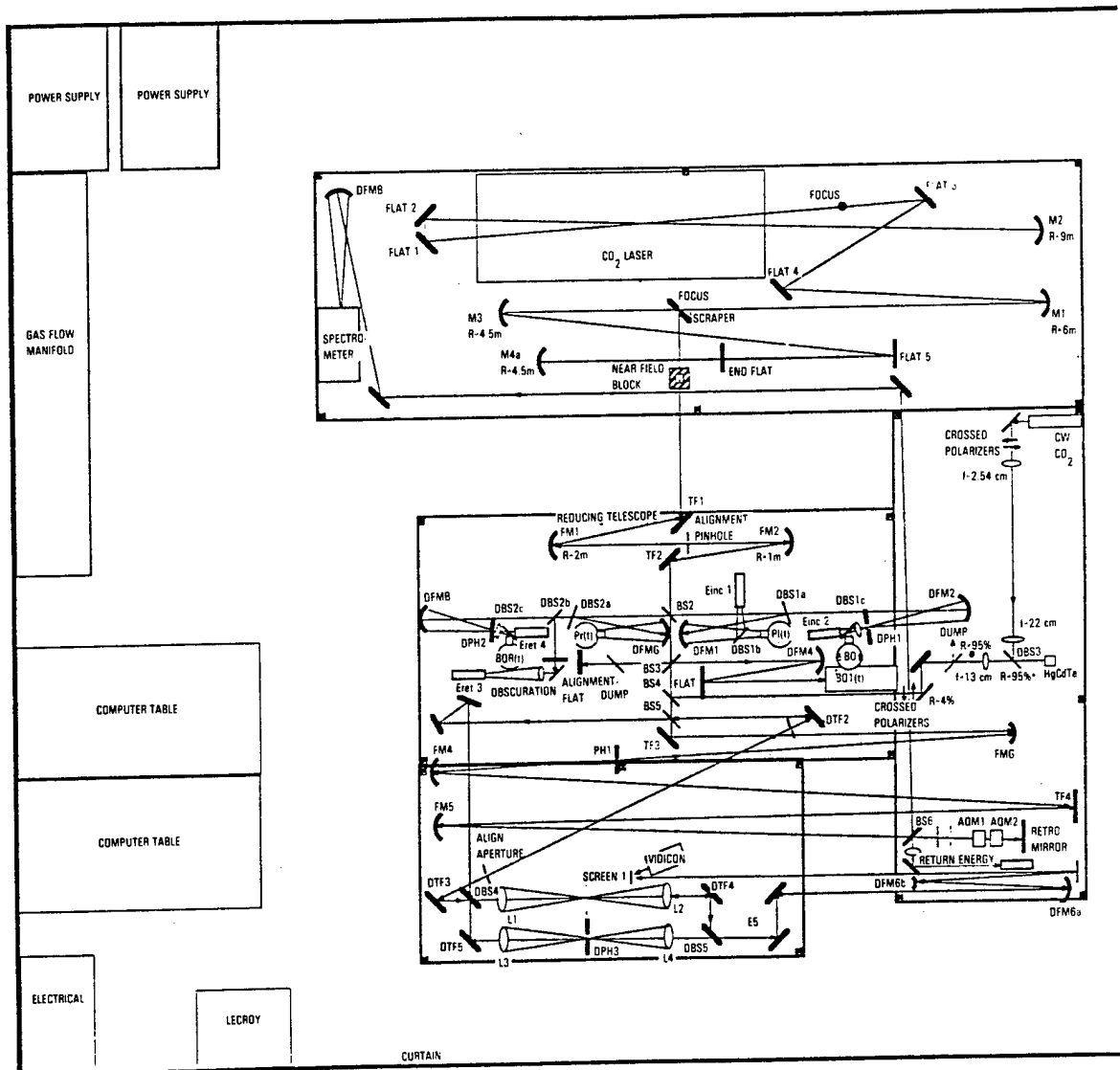


Figure 6-8. Detailed NBSW Optical Train and Diagnostics Layout

the individual beamsplitters and mirrors do not degrade the beam by a measureable amount. The use of transmissive elements is minimized to prevent uncontrolled feedback into the resonator.

The length of the optical train from scraper to return mirror is ~27.9 m. The return mirror is used to vary the alignment of the frequency-shifted return beam in the horizontal direction, i.e., parallel to the plane of the optical bench. A quarter-wave plate and polarizer are added to the optical train for the ring-resonator experiments since this resonator produces circular polarization and the optical train requires vertical, s, polarization. Also, at  $M = 2$  for NBSW and  $M = 1.5$  for the ring resonator, the demagnification of the first telescope is 4:1 instead of 2:1. The demagnification increases to 6.2:1 for the  $M = 1.77$  ring resonator.

The acousto-optic modulators depicted in Figure 6-10 are used to simulate the SBS frequency shift of the return beam and also to attenuate the return beam from a maximum return fraction of approximately  $1 \times 10^{-2}$  to  $1 \times 10^{-5}$ . The AOMs are turned on for  $500 \mu s$ , ~590  $\mu s$  after the beginning of the pulse. Thus, it is possible to obtain data without return and with return on a single shot. Two AOMs are used in series and double passed. Figure 6-9 illustrates the orientation of the two AOMs. The first AOM upshifts the frequency of the incident beam, and the first order exists AOM 1 at the Bragg angle. This beam hits the second AOM, which downshifts the beam by a greater amount. The first order from the second AOM hits the return end mirror at normal incidence and then retraces its path through the AOMs and back to the resonator. The net frequency shift is the difference between the AOM frequency settings multiplied by a factor of 2. Increments as fine as 1 kHz can be obtained. The maximum frequency shift attainable in this configuration is 40 MHz since the AOMs have individual frequency ranges of 30 to 40 MHz and 40 to 50 MHz, respectively. Shifts between 0 MHz and the longitudinal mode spacing for the given resonator are typically used. The AOM RF power setting is used to attenuate the return beam.

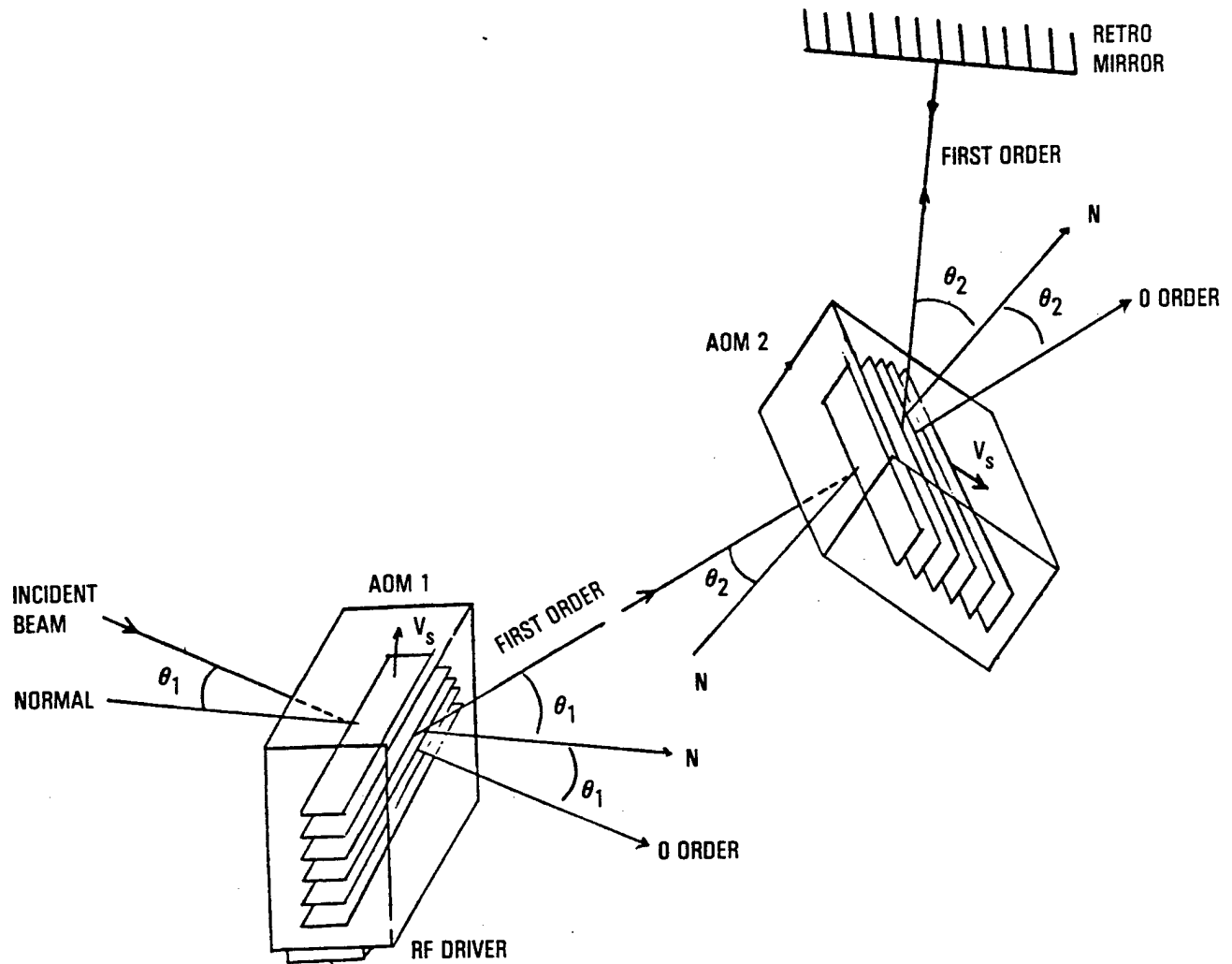


Figure 6-9. Acousto-optic Modulators Used to Frequency Shift Return Beam

The diagnostics are shown in Figure 6-8. Beam quality versus time is the primary diagnostic. Beam-quality measurements can be made just before and just after the AOMs are turned on, i.e., with and without the return beam within the same pulse. Time-resolved beam quality is measured by HgCdTe detectors with a bandwidth of approximately 10 MHz, which record power versus time for the total outcoupled power and for power through a diffraction-limited aperture. Photographs of the oscilloscope traces serve as quick-look data. Joulemeters record the outcoupled beam energy, energy through the diffraction limited aperture, and the return beam energy.

The frequency content of the CO<sub>2</sub> laser output is monitored by the heterodyne diagnostic. This consists of a signal beam from the pulsed CO<sub>2</sub> device mixed with a strong local oscillator beam from a 3 W, frequency-stabilized, CW CO<sub>2</sub> probe laser. The combination of these two beams is detected by another HgCdTe detector with bandwidth approximately 500 MHz. The sampling rate of the associated digitizer allows detection of signals up to a frequency of 100 MHz.

Diagnostics also include return beam alignment, near-field intensity, and spectral content. The horizontal and vertical alignment of the return beam is monitored by two linear Spiricon pyroelectric arrays with 256 elements with 100- $\mu$ m center-to-center spacing. The alignment can be adjusted from shot to shot, real-time, by observing the output from the linear arrays on an oscilloscope. Time-integrated near-field intensity is measured with an IR vidicon placed at the image of the near field and is recorded with a VCR. A spectrometer with phosphor display measures the time integrated spectral content of the laser output.

Two computers are dedicated to data acquisition, and Everex AT and an XT. Figure 6-10 illustrates the diagnostic control structure. The data are acquired by the LeCroy transient digitizers and frame grabber. An external timing circuit with manual control is used to arm the system and acquire the data. Multiple pulses can be acquired and downloaded to floppy disk as needed. Oscilloscopes provide quick-look data for the heterodyne and beam-quality diagnostics.

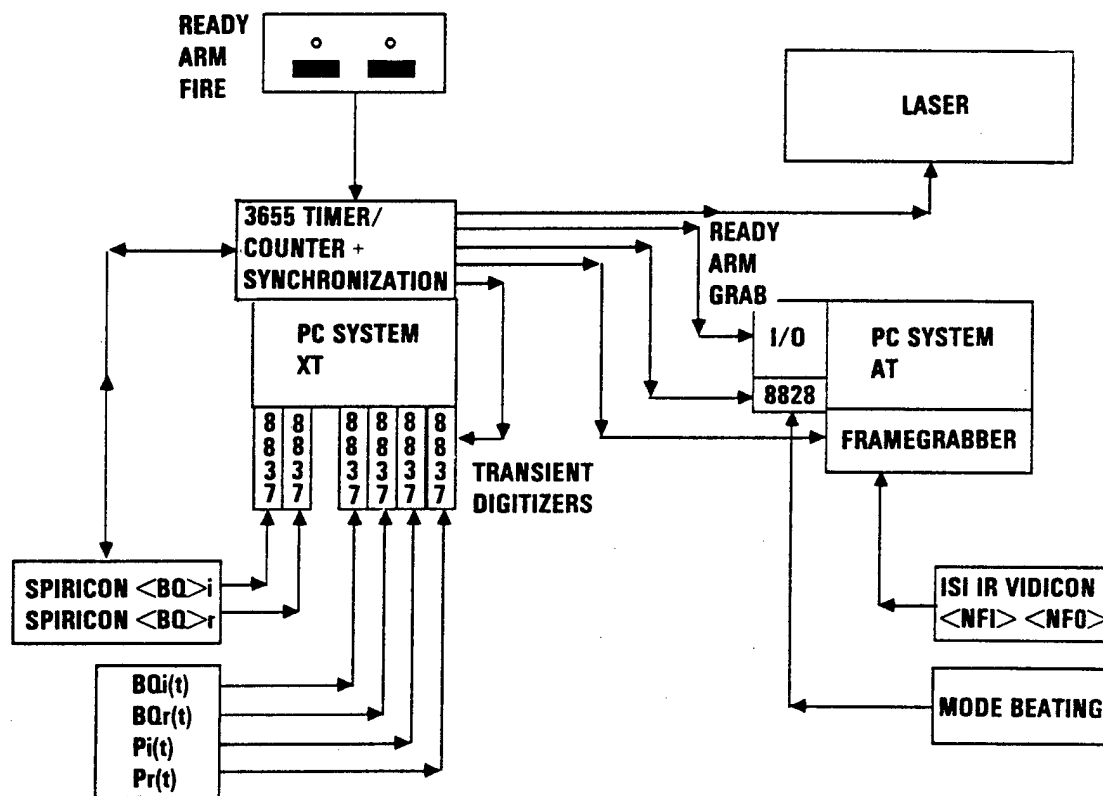


Figure 6-10. CO<sub>2</sub> Oscillator Isolation Experiment Diagnostic Control Structure

## 6.4 EXPERIMENTAL RESULTS

The main oscillator isolation tests study the dependence of beam-quality degradation on return energy fraction, return frequency shift, return beam alignment, and resonator magnification. The results for the negative branch unstable standing-wave resonator and the negative-branch ring resonator are reported in Sections 6.4.1 and 6.4.2, respectively.

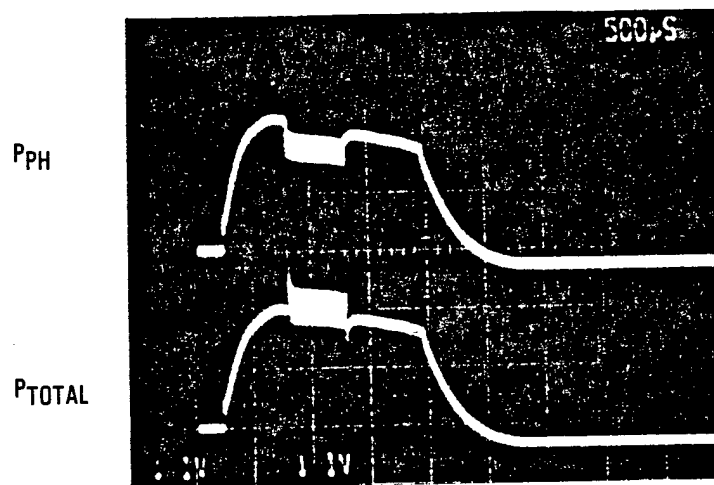
### 6.4.1 Negative Branch Unstable SW Resonator (CZAR)

The characteristics of the negative branch unstable standing-wave resonator were described in Section 6.3.2.1.

#### 6.4.1.1 Negative Branch Standing Wave Resonator Results for $M = 1.5$

The first and lowest magnification studied for the NBSW resonator is  $M = 1.5$ . Several hundred shots were recorded and analyzed to study the effect of feedback in this resonator.

Frequency shifts between 0 MHz and 9.196 MHz, i.e.,  $c/2L$ , and return fractions between 0 and  $3 \times 10^{-3}$  were studied. Small return fractions on the order of  $10^{-3}$  were sufficient to cause substantial degradations in beam quality. Data for greater return fractions became difficult to reduce as multiple frequencies in the laser output were observed and obscured the mean value of the power versus time traces. Beam-quality degradation is calculated from the two photodiode traces for power through the pinhole and total power versus time. Figure 6-11 shows typical traces for a return frequency of 6.4 MHz and return fraction of  $1 \times 10^{-3}$ . The upper trace is the power transmitted through a diffraction limited pinhole, and the lower trace is total power. The AOM (i.e., return beam) is on for approximately 500  $\mu$ s midway through the pulse as is evidenced by the beat frequency of 6.4 MHz (homodyne) present on both traces. Note the average decrease in power through the pinhole compared to the total power when the feedback is present. Independent measurements made using the Spiricon arrays verified that this drop in power through the pinhole was a result of beam quality degradation as opposed to a simple tilting of the beam. The percentage difference between the average beam quality before the return is on and while feedback is present is defined as the beam-quality degradation. Figure 6-12 shows the beam-quality degradation as a function of return for



$$R = 1 \times 10^{-3} \quad \Delta BQ = 12.2\%$$

Figure 6-11. Power Versus Time for NBSW Resonator,  $M = 1.5$ ,  $\Delta\nu = 6.4$  MHz



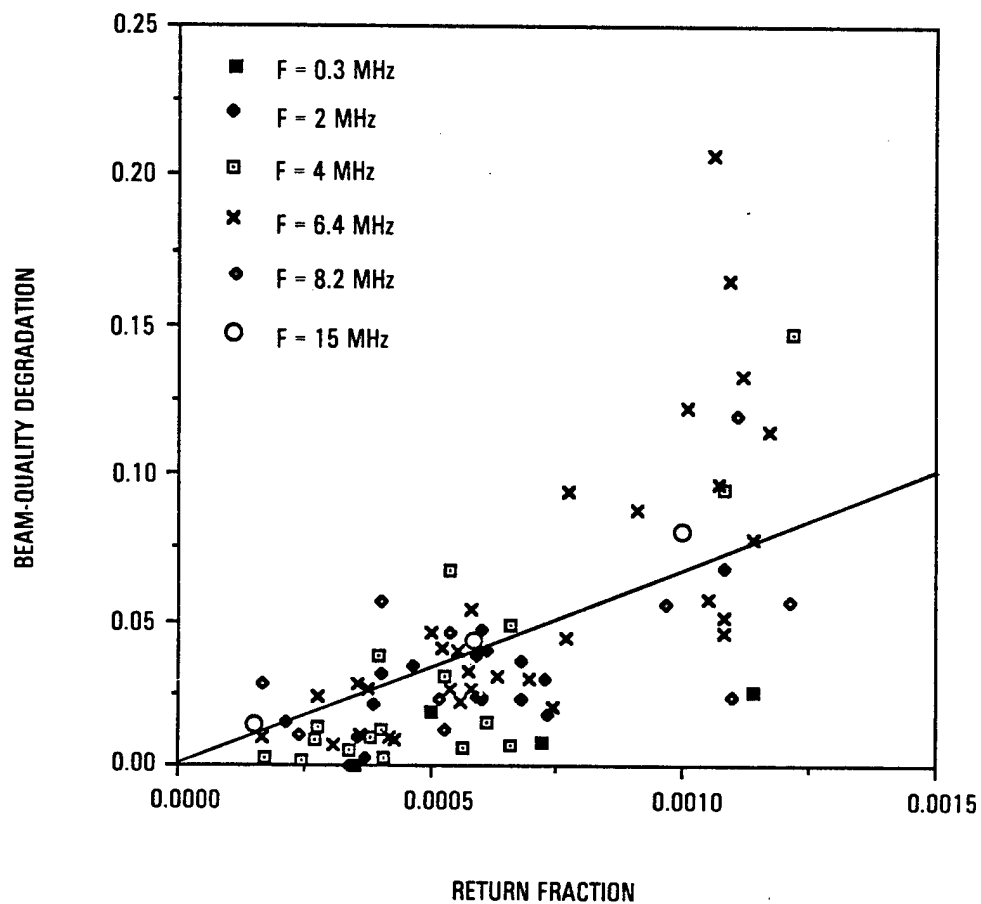


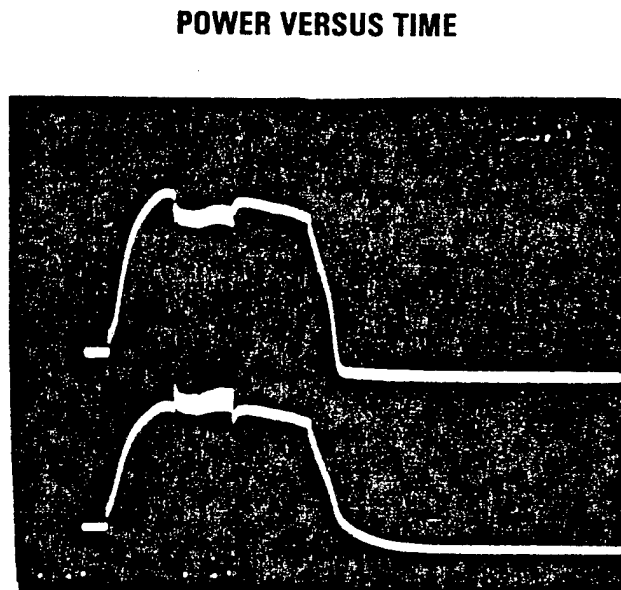
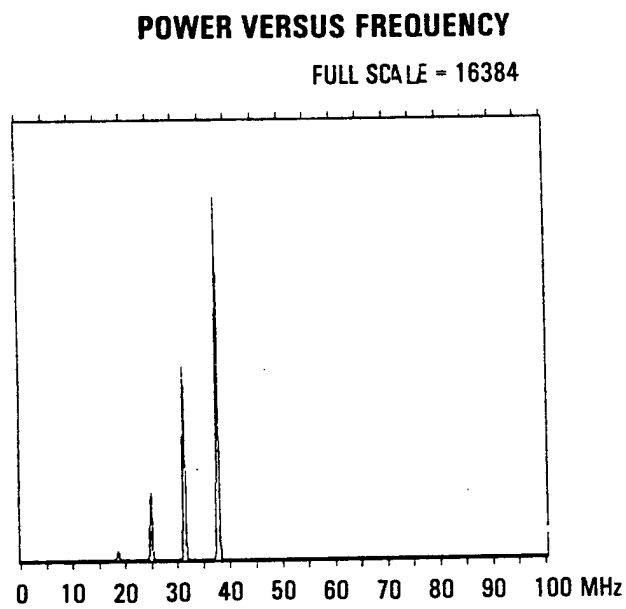
Figure 6-12. Beam-Quality Degradation Versus Return for NBSW Resonator,  $M = 1.5$

return frequencies greater than 0 MHz. As more power is returned to the resonator, the beam-quality degradation increases. A return of approximately  $7.0 \times 10^{-4}$  is sufficient to cause a 5% degradation in beam quality.

For very high returns, on the order of  $1 \times 10^{-3}$ , there are multiple-frequency shifts (cascading) that occur within the 2 ms pulse. The mode buildup time and optical train round-trip time combined is less than the AOM on time or pulse duration, i.e.,  $0.5 \mu\text{s} + 93 \text{ ns} < 500 \mu\text{s}$ , or 2 ms. Hence, the frequency-shifted return beam has time to establish itself as a mode and serve as output from the resonator to be frequency shifted again as it reaches the AOMs. Heterodyne diagnostic data in Figure 6-13 show the frequency content of the laser output. Note the multiple shifts of 6.4 MHz for this high return. Successive frequency shifts move farther from the lowest loss mode and a large degradation in beam quality is observed. Experimentally, no beam-quality dependence on return-beam frequency greater than zero has been observed for the negative-branch standing-wave resonator. There is a 5% degradation in beam quality for a return fraction of approximately  $7 \times 10^{-4}$  for frequencies 0.3, 2.0, 4.0, 6.4, 8.2, and 9.196 MHz. For a return without a frequency shift, the beam quality did not degrade for returns as high as  $7 \times 10^{-4}$ ; however, as many as three modes spaced by  $c/2L$  were present.

The response of the resonator to the return was sensitive to environmental conditions such as temperature and humidity. Also, the resonator and return beam were aligned as often as twice daily. Temperature fluctuations and slightly different resonator cavity alignments can cause a difference in resonator length and shift the position of the lowest loss mode with respect to the gain curve. This may change the effective gain that the return mode experiences which affects the amount of beam quality degradation. These sensitivities are exhibited as scatter in the data. The data for several return frequencies were typically taken over a few days.

The amplification of the return shows little dependence upon return except for zero frequency shift. The amplification is found experimentally to be approximately 150 for frequency shifts greater than zero. This is



$\Delta\nu = 6.4 \text{ MHz}$   
 $R = 1.17 \times 10^{-3}$   
 $\Delta BQ = 11.4\%$

Figure 6-13. Frequency Content of Output Beam, NBSW Resonator,  $M = 1.5$

illustrated in Figure 6-14 where return fraction versus the quantity derived in Section 6.2,  $[(1 + \Delta BQ)^2 - 1]/[1 + \Delta BQ]^2$ , is plotted for  $M = 1.5$  and  $M = 2.0$  at 6.4 MHz so that the corresponding slope of the best fit line is the return beam amplification. Analysis results are also plotted and show good comparison with experimental data.

Analysis as presented in detail in Section 6.2 shows that the amplification of the fed-back beam is the result of three factors: an amplification factor representing the gain experienced walking into and back out of the Fresnel core, a diffractive loss factor, and a frequency-dependent factor representing regenerative amplification. Analysis predicts amplifications in the range of 91 to 201 ( $M = 1.5$ ) and 840 to 1078 ( $M = 2.0$ ) for the standing-wave resonator as shown in Figure 6-14. When the fed-back beam returns at a frequency that is different than any of the lowest loss transverse modes, it excites a higher order mode with poor beam quality. As predicted by analysis, the amplification of the return mode is greater for the higher ( $M = 2$ ) magnification standing-wave resonator and, thus, beam-quality degradation is greater.

The effect of return beam misalignment has been examined for the NBSW resonator,  $M = 1.5$ . The return mirror at the end of the optical train is used to misalign the beam in a plane parallel to the optical bench while maintaining vertical alignment. The range of misalignment is limited by the clear apertures of the AOMs and is approximately  $\pm 300 \mu\text{rad}$ . The amount of angular deviation is tracked in increments of  $7.5 \mu\text{rad}$  by two linear Spiricon arrays placed vertically and horizontally in the far field of the return beam. The average return fraction is approximately  $2.77 \times 10^{-4}$  for 0.3 MHz and  $2.85 \times 10^{-4}$  for 6.4 MHz. Because of the difficulty in maintaining the same return for different alignments, only a few shots were obtained at each misalignment.

The beam-quality degradation versus return beam alignment is plotted in Figure 6-15. The beam-quality degradation remains constant within measurement capability for a frequency shift of 0.3 MHz. A slight decrease in beam-quality degradation with greater misalignment is seen for the 6.4 MHz shift. The amount of beam-quality degradation for any given misalignment does exhibit a large degree of scatter as shown in Figure 6-12. Thus, to draw a quantitative conclusion, more data are

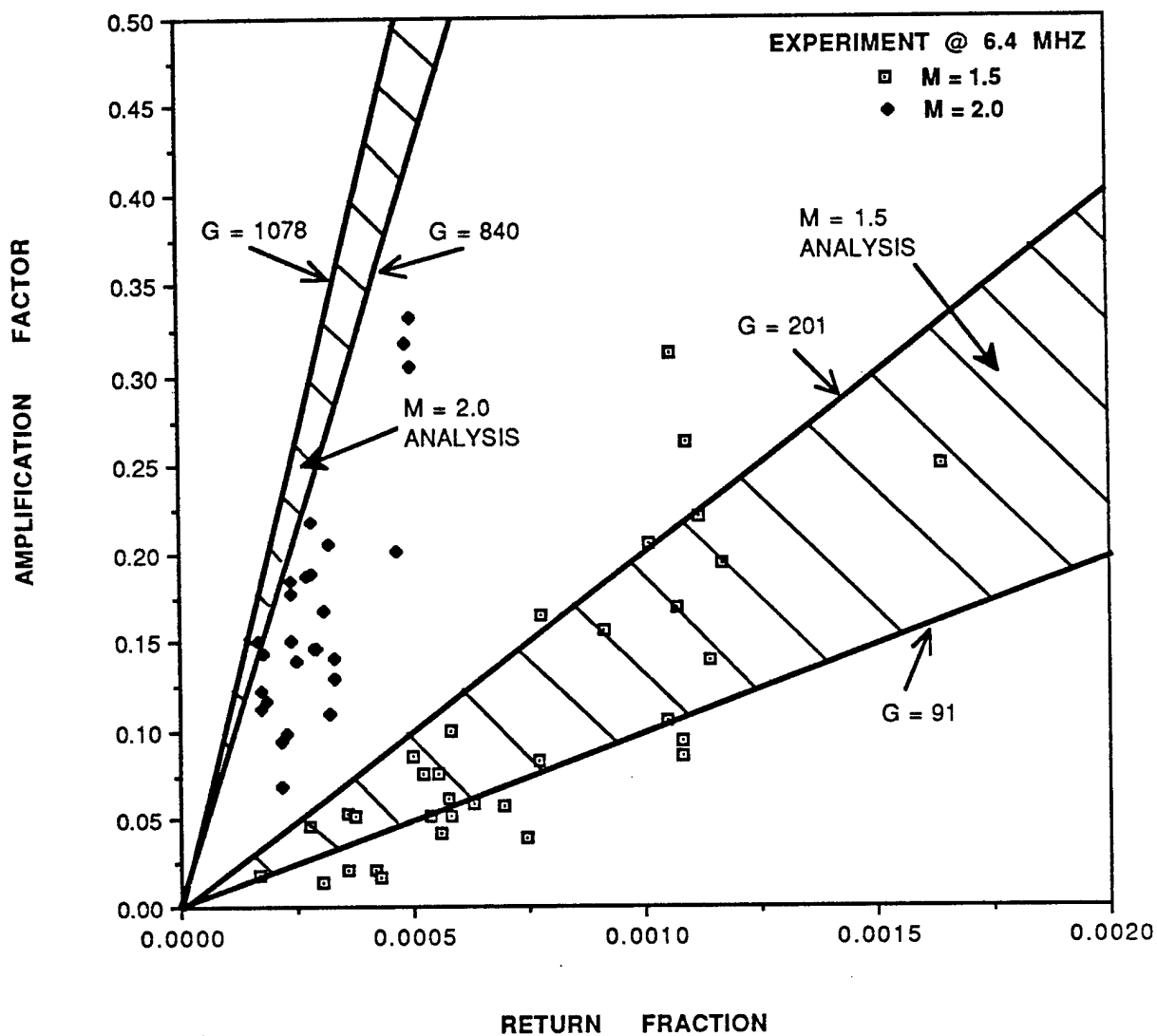


Figure 6-14. Experimental and Theoretical Return Beam Amplification for the NBSW Resonator,  $M = 1.5$  and  $2.0$  for a Frequency Shift of  $6.4$  MHz

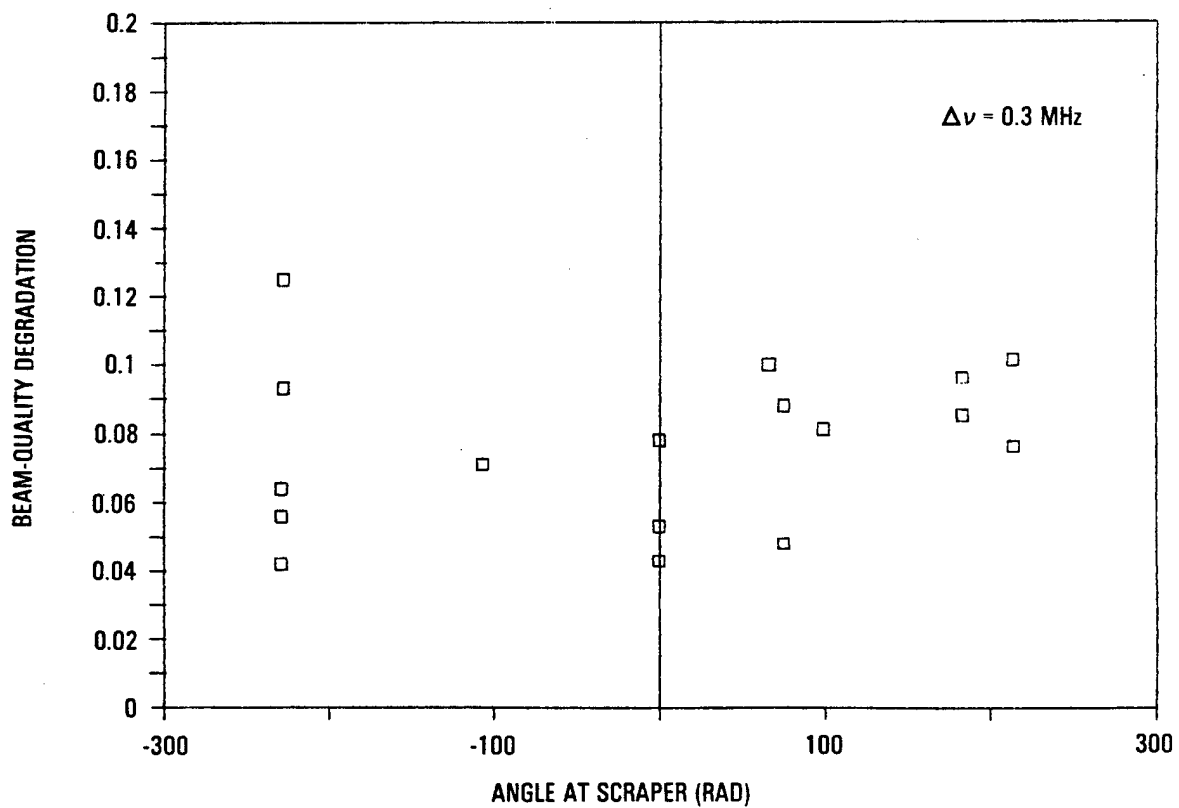
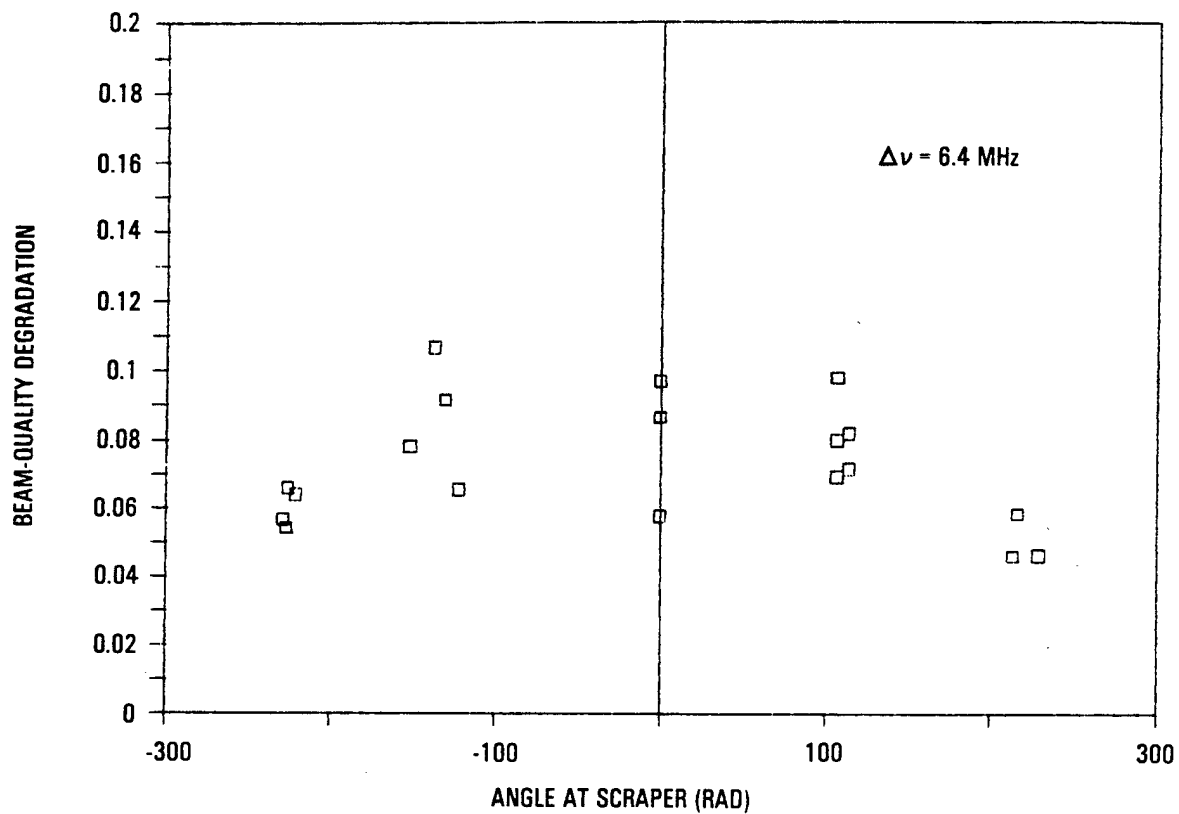


Figure 6-15. Beam Quality Degradation Versus Return Beam Alignment for NBSW Resonator,  $M = 1.5$

required for the given misalignments and the range of misalignment needs to be extended.

#### 6.4.1.2 NBSW Results for $M = 2.0$

The second and highest magnification studied for the NBSW resonator is  $M = 2.0$ . Data for frequency shifts of 0.3, 6.4, 7.5, and 9.5 MHz are reported. As described in Section 6.3.2.1, the longitudinal mode spacing for this resonator is  $\sim 9.5$  MHz.

The standing-wave resonator at  $M = 2$  exhibits greater beam-quality degradation with return than for  $M = 1.5$ . Figure 6-16 illustrates the degradation in beam quality with return for  $M = 2$  and frequency shifts of 0.3, 6.4, 7.5, and 9.5 MHz. The standing-wave resonator is five times more sensitive at  $M = 2.0$  than 1.5 (Figure 6-17). A return of  $1.5 \times 10^{-4}$  is sufficient to cause a 5% degradation in beam quality. A discussion of the theoretical dependence of magnification on beam quality degradation was included in Section 6.2.

Theoretically, both 0.3 and 6.4 MHz are relatively low loss modes. Data at 7.5 MHz are presented as a nonmode case. No dependence on return frequency is apparent. As noted previously, the amplification of the return mode is greater for higher magnification. This is illustrated experimentally in Figure 6-14 and in the power versus time traces in Figure 6-18. The amplitude of the homodyne beating is greater for  $M = 2$ .

This resonator is more sensitive to alignment of the return beam and also, daily fluctuations in room temperature. Thus, quantitative data of beam-quality degradation versus return-beam alignment were not obtained.

#### 6.4.2 Negative Branch Unstable Ring Resonator Experimental Results

The characteristics of the negative branch unstable ring resonator were described in Section 6.3.2.2.

##### 6.4.2.1 Ring Resonator Results for $M = 1.5$

The first of two magnifications studied for the ring resonator is  $M = -1.5$ . The dependence of the forward-wave output intensity and beam-quality on the return fraction and frequency shift of the return is reported. Frequency shifts of 0, 3, 6.4, 7.95 ( $c/2L$ ), and 15.9 MHz ( $c/L$ )

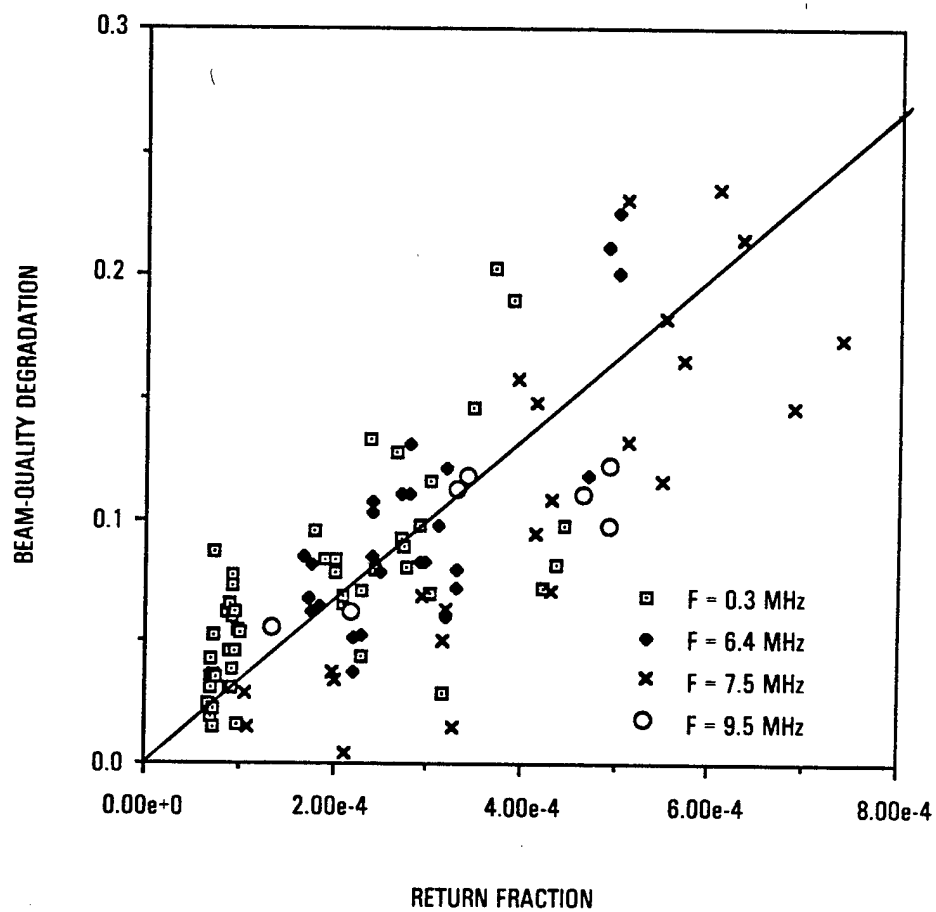


Figure 6-16. Beam-Quality Degradation Versus Return Fraction for NBSW CZAR,  $M = 2$ . (5% beam quality degradation for returns of  $1.5 \times 10^{-4}$ )



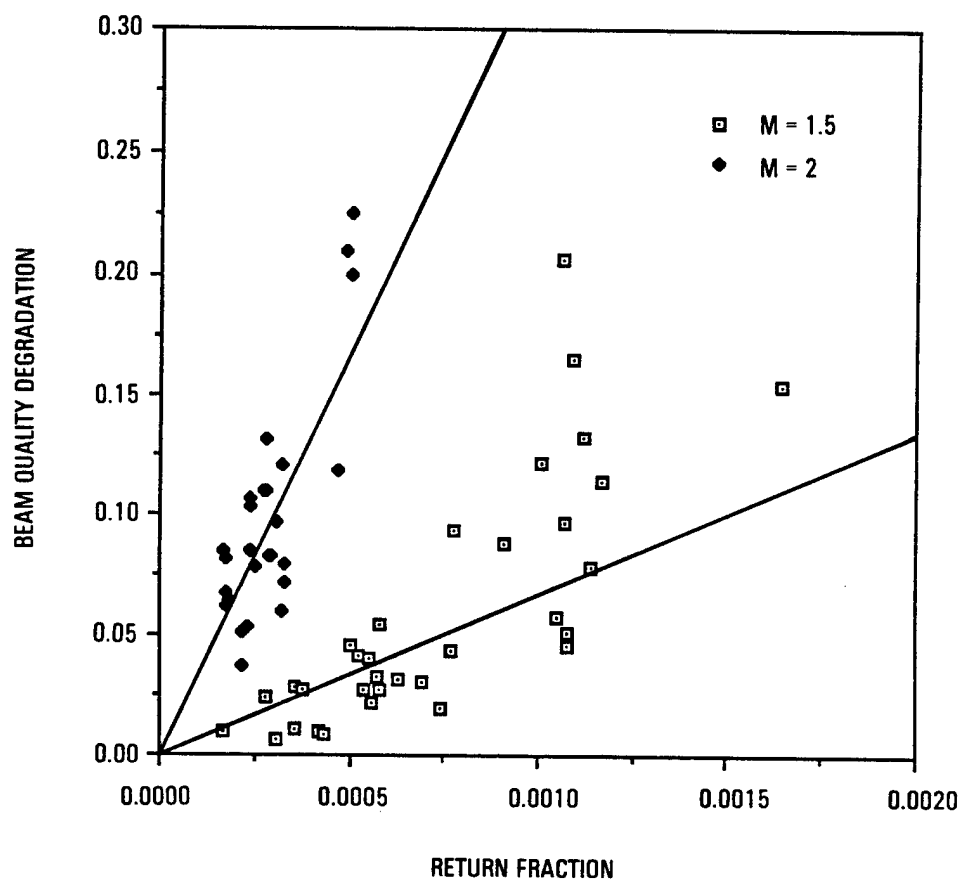


Figure 6-17. Beam Quality Degradation Versus Return for NBSW Resonator,  $\Delta\nu = 6.4$  MHz,  $M = 1.5$  and  $2.0$  ( $M = 2$  is 5 x more sensitive to return)

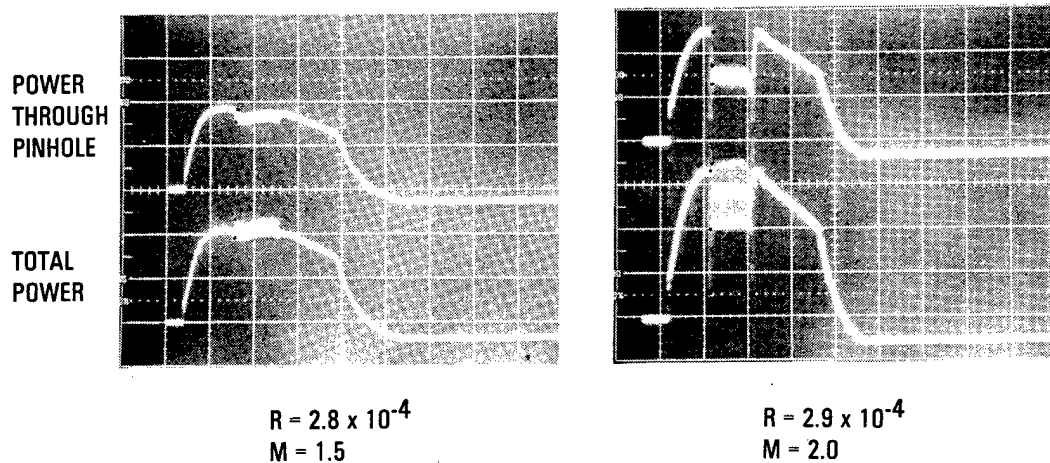


Figure 6-18. Power Versus Time for NBSW Resonators for 6.4-MHz Shift and Comparable Return. (Amplification greater for  $M = 2$  resonator)

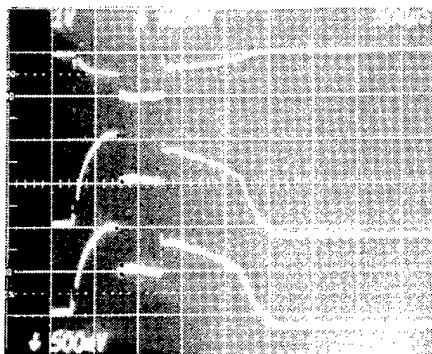
are studied, as well as shifts very near zero, e.g., 0.1, 0.2, 0.3, and 0.4 MHz. Return fractions between  $10^{-5}$  and  $10^{-2}$  and no return are typical. These ring resonators have two sets of eigenmodes, i.e., separate sets of eigenmodes for left and right circularly polarized light. Each set has a  $c/L$  spacing but with a relative offset of  $c/2L$ . Each polarization experiences a  $kL$  phase shift associated with propagation, an inversion and 90-deg rotation for every round trip in the ring resonator.

The experimental results indicate that the major effect of small return into the ring resonator is a drop in intensity of the forward wave with an increase in the reverse wave intensity. As shown in the power versus time traces in Figure 6-19, a total drop in intensity is observed without beam quality degradation. Figure 6-20 shows the intensity drop versus return fraction for frequency shifts on cavity resonance (0, 7.95, and 15.9 MHz), and nonmodes (3 and 6.4 MHz). A larger drop in forward-wave intensity is observed when the return frequency matches a cavity resonance, i.e., 0,  $c/2L$ ,  $c/L$ . For example, the ring resonator has a 10% intensity decrease for return as low as  $3 \times 10^{-4}$  and over 95% for  $2 \times 10^{-3}$  return at 0,  $c/2L$ , and  $c/L$  frequencies. It is less sensitive to return at nonmodes 3 and 6.4 MHz; an intensity drop of only 20% is observed for a return of  $2 \times 10^{-3}$ .

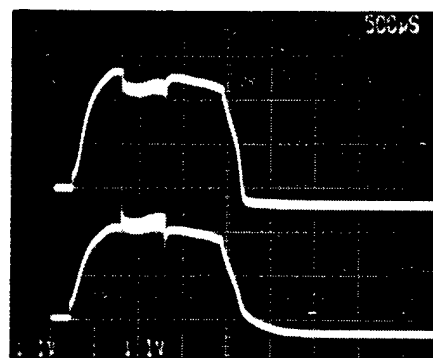
The gain of the return beam for nonmodes 3 and 6.4 MHz is shown as the slope in Figure 6-21 and is approximately equal to 150. Gain as high as 280 has also been measured. Fluctuation in the gain can be attributed to differences in daily alignment of the return mirror, resonator, and reverse wave suppressor. These data show good agreement with the analysis results derived in Section 6.5.2 in which the total gain is estimated to be between 80 and 110 for nonzero, nonresonant frequency shifts.

It is significant to note that for the ring resonator all brightness degradation caused by feedback is a result of a drop in laser power in the forward direction. No measurable beam-quality degradation is observed as shown in Figure 6-22. This is in contrast to results obtained with the standing-wave resonator where the major effect of return on brightness degradation is degradation of beam quality. In the ring resonator, the injected signal is amplified and decreases power. Beam quality is unchanged because the outcoupling is internal.

M = 1.5      F = 6.4 MHz



RING RESONATOR  
 $\Delta BQ = 0\%$   
 INTENSITY DROP = 48%  
 $R = 4.69 \times 10^{-3}$



NBSW RESONATOR  
 $\Delta BQ = 11.4\%$   
 $R = 1.17 \times 10^{-3}$   
 POWER THROUGH PINHOLE DECREASES  
 COMPARED TO TOTAL POWER WITH RETURN

Figure 6-19. Power Versus Time for Ring Resonator and NBSW Resonator,  
 M = 1.5,  $\Delta V = 6.4$  MHz

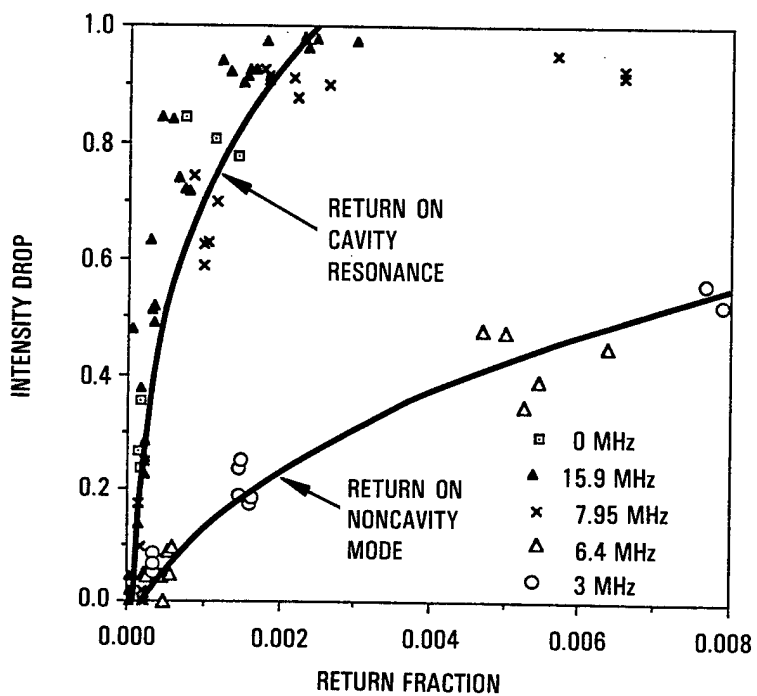


Figure 6-20. Intensity Drop Versus Return Fraction for Ring Resonator,  $M = 1.5$

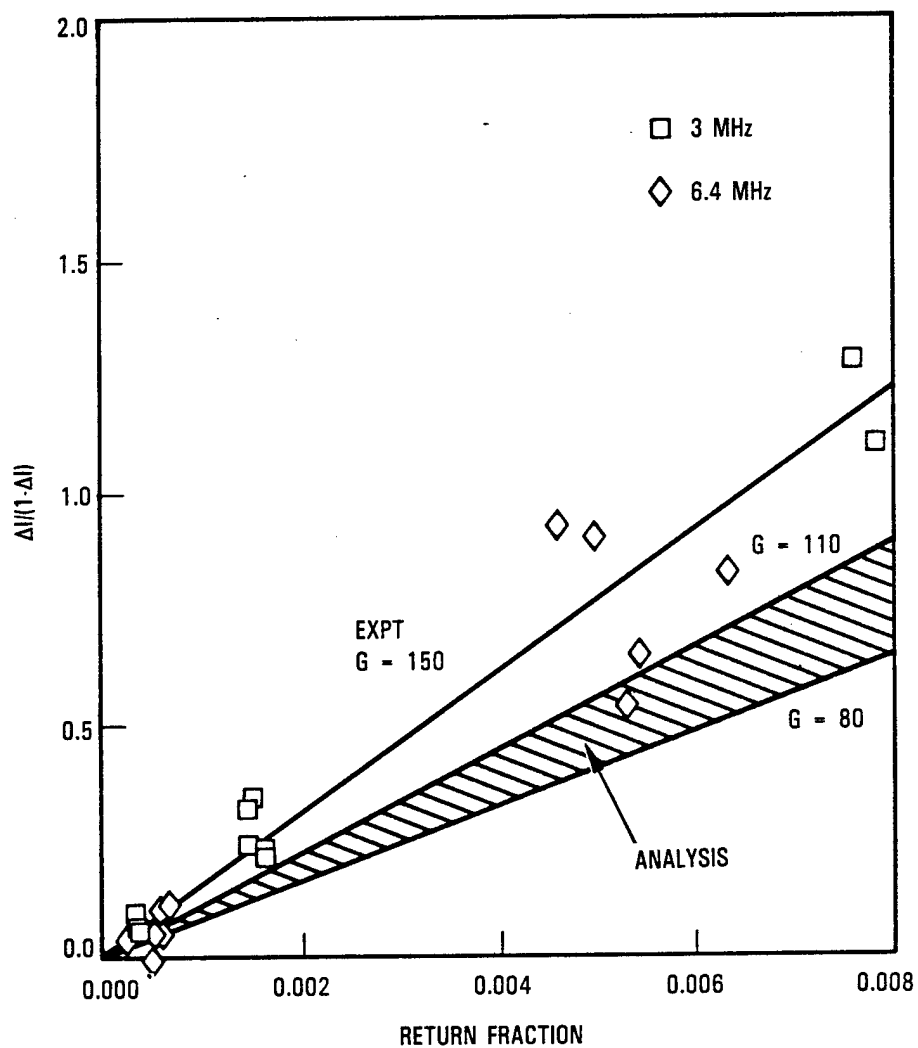


Figure 6-21. Ring Resonator,  $M = 1.5$ , Gain of Return Beam

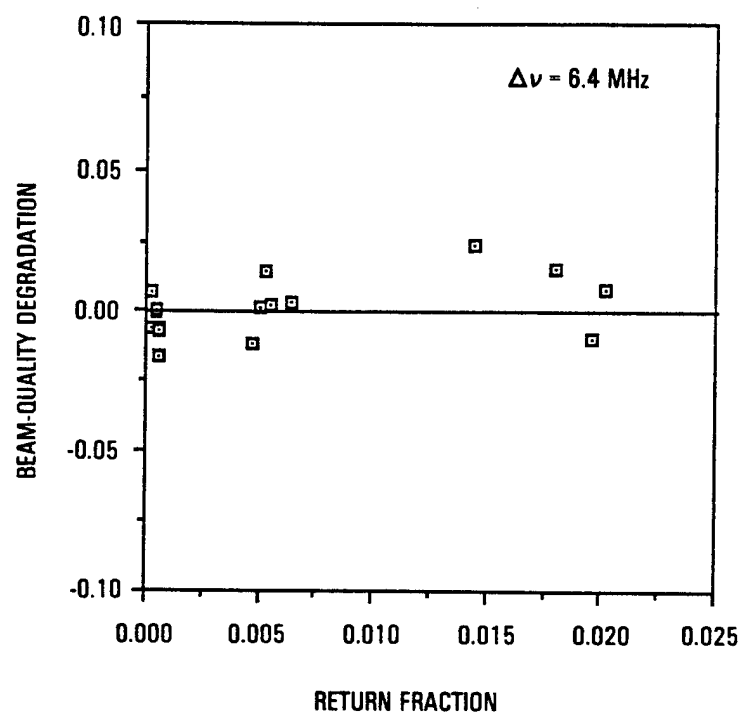


Figure 6-22. Beam-Quality Degradation Versus Return Fraction for Ring Resonator,  $M = 1.5$

The intensity drop for frequencies near zero ( $\pm 0.1$ ,  $\pm 0.2$ ,  $\pm 0.3$ , and  $\pm 0.4$ ) is plotted in Figure 6-23 for a constant return fraction of approximately  $1 \times 10^{-4}$  ( $\sigma = 0.7 \times 10^{-4}$ ). A monotonic decrease in intensity is observed with the largest drop at zero frequency shift and a minimal drop at  $\pm 0.4$  MHz. The behavior of the ring resonator for a return near a strong resonance is analogous to injection locking, where the gain is proportional to the inverse square of the frequency. This is shown experimentally in Figure 6-24 in which the relative gain is plotted versus frequency shifts of 0.1, 0.2, 0.3, and 0.4 MHz. Figure 6-25 shows the power versus time traces for frequency shifts near zero. Note the decrease in intensity drop when the return is on at successively higher frequency shifts. Also, the drop in power through the pinhole in the presence of return is comparable to the drop in total power; hence, the beam quality does not degrade with return.

The analysis results are presented in Section 6.5 and compared with these experimental values.

#### 6.4.2.2 Ring Resonator Experimental Results for $M = 1.77$

The second and highest magnification of the ring resonator is  $M = 1.77$ . Magnifications greater than this were subject to excessive clipping by the existing gain medium and associated optics and, thus, were not studied.

The ring resonator at higher magnification is more sensitive to return. The intensity drop for a return of  $5.2 \times 10^{-3}$  at 6.4 MHz is more than a factor of 2 greater for  $M = 1.77$  than for  $M = 1.5$ . The intensity drop as a function of return fraction is plotted for the nonmode frequency shifts, 3 and 6.4 MHz, in Figure 6-26. For a return of  $5.4 \times 10^{-3}$  and frequency shift of 6.4 MHz, the intensity drop is approximately 80% compared to 35% for  $M = 1.5$ . The gain of the return beam for nonmodes 3 and 6.4 MHz is shown as the slope in Figure 6-27 and is approximately equal to 1250. This is a factor of 8 higher than the gain for  $M = 1.5$ .

Analysis as derived in Section 6.5.2 predicts net amplification factors of 370 to 600 for nonresonant frequency shifts in the ring resonator,  $M = 1.77$ . The difference between experimental results and



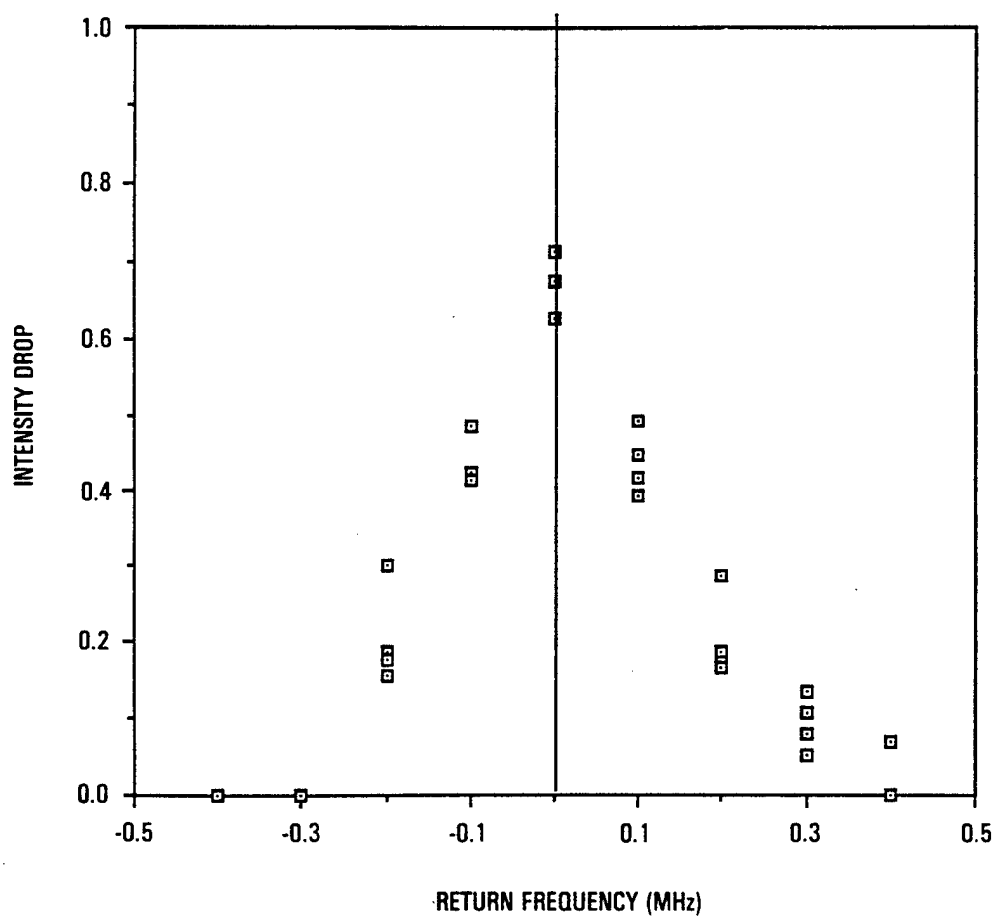


Figure 6-23. Intensity Drop Versus Frequency for Ring Resonator,  
 $M = 1.5$

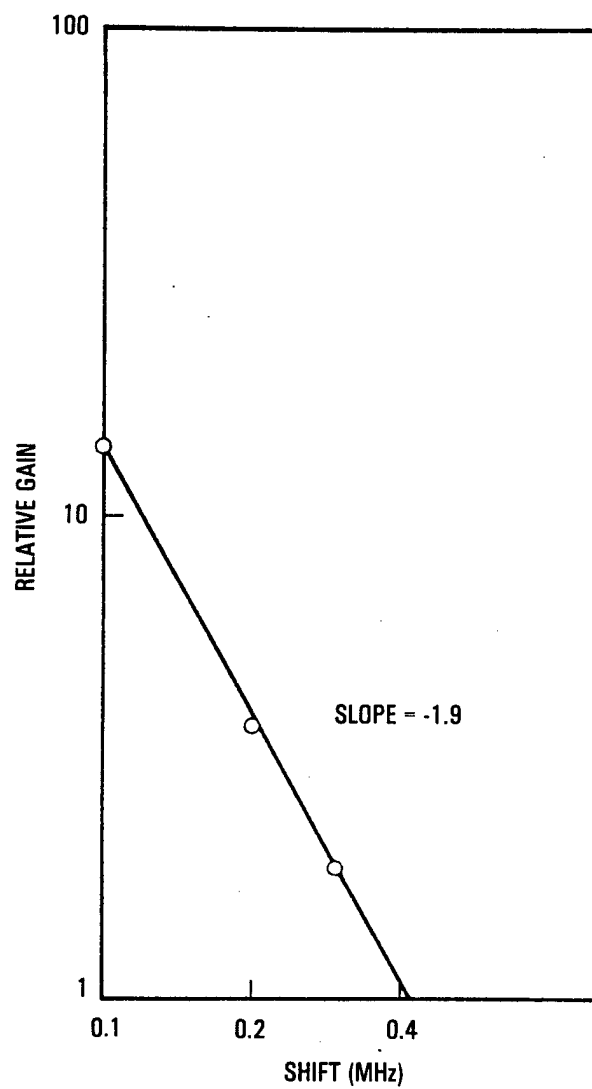


Figure 6-24. Gain Behavior Near Zero Frequency Shift

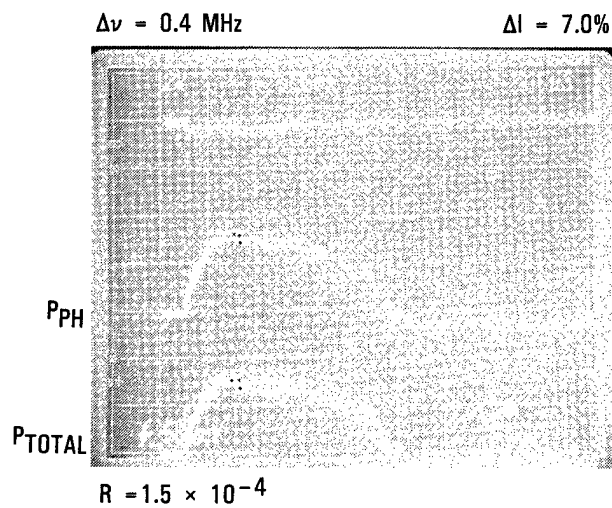
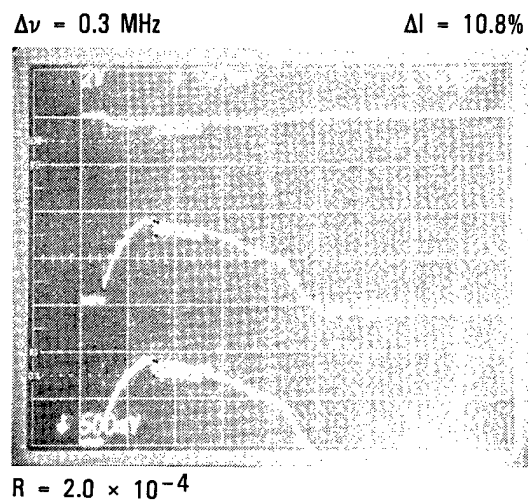
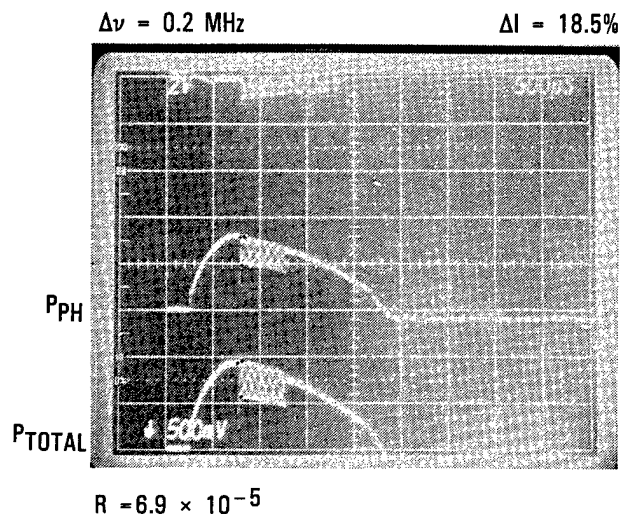
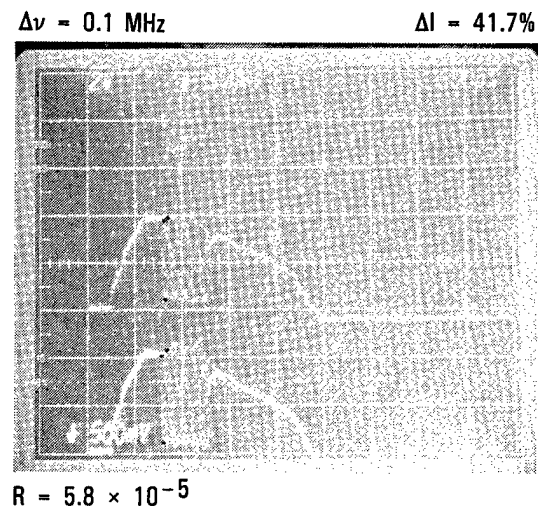
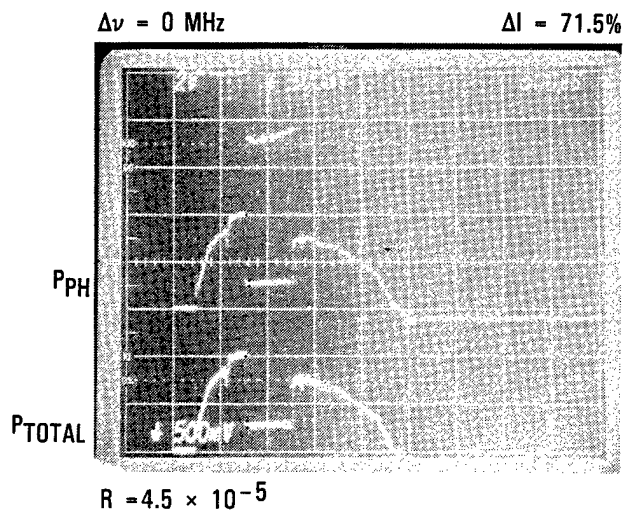


Figure 6-25. Ring Resonator, Effect of Frequency Shift Near Zero,  
 $M = 1.5$

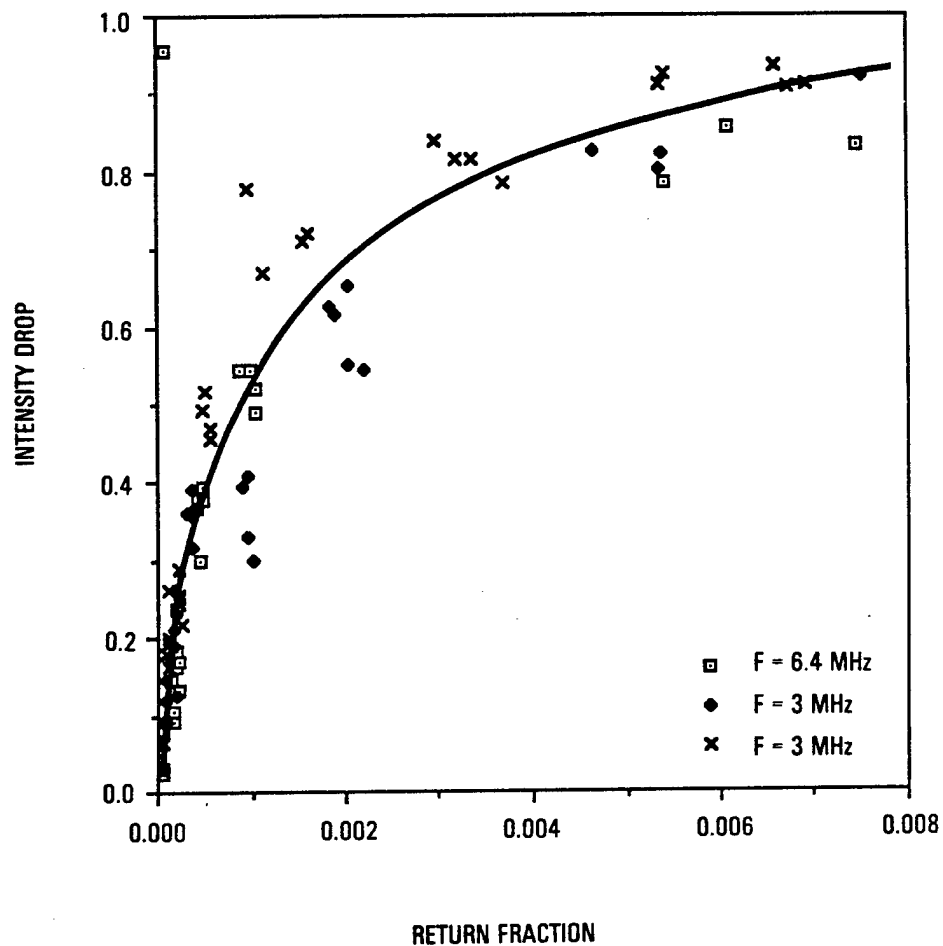


Figure 6-26. Intensity Drop for Ring Resonator,  $M = 1.77$ , as Function of Return Fraction (Nonmode frequency shifts plotted)

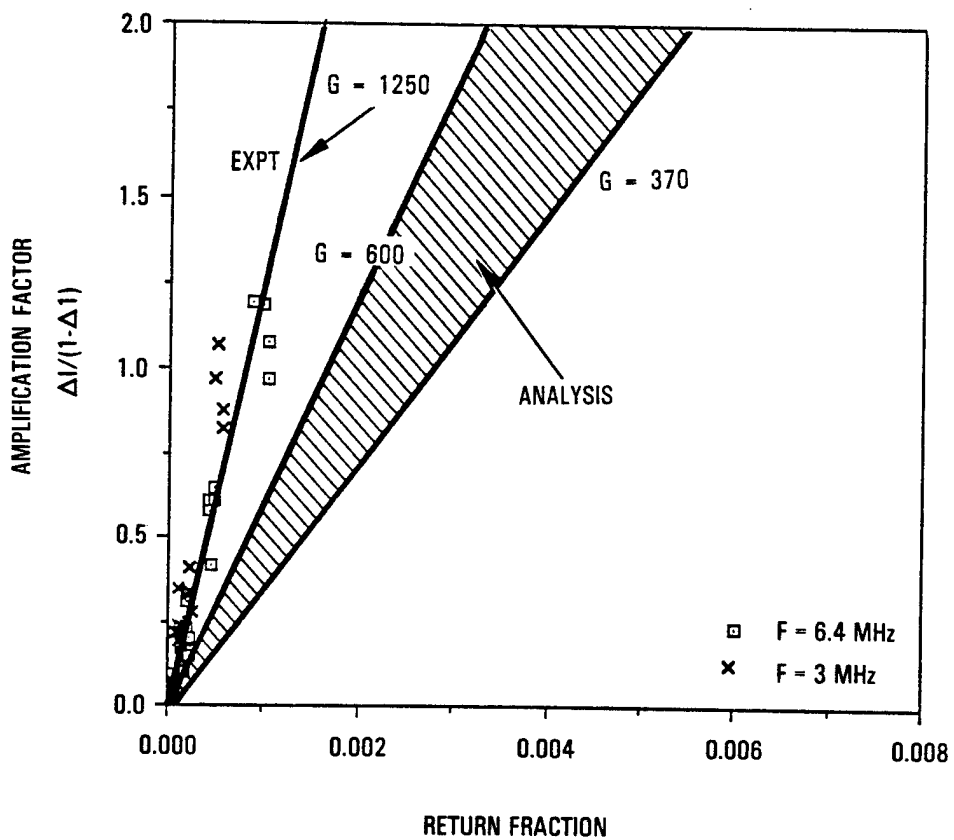


Figure 6-27. Ring Resonator,  $M = 1.77$ , Gain of Return Beam

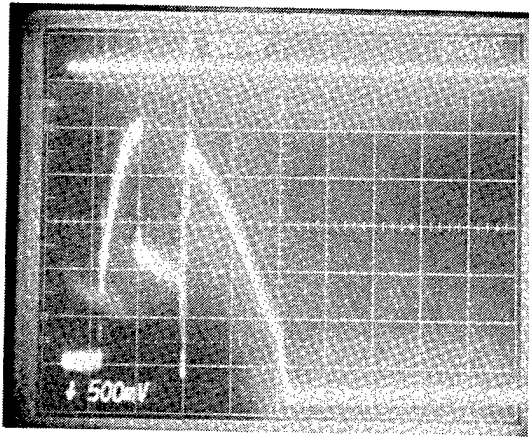
analysis may be attributed in part to the effect of the reverse wave suppressor mirror. For a perfectly aligned RWSM, some fraction of the return beam may miss the clipping aperture near the scraper. This robs additional power from the gain medium and does not emerge as part of the forward wave output.

The effect of frequency shifts near  $c/2L$  have been studied for the frequency range 9.04 to 9.44 MHz in increments of 0.1 MHz. A resonance is indicated at 9.14 MHz which shows increased intensity drop: 77% for a return of  $5.3 \times 10^{-4}$  at 9.14 MHz versus 34% for a comparable return of  $5.4 \times 10^{-4}$  at 9.44 MHz.

The frequency dependence at resonance is sensitive to the effectiveness of the reverse-wave suppressor mirror. The forward-wave intensity drop for 0 MHz shift ranges from 63 to 78% for  $M = 1.77$  at a return of  $5.5 \times 10^{-5}$ . This is comparable to results for  $M = 1.5$ , where the intensity drops between 63 and 72% for no shift at approximately  $4.5 \times 10^{-5}$  return. The scatter in the data, particularly for  $M = 1.77$  can be attributed to the effectiveness of the RWS mirror as described in Section 6.3.2.2.

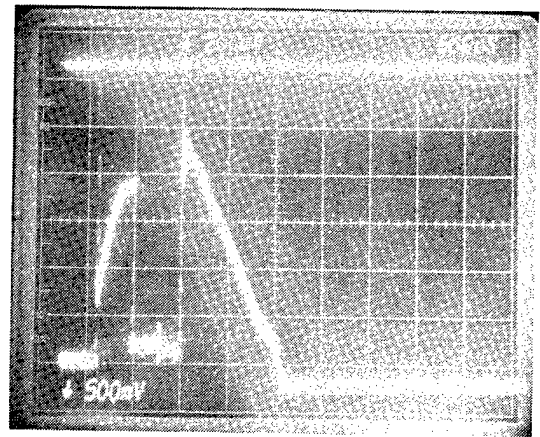
The effect of partially blocking the RWS mirror was studied for  $M = 1.77$  at 0, 3, and 9.04 MHz. The RWS is located 26.5 cm behind the scraper mirror, normal to the optical axis, and only 3 mm of the mirror is exposed in the partially blocked condition. Figure 6-28 illustrates the effect of the RWS. For no shift, there is a factor of 1.7 decrease in the outcoupled intensity when the RWS is partially blocked compared to when it is unblocked; the intensity drops for unblocked RWS and blocked at a return of approximately  $2 \times 10^{-4}$  are 55 and 90%, respectively. At a frequency shift of 9.04 MHz,  $c/2L$ , and an average return of  $4.8 \times 10^{-4}$ , there is a factor of 2.7 increase in outcoupled intensity for a partially blocked RWS; the intensity drops for unblocked and blocked cases are 59 ( $R = 3.4 \times 10^{-4}$ ) and 22% ( $R = 6.1 \times 10^{-4}$ ), respectively. For nonmodes, the intensity drop increases by a factor of 1.2 when the RWS is partially blocked, i.e., less energy is outcoupled. At 3 MHz the intensity decrease is 55% for unblocked RWS ( $R = 1.4 \times 10^{-3}$ ), and 45% for partially blocked RWS ( $R = 1.7 \times 10^{-3}$ ). If the RWS mirror is blocked more than 3 mm, the total power in the forward

$\Delta\nu = 0$  MHz UNBLOCKED RWS



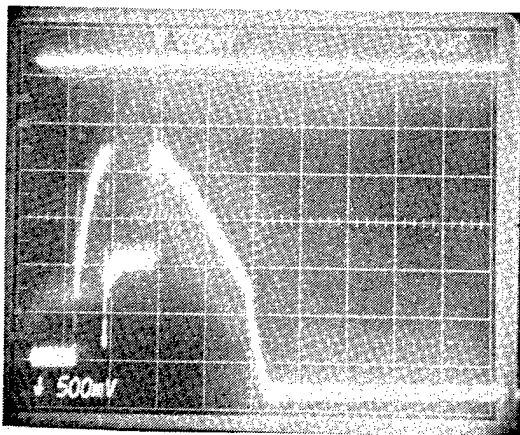
$\Delta I = 54.6\%$

$\Delta\nu = 0$  MHz PARTIALLY BLOCKED RWS



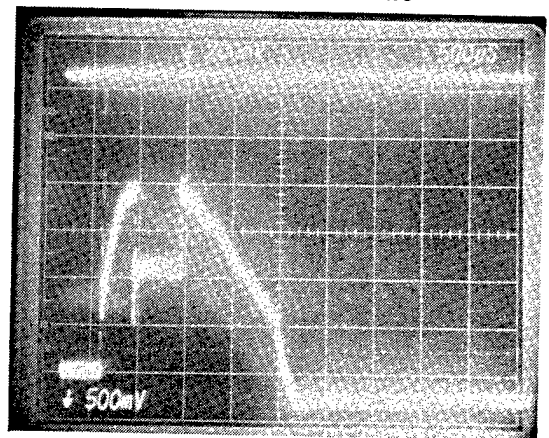
$\Delta I = 89.9\%$

$\Delta\nu = 3$  MHz UNBLOCKED RWS



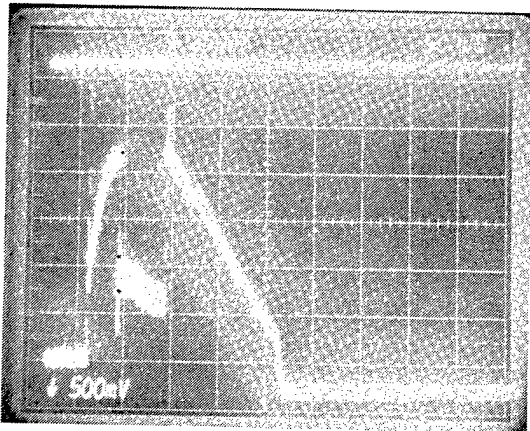
$\Delta I = 54.5\%$

$\Delta\nu = 3$  MHz PARTIALLY BLOCKED RWS



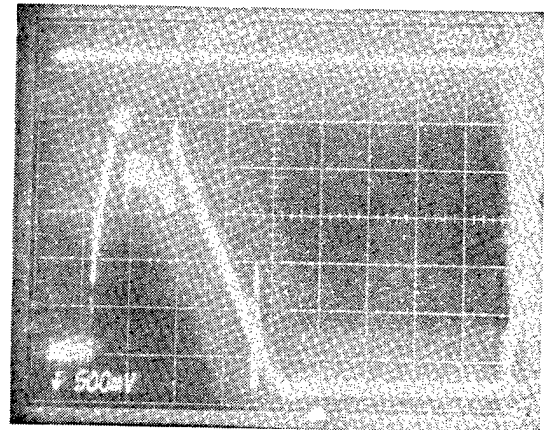
$\Delta I = 44.7\%$

$\Delta\nu = 9.04$  MHz UNBLOCKED RWS



$\Delta I = 59.2\%$

$\Delta\nu = 9.04$  MHz PARTIALLY BLOCKED RWS



$\Delta I = 22.2\%$

Figure 6-28. Effect of Partially Blocking RWS Mirror,  $M = -1.77$

wave decreases. This shows the strong dependence of the output intensity on the integrity of the reverse wave suppressor. The intensity drop of the ring resonator at  $M = 1.77$  and the unperturbed pulse shape was observed as the current, i.e., gain, of the laser was varied. The unperturbed pulse shape shows a greater falloff in power toward the end of the pulse for increased current, 3.5 amp. As the current is decreased to 2.0 amp, the unperturbed pulse approaches a square wave. Changing the gain while maintaining constant return on the order of  $1 \times 10^{-3}$  has minimal effect on the intensity drop over a current range of 2.0 to 3.5 amp; intensity drops of 61 to 57% are observed.

#### 6.4.3 Summary Comparison of Experimental Results for Standing-Wave and Ring Resonators

A brief summary of the experimental results is shown in Table 6-2, where the results for both the negative-branch unstable standing-wave resonators and the ring resonators are presented. The primary difference between the two resonator types is the degradation of beam quality. The beam quality degrades in the presence of return energy for the negative branch standing-wave resonators. However, the ring resonators experience no such beam quality degradation; the outcoupled energy in the forward wave decreases as a function of return, while the beam quality remains unchanged. The table also summarizes results for the return beam amplification, frequency dependence, and alignment sensitivity.

Despite the different responses in beam quality degradation and outcoupled energy, the relative brightness for a given resonator magnification and feedback remains the same for both types of resonators. Figure 6-29 shows experimental and theoretical results for the relative brightness as a function of return fraction for the standing-wave and ring resonators at  $M = 1.5, 1.77$  and  $2.0$  and a return beam frequency of  $6.4$  MHz. For the standing-wave resonators, Figure 6-29(a) brightness decreases linearly for small return fractions less than  $1 \times 10^{-3}$  and shows a steeper decline at higher magnification. Analysis predicts

$$B_{SW} \approx 1 - Gf$$



Table 6-2. Summary of Standing-Wave and Ring Resonator Results

	Magnification	Analysis	Experiment
Negative Branch SW Resonator			
Return-beam amplification	1.5 2.0	91 to 201 840 to 1078	150 700
BQ degradation	1.5 2.0	5% at $10^{-3}$ 5% at $10^{-4}$	5% at $7E-04$ 5% at $1.5E-04$
Frequency dependence	Both 1.5 and 2.0	NO, except at fundamental. More gain at fundamental	NO, except at fundamental. Return mode BQ good near fundamental.
Alignment sensitivity	Both 1.5 and 2.0	More sensitive near fundamental	Inconclusive
Ring Resonator			
Return beam amplification	1.5 1.77	80 to 110 370 to 600	150 - 280 1250
BQ degradation	1.5 and 1.77	NO	NO
Intensity drop (6.4 MHz nonmode)	1.5 1.77	29% to 35% 65% to 75%	35% at $5E-03$ 80% at $5E-03$
Frequency dependence	Both 1.5 and 1.77	NO, except near fundamental. More gain near fundamental	NO, except near fundamental. Intensity drop sensitive near fundamental
Alignment sensitivity	Both 1.5 and 1.77	More sensitive near fundamental	Inconclusive

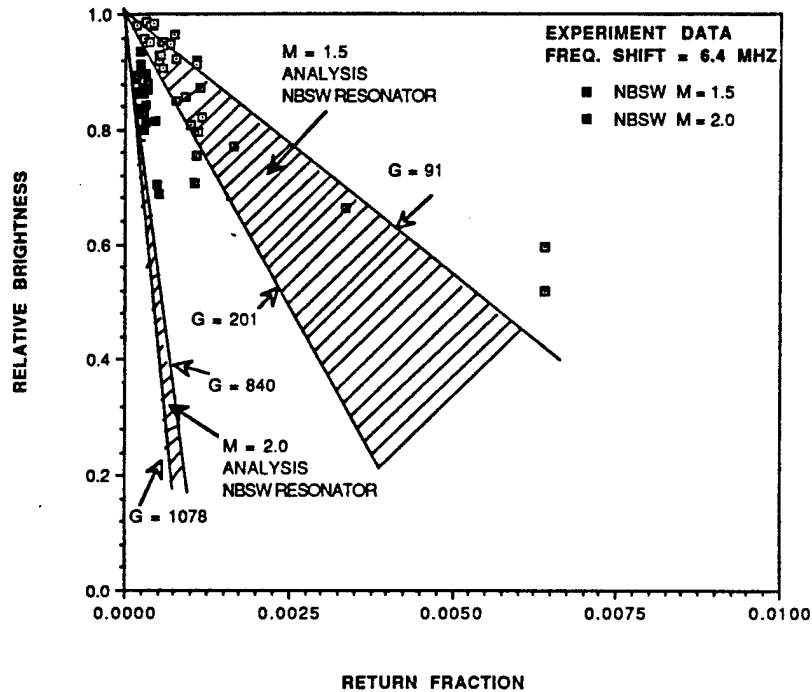


Figure 6-29(a). Experimental and Theoretical Relative Brightness Versus Return for NBSW Resonators,  $M = 1.5$  and  $2.0$ , for Frequency Shift of  $6.4$  MHz

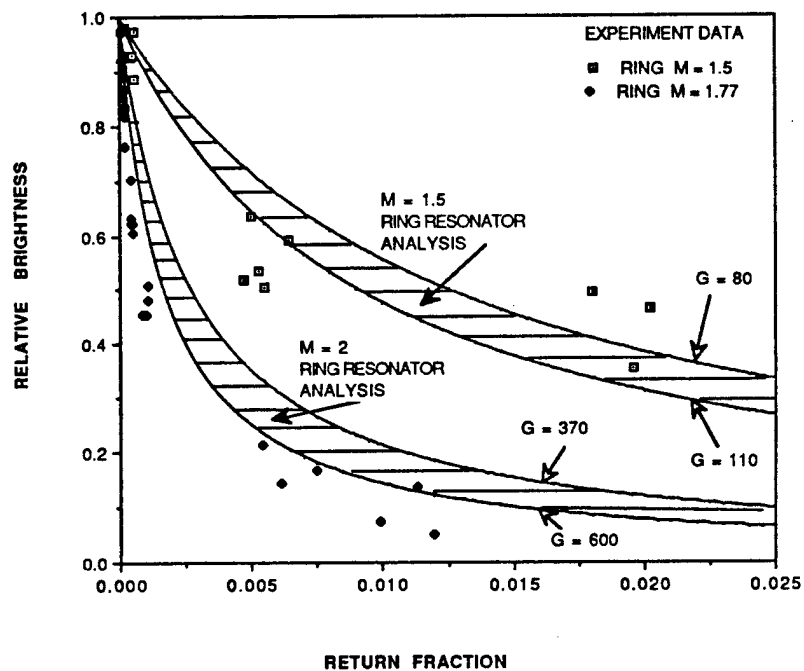


Figure 6-29(b). Experimental and Theoretical Relative Brightness Versus Return for the Ring Resonators,  $M = 1.5$  and  $1.77$ , for Frequency Shift of  $6.4$  MHz

where

G = total gain for a given magnification  
f = return fraction  
B<sub>SW</sub> = relative brightness for NBSW resonator

The ring resonators show similar behavior for very small returns (Figure 6-29(b)). However, for greater returns brightness is described by the following equation.

$$B_{RR} \approx \frac{1}{1 + Gf}$$

where G and f were defined above. Experimental data agree well with the analysis.

## 6.5 COMPARISON BETWEEN ANALYSIS AND EXPERIMENT

### 6.5.1 Standing-Wave Resonators

The MOI physical optics computer code was used to assess the number of passes required to walk into and out of the Fresnel core for both the negative branch unstable standing-wave resonators. The outcoupling fraction for each round trip pass is shown in Figure 6-30. The amplification passes are assumed to occur until outcoupling is comparable to the predicted outcoupling fraction. This occurs on the fifth pass for each resonator. The curves show that some outcoupling occurs prior to the fifth pass and these losses are accounted for by the  $G_L$  values. The inferred values for  $G_A$  and  $G_R$  are

$$\begin{aligned} M = 1.5 \quad G_A &= 58 \quad G_L = 0.66 \\ M = 2.0 \quad G_A &= 1024 \quad G_L = 0.53 \end{aligned}$$

Figure 6-31 shows pertinent eigenvalues (squared) used to infer the range of  $G(W)$  values for the two standing wave resonators.

Table 6-3 lists the first 13 eigenmodes between zero and  $c/2L$  calculated for the negative branch standing-wave resonator, magnification 1.5. Figure 6-31(a) shows the theoretical mode structure for this resonator.

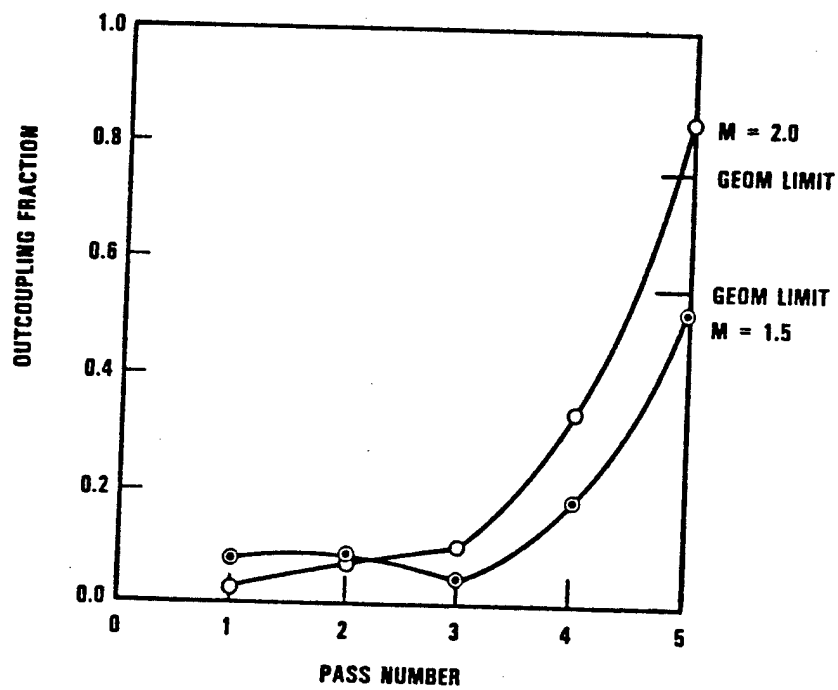
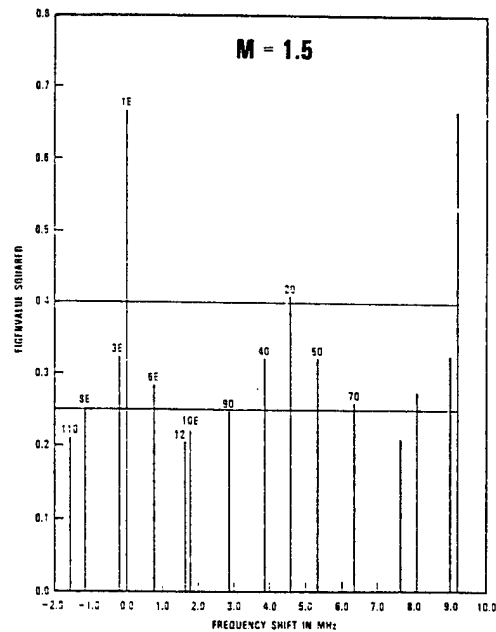
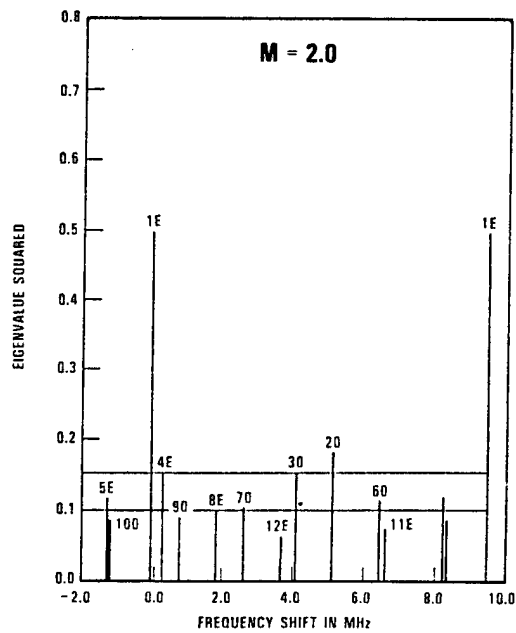


Figure 6-30. Return Beam Outcoupling Fraction Dependence on Pass Number



(a)



(b)

Figure 6-31. Eigenvalues Used to Assess NBSW G(W) Values

Table 6-3. Theoretical Eigenmodes for Standing-Wave Resonator,  $M = 1.5$

Mode No.	Frequency (MHz)	Type Symmetry	Mode No.	Frequency (MHz)	Type Symmetry
1	+0.0000	Even	8	-1.1372	Even
2	+4.5955	Odd	9	+2.8819	Odd
3	-0.1929	Even	10	+1.7961	Even
4	+3.8686	Odd	11	-1.5580	Odd
5	+5.3383	Odd	12	+1.6466	
6	+0.7637	Even	13	+9.1959	
7	+6.3396	Odd			

The theoretical eigenmodes for the negative branch standing-wave resonator,  $M = 2.0$ , are listed in Table 6-4. These eigenmodes were calculated base on a theoretical resonator length of 15.834 m. The actual experimental resonator length was approximately 15.76 m, which yields a longitudinal mode spacing of 9.519 MHz, only 0.5% difference from theoretical values. Figure 6-31(b) shows the relative strength of the theoretical modes for this resonator.

As a bound on likely values of  $G(W)$  calculations using the resonance formula in Section 6.2 were performed for both the maximum and typical values indicated on the graphs (e.g., 0.25 and 0.4 for  $M = 1.5$ ). The inferred ranges for  $G(W)$  were

$M = 1.5$	2.4 typical	5.3 maximum
$M = 2.0$	1.6 typical	2.0 maximum

For typical nonfundamental eigenmodes, the resonance halfwidths are quite large, typically of order 0.25 free spectral ranges and, therefore, substantial resonances are not anticipated. Furthermore, the amplified return will almost certainly not match a particular mode but can be decomposed into a sum of eigenmodes. This decomposition further reduces the likelihood of a strong resonance. A detailed treatment is complicated by the fact that unstable resonator eigenmodes are not orthogonal.

The inferred range of  $G_{Total}$  values compares reasonably well with the test data:

	<u><math>G_{Total}</math> (Calculated)</u>	<u>Experimental Value</u>
$M = 1.5$	90-200	150
$M = 2.0$	840-1080	700

As might be anticipated from the simple confocal telescopic resonator analyses in Section 6.2, both the theory and data exhibit a strong dependence on magnification. A universal scaling law is probably not however appropriate due to dependence on other resonator parameters.

Table 6-4. Theoretical Eigenmodes for Standing-Wave Resonator,  $M = 2.0$ ,  $L = 15.834$  m

Mode No.	Frequency (MHz)	Type Symmetry	Mode No.	Frequency (MHz)	Type Symmetry
1	+0.0000	Even	9	+0.8041	Odd
2	+5.1011	Odd	10	-1.1917	Odd
3	+4.0859	Odd	11	+6.6150	Even
4	+0.3360	Even	12	+3.6434	Even
5	-1.2458	Even	13	+5.0872	Even
6	+6.4268	Odd	14	+0.1092	Odd
7	+2.6142	Odd	15	-1.6245	Odd
8	+1.8411	Even	16	+9.4670	



Note that there was some systematic variability in the test data and that the reported values typically reflect high values. This variability may be due to gain profile and hole burning effects which are ignored in this simple model. Due to random variations in room temperature it would be anticipated that sometimes the laser fundamental mode frequency would coincide with the CO<sub>2</sub> line center. The frequency-shifted gain would then be systematically lower than the resonator threshold since it is further from line center. On the other hand, sometimes the frequency-shifted frequency may coincide with line center and, therefore, the gain would be systematically higher than the resonator operating gain. Hole burning will tend to increase the amplification above predicted values in both cases. Very approximate estimates suggest that both effects together could account for as much as a factor of approximately 2.

#### 6.5.2 Ring Resonators

For the ring resonator analyses, it was assumed that the total power "output" including both reverse and forward waves was constant. The fractional power lost due to feedback was estimated by methods similar to the CZAR analysis. Physical optics eigenvalue calculations were used to estimate saturated resonator threshold gain per pass and  $G(W)$  values for both ring resonators. Reverse-wave outcoupling was also assessed with physical optics calculations. The situation is complicated by the fact that some of the reverse-wave outcoupling occurs immediately at the aperture clipper and some occurs at the reverse-wave suppressor mirror which converts the reverse to forward propagating radiation. However, geometrically the power reflected by the RWS also outcouples at the clipper but after one additional gain medium pass. This extra gain was included in the analysis. In addition, because of the relatively gradual increase in outcoupling fraction with pass number and the extra gain due to the suppressor mirror all power outcoupled into the clipper during the buildup was summed and included in the total amplification factor estimate. This term has a modest effect on ring resonator predictions and a smaller effect on standing-wave resonator predictions which the results in Section 6.5.1 did not include.

The outcoupling ratio pass dependence for both the total net and fraction incident on the suppressor mirror are shown in Figure 6-32. Eight passes were required to reach the nominal outcoupling eigenvalue. Based on average behavior after a large number of passes (the net falls toward the eigenvalue after still more passes and the suppressor mirror value continues to oscillate), it was assumed for calculation purposes that there is a 2:1 split between reverse-wave radiation which directly impacts the clipper and radiation which impacts the reverse-wave suppressor mirror. The net inferred aggregate gain value was

$$30 + 38G(W)$$

Away from the zero frequency shift and  $c/2L$  (9 MHz) reverse-wave resonance frequency shifts, typical  $G(W)$  values ranged between 1.3 and 2 leading to a net estimate of 80 to 110 for  $G_{Total}$ . This value compares reasonably with data values which were 150 to 280.

Experiments performed near-zero frequency shift and 9 MHz exhibited the anticipated inverse square dependence on frequency mismatch expected from the  $G(W)$  discussions (e.g., Figure 6-24). As discussed in more detail later, at zero frequency shift a resonance is expected because the feedback can function as a forward "reverse" wave suppressor mirror. The resonance near 9 MHz is due to a resonance with the reverse-wave eigenfrequency. The shift in resonant frequency is a result of the change in handedness of the circular polarization which is reinjected.

Similar analyses were also performed for the  $M = 1.77$  resonator. The net inferred aggregate gain value was

$$150 + 180G(W)$$

Away from the resonances the inferred  $G(W)$  values implied net amplification factors of 370 to 600. These values are somewhat below the measured values which were typically 800 to 1200. Reverse-wave suppressor mirror effects are substantial and may account for some of the discrepancy. For nonresonant returns the analysis assumes the primary effect of the RWSM

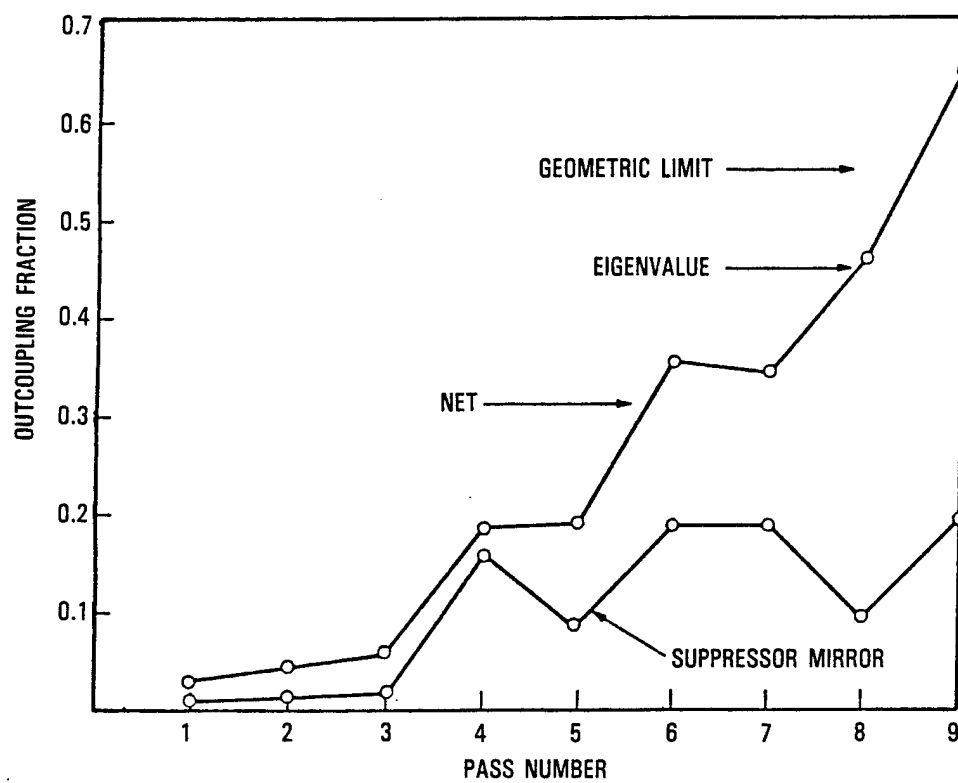


Figure 6-32. Ring Resonator Outcoupling Ratio Pass Dependence,  $M = 1.5$

is to cause a portion of the amplified reflected radiation to make one extra pass through the gain media before crashing into the clipping aperture near the scraper. Strictly speaking, if the RWSM were perfectly aligned in this manner, it would not function very well as a suppressor mirror. Some fraction of the reflected beam probably misses the aperture and robs additional power from the gain medium. Presumably this radiation is so poorly angularly matched to the forward wave that it does not emerge as part of the output.

The data obtained by partially blocking the RWSM which are summarized in Figure 6-28 were examined to clarify the effects of the RWSM. First consider the effect at zero frequency shift. At zero frequency shift one can view the feedback as another suppressor mirror which favors the reverse rather than forward wave. It is usually supposed that a RWSM is effective provided it produces returns large compared to optics scattering. However, when two RWSM's are present at "opposite ends" of the resonator there is a competition between the two and one would expect that if the effects of the RWSM were reduced by partially covering its surface then it would be easier for the feedback signal to suppress the forward wave. The data in Figure 6-28 clearly show the effect. The inferred amplification,  $G_{\text{Total}}$ , increases by a factor of 7 after the mirror is partially blocked. Far from the zero frequency-shift resonance an opposite effect is anticipated and the sensitivity to feedback should decrease. The 3 MHz frequency-shift data show the anticipated behavior. Partially covering the RWSM reduces the inferred amplification by a factor of 1.8. This is already somewhat larger (1.4 calculated) than the value assumed in the analysis. Since the RWSM was still functioning well as a reverse-wave suppressor, additional sensitivity reductions would probably have occurred if it could have been further blocked. The reduction in feedback sensitivity associated with blocking the RWSM is even greater at the 9.04 MHz,  $c/2L$  resonance. The situation is complicated because in this case the reverse wave is resonantly excited by the feedback. Possibly the increase in sensitivity to the RWSM is a result of the differing intensity and angular distribution associated with a true reverse wave as opposed to the distribution produced by the amplified 3 MHz shifted return.

### 6.5.3 Implications

The results show that there is a strong feedback sensitivity dependence on resonator parameters. Ultimately, resonator design approaches may need to consider these dependencies. It appears likely that prediction accuracy within a factor of order 2 or 3 can be made on the basis of simple analyses. Better accuracy will require development of more sophisticated models.

From a brightness standpoint, there is apparently not a large difference between ring and standing-wave resonator sensitivity to feedback. For a given magnification and level of feedback the losses in brightness caused by power degradation in the ring resonators were comparable to the losses caused by beam-quality degradation in standing-wave resonators. For applications without spatial filtering, this behavior would strongly favor the selection of ring resonators but if a spatial filter is used either choice is comparable. A ring resonator may also be more sensitive to resonance problems and therefore more care will be necessary in insuring that the SBS frequency shifted longitudinal modes do not align with either forward or reverse mode frequencies.

As an application of the methodology similar calculations were performed for the HEXDARR resonator which is used for the ALPHA device. The HEXDARR resonator does not incorporate a reverse-wave suppressor mirror so this analysis uncertainty is eliminated. However, there is an intrinsic reverse-wave suppression associated with a mismatch between the reverse wave and gain regions. Available SAI analyses of the reverse wave were used to assess this intrinsic loss. The forward and reverse mode geometric feedback ratio is 0.124. The reverse mode was predicted to lase for a feedback ratio of 0.16 but not for 0.12 or 0.14. It was therefore concluded that the additional effective loss for the reverse mode resulting from mode/gain overlap was between 0.016 and 0.036. Calculated HEXDARR eigenvalues were used to infer the regenerative amplification factor,  $G(W)$ , values. Figure 6-33 shows the predicted dependence on eigenvalue.  $E_1$  are the ALPHA eigenvalues and  $E_1^*$  includes the intrinsic suppression. The inferred values are 2 to 5 without the additional loss and 1.5 to 3 with it. Bare cavity CROQ code physical optics calculations were used to

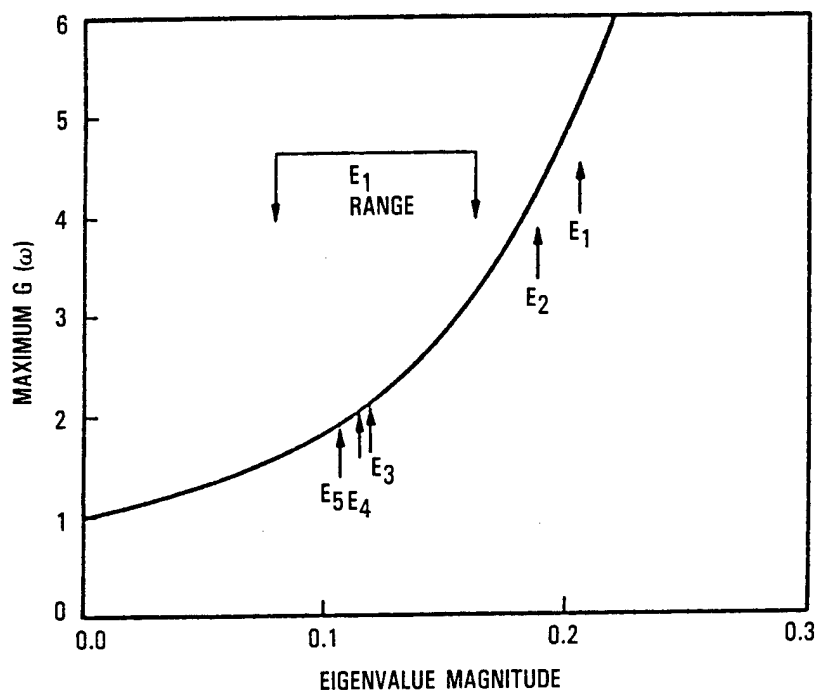


Figure 6-33. HEXDARR Regenerative Mode Gain Versus Eigenmode Magnitude

estimate  $G_{AGL}$ . The most probable inferred value was three round trips for a net value of 80. As a worst case, a maximum gain of 270 was estimated after 4.5 round trips. The inferred values for  $G_{Total}$  were most probable: 120 to 240 and worst case 600 to 1500. Assuming a 5% total power degradation criteria, the most probable inferred isolation requirement is

$$\frac{P_{return}}{P_{osc}} = 2 \text{ to } 4 \times 10^{-4}$$

Based on reverse wave analysis of HEXDARR this criteria is also sufficient to substantially limit beam-quality degradation ( $<0.2$ ) caused by the presence of the reverse wave in the Fresnel core. Isolation at these levels is well within expected capabilities.

## 7. OSCILLATOR ISOLATION VM EXPERIMENTS

### 7.1 INTRODUCTION AND MOTIVATION

The CO<sub>2</sub> oscillator isolation experiments reported in Section 6.0 provided a parametric study of factors important in assessing the effects of feedback to an oscillator for several resonator configurations. During the design of the OI CO<sub>2</sub> experiment, special attention was paid to the traceability of the results to the operation of an HF resonator, similar to ALPHA. Thus, parameters such as ratios of the homogeneous line width and SBS frequency shift to the cavity mode spacing were properly simulated in the CO<sub>2</sub> experiment. Parameters not well simulated, however, included the gain distribution and the number of modes within the Doppler bandwidth (one mode in 50 MHz for CO<sub>2</sub> versus 10 to 30 (depending on resonator length) in 400 MHz for a large-scale HF laser). To expand upon the validation of the isolation analyses performed, an HF experiment conducted on a device scalable to the ALPHA gain generator was deemed desirable. The appropriate device for this test is the ALPHA verification module (ALPHA-VM). However, an oscillator isolation experiment using the ALPHA-VM with all the parameterization covered in the CO<sub>2</sub> experiment would have been very expensive. For this reason, it was decided that a detailed ALPHA-VM isolation experiment should be preceded by a low-cost risk-reduction experiment. The primary objective of this experiment was to gain experience in using this device for isolation studies and to provide data necessary to support the design of a more detailed experiment.

The design of the oscillator isolation risk-reduction experiment using the ALPHA-VM device (termed OIVM) called for a small amount of frequency-shifted power to be fed back into an oscillator. The major goals of this experiment were:

- Gain experience in setting requirements for alignment tolerances of a frequency shifter and retro mirror to simulate a phase-conjugated return back into the oscillator assembly used
- Gain experience with diagnostics needed to measure laser degradation



- Determine whether or not oscillator performance degradation could be observed at low returns with a frequency shift.

The approach was to use the ALPHA-VM device to provide traceability to ALPHA and the SBL gain medium. The experiment was to start immediately after the completion of an NWC test series to save the cost of device activation. An existing resonator and diagnostics that had been designed for a recent experiment on the SABLE program were used to reduce design and equipment costs. An acoustic optic modulator (AOM) and retro mirror to inject feedback into the resonator with a frequency shift were added. A shutter was placed in front of the AOM to minimize flux. The tests were scheduled for 2 weeks to minimize costs associated with running the ALPHA-VM device. The experiments were not meant to be an exhaustive study of oscillator isolation at HF wavelengths but to be a bridge between CO<sub>2</sub> and HF media and to provide risk reduction for future oscillator isolation experiments to be performed on the VM as part of APEX.

## 7.2 EXPERIMENT DESCRIPTION

### 7.2.1 Resonator and High-Power Optical Train

A layout of the resonator used for the OIVM experiment is shown in Figure 7-1. The stable, double off-axis resonator consisted of an 881-in.-radius concave mirror and a 569-in.-convex mirror with a 1.9- by 8.2-cm scraper and had a magnification of 1.486. The resonator cavity length was 4.0 m giving a longitudinal mode spacing of 37.5 MHz. For the OIVM tests, a turning flat was placed at a 55° angle to the beam in front of the concave mirror so that the resonator output would favor linear S polarization, the polarization required for input to the AOM. The geometric footprint of the resonator beam is shown in Figure 7-2. A flat down beam of the scraper clipped the fangs of the beam, which were sent to a dump. The beam transmitted to the external optical train was 2.82 x 3.44 cm. A beamsplitter, BS1, placed down beam of the clipper inside the vacuum enclosure attenuated the beam before the diagnostics bench. The beam was sent from the mirror vacuum enclosure to the diagnostics bench through a sapphire outcoupling window. A mechanical shutter was used in some tests to diagnose laser behavior. This shutter was placed between the scraper and convex mirror for some tests and external to the cavity in

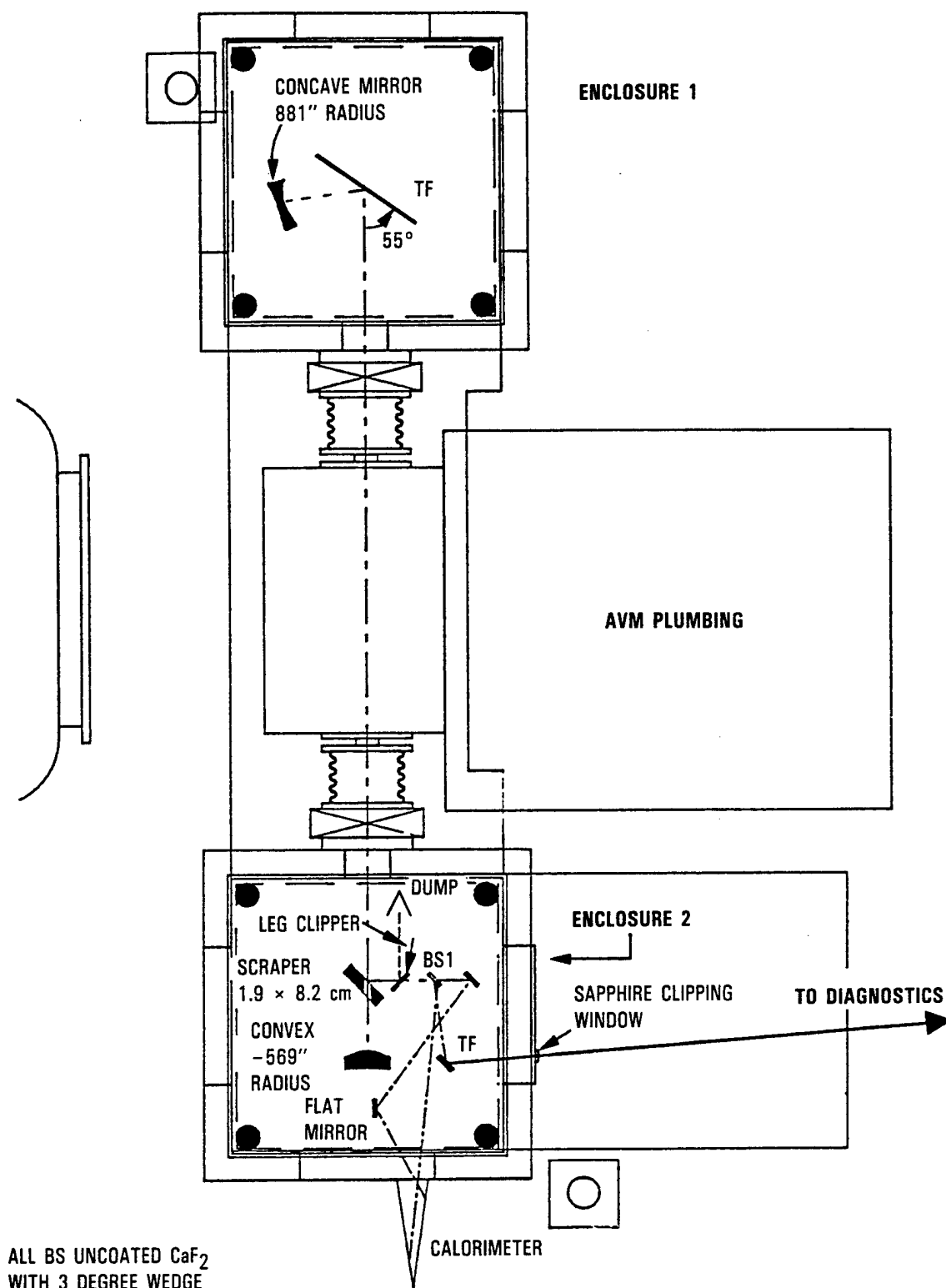


Figure 7-1. Resonator Used for OIVM Experiment

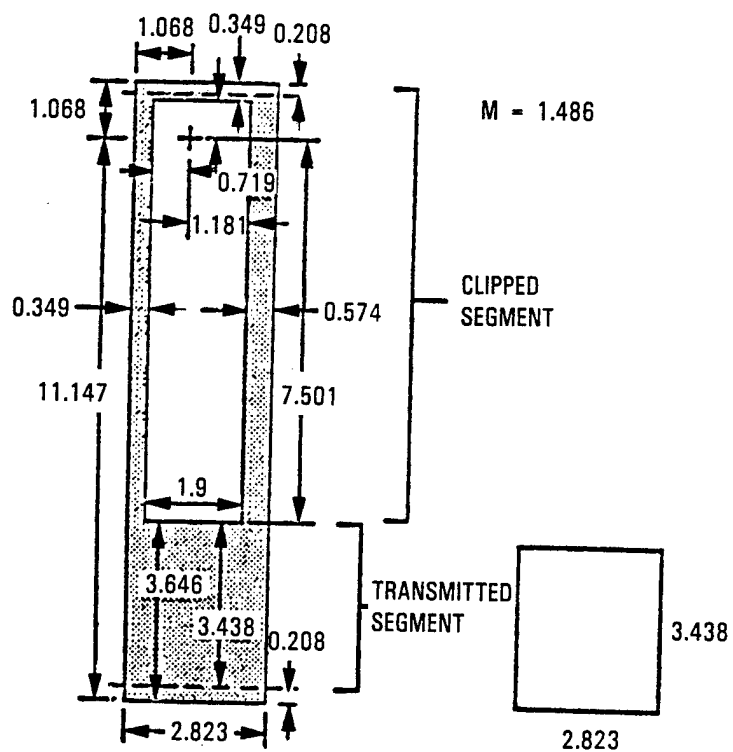


Figure 7-2. OIVM Resonator Beam Footprint Before Clipper

front of the sapphire window in other tests. Total output power of the device was measured by a calorimeter that measured the power transmitted through beamsplitter BS1. Total multiline output power started at 13.7 kW and degraded to 11 kW by the end of testing. A power of 300 W was delivered to the optical bench.

#### 7.2.2 External Optical Train

A block diagram of the external optical train is shown in Figure 7-3, and a more detailed layout is shown in Figure 7-4. The beam is first directed to a 300 lns/mm grating which separated the HF spectral lines and was oriented for vertical polarization. The  $P_2(7)$  beam then propagated to a turning flat and a demagnifying telescope. This telescope reduced the beam size so that it is smaller than the AOM aperture, as well as imaged the output of the scraper on the retro mirror. The beam was then passed through the AOM. The frequency-shifted beam at the first order Bragg angle was then retroreflected back through the AOM to double the frequency shift to 80 MHz. It passed back through the optical train, hit the scraper, and reentered the resonator.

The entire beam path outside the vacuum cavity boxes was enclosed and conditioned with dry nitrogen before a run. This prevented losses caused by atmospheric absorption. The  $P_2(7)$  line was transmitted through the atmosphere, allowing alignment to be conducted without the beam path conditioning in place. The optical train was aligned using a Helios CLI probe laser. An IRCCD camera was used to view the beam during alignment.

#### 7.2.3 Diagnostics

Sample beams were directed toward several diagnostics via beam-splitters in the main optical train. The diagnostics included spectrum, near-field intensity, power on the incident and return beams, power through a far-field pinhole, and far-field intensity.

The zero order from the grating was directed to a Norcon scanning spectrometer which recorded the total spectrum of the output. A beam-splitter in front of the spectrometer sent a portion of the beam to a rotating scatter plate. An AGA camera viewing this scatter plate recorded

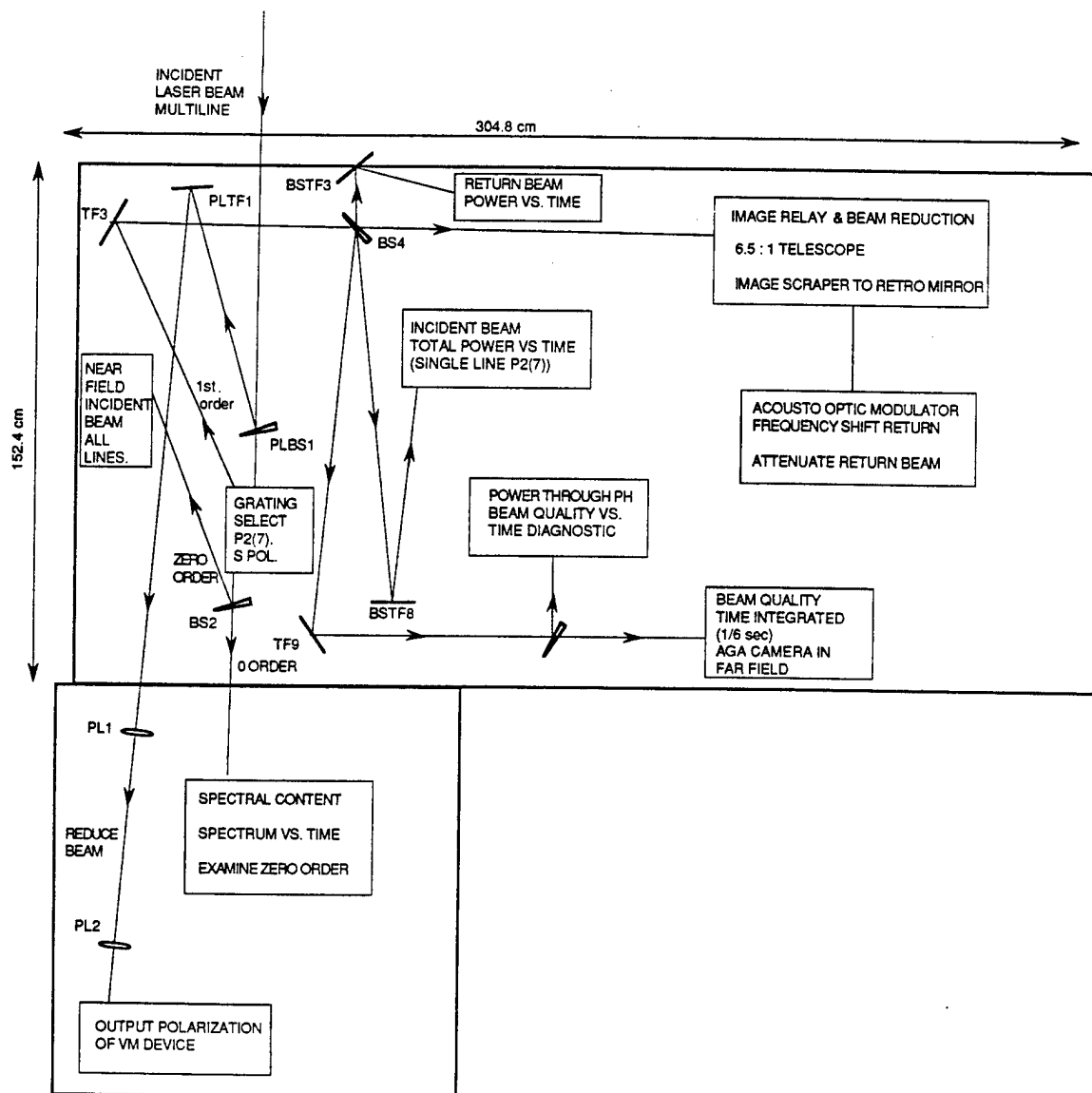


Figure 7-3. Block Diagram of External Optical Train for OIVM Experiment

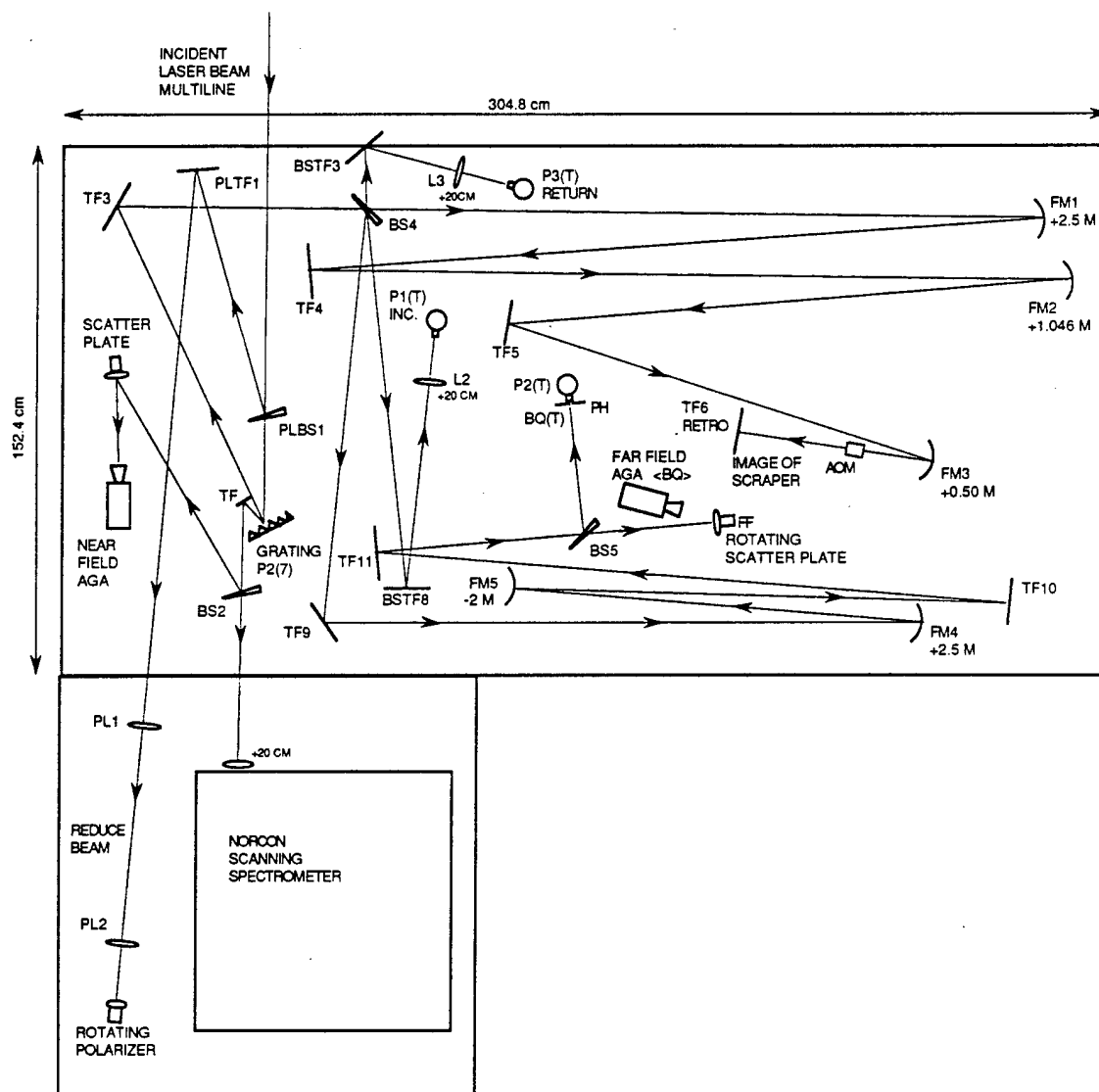


Figure 7-4. Detailed Layout of External Optical Train for OIVM Experiment

the near-field intensity. The other diagnostic beams were sampled from the main beam at beamsplitter BS4. InAs detectors measured the incident and return beam powers. An AGA camera looking at a scatter plate was used to detect far-field intensity. A power through the pinhole diagnostic was also set up to record relative beam quality as a function of time. TF3 could be aligned remotely to center the beam on the pinhole and thus manually correct for beam drift in real time. An IR CCD camera was used to observe the beam on the pinhole.

### 7.3 EXPERIMENTAL RESULTS

The first tests characterized the laser performance without a frequency shift. The near-field intensity of the beam is shown in Figure 7-5. It showed asymmetry in the horizontal direction and Fresnel ripple. The spectrum shown in Figure 7-6 indicated that  $P_2(6)$  was the dominant spectral line. The lines and their relative powers are shown in Table 7-1.

The power through the pinhole diagnostic proved not to be useful because of rapid beam drift, which prevented accurate adjustment of the manually controlled pinhole alignment mirror.

The far field of the beam recorded on the AGA camera was observed to spread in time. The major effect was an astigmatic aberration that caused a gross change in the horizontal slice plots as shown in Figure 7.3-3. The plots in this figure correspond to horizontal intensity slices across the beam taken at every fourth vertical pixel on a video screen. Four of these slice plots are required to construct an entire video frame showing a three-dimensional spot. It takes 167 ms to accumulate this entire frame. Slice plots were used because better time resolution could be observed. The peaks in the two plots in Figure 7-6 are aligned such that they represent the same vertical coordinate. Entire frames were not reconstructed because of the rapid changes from frame to frame.

Diagnostic tests were performed to determine the origin of the beam degradation. Two degradation sources were possible: (1) distortion within the resonator and (2) aberrations produced down beam of the scraper mirror. Initially, it was thought that heating of the grating was causing the change in the far-field beam. To investigate this possibility, a shutter

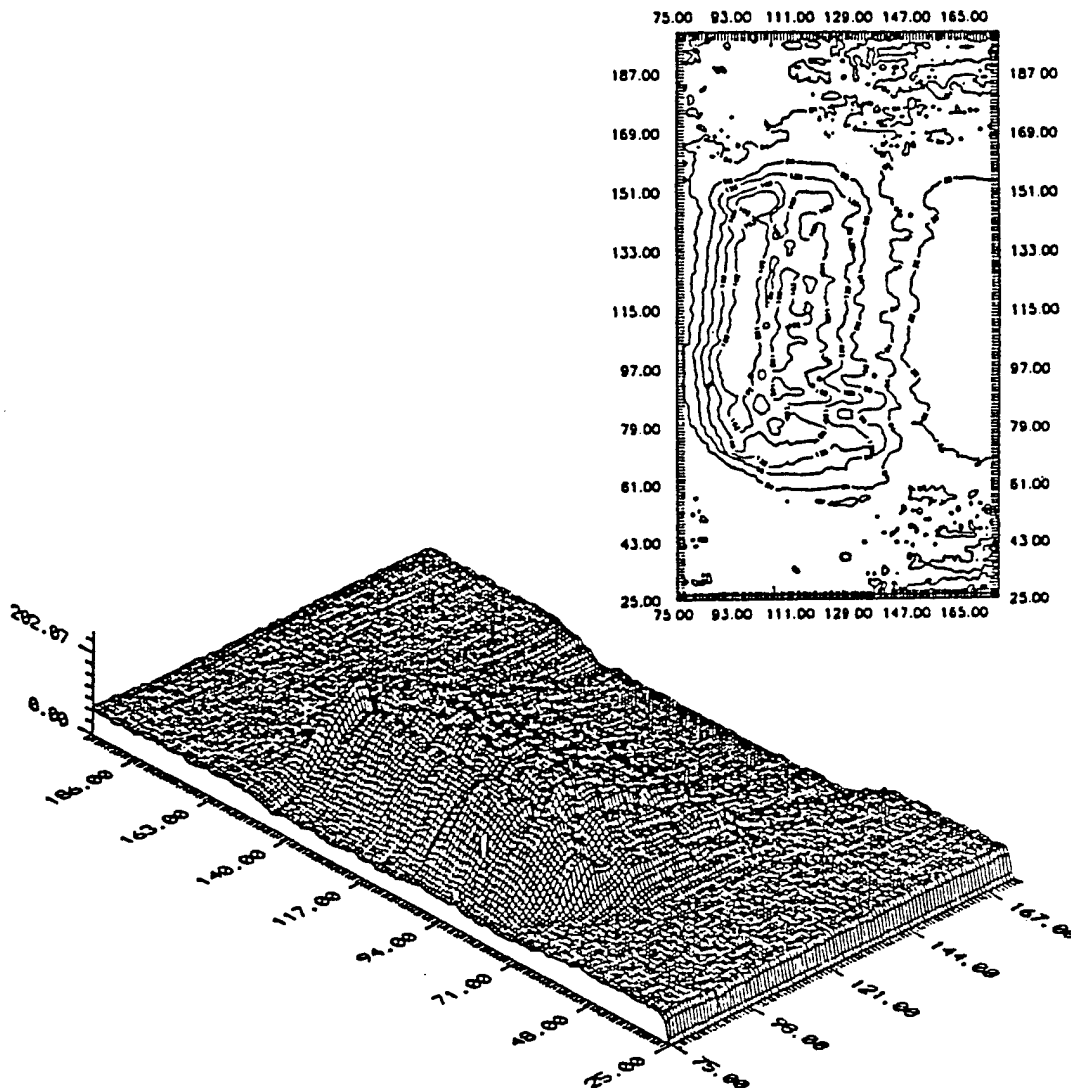


Figure 7-5. Near-Field Intensity of Propagated Beam



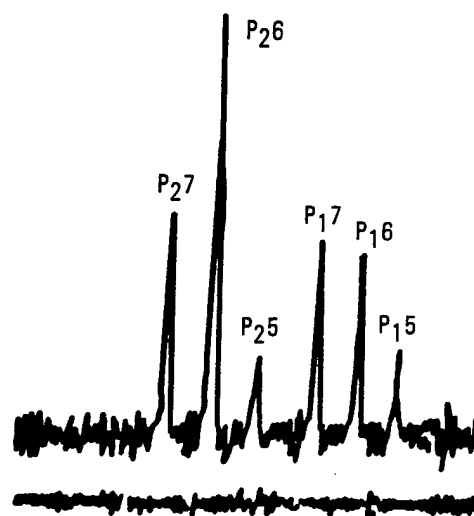
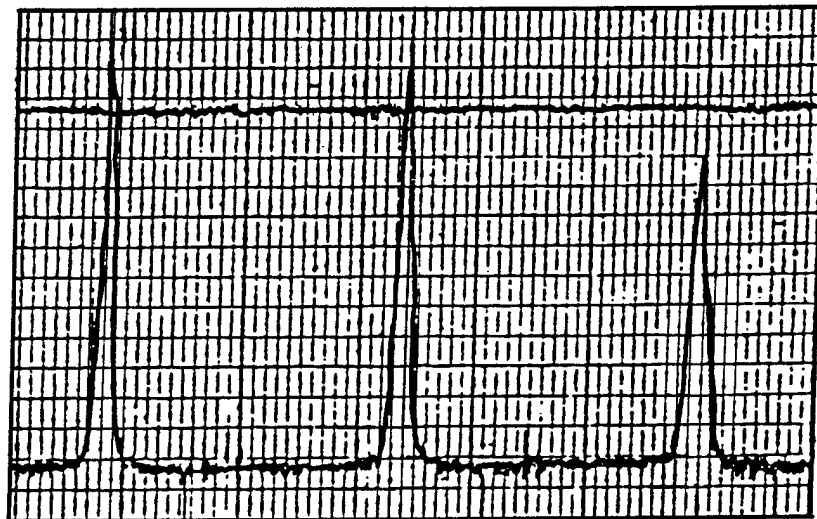


Figure 7-6. Spectrum of Laser Output



10 ms AFTER LASER ON (NO RETURN)



150 ms AFTER LASER ON (NO RETURN)

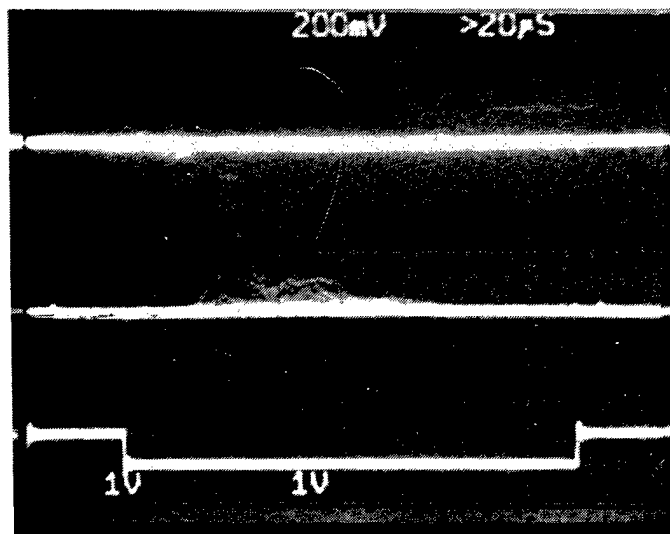
Figure 7-7. Horizontal Slice Plots of Intensity From Far-Field Diagnostic at Two Times During Testing

Table 7-1. Spectral Output of ALPHA-VM device

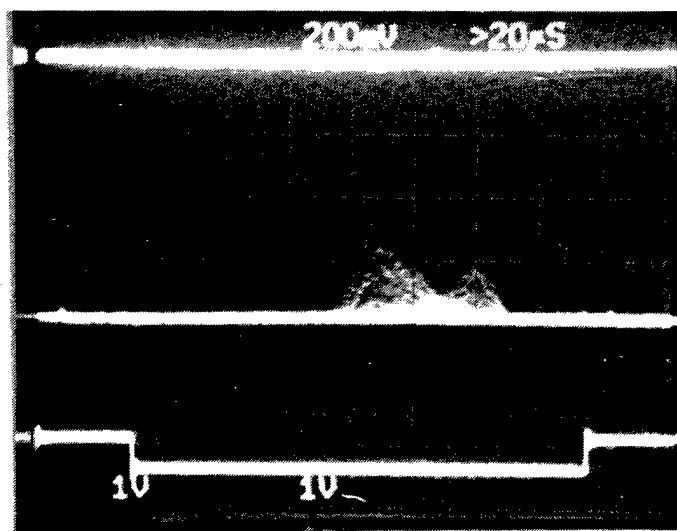
Line	Relative Intensity (%)
P <sub>2</sub> (7)	22.9
P <sub>2</sub> (6)	32.8
P <sub>2</sub> (5)	6.1
P <sub>1</sub> (7)	14.6
P <sub>1</sub> (6)	17.0
P <sub>1</sub> (5)	6.6

was placed near the sapphire outcoupling window. The laser was allowed to stabilize, the shutter was then opened, and the temporal behavior of the far-field beam was observed. When the shutter was opened, the far-field degradation was observed immediately, indicating that the beam had already degraded upstream of this shutter. To verify that the degradation source was in the resonator, a second test was performed wherein an intracavity shutter was placed between the convex mirror and the scraper. Flows were allowed to stabilize, and the shutter was opened. It was observed that the far-field beam had good beam quality initially but degraded within 200 ms to a beam quality comparable to what was seen in previous tests. This result indicated that the source of the degradation was in the laser, and it is believed that thermal distortion of the uncoated turning flat used for polarization control was responsible for the degradation.

Later observation of the far field in the run indicated the beam had stabilized to a constant poor beam quality that was rather poor (BQ ~2). The main aberration appeared to be astigmatism. Tests were conducted with the AOM on and off to determine if a further degradation in the beam could be observed with a feedback fraction as large as  $2 \times 10^{-4}$ . No observable change in the far-field beam could be observed with and without return. Scope traces showing overlapping intensity slices are shown in Figure 7-8. Careful measurement of frames with and without return indicated no



NO RETURN



RETURN  $\sim 3 \times 10^{-4} \Delta\nu = 80 \text{ MHz}$

Figure 7-8. Overlapping Slice Plots From Far-Field Diagnostic, With and Without Return

measurable change in beam spread, but does not permit conclusions on the effect of return because of the difficulty in measuring degradation of a poor quality beam.

In the next test series an intracavity shutter was used to start lasing and to trigger the AOM to turn on ~80 ms after lasing so that data with and without return could be obtained while the beam quality was still good. This test was set up when a water leak was observed in the ALPHA-VM device. The problem was diagnosed as resulting from cracks in the primary plate. The test series was terminated since estimated down time for the device would be several months. The optical bench was moved intact in case future tests could be conducted.

#### 7.4 RECOMMENDATIONS FOR FUTURE WORK

Although very little quantitative data on the effects of feedback to an oscillator were generated during this test, a great deal of information was generated regarding how to design such an experiment using the ALPHA-VM device. Such design information was the primary objective of the OIVM risk reduction experiment.

One of the more important results obtained was the observation that the rapid degradation in beam quality limited what could be done with the present configuration. At least two options exist for future tests. The simplest fix to the beam quality is to recoat the cavity mirrors and turning flat and to install a repetitive fast shutter with a relatively long off cycle to limit thermal loading on cavity optics. The AOM would then be triggered either to turn on shortly after the shutter or to be on one cycle and off the next. Use of such a shuttered resonator would require power and beam quality diagnostics with time resolution of the order of 1 ms.

Another option would be to use cooled mirrors to prevent degradation. This could be more a costly option unless mirrors were already available and would have to be evaluated carefully. Any future oscillator isolation experiments in HF will be conducted on APEX, and trades will be a part of that program.

## 8. PULSE STRETCHING EXPERIMENTS IN HF LASER

### 8.1 INTRODUCTION

The APACHE SBL concept relies on phase conjugation of CW HF amplifiers. However, experiments performed at HF wavelengths to date used PAR lasers with typical pulse lengths on the  $P_2(8)$  line of  $0.5 \mu s$ . This is about two times the phonon rise time and is in the transient regime for SBS. A pulse length approaching the CW regime for SBS would provide better traceability and scalability to an SBL or high-power CW HF phase-conjugation experiment. SBS experiments conducted with a long pulse would make extrapolation from the pulsed to the CW regime for SBS more reliable. There are two specific applications for a long-pulse laser on the APEX program. The first is for SBS experiments in a flowing gas cell. In the flowing cell, the turbulence time scale ( $>10 \mu s$ ) is an important scaling parameter. If the PAR laser pulse could be stretched to  $10 \mu s$  or greater, a scalable simulation could be performed which would validate the flowing cell concept. A second motivation for long pulses relates to the phase-conjugated pulsed HF amplifier experiment being considered for the APEX program. Here, pulsed results would have to be extrapolated to CW conditions, which would be practical only if a pulsed laser could operate in a quasi-CW regime for HF kinetics ( $\sim 10 \mu s$ ).

The possibility of achieving longer pulses with existing lasers was motivated by conversations with Dr. George Hart of W. J. Schafer Associates. He had performed kinetic code calculations for Los Alamos National Laboratories that indicated that the total pulse length of a pulsed HF/DF laser can be stretched to greater than  $30 \mu s$  by using a combination of a high Q cavity, low initiation factor ( $F/F_2$ ), and gas mixtures with low fluorine ( $\leq 45$  torr) composition. The techniques have been applied to a DF/CO<sub>2</sub> transfer laser to achieve very long pulses. He reported that DF experiments are planned at Boeing with their PCL50 device to determine the extent to which the pulse length could be stretched. However, these experiments have not yet been performed and plans do not include HF.

The objective of the experiments described in this section was to vary the parameters suggested by George Hart to:

- Determine both the total and single line pulse lengths and shapes achievable with these techniques
- Assess what penalties in energy and power are incurred by operating the laser in a long pulse mode
- Use the results to evaluate the practical limit for a pulse stretched SBS experiment using available pulsed laser devices.

The approach was to configure a PAR laser device as an oscillator with a closed-cavity resonator. Diagnostics were used to look at pulse length and shape for both the total laser pulse and for an individual line. Details of the experiment are presented in Section 8.2.

## 8.2 EXPERIMENTAL DESCRIPTION

A sketch of the experimental layout is shown in Figure 8-1. One PAR laser head is used as an oscillator. A stable resonator consisting of one concave metal mirror and one flat metal mirror separated by 13 m is used. The concave mirror has a radius of 32.5 m. A turning flat was incorporated in the resonator to allow the entire length to fit on the optical bench. Losses in the cavity occurred from scattering off the mirrors and also from scattering off the cavity windows which were canted  $5^\circ$  from normal incidence to the beam. Reflections off the cavity windows resulted in ~12% loss per pass in the resonator. Scatter off the resonator turning flat mirror was used to monitor the relative power out of the laser. This scatter was observed with two InAs detectors whose signals were recorded with a digital oscilloscope. An HF line filter, either P<sub>2</sub>(8) or P<sub>2</sub>(7), was placed in front of one of the detectors to look at single line pulse length. A 4-in. calorimeter was set to look at a reflection off one of the cavity windows. Because of difficulties in obtaining accurate absolute calorimeter energy calibrations, this calorimeter was used only for relative energy measurements.

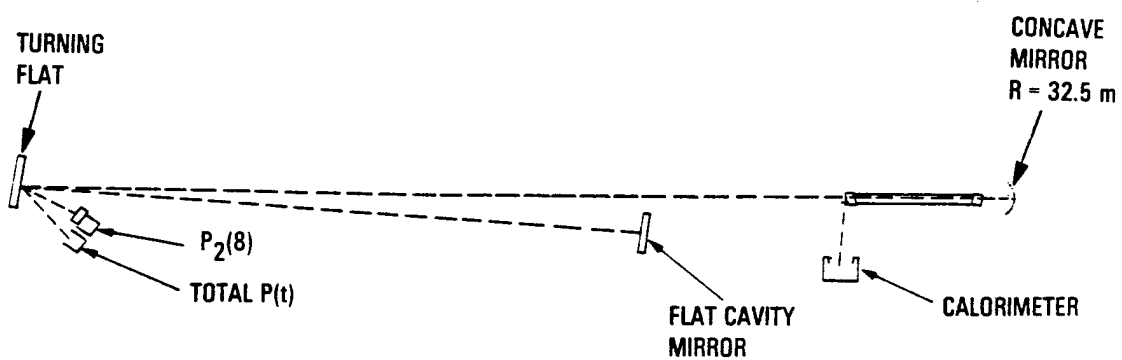


Figure 8-1. Experimental Layout for Pulse Stretching Experiments



### 8.3 EXPERIMENTAL RESULTS

Several gas mixtures and pressures were studied as a function of flashlamp voltage to control the dissociation level. The test matrix is summarized in Table 8-1.

Table 8-1. Test Matrix for Pulse Stretching Experiments

Run	F <sub>2</sub> (torr)	H <sub>2</sub> (torr)	He (torr)	O <sub>2</sub> (torr)	Pressure (torr)	Voltage (kV)
1	110	27.5	401.5	11	550	50
2	45	15	696	4	760	50
3	45	15	696	4	760	45
4	45	15	696	4	760	40
5	45	15	696	4	760	35
6	33	11	510	3	560	50
7	33	11	510	3	560	40
8	33	11	510	3	560	35
9	30	10	717	3	760	50
10	30	10	717	3	760	40

The nominal mixture for the PAR oscillator is F<sub>2</sub>/H<sub>2</sub>/He/O<sub>2</sub> = 0.2/0.05/0.73/0.02 at a pressure of 550 torr. The nominal voltage is 50 kV. The first runs established the operation of the PAR laser for the nominal operating condition with the closed cavity resonator. Power as a function of time traces are shown in Figure 8-2 for the P<sub>2</sub>(8) and P<sub>2</sub>(7) lines. In both cases, the top trace is the power in all lines.

A new gas mixture was then made with  $F_2/H_2/He/O_2 = 0.0592/0.01974/0.9158/0.00526$ . The mixture was first flashed at ~760 torr total pressure ( $F_2$  partial pressure 45 torr) with voltages of 50, 40, and 35 kV respectively. Scope traces are shown in Figure 8-3. The total pressure of the mixture was then lowered to 560 torr total pressure ( $F_2$  partial pressure 33 torr) and data taken again at 50, 40, and 35 kV. At the extreme condition of 560 torr and 35 kV, the pulse length of all lines increased to 14  $\mu s$  full width and the pulse length of the  $P_2(8)$  line increased to 10  $\mu s$  (data is shown in Figure 8-4).

Since the pulse length was extended with decreasing fluorine pressure and decreased flashlamp voltage, a new gas mixture was made that contained 30 torr of  $F_2$  at 760 torr total pressure. Some problems were encountered getting this mixture to lase reproducibly, possibly because of prereaction. Also, on some of the shots with this mixture, the oscilloscope had been accidentally reconfigured resulting in pickup of electrical noise from the flashlamps. Several shots where noise pickup was not a problem are shown in Figure 8-5 with both  $P_2(8)$  and  $P_2(7)$  line filters. These photographs, along with some earlier data, indicate that the  $P_2(8)$  line comes on late in the pulse. It appears that  $P_2(8)$  may come on even later as diluent is increased and fluorine decreased, resulting in a slower temperature rise.

The late bump on the total power normally corresponds to the  $P_2(8)$  line. This indicates that for PAR operating conditions where pulse stretching occurs, the  $P_2(7)$  line may have a longer pulse length than the  $P_2(8)$  line.

As a result of the aforementioned calorimeter calibration problems, the change in energy and peak power as a function of pulse length was not well quantified. Qualitatively, the peak power dropped by a factor of approximately 4 for the total pulse length was extended from 7  $\mu s$  to 14  $\mu s$ .

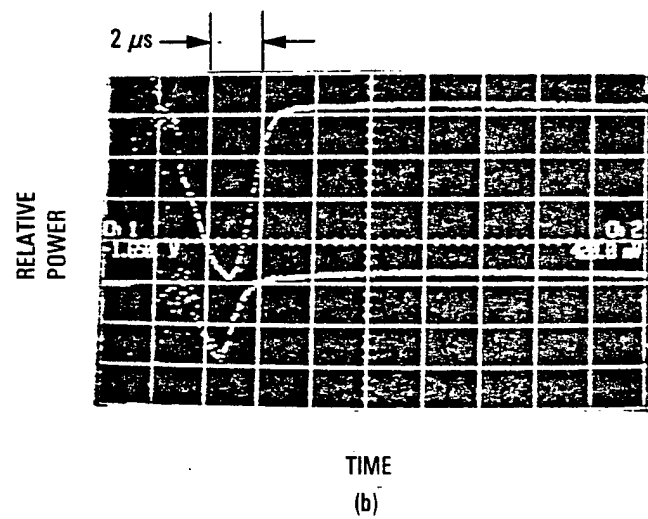
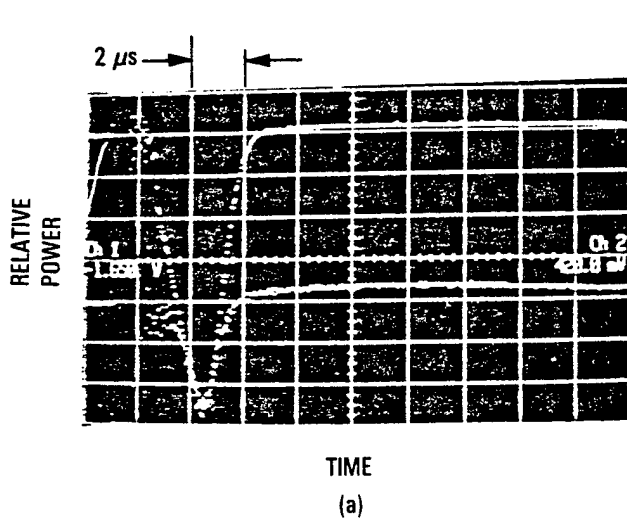


Figure 8-2. Power as Function of Time for Nominal Gas Mixture,  $F_2/H_2/He/O_2 = 110/27.5/401.5/11$ ,  $P = 550$  torr. Top traces are multilined power. (a) Bottom Trace,  $P_2(8)$  (b) Bottom Trace  $P_2(7)$

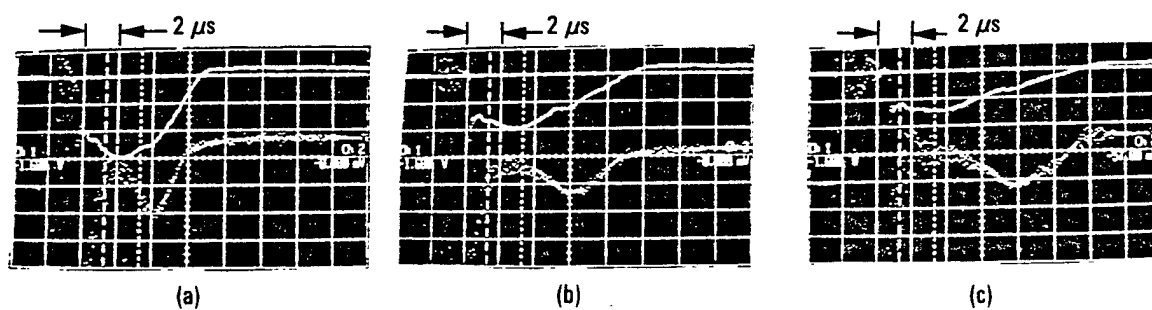


Figure 8-3. Power as Function of Time for Mixture With  $F_2/H_2/He/O_2 = 45/15/701.5/3.5$ ,  $P = 760$  torr. Top traces are multilane pulses. Bottom traces are  $P_2(8)$  pulse. (a) 50 kV, (b) 40 kV, (c) 35 kV

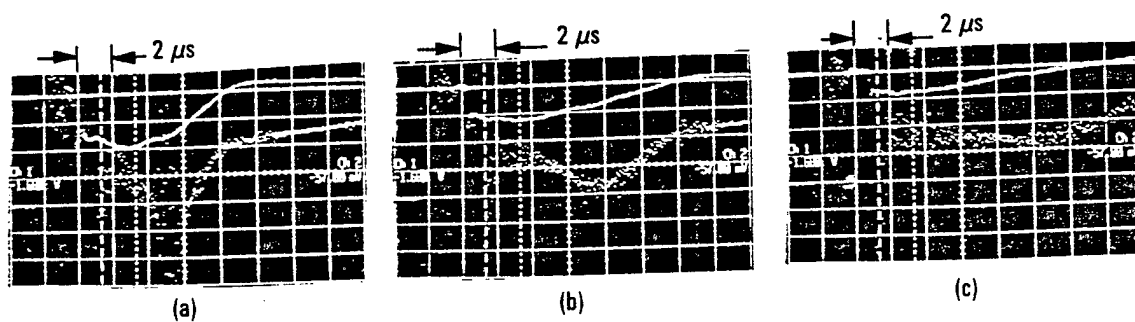


Figure 8-4. Power as Function of Time for Mixture With  $F_2/H_2/He/O_2 = 33/11/510/3$ ,  $P = 560$  torr. Top traces are multilined pulse. Bottom traces are  $P_2(8)$ . (a) 50kV, (b) 40 kV, (c) 35 kV

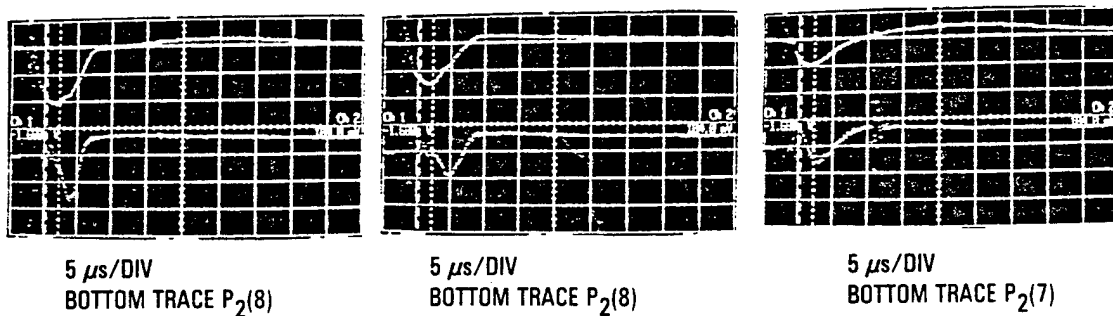


Figure 8-5. Power as Function of Time for Mixture With  
 $F_2/H_2/He/O_2 = 30/10/717/3$ ,  $P = 760$  torr

#### 8.4 DISCUSSION

These limited experiments showed that the pulse length of the PAR laser could be lengthened by adjustments in run conditions. The longest pulse achieved was 14  $\mu$ s full-width on all lines and  $\sim 10$   $\mu$ s full width on the P<sub>2</sub>(8) line. Further improvements could be obtained by even lower initiation levels and some variations in gas mixture. It was found that the P<sub>2</sub>(8) line turns on very late in the pulse for run conditions which give the longest pulses. Preliminary data indicates that operation on the P<sub>2</sub>(7) line may be preferable since it occurs nearer the peak of the total pulse and may have a somewhat longer inherent pulse length.

The major limit to this experimental setup is believed to be losses from reflections off the CaF<sub>2</sub> cavity windows. These could result in a 12% loss per pass or 24% loss round trip. This makes the Q of the cavity lower than the calculations performed by George Hart indicated were optimum. Hence, efficient long pulse operation would require either replacement of the cavity windows placed at Brewster's angle or antireflection coating the present cavity windows.

## 9. BIDIRECTIONAL AMPLIFIER CONCEPTUAL DESIGN STUDY

### 9.1 BACKGROUND/INTRODUCTION

The APACHE SBL design and other SBL designs using SBS phase conjugation employ a common master oscillator to allow phase conjugation to coherently couple multiple HF amplifiers. An inherent feature of this concept is that the phase-conjugated multiline amplifiers are bidirectional, i.e., the beam propagating toward the SBS cell and the conjugate return counterpropagate through the same amplifier medium. Furthermore, a frequency shift is introduced in the reverse direction by the SBS process. Prior to the APACHE program, very little work had been performed on such bidirectional phase-conjugated HF chemical laser amplifiers. For this reason, a bidirectional amplifier experiment was deemed appropriate to expand the data base. As part of a feasibility study to examine how such an experiment could be configured and what results obtained, a brief design study was conducted. This design was taken to the level of a Conceptual Design Review (CoDR). Future effort in this area will be expended on the APEX program. The results of the CoDR design effort are presented here.

The primary objective of the APACHE bidirectional amplifier experiment is to establish bidirectional amplifier operation with a frequency shift under conditions scalable to a high-power demonstration to be performed on the APEX program and an SBL. Derived requirements include:

- Study the effect of a frequency shift on extraction efficiency
- Study the effect of a frequency shift on forward and backward amplification
- Determine the minimum number of spectral lines on which a long-gain-length HF amplifier can be operated.

Table 9.1-1 summarizes bidirectional amplifier technical issues and their impact on either the SBL or the phase-conjugated demonstration scheduled for APEX.

There is a limited data base for the performance of single directional HF amplifiers and no data for bidirectional HF amplifiers. Multiline and selected single-line MOPA experiments were performed on the



Table 9.1-1. Bidirectional Amplifier Technical Issues

Issue	Impact
Is there a decrease in extraction efficiency with frequency shift?	<p>SBL: Could dictate larger amplifiers leading to larger system weight</p> <p>APEX: Not critical to experiment</p>
Are forward and backward amplifications equal with frequency?	<p>APEX/SBL: Sets requirements on size of master oscillator</p>
Can total amplifier power be extracted on a few lines?	<p>SBL: May relax oscillator requirement. Also simplifies SBS cell design for scenario where each line is conjugated in separate volume</p> <p>APEX: Increases likelihood of experiment success as it could give more power in a single line at SBS cell</p>

Parallel-Optical Stage, Master Oscillator Power Amplifier (POSM) program (Reference 9-1) to assess power extraction efficiencies and characterize the optical behavior of chemical laser media. The total multiline extraction efficiency in these experiments seemed consistent with amplifier theory. However, some of the single-line experiments provided confusing spectral results. More recently, Sentman et al. (References 9-2 through 9-4) performed single-pass studies of CW HF amplifiers as a function of input power, oscillator/amplifier flow-field match/mismatch, and location of the optical axis of the input beam. The studies showed that the power out of an amplifier minus the power in remained almost constant over a wide range of input powers. The studies also showed that the peak of the intensity distribution from the oscillator must be matched to the peak of the zero power gain distribution in the amplifier. Spectral studies also showed that the amplifier spectrum contained the same lines as the oscillator spectrum.

The above studies indicate that CW HF multiline amplifiers perform as expected. However, none of these studies was performed with a supersonic HF medium traceable to an SBL, and none were performed in a bidirectional mode with a frequency shift which would simulate the SBS phase conjugation. The Aerospace Corporation is currently setting up to perform bidirectional amplifier experiments with a frequency shift in an arc-driven CW HF laser. A schematic diagram of their experiment is shown in Figure 9.1-1. Their oscillator will deliver up to four longitudinal modes to the amplifier and provide a maximum power to the amplifier of approximately  $0.6 I_{\text{sat}}$ . A Faraday rotator is used for isolation. The amplifier is 18 cm long with an average small signal gain of  $0.08 \text{ cm}^{-1}$ . An acoustic optic modulator will be used to provide a frequency shift of 100 MHz. The CLAM code described in the Section 9.2 was used to model the Aerospace experiment. Figure 9.1-2 shows a plot of extraction efficiency versus input  $I/I_{\text{sat}}$ . The model indicates that differences in extraction efficiency with and without a frequency shift will range from 0 to 7% depending on the degree of amplifier saturation. Differences in forward and backward amplifications will be less than 5%. These experiments will provide data on the effect of frequency shift on extraction efficiency. However, quantitative differences between data with and without a frequency shift may be difficult to obtain

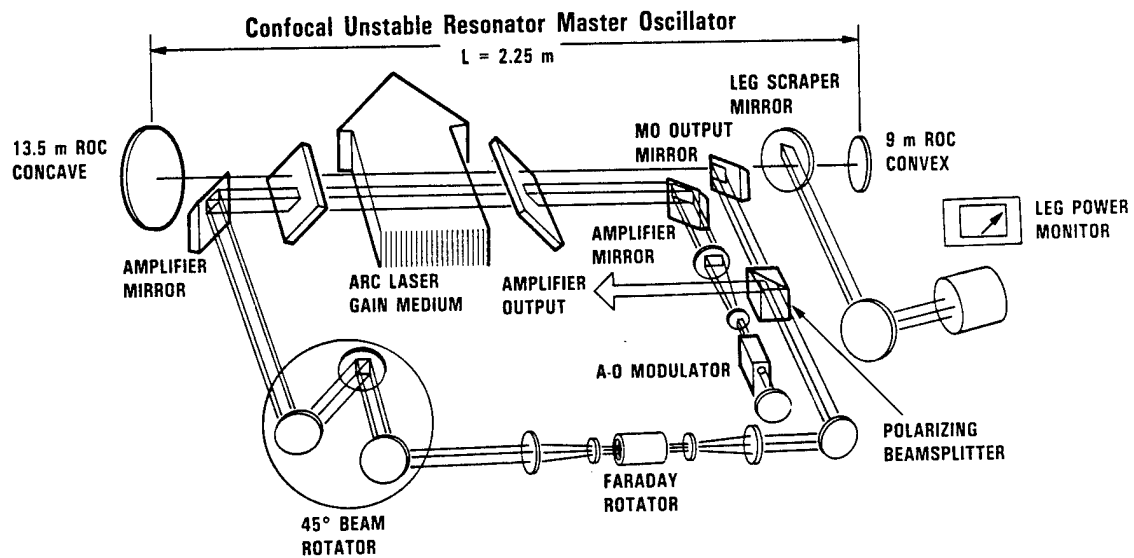


Figure 9.1-1. Aerospace Bidirectional Amplifier Experimental Setup

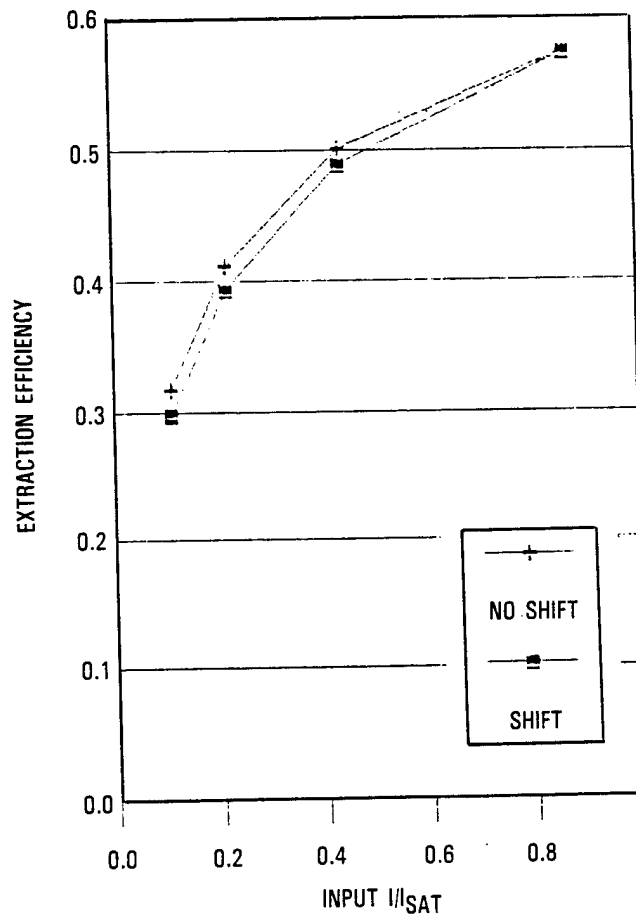


Figure 9.1-2. Predicted Extraction Efficiency Versus Input Intensity for Aerospace Experiment

because of limitations in gain length product, diagnostic accuracy, and the accuracy with which the effective reflectivities can be matched for with and without a frequency shift.

The rest of this section describes aspects of the bidirectional amplifier experiment planned for the APEX program. Section 9.2 covers amplifier modeling tools and shows predictions for SBL and ALPHA demonstration experiment amplifiers. Section 9.3 outlines experimental requirements and shows how the codes discussed in Section 9.2 were used to set some of these requirements. Section 9.4 outlines the experiment design approach and presents a conceptual design for the ALPHA-VM device. Section 9.5 presents small-signal-gain measurements that were performed early in the program to provide data used in the design.

## 9.2 AMPLIFIER MODELING AND SBL PERFORMANCE PREDICTIONS

Several amplifier models were used to help define performance of an SBL or APEX amplifier and to determine scaling relations between proposed experimental setups and an SBL or APEX demonstration experiment. Two amplifier codes, CLAM and LFCM, were used to predict bidirectional amplifier performance for an SBL, a large-scale demonstration experiment, and experimental requirements definition. The CLAM code was used to study the effects of frequency shift on a bidirectional amplifier, and the LFCM code was used to study the effect of HF kinetics on few line extraction. Description of the codes and their predictions for large systems are presented below.

### 9.2.1 CLAM Code

The CLAM code is a one-dimensional amplifier code designed to model the effects of the SBS frequency shift on amplification and extraction efficiency. It is based on the ANOM code developed under the Advanced Chemical Laser Optics Study (ACLOS) (Reference 9-5). It has two gain options. In its original form it had an HF gain model that models two cascade-connected transitions. This model is anchored to CROQ code results at one flow coordinate. Thus, the gain model is limited to the ALPHA flow condition. A simple  $g_0$ ,  $I_{\text{sat}}$  gain model was added to the CLAM code on the

APACHE program to allow comparison with other codes and to provide a mechanism to model other gain media.

Predictions of SBL bidirectional amplifier performance were made using the CLAM code. The input conditions were: amplifier length = 9 m, SBS reflectivity = 0.7, and input intensity =  $0.1 I/I_{\text{sat}}$ . The results with and without a 107-MHz frequency shift are shown in Table 9.2-1. Corresponding plots are shown in Figure 9.2-1 for the shifted and nonshifted cases. The implications are that for these conditions there is no power (and hence brightness) penalty with a frequency shift. There is also more power at the SBS cell with a frequency shift, indicating that the requirement on the master oscillator power may be smaller for a SBS phase conjugated bidirectional amplifier.

Table 9.2-1. CLAM Code Results for SBL Bidirectional Amplifier Performance, With and Without Frequency Shift

Parameter*	No Shift	Shift
I at input	0.10	0.10
I at SBS cell	1.77	2.48
I at output	22.16	22.56

\*Intensity in normalized units of  $I/I_{\text{sat}}$

Similar CLAM code calculations were performed for a possible APEX configuration, assuming ALPHA is run as an amplifier. The oscillator was assumed to be a separate device with an output power  $\sim 10X$  the power of ALPHA-VM to provide approximately  $0.5 I/I_{\text{sat}}$  input power to the ALPHA amplifier. A 25-m ring resonator was assumed for this oscillator. The amplifier assumed a two-pass ALPHA geometry with an effective gain length of 4 m. An SBS reflectivity of 0.2 was assumed to provide more power at the SBS cell. Parametric studies as a function of SBS reflectivity were not performed. Results with and without a frequency shift are shown in Table 9.2-2. Plots of intensity versus frequency from the CLAM runs with and without a frequency shift are shown in Figure 9.2-2.

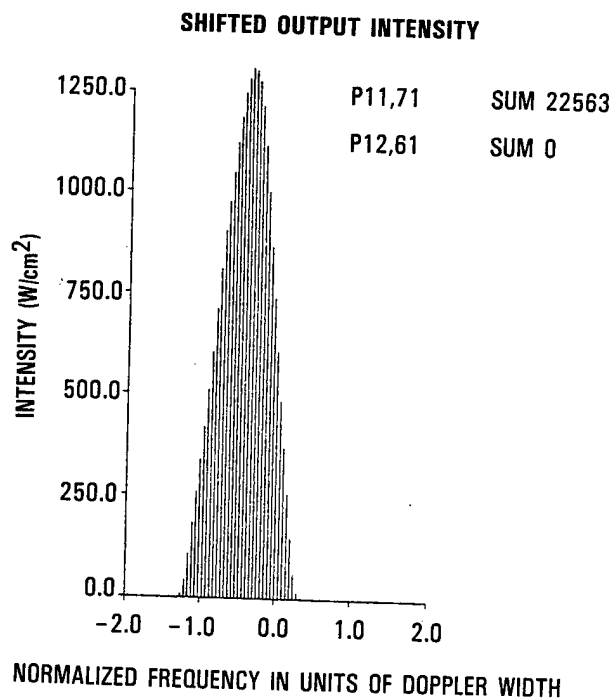
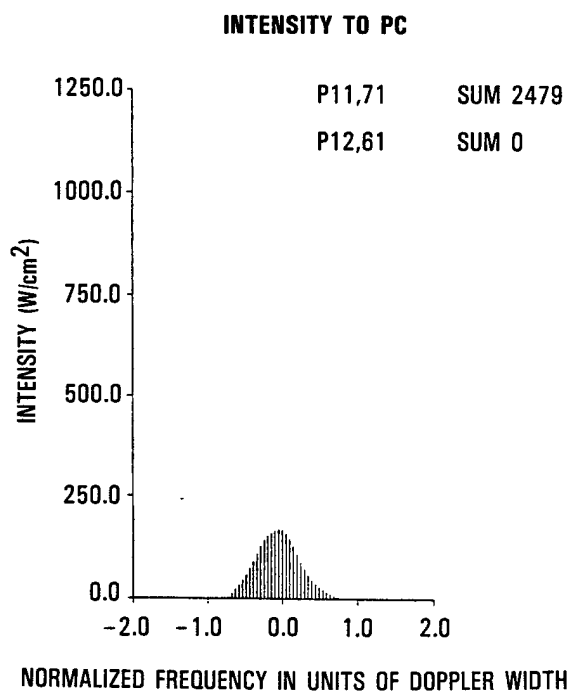
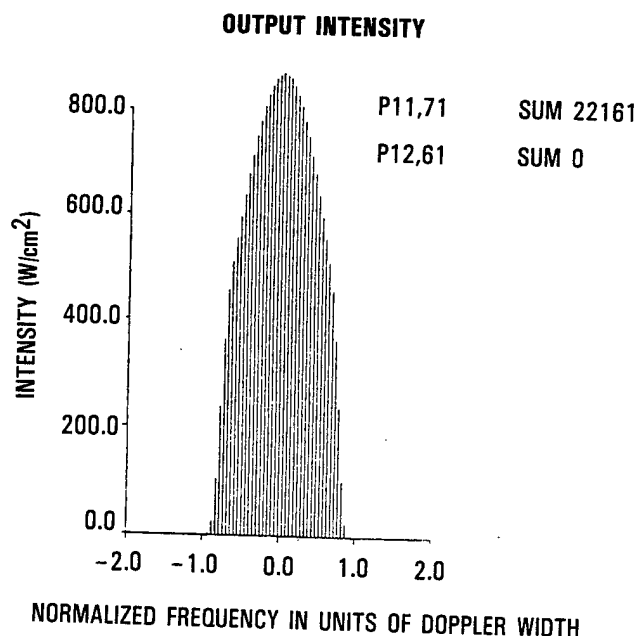
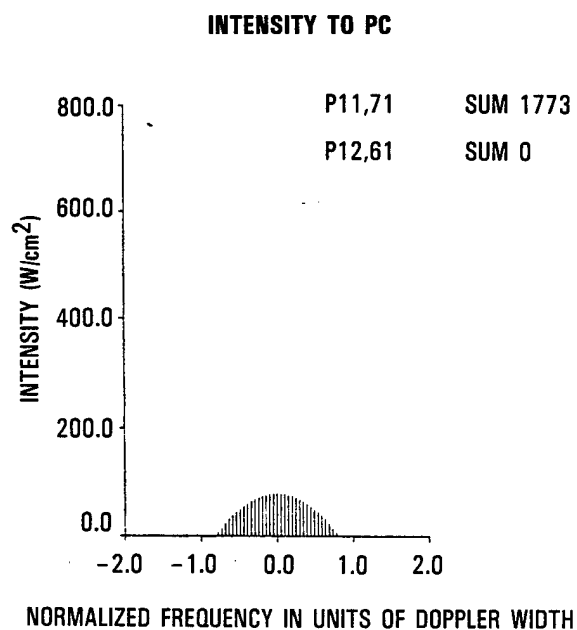


Figure 9.2-1. CLAM Code Prediction of Bidirectional Amplifier Performance for SBL

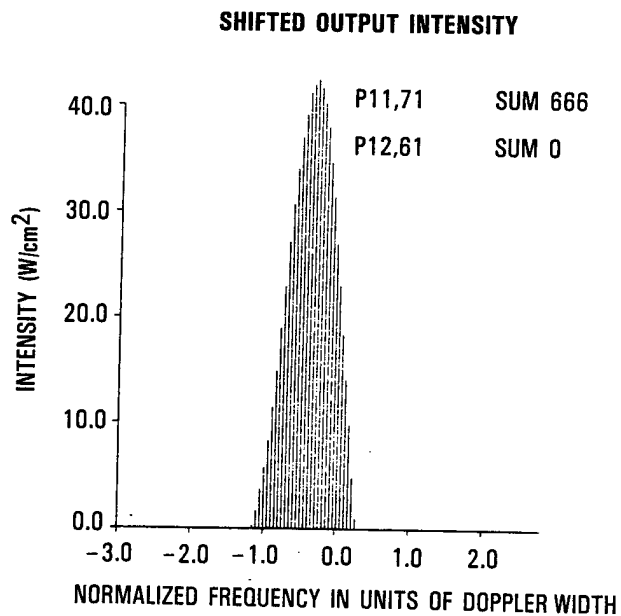
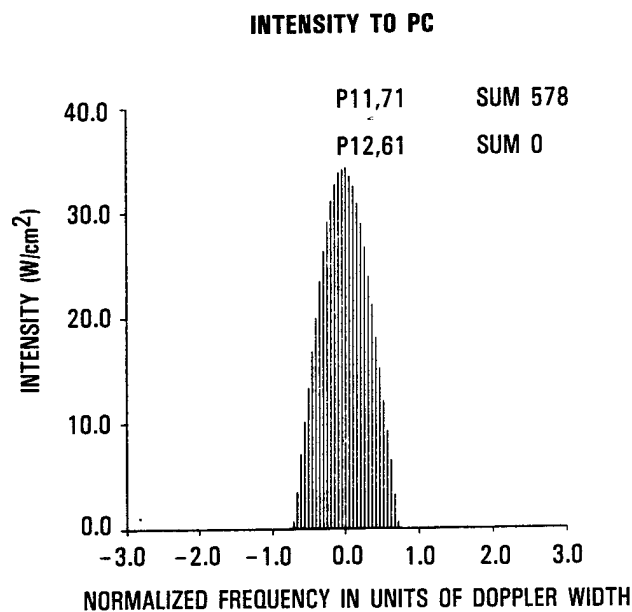
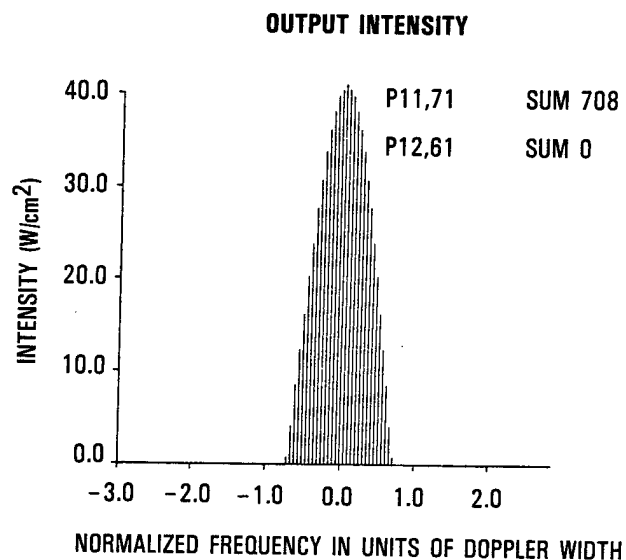
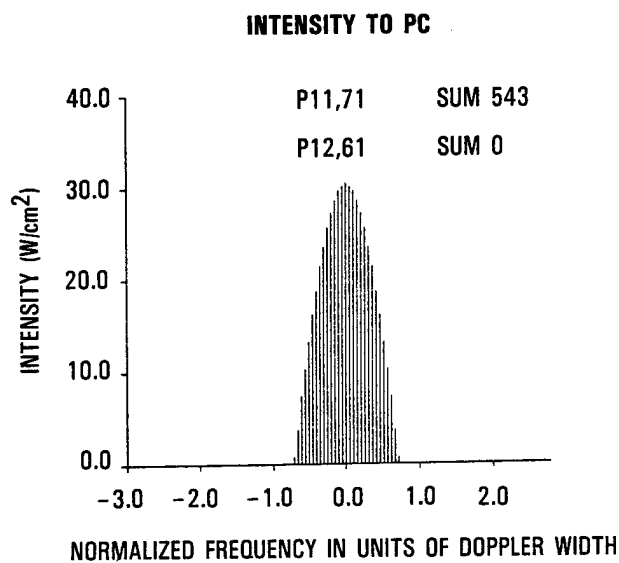


Figure 9.2-2. CLAM Code Predictions of Bidirectional Amplifier Performance for High-Power Demonstration Experiment



Table 9.2-2. CLAM Code Predictions of Intensities for ALPHA Run as Amplifier, With and Without Frequency Shift

Parameter	No Shift	Shift
I at input	0.5	0.5
I at SBS cell	2.39	2.54
I at output	3.85	3.62

The calculations indicates that the frequency shift has very little impact for the case run for an ALPHA amplifier. The output intensities are about the same with and without a frequency shift, and there is slightly more power at the SBS cell for the frequency shifted case. Comparisons of unidirectional and bidirectional amplifiers indicates that the conjugated return has a significant effect on the power reaching the SBS cell. It may be necessary to attenuate the phase conjugate beam before it reenters the amplifier to remain above threshold for SBS.

#### 9.2.2 LFCM/HF Kinetics Code

The gain model in the two-dimensional LFCM amplifier code (described in more detail in Section 4.1) was modified to include the CROQ HF gain model. The modified code has been named SLAM (slice amplifier model). The code was used to study two-line injection into an ALPHA amplifier and to assess if ASE on uninjected lines was important.

Only a few runs were made for an ALPHA amplifier to verify the correct operation of this multiline code. The extraction efficiency for four lines [ $P_1(7)$ ,  $P_1(8)$ ,  $P_2(7)$ , and  $P_2(8)$ ] was verified using CROQ code results. Two gain sheets were sufficient to provide good results at reasonable cost.

The code has the capability to run nine lines in the  $P_1$  and  $P_2$  bands. If less than nine lines are injected, ASE can be observed on the other noninjected lines. Two lines [either cascade connected  $P_2(7)$  and  $P_1(8)$  or  $P_2(8)$  and  $P_1(9)$ ] were injected to study ASE and extraction efficiency. It

was found that the output power when two lines were injected equalled that when four lines were injected. The total ASE was near 5 W, which is negligible.

### 9.3 EXPERIMENT REQUIREMENTS

In line with the stated objective of this experiment, requirements flow from the need to perform a bidirectional amplifier experiment traceable to an ALPHA demonstration experiment or an SBL. This objective gives some obvious requirements such as a CW HF gain medium for both oscillator and amplifier and the ability to provide a frequency shift to simulate an SBS reflector. Oscillator requirements are summarized in Table 9.3-1. Amplifier requirements are summarized in Table 9.3-2. Many of these requirements are self-explanatory from the table. Some of the less obvious requirements are discussed below.

#### 9.3.1 Gain Saturation as a Function of Frequency

The resonator length determines the number of longitudinal modes output from the oscillator. This in turn determines how well the amplifier will be saturated in frequency space. The CLAM code was used to predict relative saturations. Different resonator lengths were considered, and the amplifier saturated gain profiles calculated. A criterion that the magnitude of ripples in the saturated gain due to hole burning by the longitudinal modes be less than 5% gain fluctuations was set. CLAM code calculations for both the SBL and a three-pass VM with a resonator length of 4 m are shown in Figure 9.3-1. These calculations indicate that a minimum resonator length is 4 m.

#### 9.3.2 Gain Saturation in the Amplifier

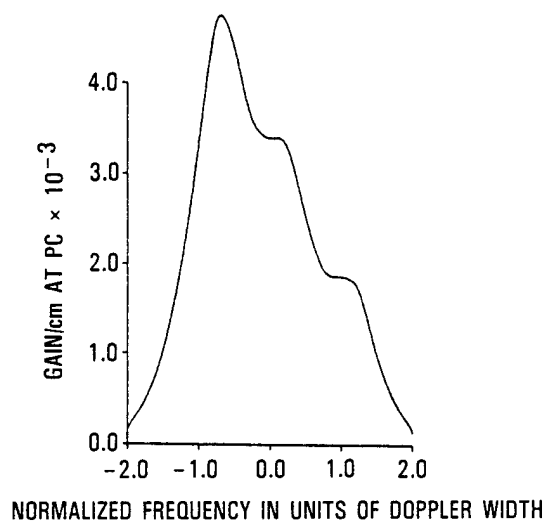
In any amplifier, the degree of saturation varies with length along the optic axis. At the end opposite the SBS cell, the required input intensity is of the order  $0.1 I/I_{\text{sat}}$ , and the intensity of the frequency shifted output is of the order  $10 I/I_{\text{sat}}$ . At the SBS end, the intensities of the frequency-shifted and nonfrequency-shifted beams are almost equal with a total intensity of  $\sim 3 I/I_{\text{sat}}$ , the ratio being determined by the SBS reflectivity. Calculations using the CLAM code were made of extraction efficiency as a function of relative input intensity with and without a

Table 9.3-1. Oscillator/Resonator Requirements

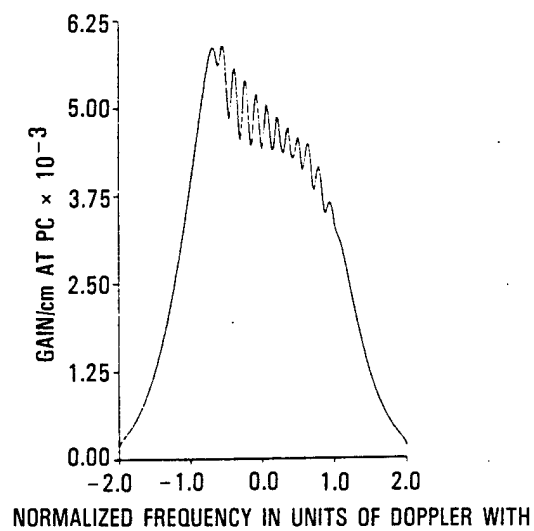
Parameter	Requirement	Justification
Gain medium	CW HF	Amplifier matching, spectrum
Resonator length	>4 m	Uniform gain saturation across Doppler gain profile
Spectrum	Variable	Need to study amplifier/oscillator spectral matching
Turn-on	Independent of amplifier	Change oscillator spectrum Preloading of amplifier
Power at amplifier	0.1 to 1 I/I <sub>sat</sub>	Need to study extraction as a function of input
Beam shape	Provide uniform illumination of amplifier aperture	Need less than 5% untapped gain in amplifier
Beam quality	<1.3	Ensure amplifier can provide good beam quality
Isolation	<10 <sup>-4</sup> of amplifier output	Ensure oscillator power and beam degrade by less than 10%

Table 9.3-2. Amplifier Requirements

Parameter	Requirement	Justification
Gain medium	CW HF (~5 torr)	Simulate ALPHA and SBL
g <sub>0</sub> L	TBD, as long as possible	Traceability to SBL
Fresnel number	Large enough to maintain image through amplifier	Elimination of measurement errors
Geometry	Tractable to analysis	Need analysis to scale to larger devices



**SBL**



**3-PASS VM**

Figure 9.3-1. CLAM Code Predictions for SBL and Three-Pass VM

frequency shift for a three-pass ALPHA-VM experiment ( $g_0 = 0.02 \text{ cm}^{-1}$ ,  $L = 180 \text{ cm}$ ). Results are shown in Figure 9.3-2. Similar calculations were made for a one-pass VM experiment ( $L = 60 \text{ cm}$ ). Calculations indicated that the  $g_0L$  should be greater than 1 to obtain meaningful extraction efficiency measurements. They also show that differences in extraction efficiency between shifted and unshifted cases depended on the degree of saturation, with higher extraction efficiencies anticipated for a frequency shifted beam in highly saturated experiments. For scalability to an SBL, the requirement for the total intensity (forward plus backward) is that it should be greater than  $2 I_{\text{sat}}$  to obtain scalable results.

### 9.3.3 Amplifier Gain Length Product

Two issues affect the required gain length product: ability to measure backward and forward amplifications and single-line extraction efficiency. Calculations were made of forward and backward amplifications with and without a frequency shift. These results are shown versus the number of passes through ALPHA-VM in Figure 9.3-3. Differences in forward and backward amplifications become more pronounced with higher  $g_0L$ . The  $g_0L$  should be greater than 3.5 to obtain differences between forward and backward amplifications of greater than 10%. Smaller differences would be difficult to measure with "typical" diagnostics.

Measurement of single-line extraction could set a higher  $g_0L$  requirement. This is because competition from other lines becomes more important as the gain length product is increased. This requirement could be relaxed if an additional requirement of measurement of small signal gain on unextracted lines is set.

### 9.3.4 Alignment of the Frequency Shifted Beam

A major issue affecting the frequency shifter design is how well the return beam has to be aligned to the incident beam to simulate a phase conjugated return. Calculations were performed to assess effects of misalignment of the return beam after it returns from the frequency shifter. For simplicity, the analysis assumed that the misalignment would be vertical as shown in Figure 9.3-4. The model divides the amplifier into zones as shown in the figure. Zone A sees only forward amplification.

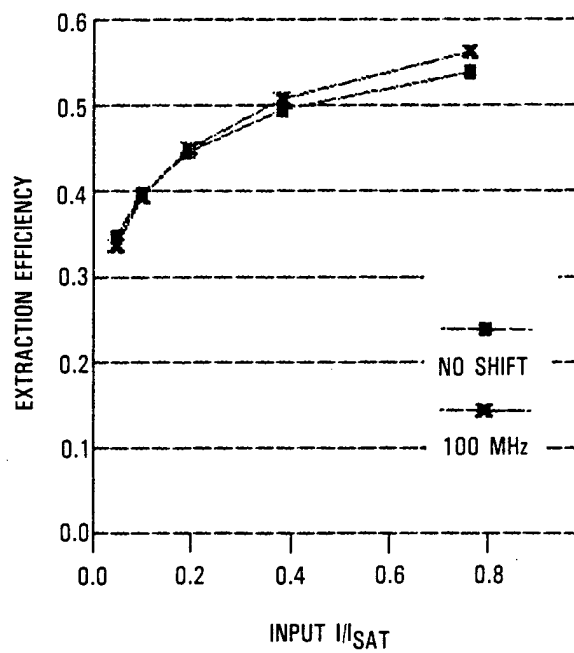


Figure 9.3-2. CLAM Code Predictions of Extraction Efficiency as Function of Input Intensity

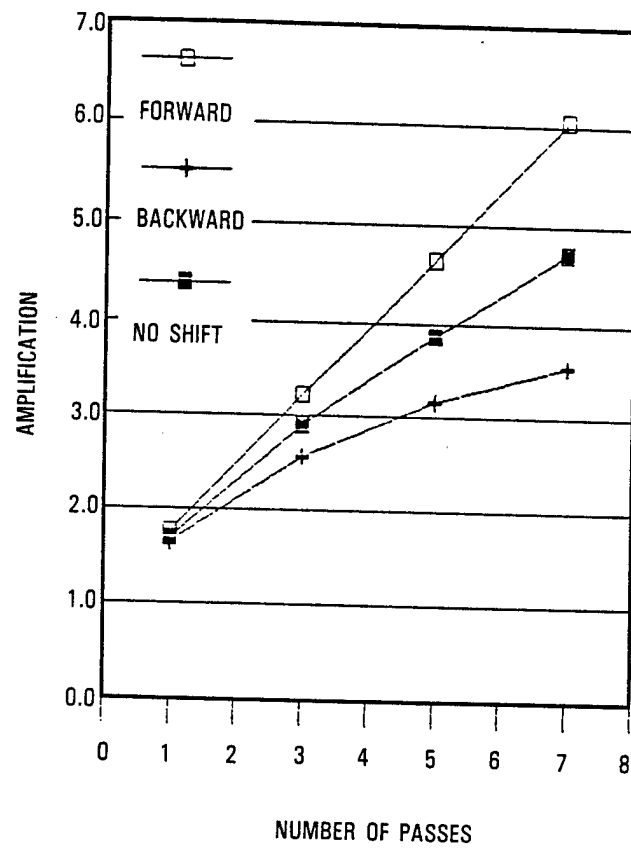


Figure 9.3-3. CLAM Code Predictions of Forward and Backward Amplifications Versus Number of Passes Through ALPHA-VM Gain Medium

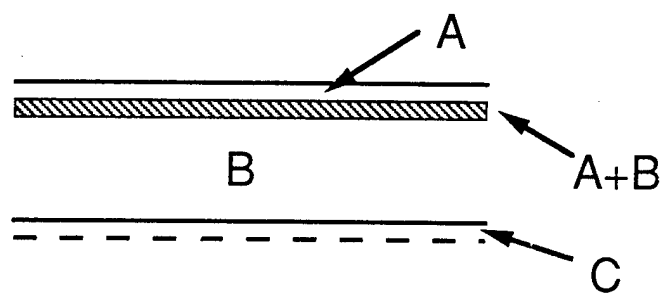


Figure 9.3-4. Geometry Used to Determine Misalignment Tolerance



Zone A+B sees the forward beam plus the return from zone A. Zone B gives the desired measurement, and zone C sees only the frequency-shifted return from zone B. A criterion that the maximum allowable error due to misalignment be less than 5% was established. For one pass through ALPHA-VM, this requirement yields a 12% offset. For three passes, this tolerance is reduced to 6%. Diffraction outside the geometric mode could also cause measurement errors. This sets a requirement on the Fresnel number of the amplifier of  $\sim 5$ .

#### 9.4 EXPERIMENT DESIGN APPROACH

##### 9.4.1 Optical Design

As part of the initial design, a trade study was performed to identify the most appropriate device to be used. Selection criteria included traceability, feasibility, cost, and schedule. The major requirement for the experiment is that it simulates SBL conditions for amplifier extraction. The ideal experiment for traceability to an SBL would be to phase conjugate a CW HF amplifier using SBS. The threshold in SBS limits the choice of lasers where phase conjugation is feasible. For example, an SBS experiment on ALPHA-VM would need a factor of greater than 30 in threshold reduction. An SBS experiment on NACL would need a threshold reduction factor between 5 and 10. The available options are summarized in Table 9.4-1. Budget and schedule considerations dictated the use of a CW device the size of ALPHA-VM or ZEBRA. A NACL experiment may be feasible but would require a 2-year schedule and a large budget. It would also depend on advances in threshold reduction and material windows.

An alternative approach would be to conjugate a pulsed HF amplifier. Unfortunately, pulsed HF lasers normally operate at high pressures of the order of 1 atm, where the medium is pressure broadened rather than Doppler broadened as in a CW device. Even a low-pressure pulsed HF device is predominantly homogeneously broadened because of the large HF-HF self-broadening constant. It would be feasible to run a pulsed laser with low concentrations of fluorine and a low outcoupling resonator to stretch the pulse into a more CW regime.

Table 9.4-1. Options for Bidirectional Amplifier Experiment

Option	Advantages	Disadvantages	Issues
AGGT risk reduction	TRW Building 67 experiment HYLYTE nozzle simulates SBL	19-cm gain length No existing gain model	Oscillator Partitioning
ALPHA-VM partitioned into oscillator/amplifier	AOM frequency shifter 60 cm gain length 12 cm gain height	5-cm gain height Expensive Mechanical	Partitioning Use of two oscillators
ZEBRA oscillator/VM amplifier	Traceable to ALPHA All of VM usable for amplifier Separate turn on of oscillator/amplifier Easier to characterize oscillator Possible for oscillator spatial filter	Frequency shifter Complexity of running Super expensive Never been done Mechanical frequency shifter	Facility flow capability Configuration
NACL partitioned into oscillator/amplifier	Phase conjugation experiment Longer gain length	Expensive Schedule	Threshold reduction SBS cell window feasibility

An experiment using the ALPHA-VM device with a mechanical frequency shifter/retro mirror to simulate the frequency shift present in phase conjugation was chosen as the baseline. A second option that will be explored is a phase-conjugation experiment on NACL which would rely on threshold reduction to work. A risk reduction experiment on the AGGT device in TRW Building 67 will also be considered. This experiment would be easy to implement as an AOM can be used as the frequency shifter. The experiment will be designed to address amplifier performance issues associated with bidirectional operation with a frequency shift.

A conceptual design which splits the ALPHA-VM device into oscillator and amplifier sections was chosen as the baseline for bidirectional amplifier tests. The 2.5- x 12.5-cm cross section of the gain volume is divided into five 2.5- x 2.5-cm sections. Square sections were chosen to maximize the Fresnel number per pass ( $N_F = 56$ ). The oscillator is an off-axis,  $M = 2$  confocal resonator. The output is clipped to maintain an unobscured beam. Two bidirectional amplifier conceptual designs were identified. The first consists of an oscillator and four bidirectional amplifiers. It is sketched in Figure 9.4-1 and shown in more detail in Figure 9.4-2. This design yields the maximum  $g_0L$  product for counterpropagating beams. The detailed design shows a set of polarizing grating rhombs for control of the spectrum into the amplifier and for isolation of the oscillator. An image relay telescope is placed after two amplifier passes to minimize diffraction losses through the long amplifier. Minimization of diffraction will facilitate modeling. The second consists of an oscillator and three preamps and one bidirectional amplifier. A sketch of this design is shown as Figure 9.4-3 and shown in more detail in Figure 9.4-4. This design provides the flexibility to study a wide range of intensities of the counterpropagating beams and, hence, would allow simulation of different sections of an SBL amplifier. In this design, the oscillator output is separated into two parts, one of which is frequency shifted, and one remains at its original frequency. The unshifted beam passes through a pair of polarizing grating rhombs and into the amplifier section. The second beam goes to a frequency shifter and then passes through three preamplifiers and a second polarizing grating rhomb before it enters the other side of the conjugated amplifier. This allows

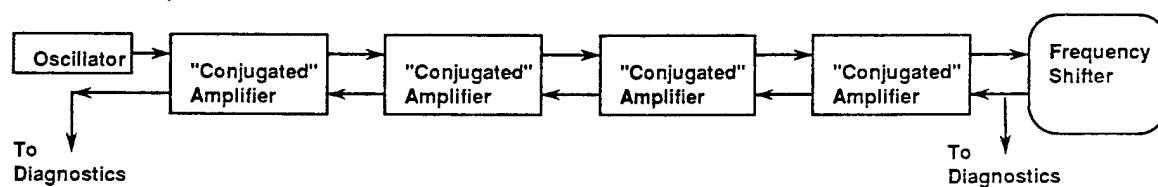


Figure 9.4-1. Sketch of Bidirectional Amplifier Concept for Oscillator and Four-Pass Amplifier

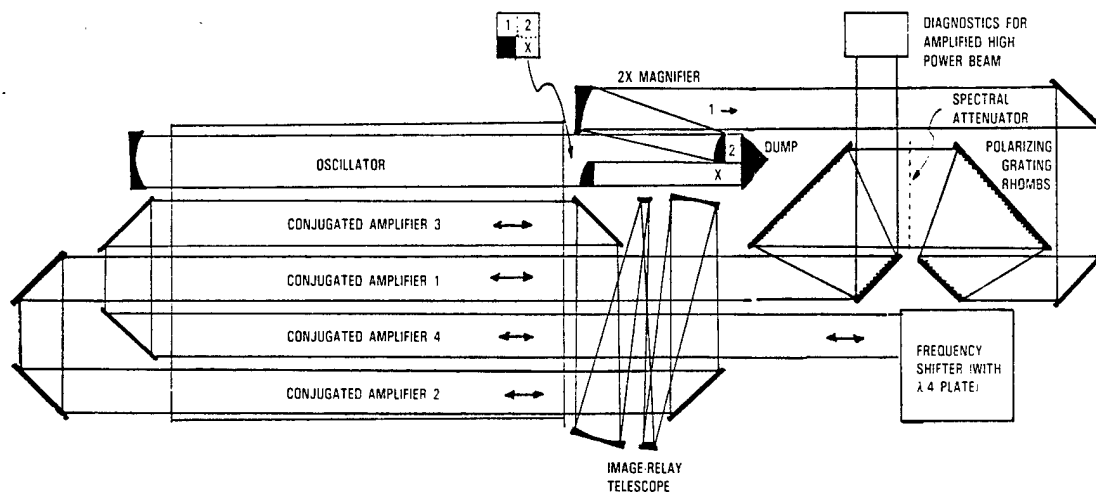


Figure 9.4-2. Bidirectional Amplifier Configuration for Oscillator and Four-Pass Amplifier

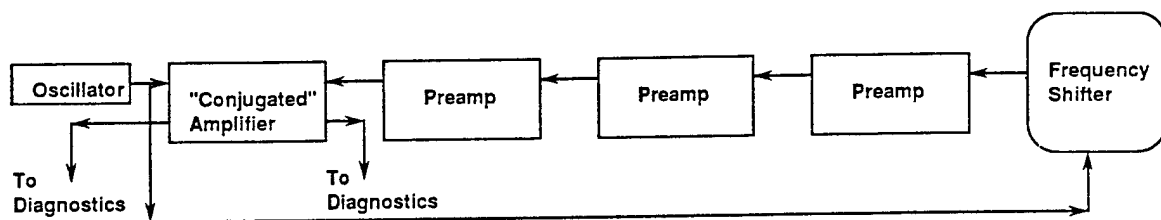


Figure 9.4-3. Sketch of Bidirectional Amplifier Experiment To Give Flexibility on Intensities of Counterpropagating Beams

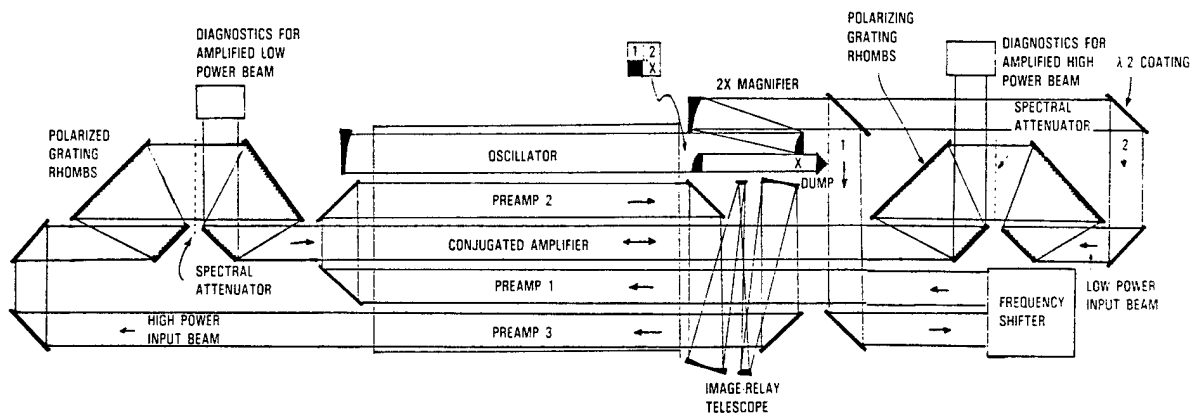


Figure 9.4-4. Bidirectional Amplifier Configuration for Greatest Intensity Range of Counterpropagating Beams

simulation of the output end of a large phase-conjugated amplifier where the output intensity is much larger than the input intensity. Both designs use a mechanical frequency shifter to provide high-efficiency simulation of the SBS Doppler shift. The polarization separation of counterpropagating beams in bidirectional amplifiers ensures oscillator isolation and simplifies experimental modeling.

The final design, procurement, integration, and testing for the bidirectional amplifier experiment will be conducted on the APEX program. Alternate concepts will be considered on that program. Advances in technology in the area of threshold reduction could lead to an SBS phase-conjugated amplifier on a sub-ALPHA scale device.

#### 9.4.2 Mechanical Frequency Shifter Design

The major requirements for a mechanical frequency shifter for a bidirectional amplifier experiment traceable to a phase-conjugated device are summarized in Table 9.4-2. The requirements for return beam parallel offset and tilt are quite stringent, placing limitations on the design.

Five concepts for the mechanical frequency were considered. These included a rotating grating shifter, a translating corner cube, an oscillating corner cube, tilted translating mirrors, and an involute wheel.

The current baseline design is a rotating grating shifter concept. The concept relies on gratings ruled on two disks which rotate counter to each other. The concept is sketched in Figures 9.4-5(a) and 9.4-5(b). The incoming beam hits the first grating at  $\sim 65^\circ$  from normal. It diffracts from this grating to the second grating and then hits a corner cube which reverses the beam. Multiple wavelengths remain parallel due to balanced geometry. Referring to Figure 9.4-5(c), the frequency shift can be shown to be equal to

$$\Delta\nu = \frac{nV}{\lambda} \sin\theta_{in} + \sin\theta_{out} = \frac{nV}{d}$$

where  $n$  is the number of grating bounces which is 4 for the concept sketched. Calculations using this formula show that the desired frequency shift could be obtained with a 30-cm-diameter radial grating ruled at 330



Table 9.4-2. Mechanical Frequency Shifter  
Design Requirements

Issue	Requirement
Shift frequency	107 MHz $\pm 10\%$
Return beam parallel offset	$< 5\%$ of beam size
Return beam tilt	$< 50 \mu\text{rad}$
Beam Size	2.54 x 2.5 cm
Maximum intensity	3 kW/cm <sup>3</sup>

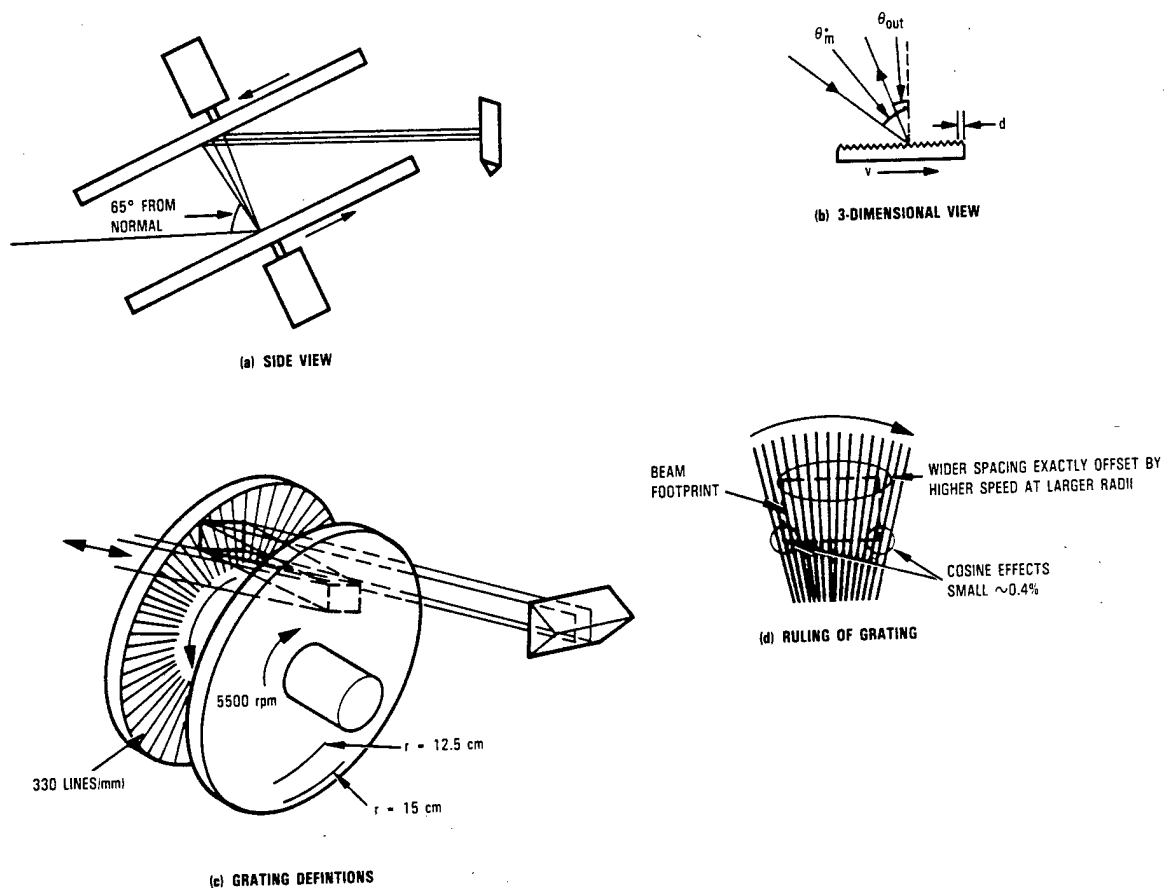


Figure 9.4-5. Rotating Grating Shifter Concept

lines/mm rotating at a radial velocity of 5500 rpm. Hyperfine, Inc., has built a 600 line/mm grating on a 20-cm disk and claims capabilities of 6000 lines/mm on 40 to 50 cm disks. The ruling of the grating on the disk is illustrated in Figure 9.4-5(d). It shows that the wider spacing at the outside edges of the disk are exactly offset by the inherent higher speed at larger radii. Cosine effects are small, of the order of 0.4%.

A translating mirror concept sketched in Figure 9.4-6 was also considered. In this concept two mirrors are rapidly translated apart giving a change in frequency due to the Doppler shift. The mirrors take a certain time to accelerate and for their motion to be damped. A relatively short time is allowed for data collection before the mirrors are decelerated. A track length greater than 1.2 m would be needed to achieve the desired velocity. A relative of the translating mirror concept is the translating corner cube sketched in Figure 9.4-7. Here corner cubes are used in place of flat mirrors to give insensitivity to jitter in moving components. A plot of the required translation velocity versus the track length is plotted in Figure 9.4-8 for either of translating mirror concepts. Assumptions made in making this plot included a constant acceleration, on  $C/C_c$ , of 0.002, a data collection time of 0.0667 s, and a deceleration time equivalent to that needed for a honeycomb to stop the mirrors. The major disadvantages of translating mirrors are their transient operation which allows only a short window of data collection time per run plus the challenging translation stage design.

The final concept considered was an involute-wheel shifter. This is sketched in Figure 9.4-9. The involute was chosen because it is always normal (retroreflecting) to lines tangent to the generating circle. The involute wheel is three to four times larger than its generating circle to maximize radial velocity uniformity and astigmatic correctability. The required spin rate is based on the edge speed of the generating circle of radius  $r$

$$\text{rpm} = \frac{60 \Delta\nu\lambda}{4 \pi r n} = 3600 \text{ rpm for } r = 10 \text{ cm, } d = 75 \text{ cm}$$

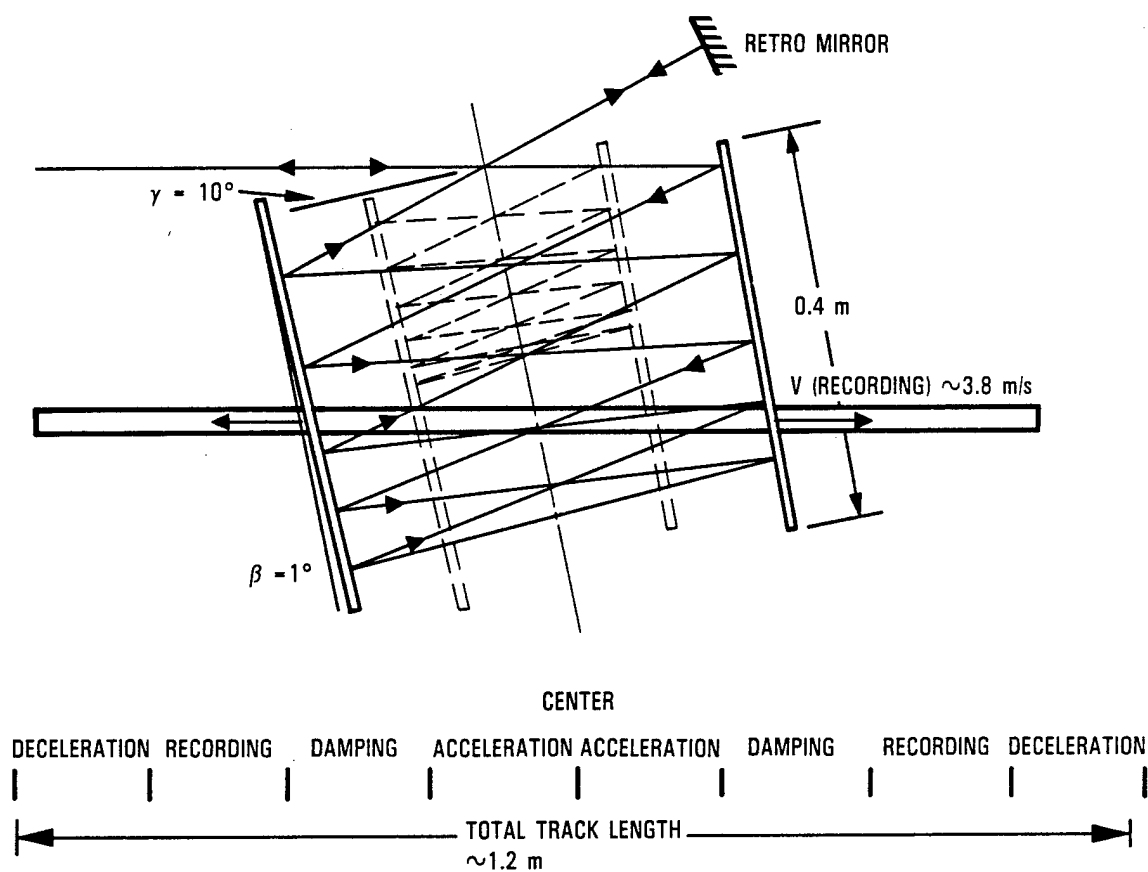


Figure 9.4-6. Translating Mirror Concept

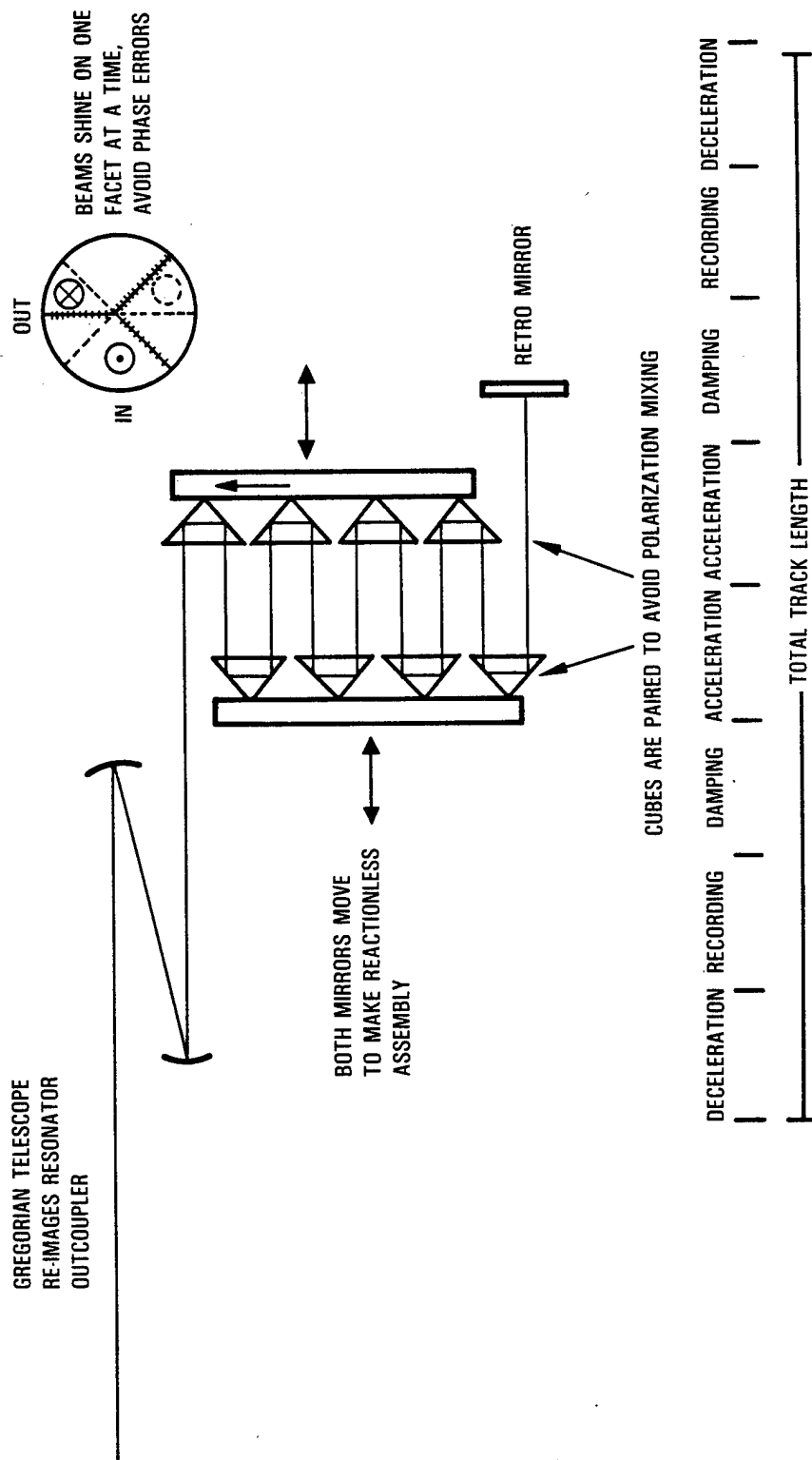


Figure 9.4-7. Translating Coner Cube Concept

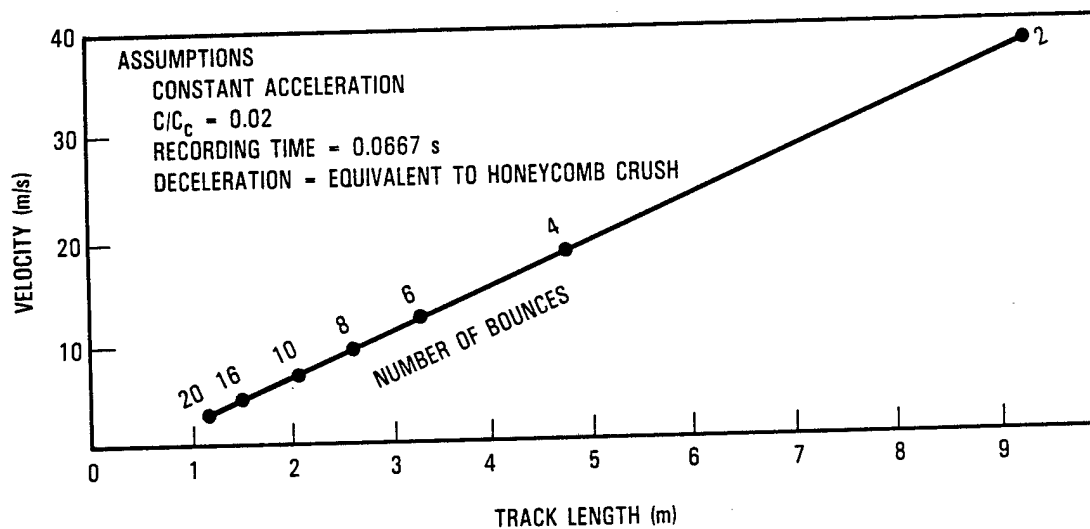


Figure 9.4-8. Velocity Required Versus Track Length for Different Numbers of Bounces

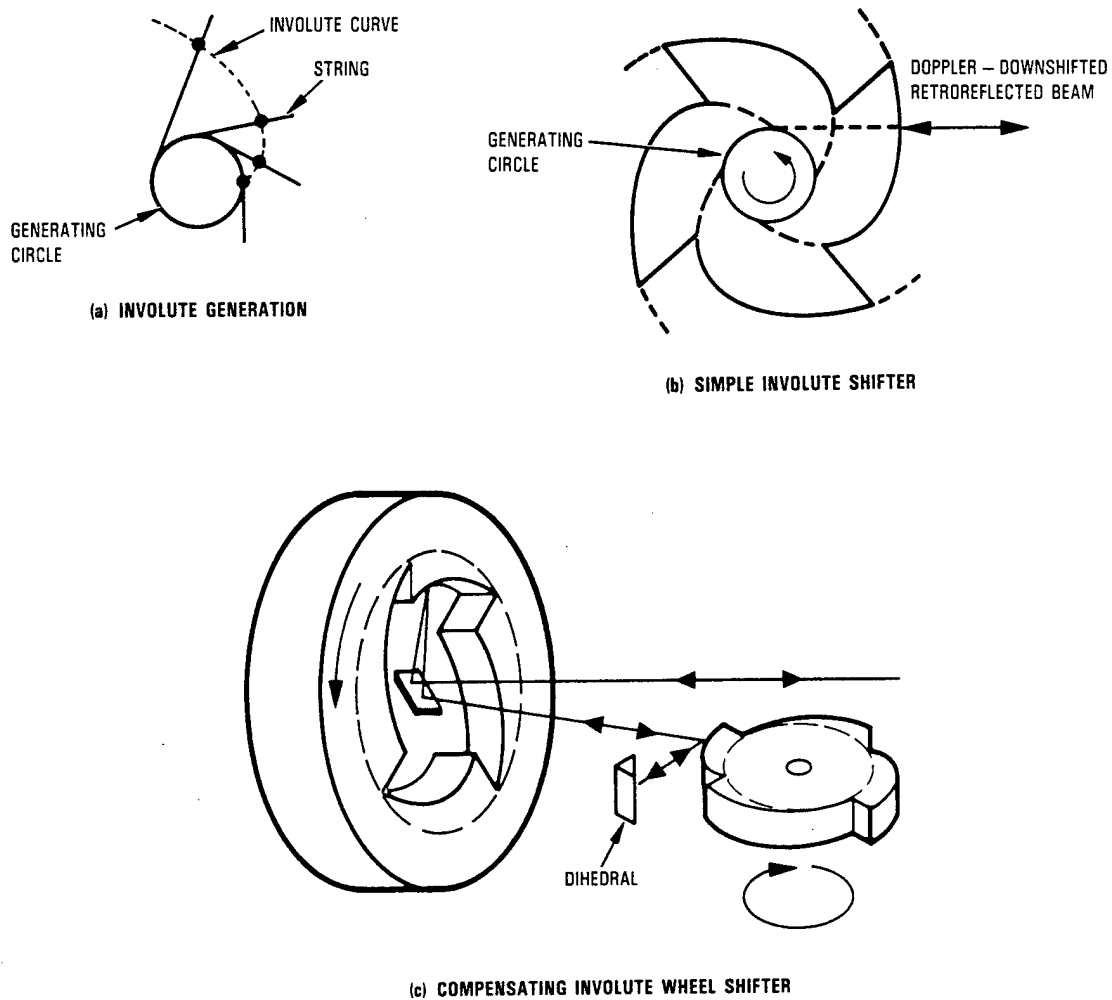


Figure 9.4-9. Internal and External Involute Wheels Compensate Astigmatic Focusing and Time-Varying Radial Velocity. Dihedral Compensates Further

where  $d$  is the wheel diameter. This concept has the advantage of high efficiency and constant operation. However, the optics are difficult to fabricate and there is a  $50\text{-}\mu\text{s}$  window on each rotation where data cannot be obtained. A more complicated version of this concept, shown in Figure 9.4-8(c), would use rotating internal and external involute wheels to compensate for astigmatic focusing and time-varying radial velocity. Use of a dihedral retromirror provides further compensation.

The concepts considered are summarized in Table 9.4-3 with advantages and disadvantages of each. The rotating grating was chosen as the baseline because of its constant operation, simple mechanical design, and its use of existing technology for grating fabrication. The translating mirror concepts were discarded basically because of their transient operation which would allow only short data collection times during a run and extensive time between runs to reset the mirrors. The rotating involute is an appealing concept but was not used as a baseline because of the difficulty in optics fabrication.

## 9.5 SMALL-SIGNAL-GAIN MEASUREMENTS

To support the design of the bidirectional amplifier experiment, information on the small-signal-gain characteristics of the ALPHA-VM device were needed. A brief small-signal-gain experiment was conducted to expand this data base. The major purpose of this experiment was to measure gain in the optical axis direction, scanning the gain aperture to look for gain nonuniformities from top to bottom of the gain medium. Previous small-signal-gain measurements on the ALPHA-VM device were taken in the horizontal direction from the center of a nozzle to the center of a base region and then integrated in the optical direction. Uniform performance of all the nozzles was assumed in extrapolation of these results to the optical axis direction.

### 9.5.1 Experiment Description

The small-signal-gain measurements were performed on the ALPHA-VM device which is shown schematically in Figure 9.5-1. The measurements were performed in the optical direction and used an eight-element detector array, scanning from strut to shroud parallel to the optical axis as shown



Table 9.4-3. Frequency Shifter Concept Evaluation

	Corner Cube Array Linear Translating/ Oscillating	Rotating Gratings	Involute Wheel	Linear Motion Flat Mirrors
Advantages	Reasonable efficiency (~60%) Insensitive to jitter in moving components Straight forward design	Demonstrated grating components Simple mechanical design Constant operation Compact	High efficiency (~90%) Constant operation Semicompact	Multiple bounces result in smaller mirrors Lower velocities Shorter track length
Disadvantages	Many reflections (~100) off surfaces Challenging translation stage design Transient operation	Low efficiency (~30%) (75% per bounce) Inaccurate shift with wavelength ( $\pm 10\%$ )	Difficult fabrication of optics 50- $\mu$ s between hiccups	Extremely high precision mirror alignment tolerances (tilt per mirror = $50/20 = 2.5 \mu$ rad)

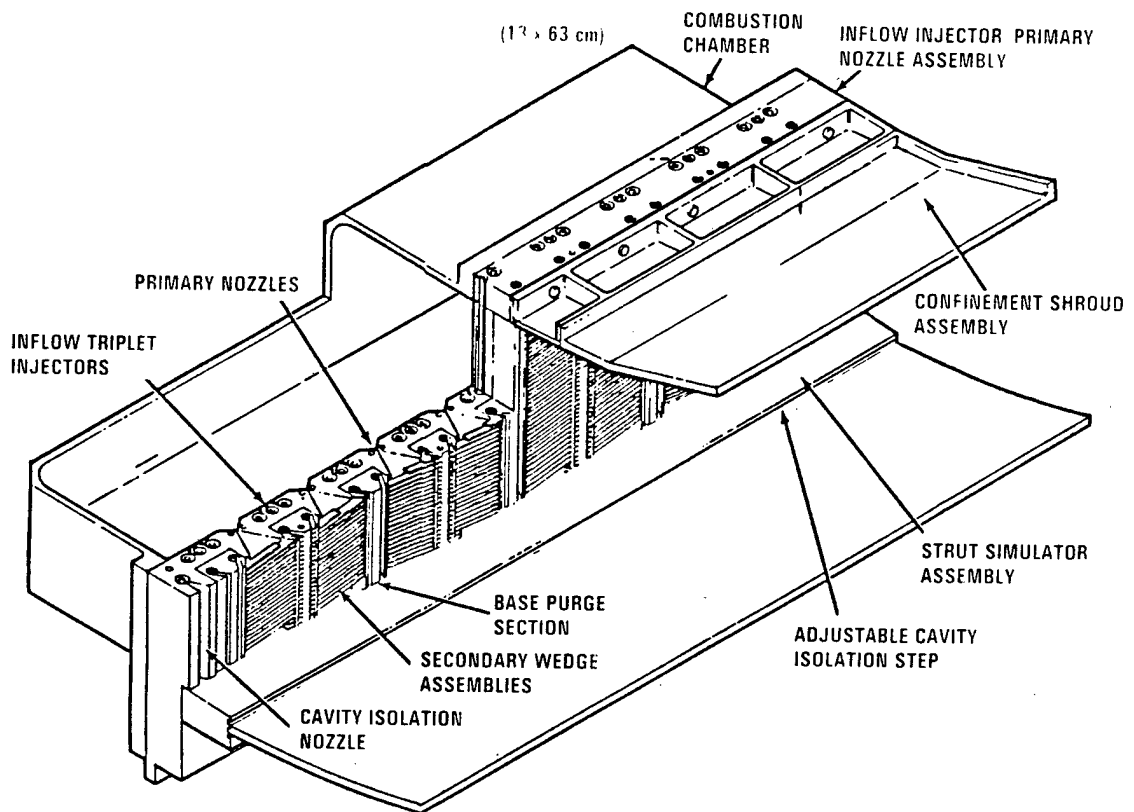


Figure 9.5-1. ALPHA VM Device

in Figure 9.5-2. Figure 9.5-3 shows the setup for previous small-signal-gain measurements on VM. They made use of the same array but scanned from the centerline of a nozzle to its corresponding base region, outward, away from the nozzle exit plan. The device was run for the nominal ALPHA flow condition listed in Table 9.5-1. Device parameters were held constant for the entire test series. Diluents flowed for 30 s before and after cavity fuel injection, while an active gain medium was on for approximately 10 s. Gain was measured in the optical axis direction.

A layout of the experiment is shown in Figure 9.5-4. A Helios miniprobe with an intracavity grating that could be tuned to most of the HF lines was used as the source for the small-signal-gain measurements. The beam passed through a calcium fluoride beam splitter, which reflected a small portion of the beam into an InAs reference detector. The remaining circular output beam was expanded via a cylindrical telescope to a rectangular beam approximately 3 X 40 mm. The rectangular beam was propagated through a calcium fluoride cavity window with a 3° wedge to a flat mirror angled at 45° to the device flow direction. The turning flat was mounted to a high-precision translation stage that translated the rectangular probe beam in the  $x_c$  or laser flow direction. This beam was incident upon an eight-element InAs detector array. The array was used to measure the signal as a function of distance from the nozzles. The detector array was mounted on a second high-precision translation stage that tracked the rectangular beam from the turning flat. Both translation stages were driven simultaneously by a TaskMaster 8138 positioning controller. The output of each detector was monitored using a PAR 124 lock-in amplifier. Data was collected with a MINC 23 microprocessor which directly calculated small signal gain.

The test procedure was to establish a baseline with only diluents running, then accumulate small signal gain data and then reestablish the baseline after a run with diluent flow.

#### 9.5.2 Experimental Results

Small signal gain was measured on the  $P_1(5)$  through  $P_1(9)$  lines and the  $P_2(6)$  through  $P_2(8)$  lines. Forty tests were performed during the time allotted to these measurements. The earlier tests were used to establish

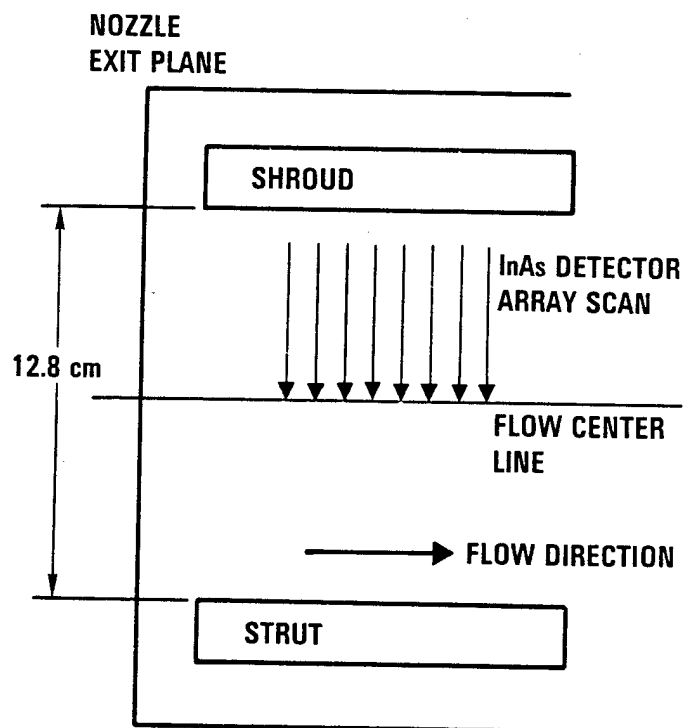


Figure 9.5-2. Schematic Experiment Showing Detector Scan From Shroud to Street

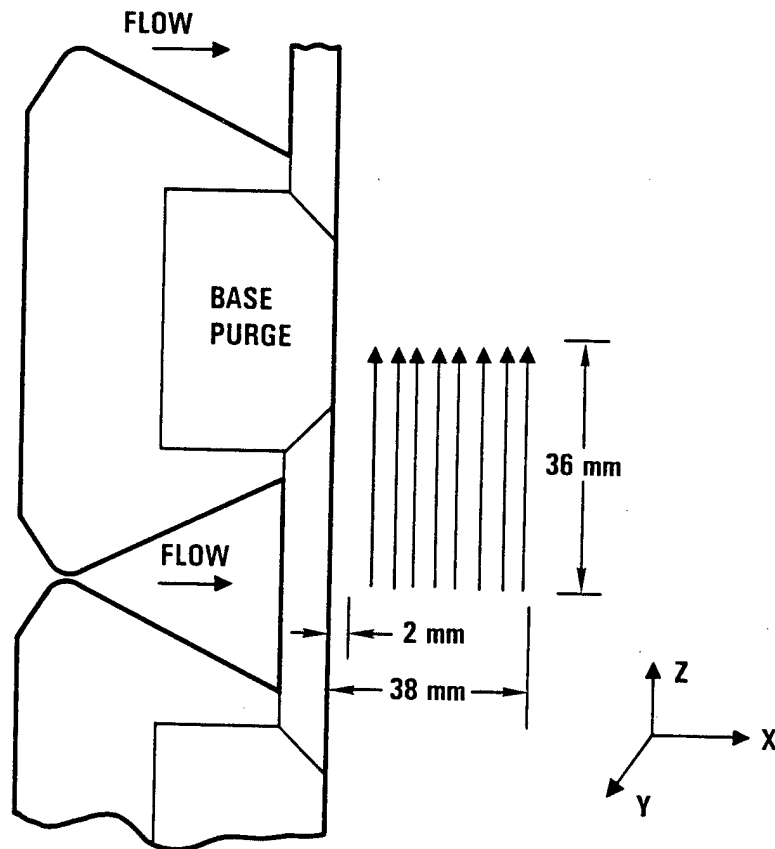


Figure 9.5-3. CLASP Small-Signal-Gain Schematic

Table 9.5-1. Nominal ALPHA-VM Run Conditions and Operating Time Line

Time	Circuit	Condition	Flow Rate (g/s)
0.0	Cavity simulant (He)	ON	30.0
5.0	Cavity fuel (He)	ON	22.0
6.0	Cavity simulant	OFF	
11.0	Cavity diluent (He)	ON	10.0
15.0	Cavity diluent	OFF	
16.0	Cavity simulant	ON	
17.0	Cavity fuel	OFF	
18.0	Shutdown		

Operation with 4 blade arrays

Combustor circuit cold flow (flowtime ~3 s each)

Combustor fuel diluent (He) = Flow 2.0 g/s

Combustor oxidizer diluent (N<sub>2</sub>) = Flow 15.0 g/s

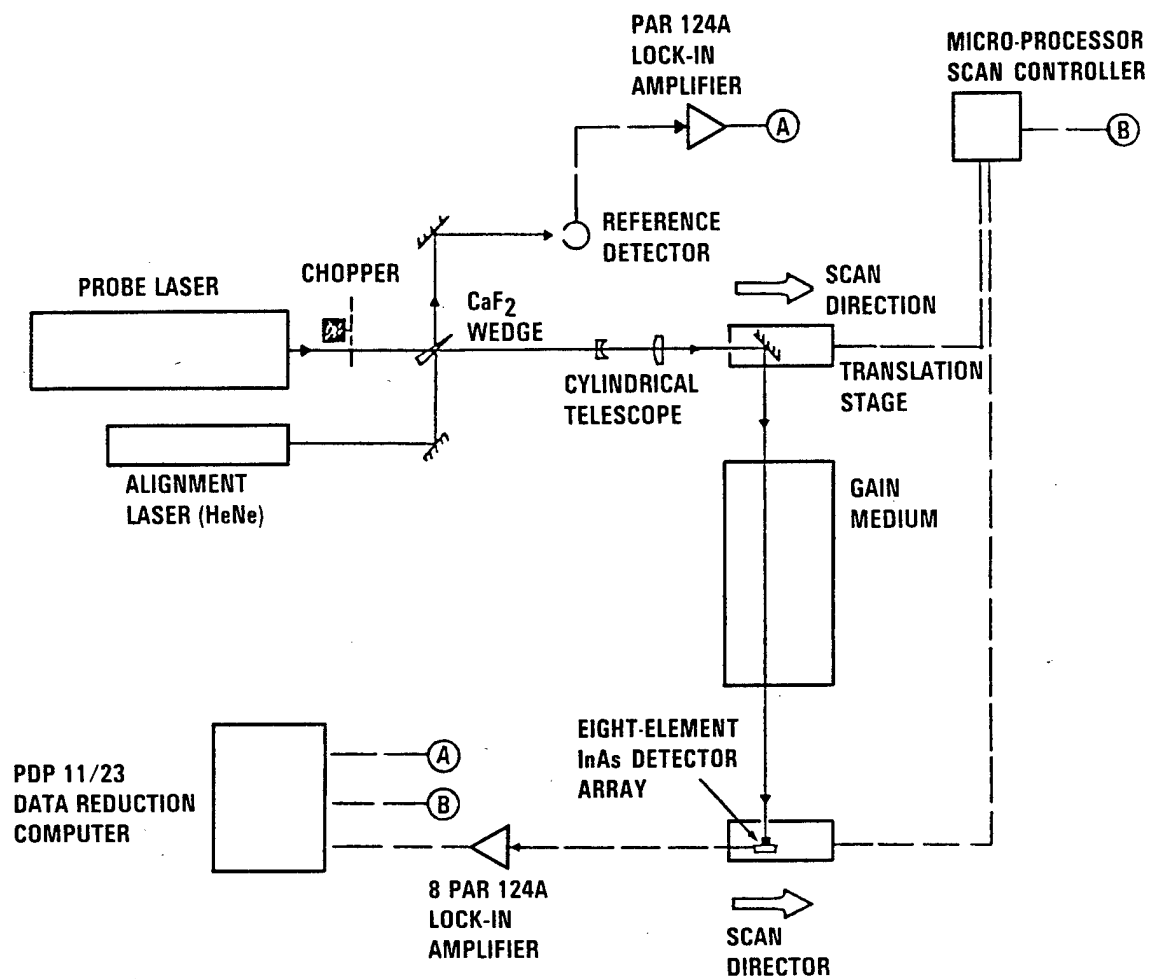


Figure 9.5-4. Small-Signal-Gain Layout

baselines and debug the system. Representative data for the lines studied are presented in this report. Figures 9.5-5 and 9.5-6 show results of small-signal-gain data as a function of position from strut to shroud for the  $P_1(6)$  and  $P_1(7)$  lines. In these runs, 0 cm corresponds to the strut position, and 12 cm to the shroud. The two traces on each plot correspond to two separate runs. Figures 9.5-7 and 9.5-8 show plots of the average small signal gain over the aperture versus position in the flow direction, where 0 cm is the nozzle position and larger numbers are downstream of the nozzle.

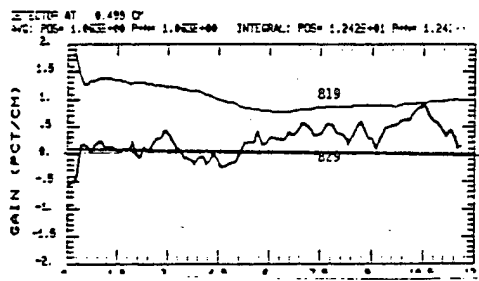
### 9.5.3 Discussion of Data

Most of the noise observed in the data was caused by instabilities in movement of the translation stages scanning the beam across the cavity. The data shown are the best noise levels that could be obtained with the equipment available for the test. Data for runs 814 and 815, shown in Figures 9.5-1 and 9.5-2, have less high-frequency noise in the 0.5 and 1.0 cm positions. In these runs, the time constant on the lock-in detectors was inadvertently set to a longer value, causing integration of the noise. The probe beam into the detector closest to the nozzles was somewhat obscured by parasitic clippers in the ALPHA-VM device. Consequently, the data at the position closest to the nozzle is somewhat suspect.

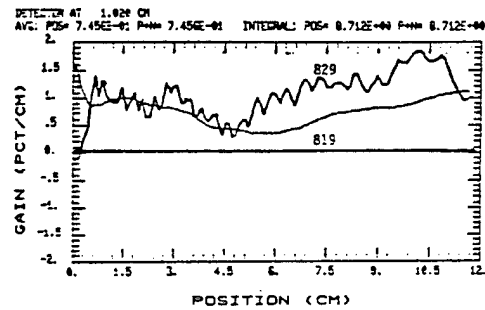
Measurement of small-signal-gain uniformity in the vertical direction was the major objective of this test series. The data show nonuniformities in the gain on the  $P_1$  lines with a dip in the gain towards the center of between 50 and 100%. The gain is generally higher on the side near the shroud. The data show more uniform gain on the  $P_2$  lines. However, there are still variations from ranging from 13 to 50%. These differences could lead to power differences between two sides of the beam. The gain on the  $P_1$  lines is more sensitive to the presence of ground state HF which is a strong absorber. If some of the absorption is bleached out during power runs, this could bring the effects of nonuniformities in the gain on the  $P_1$  lines down to the level of that of the  $P_2$  lines.



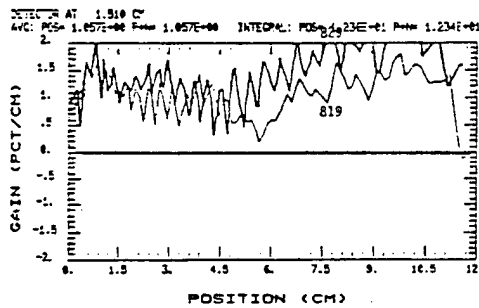
$X_C = .499\text{cm}$



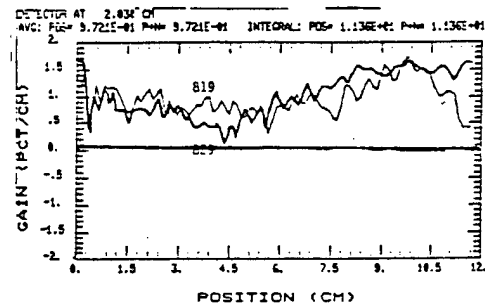
$X_C = 1.02\text{cm}$



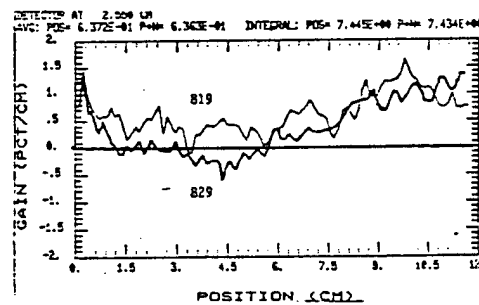
$X_C = 1.51\text{cm}$



$X_C = 2.03\text{cm}$



$X_C = 2.55\text{cm}$



$X_C = 3.05\text{cm}$

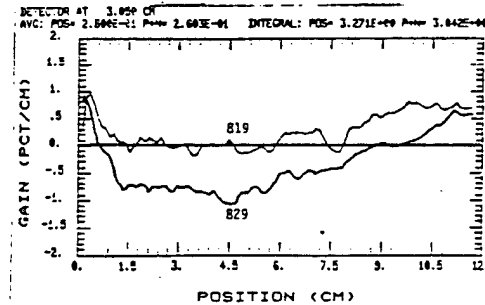
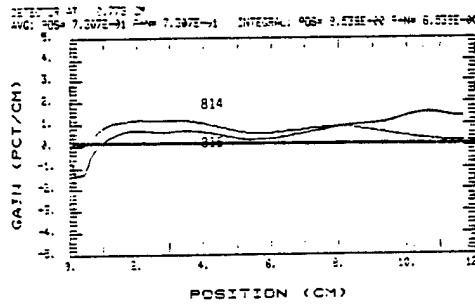
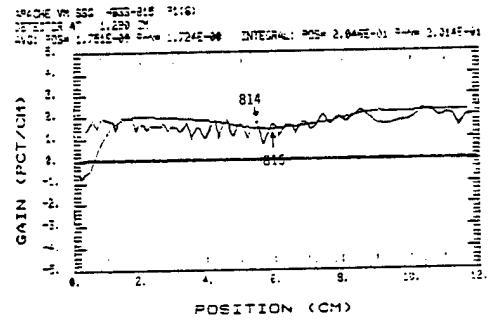


Figure 9.5-5. Gain Uniformity From Strut to Shroud,  $P_1(7)$  Line

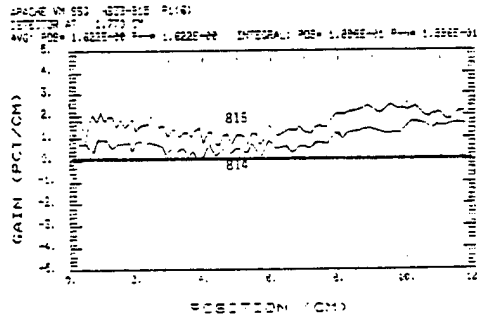
$X_C = .788\text{cm}$



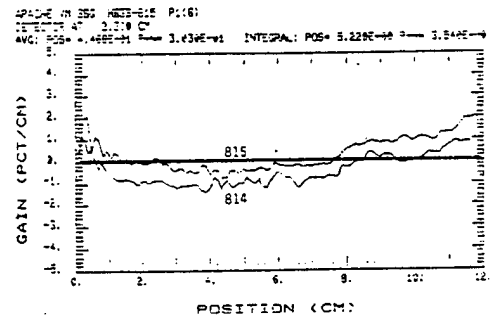
$X_C = 1.29\text{cm}$



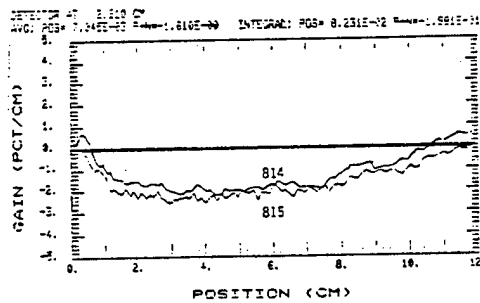
$X_C = 1.77\text{cm}$



$X_C = 2.3\text{cm}$



$X_C = 2.51\text{cm}$



$X_C = 3.32\text{cm}$

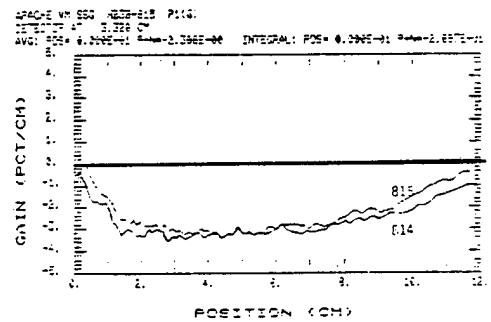


Figure 9.5-6. Gain Uniformity From Strut to Shroud, P<sub>1</sub>(6) Line

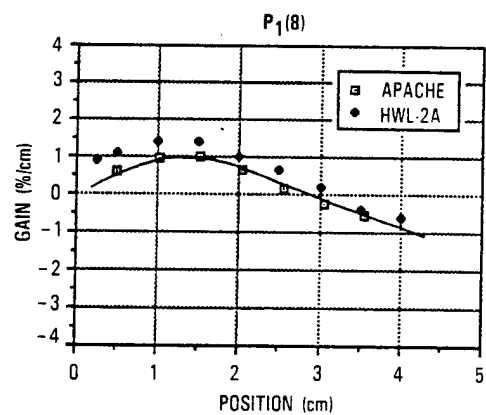
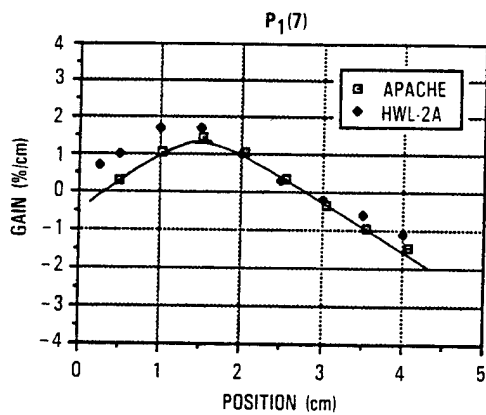
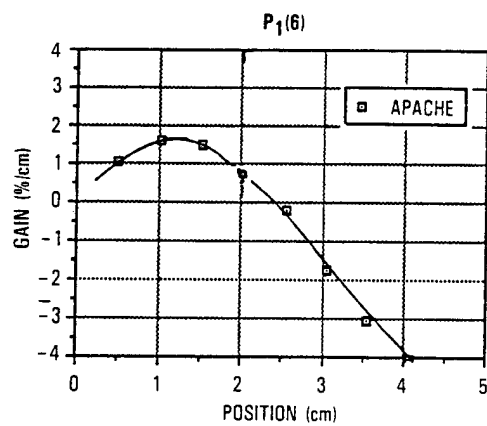
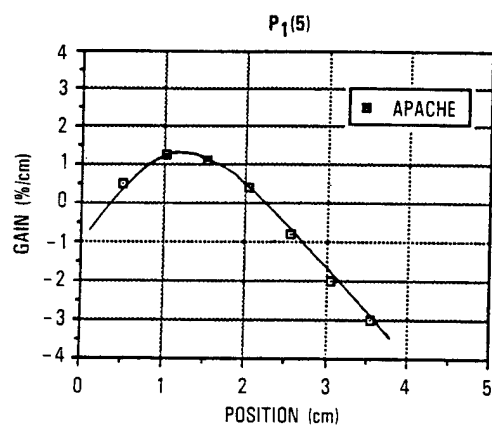


Figure 9.5-7. Averaged Small-Signal-Gain Data on  $P_1$  Lines

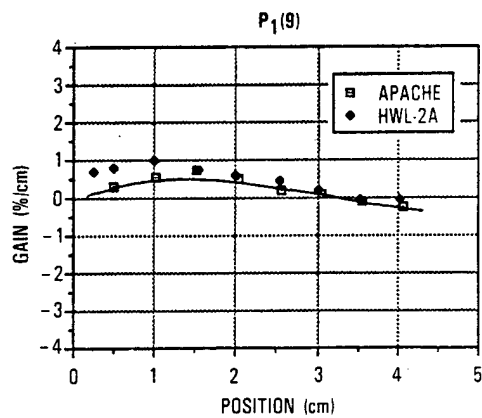
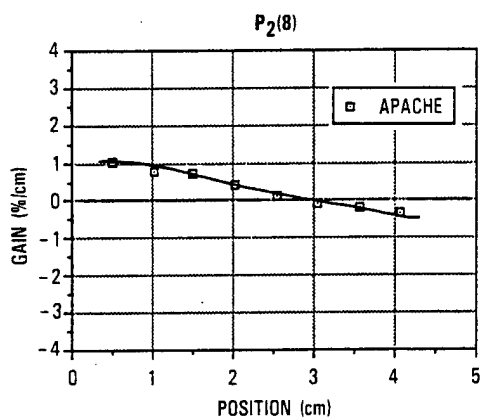
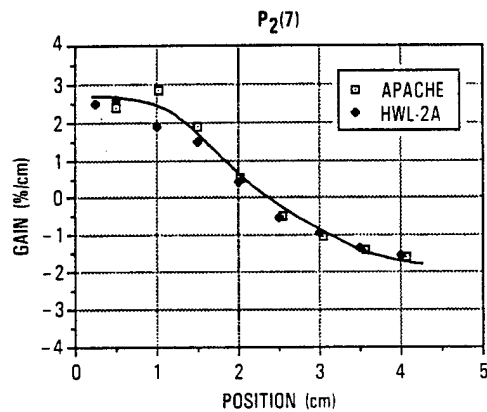
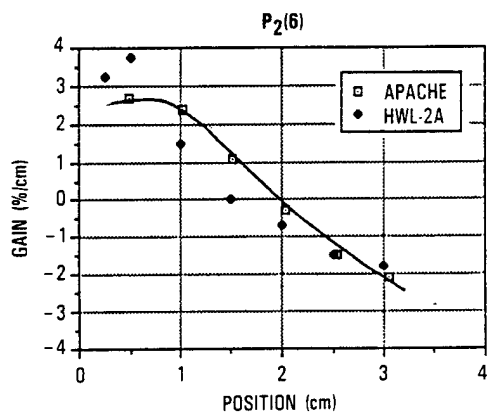


Figure 9.5-8. Averaged Small-Signal-Gain Data on  $P_2$  Lines

It is interesting to compare the small signal data obtained in these tests with those obtained on other programs. The most relevant comparison is with the small signal gain measurements obtained on the HWL-2A device which has the same nozzle configuration as ALPHA-VM but shorter gain length and hence fewer nozzle banks. This comparison is shown in plots in Figures 9.5-7 and 9.5-8. The agreement is very good considering gain is measured on two different devices with somewhat different measuring techniques. Edge effects between the two devices could easily explain the differences. Comparison between other small-signal-gain data taken on VM is difficult because that data was taken in the opposite direction (vertical) and scanned from the center of a base region to the center of a nozzle region. Measurements taken these two ways did not compare well on either HWL-2A or VM. It is speculated that this could be due to fluid dynamic effects which are not well understood. The objective of this program was not to obtain absolute small-signal-gain numbers but to measure the gain variation over the aperture of the device to aid in design of amplifier experiments planned for the ALPHA-VM device.

## 9.6 REFERENCES

- 9-1. A. W. Angelbeck et al., "Investigation of Master Oscillator Power Amplifier Systems for Chemical Lasers," AFWL-TR-74-256, September 1975.
- 9-2. L. Sentman, R. Waldo, P. Theodoropoulos, T. Nguyen, and D. Carroll, "HF Chemical Laser Amplifier Performance," AIAA 89-1906, Presented at AIAA 20th Fluid Dynamics, Plasma Dynamics and Laser Conference, Buffalo, New York, June 1989.
- 9-3. L. H. Sentman, P. Theodoropoulos, R. Waldo, T. Nguyen and R. Snipes, "An Experimental Study of CW HF Chemical Laser Amplifier Performance and Zero Power Gain," AAE 87-6, UILU ENG 87-0506, August 1987.
- 9-4. L. H. Sentman, R. E. Waldo, T. X. Nguyen, and P. T. Theodoropoulos, "CW HF Chemical Lasser Oscillator/Amplifier Performance in a MOPA Configuration," Technical Report AAE TR 88-7, UILU ENG 88-0507, July 1988.
- 9-5. D. L. Bullock, M. M. Valley, and R. S. Lipkis, "Advanced Chemical Laser Optics Study," AFWL Contract F29601-79-C-0022, July 1982.

## 10. ABSORPTION EXPERIMENT

### 10.1 MOTIVATION AND REQUIREMENTS

The minimum flow velocity of Xe in the flowing-gas SBS cell is established by the desire to avoid thermal blooming of the pump beam. This blooming results from absorption of incident radiation by the gas, and the CWCS experiment suggests the following relationship between the minimum flow speed,  $U$ , and the absorption coefficient,  $\alpha$ :

$$\frac{U}{\alpha} > 5.0 \times 10^7 \text{ cm}^2/\text{s}$$

The objective of this experiment, therefore, is to measure the absorption coefficient of research-grade Xe under conditions that simulate those expected in the APACHE SBS phase-conjugation system. Furthermore, it is desired to go beyond this objective and to measure the absorption coefficient of research-grade Xe after purification with commercially available purifiers.

The requirements for this experiment are given in Table 10-1. The conjugating medium is Xe at 40 atm of pressure at room temperature, and the wavelength of the incident CW radiation is chosen from the  $P_1$  and  $P_2$  bands of HF. The measurement technique should be able to resolve the absorption coefficient to about  $1.0 \times 10^{-5} \text{ cm}^{-1}$ .

### 10.2 EXPERIMENT APPROACH

The requirement to measure an absorption coefficient at the  $10^{-5} \text{ cm}^{-1}$  level indicates the need for a sensitive measuring technique. The two candidate methods are direct optical absorption and photo-acoustic spectroscopy. The experimental techniques are described below.

#### 10.2.1 Optical Attenuation Measurement

A direct optical attenuation measurement with an ability to measure an absorption coefficient as low as  $10^{-5} \text{ cm}^{-1}$  can be made using a differential optical technique. A diagram illustrating the technique is shown in Figure 10-1. An HF miniprobe laser is used to provide the incident radiation. It

Table 10-1. Requirements for Xe HF Absorption Experiment

Parameter	Requirement
Medium	Xe at 40 atm pressure, room temperature
Absorption coefficient resolution	$1.0 \times 10^{-5} \text{ cm}^{-1}$ (5 m/s Xe flow speed)
Baseline cleanliness	Use manufacturer specifications for research-grade Xe
HF lasing wavelengths	$P_1(5)$ , $P_1(6)$ , $P_1(7)$ , $P_1(8)$ , $P_2(5)$ , $P_2(6)$ , $P_2(7)$ , $P_2(8)$

hits a reflective chopper which alternates sending signals to a measurement path and a reference path. The measurement path contains a 155-cm-long high-pressure Xe cell. The reference path includes an attenuation wheel. At the beginning of a test, the attenuation of light through the empty test cell is balanced by adjusting the attenuation in the reference path. The change in this balance that occurs after gas is introduced into the cell indicates the absorption due to the gas. Signals from both paths are monitored by the same detector. A lock-in amplifier at the detector measures the difference between signal and reference paths. The measurement accuracy is limited by the cell length and is  $1 \times 10^{-5} \text{ cm}^{-1}$  in the 155-m cell.

#### 10.2.2 Photo-Acoustic Measurement

A second sensitive measuring technique is photo-acoustic spectroscopy (PAS). In PAS, a sample of the gas to be tested is placed in an isolated cell, and amplitude-modulated radiation at the wavelength of interest is passed through the cell. Any energy absorbed by the gas is released in the form of heat as the molecules relax, and this periodic heat release produces a fluctuating pressure signal inside the cell. This signal is picked up by a microphone located in the cell and fed to the input of a lock-in amplifier that is driven at the chopping frequency of the radiation. This synchronous detection is the reason for the high sensitivity of the method.



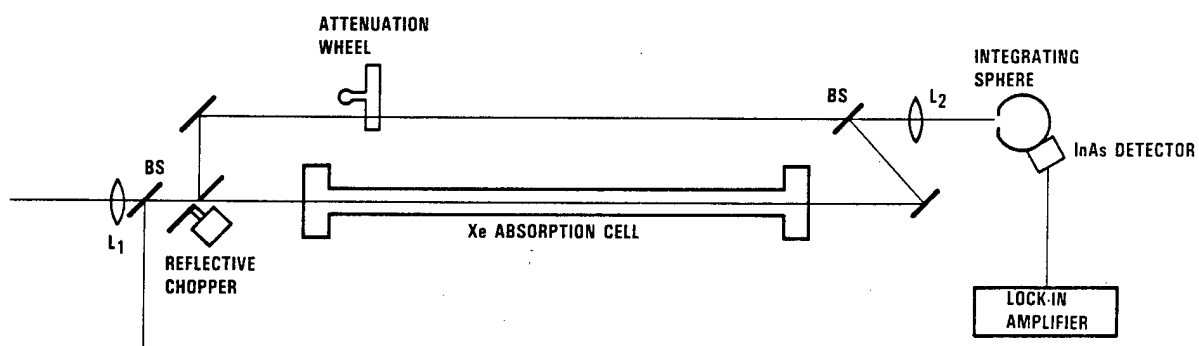


Figure 10-1. Optical Attenuation Measurement Layout

PAS is usually employed at operating pressures of near 1 atm. However, the sensitive microphones used at this pressure could not be used for a measurement at 40 atm. Consequently, a piezoelectric transducer was used in place of a standard microphone. It was subsequently found that the response of this transducer limited the sensitivity of this measurement to  $5 \times 10^{-4} \text{ cm}^{-1}$ .

A schematic of the test setup is given in Figure 10-2. A Helios Mini-Probe laser is used as the CW HF source. A PAR Model 192 chopper is used to modulate the laser light, which is then focused down into either the PAS cell or the long, optical attenuation cell. Both cells are fitted with  $\text{CaF}_2$  windows, and beamsplitters are used to monitor the laser power entering the cells; the power transmitted through the optical cell is also monitored. A PCB Model 106B50 piezoelectric transducer is used as the microphone, and a PAR Model 5210 dual-phase lock-in amplifier is used to track the microphone signal.

#### 10.2.3 Gas Handling

The gas-handling system used in the absorption experiment is illustrated in Figure 10-3. The system can admit test gases from a variety of sources, and provision has been made to mix the gases, if necessary, in a separate tank prior to transferring them into the test cells. In addition, the system can be evacuated when required.

### 10.3 EXPERIMENTAL RESULTS

Absorption measurements were made using both the optical and photo-acoustic techniques. Measurements were made on only the  $P_2(7)$  and  $P_2(8)$  lines with the optical technique. The results are given in Table 10-2. The test matrix was limited by lack of a variable attenuator for other HF wavelengths. The relatively small values obtained are encouraging, but the limited size of the data set indicates that more testing should be done to firmly establish the absorption values. Data obtained with PAS indicated that the absorption coefficients for all lines were lower than the measurement sensitivity of the technique.

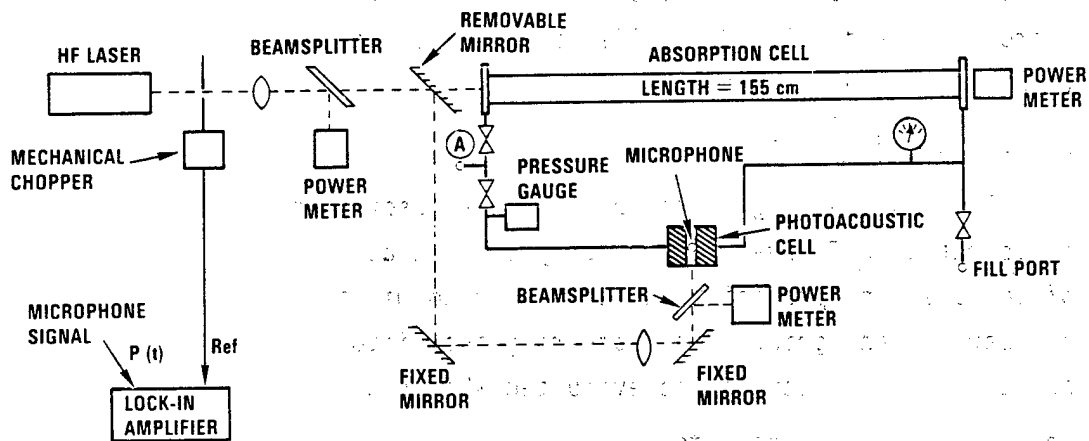


Figure 10-2. PAS Experiment Optical Layout

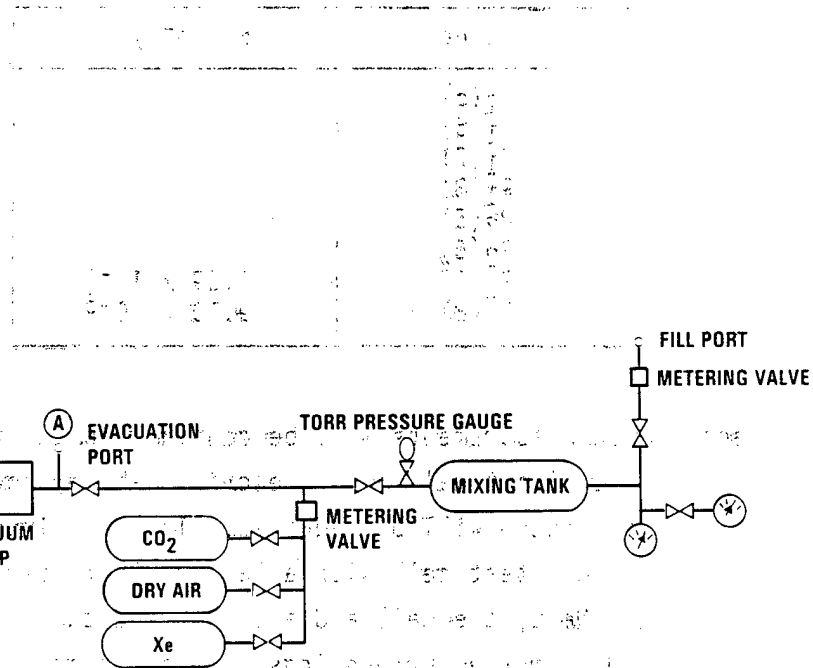


Figure 10-3. Gas-Handling System for PAS Experiment

Table 10-2. Xe HF Absorption Coefficients  
at 40 atm, Differential  
Optical Method

Line	$\alpha$ (cm <sup>-1</sup> )
P <sub>1</sub> (5)	2.59 x 10 <sup>-5</sup> 9.10 x 10 <sup>-5</sup>
P <sub>1</sub> (6)	
P <sub>1</sub> (7)	
P <sub>1</sub> (8)	
P <sub>2</sub> (5)	
P <sub>2</sub> (6)	
P <sub>2</sub> (7)	
P <sub>2</sub> (8)	

The absorption measurements will be continued under the APEX program using the differential optical method described above; however, a number of improvements to the setup will be required. The most important of these changes is to obtain a test cell with a larger clear aperture than the one presently in use. Next, the cell and all attached tubing should be thermally isolated from the surroundings. In addition, it is desired to have an active means of controlling the cell temperature. These steps are necessary to avoid scattering and drift of the beam due to random thermal gradients inside the cell. It will also be necessary to tune up the HF laser to improve its long-term stability (power, pointing, and transverse mode structure). The intensity profile of the beam transmitted through the cell should be monitored in real time to verify the transverse mode structure and to reveal any aberrations imposed on the beam by the gas in the cell. Finally, the IR detector that senses the balance between the reference and test beams should be replaced with one that has uniform response over the sensitive area.